Isogeometric Analysis of Cahn-Hilliard phase field-based Binary-Fluid-Structure Interaction based on an ALE variational formulation

Dissertation

zur Erlangung des akademischen Grades
Doctor rerum naturalium
(Dr. rer. nat.)

Der Fakultät für Mathematik
der Technischen Universität Dortmund
vorgelegt von

BABAK SAYYID HOSSEINI

August 2020

Dissertation

Isogeometric Analysis of Cahn-Hilliard phase field-based Binary-Fluid-Structure Interaction based on an ALE variational formulation

Fakultät für Mathematik
Technische Universität Dortmund

Mitglieder der Prüfungskommission:

Prof. Dr. Stefan Turek (Betreuer, Erstgutachter, Prüfer)
Prof. Dr. Matthias Möller (Betreuer, Zweitgutachter, Prüfer)
Prof. Dr. Joachim Stöckler (Prüfer)
Prof. Dr. Lorenz Schwachhöfer (Vorsitzender)

Tag der mündlichen Prüfung: 24.02.2021

To my family

Acknowledgments

I want to express my sincere gratitude to Prof. Dr. Stefan Turek and Prof. Dr. Matthias Möller who jointly supervised my dissertation.

I want to thank Prof. Dr. Stefan Turek for accepting me as a PhD student and giving me the trust and academic freedom to conduct research in those areas of his overall research scope that were particularly exciting for me. The trust and confidence that he has placed in me by giving me this opportunity is highly appreciated, given that I had completed my master's degree many years ago and was tied to the industrial world as of applying for a PhD program. In fact, this doctorate has been completed under the conditions of continuing to work half of the time in the industry. I want to thank Prof. Dr. Stefan Turek for making this possible despite these odds and also for making it possible for me to participate in international academic conferences that were always inspiring to me.

I also want to thank my second and remote supervisor Prof. Dr. Matthias Möller for accepting to co-supervise my work and for introducing me to the topic Isogeometric Analysis. It is highly appreciated that he kept supervising me despite the distance-related difficulties that arise with moving to a new university. I profited very much from the various very fruitful academic discussions I had with Prof. Dr. Matthias Möller and have learned a lot from him. Moreover, I want to thank him for inviting me to give a talk at his new working place and for constantly encouraging me to participate in relevant conferences. I am very grateful for the confidence and trust that he has always placed in me.

My thanks go to both supervisors for an always friendly and respectful working atmosphere. They have helped me to become an independent researcher, and if it weren't for them, this work would not be possible, at least not in this form.

Beside my supervisors, I want to send special thanks to Prof. Dr. Sebastian Aland for the very delightful discussions we had over many years. I especially appreciate his invitation to Dresden and the time he has invested in Dresden for our deeply technical discussion sessions and hope to be able to compensate it.

I want to also thank everyone at LS III (Math, TU Dortmund) for the very friendly and fruitful atmosphere you all have contributed to. Special thanks go to Christian Palmes, Masoud Nickaeen, Evren Bayraktar, Otto Mierka, Justus Klipstein, Steffen Basting, Michael Köster, Sven Buijssen, Omid Ahmadi, Amin Safi, and Abderrahim Ouazzi for the very nice discussions and precious moments I had with you over these years.

My deep gratitude goes to everyone that is or has been part of my life and who has struggled with me and has shown love to me during the struggle of conducting this work. This also includes my very appreciated colleague Frank Weller who always had my back and showed me what perfection is.

This work would have not been possible without the self-sacrificing support of my beloved family. Thank you very much: Zohre, Morteza, Nushin, Pete, Pari, and Till.

Contents

Chapter 1

Introduction

1.1 Background, motivation and objectives

The fascinating phenomenon of *Elasto-capillarity*[1] refers to the ability of capillary forces or surface tensions to deform elastic solids through a complex interplay between the energy of the surfaces (interfaces) and the elastic strain energy in the solid bulk. The described configuration – exemplary depicted in Figure 1.1 – gives rise to a three-phase system featuring a fluid-fluid interface (for instance the interface of a liquid and an ambient fluid such as air) and two additional interfaces separating the solid from the first and second fluids, respectively. Considering the effects of a fluid on human-built structures to be generally given by its weight (e.g. hydrostatic pressure) or its flow (e.g. inertia of a fluid in motion yielding drag and lift forces), the ever increasing interest in the fabrication of micro-devices raises attention to another type of interaction of fluids with human-built structures – the surface tension force. Albeit negligible at macroscopic scales, capillary forces become dominant at submillimetric scales. At small scales, that is mm to nm scale, the interaction of multiple fluids and a solid tends to become increasingly dominated by capillary forces as the length L of a structure keeps decreasing. With reference to scaling laws, capillary forces are proportional to L, whereas elastic forces or pressure forces (e.g. wind drag) are proportional to L^2, and volume

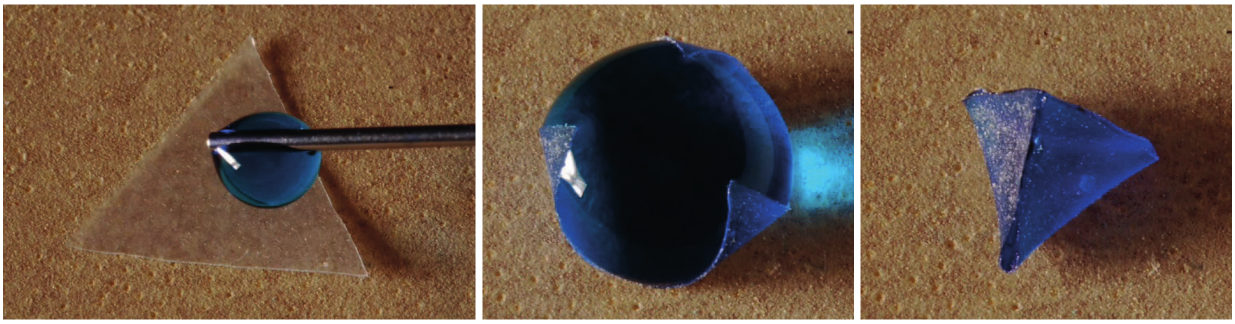

Figure 1.1: Capillary origami: A droplet deposited on a thin elastic sheet may bend the sheet and ultimately lead to the complete wrapping of the droplet. The image is reprinted from [121] with permission.

---

[1] Notion may be represented in lower case letters in the sequel.

forces scale proportionally to L^3 [126]. Therefore, downscaling a given structure implies a much faster decay of pressure and body forces in comparison to capillary forces, rendering the latter dominant after a certain size threshold. Denoting a fluid's surface tension and mass density with γ and ρ , respectively, and the gravitational acceleration with g, in terms of length scale, capillarity becomes dominant over gravity below the capillary length $l_c = \sqrt{\gamma/(\rho g)}$. Elasto-capillarity related phenomena are ubiquitous in nature as well as in high-tech (micro-/nanodevice manufacturing) industry. Examples for capillary interactions include the cohesion of sandcastles, the bending of slender structures that induces the bundling of fiber arrays (e.g. assembly of wet hair into bundles), and thin sheets that may partially wrap liquid droplets (e.g. capillary origami as depicted in Figure 1.1). Another example with biophysical background is the complete or partial collapse of pulmonary alveoli due to capillary forces with possibly fatal consequences. Elasto-capillarity is also of high relevance in high-tech micro and nano technologies. In fact, small scale devices such as e.g. microelectromechanical systems exhibit slender internal structures that are often created by wet lithography. This process involves selectively etching a layer of photosensitive resin into a given micostructure and rinsing the removed material in a solvent. During the drying process, capillary bridges may attract, deform or break slender flexible parts leading to severe damage ("stiction" phenomenon in design of micostructures) [126].

The motivation and at the same time the objective of the work presented in this thesis is to develop a computational model and simulation technique capable of capturing the complex physics behind the intriguing phenomena of Elasto-capillarity. A sophisticated enough numerical method may provide further insights in its complex dynamics and eventually leverage better designs of submillimetric technology. The significance of such numerical methods is given by the fact that it often turns out to be very difficult and expensive to perform corresponding experimental measurements. On that note we also want to point out that certain compounds such as bicontinuous interfacially jammed emulsion gels[2] for instance, even have been first proposed on the basis of numerical simulations and only then verified experimentally [3]. As another source of motivation to pursue this work we want to mention the tremendous and therefore challenging complexity posed by the multiphysics nature of the underlying problem, dubbed *Elasto-Capillary Fluid-Structure Interaction*[1] or *Binary-Fluid-Structure Interaction*[1] (BFSI).

One of the components of BFSI is *Multiphase Flow*[1] comprising the flow of materials with different phases (e.g. gas, liquid, etc.), or the flow of materials with different chemical properties in the same phase, such as oil and water. In this light, Two-phase Flow[1] problems – to whom we also refer to as Binary-fluid Flow[1] problems – either represent immiscible dual-species flow problems, or dual-phase single-species flow problems. In two-phase flows, the fluids are segregated by a very thin interfacial region where surface tension effects and mass transfer due to chemical reactions may appear. Multiphase flows are ubiquitous in nature and industrial systems and are quite challenging from the point of view of mathematical modeling and simulation due to the complex physical interaction between the involved fluids including topological changes and the complexity of having to deal with unknown moving fluid-fluid interfaces. As for methodologies to address the moving interface problem, there are various methods such as for instance the volume-of-fluid, front tracking, immersed boundary, level-set and phase field methods (cf. [78, 135]). While the class of Lagrangian interface motion techniques track individual boundary points, the interface is implicitly represented by an indicator function in interface motion techniques of Eulerian type, such as the volume-of-fluid or level-set methods for instance. The phase field method – also known as the diffuse interface method – is based on models of fluid free energy and has a solid theoret-

---

[2] Mixture of two or more usually immiscible liquids whose segregation is prevented by an additional emulsifier. The latter may for instance be a layer of colloid particles absorbed into the fluid-fluid interface.

ical foundation in thermodynamics and statistical mechanics. It may therefore be perceived as a physically motivated extension of the level-set or volume-of-fluid methods. It differs from other Eulerian interface motion techniques by virtue of the fact that it does not feature a sharp, but a diffuse interface of finite width whose dynamics are governed by the joint minimization of a double well chemical energy and a gradient-squared surface energy – both being constituents of the fluid free energy. In the phase field framework, the interface is modeled by a function $\varphi(x, t)$ which represents the concentration of the fluids. The function $\varphi(x, t)$, also referred to as the order parameter, or the phase field, attains a distinct constant value in each phase and rapidly, but smoothly, changes in the interface region between the phases. For a binary fluid, a usual assumption is that φ takes values between -1 and 1, or 0 and 1. The relaxation of the order parameter is driven by local minimization of the fluid free energy subject to the phase field conservation. As a result, complex interface dynamics such as coalescence or segregation can be captured without any special procedures [13, 142]. Diffuse interface models allow the modeling of interfacial forces as continuum forces with the effect that delta-function forces and discontinuities at the interface are smoothed by smearing them over thin yet numerically resolvable layers. Moreover, they describe the surface tension as the excess free energy per unit surface area concentrated at the interface. Particularly for two-phase flows, diffuse interface models have gained a lot of attention due to their ability to easily handle moving contact lines and topological transitions without any need for reinitialization or advective stabilization. At this point we recall our main objective of developing a numerical simulation model that is well suited for binary-fluid-structure interaction. The first call to be made to this end is the careful selection of a fluid-fluid interface motion technique after weighing up the advantages and disadvantages of the various techniques available. The solid physical background of the (diffuse interface) phase field method, its approach to handle interfacial forces, and its ability to easily handle topological transitions like droplet coalescence or break-up led us to the decision to adopt a phase field model in this work. More specifically, we use the fourth-order parabolic Cahn-Hilliard equation(s) describing the spinodal decomposition of a two-component mixture. It requires the specification of a so-called mobility coefficient and a diffuse interface width – both turning out to be non-trivial and therefore tunable parameters. In particular, the answer to the question how to select the diffuse interface thickness is non-obvious. In fact, given an actually measured interface thickness of the order $10^{-10}\,\mathrm{m}$ and other problem length scales typically multiple orders of magnitude larger in size, numerical simulations adopting the phase field model face the outrageous difficulty of how to deal with this disparity in scales. However, since large scale disparities often render computations at this level of resolution practically not feasible, the common practice is to inflate the interface thickness to the smallest computationally affordable value. Unfortunately, this is accompanied by numerical complications. To give an example, a poorly resolved interface may violate the boundedness of the phase field function to the value range given by the pure phase indicators [166] and consequently deteriorate the model's stability. For this issue we refer to the above mentioned reference – a research analyzing the spontaneous shrinkage of drops in phase field simulations. Moreover, interfaces too large a size (thickness) were shown [4–6] to introduce additional diffusion into the problem, making adequate counteractive measures possibly necessary. The commitment to a phase field-based interface motion technique immediately gives rise to the next question, namely how to couple the corresponding equations (e.g. Cahn-Hilliard equations) to the (incompressible) flow equations (Navier-Stokes equations), or to put it differently, which of the many Navier-Stokes-Cahn-Hilliard (NSCH) models to use. These models differ from each other by a group of quite diverse criteria, one of them being e.g. the treatment of the density, that is, considering it constant or variable. Moreover, not all models are based on a divergence-free velocity field and the modeling of extra contributions of additional forces to the stress tensor such as e.g. the surface tension induced capillary forces is quite varied across the models. While for some models no energy inequalities are known, others are shown to admit an energy law and to be thermodynamically consistent. For the latter to hold, some of the affected models are extended by additional terms. Each of these models has its own advantages and disadvantages in terms of suitability for particular flow scenarios, physical consistency and implementation simplicity. That said, the identification of a reasonable model in the context of this work turned up to be a time consuming and tedious process. This is founded on the fact that there are quite a number of different models at one's disposal, each having a distinct set of traits determining its overall suitability. As an additional reason, we identify the lack of a consolidated inventory with emphasis on the most essential features and shortcomings of each model. All the questions raised and issues presented so far in association with two-phase flow will be dealt with in a dedicated chapter of this work. We will present a solution therein that fits well in the framework of BFSI.

Another component of BFSI is *Fluid-Structure Interaction*[1] (FSI) referring to the interaction of a deformable solid with fluid flow. FSI poses already by itself a multiphysics problem due to the mutual dependence between the fluid and solid parts of the continuum, and therefore requires the combination of fluid and structural mechanics. At the contact interface, the solid experiences forces exerted by the fluid stresses – forces that can significantly affect the solid's motion and deformation. The deformed solid and its motion in turn imply a modified fluid flow domain with obvious causal relationship with changes to the fluid's velocity and pressure and therefore its stress. This completes the dependency cycle. FSI problems are omnipresent in nature – just to name a few scenarios, we refer to the inflation of a balloon, the motion of a tree subject to wind, the fluttering of aircraft wings, the interaction of blood and heart valves and wind induced deflection of wind-turbine blades. The aspect of omnipresency in nature and the desire to perform simulations "as realistic as it gets", render FSI a very relevant, attractive and active field of research. As far as theoretical considerations, the application of analytical methods to non-toy fluid flow and structure deformation problems is already quite limited, let alone FSI problems. This is due to the time-dependent and inherently nonlinear nature of FSI. That being said, in recent decades a significant amount of attention has been put to the development of *computational* FSI methods with focus on robustness, efficiency and applicability to geometrically complex domains in 3D. There exist different FSI solution algorithms falling into the categories of monolithic or partitioned approaches, each coming along with its own traits in terms of robustness, complexity and applicability. Partitioned FSI techniques often face instabilities when the solid mass density ρ_s approaches the fluid mass density ρ_f (Added mass effect). Besides, for the convergence of a partitioned FSI problem, typically a few rounds of iteration are necessary, where in each round the respective problems are solved one at a time. These deficiencies are avoided by an implicit and monolithic solution approach that takes the full fluid-structure interaction problem as one coupled unity, without partitioning. When modeling the coupled dynamics of FSI, one is additionally confronted with the dilemma that the fluid model is naturally based on an Eulerian perspective while it is very natural to express the solid problem in Lagrangian formulation. With regard to the achievement of the objectives of this work, at this point, the question arises which approach to take from here. Given the fact that each approach has its individual flaws and hassles, it turns out to be non-obvious how to answer the question asked. We address in this work the above presented FSI affiliated questions and dilemmas and present a solution that resonates well with binary-fluid-structure interaction. Our approach is also well suited for those FSI problems, where both the fluid and the solid are allowed to have identical mass densities. This occurs often in biomechanical contexts such as in the case of blood flow inside an artery, where it holds $\rho_f/\rho_s \approx 1$. In the sense of a short prospect, we want to mention at this point that we have chosen to work with the very robust and widely applicable monolithic approach that comes at the cost of a high implementation complexity. The monolithic approach we take, uses a fully coupled Arbitrary Lagrangian-Eulerian (ALE) variational formulation of the whole FSI problem (cf. [84])

and applies a Galerkin method for the discretization of the partial differential equations involved. This approach solves the difficulty of a common variational description and facilitates a consistent Galerkin discretization of the FSI problem.

In the above two paragraphs we have shed light on each of the two necessary components of BFSI and the challenging problems associated with each one of them. Binary-fluid-structure interaction, however, means nothing less than considering the highly complex interaction of two immiscible (and incompressible) fluids with both, each other, and an elastic solid. While multiphase flow problems and classical (single fluid) fluid-structure interaction problems have seen a vast amount of research – as of conducting the research for this work and to the best of author's knowledge – only a few published articles exist on the computational investigation of the complex mechanical interaction of multiple fluids with deformable solids. We consider the article [28] published by J. Bueno et al. as the first and therefore pioneering work in this field. The authors employ a strongly coupled algorithm for the solution of the Elasto-capillarity problem. Unfortunately it remained not exactly clear to us what "strongly coupled" is supposed to mean in the context of this article. This notion is for instance often used in the context of partitioned FSI algorithms and represents repetitively solving the fluid and solid subproblems after each other, until the difference of the field values (displacement, velocity, etc.) of the fluid and solid parts of the domain fall below a given bound along the fluid-solid interface. If this is the modus operandi of the above article, then the NSCH equations are solved altogether, but separated from the equations of Elastodynamics. This would then correspond to a partitioned FSI approach that is prone to instability issues when the fluid mass densities approach each other. Bueno et al. also published the following articles in the context of interaction of complex fluids with solids: [26, 27]. The next articles [151, 152] on computational investigations of Elasto-capillarity published by the research group around E. H. van Brummelen et al. also take a partitioned FSI approach as described above and solve the NSCH equations separated from the solid equations. The non-robustness of this FSI approach may be concluded from the data published in these articles. However, we want to mention that according to a presentation held at the Isogeometric Analysis (IGA) 2019 conference, Brummelen presented – to the best of author's knowledge – a yet unpublished work on monolithic elasto-capillary FSI to circumvent the non-robustness issue. The scarcity of research on the numerical analysis of elasto-capillary fluid-structure interaction is attributed to the complexity of the endeavor to combine two fundamentally different problems (fluid flow, structure deformation) with the added complexity of having to cope with a dual-species fluid. To put it in a colleague's words: "binary-fluid-structure interaction is tricky". It inherits all the complexities inherent to the two-phase flow and fluid-structure interaction subproblems and mixes in its very own characteristic traits – features like *fluid-solid surface tension*[3], *contact line motion*[4], and *dynamic wetting*[5]. Fortunately, the usage of phase field models endowed with appropriate boundary conditions is a great relief in this matter, as they come up with an intrinsic description of wetting on solid surfaces. This trait pictures them as ideally suited for the modeling and simulation of BFSI problems and was one of the reasons why we made the call to adopt a phase field model. In terms of methodology the approach pursued in this work differs from those of the above cited previous works. More specifically, we start with solving the Cahn-Hilliard phase field equations using the available flow velocity field. Next, we monolithically solve the fluid-structure interaction problem using the available phase field values. The motivation for this approach is twofold: First, following a monolithic FSI approach based on an Arbitrary

---

[3] In binary-fluid-structure interaction one considers three interfaces, the fluid-fluid interface and the interfaces between each of the involved fluids and the solid. Each of these three interfaces is endowed with its own surface tension.

[4] The three-phases in binary-fluid-structure interaction meet at a contact line.

[5] Wetting refers to the study of the behavior (spreading) of a liquid that is in contact with the surface of a solid (or another liquid), cf. Section 6.2.

Lagrangian-Eulerian formulation renders almost all terms in the Navier-Stokes equations nonlinear and induces additional geometrical nonlinearities that express themselves through nonlinear couplings of the displacement, velocity, and pressure variables. This makes the "pen and paper" derivation of the Fréchet derivative (Jacobian) of the respective partial differential operator not exactly easy. Second, a large number of coupled field variables negatively impacts the bandwidth and fill-in state of the system matrices obtained from the discretization process. These two reasons led us to the idea not to worsen the above mentioned issues by mixing in two more field variables (phase field, chemical potential) from the phase field model. That said, we consider our approach as "quasi-"monolithic as the phase field equations are solved separately from the monolithically solved variable fluid density and viscosity FSI equations.

We consistently apply the relatively novel technique of Isogeometric Analysis for the spatial discretization of all partial differential equations treated in this work. Isogeometric Analysis can be considered as a generalization of standard Finite Element Analysis (FEA) with the addition of unique features such as the ability to perform computations on exact representation of complex geometries, the usage of "spline"-type basis functions (e.g. B-spline, NURBS, etc.), and the ability to easily allow the setup of approximation spaces with high and possibly varying continuity across the computational domain. All numerical results presented in this work are obtained from an Isogeometric Finite Element Analysis kernel that the author has developed from scratch in the context of this thesis.

1.2 Outline of the thesis

The complexity of the multiphysics problem tackled in this work made it necessary to dissect the overall problem into several subproblems that are treated in corresponding thematic building blocks (cf. Figure 1.2). Our partition provides the following major blocks

(i) Single-phase flow (*),

(ii) Two-phase flow (**),

(iii) Fluid-Structure Interaction (**),

(iv) Binary-Fluid-Structure Interaction (***),

where the number of asterisks gives a rough idea about the level of complexity inherent in the respective subproblems. While in terms of the conceptual design of this thesis it was straight forward to identify the above blocks, it turned up to be very difficult to identify a level of presentation detail that on the one hand does justice to the complexity of each subproblem, and on the other hand respects the bounds or scope of such a thesis. This is definitely attributed to the large number of components that only together complete the big picture. Considering the fact that numerical simulation of two-phase flow or fluid-structure interaction problems alone contain enough complexity for a PhD thesis, it was challenging to present just the right amount of content in each subproblem chapter in the spirit of the mentioned constraints. Excluding the present introductory chapter, the outline of this thesis is as follows:

Chapter 2 is devoted to a brief review of continuum mechanics, conservation equations and the Arbitrary-Lagrangian-Eulerian (ALE) concept. The motivation for this is as follows: All physical problems considered in this work are based on continuum mechanical models. Moreover, the partial differential equations considered in different chapters of this work are based on conservation

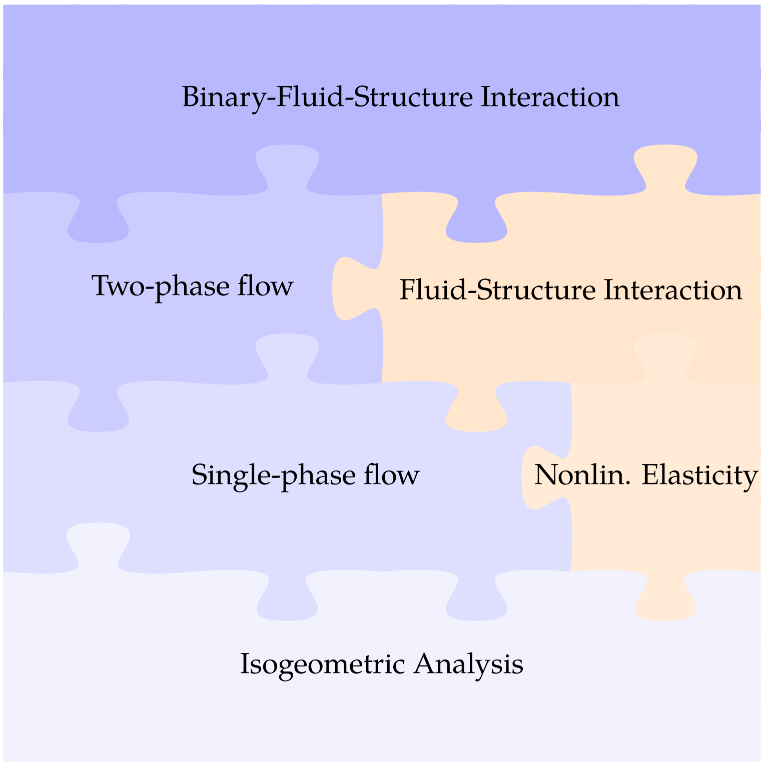

Figure 1.2: Structure of thematic building blocks with vertical dependency structure.

equations that we present in a consolidated manner in this chapter. The ALE concept is reviewed as it is a key ingredient in our fluid-structure interaction as well as binary-fluid-structure interaction models.

In Chapter 3 we lay the foundation for the treatment of the fluid-related subproblems of binary-fluid-structure interaction. We apply Isogeometric Analysis to the steady and transient Navier-Stokes equations and numerically solve a series of benchmark problems for the validation of the component in charge with single-phase fluid flow. This chapter embeds a brief overview over a few selected topics of Isogeometric Analysis. The reason we did not devote a separate chapter to Isogeometric Analysis and have rather opted for a concise embedded section is motivated by the circumstance that Isogeometric Analysis is a vast topic and we considered it enough to just present a selected set of its features relevant to this work.

Chapter 4 is devoted to the two-phase flow component of the binary-fluid-structure interaction problem. The two-phase flow model we employ is based on the Cahn-Hilliard phase field model that is also addressed in this chapter.

In Chapter 5 we present our monolithic fluid-structure interaction model that is restricted to one (Newtonian) fluid. We dissect the fluid-structure interaction problem and discuss the standalone solid deformation problem (Elastostatics, Elastodynamics) before moving on to the complex interaction of solids and fluids. With the author's background being in fluid mechanics, this chapter has been designed with the objective to provide that type and amount of information that a reader with a similar background in structural mechanics can understand and reproduce the presented work.

Chapter 6 ultimately integrates all previous results and presents a "quasi"-monolithic model for binary-fluid-structure interaction. It heavily draws on the detailed descriptions provided in the FSI Chapter 5.

1.2.1 Already published contributions

This thesis contains results that are already published in the following refereed publications and for which Babak Sayyid Hosseini has – as the main author – provided decisive contributions:

- [81] B. S. Hosseini, M. Möller and S. Turek. Isogeometric Analysis of the Navier-Stokes equations with Taylor-Hood B-spline elements. Applied Mathematics and Computation, 267:264-281, 2015
- [82] B. S. Hosseini, S. Turek, M. Möller and C. Palmes. Isogeometric Analysis of the Navier–Stokes–Cahn–Hilliard equations with application to incompressible two-phase flows. Journal of Computational Physics, 348:171-194, 2017
- [80] B. S. Hosseini and M. Möller. Phase Field–Based Incompressible Two–Component Liquid Flow Simulation. Numerical Methods for Flows. Lecture Notes in Computational Science and Engineering, 132:165-176, Springer, 2020

Moreover, the author of this thesis has additionally collaborated in the creation of the following refereed publication:

- [114] C. Palmes, B. Funke and B. S. Hosseini. Nonparametric low-frequency Lévy copula estimation in a general framework. Journal of Nonparametric Statistics, 30(3):523-555, 2018

Chapter 2

Continuum mechanics and conservation equations

A brief introduction into continuum mechanics based on [33, 47, 73, 98, 108] is in order as this thesis covers multiphysics problems that are based on the description of matter as a continuum. This chapter is not intended to be comprehensive. Our focus lies on the ingredients necessary for the isogeometric finite element formulation of fluid and solid problems and their combination. For a comprehensive introduction we refer to the above listed references and the references therein.

Continuum theory is known as the theory that has the objective to describe relationships among phenomena neglecting the structure of material on very small scales (e.g. molecular level[6]). While a description of the dynamics of microstructures including molecules, atoms and subatomic structures is possible with fundamental physical laws, their realization often remains not feasible, for a huge number of individual particles has to be tracked. For instance, the tracking of more than 10^{25} molecules in a liter of water is considered daunting, let alone larger fluid bodies. Matter is regarded in continuum theory as indefinitely divisible and one accepts the concept of an infinitesimal material volume, referred to as a particle in the continuum. Such a particle has neighboring particles in the continuum and the totality of the infinitesimal volumes form a body $B \subset \mathcal{E}$, where $\mathcal{E}$ denotes the Euclidean space. So, instead of tracking every single particle, the continuum approach considers averaged properties of the complete volume in the form of local density distributions. For instance, $\boldsymbol{v}(\boldsymbol{x}, t)$, denotes the average velocity of whatever particle may be in position $\boldsymbol{x}$ at a given time t.

The justification of continuum theory as a suitable model depends on the given situation. It adequately describes the behavior of real materials in many circumstances and more than 200 years of experience have justified this theory in wide variety of situations. However, its suitability is subject to some restrictions. For instance, for the propagation of waves of extremely small wavelength, it yields results that do not reflect experimental observations [98].

Continuum mechanics deals with the study of materials response to loading conditions. The study comprises motion and deformation (also known as kinematics), stress, and fundamental physical laws (balance laws) governing the motion of a continuum. These topics are discussed in the following.

---

[6] Molecular-statistical theory is to be considered for very small scales.

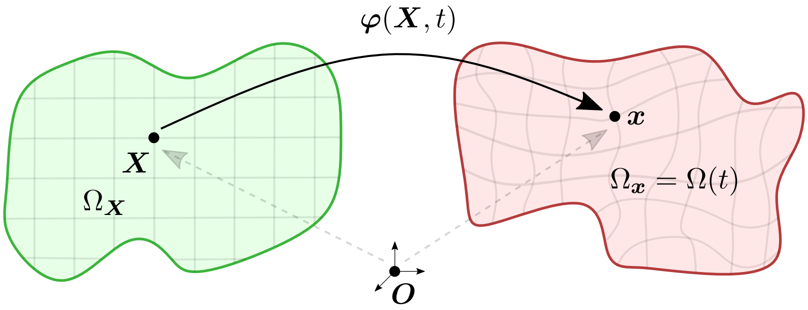

Figure 2.1: The initial ($\Omega_{\boldsymbol{X}}$) and current ($\Omega_{\boldsymbol{x}}$) domains in the Lagrangian description of motion.

2.1 Kinematics and deformation gradient

Kinematics is the study of motion and deformation. Continuum mechanics considers the concept of two domains (reference frames): the *initial* (*and undeformed*) *material domain* $\Omega_{\boldsymbol{X}} \subset \mathbb{R}^d$ also known as the *reference domain* and comprised of material particle positions $\boldsymbol{X}$, and the *current* (*and deformed*) *spatial domain* $\Omega_{\boldsymbol{x}}$ encompassing spatial points $\boldsymbol{x}$ at time t. For the depiction of these domains, we refer to Figure 2.1. Note that the depicted points $\boldsymbol{X}$ and $\boldsymbol{x}$ may just as well be described with corresponding (position) vectors $\boldsymbol{X}$ and $\boldsymbol{x}$ starting from the origin $\boldsymbol{O}$ of a global cartesian coordinate system. Therefore, in the following it proves to be illustrative to refer to *points* $(\boldsymbol{X}, \boldsymbol{x})$ or *vectors* $(\boldsymbol{X}, \boldsymbol{x})$ (displacements), depending on the circumstance we want to accentuate.

$\Omega_{\boldsymbol{X}}$ and $\Omega_{\boldsymbol{x}}$ are bounded open sets in $\mathbb{R}^d$, where d represents the spatial dimensions. In this work we consider two-dimensional problems, nevertheless for generality we set $d = 3$ and therefore $\mathcal{E} = \mathbb{R}^3$.

2.1.0.1 Lagrangian-to-Eulerian map φ

Looking at the initial (undeformed) body B being represented by the closure of the domain $\Omega_{\boldsymbol{X}}$, we are interested in its motion and deformation as it experiences forces. A *deformation* of $\overline{\Omega}_{\boldsymbol{X}}$ is a smooth enough, injective, and orientation preserving mapping

$$\begin{aligned} \varphi\colon \overline{\Omega}_{\boldsymbol{X}} \times [0,T] &\longrightarrow \overline{\Omega}_{\boldsymbol{x}} \times [0,T] \\ (\boldsymbol{X},t) &\longmapsto \varphi(\boldsymbol{X},t) = (\boldsymbol{x},t) \end{aligned} \tag{2.1}$$

which for each time instance $t \in I = [0,T]$ associates each point $\boldsymbol{X} \in \overline{\Omega}_{\boldsymbol{X}}$ of a material domain to a new position $\boldsymbol{x} \in \overline{\Omega}_{\boldsymbol{x}}$ of the spatial domain. In the above mapping φ, the spatial coordinate $\boldsymbol{x}$ depends on both, the material particle coordinate $\boldsymbol{X}$ and time t. The mapping φ defines for every fixed instant t a *configuration*[7] in the spatial domain. The physical time is measured with the same variable t in both domains. The coordinates X_1, X_2 of every point $\boldsymbol{X} \in \overline{\Omega}_{\boldsymbol{X}}$ are known as *Lagrangian coordinates* and correspondingly the coordinates x_1, x_2 of every point $\boldsymbol{x} \in \overline{\Omega}_{\boldsymbol{x}}$ are known as *Eulerian coordinates*. Therefore, the motion of a deformable body can be observed and described from either the initial configuration coordinate frame $\boldsymbol{X}$, or the current configuration coordinate frame $\boldsymbol{x}$.

Note that the deformation mapping φ can be expressed with a displacement function $\boldsymbol{u} : \overline{\Omega}_{\boldsymbol{X}} \times I \to \mathbb{R}^3$ as

$$\varphi(\boldsymbol{X},t) = \boldsymbol{X} + \boldsymbol{u}(\boldsymbol{X},t). \tag{2.2}$$

---

[7] A configuration can be seen as the embedding of a material body into some region in space.

Obviously, the initial domain $\overline{\Omega}_{\boldsymbol{X}}$ is obtained (in the absence of displacements) by the identity map $\boldsymbol{\varphi}_0 := \boldsymbol{\varphi}(\cdot, 0) = \textsc{id}(\cdot)$ and its *motion* as a series of mappings $\boldsymbol{\varphi}_t := \boldsymbol{\varphi}(\boldsymbol{X}, t)$ for $t \in I$ and non-zero displacements $\boldsymbol{u}(t)$.

The representation of the gradient of the mapping $\boldsymbol{\varphi}(\boldsymbol{X}, t)$ in matrix notation

$$\frac{\partial \boldsymbol{\varphi}}{\partial(\boldsymbol{X}, t)} = \begin{pmatrix} \frac{\partial \boldsymbol{x}}{\partial \boldsymbol{X}} & \frac{\partial \boldsymbol{x}}{\partial t} \\ \\ \frac{\partial t}{\partial \boldsymbol{X}} & \frac{\partial t}{\partial t} \end{pmatrix} = \begin{pmatrix} \frac{\partial \boldsymbol{x}}{\partial \boldsymbol{X}} & \boldsymbol{v} \\ \\ \boldsymbol{0}^T & 1 \end{pmatrix} \tag{2.3}$$

comes in handy for the deduction of the *material velocity*

$$\boldsymbol{v}(\boldsymbol{X}, t) = \frac{\partial \boldsymbol{\varphi}}{\partial t}\bigg|_{\boldsymbol{X}} = \dot{\boldsymbol{\varphi}} = \frac{\partial \boldsymbol{x}}{\partial t}\bigg|_{\boldsymbol{X}} = \frac{\partial\,(\boldsymbol{X} + \boldsymbol{u})}{\partial t}\bigg|_{\boldsymbol{X}} = \frac{\partial \boldsymbol{u}}{\partial t}\bigg|_{\boldsymbol{X}} = \dot{\boldsymbol{u}}, \tag{2.4}$$

where $\big|_{\boldsymbol{X}}$ stands for holding the material coordinate $\boldsymbol{X}$ fixed and $\frac{\partial \boldsymbol{X}}{\partial t}\Big|_{\boldsymbol{X}}$ can be seen as the temporal derivative of the identity mapping $\boldsymbol{X} = \boldsymbol{\varphi}(\boldsymbol{X}, 0) = \textsc{id}(\boldsymbol{X})$. For each point $\boldsymbol{X}$ and time instance $t > t_0$, the mapping $\boldsymbol{\varphi}$ needs to ensure $\det(\partial \boldsymbol{x}/\partial \boldsymbol{X}) > 0$ in order to impose both injectivity and orientation preservation of the reference axes.

With the definition of the material velocity $\boldsymbol{v}$ at hand, the Lagrangian time derivative of a scalar function $\alpha : \Omega_x \to \mathbb{R}$ can be expressed in terms of the Eulerian reference frame:

$$\dot{\alpha}(\boldsymbol{x}, t) = \frac{\partial \alpha(\boldsymbol{x}, t)}{\partial t}\bigg|_{\boldsymbol{X}} = \frac{\partial \alpha(\boldsymbol{\varphi}(\boldsymbol{X}, t), t)}{\partial t}\bigg|_{\boldsymbol{X}} = \frac{\partial \alpha}{\partial t}\bigg|_{\boldsymbol{x}} + \nabla_{\boldsymbol{x}}\,\alpha \cdot \frac{\partial \boldsymbol{\varphi}}{\partial t}\bigg|_{\boldsymbol{X}} = \frac{\partial \alpha}{\partial t}\bigg|_{\boldsymbol{x}} + \boldsymbol{v} \cdot \nabla_{\boldsymbol{x}}\,\alpha. \tag{2.5}$$

Remark 2.1.1. *Above, the subscript after the gradient operator ($\nabla_{(\cdot)}$) denotes the domain with respect to which the gradient is to be considered. On that note, $\nabla_{\boldsymbol{x}}$ and $\nabla_{\boldsymbol{X}}$ denote the gradient operator in the spatial and reference domains, respectively. In order to ease notation, in the following, we may omit the subscript for the spatial gradient and use the notation $\nabla(\cdot)$ instead of $\nabla_{\boldsymbol{x}}(\cdot)$. We apply these notational conventions also to the divergence operator. Moreover, in the spirit of consistent application of these notational conventions, we also define $\Omega_{\boldsymbol{x}} \equiv \Omega$ and $\Gamma_{\boldsymbol{x}} = \partial\Omega_{\boldsymbol{x}} \equiv \partial\Omega = \Gamma$.*

For the analysis of the deformation of the reference configuration to the deformed (current) configuration we fade out the dependency on time and reduce (2.1) to

$$\boldsymbol{x} = \boldsymbol{\varphi}(\boldsymbol{X}). \tag{2.6}$$

Now, the Jacobian matrix of the deformation mapping $\boldsymbol{\varphi}(\boldsymbol{X})$ yields the *Deformation gradient* $\boldsymbol{F} : \overline{\Omega}_{\boldsymbol{X}} \to \mathbb{R}^{3\times 3}$ which we denote by

$$\boldsymbol{F} := \boldsymbol{F}(\boldsymbol{X}, \boldsymbol{u}) := \frac{\partial \boldsymbol{\varphi}}{\partial \boldsymbol{X}} = \nabla_{\boldsymbol{X}} \boldsymbol{\varphi}(\boldsymbol{X}) = \frac{\partial \boldsymbol{x}}{\partial \boldsymbol{X}} = \frac{\partial(\boldsymbol{X} + \boldsymbol{u})}{\partial \boldsymbol{X}} = \frac{\partial \boldsymbol{X}}{\partial \boldsymbol{X}} + \frac{\partial \boldsymbol{u}}{\partial \boldsymbol{X}} = \boldsymbol{I} + \nabla_{\boldsymbol{X}}\,\boldsymbol{u}. \tag{2.7}$$

Above, $\boldsymbol{I}$ represents the identity tensor in $\mathbb{R}^{3\times 3}$ and $\partial \boldsymbol{u}/\partial \boldsymbol{X}$ is the *displacement gradient*. For the depiction of the action of the deformation gradient $\boldsymbol{F}$, we refer to Figure 2.2 showing material points $\boldsymbol{P}_1$ and $\boldsymbol{P}_2$ undergoing individual displacements $\boldsymbol{u}(\cdot, t)$ with the effect of arriving at positions

$$\boldsymbol{x} = \boldsymbol{X} + \boldsymbol{u}(\boldsymbol{X}, t) \tag{2.8}$$

and

$$\boldsymbol{x} + \mathrm{d}\boldsymbol{x} = \boldsymbol{X} + \mathrm{d}\boldsymbol{X} + \boldsymbol{u}(\boldsymbol{X} + \mathrm{d}\boldsymbol{X}, t), \tag{2.9}$$

respectively. With the above relations, the differential length $\mathrm{d}\boldsymbol{x}$ may be expressed as

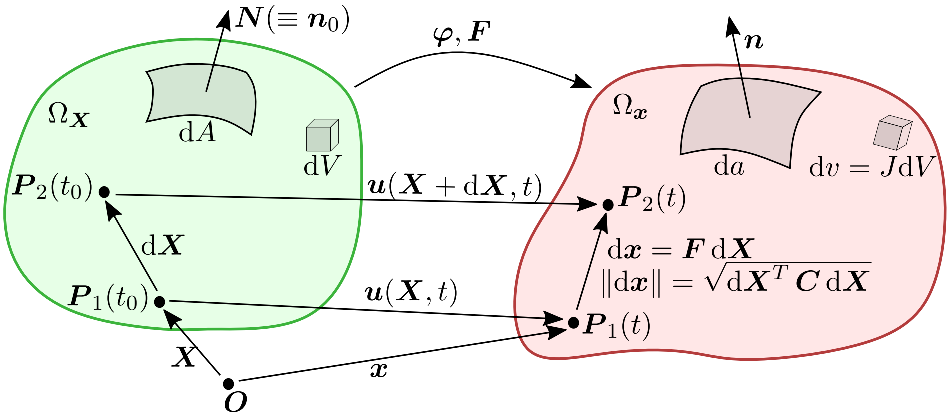

Figure 2.2: Transformation of infinitesimal line segment $\mathrm{d}\boldsymbol{X}$ to $\mathrm{d}\boldsymbol{x}$ via the deformation gradient $\boldsymbol{F}$. The squared segment length in the current configuration is obtained with $||\mathrm{d}\boldsymbol{x}||^2 = \mathrm{d}\boldsymbol{X}^T\boldsymbol{C}\,\mathrm{d}\boldsymbol{X}$, where $\boldsymbol{C} = \boldsymbol{F}^T\boldsymbol{F}$ is the right Cauchy-Green tensor.

$$\begin{aligned} \mathrm{d}\boldsymbol{x} &= \mathrm{d}\boldsymbol{X} + \boldsymbol{u}(\boldsymbol{X} + \mathrm{d}\boldsymbol{X}, t) - \boldsymbol{u}(\boldsymbol{X}, t) \\ &= \mathrm{d}\boldsymbol{X} + (\nabla_{\boldsymbol{X}}\,\boldsymbol{u})\,\mathrm{d}\boldsymbol{X} + o(\|\mathrm{d}\boldsymbol{X}\|^2) \\ &= (\boldsymbol{I} + \nabla_{\boldsymbol{X}}\,\boldsymbol{u})\,\mathrm{d}\boldsymbol{X} + o(\|\mathrm{d}\boldsymbol{X}\|^2) \\ &= \boldsymbol{F}\,\mathrm{d}\boldsymbol{X} + o(\|\mathrm{d}\boldsymbol{X}\|^2). \end{aligned} \tag{2.10}$$

Equation (2.10) states that the deformation gradient $\boldsymbol{F}$ maps an initial undeformed differential length vector $\mathrm{d}\boldsymbol{X}$ in the reference configuration $\Omega_{\boldsymbol{X}}$ to its deformed result $\mathrm{d}\boldsymbol{x}$ in the current configuration $\Omega_{\boldsymbol{x}}$. Therefore, the deformation gradient denotes the local change of relative position under deformation and its determinant

$$J := \det(\boldsymbol{F}) \tag{2.11}$$

represents the local change of volume. The latter statement is demonstrated via the relation

$$\begin{aligned} \mathrm{d}v &= |\mathrm{d}\boldsymbol{x}_1 \cdot (\mathrm{d}\boldsymbol{x}_2 \times \mathrm{d}\boldsymbol{x}_3)| \\ &= |\det(\mathrm{d}\boldsymbol{x}_1, \mathrm{d}\boldsymbol{x}_2, \mathrm{d}\boldsymbol{x}_3)| \\ &= |\det(\boldsymbol{F}\,\mathrm{d}\boldsymbol{X}_1, \boldsymbol{F}\,\mathrm{d}\boldsymbol{X}_2, \boldsymbol{F}\,\mathrm{d}\boldsymbol{X}_3)| \\ &\overset{(J>0)}{=} \det(\boldsymbol{F})\,|\det(\mathrm{d}\boldsymbol{X}_1, \mathrm{d}\boldsymbol{X}_2, \mathrm{d}\boldsymbol{X}_3)| \\ &= \det(\boldsymbol{F})\,|\mathrm{d}\boldsymbol{X}_1 \cdot (\mathrm{d}\boldsymbol{X}_2 \times \mathrm{d}\boldsymbol{X}_3)| \\ &= J\,\mathrm{d}V, \end{aligned} \tag{2.12}$$

where dV and dv represent the volumes of differential parallelepipeds – spanned by the basis vectors $(\mathrm{d}\boldsymbol{X}_1, \mathrm{d}\boldsymbol{X}_2, \mathrm{d}\boldsymbol{X}_3)$ and $(\mathrm{d}\boldsymbol{x}_1, \mathrm{d}\boldsymbol{x}_2, \mathrm{d}\boldsymbol{x}_3)$ – in the reference and current domains, respectively.

With the definition of the *cofactor matrix* of an invertible matrix $\boldsymbol{A}$

$$\mathbf{Cof}\;\boldsymbol{A} = (\det\boldsymbol{A})\boldsymbol{A}^{-T} \tag{2.13}$$

the relation between the areas in the deformed and reference configuration is given by the following theorem.

Theorem 2.1.1 (Nanson's formula). *Let* $\mathrm{d}\boldsymbol{A} \equiv \mathrm{d}A\,\boldsymbol{N}$ *and* $\mathrm{d}\boldsymbol{a} \equiv \mathrm{d}a\,\boldsymbol{n}$ *be the infinitesimal vector surface area elements of an undeformed body* B *and a deformed body* $\boldsymbol{\varphi}(B)$, *respectively, and let* $\boldsymbol{N}(\equiv \boldsymbol{n}_0)$ *and* $\boldsymbol{n}$ *denote the outward unit normal vectors at the corresponding domain boundaries. Then the transformation of surface area elements between* B *and* $\boldsymbol{\varphi}(B)$ *is given by Nanson's formula*

$$\mathrm{d}\boldsymbol{a} = \boldsymbol{n}\,\mathrm{d}a = J\boldsymbol{F}^{-T}\boldsymbol{N}\,\mathrm{d}A = \mathbf{Cof}\,\boldsymbol{F}\boldsymbol{N}\,\mathrm{d}A = J\boldsymbol{F}^{-T}\,\mathrm{d}\boldsymbol{A}. \tag{2.14}$$

Proof. In the deformed body $\boldsymbol{\varphi}(B)$, we consider an infinitesimal vector surface area element $\mathrm{d}\boldsymbol{a} \equiv \mathrm{d}a\,\boldsymbol{n} = \mathrm{d}\boldsymbol{x}_2 \times \mathrm{d}\boldsymbol{x}_3$ in the tangent plane given by the vectors $\mathrm{d}\boldsymbol{x}_2$ and $\mathrm{d}\boldsymbol{x}_3$ and extrude it along the infinitesimal increment $\mathrm{d}\boldsymbol{x}_1$. Following (2.12) and assuming non-negative volumes dv and dV (through proper orientation of the involved vectors $\boldsymbol{x}_i$ and $\boldsymbol{X}_i$ in the scalar triple product), the following relation

$$\mathrm{d}\boldsymbol{x}_1 \cdot (\mathrm{d}\boldsymbol{x}_2 \times \mathrm{d}\boldsymbol{x}_3) = \mathrm{d}v = J\,\mathrm{d}V = J\,\mathrm{d}\boldsymbol{X}_1 \cdot (\mathrm{d}\boldsymbol{X}_2 \times \mathrm{d}\boldsymbol{X}_3)$$

holds for the measure of the extruded volume, where $\mathrm{d}\boldsymbol{X}_2 \times \mathrm{d}\boldsymbol{X}_3 = \boldsymbol{N}\,\mathrm{d}A$ is the corresponding vector surface area element in the undeformed body B. Then (2.14) is obtained from the above expression as follows

$$\begin{aligned}
\boldsymbol{F}\,\mathrm{d}\boldsymbol{X}_1 \cdot (\mathrm{d}\boldsymbol{x}_2 \times \mathrm{d}\boldsymbol{x}_3) &= J\,\mathrm{d}\boldsymbol{X}_1 \cdot (\mathrm{d}\boldsymbol{X}_2 \times \mathrm{d}\boldsymbol{X}_3)\\
\mathrm{d}\boldsymbol{X}_1 \cdot (\boldsymbol{F}^T(\mathrm{d}\boldsymbol{x}_2 \times \mathrm{d}\boldsymbol{x}_3)) &= \mathrm{d}\boldsymbol{X}_1 \cdot (J(\mathrm{d}\boldsymbol{X}_2 \times \mathrm{d}\boldsymbol{X}_3))\\
\boldsymbol{F}^T\,\boldsymbol{n}\,\mathrm{d}a &= J\boldsymbol{N}\,\mathrm{d}A\\
\boldsymbol{n}\,\mathrm{d}a &= J\boldsymbol{F}^{-T}\,\boldsymbol{N}\,\mathrm{d}A\\
\mathrm{d}\boldsymbol{a} &= J\,\boldsymbol{F}^{-T}\,\mathrm{d}\boldsymbol{A}
\end{aligned}$$

□

Remark 2.1.2. *The unit outer normal vectors* $\boldsymbol{n}$ *and* $\boldsymbol{N}$ *at the points* $\boldsymbol{x} = \boldsymbol{\varphi}(\boldsymbol{X})$ *are related by*

$$\boldsymbol{n} = \frac{\mathbf{Cof}\,\nabla_{\boldsymbol{X}}\boldsymbol{\varphi}(\boldsymbol{X})\boldsymbol{N}}{\|\mathbf{Cof}\,\nabla_{\boldsymbol{X}}\boldsymbol{\varphi}(\boldsymbol{X})\boldsymbol{N}\|} = \frac{\boldsymbol{F}^{-T}\boldsymbol{N}}{\|\boldsymbol{F}^{-T}\boldsymbol{N}\|}.$$

This yields the following relation for the area elements in the undeformed and deformed configuration:

$$\begin{aligned}
\boldsymbol{n}\,\mathrm{d}a &= J\boldsymbol{F}^{-T}\,\boldsymbol{N}\,\mathrm{d}A\\
\frac{\boldsymbol{F}^{-T}\boldsymbol{N}}{\|\boldsymbol{F}^{-T}\boldsymbol{N}\|}\,\mathrm{d}a &= J\boldsymbol{F}^{-T}\,\boldsymbol{N}\,\mathrm{d}A\\
\mathrm{d}a &= J\,\left\|\boldsymbol{F}^{-T}\boldsymbol{N}\right\|\,\mathrm{d}A = \|\mathbf{Cof}\,\nabla_{\boldsymbol{X}}\boldsymbol{\varphi}(\boldsymbol{X})\boldsymbol{N}\|\,\mathrm{d}A.
\end{aligned} \tag{2.15}$$

2.2 Strain and rate of deformation

In continuum mechanics the *strain* of a body refers to the change in its shape as a result of the action of an external force. Excluding rigid body motion, these shape changes are given through relative displacements of particles in a body causing length change (stretch) and angle change (shear). Corresponding deformations are represented by the strain tensor.

Different strain measures are at one's disposal depending on the nature of the (deformation) problem under consideration and in particular depending on the configuration (initial or current) w.r.t. which the strain is defined. For instance, the *infinitesimal strain theory* involving the *infinitesimal strain tensor*

$$\boldsymbol{\varepsilon} = \frac{1}{2}\left(\nabla_{\boldsymbol{X}}\boldsymbol{u} + (\nabla_{\boldsymbol{X}}\boldsymbol{u})^T\right) = \frac{1}{2}\left(\boldsymbol{F} + \boldsymbol{F}^T\right) - \boldsymbol{I}, \tag{2.16}$$

is suitable for the analysis of deformation of materials exhibiting elastic behavior under the constraint of infinitesimal strains and rotations. This implies that the reference (undeformed) and current (deformed) configurations of a body can be assumed identical. The notion infinitesimal strain is a misnomer since actually only the rotations, not the strains, need to be infinitesimal in order to accurately use the small strain equations. In fact, in equation (2.16), plugging a rotation matrix w.r.t. the rotation angle $\theta > 0$ into $\boldsymbol{F}$, yields a strain tensor $\boldsymbol{\varepsilon}$ whose scaling components (on the main diagonal) are non-zero. For the above rotation only example, this measure erroneously indicates strain despite the fact that the object has not deformed at all. The errors obviously grow with increasing θ. So far we have shown the shortcoming of the infinitesimal strain tensor for the scenario where a deformation involves rotations. We assess next the complementary scenario where rotations are ruled out ($\boldsymbol{R} = \boldsymbol{I}$). To this end we perform a polar decomposition

$$\boldsymbol{F} = \boldsymbol{R}\boldsymbol{U} = \boldsymbol{V}\boldsymbol{R} \tag{2.17}$$

- a process in which the gradient of a deformation is expressed as the product of a rotation matrix $\boldsymbol{R}$ and a left stretch matrix $\boldsymbol{V}$ or a right stretch matrix $\boldsymbol{U}$. Taking the symmetric right stretch tensor $\boldsymbol{U} = \boldsymbol{U}^T$ for instance, the tensor $\boldsymbol{U} - \boldsymbol{I}$ satisfies the classical mechanical definitions of normal and shear strains and is very well suited to be used as a strain tensor. At this point the question arises how well does $\boldsymbol{\varepsilon}$ represent $\boldsymbol{U} - \boldsymbol{I}$. To answer this, we insert the polar decomposition $\boldsymbol{F} = \boldsymbol{R}\boldsymbol{U}$ into (2.16), so as to obtain

$$\begin{aligned} \boldsymbol{\varepsilon} &= \frac{1}{2}\left(\boldsymbol{F} + \boldsymbol{F}^T\right) - \boldsymbol{I} \\ &= \frac{1}{2}\left(\boldsymbol{R}\boldsymbol{U} + \boldsymbol{U}^T\boldsymbol{R}^T\right) - \boldsymbol{I}. \end{aligned} \tag{2.18}$$

Since in the absence of rotations, the above expression reduces to

$$\boldsymbol{\varepsilon} = \boldsymbol{U} - \boldsymbol{I}, \tag{2.19}$$

it becomes obvious that the essential limitation of the infinitesimal strain tensor $\boldsymbol{\varepsilon}$ is given by its admissibility for infinitesimal rotations only. For larger (finite) rotations the computed strains will lose accuracy.

If on the other hand the deformation involves rotations and strains that are arbitrary large, the *finite strain theory*, also known as *large deformation theory*, is a reasonable choice. Note that this case requires a clear distinction between the reference and current configurations of the continuum as they end up to differ significantly under deformation.

In the following we will briefly introduce some common strain measures, where the deformation gradient $\boldsymbol{F}$ is shown to be a core ingredient.

Let $\mathrm{d}s = \|\mathrm{d}\boldsymbol{x}\|$ and $\mathrm{d}S = \|\mathrm{d}\boldsymbol{X}\|$ denote the lengths of the differential segments $\mathrm{d}\boldsymbol{X}$ and $\mathrm{d}\boldsymbol{x}$, respectively. Then, their relation can be obtained using the projection of $\mathrm{d}\boldsymbol{x}$ on itself:

$$\begin{aligned} \mathrm{d}\boldsymbol{x} \cdot \mathrm{d}\boldsymbol{x} = \boldsymbol{F}\,\mathrm{d}\boldsymbol{X} \cdot \boldsymbol{F}\,\mathrm{d}\boldsymbol{X} + o(\|\mathrm{d}\boldsymbol{X}\|^2) &= \mathrm{d}\boldsymbol{X} \cdot \left(\boldsymbol{F}^T\boldsymbol{F}\right)\,\mathrm{d}\boldsymbol{X} + o(\|\mathrm{d}\boldsymbol{X}\|^2) \\ \mathrm{d}s^2 = \mathrm{d}\boldsymbol{X} \cdot \boldsymbol{C}\,\mathrm{d}\boldsymbol{X} + o(\mathrm{d}S^2), & \end{aligned} \tag{2.20}$$

where

$$\begin{aligned} \boldsymbol{C} &= \boldsymbol{F}^T\boldsymbol{F} \\ &= (\boldsymbol{I} + \nabla_{\boldsymbol{X}}\,\boldsymbol{u})^T\,(\boldsymbol{I} + \nabla_{\boldsymbol{X}}\,\boldsymbol{u}) \\ &= \boldsymbol{I} + \nabla_{\boldsymbol{X}}\,\boldsymbol{u} + (\nabla_{\boldsymbol{X}}\,\boldsymbol{u})^T + (\nabla_{\boldsymbol{X}}\,\boldsymbol{u})^T\,\nabla_{\boldsymbol{X}}\,\boldsymbol{u} \end{aligned} \tag{2.21}$$

represents the *right Cauchy-Green strain tensor*. This symmetric and positive definite tensor describes the squared length *scaling* of a line segment in direction $\mathrm{d}\boldsymbol{X} = \boldsymbol{P}_2(t_0) - \boldsymbol{P}_1(t_0)$ and is a strain measure suitable for large (finite) deformations. A deformation is rigid, if and only if $\boldsymbol{C} = \boldsymbol{I}$.

Another widely used strain measure for large deformations is given by the symmetric *Green-St. Venant strain tensor*:

$$\begin{aligned} \boldsymbol{E} &= \frac{1}{2}\,(\boldsymbol{C} - \boldsymbol{I}) \\ &= \frac{1}{2}\left(\boldsymbol{F}^T\boldsymbol{F} - \boldsymbol{I}\right) \\ &= \frac{1}{2}\left(\boldsymbol{F}^T\boldsymbol{F} - \boldsymbol{F}^T - \boldsymbol{F} + \boldsymbol{I} + \boldsymbol{F} + \boldsymbol{F}^T - 2\boldsymbol{I}\right) \\ &= \frac{1}{2}\left(\boldsymbol{F} + \boldsymbol{F}^T\right) - \boldsymbol{I} + \frac{1}{2}\left(\boldsymbol{F}^T\boldsymbol{F} - \boldsymbol{F} - \boldsymbol{F}^T + \boldsymbol{I}\right) \\ &= \frac{1}{2}\left(\boldsymbol{F} + \boldsymbol{F}^T - \boldsymbol{I} - \boldsymbol{I}\right) + \frac{1}{2}\,(\boldsymbol{F} - \boldsymbol{I})^T\,(\boldsymbol{F} - \boldsymbol{I}) \\ &= \frac{1}{2}\left(\boldsymbol{F} - \boldsymbol{I} + (\boldsymbol{F} - \boldsymbol{I})^T\right) + \frac{1}{2}\,(\nabla_{\boldsymbol{X}}\boldsymbol{u})^T\,\nabla_{\boldsymbol{X}}\boldsymbol{u} \\ &= \underbrace{\frac{1}{2}\left(\nabla_{\boldsymbol{X}}\boldsymbol{u} + (\nabla_{\boldsymbol{X}}\boldsymbol{u})^T\right)}_{\boldsymbol{\varepsilon}:=\text{Infinitesimal strain tensor}} + \frac{1}{2}\,(\nabla_{\boldsymbol{X}}\boldsymbol{u})^T\,\nabla_{\boldsymbol{X}}\boldsymbol{u} \\ &= \frac{1}{2}\left(\nabla_{\boldsymbol{X}}\boldsymbol{u} + (\nabla_{\boldsymbol{X}}\boldsymbol{u})^T + (\nabla_{\boldsymbol{X}}\boldsymbol{u})^T\,\nabla_{\boldsymbol{X}}\boldsymbol{u}\right) \end{aligned} \tag{2.22}$$

This strain gauge - used in calculations where large shape changes are expected - measures the squared length *change* of a line-segment $\mathrm{d}\boldsymbol{X} = \boldsymbol{P}_2(t_0) - \boldsymbol{P}_1(t_0)$ under deformation:

$$\begin{aligned} \frac{1}{2}\left(\|\mathrm{d}\boldsymbol{x}\|^2 - \|\mathrm{d}\boldsymbol{X}\|^2\right) &= \frac{1}{2}\left((\mathrm{d}\boldsymbol{X})^T\,\boldsymbol{C}\,\mathrm{d}\boldsymbol{X} + o(\|\mathrm{d}\boldsymbol{X}\|^2) - (\mathrm{d}\boldsymbol{X})^T\,\mathrm{d}\boldsymbol{X}\right) \\ &\approx (\mathrm{d}\boldsymbol{X})^T\left(\frac{1}{2}(\boldsymbol{C} - \boldsymbol{I})\right)\mathrm{d}\boldsymbol{X} \\ &= (\mathrm{d}\boldsymbol{X})^T\,\boldsymbol{E}\,\mathrm{d}\boldsymbol{X}. \end{aligned} \tag{2.23}$$

Equation (2.22) clearly illustrates that $\boldsymbol{E}$ is obtained from the combination of the infinitesimal strain tensor $\boldsymbol{\varepsilon}$ and terms quadratic in $\boldsymbol{u}$. The latter render the Green-St. Venant strain tensor rotation independent. However, this comes at a price: The quadratic terms that successfully eliminated the rotational dependency, unfortunately alter the strain components from the desired ($\varepsilon_x = \partial u_x/\partial X = (L - L_0)/L_0 = \Delta L/L_0$) values when the strains (not the rotations this time, but actual strains ($\boldsymbol{U}$)) are large. For small strains, the Green-St. Venant strain tensor and $\boldsymbol{U} - \boldsymbol{I}$ become very close to each other, regardless of the level of rotation, while the infinitesimal strain tensor $\boldsymbol{\varepsilon}$ fails to do so.

Note that both $\boldsymbol{C}$ and $\boldsymbol{E}$ are nonlinear functions of $\boldsymbol{u}$. In applications involving very small displacement gradients, such as in linearized elasticity, the terms nonlinear in $\boldsymbol{u}$ are in fact omitted, yielding linearized versions of (2.21) and (2.22) that are represented through

$$\boldsymbol{c} = \boldsymbol{I} + \nabla_{\boldsymbol{X}}\,\boldsymbol{u} + (\nabla_{\boldsymbol{X}}\,\boldsymbol{u})^T\,, \tag{2.24}$$

and equation (2.16), respectively.

After the introduction of deformation and its gradient, in the sequel, we will briefly discuss the concept of the temporal variation of the deformation gradient. As will be shown in Section 2.3, it is a key ingredient in the modeling of internal material forces (stresses). Differentiation of the deformation gradient w.r.t. time, yields

$$\dot{\boldsymbol{F}} = \frac{d}{dt}\left(\frac{\partial \boldsymbol{x}}{\partial \boldsymbol{X}}\right) = \frac{\partial}{\partial \boldsymbol{X}}\left(\frac{\mathrm{d}\boldsymbol{x}}{dt}\right) = \frac{\partial \boldsymbol{v}}{\partial \boldsymbol{X}} = \frac{\partial \boldsymbol{v}}{\partial \boldsymbol{x}}\frac{\partial \boldsymbol{x}}{\partial \boldsymbol{X}} = \nabla_{\boldsymbol{x}}\boldsymbol{v}\,\boldsymbol{F}, \tag{2.25}$$

where $\nabla_{\boldsymbol{x}}\boldsymbol{v}$ denotes the *spatial velocity gradient*. The velocity gradient can be decomposed into its symmetric and antisymmetric parts as

$$\nabla \boldsymbol{v} = \nabla^s \boldsymbol{v} + \nabla^w \boldsymbol{v}, \quad \text{where} \quad \begin{cases} \nabla^s := \frac{1}{2}\left(\nabla + \nabla^T\right), & \text{and} \\ \nabla^w := \frac{1}{2}\left(\nabla - \nabla^T\right). \end{cases} \tag{2.26}$$

The symmetric tensor ∇^s is called the *rate of deformation (or strain rate) tensor* and the antisymmetric tensor ∇^w is called the *vorticity (or spin) tensor.*

2.3 Stress

A body $\mathcal{B}$ exposed to applied forces experiences a deformation $\boldsymbol{\varphi}$. In the deformed configuration $\Omega_{\boldsymbol{x}}$ the body is subject to *applied body forces* that are defined by a vector field

$$\boldsymbol{f} := \Omega_{\boldsymbol{x}} \to \mathbb{R}^3,$$

called the density of the applied body force per unit volume $\mathrm{d}v$ in the deformed configuration, and *applied surface forces* that are defined by a vector field

$$\boldsymbol{g} := \Gamma_{1,\boldsymbol{x}} \to \mathbb{R}^3,$$

called the density of the applied surface force per unit area $\mathrm{d}a$ of a subset $\Gamma_{1,\boldsymbol{x}} \subset \Gamma_{\boldsymbol{x}}$ of the boundary $\Gamma_{\boldsymbol{x}} := \partial\Omega_{\boldsymbol{x}}$ in the deformed configuration.

Remark 2.3.1. *Let*

$$\boldsymbol{b} := \Omega_{\boldsymbol{x}} \to \mathbb{R}^3,$$

denote the density of the applied body forces per unit mass in the deformed configuration. Then, the applied body forces can be alternatively defined as

$$\boldsymbol{f} = \rho \boldsymbol{b}, \tag{2.27}$$

where $\rho : \Omega_{\boldsymbol{x}} \to \mathbb{R}$ *denotes the mass density in the deformed configuration, such that the mass for every* $\mathrm{d}x$*-measurable subset* $A_{\boldsymbol{x}}$ *of* $\bar{\Omega}_{\boldsymbol{x}}$ *is given by the integral* $\int_{A_{\boldsymbol{x}}} \rho(\boldsymbol{x})\,\mathrm{d}v$*. For this it is assumed that*

$$\rho(\boldsymbol{x}) > 0 \quad \forall \boldsymbol{x} \in \Omega_{\boldsymbol{x}}.$$

As shown in the sequel, these applied forces cause a change in the internal state of the body for whose characterization the following axiom is fundamental.

Axiom 2.3.1 (Stress principle of Euler and Cauchy). *For a body occupying a deformed configuration* $\bar{\Omega}_{\boldsymbol{x}}$ *and loaded with body force densities* $\boldsymbol{f} = \Omega_{\boldsymbol{x}} \to \mathbb{R}^3$ *and surface force densities* $\boldsymbol{g} = \Gamma_{1,\boldsymbol{x}} \to \mathbb{R}^3$*, there* *exists a vector field*

$$\boldsymbol{t}\colon \bar{\Omega}_{\boldsymbol{x}} \times \boldsymbol{S}_1 \to \mathbb{R}^3, \text{ where } \boldsymbol{S}_1 = \{\boldsymbol{v} \in \mathbb{R}^3; \|\boldsymbol{v}\| = 1\}, \tag{2.28}$$

such that:

1. *For arbitrary subsets* $A_{\boldsymbol{x}} \subset \bar{\Omega}_{\boldsymbol{x}}$ *and for any point* $\boldsymbol{x} \in \Gamma_{1,\boldsymbol{x}} \cap \partial A_{\boldsymbol{x}}$ *where the unit outer normal vector* $\boldsymbol{n}$ *to* $\Gamma_{1,\boldsymbol{x}} \cap \partial A_{\boldsymbol{x}}$ *exists,*
$$\boldsymbol{t}(\boldsymbol{x}, \boldsymbol{n}) = \boldsymbol{g}(\boldsymbol{x}).$$

2. *Axiom of (linear) force balance: For any subdomain* $A_{\boldsymbol{x}} \subset \bar{\Omega}_{\boldsymbol{x}}$
$$\int_{A_{\boldsymbol{x}}} \boldsymbol{f}(\boldsymbol{x})\, \mathrm{d}v + \int_{\partial A_{\boldsymbol{x}}} \boldsymbol{t}(\boldsymbol{x}, \boldsymbol{n})\, \mathrm{d}a = \boldsymbol{0}, \tag{2.29}$$
where $\boldsymbol{n}$ *is the unit outer normal vector along* $\partial A_{\boldsymbol{x}}$.

3. *Axiom of moment or torque (rotational force) balance: For any subdomain* $A_{\boldsymbol{x}} \subset \bar{\Omega}_{\boldsymbol{x}}$,
$$\int_{A_{\boldsymbol{x}}} \boldsymbol{x} \times \boldsymbol{f}(\boldsymbol{x})\, \mathrm{d}v + \int_{\partial A_{\boldsymbol{x}}} \boldsymbol{x} \times \boldsymbol{t}(\boldsymbol{x}, \boldsymbol{n})\, \mathrm{d}a = \boldsymbol{0}. \tag{2.30}$$

The above axiom asserts for any subdomain $A_{\boldsymbol{x}}$ of the deformed configuration $\bar{\Omega}_{\boldsymbol{x}}$ and $\boldsymbol{x} \in \partial A_{\boldsymbol{x}}$ the existence of elementary surface forces $\boldsymbol{t}(\boldsymbol{x}, \boldsymbol{n})\, \mathrm{d}a$ along the boundary $\partial A_{\boldsymbol{x}}$ with unit outer normal vector $\boldsymbol{n}$. The stress vectors $\boldsymbol{t}(\boldsymbol{x}, \boldsymbol{n})$ completely represent the forces $\int_{A_{\boldsymbol{x}}} (\cdot)\, \mathrm{d}v$ which are exerted on a region $A_{\boldsymbol{x}}$ by the material outside. Similarly, the interior material exerts the same total force on the exterior by Newton's law of action and reaction. At a point $\boldsymbol{x} \in \partial A_{\boldsymbol{x}} \subset A_{\boldsymbol{x}}$, the elementary surface force depends on the subdomain $A_{\boldsymbol{x}}$ *only* via the normal vector $\boldsymbol{n}$ to $\partial A_{\boldsymbol{x}}$ at $\boldsymbol{x}$. Moreover, the axiom asserts that any subdomain $A_{\boldsymbol{x}} \subseteq \bar{\Omega}_{\boldsymbol{x}}$ is in static equilibrium in the sense that the resultant force (linear force) and torque (rotational force) vectors in (2.29) and (2.30) vanish.

The stress principle asserts a linear dependence of $\boldsymbol{t}$ on $\boldsymbol{n}$, that is, at each point $\boldsymbol{x} \in \bar{\Omega}_{\boldsymbol{x}}$, there exists a symmetric tensor $\boldsymbol{\sigma}(\boldsymbol{x}) \in \mathbb{M}^3$ such that $\boldsymbol{t}(\boldsymbol{x}, \boldsymbol{n}) = \boldsymbol{\sigma}(\boldsymbol{x})\, \boldsymbol{n}$ for all $\boldsymbol{n} \in \boldsymbol{S}_1$. Moreover, it states that the tensor field $\boldsymbol{\sigma}\colon \Omega_{\boldsymbol{x}} \to \mathbb{M}^3$ and the vector fields $\boldsymbol{f}\colon \Omega_{\boldsymbol{x}} \to \mathbb{R}^3$ and $\boldsymbol{g}\colon \Gamma_{1,\boldsymbol{x}} \to \mathbb{R}^3$ are related by a partial differential equation in $\Omega_{\boldsymbol{x}}$, and a boundary condition on $\Gamma_{1,\boldsymbol{x}}$, respectively. These consequences of the stress principle are formalized in the following theorem:

Theorem 2.3.1 (Cauchy's theorem). *Let the applied body force density* $\boldsymbol{f}\colon \bar{\Omega}_{\boldsymbol{x}} \to \mathbb{R}^3$ *be continuous, and let the Cauchy stress vector field* $\boldsymbol{t}\colon (\boldsymbol{x}, \boldsymbol{n}) \in \bar{\Omega}_{\boldsymbol{x}} \times \boldsymbol{S}_1 \to \boldsymbol{t}(\boldsymbol{x}, \boldsymbol{n}) \in \mathbb{R}^3$ *be continuously differentiable with respect to* $\boldsymbol{x} \in \bar{\Omega}_{\boldsymbol{x}}$ *for each* $\boldsymbol{n} \in \boldsymbol{S}_1$ *and continuous with respect to* $\boldsymbol{n} \in \boldsymbol{S}_1$ *for each* $\boldsymbol{x} \in \bar{\Omega}_{\boldsymbol{x}}$. *Then the axioms of force and moment balance (Axiom 2.3.1) imply the existence of a continuously differentiable tensor field* $\boldsymbol{\sigma}\colon \boldsymbol{x} \in \bar{\Omega}_{\boldsymbol{x}} \to \boldsymbol{\sigma}(\boldsymbol{x}) \in \mathbb{M}^3$, *such that the Cauchy stress vector satisfies*

$$\boldsymbol{t}(\boldsymbol{x}, \boldsymbol{n}) = \boldsymbol{\sigma}(\boldsymbol{x})\, \boldsymbol{n} \quad \forall \boldsymbol{x} \in \bar{\Omega}_{\boldsymbol{x}}, \forall \boldsymbol{n} \in \boldsymbol{S}_1, \tag{2.31}$$

and such that

$$\begin{aligned} -\nabla \cdot \boldsymbol{\sigma}(\boldsymbol{x}) &= \boldsymbol{f}(\boldsymbol{x}) && \forall \boldsymbol{x} \in \Omega_{\boldsymbol{x}}, \\ \boldsymbol{\sigma}(\boldsymbol{x}) &= \boldsymbol{\sigma}(\boldsymbol{x})^T && \forall \boldsymbol{x} \in \bar{\Omega}_{\boldsymbol{x}}, \\ \boldsymbol{\sigma}(\boldsymbol{x})\, \boldsymbol{n} &= \boldsymbol{g}(\boldsymbol{x}) && \forall \boldsymbol{x} \in \Gamma_{1,\boldsymbol{x}}, \end{aligned}$$

where $\boldsymbol{n}$ *denotes the unit outer normal vector along* $\Gamma_{1,\boldsymbol{x}}$.

Proof. See [33]. □

The symmetric spatial tensor $\boldsymbol{\sigma}(\boldsymbol{x})$ is called the *Cauchy stress tensor* at point $\boldsymbol{x}$. It is also called the *true stress tensor* because it is a true measure for the force per unit area in the current, deformed configuration. For small deformations there is no distinction to be made between the deformed and undeformed configurations and the Cauchy stress tensor is a reasonable choice for the description of the action of forces. However, for large deformations such as those arising in nonlinear elasticity, using the deformed configuration, the area to divide the force by and the equilibrium equations involved are implicitly dependent on the yet unknown deformation which makes it necessary to refer to a reference configuration instead. With the necessity to pull back the stress to a reference configuration, a definition establishing a correspondence between tensor fields defined over the reference and deformed configurations is in order:

Definition 2.3.1 (Piola transform of a tensor field). *Let $\boldsymbol{\varphi}$ be in injective deformation on $\bar{\Omega}_{\boldsymbol{X}}$, such that the matrix $\nabla\boldsymbol{\varphi}$ is invertible at all points of the reference configuration. Then, if $\boldsymbol{T}^{\boldsymbol{\varphi}}(\boldsymbol{x})$ is a tensor defined at the point $\boldsymbol{x} = \boldsymbol{\varphi}(\boldsymbol{X})$ of the deformed configuration, we associate with $\boldsymbol{T}^{\boldsymbol{\varphi}}(\boldsymbol{x})$ a tensor $\boldsymbol{T}(\boldsymbol{X})$ defined at the point $\boldsymbol{X}$ of the reference configuration by:*

$$\boldsymbol{T}(\boldsymbol{X}) := \underbrace{(\det \nabla_{\boldsymbol{X}} \boldsymbol{\varphi}(\boldsymbol{X}))}_{J} \boldsymbol{T}^{\boldsymbol{\varphi}}(\boldsymbol{x}) \underbrace{\nabla_{\boldsymbol{X}} \boldsymbol{\varphi}(\boldsymbol{X})^{-T}}_{\boldsymbol{F}^{-T}} \tag{2.32}$$

Theorem 2.3.2 (Properties of the Piola transform). *Let $\boldsymbol{T} \colon \bar{\Omega}_{\boldsymbol{X}} \to \mathbb{M}^3$ denote the Piola transform of $\boldsymbol{T}^{\boldsymbol{\varphi}} \colon \bar{\Omega}_{\boldsymbol{x}} \to \mathbb{M}^3$. Then*

$$\nabla_{\boldsymbol{X}} \cdot \boldsymbol{T}(\boldsymbol{X}) = (\det \nabla_{\boldsymbol{X}} \boldsymbol{\varphi}(\boldsymbol{X}))\, \nabla_{\boldsymbol{x}} \cdot \boldsymbol{T}^{\boldsymbol{\varphi}}(\boldsymbol{x}) \qquad \forall \boldsymbol{x} = \boldsymbol{\varphi}(\boldsymbol{X}), \boldsymbol{X} \in \bar{\Omega}_{\boldsymbol{X}}, \tag{2.33a}$$

$$\boldsymbol{T}(\boldsymbol{X})\, \boldsymbol{n}_0 \, \mathrm{d}A = \boldsymbol{T}^{\boldsymbol{\varphi}}(\boldsymbol{x})\, \boldsymbol{n} \, \mathrm{d}a, \qquad \forall \boldsymbol{x} = \boldsymbol{\varphi}(\boldsymbol{X}), \boldsymbol{X} \in \partial\Omega_{\boldsymbol{X}}. \tag{2.33b}$$

The area elements $\mathrm{d}A$ and $\mathrm{d}a$ at the points $\boldsymbol{X} \in \partial\Omega_{\boldsymbol{X}}$ and $\boldsymbol{x} = \boldsymbol{\varphi}(\boldsymbol{X}) \in \partial\Omega_{\boldsymbol{x}}$, with respective unit outer normal vectors $\boldsymbol{n}_0$ and $\boldsymbol{n}$, are related by

$$\det \nabla_{\boldsymbol{X}} \boldsymbol{\varphi}(\boldsymbol{X}) \left\| \nabla_{\boldsymbol{X}} \boldsymbol{\varphi}(\boldsymbol{X})^{-T} \boldsymbol{n}_0 \right\| \mathrm{d}A = \left\| \mathbf{Cof}\, \nabla_{\boldsymbol{X}} \boldsymbol{\varphi}(\boldsymbol{X}) \boldsymbol{n}_0 \right\| \mathrm{d}A = \mathrm{d}a. \tag{2.34}$$

Proof. See [33]. □

With Definition 2.3.1 at hand, using the Piola transform of the Cauchy stress tensor, we obtain a tensor $\boldsymbol{P} \colon \bar{\Omega}_{\boldsymbol{X}} \to \mathbb{M}^3$ with

$$\boldsymbol{P}(\boldsymbol{X}) = J \boldsymbol{\sigma} \boldsymbol{F}^{-T} \tag{2.35}$$

which we refer to as the *first Piola-Kirchhoff stress tensor*. The first Piola-Kirchhoff stress tensor $\boldsymbol{P}$, relates the force acting in the current configuration on a vector element of surface ($\boldsymbol{n}\mathrm{d}a$) to the corresponding vector element of surface in the reference configuration ($\boldsymbol{N}\mathrm{d}A$) and is in general not symmetric. Since it relates to both configurations, it is a two-point tensor. We also define the *first Piola-Kirchhoff stress vector* $\boldsymbol{t}_0 \colon \bar{\Omega}_{\boldsymbol{X}} \to \mathbb{R}^3$ as

$$\boldsymbol{t}_0(\boldsymbol{X}, \boldsymbol{n}_0)\, \mathrm{d}A = \boldsymbol{t}(\boldsymbol{x}, \boldsymbol{n})\, \mathrm{d}a, \tag{2.36}$$

that together with

$$\boldsymbol{P}(\boldsymbol{X}) \boldsymbol{n}_0 \, \mathrm{d}A = \boldsymbol{\sigma}(\boldsymbol{x}) \boldsymbol{n} \, \mathrm{d}a \quad \forall \boldsymbol{x} = \boldsymbol{\varphi}(\boldsymbol{X}), \boldsymbol{X} \in \partial\Omega_{\boldsymbol{X}}, \tag{2.37}$$

yields the counter piece of equation (2.31) in the reference configuration:

$$\boldsymbol{t}_0(\boldsymbol{X}, \boldsymbol{n}_0) = \boldsymbol{P} \boldsymbol{n}_0 \quad \forall \boldsymbol{X} \in \bar{\Omega}_{\boldsymbol{X}}, \forall \boldsymbol{n}_0 \in \boldsymbol{S}_1. \tag{2.38}$$

The Cauchy traction (2.31) and the first Piola-Kirchhoff traction (2.38) differ as follows: The former is the actual physical force per area on the element in the current configuration, whereas the latter is a pure fictitious quantity representing the force acting on an element in the current configuration divided by the area of the corresponding element in the reference configuration.

The relation between the divergence of the Cauchy stress tensor and the divergence of first Piola-Kirchhoff stress tensor follows directly from equation (2.33a):

$$\nabla_{\boldsymbol{X}} \cdot \boldsymbol{P}(\boldsymbol{X}) = (\det \nabla_{\boldsymbol{X}} \boldsymbol{\varphi}(\boldsymbol{X}))\, \nabla_{\boldsymbol{x}} \cdot \boldsymbol{\sigma}(\boldsymbol{x}). \tag{2.39}$$

The lack of symmetry of $\boldsymbol{P}$ has led to the usage of the symmetric and more popular *second Piola-Kirchhoff stress tensor* $\boldsymbol{S} \colon \bar{\Omega}_{\boldsymbol{X}} \to \mathbb{M}^3$, defined as

$$\boldsymbol{S}(\boldsymbol{X}) = \boldsymbol{F}^{-1}\boldsymbol{P} = J\boldsymbol{F}^{-1}\boldsymbol{\sigma}\boldsymbol{F}^{-T}. \tag{2.40}$$

The second Piola-Kirchhoff stress tensor does not admit a physical interpretation. It may be helpful to think of it as follows, though: Given a force vector in the current configuration and the corresponding (fictitious) force vector in the undeformed configuration, the second Piola-Kirchhoff stress tensor is this (fictitious) force divided by the corresponding area element in the reference configuration.

2.4 Transformations between the reference and current configurations

In this section we touch upon the operations to be applied to scalar, vectorial and tensorial quantities as they are transformed (pulled back or pushed forward) from one domain to another. We start off with a theorem that generalizes the concept of integration by substitution and provides a description for the behaviors of integrals under coordinate transformations:

Theorem 2.4.1 (Transformationssatz). *Let $U, V \subset \mathbb{R}^d$ be open sets and let $\Phi \colon U \to V$ be a diffeomorphism. Then, a function f on V is integrable on V, if and only if $(f \circ \Phi) \cdot |\det(D\Phi)|$ is integrable on U. In this case we have*

$$\int_U f(\Phi(x)) \cdot |\det(D\Phi(x))| \,\mathrm{d}x = \int_V f(y)\,\mathrm{d}y, \tag{2.41}$$

where $D\Phi(x)$ and $\det(D\Phi(x))$, denote the jacobian matrix and its determinant, respectively.

Proof. See [96]. □

With regard to our discussion on the typical domains in continuum mechanics, let V denote the current domain, that is, $V \equiv \Omega_x$ and let U denote a reference domain[8] which we choose for convenience to be the initial domain: $U \equiv \Omega_X = \boldsymbol{\varphi}^{-1}(\Omega_x)$. Then for a scalar-valued function $f(\boldsymbol{x}, t) = f(\boldsymbol{\varphi}(\boldsymbol{X}), t) \in C^1(I \times \Omega_x)$ it follows from Theorem 2.4.1 and expressions (2.1), (2.10) and (2.11) that we can transform its volume integral in Ω_x to a volume integral in Ω_X:

$$\int_{\Omega_X} f(\boldsymbol{\varphi}(\boldsymbol{X}))\, J \,\mathrm{d}\Omega_X = \int_{\Omega_x} f(\boldsymbol{x})\,\mathrm{d}\Omega_x. \tag{2.42}$$

---

[8] Note that U may be chosen to be an arbitrary other domain: $U \equiv \Omega_{\chi} = \hat{\boldsymbol{\varphi}}^{-1}(\Omega_x)$ (cf. Section 2.6.1).

For the gradient of the scalar field f, the following relation is derived using the chain rule:

$$\nabla_{\boldsymbol{X}} f(\boldsymbol{\varphi}(\boldsymbol{X})) = \frac{\partial f(\boldsymbol{\varphi}(\boldsymbol{X}))}{\partial \boldsymbol{X}} = \frac{\partial f(\boldsymbol{\varphi}(\boldsymbol{X}))}{\partial \boldsymbol{\varphi}(\boldsymbol{X})} \frac{\partial \boldsymbol{\varphi}(\boldsymbol{X})}{\partial \boldsymbol{X}} = \frac{\partial f(\boldsymbol{x})}{\partial \boldsymbol{x}} \frac{\partial \boldsymbol{x}}{\partial \boldsymbol{X}} = \left((\nabla_{\boldsymbol{x}} f(\boldsymbol{x}))^T \boldsymbol{F}\right)^T = \boldsymbol{F}^T \nabla_{\boldsymbol{x}} f(\boldsymbol{x}). \tag{2.43}$$

When it comes to the transformation of vectors, we recall the Piola transformation rule: Let $\boldsymbol{v} : \Omega_x \to \mathbb{R}^3$ denote a differentiable vector field in the spatial domain. Then the Piola transform of $\boldsymbol{v}$ (cf. contravariant Piola mapping [125])

$$\boldsymbol{v}_0 = J\boldsymbol{F}^{-1}\boldsymbol{v} \tag{2.44}$$

yields a corresponding vector field $\boldsymbol{v}_0 : \Omega_X \to \mathbb{R}^3$ in the reference domain (cf. (2.32) , [125], and [18]).

In this case the following relation holds

$$\int_{\Omega_{\boldsymbol{X}}} \nabla_{\boldsymbol{X}} \cdot (J\boldsymbol{F}^{-1}\boldsymbol{v}) \, \mathrm{d}\Omega_X = \int_{\Omega_{\boldsymbol{x}}} \nabla_{\boldsymbol{x}} \cdot \boldsymbol{v} \, \mathrm{d}\Omega_x. \tag{2.45}$$

Proof.

$$\begin{aligned}
&\int_{\Omega_{\boldsymbol{x}}} \nabla_{\boldsymbol{x}} \cdot \boldsymbol{v} \, \mathrm{d}\Omega_x \\
\overset{(2.50)}{=} &\int_{\partial\Omega_{\boldsymbol{x}}} \boldsymbol{v} \cdot \boldsymbol{n} \, \mathrm{d}\partial\Omega_x \\
\overset{(2.14)}{=} &\int_{\partial\Omega_{\boldsymbol{X}}} \boldsymbol{v} \cdot (\mathbf{Cof}\, \boldsymbol{F}\boldsymbol{N}) \, \mathrm{d}\partial\Omega_X \\
\overset{(2.13)}{=} &\int_{\partial\Omega_{\boldsymbol{X}}} \boldsymbol{v} \cdot (J\boldsymbol{F}^{-T}\boldsymbol{N}) \, \mathrm{d}\partial\Omega_X \\
= &\int_{\partial\Omega_{\boldsymbol{X}}} (J\boldsymbol{F}^{-1}\boldsymbol{v}) \cdot \boldsymbol{N} \, \mathrm{d}\partial\Omega_X \\
\overset{(2.50)}{=} &\int_{\Omega_{\boldsymbol{X}}} \nabla_{\boldsymbol{X}} \cdot (J\boldsymbol{F}^{-1}\boldsymbol{v}) \, \mathrm{d}\Omega_X.
\end{aligned}$$

□

Further, Lemma 2.12 of [123] reports the following relation to hold in a point-wise sense:

$$\nabla_{\boldsymbol{X}} \cdot (J\boldsymbol{F}^{-1}\boldsymbol{v}) = J\nabla_{\boldsymbol{x}} \cdot \boldsymbol{v}. \tag{2.46}$$

Moreover, on every volume $\mathrm{d}\Omega_x (\equiv dv)$ with corresponding reference volume $\mathrm{d}\Omega_X (\equiv dV)$ it holds

$$\int_{\partial\Omega_{\boldsymbol{X}}} \left(J\boldsymbol{F}^{-1}\boldsymbol{v}\right) \cdot \boldsymbol{N} \, \mathrm{d}A = \int_{\partial\Omega_{\boldsymbol{x}}} \boldsymbol{v} \cdot \boldsymbol{n} \, \mathrm{d}a. \tag{2.47}$$

Proof. A proof of this relation can be found e.g. in [123] (Lemma 2.12: Piola transformation of a differentiable vector field). □

In analogy to (2.43) we obtain the following relation for the gradient of $\boldsymbol{v}$ in the reference and spatial domains:

$$\nabla_{\boldsymbol{X}}\boldsymbol{v}(\boldsymbol{\varphi}(\boldsymbol{X})) = \frac{\partial \boldsymbol{v}(\boldsymbol{\varphi}(\boldsymbol{X}))}{\partial \boldsymbol{X}} = \frac{\partial \boldsymbol{v}(\boldsymbol{\varphi}(\boldsymbol{X}))}{\partial \boldsymbol{\varphi}(\boldsymbol{X})}\frac{\partial \boldsymbol{\varphi}(\boldsymbol{X})}{\partial \boldsymbol{X}} = \frac{\partial \boldsymbol{v}(\boldsymbol{x})}{\partial \boldsymbol{x}}\frac{\partial \boldsymbol{x}}{\partial \boldsymbol{X}} = \nabla_{\boldsymbol{x}}\, \boldsymbol{v}(\boldsymbol{x})\boldsymbol{F}. \tag{2.48}$$

Eventually, we conclude this section's discussion on transformation rules with the definition of the Piola identity which is used in Section 2.6.2.

Theorem 2.4.2 (Piola identity).

$$\nabla_{\boldsymbol{X}} \cdot (\mathbf{Cof}\, \boldsymbol{F}) = \nabla_{\boldsymbol{X}} \cdot \left(J\boldsymbol{F}^{-T}\right) = 0. \tag{2.49}$$

Proof. A proof of the Piola identity can be found in [33]. □

2.5 Conservation principles

In this section we provide the field equations expressing the principles of conservation of *mass* and *momentum*. *Entropy balance* and the conservation principles of other important physical properties such as *total energy* are not discussed since they are not considered in the models used in this work. For the derivation of the considered conservation equations, we will make use of the Gauss divergence theorem and the Reynolds transport theorem which are specified in the sequel without proof:

Theorem 2.5.1 (Gauss divergence theorem). *Let V be a region in space with boundary ∂V. Then the volume integral of the divergence $\nabla \cdot \boldsymbol{f}$ of $\boldsymbol{f}$ over V and the surface integral of $\boldsymbol{f}$ over the boundary ∂V of V are related by*

$$\int_V \nabla \cdot \boldsymbol{f}\, \mathrm{d}V = \int_S \boldsymbol{f} \cdot \boldsymbol{n}\, \mathrm{d}S. \tag{2.50}$$

Theorem 2.5.2 (Reynolds transport theorem). *Let $f(\boldsymbol{x}, t)$ be a smooth scalar-, vector- or tensor-valued function of spatial coordinates $\boldsymbol{x}$ and time t. Moreover, let $V_t \equiv V_m \subset \mathbb{R}^3$ be the domain of a moving material volume that consists of the same material particles at all times and let the surface $S_t = \partial V_t$ denote its time dependent boundary driven by the motion of material particles. Besides, let V_c be a fixed in space control volume coinciding with the moving material volume V_t at time instance t. Analogously let the control surface S_c coincide at time instance t with S_t. Then,*

$$\begin{aligned}\frac{D}{Dt}\int_{V_t} f(\boldsymbol{x}, t)\, \mathrm{d}V &= \int_{V_c \equiv V_t} \frac{\partial f(\boldsymbol{x}, t)}{\partial t}\, \mathrm{d}V + \int_{S_c \equiv S_t} f(\boldsymbol{x}, t)\, \boldsymbol{v} \cdot \boldsymbol{n}\, \mathrm{d}S \\ &= \int_{V_c \equiv V_t} \left(\frac{\partial f(\boldsymbol{x}, t)}{\partial t} + \nabla \cdot (f\boldsymbol{v})\right) \mathrm{d}V \\ &= \int_{V_c \equiv V_t} \left(\frac{\partial f(\boldsymbol{x}, t)}{\partial t} + \boldsymbol{v} \cdot \nabla f + f\nabla \cdot \boldsymbol{v}\right) \mathrm{d}V \\ &= \int_{V_c \equiv V_t} \left(\frac{Df(\boldsymbol{x}, t)}{Dt} + f\nabla \cdot \boldsymbol{v}\right) \mathrm{d}V.\end{aligned} \tag{2.51}$$

Above, in the surface integral, $\boldsymbol{n}$ represents the outward unit normal vector to S_t at time t and $\boldsymbol{v}$ denotes the material velocity of points on boundary S_t.

2.5.1 Conservation of mass

The global principle of conservation of mass requires the total mass of a fixed part V_m of a material volume to remain constant at all times, that is

$$\frac{D}{Dt}\int_{V_m}\rho\,\mathrm{d}V = 0. \tag{2.52}$$

In the spirit of the Eulerian point of view, let $V_c \subset \mathbb{R}^3$ denote a fixed finite control volume and let S_c denote its surface. Then conservation of mass requires that the net mass flow out of the control volume V_c through its surface S_c is equal to the time rate of decrease of mass inside the control volume, i.e.,

$$\int_{S_c}\rho\boldsymbol{v}\cdot\boldsymbol{n}\,\mathrm{d}S = -\frac{\partial}{\partial t}\int_{V_c}\rho\,\mathrm{d}V. \tag{2.53}$$

Above, ρ is the mass density, and for a point on the control surface, $\boldsymbol{n}$ and $\boldsymbol{v}$ denote the outward oriented surface unit normal and the velocity, respectively. Rewriting equation (2.53) as

$$\frac{\partial}{\partial t}\int_{V_c}\rho\,\mathrm{d}V + \int_{S_c}\rho\boldsymbol{v}\cdot\boldsymbol{n}\,\mathrm{d}S = 0, \tag{2.54}$$

we obtain the *continuity equation in conservative integral form.* Next, owing to the constancy of the fixed control volume's integration limits, we pull the derivative into the volume integral and apply the divergence theorem to the surface integral in order to obtain

$$\int_{V_c}\frac{\partial\rho}{\partial t}\,\mathrm{d}V + \int_{V_c}\nabla\cdot(\rho\boldsymbol{v})\,\mathrm{d}V = \int_{V_c}\left(\frac{\partial\rho}{\partial t} + \nabla\cdot(\rho\boldsymbol{v})\right)\mathrm{d}V = 0. \tag{2.55}$$

Note that the left hand side of the above equation may just as well be obtained from the application of the Reynolds transport theorem to equation (2.52). Due to the arbitrariness of the finite control volume V, the only way for the above integral to become zero is when the integrand is zero at every point of V. In the sequel, we will refer to this argument as the *localization argument*. Its usage leads to the current configuration's *continuity equation in conservative differential form*:

$$\frac{\partial\rho}{\partial t} + \nabla\cdot(\rho\boldsymbol{v}) = \frac{\partial\rho}{\partial t} + \boldsymbol{v}\cdot\nabla\rho + \rho\nabla\cdot\boldsymbol{v} = 0. \tag{2.56}$$

The corresponding *non-conservative differential form* is obtained using the material derivative $\frac{D(\cdot)}{Dt} = \frac{\partial(\cdot)}{\partial t} + \boldsymbol{v}\cdot\nabla(\cdot)$:

$$\frac{D\rho}{Dt} + \rho\nabla\cdot\boldsymbol{v} = 0. \tag{2.57}$$

2.5.2 Conservation of linear momentum

According to the global principle of conservation of linear momentum, the total force acting on any fixed part of a body, equates the rate of change of the linear momentum $\rho\boldsymbol{v}$ of the part. This can be written as

$$\frac{D}{Dt}\int_{V_m}\rho\boldsymbol{v}\,\mathrm{d}V = \int_{S_c}\boldsymbol{t}\,\mathrm{d}S + \int_{V_c}\rho\boldsymbol{b}\,\mathrm{d}V, \tag{2.58}$$

where $\boldsymbol{b}$ and $\boldsymbol{t}$ represent the body and surface force densities, respectively. Using the Reynolds transport theorem, the divergence theorem and equation (2.31), the above equation can be rewritten as

$$
\begin{aligned}
\int_{V_c} \frac{\partial(\rho \boldsymbol{v})}{\partial t}\,\mathrm{d}V + \int_{S_c} ((\rho \boldsymbol{v}) \otimes \boldsymbol{v}) \cdot \boldsymbol{n}\,\mathrm{d}S &= \int_{S_c} \boldsymbol{\sigma} \boldsymbol{n}\,\mathrm{d}S + \int_{V_c} \rho \boldsymbol{b}\,\mathrm{d}V, \\
\int_{V_c} \frac{\partial(\rho \boldsymbol{v})}{\partial t} + \nabla \cdot ((\rho \boldsymbol{v}) \otimes \boldsymbol{v})\,\mathrm{d}V &= \int_{V_c} \nabla \cdot \boldsymbol{\sigma}\,\mathrm{d}V + \int_{V_c} \rho \boldsymbol{b}\,\mathrm{d}V, \\
\int_{V_c} \left(\frac{\partial(\rho \boldsymbol{v})}{\partial t} + \nabla \cdot ((\rho \boldsymbol{v}) \otimes \boldsymbol{v}) - \nabla \cdot \boldsymbol{\sigma} - \rho \boldsymbol{b} \right) \mathrm{d}V = 0
\end{aligned}
\tag{2.59}
$$

in order to obtain the *linear momentum equation in conservative integral form*. With the same argument used in the derivation of equation (2.56), we obtain the *linear momentum equation in conservative differential form*:

$$
\frac{\partial(\rho \boldsymbol{v})}{\partial t} + \nabla \cdot ((\rho \boldsymbol{v}) \otimes \boldsymbol{v}) = \nabla \cdot \boldsymbol{\sigma} + \rho \boldsymbol{b}. \tag{2.60}
$$

Taking equation (2.59) as point of departure, the *linear momentum equation in non-conservative integral form* is derived as:

$$
\begin{aligned}
\int_{V_c} \frac{\partial(\rho \boldsymbol{v})}{\partial t} + \nabla \cdot ((\rho \boldsymbol{v}) \otimes \boldsymbol{v})\,\mathrm{d}V &= \int_{V_c} \nabla \cdot \boldsymbol{\sigma}\,\mathrm{d}V + \int_{V_c} \rho \boldsymbol{b}\,\mathrm{d}V, \\
\int_{V_c} \frac{\partial(\rho \boldsymbol{v})}{\partial t} + \boldsymbol{v} \nabla \cdot (\rho \boldsymbol{v}) + ((\rho \boldsymbol{v}) \cdot \nabla)\, \boldsymbol{v}\,\mathrm{d}V &= \int_{V_c} \nabla \cdot \boldsymbol{\sigma} + \rho \boldsymbol{b}\,\mathrm{d}V, \\
\int_{V_c} \rho \frac{\partial \boldsymbol{v}}{\partial t} + \boldsymbol{v} \frac{\partial \rho}{\partial t} + ((\rho \boldsymbol{v}) \cdot \nabla)\, \boldsymbol{v} + \boldsymbol{v} \nabla \cdot (\rho \boldsymbol{v})\,\mathrm{d}V &= \int_{V_c} \nabla \cdot \boldsymbol{\sigma} + \rho \boldsymbol{b}\,\mathrm{d}V, \\
\int_{V_c} \rho \left(\frac{\partial \boldsymbol{v}}{\partial t} + (\boldsymbol{v} \cdot \nabla)\, \boldsymbol{v} \right) + \boldsymbol{v} \left(\frac{\partial \rho}{\partial t} + \nabla \cdot (\rho \boldsymbol{v}) \right) \mathrm{d}V &= \int_{V_c} \nabla \cdot \boldsymbol{\sigma} + \rho \boldsymbol{b}\,\mathrm{d}V, \\
\int_{V_c} \rho \frac{D \boldsymbol{v}}{D t}\,\mathrm{d}V &= \int_{V_c} \nabla \cdot \boldsymbol{\sigma} + \rho \boldsymbol{b}\,\mathrm{d}V, \\
\int_{V_c} \left(\rho \frac{D \boldsymbol{v}}{D t} - \nabla \cdot \boldsymbol{\sigma} - \rho \boldsymbol{b} \right) \mathrm{d}V &= 0.
\end{aligned}
\tag{2.61}
$$

Localizing the above equation in space, yields the *linear momentum equation in non-conservative differential form*:

$$
\rho \frac{D \boldsymbol{v}}{D t} = \nabla \cdot \boldsymbol{\sigma} + \rho \boldsymbol{b}. \tag{2.62}
$$

2.5.3 Conservation of angular momentum

The global principle of conservation of angular momentum states that the time rate of change of the total angular momentum $\boldsymbol{L}(V(t))$ of a body is balanced with the angular momentum exchange due to the torque $\boldsymbol{\tau}$ composed of the surface force $\int_{S_c} \boldsymbol{r} \times \boldsymbol{t}\,\mathrm{d}S$ and body force $\int_{V_c} \boldsymbol{r} \times (\rho \boldsymbol{b})\,\mathrm{d}V$, that is

$$
\begin{aligned}
\underbrace{\frac{D}{Dt} \int_{V_m} \boldsymbol{r} \times (\rho \boldsymbol{v})\,\mathrm{d}V}_{\boldsymbol{L}(V(t))} &= \underbrace{\int_{S_c} \boldsymbol{r} \times \boldsymbol{t}\,\mathrm{d}S + \int_{V_c} \boldsymbol{r} \times (\rho \boldsymbol{b})\,\mathrm{d}V}_{\boldsymbol{\tau}} \\
&= \int_{S_c} \boldsymbol{r} \times (\boldsymbol{\sigma} \boldsymbol{n})\,\mathrm{d}S + \int_{V_c} \boldsymbol{r} \times (\rho \boldsymbol{b})\,\mathrm{d}V.
\end{aligned}
\tag{2.63}
$$

Above, $\boldsymbol{r}$ is a position vector for a general particle relative to some origin. Eventually, applying the Reynolds transport theorem to the above equation, yields

$$\int_{V_m} \frac{\partial}{\partial t}(\boldsymbol{r} \times (\rho \boldsymbol{v}))\,\mathrm{d}V + \int_{S_c} (\boldsymbol{r} \times (\rho \boldsymbol{v}))\,\boldsymbol{v} \cdot \boldsymbol{n}\,\mathrm{d}S = \int_{S_c} \boldsymbol{r} \times (\boldsymbol{\sigma} \boldsymbol{n})\,\mathrm{d}S + \int_{V_c} \boldsymbol{r} \times (\rho \boldsymbol{b})\,\mathrm{d}V. \tag{2.64}$$

The above equation can be interpreted as follows: The total rate of change of angular momentum plus the total net rate of outflow of angular momentum across the control surface S_c (left hand side) is equal to the total torque about a fixed point due to surface and body forces acting on the material instantaneously inside a control volume (right hand side).

2.6 Conservation principles in different coordinate systems

Continuum mechanics comes with two different viewpoints of motion: the *Lagrangian* and the *Eulerian* viewpoints.

In the context of the Lagrangian viewpoint of motion we consider a material body occupying an initial/reference/undeformed material domain $\Omega_{\boldsymbol{X}}$. The motion of the body is broken down to the motion of its individual material particles. The motion of an individual material particle in turn is parametrized by its reference position $\boldsymbol{X}$ through the mapping (2.1) and equation (2.2). For the Lagrangian kinematical description we consider an arbitrary computational mesh inside the reference configuration and refer to the corresponding nodes as mesh particles. The latter are sticky to the material particles, and therefore, as a material body experiences motion and deformations, so does the computational mesh. The Lagrangian viewpoint of motion comes with the benefit of the ability to track the motion of individual particles and interfaces, however, at the cost of potentially severe mesh deformations with possibly fatal implications on numerical algorithms. In the realm of mesh-based numerical methods, the Lagrangian description comes in handy in problems involving small to moderate material deformations such as in solid mechanics.

In fluid mechanics on the other hand, where one has to deal with extreme deformations of the continuum (fluid body), it is in general neither reasonable nor feasible to employ the Lagrangian approach due to the above addressed mesh distortion issues. The Eulerian formulation avoids these issues by giving up on tracking individual material particles and using instead a fixed computational mesh with respect to which the material moves and deforms. The quantities of interest in the continuum such as e.g. density and velocity are then sampled at fixed locations (e.g. grid line intersections) with the drawback of not any longer knowing to which material particle the current quantity of interest at a sample location is associated to. The evaluated quantity then literally belongs to the "random" particle that happens to pass the sample location at the time of sampling. Moreover, by contrast to the Lagrangian description, tracking material interfaces turns now significantly more difficult since they end up arbitrarily intersecting Eulerian grid cells.

2.6.1 Arbitrary Lagrangian-Eulerian approach

In the previous section we have briefly discussed the Lagrangian and Eulerian descriptions together with their individual benefits and shortcomings. We recall that in the Lagrangian approach the mesh deforms together with the matter and therefore, at any time instance, one has a sharp and easy to access material interface. This is without any doubt very appealing, however, the question remains how to avoid potentially massive mesh deformations that prevent the success of numerical algorithms. If we consider – in a limit sense – a severely deformed mesh associated with the Lagrangian approach as one extreme and a not at all deformed mesh in affiliation with the Eulerian approach as the other extreme, a moderately deformed mesh in between may allow to find solutions to computational mechanics problems which would otherwise not be possible with heavily distorted meshes of a purely Lagrangian approach. Therefore, it is pleasant to have a method which combines the benefits of both approaches, that is, on the one hand allowing to track moving material interfaces in the spirit of the Lagrangian approach, and on the other hand allowing to temper mesh distortions by a user specified mesh deformation function independent of the material deformation.

A general description designed to combine the benefits of the Lagrangian and Eulerian descriptions in the sense of the idea presented above is given by the *Arbitrary Lagrangian-Eulerian* (ALE) description of motion. The ALE description neither uses the material domain $\Omega_{\boldsymbol{X}}$ nor the spatial domain $\Omega_{\boldsymbol{x}}$ as the reference. Instead, a third domain $\Omega_{\boldsymbol{\chi}}$, denoted as the *referential domain*, comes to fruition where accordingly the grid points are identified with referential coordinates $\boldsymbol{\chi}$. In a sense, the referential domain can be thought of as a *virtual material* (or *mesh*) domain which deforms according to an arbitrarily chosen law. We refer to Figure 2.3 for the depiction of the ALE domains

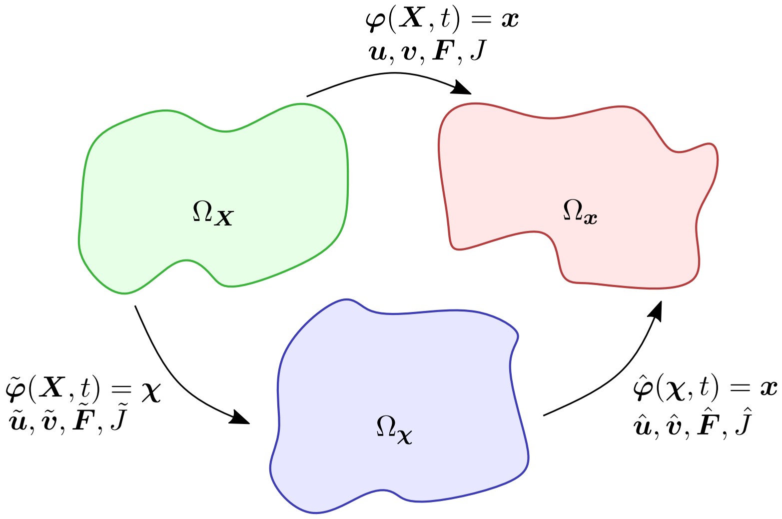

Figure 2.3: Domains involved in the ALE method and corresponding coordinate mappings.

and the bijective mappings relating coordinates between these domains. In the ALE description the domain is in motion but the motion is independent of the motion of material particles. The material particles are in relative motion with respect to the referential domain's motion. The referential domain $\Omega_{\boldsymbol{\chi}}$ is mapped to the material and spatial domains via the bijective maps $\tilde{\boldsymbol{\varphi}}^{-1}$ and $\hat{\boldsymbol{\varphi}}$, respectively. Note that the particle motion $\boldsymbol{\varphi}$ can now be also expressed as

$$\boldsymbol{\varphi} = \hat{\boldsymbol{\varphi}} \circ \tilde{\boldsymbol{\varphi}} \tag{2.65}$$

revealing a dependency structure among the three mappings $\boldsymbol{\varphi}, \tilde{\boldsymbol{\varphi}}$ and $\hat{\boldsymbol{\varphi}}$. In what follows, we proceed with the introduction of the *Lagrangian-to-Referential map* $\tilde{\boldsymbol{\varphi}}$ and *Referential-to-Eulerian map* $\hat{\boldsymbol{\varphi}}$.

2.6.1.1 Lagrangian-to-Referential map $\tilde{\boldsymbol{\varphi}}$

The smooth enough, injective, and orientation preserving mapping from the material domain to the referential domain, dubbed $\tilde{\boldsymbol{\varphi}}$, is defined as

$$\begin{aligned} \tilde{\boldsymbol{\varphi}} \colon \overline{\Omega}_{\boldsymbol{X}} \times [0,T] &\longrightarrow \overline{\Omega}_{\boldsymbol{\chi}} \times [0,T] \\ (\boldsymbol{X},t) &\longmapsto \tilde{\boldsymbol{\varphi}}(\boldsymbol{X},t) = (\boldsymbol{\chi},t), \end{aligned} \tag{2.66}$$

and can be interpreted to track the motion of the referential frame as seen from the Lagrangian reference frame. The gradient of the map $\tilde{\boldsymbol{\varphi}}$

$$\frac{\partial \tilde{\boldsymbol{\varphi}}}{\partial(\boldsymbol{X},t)} = \begin{pmatrix} \frac{\partial \boldsymbol{\chi}}{\partial \boldsymbol{X}} & \tilde{\boldsymbol{v}} \\ \boldsymbol{0}^T & 1 \end{pmatrix} \tag{2.67}$$

reveals the quantity

$$\tilde{\boldsymbol{v}}(\boldsymbol{X},t) = \frac{\partial \tilde{\boldsymbol{\varphi}}}{\partial t}\bigg|_{\boldsymbol{X}} = \frac{\partial \boldsymbol{\chi}}{\partial t}\bigg|_{\boldsymbol{X}} = \frac{\partial(\boldsymbol{X}+\tilde{\boldsymbol{u}})}{\partial t}\bigg|_{\boldsymbol{X}} = \frac{\partial \tilde{\boldsymbol{u}}}{\partial t}\bigg|_{\boldsymbol{X}} \tag{2.68}$$

that can be interpreted[9] as the velocity of the referential frame as observed from the Lagrangian frame [133]. Therefore,

$$\tilde{\boldsymbol{u}} = \tilde{\boldsymbol{\varphi}}(\boldsymbol{X},t) - \tilde{\boldsymbol{\varphi}}(\boldsymbol{X},0) = \tilde{\boldsymbol{\varphi}}(\boldsymbol{X},t) - \boldsymbol{X} \tag{2.69}$$

can be interpreted to represent the mesh displacement as observed from the Lagrangian reference frame. The deformation gradient and the Jacobian determinant of this map, read

$$\begin{aligned} &\tilde{\boldsymbol{F}} := \tilde{\boldsymbol{F}}(\boldsymbol{X},\tilde{\boldsymbol{u}}) := \frac{\partial \tilde{\boldsymbol{\varphi}}}{\partial \boldsymbol{X}} = \nabla_{\boldsymbol{X}} \tilde{\boldsymbol{\varphi}}(\boldsymbol{X}) = \frac{\partial \boldsymbol{\chi}}{\partial \boldsymbol{X}} = \frac{\partial(\boldsymbol{X}+\tilde{\boldsymbol{u}})}{\partial \boldsymbol{X}} = \frac{\partial \boldsymbol{X}}{\partial \boldsymbol{X}} + \frac{\partial \tilde{\boldsymbol{u}}}{\partial \boldsymbol{X}} = \boldsymbol{I} + \nabla_{\boldsymbol{X}}\, \tilde{\boldsymbol{u}}, \\ &\tilde{J} := \det(\tilde{\boldsymbol{F}}). \end{aligned} \tag{2.70}$$

With the definition of $\tilde{\boldsymbol{v}}$ at hand, the Lagrangian time derivative of a scalar function $\alpha : \Omega_{\chi} \to \mathbb{R}$ can be expressed in terms of the referential frame:

$$\dot{\alpha}(\boldsymbol{\chi},t) = \frac{\partial \alpha(\boldsymbol{\chi},t)}{\partial t}\bigg|_{\boldsymbol{X}} = \frac{\partial \alpha(\tilde{\boldsymbol{\varphi}}(\boldsymbol{X},t),t)}{\partial t}\bigg|_{\boldsymbol{X}} = \frac{\partial \alpha}{\partial t}\bigg|_{\boldsymbol{\chi}} + \nabla_{\boldsymbol{\chi}}\, \alpha \cdot \frac{\partial \tilde{\boldsymbol{\varphi}}}{\partial t}\bigg|_{\boldsymbol{X}} = \frac{\partial \alpha}{\partial t}\bigg|_{\boldsymbol{\chi}} + \tilde{\boldsymbol{v}} \cdot \nabla_{\boldsymbol{\chi}}\, \alpha. \tag{2.71}$$

2.6.1.2 Referential-to-Eulerian map $\hat{\boldsymbol{\varphi}}$

Coordinates $\boldsymbol{\chi}$ from the referential domain $\overline{\Omega}_{\boldsymbol{\chi}}$ are mapped to the spatial domain via the smooth enough, injective, and orientation preserving map

$$\begin{aligned} \hat{\boldsymbol{\varphi}} \colon \overline{\Omega}_{\boldsymbol{\chi}} \times [0,T] &\longrightarrow \overline{\Omega}_{\boldsymbol{x}} \times [0,T] \\ (\boldsymbol{\chi},t) &\longmapsto \hat{\boldsymbol{\varphi}}(\boldsymbol{\chi},t) = (\boldsymbol{x},t). \end{aligned} \tag{2.72}$$

Analogous to (2.2) the deformation mapping $\hat{\boldsymbol{\varphi}}$ can be expressed with a displacement function $\hat{\boldsymbol{u}} : \overline{\Omega}_{\boldsymbol{\chi}} \times [0,T] \to \mathbb{R}^3$ as

$$\hat{\boldsymbol{\varphi}}(\boldsymbol{\chi},t) = \boldsymbol{\chi} + \hat{\boldsymbol{u}}(\boldsymbol{\chi},t). \tag{2.73}$$

---

[9] Note that Donea et al. [47] provide an alternative interpretation for $\tilde{\boldsymbol{v}}$, they interpret it as the particle velocity as seen from the referential domain $\Omega_{\boldsymbol{\chi}}$.

The gradient of the referential-to-spatial mapping (2.72) is

$$\frac{\partial \hat{\boldsymbol{\varphi}}}{\partial(\boldsymbol{\chi}, t)} = \begin{pmatrix} \frac{\partial \boldsymbol{x}}{\partial \boldsymbol{\chi}} & \hat{\boldsymbol{v}} \\ \\ \boldsymbol{0}^T & 1 \end{pmatrix}, \tag{2.74}$$

where

$$\hat{\boldsymbol{v}}(\boldsymbol{\chi}, t) = \frac{\partial \hat{\boldsymbol{\varphi}}}{\partial t}\bigg|_{\boldsymbol{\chi}} = \frac{\partial \boldsymbol{x}}{\partial t}\bigg|_{\boldsymbol{\chi}} = \frac{\partial(\boldsymbol{\chi} + \hat{\boldsymbol{u}})}{\partial t}\bigg|_{\boldsymbol{\chi}} = \frac{\partial \hat{\boldsymbol{u}}}{\partial t}\bigg|_{\boldsymbol{\chi}} \tag{2.75}$$

indicates the referential velocity also known as the *mesh velocity*. Accordingly, the *mesh deformation gradient* $\hat{\boldsymbol{F}}$ and the *mesh Jacobian determinant* $\hat{J}$ are defined as

$$\begin{aligned} \hat{\boldsymbol{F}} &:= \hat{\boldsymbol{F}}(\boldsymbol{\chi}, \hat{\boldsymbol{u}}) := \frac{\partial \hat{\boldsymbol{\varphi}}}{\partial \boldsymbol{\chi}} = \nabla_{\boldsymbol{\chi}} \hat{\boldsymbol{\varphi}}(\boldsymbol{\chi}) = \frac{\partial \boldsymbol{x}}{\partial \boldsymbol{\chi}} = \frac{\partial(\boldsymbol{\chi} + \hat{\boldsymbol{u}})}{\partial \boldsymbol{\chi}} = \frac{\partial \boldsymbol{\chi}}{\partial \boldsymbol{\chi}} + \frac{\partial \hat{\boldsymbol{u}}}{\partial \boldsymbol{\chi}} = \boldsymbol{I} + \nabla_{\boldsymbol{\chi}} \hat{\boldsymbol{u}}, \\ \hat{J} &:= \det(\hat{\boldsymbol{F}}). \end{aligned} \tag{2.76}$$

Note that equation (2.75) involves a referential time derivative. The referential time derivative of a scalar function $\alpha : \Omega_x \to \mathbb{R}$ reads

$$\frac{\partial \alpha(\boldsymbol{x}, t)}{\partial t}\bigg|_{\boldsymbol{\chi}} = \frac{\partial \alpha(\hat{\boldsymbol{\varphi}}(\boldsymbol{\chi}, t), t)}{\partial t}\bigg|_{\boldsymbol{\chi}} = \frac{\partial \alpha}{\partial t}\bigg|_{\boldsymbol{x}} + \nabla_{\boldsymbol{x}} \alpha \cdot \frac{\partial \hat{\boldsymbol{\varphi}}}{\partial t}\bigg|_{\boldsymbol{\chi}} = \frac{\partial \alpha}{\partial t}\bigg|_{\boldsymbol{x}} + \hat{\boldsymbol{v}} \cdot \nabla_{\boldsymbol{x}} \alpha. \tag{2.77}$$

Application of the chain rule of differentiation to $\boldsymbol{\varphi} = \hat{\boldsymbol{\varphi}} \circ \tilde{\boldsymbol{\varphi}} = \hat{\boldsymbol{\varphi}}(\tilde{\boldsymbol{\varphi}})$ yields the following relation among the derivatives of the involved mappings:

$$\frac{\partial \boldsymbol{\varphi}(\boldsymbol{X}, \boldsymbol{t})}{\partial(\boldsymbol{X}, t)} = \frac{\partial \hat{\boldsymbol{\varphi}}(\tilde{\boldsymbol{\varphi}}(\boldsymbol{X}, t))}{\partial(\boldsymbol{\chi}, t)} \frac{\partial \tilde{\boldsymbol{\varphi}}(\boldsymbol{X}, t)}{\partial(\boldsymbol{X}, t)} = \frac{\partial \hat{\boldsymbol{\varphi}}(\boldsymbol{\chi}, t)}{\partial(\boldsymbol{\chi}, t)} \frac{\partial \tilde{\boldsymbol{\varphi}}(\boldsymbol{X}, t)}{\partial(\boldsymbol{X}, t)}. \tag{2.78}$$

Using equations (2.3), (2.74) and (2.67), equation (2.78) can be written as

$$\begin{pmatrix} \frac{\partial \boldsymbol{x}}{\partial \boldsymbol{X}} & \boldsymbol{v} \\ \\ \boldsymbol{0}^T & 1 \end{pmatrix} = \begin{pmatrix} \frac{\partial \boldsymbol{x}}{\partial \boldsymbol{\chi}} & \hat{\boldsymbol{v}} \\ \\ \boldsymbol{0}^T & 1 \end{pmatrix} \begin{pmatrix} \frac{\partial \boldsymbol{\chi}}{\partial \boldsymbol{X}} & \tilde{\boldsymbol{v}} \\ \\ \boldsymbol{0}^T & 1 \end{pmatrix}, \tag{2.79}$$

which discloses the following structure

$$\boldsymbol{v} = \frac{\partial \boldsymbol{x}}{\partial \boldsymbol{\chi}} \cdot \tilde{\boldsymbol{v}} + \hat{\boldsymbol{v}} \tag{2.80}$$

among the material velocity $\boldsymbol{v}$, the mesh velocity $\hat{\boldsymbol{v}}$ and the particle velocity $\tilde{\boldsymbol{v}}$ as seen from the referential domain. Equation (2.80), rewritten, now allows to define a *convective velocity*

$$\boldsymbol{c} := \boldsymbol{v} - \hat{\boldsymbol{v}} = \frac{\partial \boldsymbol{x}}{\partial \boldsymbol{\chi}} \cdot \tilde{\boldsymbol{v}} = \hat{\boldsymbol{F}} \cdot \tilde{\boldsymbol{v}}, \tag{2.81}$$

representing the particle velocity relative to the mesh, as seen from the spatial[10] domain $\Omega_{\boldsymbol{x}}$. Note that due to (2.81), $\tilde{\boldsymbol{v}}$ may now be represented as

$$\tilde{\boldsymbol{v}} = \hat{\boldsymbol{F}}^{-1} \cdot \boldsymbol{c}. \tag{2.82}$$

---

[10] Note that both $\boldsymbol{v} = \frac{\partial \boldsymbol{x}}{\partial t}\big|_{\boldsymbol{X}}$ and $\hat{\boldsymbol{v}} = \frac{\partial \boldsymbol{x}}{\partial t}\big|_{\boldsymbol{\chi}}$ are variations of the spatial coordinate $\boldsymbol{x}$.

For the expression of the conservation laws in the ALE framework, we need to establish a relation between the spatial time derivative, the referential time derivative and the material (time) derivative. To this end, we consider a scalar physical quantity, represented in the spatial, referential and material domains by $f(\boldsymbol{x},t)$, $f^*(\boldsymbol{\chi},t)$ and $f^{**}(\boldsymbol{X},t)$, respectively. The particle-motion describing mapping $\boldsymbol{\varphi}$, allows to relate the material description $f^{**}(\boldsymbol{X},t)$ and the spatial description $f(\boldsymbol{x},t)$ of the physical quantity as

$$f^{**}(\boldsymbol{X},t) = f(\boldsymbol{\varphi}(\boldsymbol{X},t),t) = f(\boldsymbol{x},t) \circ \boldsymbol{\varphi}(\boldsymbol{X},t). \tag{2.83}$$

Then, from the gradient of the above expression

$$\frac{\partial f^{**}(\boldsymbol{X},t)}{\partial(\boldsymbol{X},t)} = \frac{\partial f(\boldsymbol{x},t)}{\partial(\boldsymbol{x},t)} \frac{\partial \boldsymbol{\varphi}(\boldsymbol{X},t)}{\partial(\boldsymbol{X},t)} \tag{2.84}$$

written in matrix form

$$\begin{pmatrix} \dfrac{\partial f^{**}}{\partial \boldsymbol{X}} & \dfrac{\partial f^{**}}{\partial t} \end{pmatrix} = \begin{pmatrix} \dfrac{\partial f}{\partial \boldsymbol{x}} & \dfrac{\partial f}{\partial t} \end{pmatrix} \begin{pmatrix} \frac{\partial \boldsymbol{x}}{\partial \boldsymbol{X}} & \boldsymbol{v} \\ \mathbf{0}^T & 1 \end{pmatrix} \tag{2.85}$$

one can deduce the following expression

$$\frac{\partial f^{**}}{\partial t} = \frac{\partial f}{\partial t} + \frac{\partial f}{\partial \boldsymbol{x}} \cdot \boldsymbol{v} \tag{2.86}$$

which in alternative notation

$$\left.\frac{\partial f}{\partial t}\right|_{\boldsymbol{X}} = \left.\frac{\partial f}{\partial t}\right|_{\boldsymbol{x}} + \boldsymbol{v} \cdot \frac{\partial f}{\partial \boldsymbol{x}} = \left.\frac{\partial f}{\partial t}\right|_{\boldsymbol{x}} + \boldsymbol{v} \cdot \nabla_{\boldsymbol{x}} f \qquad \text{or} \qquad \frac{Df}{Dt} = \frac{\partial f}{\partial t} + \boldsymbol{v} \cdot \nabla f \tag{2.87}$$

reveals the relation between the material (time) derivative $\frac{D(\cdot)}{Dt} := \frac{\partial(\cdot)}{\partial t}\big|_{\boldsymbol{X}}$ and spatial time derivative $\frac{\partial(\cdot)}{\partial t} := \frac{\partial(\cdot)}{\partial t}\big|_{\boldsymbol{x}}$. Equation (2.87) implies that the temporal variation of a physical quantity for a particle $\boldsymbol{X}$ is equal to the sum of a local variation and a convective term attributed to the relative motion between the material and spatial systems.

Next, the relation between the material and spatial time derivatives is extended to include the referential time derivative. Analogous to (2.83), the mapping $\tilde{\boldsymbol{\varphi}}$ allows to relate the material description $f^{**}(\boldsymbol{X},t)$ and the referential description $f^*(\boldsymbol{\chi},t)$ of the physical quantity as

$$f^{**}(\boldsymbol{X},t) = f^*(\tilde{\boldsymbol{\varphi}}(\boldsymbol{X},t),t) = f^*(\boldsymbol{\chi},t) \circ \tilde{\boldsymbol{\varphi}}(\boldsymbol{X},t). \tag{2.88}$$

Then, from the gradient of the above expression

$$\frac{\partial f^{**}(\boldsymbol{X},t)}{\partial(\boldsymbol{X},t)} = \frac{\partial f^*(\boldsymbol{\chi},t)}{\partial(\boldsymbol{\chi},t)} \frac{\partial \tilde{\boldsymbol{\varphi}}(\boldsymbol{X},t)}{\partial(\boldsymbol{X},t)} \tag{2.89}$$

written in matrix form

$$\begin{pmatrix} \dfrac{\partial f^{**}}{\partial \boldsymbol{X}} & \dfrac{\partial f^{**}}{\partial t} \end{pmatrix} = \begin{pmatrix} \dfrac{\partial f^*}{\partial \boldsymbol{\chi}} & \dfrac{\partial f^*}{\partial t} \end{pmatrix} \begin{pmatrix} \frac{\partial \boldsymbol{\chi}}{\partial \boldsymbol{X}} & \tilde{\boldsymbol{v}} \\ \mathbf{0}^T & 1 \end{pmatrix} \tag{2.90}$$

one can deduce the following expression

$$\frac{\partial f^{**}}{\partial t} = \frac{\partial f^{*}}{\partial t} + \frac{\partial f^{*}}{\partial \boldsymbol{\chi}} \cdot \tilde{\boldsymbol{v}} \tag{2.91}$$

which in alternative notation

$$\left.\frac{\partial f}{\partial t}\right|_{\boldsymbol{X}} = \left.\frac{\partial f}{\partial t}\right|_{\boldsymbol{\chi}} + \tilde{\boldsymbol{v}} \cdot \frac{\partial f}{\partial \boldsymbol{\chi}} = \left.\frac{\partial f}{\partial t}\right|_{\boldsymbol{\chi}} + \tilde{\boldsymbol{v}} \cdot \nabla_{\boldsymbol{\chi}} f \tag{2.92}$$

reveals the relation between the material (time) derivative $\frac{\partial(\cdot)}{\partial t}\big|_{\boldsymbol{X}}$ and referential time derivative $\frac{\partial(\cdot)}{\partial t}\big|_{\boldsymbol{\chi}}$. We want to point out that in equation (2.92) the gradient is to be evaluated with respect to the referential domain. However, since it is in general more convenient to work in the spatial or material domains, the above equation can be rewritten such that the referential gradient is replaced with the spatial one:

$$\begin{aligned} \left.\frac{\partial f}{\partial t}\right|_{\boldsymbol{X}} &= \left.\frac{\partial f}{\partial t}\right|_{\boldsymbol{\chi}} + \tilde{\boldsymbol{v}} \cdot \nabla_{\boldsymbol{\chi}} f \\ &= \left.\frac{\partial f}{\partial t}\right|_{\boldsymbol{\chi}} + \tilde{\boldsymbol{v}} \cdot \frac{\partial f}{\partial \boldsymbol{\chi}} \\ &= \left.\frac{\partial f}{\partial t}\right|_{\boldsymbol{\chi}} + \tilde{\boldsymbol{v}} \cdot \frac{\partial \boldsymbol{x}}{\partial \boldsymbol{\chi}} \frac{\partial f}{\partial \boldsymbol{x}} \\ &= \left.\frac{\partial f}{\partial t}\right|_{\boldsymbol{\chi}} + \boldsymbol{c} \cdot \frac{\partial f}{\partial \boldsymbol{x}} \\ &= \left.\frac{\partial f}{\partial t}\right|_{\boldsymbol{\chi}} + \boldsymbol{c} \cdot \nabla_{\boldsymbol{x}} f \end{aligned} \tag{2.93}$$

The above relation for the Lagrangian time derivative can be alternatively derived as follows

$$\begin{aligned} \dot{f} &= \left.\frac{\partial f(\boldsymbol{x}, \boldsymbol{t})}{\partial t}\right|_{\boldsymbol{X}} = \left.\frac{\partial f(\boldsymbol{\varphi}(\boldsymbol{X}, t), t)}{\partial t}\right|_{\boldsymbol{X}} \\ &\overset{(2.5)}{=} \left.\frac{\partial f}{\partial t}\right|_{\boldsymbol{x}} + \boldsymbol{v} \cdot \nabla_{\boldsymbol{x}} f \\ &\overset{(2.77)}{=} \left.\frac{\partial f}{\partial t}\right|_{\boldsymbol{\chi}} - \hat{\boldsymbol{v}} \cdot \nabla_{\boldsymbol{x}} f + \boldsymbol{v} \cdot \nabla_{\boldsymbol{x}} f \\ &= \left.\frac{\partial f}{\partial t}\right|_{\boldsymbol{\chi}} + \boldsymbol{c} \cdot \nabla_{\boldsymbol{x}} f \end{aligned} \tag{2.94}$$

Equation (2.93) expresses the fundamental ALE relation between the material (time) derivative, the referential time derivative and the spatial gradient. It implies that the temporal variation of a physical quantity for a particle $\boldsymbol{X}$ is equal to the sum of its local derivative (with the reference coordinate $\boldsymbol{\chi}$ held fixed) and a convective term taking account the relative velocity $\boldsymbol{c} = \boldsymbol{v} - \hat{\boldsymbol{v}}$ between the material and the referential systems. As shown in the sequel, the ALE formulation can be seen as a generalization of the Lagrangian and Eulerian formulations. The choice $\tilde{\boldsymbol{\varphi}}^{-1} = \boldsymbol{I}$ results according to (2.66) to $\boldsymbol{X} \equiv \boldsymbol{\chi}$ and gives rise to a Lagrangian description. Since the material velocity $\boldsymbol{v}(\boldsymbol{X}, t) = \frac{\partial \boldsymbol{x}}{\partial t}\big|_{\boldsymbol{X}}$ and the mesh velocity $\hat{\boldsymbol{v}}(\boldsymbol{\chi}, t) = \frac{\partial \boldsymbol{x}}{\partial t}\big|_{\boldsymbol{\chi}}$ coincide in this description, the convective velocity $\boldsymbol{c}$ vanishes. As a consequence, the convective derivative vanishes altogether and the total derivative reduces to a simple time derivative: $\frac{\partial f}{\partial t}\big|_{\boldsymbol{X}} = \frac{\partial f}{\partial t}\big|_{\boldsymbol{\chi}}$. The choice $\hat{\boldsymbol{\varphi}} = \boldsymbol{I}$ on the other hand, results according to (2.72) and (2.74) in $\boldsymbol{x} \equiv \boldsymbol{\chi}$ and $\hat{\boldsymbol{v}}(\boldsymbol{\chi}, t) = 0$, respectively, and gives rise to an Eulerian description. With a zero mesh velocity in the Eulerian description, the convective velocity is simply the particle velocity, that is $\boldsymbol{c} = \boldsymbol{v}$.

By way of illustration we derive the material acceleration $\boldsymbol{a}$ in Lagrangian, Eulerian and ALE formulations, with the corresponding equations given in the same order:

$$\boldsymbol{a} = \left.\frac{\partial \boldsymbol{v}}{\partial t}\right|_{\boldsymbol{X}} \tag{2.95a}$$

$$\boldsymbol{a} = \left.\frac{\partial \boldsymbol{v}}{\partial t}\right|_{\boldsymbol{x}} + \boldsymbol{v}\,\frac{\partial \boldsymbol{v}}{\partial \boldsymbol{x}} = \left.\frac{\partial \boldsymbol{v}}{\partial t}\right|_{\boldsymbol{x}} + \boldsymbol{v}\,\nabla_{\boldsymbol{x}}\boldsymbol{v} \tag{2.95b}$$

$$\boldsymbol{a} = \left.\frac{\partial \boldsymbol{v}}{\partial t}\right|_{\boldsymbol{\chi}} + \boldsymbol{c}\,\frac{\partial \boldsymbol{v}}{\partial \boldsymbol{x}} = \left.\frac{\partial \boldsymbol{v}}{\partial t}\right|_{\boldsymbol{\chi}} + (\boldsymbol{v} - \hat{\boldsymbol{v}})\,\nabla_{\boldsymbol{x}}\boldsymbol{v} \tag{2.95c}$$

2.6.2 Conservation equations in ALE formulation

The ALE framework requires the governing equations to be represented with respect to the referential domain. Therefore, in the following, the ALE formulation of the conservation equations for mass and linear momentum is presented, and shown to be a general representation inasmuch as it comes with the ability to be mapped to the conservation equations presented in Section 2.5. For the derivation of these equations, we refer to [17, 133].

2.6.2.1 Mass conservation equations in ALE formulation

The conservative form of the mass conservation equation written with respect to the referential domain Ω_χ is

$$\int_{\Omega_\chi} \left.\frac{\partial(\hat{J}\rho)}{\partial t}\right|_{\boldsymbol{\chi}} + \nabla_{\boldsymbol{\chi}} \cdot \left(\hat{J}\hat{\boldsymbol{F}}^{-1}\rho\,(\boldsymbol{v} - \hat{\boldsymbol{v}})\right)\,\mathrm{d}\Omega_\chi = 0 \tag{2.96}$$

which together with relation (2.82) can be written as

$$\int_{\Omega_\chi} \left.\frac{\partial(\hat{J}\rho)}{\partial t}\right|_{\boldsymbol{\chi}} + \nabla_{\boldsymbol{\chi}} \cdot \left(\hat{J}\rho\,\tilde{\boldsymbol{v}}\right)\,\mathrm{d}\Omega_\chi = 0. \tag{2.97}$$

Note that choosing the referential domain to be the material domain, that is, setting $\Omega_\chi = \Omega_X, \hat{\boldsymbol{v}} = \boldsymbol{v}, \hat{\boldsymbol{F}} = \boldsymbol{F}$ and $\hat{J} = J$, equation (2.96) yields the mass conservation law on the material domain:

$$\int_{\Omega_X} \left.\frac{\partial \rho_0}{\partial t}\right|_{\boldsymbol{X}} \mathrm{d}\Omega_X = 0, \tag{2.98}$$

where

$$\rho_0 = J\rho \tag{2.99}$$

denotes the mass density in the initial configuration.

On the other hand, setting $\Omega_\chi = \Omega_x$ implies $\hat{\boldsymbol{v}} = 0, \hat{\boldsymbol{F}} = \boldsymbol{I}$ and $\hat{J} = 1$ and as a consequence equation (2.96) yields the conservative form of the mass conservation equation (cf. (2.55)) written with respect to the spatial domain $\Omega_{\boldsymbol{x}}$:

$$\int_{\Omega_x} \left.\frac{\partial \rho}{\partial t}\right|_{\boldsymbol{x}} + \nabla_{\boldsymbol{x}} \cdot (\rho \boldsymbol{v})\,\mathrm{d}\Omega_x = 0. \tag{2.100}$$

Using the referential Piola identity, that is, the Piola identity (2.49) with regard to the map $\hat{\boldsymbol{\varphi}}$

$$\nabla_{\boldsymbol{\chi}} \cdot \left(\hat{J} \hat{\boldsymbol{F}}^{-T} \right) = 0, \tag{2.101}$$

and the transformation rules introduced in Section 2.4 now with respect to the map $\hat{\boldsymbol{\varphi}}$, equation (2.96) can be pushed forward to the current configuration, yielding a so-called *mixed* or *hybrid* form of the conservative mass conservation equation involving a referential time derivative and a spatial gradient:

$$\int_{\Omega_x = \hat{\varphi}(\Omega_\chi)} \hat{J}^{-1} \frac{\partial (\hat{J}\rho)}{\partial t}\bigg|_{\boldsymbol{\chi}} + \nabla_{\boldsymbol{x}} \cdot \left(\rho \left(\boldsymbol{v} - \hat{\boldsymbol{v}} \right) \right) \, \mathrm{d}\Omega_x = 0. \tag{2.102}$$

By means of the localization argument, the corresponding conservative differential (local) form is then simply

$$\hat{J}^{-1} \frac{\partial (\hat{J}\rho)}{\partial t}\bigg|_{\boldsymbol{\chi}} + \nabla_{\boldsymbol{x}} \cdot \left(\rho \left(\boldsymbol{v} - \hat{\boldsymbol{v}} \right) \right) = 0. \tag{2.103}$$

Using the identity

$$\frac{\partial \hat{J}}{\partial t}\bigg|_{\boldsymbol{\chi}} = \hat{J} \nabla_{\boldsymbol{x}} \cdot \hat{\boldsymbol{v}}, \tag{2.104}$$

and (2.46), the non-conservative (advective) form of the mass conservation equation written with respect to the referential domain Ω_χ is

$$\begin{aligned}
0 &= \int_{\Omega_\chi} \frac{\partial (\hat{J}\rho)}{\partial t}\bigg|_{\boldsymbol{\chi}} + \nabla_{\boldsymbol{\chi}} \cdot \left(\hat{J} \hat{\boldsymbol{F}}^{-1} \rho \boldsymbol{c} \right) \mathrm{d}\Omega_\chi \\
&= \int_{\Omega_\chi} \hat{J} \frac{\partial \rho}{\partial t}\bigg|_{\boldsymbol{\chi}} + \rho \frac{\partial \hat{J}}{\partial t}\bigg|_{\boldsymbol{\chi}} + \hat{J} \hat{\boldsymbol{F}}^{-1} \boldsymbol{c} \nabla_{\boldsymbol{\chi}} \rho + \rho \nabla_{\boldsymbol{\chi}} \cdot \left(\hat{J} \hat{\boldsymbol{F}}^{-1} \boldsymbol{v} \right) - \rho \nabla_{\boldsymbol{\chi}} \cdot \left(\hat{J} \hat{\boldsymbol{F}}^{-1} \hat{\boldsymbol{v}} \right) \mathrm{d}\Omega_\chi \\
&= \int_{\Omega_\chi} \hat{J} \frac{\partial \rho}{\partial t}\bigg|_{\boldsymbol{\chi}} + \rho \hat{J} \nabla_{\boldsymbol{x}} \cdot \hat{\boldsymbol{v}} + \hat{J} \hat{\boldsymbol{F}}^{-1} \boldsymbol{c} \nabla_{\boldsymbol{\chi}} \rho + \rho \nabla_{\boldsymbol{\chi}} \cdot \left(\hat{J} \hat{\boldsymbol{F}}^{-1} \boldsymbol{v} \right) - \rho \nabla_{\boldsymbol{\chi}} \cdot \left(\hat{J} \hat{\boldsymbol{F}}^{-1} \hat{\boldsymbol{v}} \right) \mathrm{d}\Omega_\chi \\
&= \int_{\Omega_\chi} \hat{J} \frac{\partial \rho}{\partial t}\bigg|_{\boldsymbol{\chi}} + \rho \nabla_{\boldsymbol{\chi}} \cdot \left(\hat{J} \hat{\boldsymbol{F}}^{-1} \hat{\boldsymbol{v}} \right) + \hat{J} \hat{\boldsymbol{F}}^{-1} \boldsymbol{c} \nabla_{\boldsymbol{\chi}} \rho + \rho \nabla_{\boldsymbol{\chi}} \cdot \left(\hat{J} \hat{\boldsymbol{F}}^{-1} \boldsymbol{v} \right) - \rho \nabla_{\boldsymbol{\chi}} \cdot \left(\hat{J} \hat{\boldsymbol{F}}^{-1} \hat{\boldsymbol{v}} \right) \mathrm{d}\Omega_\chi \\
&= \int_{\Omega_\chi} \hat{J} \frac{\partial \rho}{\partial t}\bigg|_{\boldsymbol{\chi}} + \hat{J} \hat{\boldsymbol{F}}^{-1} \boldsymbol{c} \nabla_{\boldsymbol{\chi}} \rho + \rho \nabla_{\boldsymbol{\chi}} \cdot \left(\hat{J} \hat{\boldsymbol{F}}^{-1} \boldsymbol{v} \right) \mathrm{d}\Omega_\chi .
\end{aligned} \tag{2.105}$$

Equation (2.105) may be pushed forward to the current configuration in order to obtain the advective and mixed form of the mass conservation equation written with respect to the spatial domain:

$$\int_{\Omega_x = \hat{\varphi}(\Omega_\chi)} \frac{\partial \rho}{\partial t}\bigg|_{\boldsymbol{\chi}} + \boldsymbol{c} \cdot \nabla_{\boldsymbol{x}} \rho + \rho \nabla_{\boldsymbol{x}} \cdot \boldsymbol{v} \, \mathrm{d}\Omega_x = 0. \tag{2.106}$$

Note that using expression (2.94) the above equation may be written as

$$\begin{aligned}
&\int_{\Omega_x = \hat{\varphi}(\Omega_\chi)} \frac{\partial \rho}{\partial t}\bigg|_{\boldsymbol{x}} + \boldsymbol{v} \cdot \nabla_{\boldsymbol{x}} \rho + \rho \nabla_{\boldsymbol{x}} \cdot \boldsymbol{v} \, \mathrm{d}\Omega_x = 0, \qquad \text{or} \\
&\int_{\Omega_x = \hat{\varphi}(\Omega_\chi)} \frac{\partial \rho}{\partial t}\bigg|_{\boldsymbol{X}} + \rho \nabla_{\boldsymbol{x}} \cdot \boldsymbol{v} \, \mathrm{d}\Omega_x = 0,
\end{aligned} \tag{2.107}$$

where the local form of the latter expression, that is

$$\left.\frac{\partial \rho}{\partial t}\right|_{\boldsymbol{X}} + \rho \nabla_{\boldsymbol{x}} \cdot \boldsymbol{v} = 0 \tag{2.108}$$

is nothing but the non-conservative differential form (2.57).

Remark 2.6.1. *Using the identity*

$$\left.\frac{\partial J}{\partial t}\right|_{\boldsymbol{X}} = J \nabla_{\boldsymbol{x}} \cdot \boldsymbol{v},$$

the Lagrangian description of the mass conservation equation, given through the local form of (2.98)*, is recovered from* (2.108) *as follows*

$$\left.\frac{\partial (\rho J)}{\partial t}\right|_{\boldsymbol{X}} = \rho \left.\frac{\partial J}{\partial t}\right|_{\boldsymbol{X}} + J \left.\frac{\partial \rho}{\partial t}\right|_{\boldsymbol{X}} = \rho J \nabla_{\boldsymbol{x}} \cdot \boldsymbol{v} + J \left.\frac{\partial \rho}{\partial t}\right|_{\boldsymbol{X}} = \rho J \nabla_{\boldsymbol{x}} \cdot \boldsymbol{v} - J \rho \nabla_{\boldsymbol{x}} \cdot \boldsymbol{v} = 0. \tag{2.109}$$

2.6.2.2 Linear momentum conservation equations in ALE formulation

The conservative form of the linear momentum conservation equation written with respect to the referential domain Ω_χ is

$$\int_{\Omega_\chi} \left.\frac{\partial (\hat{J} \rho \boldsymbol{v})}{\partial t}\right|_{\boldsymbol{\chi}} + \nabla_{\boldsymbol{\chi}} \cdot \left((\rho \boldsymbol{v} \otimes (\boldsymbol{v} - \hat{\boldsymbol{v}}) - \boldsymbol{\sigma}) \hat{J} \hat{\boldsymbol{F}}^{-T} \right) - \hat{J} \rho \boldsymbol{b} \, \mathrm{d}\Omega_\chi = 0 \tag{2.110}$$

which together with the definition $\hat{\boldsymbol{P}} = \hat{J} \boldsymbol{\sigma} \hat{\boldsymbol{F}}^{-T}$ for the first Piola-Kirchhoff stress tensor w.r.t. the map $\hat{\boldsymbol{\varphi}}$ and relation (2.82) can be written as

$$\int_{\Omega_\chi} \left.\frac{\partial (\hat{J} \rho \boldsymbol{v})}{\partial t}\right|_{\boldsymbol{\chi}} + \nabla_{\boldsymbol{\chi}} \cdot \left((\hat{J} \rho \boldsymbol{v}) \otimes \tilde{\boldsymbol{v}} - \hat{\boldsymbol{P}} \right) - \hat{J} \rho \boldsymbol{b} \, \mathrm{d}\Omega_\chi = 0. \tag{2.111}$$

With the prerequisites for the derivation of equation (2.98), the linear momentum conservation law on the material domain Ω_X is obtained from equation (2.110) as

$$\begin{aligned} &\int_{\Omega_X} \left.\frac{\partial (J \rho \boldsymbol{v})}{\partial t}\right|_{\boldsymbol{X}} - \nabla_{\boldsymbol{X}} \cdot \left(J \boldsymbol{\sigma} \boldsymbol{F}^{-T} \right) - J \rho \boldsymbol{b} \, \mathrm{d}\Omega_X = 0, \qquad \text{or} \\ &\int_{\Omega_X} \left.\frac{\partial (\rho_0 \boldsymbol{v})}{\partial t}\right|_{\boldsymbol{X}} - \nabla_{\boldsymbol{X}} \cdot \boldsymbol{P} - \rho_0 \boldsymbol{b} \, \mathrm{d}\Omega_X = 0, \end{aligned} \tag{2.112}$$

where $\boldsymbol{P}$ is the first Piola-Kirchhoff stress tensor w.r.t. the map $\boldsymbol{\varphi}$ (cf. equation (2.35)). By analogy to the mass conservation case, the application of the prerequisites of equation (2.100) to (2.110), yields the conservative linear momentum conservation equation (cf. (2.59)) expressed with respect to the spatial domain Ω_x:

$$\int_{\Omega_x} \left.\frac{\partial (\rho \boldsymbol{v})}{\partial t}\right|_{\boldsymbol{x}} + \nabla_{\boldsymbol{x}} \cdot (\rho \boldsymbol{v} \otimes \boldsymbol{v} - \boldsymbol{\sigma}) - \rho \boldsymbol{b} \, \mathrm{d}\Omega_x = 0. \tag{2.113}$$

The push forward of equation (2.110) to the current configuration yields

$$\int_{\Omega_x = \hat{\varphi}(\Omega_\chi)} \hat{J}^{-1} \left.\frac{\partial (\hat{J} \rho \boldsymbol{v})}{\partial t}\right|_{\boldsymbol{\chi}} + \nabla_{\boldsymbol{x}} \cdot (\rho \boldsymbol{v} \otimes (\boldsymbol{v} - \hat{\boldsymbol{v}}) - \boldsymbol{\sigma}) - \rho \boldsymbol{b} \, \mathrm{d}\Omega_x = 0, \tag{2.114}$$

from which the following conservative differential (local) form is obtained after localization

$$\hat{J}^{-1}\frac{\partial(\hat{J}\rho\boldsymbol{v})}{\partial t}\bigg|_{\boldsymbol{\chi}} + \nabla_{\boldsymbol{x}}\cdot\left(\rho\boldsymbol{v}\otimes(\boldsymbol{v}-\hat{\boldsymbol{v}})-\boldsymbol{\sigma}\right)-\rho\boldsymbol{b}=0. \tag{2.115}$$

The non-conservative (advective) form of the linear momentum conservation equation written with respect to the referential domain Ω_χ is given through the expression

$$\int_{\Omega_\chi}\hat{J}\rho\frac{\partial\boldsymbol{v}}{\partial t}\bigg|_{\boldsymbol{\chi}} + \hat{J}\rho\nabla_{\boldsymbol{\chi}}\boldsymbol{v}\left(\hat{\boldsymbol{F}}^{-1}\boldsymbol{c}\right)-\nabla_{\boldsymbol{\chi}}\cdot\left(\hat{J}\boldsymbol{\sigma}\hat{\boldsymbol{F}}^{-T}\right)-\hat{J}\rho\boldsymbol{b}\,\mathrm{d}\Omega_\chi=0 \tag{2.116}$$

which, using $\hat{\boldsymbol{P}}$ and (2.82), can also be written as

$$\int_{\Omega_\chi}\hat{J}\rho\frac{\partial\boldsymbol{v}}{\partial t}\bigg|_{\boldsymbol{\chi}} + \hat{J}\rho\left(\nabla_{\boldsymbol{\chi}}\boldsymbol{v}\right)\tilde{\boldsymbol{v}}-\nabla_{\boldsymbol{\chi}}\cdot\hat{\boldsymbol{P}}-\hat{J}\rho\boldsymbol{b}\,\mathrm{d}\Omega_\chi=0. \tag{2.117}$$

Just as (2.113) was obtained from (2.110), we will show in the sequel that the equation for the non-conservative linear momentum conservation written with respect to the spatial domain can be obtained from the corresponding non-conservative ALE form (2.116). With the prerequisites for the derivation of equation (2.100), the ALE form (2.116) yields

$$\int_{\Omega_x}\rho\frac{\partial\boldsymbol{v}}{\partial t}\bigg|_{\boldsymbol{x}} + \rho\,\boldsymbol{v}\cdot\nabla_{\boldsymbol{x}}\boldsymbol{v}-\nabla_{\boldsymbol{x}}\cdot\boldsymbol{\sigma}-\rho\boldsymbol{b}\,\mathrm{d}\Omega_x=0, \tag{2.118}$$

whose local form

$$\rho\frac{\partial\boldsymbol{v}}{\partial t}\bigg|_{\boldsymbol{x}} + \rho\,\boldsymbol{v}\cdot\nabla_{\boldsymbol{x}}\boldsymbol{v}-\nabla_{\boldsymbol{x}}\cdot\boldsymbol{\sigma}-\rho\boldsymbol{b}=\rho\frac{D\boldsymbol{v}}{Dt}-\nabla_{\boldsymbol{x}}\cdot\boldsymbol{\sigma}-\rho\boldsymbol{b}=0 \tag{2.119}$$

is nothing but (2.62).

Eventually, pushing forward equation (2.116) to the current configuration, yields the corresponding mixed or hybrid form

$$\int_{\Omega_x=\hat{\varphi}(\Omega_\chi)}\rho\frac{\partial\boldsymbol{v}}{\partial t}\bigg|_{\boldsymbol{\chi}} + \rho\left(\nabla_{\boldsymbol{x}}\boldsymbol{v}\right)\boldsymbol{c}-\nabla_{\boldsymbol{x}}\cdot\boldsymbol{\sigma}-\rho\boldsymbol{b}\,\mathrm{d}\Omega_x=0. \tag{2.120}$$

Chapter 3

Single-phase flow

3.1 Introduction

Breaking down the multiphysics problem of binary-fluid-structure interaction into its essential parts, one of these parts is the two-phase (or binary-fluid) flow problem that is treated in Chapter 4. The two-phase flow problem, however, is built on top of the standard or "single-phase" flow problem to whom we have dedicated the present chapter. This chapter lays the foundation for the simulation of the fluid part of the overall BFSI problem. More specifically, in this chapter we are concerned with the application and assessment of the Isogeometric Analysis approach to fluid flows with respect to well known benchmark problems. The assessments performed in this chapter are crucial for the validation of intermediate results prior to moving on to more complex problems.

That being said, we present our numerical results for the lid-driven cavity flow problem (including its regularized version) using different B-spline approximation spaces, and compare them to reference results from literature. Moreover, in addition to comparisons with classical references, we will whenever feasible take into consideration the results of two recently published articles [54, 144] on the application of Galerkin-based IGA to the cavity flow problem. The analysis presented in [144] is based on a scalar stream function formulation of the Navier-Stokes equations, while [54] uses divergence-conforming B-splines which may be interpreted as smooth generalizations of Raviart-Thomas elements. We extend this Galerkin IGA-based row of results for cavity flow with data obtained from the application of smooth generalizations of Taylor-Hood elements. Despite the fact that investigations of lid-driven cavity type model problems do not necessarily reflect the current spirit of time, they are nonetheless a natural first choice in computational fluid dynamics when it comes to assessing the properties of a novel numerical technique.

Subsequent to lid-driven cavity, we eventually proceed to present and assess approximated physical quantities such as the drag and lift coefficients obtained for the flow around cylinder benchmark, whereby a multi-patch discretization approach is adopted. For the scenarios addressed, Isogeometric Analysis is applied to the steady-state as well as to the transient incompressible Navier-Stokes equations. For the equations under consideration are of nonlinear nature, we decided to provide a rather detailed insight concerning their treatment. The efficient solution of the discretized system of equations using iterative solution techniques such as, for instance, multigrid is not addressed in this work. Preliminary research results are underway and will be presented in a forthcoming publication. In numerical studies performed in this work, all systems of equations have been solved with a direct solver.

The outline of this chapter is as follows: Section 3.2 is devoted to a concise introduction to a few chosen aspects of Isogeometric Analysis that we considered relevant for this work. This presentation is quite brief and notationally oriented. A more complete introduction to NURBS and Isogeometric Analysis can be found in [16, 37, 119]. Section 3.3 formalizes Taylor-Hood like discrete approximation spaces being used in different peculiarities throughout this chapter. Section 3.4 is dedicated to the presentation of the governing equations and their variational forms. The numerical results are showcased in Section 3.5. In particular, in Sections 3.5.2 and 3.5.4, numerical results of Isogeometric Analysis of lid-driven cavity flow and flow around cylinder are presented and compared with reference results from literature. Section 3.6 is dedicated to a short summary in addition to drawn conclusions.

3.2 Intermezzo – A digest of a few chosen aspects of IGA

Consistently applying Galerkin-based Isogeometric Analysis for the discretization of various partial differential equations considered throughout this work, makes it necessary to at least briefly address this new paradigm in the numerical approximation of PDEs. Towards this end, this section provides a very concise overview over some aspects of Galerkin-based Isogeometric Analysis that are relevant to this work. This includes a few notes on the general idea, the utilized basis functions, geometry representations, and the existence, uniqueness and convergence of solutions. The idea is just to fix the notation for everything that is IGA-related in the present and subsequent chapters of this work. We deliberately refrain from dedicating an entire chapter to IGA, since the topic is very comprehensive and its description outside the scope of this work. We consider an "intermezzo" in the form of this (embedded) section to be more appropriate. For a detailed introduction to IGA we refer to standard text books such as [30, 37].

The Isogeometric Analysis technique, developed by Hughes et al. [37], is a powerful numerical technique aiming to bridge the gap between the worlds of computer-aided engineering (CAE) and computer-aided design (CAD). It combines the benefits of Finite Element Analysis (FEA) with the ability of an exact representation of complex computational domains via an elegant mathematical description in the form of uni-, bi- or trivariate non-uniform rational B-splines. Non-Uniform Rational B-splines (NURBS) are the de facto industry standard when it comes to modeling complex geometries, while FEA is a numerical approximation technique that is widely used in computational mechanics.

NURBS and FEA utilize basis functions for the representation of geometry and approximation of field variables, respectively. In order to close the gap between the two technologies, Isogeometric Analysis adopts the B-spline, NURBS or T-spline (see [37]) geometry as the computational domain and utilizes its basis functions to construct both trial and test spaces in the discrete variational formulation of differential problems. The usage of these functions allows the construction of approximation spaces exhibiting higher regularity ($\mathcal{C}^{\geq 0}$) which – depending on the problem to be solved – may be beneficial compared to standard finite element spaces. For instance, Cottrell, Hughes and Reali showed in their study of refinement and continuity in isogeometric structural analysis [38] that increased smoothness leads to a significant increase in accuracy for the problems of structural vibrations over the classical $\mathcal{C}^0$ continuous p-method of FEA. Isogeometric Analysis has been successfully applied to high order partial differential equations (PDEs) from a wide range of fields of computational mechanics. In fact, primal variational formulations of high order PDEs such as Navier-Stokes-Korteweg (3rd order spatial derivatives) or Cahn-Hilliard (4th order spatial derivatives) require piecewise smooth and globally $\mathcal{C}^1$ continuous basis functions. Note that the number of finite elements possessing $\mathcal{C}^1$ continuity and being applicable to complex geometries is already very limited in two dimensions [75, 76]. The Isogeometric Analysis technology features a unique combination of attributes, namely, superior accuracy on degree of freedom basis, robustness, two- and three-dimensional geometric flexibility, compact support, and the possibility for $\mathcal{C}^{\geq 0}$ continuity [37].

Galerkin-based Isogeometric Analysis adopts spline (B-spline/NURBS, etc.) basis functions for analysis as well as for the description of the geometry (computational domain). Just like in FEA, a discrete approximation space – based on the span of the basis functions in charge – is constructed and eventually used in the framework of a Galerkin procedure for the numerical approximation of the solution of partial differential equations[11].

Recalling reference ($\tilde{\Omega}$) and physical domains (Ω) in FEA, using B-splines/NURBS, one additional domain – the parametric spline domain ($\hat{\Omega}$) – needs to be considered as well (see Fig. 3.1). We follow this requirement and present an insight in the traits of spline-based discrete approximation spaces in the sequel.

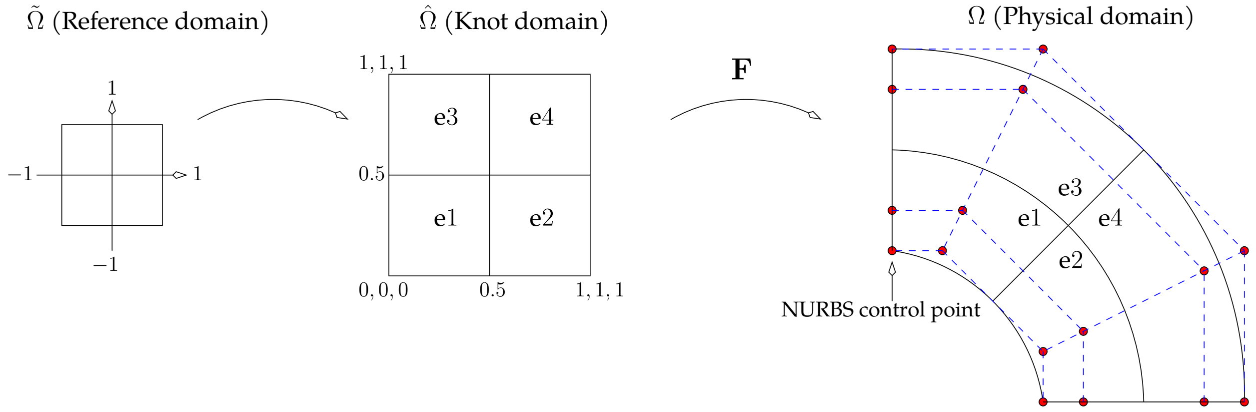

Figure 3.1: Domains involved in Isogeometric Analysis. Left: Reference domain used to evaluate integrals; Center: Exemplary parametric spline domain with knot vectors $\Xi_u = \Xi_v := \{0, 0, 0, 0.5, 1, 1, 1\}$ defining four elements $(e0, \dots, e3)$, two in each parametric direction. Right: Image of the knot space coordinates under the parametrization $\mathbf{F}$.

3.2.1 Basis functions

Given two positive integers p and n, we introduce the ordered knot vector

$$\Xi := \{0 = \xi_1, \xi_2, \dots, \xi_m = 1\}, \tag{3.1}$$

whereby repetitions of the $m = n+p+1$ knots ξ_i are allowed: $\xi_1 \leq \xi_2 \leq \cdots \leq \xi_m$. Note that in (3.1) the values of Ξ are normalized to the range $[0, 1]$ merely for the sake of clarity and not restricted in range otherwise. Besides, we assume that Ξ is an open knot vector, that is, the first and last knots have multiplicity $p + 1$: $\Xi = \{\underbrace{0, \dots, 0}_{p+1}, \xi_{p+2}, \dots, \xi_{m-p-1}, \underbrace{1, \dots, 1}_{p+1}\}$.

---

[11] We point out on a side note that IGA is not restricted to the Galerkin framework and has as a matter of fact been successfully used with Collocation techniques as well, see for instance [8, 130].

Let the (univariate) B-spline basis functions of degree[12] p be denoted by $B_{i,p}(\xi)$, for $i = 1, \ldots, n$. Then, the ith B-spline basis function is a piecewise polynomial function and it is recursively defined by the Cox-de Boor recursion formula:

$$\begin{aligned} B_{i,0}(\xi) &= \begin{cases} 1, & \text{if } \xi_i \leq \xi < \xi_{i+1} \\ 0, & \text{otherwise} \end{cases} \\ B_{i,p}(\xi) &= \frac{\xi - \xi_i}{\xi_{i+p} - \xi_i} B_{i,p-1}(\xi) + \frac{\xi_{i+p+1} - \xi}{\xi_{i+p+1} - \xi_{i+1}} B_{i+1,p-1}(\xi), \quad p > 0. \end{aligned} \tag{3.2}$$

At knot ξ_i the basis functions have $\alpha := p - r_i$ continuous derivatives, where r_i denotes the multiplicity of knot ξ_i. The quantity α is bounded from below and above by $-1 \leq \alpha \leq p - 1$. Thus, the maximum multiplicity allowed is $r_i = p + 1$, rendering the basis functions at ξ_i discontinuous as it is the case at the boundaries of the interval. Each basis function $B_{i,p}$ is non-negative over the entire domain, that is, $B_{i,p}(\xi) \geq 0, \forall \xi$ and has a local support property: $B_{i,p}(\xi) = 0$, if ξ is outside the interval $[\xi_i, \xi_{i+p+1})$. The half-open interval $[\xi_i, \xi_{i+1})$ is referred to as a knot span (ith knot span; possibly of zero length) or element in IGA speak. Moreover, the B-spline basis functions are linearly independent and constitute a partition of unity, that is,

$$\sum_{i=1}^{n} B_{i,p}(\xi) = 1, \text{ for all } \xi \in [0, 1]. \tag{3.3}$$

Figure 3.2 illustrates the basis functions of degree 2 of an exemplary knot vector exhibiting different levels of continuity. Due to the recursive definition (3.2), the derivative of the ith B-spline basis function is given by

$$\frac{d}{d\xi} B_{i,p}(\xi) = B'_{i,p}(\xi) = \frac{p}{\xi_{i+p} - \xi_i} B_{i,p-1}(\xi) - \frac{p}{\xi_{i+p+1} - \xi_{i+1}} B_{i+1,p-1}(\xi) \tag{3.4}$$

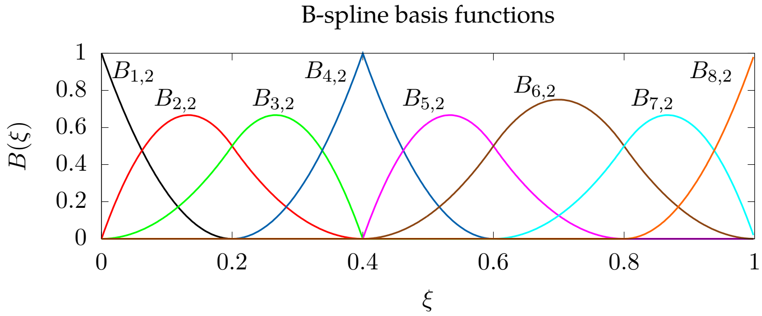

Figure 3.2: Plot of B-spline basis functions of degree 2 corresponding to the open knot vector $\Xi := \{0, 0, 0, 0.2, 0.4, 0.4, 0.6, 0.8, 1, 1, 1\}$. Due to the open knot vector trait, the first and last basis functions are interpolatory, that is, they take the value 1 at the first and last knot. At an interior knot ξ_i the continuity is $\mathcal{C}^{p-r_i}$ with r_i denoting the multiplicity of knot ξ_i. Due to the multiplicity $r_5 = 2$ of knot $\xi_5 = 0.4$, the continuity of the basis functions across this parametric point is $\mathcal{C}^{p-2} = \mathcal{C}^0$, while at the other interior knots the continuity is $\mathcal{C}^{p-1} = \mathcal{C}^1$.

---

[12] *Degree* and *order* are differently defined in geometry and analysis contexts. For instance, a quadratic polynomial has for Geometers degree 2 and order 3 (degree + 1), whereas for Analysts the same polynomial is of order 2. The latter use the notion degree and order synonymously. We adhere to this convention in this work.

which is a combination of lower order B-spline functions. The generalization to higher derivatives is straightforward by simply differentiating each side of the above relation.

Univariate rational B-spline basis functions are obtained by augmenting the set of B-spline basis functions with weights w_i and defining

$$\begin{aligned} R_{i,p}(\xi) &= \frac{B_{i,p}(\xi)w_i}{W(\xi)}, \\ W(\xi) &= \sum_{j=1}^{n} B_{j,p}(\xi)w_j. \end{aligned} \tag{3.5}$$

Above, the function $R_{i,p}(\xi)$ represents a projective transformation [119] using the polynomial weighting function $W(\xi)$. The derivative of the NURBS basis function $R_{i,p}(\xi)$ is obtained by applying the quotient rule:

$$\begin{aligned} \frac{d}{d\xi}R_{i,p}(\xi) &= w_i\frac{B'_{i,p}(\xi)W(\xi) - B_{i,p}(\xi)W'(\xi)}{W^2(\xi)}, \\ W'(\xi) &= \sum_{i=1}^{n} B'_{i,p}(\xi)w_i. \end{aligned} \tag{3.6}$$

By setting all weighting coefficients equal to one it follows that B-splines are just a special case of NURBS.

The space of B-splines of degree p and regularity α determined by the knot vector Ξ is spanned by the basis functions $B_{i,p}$ and will be denoted by

$$\mathcal{S}^p_\alpha \equiv \mathcal{S}^p_\alpha(\Xi, p) := \operatorname{span}\{B_{i,p}\}_{i=1}^n. \tag{3.7}$$

Analogously, we define the space spanned by rational B-spline basis functions as

$$\mathcal{N}^p_\alpha \equiv \mathcal{N}^p_\alpha(\Xi, p, w) := \operatorname{span}\{R_{i,p}\}_{i=1}^n. \tag{3.8}$$

The definition of univariate B-spline spaces can readily be extended to higher dimensions. To this end, we consider d knot vectors Ξ_β, $1 \leq \beta \leq d$ and an open parametric domain $(0,1)^d \in \mathbb{R}^d$. The knot vectors Ξ_β partition the parametric domain $(0,1)^d$ into d-dimensional open knot spans, or elements, and thus yield a mesh $\mathcal{Q}$ being defined as

$$\mathcal{Q} \equiv \mathcal{Q}(\Xi_1, \ldots, \Xi_d) := \{Q = \otimes_{\beta=1}^d(\xi_{i_\beta,\beta}, \xi_{i_\beta+1,\beta}) \mid Q \neq \emptyset,\ 1 \leq i < m_\beta\} \tag{3.9}$$

For an element $Q \in \mathcal{Q}$, we set $h_Q = \text{diam}(Q)$, and define the global mesh size $h = \max\{h_Q, Q \in \mathcal{Q}\}$. We define the tensor product B-spline and NURBS basis functions as

$$B_{i_1,\ldots,i_d} := B_{i_1,1} \otimes \cdots \otimes B_{i_d,d}, \quad i_1 = 1,\ldots,n_1, \quad i_d = 1,\ldots,n_d \tag{3.10}$$

and

$$R_{i_1,\ldots,i_d} := R_{i_1,1} \otimes \cdots \otimes R_{i_d,d}, \quad i_1 = 1,\ldots,n_1, \quad i_d = 1,\ldots,n_d, \tag{3.11}$$

respectively. For $d = 2$ for instance, the bivariate B-spline and NURBS basis functions (and derivatives) of degrees p and q in the respective directions, are defined as

$$\begin{aligned} B_{i,j}^{p,q}(\xi,\eta) &= B_{i,p}(\xi)B_{j,q}(\eta), \\ \frac{\partial B_{i,j}^{p,q}(\xi,\eta)}{\partial\xi} &= \frac{d}{d\xi}\Big(B_{i,p}(\xi)\Big)B_{j,q}(\eta), \\ \frac{\partial B_{i,j}^{p,q}(\xi,\eta)}{\partial\eta} &= B_{i,p}(\xi)\frac{d}{d\eta}\Big(B_{j,q}(\eta)\Big), \end{aligned} \tag{3.12}$$

$$R_{i,j}^{p,q}(\xi,\eta) = \frac{B_{i,p}(\xi)B_{j,q}(\eta)w_{i,j}}{W(\xi,\eta)}, \quad W(\xi,\eta) = \sum_{i=1}^{n}\sum_{j=1}^{m} B_{i,p}(\xi)B_{j,q}(\eta)w_{i,j}. \tag{3.13}$$

$$\begin{aligned} \frac{\partial R_{i,j}^{p,q}(\xi,\eta)}{\partial\xi} &= w_{i,j}\frac{B'_{i,p}(\xi)B_{j,q}(\eta)W(\xi,\eta) - B_{i,p}(\xi)B_{j,q}(\eta)W'_\xi(\xi,\eta)}{W^2(\xi,\eta)}, \\ \frac{\partial R_{i,j}^{p,q}(\xi,\eta)}{\partial\eta} &= w_{i,j}\frac{B_{i,p}(\xi)B'_{j,q}(\eta)W(\xi,\eta) - B_{i,p}(\xi)B_{j,q}(\eta)W'_\eta(\xi,\eta)}{W^2(\xi,\eta)}, \\ W'_\xi(\xi,\eta) &= \sum_{i=1}^{n}\sum_{j=1}^{m} B'_{i,p}(\xi)B_{j,q}(\eta)w_{i,j}, \quad W'_\eta(\xi,\eta) = \sum_{i=1}^{n}\sum_{j=1}^{m} B_{i,p}(\xi)B'_{j,q}(\eta)w_{i,j}. \end{aligned} \tag{3.14}$$

Then, the tensor product B-spline and NURBS spaces, spanned by the respective basis functions, are defined as

$$\mathcal{S} \equiv \mathcal{S}_{\alpha_1,\dots,\alpha_d}^{p_1,\dots,p_d} \equiv \mathcal{S}_{\alpha_1,\dots,\alpha_d}^{p_1,\dots,p_d}(\mathcal{Q}) := \mathcal{S}_{\alpha_1}^{p_1} \otimes \cdots \otimes \mathcal{S}_{\alpha_d}^{p_d} = \operatorname{span}\{B_{i_1\dots i_d}\}_{i_1=1,\dots,i_d=1}^{n_1,\dots,n_d} \tag{3.15}$$

and

$$\mathcal{N} \equiv \mathcal{N}_{\alpha_1,\dots,\alpha_d}^{p_1,\dots,p_d} \equiv \mathcal{N}_{\alpha_1,\dots,\alpha_d}^{p_1,\dots,p_d}(\mathcal{Q}) := \mathcal{N}_{\alpha_1}^{p_1} \otimes \cdots \otimes \mathcal{N}_{\alpha_d}^{p_d} = \operatorname{span}\{R_{i_1\dots i_d}\}_{i_1=1,\dots,i_d=1}^{n_1,\dots,n_d}, \tag{3.16}$$

respectively. The space $\mathcal{S}_{\alpha_1,\dots,\alpha_d}^{p_1,\dots,p_d}$ is fully characterized by the mesh $\mathcal{Q}$, the degrees $p_1,\dots,p_d$ of basis functions and their continuities $\alpha_1,\dots,\alpha_d$. The minimum regularity/continuity of the space is $\alpha := \min\{\alpha_i, i \in (1,d)\}$. A mesh stack $\{\mathcal{Q}_h\}_{h\le h_0}$, with affiliated spaces $(\mathcal{S}_h,\mathcal{N}_h)$, can be constructed via knot insertion as described, e.g., in [37] from an initial coarse mesh $\mathcal{Q}_0$, with the global mesh size h pointing to a refinement level index.

For a representation of the elements in the physical domain Ω, the mesh $\mathcal{Q}$ is mapped to the physical space via a NURBS geometrical map $\mathbf{F} : \hat{\Omega} \to \Omega$

$$\mathbf{F} = \sum_{i_1=1}^{n_1}\cdots\sum_{i_d=1}^{n_d} R_{i_1,\dots,i_d}(\xi_{i_1},\dots,\xi_{i_d})\mathbf{P}_{i_1,\dots,i_d} \tag{3.17}$$

yielding a mesh $\mathcal{K}$, with

$$\mathcal{K} = \mathbf{F}(Q) := \{\mathbf{F}(\boldsymbol{\xi}) \,|\, \boldsymbol{\xi} \in Q\}. \tag{3.18}$$

In equation (3.17), $\mathbf{P}$, denotes a homogeneous NURBS control point uniquely addressed in the NURBS tensor product mesh by its indices. $\mathbf{F}$ denotes a parametrization of the physical domain Ω and we assume that it is invertible, with smooth inverse, on each element $Q \in \mathcal{Q}$. With the definition of $\mathbf{F}$ in hand, the space $\mathcal{V}$ of NURBS basis functions on Ω, being the *push-forward* of the space $\mathcal{N}$, is defined as

$$\mathcal{V}_{\alpha_1,\dots,\alpha_d}^{p_1,\dots,p_d} \equiv \mathcal{V}_{\alpha_1,\dots,\alpha_d}^{p_1,\dots,p_d}(\mathcal{K}) := \mathcal{V}_{\alpha_1}^{p_1} \otimes \cdots \otimes \mathcal{V}_{\alpha_d}^{p_d} = \operatorname{span}\{R_{i_1\dots i_d}^{\text{phys}} = R_{i_1\dots i_d} \circ \mathbf{F}^{-1}\}_{i_1=1,\dots,i_d=1}^{n_1,\dots,n_d} \tag{3.19}$$

3.2.2 Geometry representation

Isogeometric Analysis is based on the idea to perform analysis directly on the geometries that are used in CAD, and to use the same functions that exactly describe geometry also for analysis. Since it is very common in CAD to describe geometries with NURBS and we have already presented their basis functions, in the sequel we will briefly present a few key aspects of geometry representation that are relevant for the present work. Linear combinations of B-spline or NURBS basis functions can be used to describe geometry in $\mathbb{R}^d$. We will briefly discuss the concept for B-splines and show how it extends to NURBS. Given n pth-degree B-spline basis functions, $B_{i,p}, i = 1, 2, \dots, n$ defined on the knot vector

$$\Xi = \{\xi_1, \dots \xi_{m=n+p+1}\} = \{\underbrace{0, \dots, 0}_{p+1}, \xi_{p+2}, \dots, \xi_{m-p-1}, \underbrace{1, \dots, 1}_{p+1}\}$$

and corresponding vector-valued coefficients also known as control points $\mathbf{P}_i \in \mathbb{R}^d, i = 1, 2, \dots, n$, a piecewise polynomial B-spline curve of degree p is given by

$$\mathbf{C}(\xi) = \sum_{i=1}^{n} B_{i,p}(\xi)\mathbf{P}_i, \quad 0 \leq \xi \leq 1. \tag{3.20}$$

A piecewise linear interpolation of the control points yields a so-called control polygon. Note that higher dimensional geometries such as surfaces and volumes can be easily created from the tensor product of B-spline curves. For instance, given a control net $\{\mathbf{P}_{i,j}\}, i = 1, \dots, n,\ j = 1, \dots, m$, polynomial degrees p and q, and univariate B-spline basis functions $B_{i,p}(\xi)$ and $B_{j,q}(\eta)$ respectively defined on knot vectors

$$\Xi = \{\xi_1, \dots \xi_{r=n+p+1}\} = \{\underbrace{0, \dots, 0}_{p+1}, \xi_{p+2}, \dots, \xi_{r-p-1}, \underbrace{1, \dots, 1}_{p+1}\}, \text{ and}$$
$$E = \{\eta_1, \dots \eta_{s=m+q+1}\} = \{\underbrace{0, \dots, 1}_{q+1}, \xi_{q+2}, \dots, \xi_{s-q-1}, \underbrace{1, \dots, 1}_{q+1}\},$$

a tensor product B-spline surface is defined by the following expression

$$\mathbf{S}(\xi, \eta) = \sum_{i=1}^{n} \sum_{j=1}^{m} B_{i,p}(\xi) B_{j,q}(\eta) \mathbf{P}_{i,j}, \quad 0 \leq \xi, \eta \leq 1. \tag{3.21}$$

Tensor product B-spline volumes (a.k.a. solids) can be created likewise. B-spline and NURBS geometries have various interesting properties whose discussion is, however, outside the scope of this work. We refer to [119] for more information on this topic. While B-splines are capable of describing complex geometries with a fairly little amount of control points, they fail to *exactly* represent conic sections such as circles or ellipses. To give an example, a unit circle in the xy plane, centered at the origin, cannot be represented using polynomial coordinate functions [119]. This shortcoming is eliminated by NURBS due to their ability to exactly represent all conic sections, and therefore giving rise to the exact representation of spheres, cylinders, tori, and ellipsoids. NURBS address this shortcoming of B-splines by means of *rational functions* that are defined as the ratio of two polynomials. More specifically, conic curves including the circle can be represented with rational functions of the form

$$x(\xi) = \frac{X(\xi)}{W(\xi)}, \quad y(\xi) = \frac{Y(\xi)}{W(\xi)}, \tag{3.22}$$

where $X(\xi), Y(\xi)$, and $W(\xi)$ are polynomials, and each of the coordinate functions has the same denominator. Inspired by projective geometry, the idea is to use *homogeneous coordinates* to represent a *rational* curve in n-dimensional space with a *polynomial* curve in $(n+1)$-dimensional space [119]. In three-dimensional Euclidean space for instance, a point $\mathbf{P} = (x, y, z) \in \mathbb{R}^3$ is augmented with a weight $w \neq 0$ so as to obtain a homogeneous-coordinate point $\mathbf{P}^w = (wx, wy, wz, w) = (X, Y, Z, W) \in \mathbb{R}^4$. Note that $\mathbf{P}$ is obtained by the projection of $\mathbf{P}^w$ onto the $W = 1$ hyperplane by a ray through the origin. The corresponding operator is a perspective map H with center at the origin, reading

$$\mathbf{P} = H\{\mathbf{P}^w\} = H\{(X, Y, Z, W)\} = \begin{cases} (\frac{X}{W}, \frac{Y}{W}, \frac{Z}{W}) & \text{if } W \neq 0, \\ \text{direction } (X, Y, Z) & \text{if } W = 0. \end{cases} \tag{3.23}$$

Now, given a set of control points $\{\mathbf{P}_i\}$ and corresponding weights w_i, a nonrational (piecewise polynomial) B-spline curve of degree p in four-dimensional space is given through the following definition

$$\mathbf{C}^w(\xi) = \sum_{i=1}^{n} B_{i,p}(\xi)\mathbf{P}_i^w, \tag{3.24}$$

where $\{\mathbf{P}_i^w = (w_i x_i, w_i y_i, w_i z_i, w_i)\}$ represents a set of weighted control points. Note that the coordinate functions of the curve described in (3.24) read

$$X(\xi) = \sum_{i=1}^{n} B_{i,p}(\xi) w_i x_i,\ Y(\xi) = \sum_{i=1}^{n} B_{i,p}(\xi) w_i y_i,\ Z(\xi) = \sum_{i=1}^{n} B_{i,p}(\xi) w_i z_i,\ W(\xi) = \sum_{i=1}^{n} B_{i,p}(\xi) w_i. \tag{3.25}$$

The coordinate functions of the corresponding rational B-spline curve $\mathbf{C}(\xi)$ in three-dimensional space are obtained through the application of the perspective map (3.23) to $\mathbf{C}^w(\xi)$:

$$x(\xi) = \frac{X(\xi)}{W(\xi)} = \frac{\sum_{i=1}^{n} B_{i,p}(\xi) w_i x_i}{\sum_{i=1}^{n} B_{i,p}(\xi) w_i},\ y(\xi) = \frac{Y(\xi)}{W(\xi)} = \frac{\sum_{i=1}^{n} B_{i,p}(\xi) w_i y_i}{\sum_{i=1}^{n} B_{i,p}(\xi) w_i},\ z(\xi) = \frac{Z(\xi)}{W(\xi)} = \frac{\sum_{i=1}^{n} B_{i,p}(\xi) w_i z_i}{\sum_{i=1}^{n} B_{i,p}(\xi) w_i}. \tag{3.26}$$

Therefore, the NURBS curve $\mathbf{C}(\xi)$ may be expressed as

$$\mathbf{C}(\xi) = (x(\xi), y(\xi), z(\xi)) = \frac{\sum_{i=1}^{n} B_{i,p}(\xi) w_i (x_i, y_i, z_i)}{\sum_{i=1}^{n} B_{i,p}(\xi) w_i} = \frac{\sum_{i=1}^{n} B_{i,p}(\xi) w_i \mathbf{P}_i}{\sum_{i=1}^{n} B_{i,p}(\xi) w_i} = \sum_{i=1}^{n} R_{i,p}(\xi)\mathbf{P}_i, \tag{3.27}$$

using rational basis functions $R_{i,p}(\xi)$ as defined in (3.5). Clearly, the application of the perspective map H to the piecewise polynomial curve $\mathbf{C}^w(\xi)$, that is,

$$\mathbf{C}(\xi) = H\{\mathbf{C}^w(\xi)\} = H\left\{\sum_{i=1}^{n} B_{i,p}(\xi)\mathbf{P}_i^w\right\}, \tag{3.28}$$

yields the corresponding rational B-spline curve (piecewise rational) in three-dimensional space. We conclude the geometry representation discussion with the presentation of the definition for a NURBS surface. The definition of a NURBS volume exhibits an analogous structure. Given a control net $\{\mathbf{P}_{i,j}\}, i = 1, \ldots, n,\ j = 1, \ldots, m$ and corresponding weights $w_{i,j}$, polynomial degrees p and q, and univariate B-spline basis functions $B_{i,p}(\xi)$ and $B_{j,q}(\eta)$ respectively defined on knot vectors

$$\Xi = \{\xi_1, \dots \xi_{r=n+p+1}\} = \{\underbrace{0, \dots, 0}_{p+1}, \xi_{p+2}, \dots, \xi_{r-p-1}, \underbrace{1, \dots, 1}_{p+1}\}, \text{ and}$$

$$E = \{\eta_1, \dots \eta_{s=m+q+1}\} = \{\underbrace{0, \dots, 0}_{q+1}, \xi_{q+2}, \dots, \xi_{s-q-1}, \underbrace{1, \dots, 1}_{q+1}\},$$

a NURBS surface of degree p in the ξ direction and degree q in the η direction is a bivariate vector-valued piecewise rational function, defined as

$$\mathbf{S}(\xi, \eta) = \frac{\sum_{i=1}^{n} \sum_{j=1}^{m} B_{i,p}(\xi) B_{j,q}(\eta) w_{i,j} \mathbf{P}_{i,j}}{\sum_{i=1}^{n} \sum_{j=1}^{m} B_{i,p}(\xi) B_{j,q}(\eta) w_{i,j}}, \quad 0 \leq \xi, \eta \leq 1. \tag{3.29}$$

Using the rational basis functions (3.14), Equation (3.29) can be written as

$$\mathbf{S}(\xi, \eta) = \sum_{i=1}^{n} \sum_{j=1}^{m} R_{i,j}^{p,q}(\xi, \eta) \mathbf{P}_{i,j}. \tag{3.30}$$

Just like with NURBS curves, it is convenient to represent NURBS surfaces with homogeneous coordinates, that is

$$\mathbf{S}^w(\xi, \eta) = \sum_{i=1}^{n} \sum_{j=1}^{m} B_{i,p}(\xi) B_{j,q}(\eta) \mathbf{P}_{i,j}^w, \tag{3.31}$$

where $\mathbf{P}_{i,j}^w = (w_{i,j} x_{i,j}, w_{i,j} y_{i,j}, w_{i,j} z_{i,j}, w_{i,j})$. Then, the application of the perspective map H to the tensor product piecewise polynomial surface $\mathbf{S}^w(\xi, \eta)$ in four-dimensional space yields the corresponding piecewise rational surface in $\mathbb{R}^3$: $\mathbf{S}(\xi, \eta) = H\{\mathbf{S}^w(\xi, \eta)\}$. We refer to Figure 3.3 for the demonstration of a few simple examples of NURBS geometries.

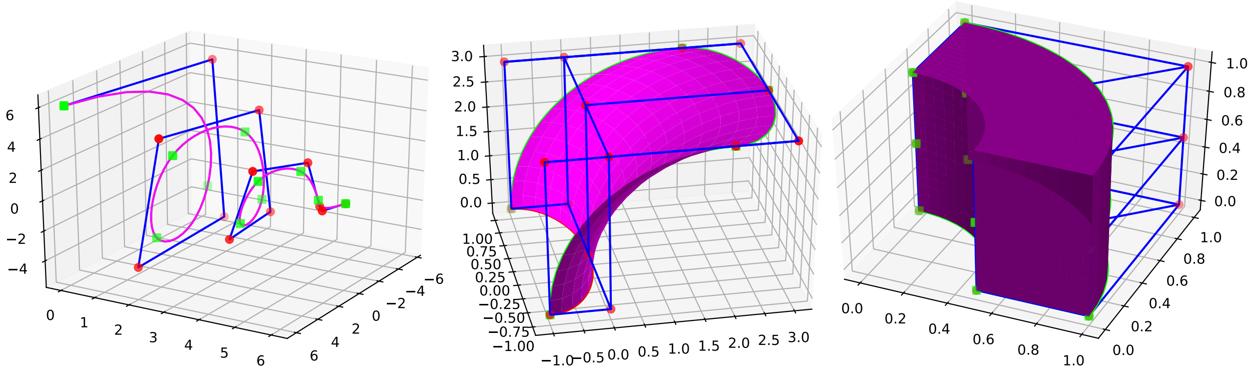

Figure 3.3: Examples of univariate (curve), bivariate (surface), and trivariate (volume) NURBS geometries depicted in magenta color. The NURBS control points and control polygon are drawn in red and blue, respectively. The green points represent the knots (element boundaries).

3.2.3 Galerkin-based Isogeometric Analysis

Galerkin-based Isogeometric Analysis ([13]IGA) is one of the numerical methods in the class of Isogeometric methods and can be seen as spline-based Galerkin FEA. The typical class of splines used are

---

[13] In the sequel we abbreviate Galerkin-based Isogeometric Analysis with IGA.

B-splines and NURBS, however the method has been extended in recent years to utilize additional spline types such as Truncated Hierarchic B-splines, T-splines, etc. allowing for local refinement. IGA uses basis functions that satisfy the partition of unity property (cf. Equation (3.3)), and naturally adheres to the *isoparametric concept* by using the same basis for geometry and analysis. In the context of mappings between the reference and physical elements in FEA, isoparametric mappings are those mappings whose polynomial degree coincides with that of the trial functions. They are very useful for discretizing domains with curvilinear boundaries. For instance, given basis functions $B_{i,j}^{p,q}(\xi,\eta)$ of degrees p and q in the respective spatial directions, and letting n_{en} denote the number of basis functions with support on element e, the (isoparametric) transformation

$$(x,y)^T = F_e(\xi,\eta) = \sum_{i=1}^{n_{en}} (x_i, y_i)^T B_{i,j}^{p,q}(\xi,\eta), \quad 0 \le \xi, \eta \le 1. \tag{3.32}$$

maps an element (segment) $\hat{\Omega}^e \equiv [\xi_i, \xi_{i+1}] \times [\eta_i, \eta_{i+1}]$ in the parametric domain $\hat{\Omega}$ to an element Ω^e in the (xy)-plane with possibly curved edges according the the degrees of p and q. Likewise, considering a 1D scenario for simplicity, given basis functions $B_{i,p}$ that satisfy the partition of unity property, and a corresponding basis $\{B_{i,p}\}_{i=1}^n$ for a solution space, a discrete approximation function $\hat{u}_h : \hat{\Omega} \to \mathbb{R}$ from this space may be expressed as

$$\hat{u}_h = \sum_{i=1}^{n} c_i B_i^p(\xi), \tag{3.33}$$

with c_i denoting the coefficients. Note that any reasonably smooth isoparametric basis that is also a partition of unity constitutes the most basic convergence requirements in many numerical methods. As discussed in [37, 87], a basis that is (i) complete, (ii) $\mathcal{C}^1$ inside the elements, and (iii) $\mathcal{C}^0$ on the element boundaries, satisfies the sufficient conditions for a basic proof of convergence of the Galerkin solution to the exact solution for a large class of problems. For the first condition - completeness - all linear functions on any given element Ω^e must be representable by the basis. Conditions (ii) and (iii) pose no restrictions either, as it is easy to setup a (spline) basis with functions that are smooth ($\mathcal{C}^\infty$) in the element interiors and (excluding Discontinuous Galerkin methods) at least $\mathcal{C}^0$ on the element boundaries. As for condition (i), the isoparametric concept and the partition of unity - both inherent in IGA - are enough to ensure completeness [37]. Convergent methods for many different element technologies including NURBS are essentially attributed to these traits in the context of IGA.

Galerkin-based IGA may be considered as an expansion and powerful generalization of traditional finite elements analysis. The basic operating principle of IGA and its similarity to FEA is best explained with a simple boundary value problem. To this end we consider a Poisson's problem with Dirichlet, Neumann, and Robin boundary conditions requiring to split the boundary $\partial\Omega$ of the computational domain Ω into corresponding parts. The strong form of this boundary value problem requires to find $u : \bar{\Omega} \to \mathbb{R}$ such that

$$-\nabla \cdot (\nu \nabla u) = f \quad \text{in } \Omega, \tag{3.34a}$$

$$u = g \quad \text{on } \Gamma_D, \tag{3.34b}$$

$$\nu \frac{\partial u}{\partial \boldsymbol{n}} = h \quad \text{on } \Gamma_N, \tag{3.34c}$$

$$\beta u + \nu \frac{\partial u}{\partial \boldsymbol{n}} = r \quad \text{on } \Gamma_R, \tag{3.34d}$$

where ν is a scalar and $\boldsymbol{n}$ denotes the unit normal vector pointing outside the computational domain Ω. The boundary of the latter is partitioned into nonoverlapping Dirichlet (Γ_D), Neumann (Γ_N), and Robin (Γ_R) segments, that is, $\overline{\Gamma_D \cup \Gamma_N \cup \Gamma_R} = \Gamma = \partial\Omega, \Gamma_D \cap \Gamma_N \cap \Gamma_R = \emptyset$, and the given functions $g : \Gamma_D \to \mathbb{R}, h : \Gamma_N \to \mathbb{R}, r : \Gamma_R \to \mathbb{R}$ represent Dirichlet, Neumann, and Robin boundary condition functions on the respective segments.

The variational formulation of this problem reads:

Problem 3.2.1. *Let $\mathcal{T} := \{u \in \mathcal{H}^1(\Omega) : u = g \text{ on } \Gamma_D\}$ denote a space of trial functions, and let $\mathcal{W} := \{w \in \mathcal{H}^1(\Omega) : w = 0 \text{ on } \Gamma_D\}$ be a space of functions with vanishing trace on Γ_D - a space of test/weighting functions. Given the bilinear form*

$$a(u, w) := \int_\Omega \nu \nabla w \cdot \nabla u \, \mathrm{d}\Omega + \beta \int_{\Gamma_R} wu \, \mathrm{d}\Gamma, \tag{3.35}$$

and the linear form

$$b(w) := \int_\Omega wf \, \mathrm{d}\Omega + \int_{\Gamma_N} wh \, \mathrm{d}\Gamma + \int_{\Gamma_R} wr \, \mathrm{d}\Gamma, \tag{3.36}$$

find $u \in \mathcal{T}$, such that

$$a(u, w) = b(w) \quad \forall w \in \mathcal{W}. \tag{3.37}$$

This problem formulation directly leads to the variational formulation of the corresponding discrete problem that we define as follows:

Problem 3.2.2. *Let $\mathcal{S}^p_\alpha$ denote a spline space that, for instance, for B-spline and NURBS is defined through equations (3.15) and (3.16), respectively. Moreover, let $\hat{\mathcal{T}}_h$ denote a discrete trial space in the parametric spline domain and let $\mathcal{T}_h = \{u_h \in \mathcal{T} \cap \mathcal{S}^p_\alpha : u_h = \hat{u}_h \circ \mathbf{F}^{-1}, \hat{u}_h \in \hat{\mathcal{T}}_h\}$ denote its counterpart in the physical domain Ω, where $\mathbf{F} : \hat{\Omega} \to \Omega$ is a parametrization of Ω (NURBS geometrical map as defined in (3.17)). Given the bilinear form*

$$a(u_h, w_h) := \int_\Omega \nu \nabla w_h \cdot \nabla u_h \, \mathrm{d}\Omega + \beta \int_{\Gamma_R} w_h u_h \, \mathrm{d}\Gamma, \tag{3.38}$$

and the linear form

$$b(w_h) := \int_\Omega w_h f \, \mathrm{d}\Omega + \int_{\Gamma_N} w_h h \, \mathrm{d}\Gamma + \int_{\Gamma_R} w_h r \, \mathrm{d}\Gamma, \tag{3.39}$$

find $u_h \in \mathcal{T}_h$, such that

$$a(u_h, w_h) = b(w_h) \quad \forall w_h \in \mathcal{T}_h. \tag{3.40}$$

For the solution of Problem 3.2.2 it is necessary to define bases for the discrete spaces $\hat{\mathcal{T}}_h$ and $\mathcal{T}_h$, whose dimensions is denoted by $N_h = \dim(\hat{\mathcal{T}}_h) = \dim(\mathcal{T}_h)$. We let a basis for $\hat{\mathcal{T}}_h$ be given by $\{\hat{v}_i\}_{i=1}^{N_h}$, and using the parametrization $\mathbf{F}$, we define a basis for $\mathcal{T}_h$ by $\{v_i = \hat{v}_i \circ \mathbf{F}^{-1}\}_{i=1}^{N_h}$. With these bases at hand, we consider for trial and test functions $u(\boldsymbol{x})$ and $w(\boldsymbol{x})$ and their gradients approximations of the form

$$
\begin{aligned}
u(\boldsymbol{x}) \approx u_h(\boldsymbol{x}) &= \sum_{j=1}^{N_h} c_j v_j = \sum_{j=1}^{N_h} c_j \left(\hat{v}_j \circ \mathbf{F}^{-1}\right), \\
w(\boldsymbol{x}) \approx w_h(\boldsymbol{x}) &= \sum_{i=1}^{N_h} d_i v_i = \sum_{i=1}^{N_h} d_i \left(\hat{v}_i \circ \mathbf{F}^{-1}\right), \\
\nabla u(\boldsymbol{x}) \approx \nabla u_h(\boldsymbol{x}) &= \sum_{j=1}^{N_h} c_j \nabla v_j = \sum_{j=1}^{N_h} c_j (D\mathbf{F})^{-T} \left(\nabla \hat{v}_j \circ \mathbf{F}^{-1}\right), \\
\nabla w(\boldsymbol{x}) \approx \nabla w_h(\boldsymbol{x}) &= \sum_{i=1}^{N_h} d_i \nabla v_i = \sum_{i=1}^{N_h} d_i (D\mathbf{F})^{-T} \left(\nabla \hat{v}_i \circ \mathbf{F}^{-1}\right),
\end{aligned}
\tag{3.41}
$$

where $D\mathbf{F}$ denotes the Jacobian matrix of the parametrization $\mathbf{F}$, and $(D\mathbf{F})^{-T}$ is its inverse transpose. Ultimately, inserting the substitutions presented in (3.41) into (3.40), that is,

$$
a\left(v_i, \sum_{j=1}^{N_h} v_j c_j\right) = \sum_{j=1}^{N_h} a(v_i, v_j) c_j = b(v_i), \quad i = 1, \ldots, N_h, \tag{3.42}
$$

leads to the following discrete system

$$
\boldsymbol{d}^T [\boldsymbol{A}\boldsymbol{c} - \boldsymbol{b}] = \boldsymbol{0}, \tag{3.43}
$$

with system matrix $\boldsymbol{A}$, right hand side vector $\boldsymbol{b}$, and the vector $\boldsymbol{c}$ of unknown coefficients. The requirement that (3.40) has to hold for all test functions $w_h \in \mathcal{T}_h$ is equivalent to the requirement to satisfy (3.43) for all choices of coefficient vectors $\boldsymbol{d}$, and the only possibility for this to happen is when $\boldsymbol{c}$ is the solution of the linear algebraic system

$$
\underbrace{\begin{bmatrix} a(v_1, v_1) & \ldots & a(v_1, v_{N_h}) \\ \vdots & \ddots & \vdots \\ a(v_{N_h}, v_1) & \ldots & a(v_{N_h}, v_{N_h}) \end{bmatrix}}_{\boldsymbol{A}}
\underbrace{\begin{bmatrix} c_1 \\ \vdots \\ c_{N_h} \end{bmatrix}}_{\boldsymbol{c}}
=
\underbrace{\begin{bmatrix} b(v_1) \\ \vdots \\ b(v_{N_h}) \end{bmatrix}}_{\boldsymbol{b}}. \tag{3.44}
$$

Except the imposition of Dirichlet boundary conditions, the further procedure involving the assembly process and the numerical integration of the integrals pretty much resembles that of standard FEA and is therefore not further discussed. The non-interpolatory basis of the discrete approximation spaces used in IGA render the imposition of Dirichlet boundary conditions a bit more involved than in standard FEA. For a brief discussion of the means to address this issue, we recall the Dirichlet boundary condition function g (cf. (3.34b)) of our model problem and assume there exists a *lifting* function $g_h \in \mathcal{T}_h$ such that $g_h|_{\Gamma_D} = g$, if g exists in the NURBS space. For constant g - covering the case of homogeneous Dirichlet boundary conditions - the partition of unity property of the B-spline/NURBS basis functions ensures that it is enough to just prescribe the constant value to the respective coefficients. Functions of higher order that exist in the NURBS space may in principle be set by a proper choice of the control variables. For functions that do not exist in the NURBS space the lifting is just an approximation $g_h|_{\Gamma_D} \approx g$. Interpolating g with the control points is at times a feasible option, however, it yields a g_h with a certain not necessarily uniform offset to g. A better lifting may be found by a least-squares fit of the prescribed Dirichlet data or by an $\mathcal{L}^2$-projection of g into the solution space.

3.2.4 A review of classical results on existence, uniqueness and convergence of solutions

In this section we will briefly review the most relevant results on the existence, uniqueness and convergence of Finite Element (FE) and (Galerkin-based) [13]IGA solutions without proofs and cite sources in which these topics are treated with a significantly higher level of detail. FE theory heavily draws on *Functional Analysis* and is embedded in an elegant framework enabling accurate *a priori* and *a posteriori* estimates of discretization errors and convergence rates. With IGA being a generalization of standard FEA, the results on existence and uniqueness of solutions directly apply to IGA as well. As far as convergence is concerned, the approximation properties of NURBS are harder to determine than those of standard polynomials used in FEA. We concisely review the approximation properties of B-spline and NURBS spaces and contrast the convergence rates of solutions obtained with IGA and standard FEA. The results and concepts presented are discussed on the basis of the variational Problem 3.2.3 for which the following conditions are expected to hold:

$$\begin{cases} 1. \quad (\mathcal{H}, (\cdot,\cdot)) \text{ is a Hilbert space.} \\ 2. \quad \mathcal{V} \text{ is a (closed) subspace of } \mathcal{H}. \\ 3. \quad a(\cdot,\cdot) \text{ is a continuous and coercive bilinear form on } \mathcal{V} \textit{ that is not necessarily symmetric.} \end{cases} \tag{3.45}$$

Note that our model Problem 3.2.1 (Poisson) is a special case of Problem 3.2.3 with a symmetric bilinear form.

Problem 3.2.3 (Nonsymmetric variational problem). *Let $\mathcal{V}$ be a Hilbert space and let $\mathcal{V}'$ denote its dual space. Find $u \in \mathcal{V}$, such that*

$$a(u,w) = F(w) \quad \forall w \in \mathcal{V}, \tag{3.46}$$

where $F \in \mathcal{V}'$ is a continuous linear functional, and $a(\cdot,\cdot)$ is a continuous and coercive bilinear form.

We recall the definitions of a few notions used in the above problem formulation:

Definition 3.2.1. *A bilinear form $a(\cdot,\cdot)$ on a normed linear space $\mathcal{H}$ is called* ***bounded*** *(or* ***continuous****), if $\exists\, C < \infty$, such that*

$$|a(v,w)| \leq C \, \|v\|_{\mathcal{H}} \, \|w\|_{\mathcal{H}} \quad \forall v, w \in \mathcal{H},$$

and ***coercive*** *(a.k.a.* ***H-Elliptic****,* ***elliptic****, or* ***positive definite****) on $\mathcal{V} \subset \mathcal{H}$, if $\exists\, \alpha > 0$, such that*

$$a(v,v) \geq \alpha \, \|v\|^2_{\mathcal{H}} \quad \forall v \in \mathcal{V}.$$

Every H-elliptic bilinear form $a(\cdot,\cdot)$ induces a norm - a so-called energy norm defined as

$$\|v\|_a := \sqrt{a(v,v)}.$$

The subscripts a reflects the fact that the norm has been induced by the bilinear form $a(\cdot,\cdot)$.

The dual space $\mathcal{B}'$ to a Banach space $\mathcal{B}$ is a set of linear functionals on $\mathcal{B}$. A linear functional L on a linear space $\mathcal{B}$ is a linear function from $\mathcal{B}$ into the set of real numbers ($L : \mathcal{B} \to \mathbb{R}$), such that

$$L(u + \alpha v) = L(u) + \alpha L(v) \quad \forall u, v \in \mathcal{B}, a \in \mathbb{R}.$$

Proposition 3.2.1. *A linear functional L on a Banach space $\mathcal{B}$ is continuous, if and only if it is bounded, i.e., if $\exists\, C < \infty$, such that*

$$|L(v)| \leq C \, \|v\|_{\mathcal{B}} \quad \forall v \in \mathcal{B}.$$

Proof. See [23]. □

Now, given the variational problem (3.46), we want to answer the following questions:

(i) Does the problem have a solution (u), and if so, is it unique?

(ii) Let $\mathcal{V}_h$ be a finite dimensional function space and let $u_h \in \mathcal{V}_h$ be the solution obtained from the Galerkin FEA/IGA method. Is this solution optimal? That is, is u_h optimal in the sense that the error $u - u_h$ satisfies

$$\|u - u_h\| = \min_{v_h \in \mathcal{V}_h} \|u - v_h\| \tag{3.47}$$

in an appropriate norm?

(iii) What is an upper bound for the right hand side of (3.47), i.e., how good does an optimal interpolant $\mathcal{I}_h u$ in the space $\mathcal{V}_h$ approximate the solution u of a variational problem?

The existence and uniqueness of the solution to (3.46) is guaranteed by the Lax-Milgram theorem yielding an answer to question (i).

Theorem 3.2.1 (Lax-Milgram lemma). *Let $(\mathcal{V}, (\cdot,\cdot))$ denote a Hilbert space. Given a bounded (continuous) and coercive bilinear form $a(\cdot,\cdot)$ on $\mathcal{V}$ and a continuous linear functional $F \in \mathcal{V}'$, there exists a unique $u \in \mathcal{V}$, such that*

$$a(u, w) = F(w) \quad \forall w \in \mathcal{V}. \tag{3.48}$$

Proof. A proof of this can be found in [23]. □

We proceed with a discussion on question (ii). There is a connection between self-adjoint differential problems such as the Poisson problem (3.34) (with homogeneous Dirichlet data) and the minimization of the energy functional

$$J(v) := a(v, v) - 2(f, v), \tag{3.49}$$

with bilinear and linear forms according to (3.35) and (3.36). More specifically, $J(v)$ attains its minimum value for the solution $u \in \mathcal{H}_0^1(I)$ of the Galerkin weak form (3.37). Contrariwise, the solution of the minimization problem:

$$\text{Find } v \in \mathcal{H}_0^1 \text{ such that } J(v) \longrightarrow \min! \tag{3.50}$$

is also a solution to the Galerkin weak form (3.37). It can be concluded from the above, that the solution of the Galerkin problem (3.37) is optimal in the sense of minimizing (3.49).

Theorem 3.2.2. *The function $u \in \mathcal{H}_0^1(I)$ that minimizes the energy functional (3.49) is the one that satisfies the Galerkin weak from (3.37) and vice versa.*

Proof. A proof of this relation can for instance be found in [22, 60]. □

The estimation of the error $\|u - u_h\|$ in (3.47) requires access to the discrete (finite dimensional) solution u_h. In order to obtain u_h, we consider a finite dimensional subspace $\mathcal{V}_h \subset \mathcal{H}_0^1(I)$ and replace in (3.46) the functions u and w with their discrete counterparts. This yields the corresponding discrete variational problem, reading: Find $u_h \in \mathcal{V}_h$ satisfying

$$a(u_h, w_h) = F(w_h) \quad \forall w_h \in \mathcal{V}_h. \tag{3.51}$$

As a subspace of $\mathcal{H}_0^1(I)$, the discrete space $\mathcal{V}_h$ satisfies the prerequisites of the Lax-Milgram lemma, allowing it to guarantee the existence and uniqueness of a solution $u_h \in \mathcal{V}_h$ for the discrete problem (3.51). The following theorem shows that the discrete solution u_h is the near-best fit to the solution u of the continuous problem, or *optimal* in the sense that the error $\|u - u_h\|_{\mathcal{V}}$ is proportional to the best it can be in the subspace $\mathcal{V}_h$.

Theorem 3.2.3 (Céa's lemma). *Let u be the solution of the continuous problem (3.46). Under the same conditions (cf. (3.45)) as for Theorem 3.2.1 (Lax-Milgram lemma), the discrete problem (3.51) has a unique solution u_h for which it holds*

$$\|u - u_h\|_{\mathcal{V}} \leq \frac{C}{\alpha} \min_{v_h \in \mathcal{V}_h} \|u - v_h\|_{\mathcal{V}}\,, \tag{3.52}$$

with C and α denoting the continuity and coercivity constant of $a(\cdot,\cdot)$ on $\mathcal{V}$. The discrete solution u_h from the subspace $\mathcal{V}_h$ is quasi-optimal - it is at most by the constant $\frac{C}{\alpha}$ worse than the best approximation for u in $\mathcal{V}_h$.

Proof. Proofs of Céa's lemma can be found in [22, 23], for example. □

With question (ii) being answered by Céa's lemma, it remains to discuss about an upper bound for the error $\|u - v_h\|_{\mathcal{V}}$ in (3.52). To this end, let the solutions $u \in \mathcal{H}^k(\Omega)$ and $u_h \in \mathcal{V}_h$ of a continuous and the corresponding discrete variational problem satisfy (cf. Céa's lemma)

$$\|u - u_h\|_{\mathcal{H}^k(\Omega)} \leq c_0 \min_{v_h \in \mathcal{V}_h} \|u - v_h\|_{\mathcal{H}^k(\Omega)}\,. \tag{3.53}$$

An upper bound for the right hand side of (3.53) is obtained by considering the error of an interpolant $\mathcal{I}_h u \in \mathcal{V}_h$ of u. The existence of a smooth enough u and an interpolant $\mathcal{I}_h u$, such that

$$\|u - \mathcal{I}_h u\|_{\mathcal{H}^k(\Omega)} \leq C h^{l-k} \|u\|_{\mathcal{H}^l(\Omega)}\,, \tag{3.54}$$

for $0 \leq k \leq l$, implies

$$\|u - u_h\|_{\mathcal{H}^k(\Omega)} \leq c_1 h^{l-k} \|u\|_{\mathcal{H}^l(\Omega)}\,. \tag{3.55}$$

Remark 3.2.1. *The approach for the construction of the estimate presented in (3.54) is to obtain a bound for the interpolation error on each element and eventually sum over all elements to get a global interpolation error result (cf. [23], Theorem (4.4.20)). In this context, the Bramble-Hilbert Lemma (cf. [23]) is an important building block. It describes a bound for the error of an approximation of a function $u \in \mathcal{W}^{m,p}$ by a polynomial of order at most $m - 1$ in terms of m-th order derivatives of u.*

The following theorem presents a finite element convergence estimate for the more general case in which u may lack the required smoothness for the interpolant $\mathcal{I}_h u$ to be well defined.

Theorem 3.2.4. *Let the optimality constraint (3.53) hold for any $u \in \mathcal{H}^k(\Omega)$ and let the interpolation estimate (3.55) hold for any $u \in \mathcal{H}^t(\Omega)$, where $k, l, t \in \mathbb{N}$ with $k < l < t$. Then, for any $u \in \mathcal{H}^l(\Omega)$ it holds*

$$\|u - u_h\|_{\mathcal{H}^k(\Omega)} \leq C h^{\beta = l-k} \|u\|_{\mathcal{H}^l(\Omega)}\,. \tag{3.56}$$

Proof. For a proof of this theorem and results leading to it we refer to the proofs of Theorems (4.4.20) and (14.3.3) in [23], the proof of Theorem (6.4) in [22], and to the proofs of Theorems (4.6.5), (7.2.3), and (7.2.4) in [60]. □

Remark 3.2.2. *In (3.56), $\beta = l - k$ denotes the order of convergence. It is a measure for how the error of order $O(h^\beta)$ changes under h-refinement ($h \to 0$).*

The convergence estimate (3.56) has been developed for standard finite elements. With Céa's lemma holding for both FEM and Galerkin-based IGA, it remains to discuss the interpolation error for the latter. With that being said, a concise review of some of the approximation properties of the NURBS space based on [16, 131] is presented in the sequel.

When it comes to the construction of an estimate similar to (3.56) for the order of convergence of an IGA solution u_h, one faces several difficulties. The first complication is caused by the large support of B-spline/NURBS (abbreviated with spline for the rest of this section) basis functions (cf. Figure 3.2). Standard interpolation estimates work on element level. They estimate an error bound by seeking a best fit within each element, and ultimately aggregate these bounds to obtain an error bound for the whole domain. This is non-trivial in case of spline basis functions as the support of a spline basis function spans in general more than one element.

Therefore, in the course of trying to fit a function over an element Q, one can not determine optimal control variables (coefficients) by considering each element individually. Instead, a so-called *support extension*

$$\tilde{Q} := \otimes_{\beta=1}^{d} (\xi_{i-p,\beta}, \xi_{i+p+1,\beta}) \tag{3.57}$$

of Q needs to be considered which is the union of the supports of all basis functions whose support intersects Q. Additional difficulties arise by virtue of the fact that the continuity (regularity) of a spline basis function is allowed to differ along the domain. In order to address this issue in the convergence analysis, the authors of [16] introduce so-called "bent" Sobolev spaces in which the continuity may vary throughout the domain. These spaces are intermediate between standard Sobolev spaces and so-called "broken" Sobolev spaces known from Discontinuous Galerkin methods. A *bent Sobolev space* of order $m \in \mathbb{N}$ is defined as

$$\tilde{\mathcal{H}}^m := \begin{cases} u \in \mathcal{L}^2((0,1)^d) \text{ such that} \\ u_{|Q} \in \mathcal{H}^m(Q), \forall Q \in \mathcal{Q}, \text{ and} \\ \nabla^k(u_{|Q_1}) = \nabla^k(u_{|Q_2}) \text{ on } \partial Q_1 \cap \partial Q_2, \\ \forall k \in \mathbb{N} \text{ with } 0 \le k \le \min\{m_{Q_1,Q_2}, m-1\} \\ \forall Q_1, Q_2 \text{ with } \partial Q_1 \cap \partial Q_2 \neq \emptyset, \end{cases} \tag{3.58}$$

where ∇^k represents the k-th order partial derivative operator, and m_{Q_1,Q_2} denotes the number of continuous derivatives across the common $(d-1)$-dimensional face $\partial Q_1 \cap \partial Q_2$ of two adjacent elements Q_1 and Q_2. The Hilbert space (3.58) is endowed with the seminorms

$$|u|^2_{\tilde{\mathcal{H}}^i} := \sum_{Q \in \mathcal{Q}} |u|^2_{\mathcal{H}^i(Q)}, \ 0 \le i \le m, \tag{3.59}$$

and norm

$$\|u\|^2_{\tilde{\mathcal{H}}^m} := \sum_{i=0}^{m} |u|^2_{\tilde{\mathcal{H}}^i}. \tag{3.60}$$

With the definitions of a bent Sobolev space and a support extension at hand the next step towards establishing an estimate similar to (3.56) requires to inspect the local approximation properties of the B-spline space $\mathcal{S}$ (cf. (3.15)) in the parametric domain. To this end [16] presents an extension of the classical Bramble-Hilbert lemma, reading

Lemma 3.2.1. *Let $k, l \in \mathbb{N}$ with $0 \le k \le l \le p+1$, where*

$$p := \min_{1 \le \beta \le d} p_\beta.$$

Given an element $Q \in \mathcal{Q}_h$ (cf. Page 40), a support extension $\tilde{Q}$, and a function $u \in \tilde{\mathcal{H}}^l_h$, there exists an $s \in \mathcal{S}_h$ such that

$$|u - s|_{\tilde{\mathcal{H}}^k_h(\tilde{Q})} \le C h_Q^{l-k} |u|_{\tilde{\mathcal{H}}^l_h(\tilde{Q})}. \tag{3.61}$$

Proof. See proof of Lemma 3.1. in [16]. □

Next, let $s \in \mathcal{S}_h$ in (3.61) be given by a projector $\Pi_{\mathcal{S}_h} : \mathcal{L}^2((0,1)^d) \to \mathcal{S}_h$ on the B-spline space $\mathcal{S}_h$ as introduced in [131, Chapter 12]. In present notation, the projector reads

$$\Pi_{\mathcal{S}_h} u := \sum_{i_1=1,\dots,i_d=1}^{n_1,\dots,n_d} (\lambda_{i_1,\dots,i_d} u) B_{i_1,\dots,i_d}, \quad \forall u \in \mathcal{L}^2((0,1)^d), \tag{3.62}$$

with $\lambda_{i_1,\dots,i_d}$ denoting *dual* basis functionals, i.e.,

$$\begin{aligned} \lambda_{j_1,\dots,j_d} B_{i_1,\dots,i_d} &= 1 \quad \text{if } j_\beta = i_\beta, \forall 1 \le \beta \le d, \\ \lambda_{j_1,\dots,j_d} B_{i_1,\dots,i_d} &= 0 \quad \text{otherwise.} \end{aligned} \tag{3.63}$$

The characteristic traits of the projector on the B-spline space $\mathcal{S}_h$ is presented by the following

Lemma 3.2.2.

$$\begin{aligned} \Pi_{\mathcal{S}_h} s &= s & &\forall s \in \mathcal{S}_h \ (\textit{spline preserving}), \\ \|\Pi_{\mathcal{S}_h} u\|_{\mathcal{L}^2(Q)} &\le C \, \|u\|_{\mathcal{L}^2(\tilde{Q})} & &\forall u \in \mathcal{L}^2((0,1)^d), \forall Q \in \mathcal{Q}_h \ (\textit{stability}), \end{aligned} \tag{3.64}$$

Proof. See [131, Proof of Theorem 12.6]. □

These traits are used in [16] to establish the following approximation property of the B-spline space $\mathcal{S}_h$ on the patch $(0,1)^d$:

Lemma 3.2.3. *Let $\Pi_{\mathcal{S}_h} : \mathcal{L}^2((0,1)^d) \to \mathcal{S}_h$ satisfy (3.64), and let $k, l \in \mathbb{N}$ with $0 \le k \le l \le p+1$. Then, $\forall Q \in \mathcal{Q}_h$ it holds*

$$|u - \Pi_{\mathcal{S}_h} u|_{\mathcal{H}^k(Q)} \le C h_Q^{l-k} |u|_{\tilde{\mathcal{H}}^l(\tilde{Q})} \quad \forall u \in \tilde{\mathcal{H}}^l_h(\tilde{Q}) \cap \mathcal{L}^2((0,1)^d). \tag{3.65}$$

Proof. The proof of this estimate is given in [16]. □

Further, when it comes to the approximation property of the NURBS space $\mathcal{N}_h$ on the patch

$(0,1)^d$, a result similar to (3.65) is presented in [16] using the projector

$$\begin{aligned} &\Pi_{\mathcal{N}_h} : \mathcal{L}^2((0,1)^d) \to \mathcal{N}_h \\ &\Pi_{\mathcal{N}_h} u := \frac{\Pi_{\mathcal{S}_h}(wu)}{W}, \quad \forall u \in \mathcal{L}^2((0,1)^d) \\ &W := \sum_{i_1=1}^{n_1} \cdots \sum_{i_d=1}^{n_d} w_{i_1,\dots,i_d} B_{i_1,\dots,i_d} \end{aligned} \tag{3.66}$$

on the NURBS space $\mathcal{N}_h$. It reads:

Lemma 3.2.4. *Let $k, l \in \mathbb{N}$ with $0 \leq k \leq l \leq p+1$. Then, $\forall Q \in \mathcal{Q}_h$ it holds*

$$|u - \Pi_{\mathcal{N}_h} u|_{\mathcal{H}^k(Q)} \leq C_{shape}\, h_Q^{l-k} \, \|u\|_{\tilde{\mathcal{H}}_h^l(\tilde{Q})} \quad \forall u \in \tilde{\mathcal{H}}_h^l. \tag{3.67}$$

Proof. We refer to [16] for the proof of this estimate. □

Remark 3.2.3. *The constant C_{shape} (possibly different at each occurrence) depends on the shape of Ω, but not on its size h. More specifically, it depends only on the dimensionless functions $W/\|W\|_{\mathcal{L}^\infty(\Omega)}$ and $\nabla \mathbf{F}/\|\nabla \mathbf{F}\|_{\mathcal{L}^\infty(\Omega)}$, where $\nabla \mathbf{F}$ - the gradient of the mapping $\mathbf{F}$ - is the matrix of partial derivatives of the coordinate components of $\mathbf{F}$. Note that the geometry weights w in the weighting function W (cf. (3.66), (3.5)) have an influence on the geometry shape.*

The Lemmata 3.2.3 and 3.2.4 contain the respective results for approximation with B-splines and NURBS in the parametric spline domain $\hat{\Omega}$ (normalized to $(0,1)^d$ without loss of generality). We proceed with the presentation of the results for the approximation with NURBS in the physical domain Ω. This requires a) an estimate for the change of variable from the parametric to the physical domain, as presented by Lemma 3.5 of [16], and b) a push forward of the NURBS projector $\Pi_{\mathcal{N}_h}$, defined as

$$\begin{aligned} &\Pi_{\mathcal{V}_h} : \mathcal{L}^2(\Omega) \to \mathcal{V}_h \\ &\Pi_{\mathcal{V}_h} v := \Pi_{\mathcal{N}_h}(v \circ \mathbf{F}) \circ \mathbf{F}^{-1} \quad \forall v \in \mathcal{L}^2(\Omega). \end{aligned} \tag{3.68}$$

The approximation properties of the push forward of the NURBS projector are stated through the following

Theorem 3.2.5. *Let $k, l \in \mathbb{N}$ with $0 \leq k \leq l \leq p+1$. Given an element $Q \in \mathcal{Q}_h$, its support extension $\tilde{Q}$, and their respective images under the geometrical mapping $\mathbf{F}$, that is, $K = \mathbf{F}(Q)$ and $\tilde{K} = \mathbf{F}(\tilde{Q})$, it holds*

$$|u - \Pi_{\mathcal{V}_h} u|_{\mathcal{H}^k(K)} \leq C_{shape}\, h_K^{l-k} \sum_{i=0}^{l} \|\nabla \mathbf{F}\|_{\mathcal{L}^\infty(\tilde{Q})}^{i-l} \, |u|_{\mathcal{H}^i(\tilde{K})} \quad \forall u \in \mathcal{L}^2(\Omega) \cap \mathcal{H}^l(\tilde{K}), \tag{3.69}$$

where $h_K = \|\nabla \mathbf{F}\|_{\mathcal{L}^\infty(Q)} h_Q$ denotes the element size in the physical domain.

Proof. See [16]. □

The above theorem provides a local error estimate on the element level (K). Summing up the local error estimates for all elements eventually leads to the following global error estimate for approximation with NURBS in the physical domain:

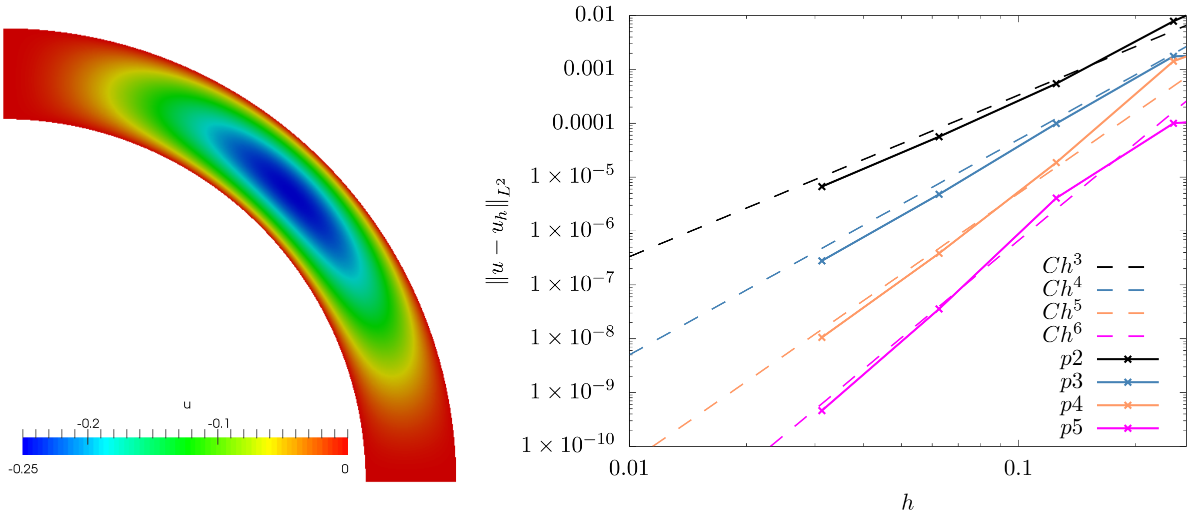

Figure 3.4: Solution of the Poisson problem (3.71) on an exact quarter ring exhibiting optimal order of convergence.

Theorem 3.2.6. *Let $k, l \in \mathbb{N}$ with $0 \le k \le l \le p+1$. Then it holds*

$$\sum_{K\in\mathcal{K}_h} |u-\Pi_{\mathcal{V}_h}u|^2_{\tilde{\mathcal{H}}^k_h(K)} \le C_{shape} \sum_{K\in\mathcal{K}_h} h_K^{2(l-k)} \sum_{i=0}^{l} \|\nabla\mathbf{F}\|^{2(i-l)}_{\mathcal{L}^\infty(\mathbf{F}^{-1}(K))} |u|^2_{\mathcal{H}^i(K)} \quad \forall u \in \mathcal{H}^l(\Omega). \tag{3.70}$$

Proof. See [16]. ☐

The fact that an Isogeometric Analysis solution u_h is quasi-optimal in the sense that is at most by a constant factor worse than the best approximation for the exact solution u (cf. (3.52)) satisfying the variational Problem 3.2.3, and the the approximation error $u - \Pi_{\mathcal{V}_h}u$ being estimated as in Theorem 3.70, leads to the following conclusion: The IGA solution obtained with NURBS of order p has the same order of convergence as a corresponding FEA solution using polynomial basis functions of order p [16, 37]. By way of example, we refer at this point to Figure 3.4 showing an IGA solution of the Poisson problem (3.71) with optimal order of convergence. NURBS have accuracy advantages over classical finite elements due to their increased smoothness. The usage of smooth NURBS basis functions is often shown [37] to yield superior accuracy per degree-of-freedom than classical FEA basis functions of the same order. Moreover, refining a NURBS mesh so as to maintain $p-1$ continuity (k-refinement, cf. [37]), introduces much less degrees-of-freedom than it is the case with standard element bisection (h-refinement) in classical FEA. This implies that NURBS can converge at the same rate as FEA polynomials, while remaining much more efficient [37].

Example: Poisson problem on a quarter ring (with problem data and exact solution according to [143])

$$\text{find } u : \Omega \to \mathbb{R} : \begin{cases} -\nabla\cdot(\mu\nabla u) = f & \text{in } \Omega \\ u = g & \text{on } \Gamma_D \\ \mu\nabla u\cdot\boldsymbol{n} = h & \text{on } \Gamma_N \end{cases} \tag{3.71}$$

3.3 Discrete approximation spaces

For an Isogeometric Analysis-based approximation of the unknowns of the PDEs considered in this work (see Section 3.4), suitable B-spline or NURBS spaces, as defined in Section 3.2, need to be specified. For the approximation of the velocity and pressure functions, we use LBB-stable Taylor-Hood-like B-spline space pairs $\hat{\mathbf{V}}_h^{TH}/\hat{Q}_h^{TH}$ [29], being defined in the parametric domain $\hat{\Omega}$ as

$$\begin{aligned} \hat{\mathbf{V}}_h^{TH} &\equiv \hat{\mathbf{V}}_h^{TH}(\mathbf{p},\boldsymbol{\alpha}) = \boldsymbol{\mathcal{S}}_{\alpha,\alpha}^{p+1,p+1} = \mathcal{S}_{\alpha,\alpha}^{p+1,p+1} \times \mathcal{S}_{\alpha,\alpha}^{p+1,p+1}, \\ \hat{Q}_h^{TH} &\equiv \hat{Q}_h^{TH}(\mathbf{p},\boldsymbol{\alpha}) = \mathcal{S}_{\alpha,\alpha}^{p,p}. \end{aligned} \tag{3.72}$$

With the definition of finite dimensional spaces $\hat{\mathbf{V}}_h^{TH}$ and $\hat{Q}_h^{TH}$ in hand, we proceed to construct the corresponding spaces $\mathbf{V}_h^{TH}$ and Q_h^{TH} in the physical domain Ω. Taylor-Hood spaces $\hat{\mathbf{V}}_h^{TH}/\hat{Q}_h^{TH}$ can be mapped to the physical domain via a component-wise mapping [29] using the parametrization $\mathbf{F}:\hat{\Omega}\to\Omega$, i.e.

$$\mathbf{V}_h^{TH} = \{\mathbf{v}_h = \hat{\mathbf{v}}_h \circ \mathbf{F}^{-1}, \hat{\mathbf{v}}_h \in \hat{\mathbf{V}}_h^{TH}\}, \qquad Q_h^{TH} = \{q_h = \hat{q}_h \circ \mathbf{F}^{-1}, \hat{q}_h \in \hat{Q}_h^{TH}\}. \tag{3.73}$$

Note that these spaces may be alternatively set up to use NURBS instead of B-spline basis functions. Throughout this work, whenever a specific discrete B-spline or NURBS approximation space is addressed, we introduce – for the sake of brevity – the convention to refer to its presentation w.r.t. the parametric domain $\hat{\Omega}$, as shown in (4.32).

3.4 Governing equations of incompressible Newtonian flow

For stationary flow scenarios considered in this chapter, the governing equations to be solved are the steady-state incompressible Navier-Stokes equations represented in strong form as

$$-\nu\nabla^2\boldsymbol{v} + (\boldsymbol{v}\cdot\nabla)\boldsymbol{v} + \nabla p = \boldsymbol{b} \quad \text{in } \Omega, \tag{3.74a}$$

$$\nabla\cdot\boldsymbol{v} = 0 \quad \text{in } \Omega, \tag{3.74b}$$

$$\boldsymbol{v} = \boldsymbol{v}_D \quad \text{on } \Gamma_D, \tag{3.74c}$$

$$-p\boldsymbol{n} + \nu(\boldsymbol{n}\cdot\nabla)\boldsymbol{v} = \boldsymbol{t} \quad \text{on } \Gamma_N, \tag{3.74d}$$

where $\Omega \subset \mathbb{R}^2$ is a bounded domain, ρ is the density, μ represents the dynamic viscosity, $\nu = \mu/\rho$ is the kinematic viscosity, $p = P/\rho$ denotes the normalized pressure, $\boldsymbol{b}$ is the body force term, $\boldsymbol{v}_D$ is the value of the velocity Dirichlet boundary conditions on the Dirichlet boundary Γ_D, $\boldsymbol{t}$ is the prescribed traction force on the Neumann boundary Γ_N, and $\boldsymbol{n}$ is the outward unit normal vector on the boundary. The kinematic viscosity and the density of the fluid are assumed to be constant. The first and second equations in (3.74) are the momentum and continuity equations, respectively.

Their continuous mixed variational formulation reads: Find $\boldsymbol{v} \in \left(\boldsymbol{\mathcal{H}}^1_{0,\Gamma_D}(\Omega) + \bar{\boldsymbol{v}}\right)$ and $p \in \mathcal{L}_2(\Omega)/\mathbb{R}$ such that for all $(\boldsymbol{w},q) \in \boldsymbol{\mathcal{H}}^1_{0,\Gamma_D}(\Omega) \times \mathcal{L}_2(\Omega)/\mathbb{R}$ it holds

$$\begin{cases} a(\boldsymbol{w},\boldsymbol{v}) + c(\boldsymbol{v};\boldsymbol{w},\boldsymbol{v}) + b(\boldsymbol{w},p) = \ (\boldsymbol{w},\boldsymbol{b}) + (\boldsymbol{w},\boldsymbol{t})_{\Gamma_N} \\ b(\boldsymbol{v},q) = 0, \end{cases} \tag{3.75}$$

where $\mathcal{L}_2$ and $\boldsymbol{\mathcal{H}}^1$ are Sobolev spaces as defined in [2],

$$\boldsymbol{\mathcal{H}}^1_{0,\Gamma_D}(\Omega) \equiv \boldsymbol{\mathcal{H}}^1_0(\Omega;\Gamma_D) := \{\boldsymbol{z} \in \boldsymbol{\mathcal{H}}^1(\Omega) \mid \boldsymbol{z} = 0 \text{ on } \Gamma_D\} \tag{3.76}$$

is the space of functions in $\boldsymbol{\mathcal{H}}^1$ with vanishing trace on Γ_D, and $\bar{\boldsymbol{v}}$ is any function in $\boldsymbol{\mathcal{H}}^1$ such that $\bar{\boldsymbol{v}} = \boldsymbol{v}_D$ on Γ_D.

Replacement of the linear-, bilinear- and trilinear forms with their respective definitions and application of integration by parts to (3.75) yields

$$\begin{aligned} &\underbrace{\nu\int_\Omega \nabla\boldsymbol{w} : \nabla\boldsymbol{v}\,\mathrm{d}\Omega}_{a(\boldsymbol{w},\boldsymbol{v})} + \underbrace{\int_\Omega \boldsymbol{w}\cdot\boldsymbol{v}\cdot\nabla\boldsymbol{v}\,\mathrm{d}\Omega}_{c(\boldsymbol{v};\boldsymbol{w},\boldsymbol{v})} - \underbrace{\int_\Omega \nabla\cdot\boldsymbol{w}p\,\mathrm{d}\Omega}_{b(\boldsymbol{w},p)} + \underbrace{\int_\Omega q\nabla\cdot\boldsymbol{v}\,\mathrm{d}\Omega}_{b(\boldsymbol{v},q)} = \\ &\underbrace{\int_\Omega \boldsymbol{w}\cdot\boldsymbol{b}\,\mathrm{d}\Omega}_{(\boldsymbol{w},\boldsymbol{b})} + \underbrace{\int_{\Gamma_N} \nu\boldsymbol{w}\cdot(\nabla\boldsymbol{v}\cdot\boldsymbol{n})\,\mathrm{d}\Gamma_N - \int_{\Gamma_N} p\boldsymbol{w}\cdot\boldsymbol{n}\,\mathrm{d}\Gamma_N}_{(\boldsymbol{w},\boldsymbol{t})_{\Gamma_N}} \end{aligned} \tag{3.77}$$

A downcast of the variational formulation (3.75) to the discrete level gives rise to the problem statement

$$\begin{cases} \text{Find } \boldsymbol{v}_h \in \{\boldsymbol{\mathcal{H}}^1_{0,\Gamma_D}(\Omega) + \bar{\boldsymbol{v}}\} \cap \mathbf{V}_h^{TH} \text{ and } p_h \in \mathcal{L}_2(\Omega)/\mathbb{R} \cap Q_h^{TH}, \text{such that} \\ \forall(\boldsymbol{w}_h, q_h) \in \boldsymbol{\mathcal{H}}^1_{0,\Gamma_D}(\Omega) \cap \mathbf{V}_h^{TH} \times \mathcal{L}_2(\Omega)/\mathbb{R} \cap Q_h^{TH} \\ a(\boldsymbol{w}_h,\boldsymbol{v}_h) + c(\boldsymbol{v}_h;\boldsymbol{w}_h,\boldsymbol{v}_h) + b(\boldsymbol{w}_h,p_h) = (\boldsymbol{w}_h,\boldsymbol{b}_h) + (\boldsymbol{w}_h,\boldsymbol{t}_h)_{\Gamma_N} \\ b(\boldsymbol{v}_h,q_h) = 0, \end{cases} \tag{3.78}$$

with superscript h dubbing the mesh family index.

In addition to the stationary flow around a circular obstacle model problem, we also consider its unsteady counterpart (see Section 3.5.4). In the latter case, the unsteady incompressible Navier-Stokes equations, defined as

$$\frac{\partial\boldsymbol{v}}{\partial t} - \nu\nabla^2\boldsymbol{v} + (\boldsymbol{v}\cdot\nabla)\boldsymbol{v} + \nabla p = \boldsymbol{b} \quad \text{in } \Omega\times(0,T), \tag{3.79a}$$

$$\nabla\cdot\boldsymbol{v} = 0 \quad \text{in } \Omega\times(0,T), \tag{3.79b}$$

$$\boldsymbol{v} = \boldsymbol{v}_D \quad \text{on } \Gamma_D\times(0,T), \tag{3.79c}$$

$$-p\boldsymbol{n} + \nu(\boldsymbol{n}\cdot\nabla)\boldsymbol{v} = \boldsymbol{t} \quad \text{on } \Gamma_N\times(0,T), \tag{3.79d}$$

$$\boldsymbol{v}(\boldsymbol{x},0) = \boldsymbol{v}_0(\boldsymbol{x}) \quad \text{in } \Omega, \tag{3.79e}$$

are solved in time, whereby the initial condition is required to satisfy $\nabla\cdot\boldsymbol{v}_0 = 0$. The corresponding variational problem reads: Find $\boldsymbol{v}(\boldsymbol{x},t) \in \big(\boldsymbol{\mathcal{H}}^1_{0,\Gamma_D}(\Omega) + \bar{\boldsymbol{v}}\big)\times(0,T)$ and $p(\boldsymbol{x},t) \in \mathcal{L}_2(\Omega)\times(0,T)$, such that for all $(\boldsymbol{w},q) \in \boldsymbol{\mathcal{H}}^1_{0,\Gamma_D}(\Omega)\times\mathcal{L}_2(\Omega)/\mathbb{R}$ it holds

$$\begin{cases} (\boldsymbol{w},\boldsymbol{v}_t) + a(\boldsymbol{w},\boldsymbol{v}) + c(\boldsymbol{v};\boldsymbol{w},\boldsymbol{v}) + b(\boldsymbol{w},p) = (\boldsymbol{w},\boldsymbol{b}) + (\boldsymbol{w},\boldsymbol{t})_{\Gamma_N} \\ b(\boldsymbol{v},q) = 0 \end{cases} \tag{3.80}$$

Analogously, the semi-discretized counterpart of the variational formulation (4.43) reads:

$$
\begin{cases}
\text{Find } \boldsymbol{v}_h \in \left(\boldsymbol{\mathcal{H}}^1_{0,\Gamma_D}(\Omega) + \bar{\boldsymbol{v}}\right) \cap \mathbf{V}_h^{TH} \times (0,T) \;\text{ and }\; p_h \in \mathcal{L}_2(\Omega)/\mathbb{R} \cap Q_h^{TH} \times (0,T), \text{such that} \\
\forall (\boldsymbol{w}_h, q_h) \in \boldsymbol{\mathcal{H}}^1_{0,\Gamma_D}(\Omega) \cap \mathbf{V}_h^{TH} \times \mathcal{L}_2(\Omega)/\mathbb{R} \cap Q_h^{TH} \\
(\boldsymbol{w}_h, \partial_t \boldsymbol{v}_h) + a(\boldsymbol{w}_h, \boldsymbol{v}_h) + c(\boldsymbol{v}_h; \boldsymbol{w}_h, \boldsymbol{v}_h) + b(\boldsymbol{w}_h, p_h) = \; (\boldsymbol{w}_h, \boldsymbol{b}_h) + (\boldsymbol{w}_h, \boldsymbol{t}_h)_{\Gamma_N} \\
b(\boldsymbol{v}_h, q_h) = 0
\end{cases}
\tag{3.81}
$$

Since the nonlinear nature of the Navier-Stokes equations involves a great deal of complexity, we deliver in Section 3.4.1 an insight into the handling of the nonlinearity aspect.

3.4.1 Treatment of nonlinearity

The treatment of nonlinearity is showcased for the steady Navier-Stokes system as presented in equation (3.74). This choice is motivated by the desire to keep this section as brief as possible. Note that the same principles for the treatment of nonlinearity apply to the unsteady Navier-Stokes system as well.

Let the nonlinear system (3.74) be presented in operator form as

$$
\mathcal{L}(\boldsymbol{u}) = \boldsymbol{b} \qquad \text{with } \boldsymbol{u} = (\boldsymbol{v}, p), \tag{3.82}
$$

and let it be disassembled as $\mathcal{L} = \mathcal{L}_A \oplus \mathcal{L}_V \oplus \mathcal{L}_G \oplus \mathcal{L}_D$, with operators $\mathcal{L}_A = \boldsymbol{v} \cdot \nabla \boldsymbol{v}$, $\mathcal{L}_V = -\nu \nabla^2 \boldsymbol{v}$, $\mathcal{L}_G = \nabla p$ and $\mathcal{L}_D = \nabla \cdot \boldsymbol{v}$.

In order to solve equation (3.82), an iterative procedure is required which, starting from an initial guess for the unknowns, linearizes in every relaxation step the nonlinear system based on the current solution $\boldsymbol{u}^n$, and eventually solves the resulting system of linear equations. The iteration is advanced until a stopping criteria such as convergence is achieved.

Since the only nonlinear term in equation (3.82) is given by the advection operator $\mathcal{L}_A$, we linearize the latter via a generalized Taylor expansion of $\mathcal{L}_A$ about the current iterate of the velocity function $\boldsymbol{v}^n$ and ignore higher order terms $O(|\delta \boldsymbol{v}|^2)$. A Newton linearization of $\mathcal{L}_A$ is derived as:

$$
\begin{aligned}
\mathcal{L}_A(\boldsymbol{v}) &= \mathcal{L}_A(\boldsymbol{v}^n) + \left.\frac{d\mathcal{L}_A(\boldsymbol{v}^n + \epsilon \delta \boldsymbol{v})}{d\epsilon}\right|_{\epsilon=0} + O(|\delta \boldsymbol{v}|^2) \\
&\approx \boldsymbol{v}^n \cdot \nabla \boldsymbol{v}^n + \left.\frac{d[(\boldsymbol{v}^n + \epsilon \delta \boldsymbol{v}) \cdot \nabla (\boldsymbol{v}^n + \epsilon \delta \boldsymbol{v})]}{d\epsilon}\right|_{\epsilon=0} \\
&= \boldsymbol{v}^n \cdot \nabla \boldsymbol{v}^n + \left.\frac{d[\boldsymbol{v}^n \cdot \nabla (\boldsymbol{v}^n + \epsilon \delta \boldsymbol{v}) + \epsilon \delta \boldsymbol{v} \cdot \nabla (\boldsymbol{v}^n + \epsilon \delta \boldsymbol{v})]}{d\epsilon}\right|_{\epsilon=0} \\
&= \boldsymbol{v}^n \cdot \nabla \boldsymbol{v}^n + \left.\frac{d[\boldsymbol{v}^n \cdot \nabla \boldsymbol{v}^n + \boldsymbol{v}^n \cdot \nabla \epsilon \delta \boldsymbol{v} + \epsilon \delta \boldsymbol{v} \cdot \nabla \boldsymbol{v}^n + \epsilon^2 \delta \boldsymbol{v} \cdot \nabla \delta \boldsymbol{v}]}{d\epsilon}\right|_{\epsilon=0} \\
&= \boldsymbol{v}^n \cdot \nabla \boldsymbol{v}^n + \boldsymbol{v}^n \cdot \nabla \delta \boldsymbol{v} + \delta \boldsymbol{v} \cdot \nabla \boldsymbol{v}^n = \boldsymbol{v}^n \cdot \nabla \boldsymbol{v}^n + \boldsymbol{v}^n \cdot \nabla (\boldsymbol{v} - \boldsymbol{v}^n) + (\boldsymbol{v} - \boldsymbol{v}^n) \cdot \nabla \boldsymbol{v}^n \\
&= \boldsymbol{v}^n \cdot \nabla \boldsymbol{v}^n + \boldsymbol{v}^n \cdot \nabla \boldsymbol{v} - \boldsymbol{v}^n \cdot \nabla \boldsymbol{v}^n + \boldsymbol{v} \cdot \nabla \boldsymbol{v}^n - \boldsymbol{v}^n \cdot \nabla \boldsymbol{v}^n \\
&= \boldsymbol{v}^n \cdot \nabla \boldsymbol{v} + \boldsymbol{v} \cdot \nabla \boldsymbol{v}^n - \boldsymbol{v}^n \cdot \nabla \boldsymbol{v}^n
\end{aligned}
\tag{3.83}
$$

Note that alternative linearizations are considered in different Picard iteration variants where $\mathcal{L}_A$ is taken either as $\mathcal{L}_A \approx \boldsymbol{v}^n \cdot \nabla \boldsymbol{v}$, $\mathcal{L}_A \approx \boldsymbol{v} \cdot \nabla \boldsymbol{v}^n$ or $\mathcal{L}_A \approx \boldsymbol{v}^n \cdot \nabla \boldsymbol{v}^n$.

3.5 Numerical results

This chapter is dedicated to the presentation of our numerical results obtained with isogeometric finite elements. As aforementioned, the lid-driven cavity flow and flow around cylinder serve as model problems, each discussed in a separate section (3.5.2, 3.5.4) in the sequel. Due to the lack of closed form analytical solutions for either benchmark flow scenarios, we first present in section 3.5.1 our obtained order of convergence for a stationary Stokes flow problem with a closed form analytical solution, before turning the attention to the principal benchmarks.

3.5.1 Order of convergence of a Stokes flow problem with analytical solution

The considered two-dimensional stokes flow problem consists of finding a velocity field $\boldsymbol{v} = (v_1, v_2)$ and a pressure p on the square domain $\Omega = (0, 1) \times (0, 1)$ such that

$$\begin{aligned} -\nu\nabla^2\boldsymbol{v} + \nabla p &= \boldsymbol{b} && \text{in } \Omega, \\ \nabla \cdot \boldsymbol{v} &= 0 && \text{in } \Omega, \\ \boldsymbol{v} &= \boldsymbol{v}_D && \text{on } \Gamma_D, \end{aligned} \tag{3.84}$$

where the kinematic viscosity is taken as $\nu = 1$. The body force $\boldsymbol{b} = (b_1, b_2)$ and exact solution $\boldsymbol{v}^* = (v_1^*, v_2^*, p^*)$ are given as

$$\begin{aligned} b_1 &= 6x + y\cos(xy) + 2\cos(y)\sin(x), \\ b_2 &= x\cos(xy) - 2\cos(x)\sin(y), \end{aligned} \tag{3.85}$$

and

$$\begin{aligned} v_1^* &= \sin(x)\cos(y), \\ v_2^* &= -\sin(y)\cos(x), \\ p^* &= 3x^2 + \sin(xy) - 1.239811742000564725943866, \end{aligned} \tag{3.86}$$

respectively. [14] The exact solution for velocity is prescribed as Dirichlet boundary condition on all four sides of Ω, and as far as pressure is concerned, we require: $\int_\Omega p \, \mathrm{d}\Omega = 0$.

Figure 3.5 illustrates the L^2-errors of the velocity and pressure function approximations for different isogeometric discretizations with varied degrees and regularities. The results verify optimal convergence rates for both velocity and pressure. In particular, keeping the degrees fixed, the discretizations with higher regularities are shown to possess the same rate of convergence as their lower regularity counterparts, while remaining much more efficient. As elaborated in section 3.5.4.1, the efficiency is in terms of the number of degrees of freedom required to gain a certain level of accuracy.

3.5.2 Lid-driven cavity flow

The classical driven cavity flow benchmark considers a fluid in a square cavity with height $H = 1$. The left, bottom and right walls exhibit no-slip Dirichlet boundary conditions ($\boldsymbol{u} = 0$), while the top "wall" is moved with a constant speed $U = 1$. The volumetric force $\mathbf{f}$ is defined to be 0. A schematic representation of the problem statement is given in Figure 3.6. At the upper left and

---

[14] The exact solution and the corresponding body force term is kindly borrowed from the Matlab based IGA package GeoPDEs.

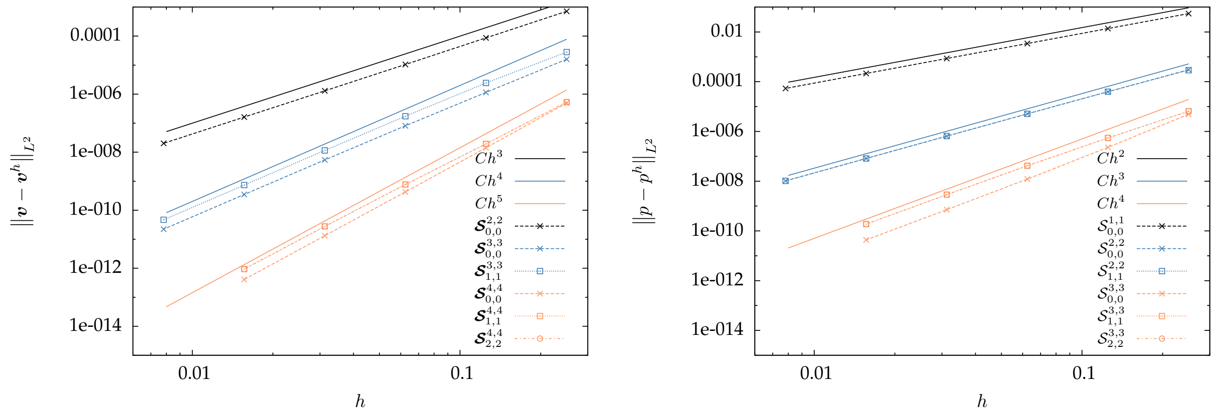

Figure 3.5: Stokes flow: L^2-errors of the velocity and pressure approximations obtained with isogeometric discretizations of various degrees and regularities.

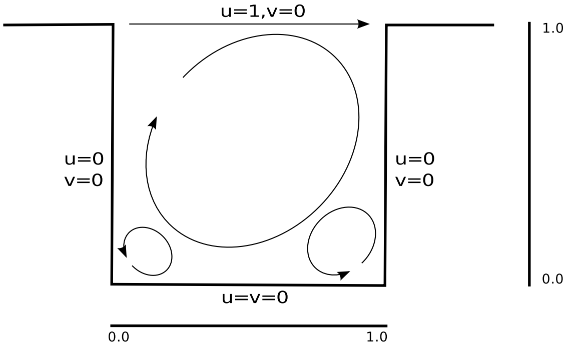

Figure 3.6: Sketch of lid-driven cavity model.

right corners, there is a discontinuity in the velocity boundary conditions producing a singularity in the pressure field at those corners. They can either be considered as part of the upper boundary or as part of the vertical walls. The former case is referred to as the "leaky" cavity rendering the latter "non-leaky". As Dirichlet boundary conditions are imposed everywhere on the boundary ($\Gamma_N = \emptyset$), pressure is in equation (3.74) only present by its gradient, and thus it is only determined up to an arbitrary constant. For a unique definition of the discrete pressure field, it is usual to either impose its average (e.g. $\int_\Omega p \, d\Omega = 0$) or fix its value at one point. We follow the latter approach and fix the value of the discrete pressure field with the value 0 at the lower left corner of the cavity.

Our results, obtained with various B-spline space-based discretizations for three consecutive mesh refinement levels $h \in [1/32, 1/64, 1/128]$ of unstretched meshes, are compared to classical reference results from the literature such as those of Ghia [65] using a second-order upwind finite difference method on a stretched mesh with 192^2 grid points. Moreover, additional comparisons are done with highly accurate, spectral method-based (Chebyshev Collocation) solutions of Botella [20] that show convergence up to seven digits. Furthermore, whenever comparable data is provided, results of two recently published articles [54, 144], both applying IGA to the cavity flow problem, are addressed. All our computations for cavity flow are performed without taking any stabilization measures for the advection term. As for the Newton iteration, the stopping criterion is considered fulfilled when the euclidean norm of the residual of equation (3.74) drops below the bound 10^{-10}.

Using the B-spline space pair $\boldsymbol{\mathcal{S}}^{2,2}_{0,0} \times \mathcal{S}^{1,1}_{0,0}$ for the approximation of the velocity and pressure functions, we present in Figure 3.7 stream function (ψ) and vorticity (ω) profiles computed for Reynolds (Re) numbers $100, 400$ and 1000. Given the circumstance that profiles for ψ and ω are provided by all mentioned references in graphical form only, we conclude the discussion on stream function and vorticity profiles with the note that visually both profiles match the corresponding profiles in the literature very well.

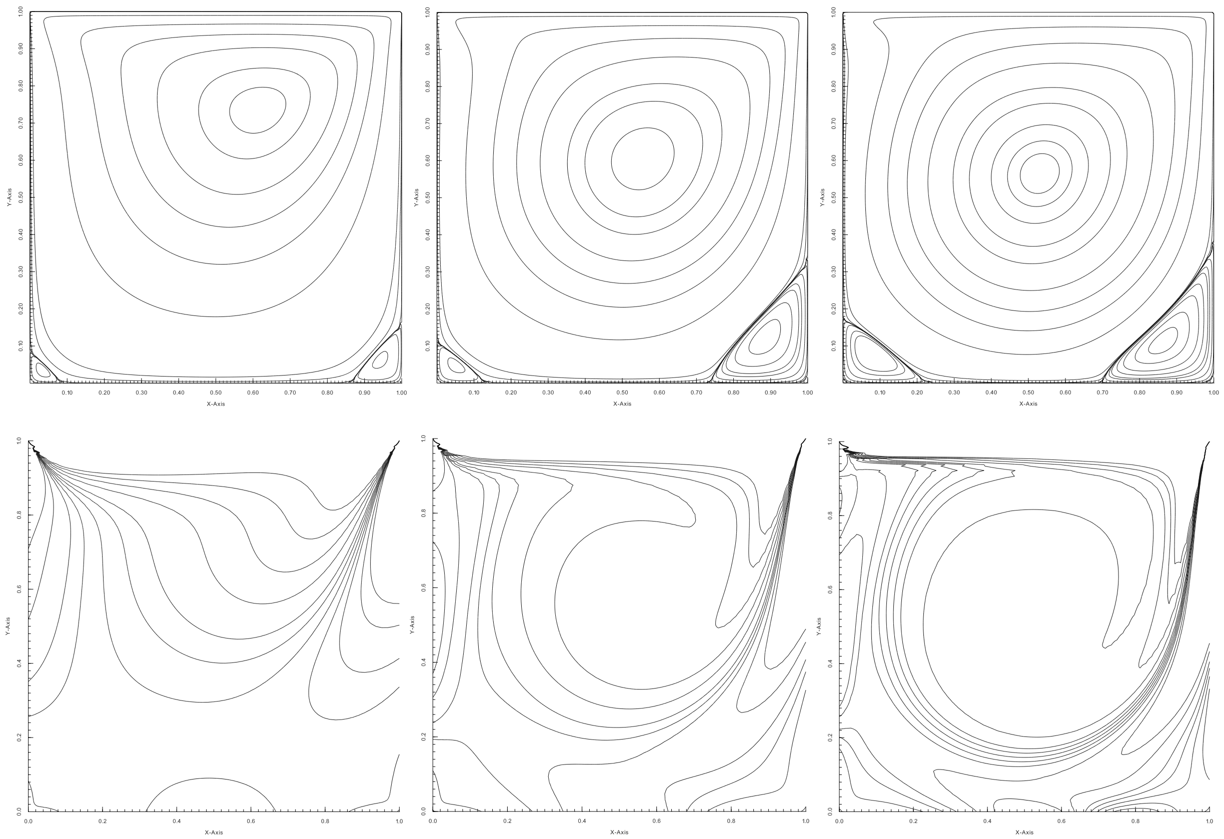

Figure 3.7: Stream function (top) and vorticity (bottom) profiles for Reynolds $100, 400$ and 1000 from left to right. Respective contour ranges for stream function and vorticity: $\psi_{iso} \in [-10^{-10}, 3 \times 10^{-3}]$, $\omega_{iso} \in [-5, 3]$. Discretization: $\boldsymbol{\mathcal{S}}^{2,2}_{0,0} \times \mathcal{S}^{1,1}_{0,0}$. $h = 1/64$ (Refinement level: 6). Number of degrees of freedom: 37507.

Remark 3.5.1. *The approach we follow for the computation of the stream function in 2D, is based on solving a Poisson equation for ψ with the scalar 2D vorticity function on the right hand side:*

$$\begin{aligned} -\nabla^2 \psi &= \omega \\ \omega = \nabla \times \boldsymbol{v} &= \frac{\partial v}{\partial x} - \frac{\partial u}{\partial y} \end{aligned} \tag{3.87}$$

Equation (3.87) is easily solvable via FEM/IGA when formulated as a unique boundary value problem in the domain Ω enclosed by the boundary Γ. We set Dirichlet boundary conditions of 0 on the entire boundary when solving for ψ.

In Table 3.1, stream function and vorticity values at the center of the main vortex are presented for Reynolds numbers $100, 400$, and 1000 and compared to the reference values of Ghia, Botella, and the stream function-based Galerkin IGA scheme of [144]. For each Reynolds number we present values for two different Isogeometric discretizations ($\boldsymbol{\mathcal{S}}_{0,0}^{2,2} \times \mathcal{S}_{0,0}^{1,1}$ and $\boldsymbol{\mathcal{S}}_{4,4}^{6,6} \times \mathcal{S}_{4,4}^{5,5}$), and additionally vary for the latter the mesh refinement among three consecutive stages. Note that in Botella's case the flow is reversed, that is, the velocity at the upper boundary is $\boldsymbol{u} = (-1, 0)$. However, the flow attributes obtained are mirror-symmetric and comparable to those of older references, such as Ghia's. Botella's results, based on a Chebyshev Collocation method with polynomial degrees as high as 160, are considered highly accurate and motivated the usage of a high degree B-splines space pair such as $\boldsymbol{\mathcal{S}}_{4,4}^{6,6} \times \mathcal{S}_{4,4}^{5,5}$. On a general note, for all Reynolds numbers under consideration, our results are considered converged and in good agreement with the references. Without any exception, both Isogeometric discretizations yield values for the position of the main vortex itself, and stream function and vorticity at the main vortex which are closer to Botella's than Ghia's results. A comparison with the stream function formulation based IGA results of [144] reveals matching positions of the main vortex up to four decimal digits for all Reynolds numbers, discretizations, and mesh refinement levels. Our stream function values match [144] very well, but are shown for Re 1000 to be minimally closer to Botella's results for both discretizations and all mesh refinement levels. Coming up next, we depict our approximations of the u- and v-velocity components along vertical and horizontal lines through the geometric center of the cavity, respectively. The corresponding profiles obtained with a $\boldsymbol{\mathcal{S}}_{0,0}^{2,2} \times \mathcal{S}_{0,0}^{1,1}$ discretization for $h \in [1/32, 1/64, 1/128]$ are presented graphically alongside those of Ghia in Figure 3.8. Except for one irregularity with respect to the v-velocity component (see Fig. 3.8) computations in the Re 400 case, the converged profiles follow the reference data of Ghia and reflect the profiles presented in the isogeometric references [54, 144].

The extrema of the velocity components along horizontal and vertical lines through the geometric center of the cavity are listed in Table 3.2 and compared to both isogeometric and the classical references. As can be seen from the tabulated data, the results of the isogeometric Taylor-Hood discretization are closest to those of Botella obtained with a spectral method.

In addition to the presented results regarding the $\boldsymbol{\mathcal{S}}_{0,0}^{2,2} \times \mathcal{S}_{0,0}^{1,1}$ discretization, we deliver additional ones associated to both an approximation space pair with higher regularity $\boldsymbol{\mathcal{S}}_{4,4}^{6,6} \times \mathcal{S}_{4,4}^{5,5}$ ($\mathcal{C}^4$) and a reversed flow direction ($\boldsymbol{u} = (-1, 0)$), such as the setup used by Botella. A graphical representation of converged velocity component and vorticity data approximated in the above described $\mathcal{C}^4$ space pair, exhibiting excellent agreement with the ones stemming from Botella's spectral method, is illustrated in Figure 3.9.

3.5.3 Regularized driven cavity flow

In the regularized lid-driven cavity flow scenario as described in [25], the flow domain is a unit square exhibiting no-slip Dirichlet boundary conditions at the vertical and lower horizontal boundaries. In order to avoid the pressure singularities in the upper left and right domain corners involved with the regular lid-driven cavity flow scenario, the regularized lid-driven cavity flow problem defines the following velocity profile on the top boundary

$$\mathbf{u}_{lid} = [-16x^2(1-x)^2, 0]. \tag{3.88}$$

In addition to the study of local quantities, it is reasonable to extend the analysis to global quantities. Towards this end, we fix the value of the discrete pressure field at the lower left domain node with

Re	Scheme	x	y	ψ	ω	$\mathrm{N_{el}}$	h	$\mathrm{N_{dof}}$	$\mathrm{N_{dof(vel.\ +\ pres.)}}$	Grid points
100	$\boldsymbol{\mathcal{S}}^{2,2}_{0,0} \times \mathcal{S}^{1,1}_{0,0}$	0.6150	0.7350	-0.103524	3.15526	32^2	1/32	9539	(8450+1089)	65^2
	$\boldsymbol{\mathcal{S}}^{2,2}_{0,0} \times \mathcal{S}^{1,1}_{0,0}$	0.6150	0.7350	-0.103517	3.15350	64^2	1/64	37507	(33282+4225)	129^2
	$\boldsymbol{\mathcal{S}}^{2,2}_{0,0} \times \mathcal{S}^{1,1}_{0,0}$	0.6150	0.7350	-0.103516	3.15377	128^2	1/128	148739	(132098+16641)	257^2
	$\boldsymbol{\mathcal{S}}^{6,6}_{4,4} \times \mathcal{S}^{5,5}_{4,4}$	0.6150	0.7350	-0.103516	3.15382	32^2	1/32	10891	(9522+1369)	69^2
	$\boldsymbol{\mathcal{S}}^{6,6}_{4,4} \times \mathcal{S}^{5,5}_{4,4}$	0.6150	0.7350	-0.103516	3.15383	64^2	1/64	40139	(35378+4761)	133^2
	$\boldsymbol{\mathcal{S}}^{6,6}_{4,4} \times \mathcal{S}^{5,5}_{4,4}$	0.6150	0.7350	-0.103516	3.15383	128^2	1/128	153931	(136242+17689)	261^2
	Ghia [65]	0.6172	0.7344	-0.103423	3.16646		1/128			129^2
	[144]	0.6150	0.7350	-0.103518		256^2	1/256	66564		258^2
400	$\boldsymbol{\mathcal{S}}^{2,2}_{0,0} \times \mathcal{S}^{1,1}_{0,0}$	0.5550	0.6050	-0.114019	2.29555	32^2	1/32	9539	(8450+1089)	65^2
	$\boldsymbol{\mathcal{S}}^{2,2}_{0,0} \times \mathcal{S}^{1,1}_{0,0}$	0.5550	0.6050	-0.113996	2.29470	64^2	1/64	37507	(33282+4225)	129^2
	$\boldsymbol{\mathcal{S}}^{2,2}_{0,0} \times \mathcal{S}^{1,1}_{0,0}$	0.5550	0.6050	-0.113989	2.29449	128^2	1/128	148739	(132098+16641)	257^2
	$\boldsymbol{\mathcal{S}}^{6,6}_{4,4} \times \mathcal{S}^{5,5}_{4,4}$	0.5550	0.6050	-0.113985	2.29448	32^2	1/32	10891	(9522+1369)	69^2
	$\boldsymbol{\mathcal{S}}^{6,6}_{4,4} \times \mathcal{S}^{5,5}_{4,4}$	0.5550	0.6050	-0.113988	2.29448	64^2	1/64	40139	(35378+4761)	133^2
	$\boldsymbol{\mathcal{S}}^{6,6}_{4,4} \times \mathcal{S}^{5,5}_{4,4}$	0.5550	0.6050	-0.113988	2.29448	128^2	1/128	153931	(136242+17689)	261^2
	Ghia [65]	0.5547	0.6055	-0.113909	2.29469		1/256			257^2
	[144]	0.5550	0.6050	-0.114031		256^2	1/256	66564		258^2
1000	$\boldsymbol{\mathcal{S}}^{2,2}_{0,0} \times \mathcal{S}^{1,1}_{0,0}$	0.5300	0.5650	-0.1189603	2.070030	32^2	1/32	9539	(8450+1089)	65^2
	$\boldsymbol{\mathcal{S}}^{2,2}_{0,0} \times \mathcal{S}^{1,1}_{0,0}$	0.5300	0.5650	-0.1189511	2.067930	64^2	1/64	37507	(33282+4225)	129^2
	$\boldsymbol{\mathcal{S}}^{2,2}_{0,0} \times \mathcal{S}^{1,1}_{0,0}$	0.5300	0.5650	-0.1189400	2.067790	128^2	1/128	148739	(132098+16641)	257^2
	$\boldsymbol{\mathcal{S}}^{6,6}_{4,4} \times \mathcal{S}^{5,5}_{4,4}$	0.5300	0.5650	-0.1189165	2.067510	32^2	1/32	10891	(9522+1369)	69^2
	$\boldsymbol{\mathcal{S}}^{6,6}_{4,4} \times \mathcal{S}^{5,5}_{4,4}$	0.5300	0.5650	-0.1189341	2.067710	64^2	1/64	40139	(35378+4761)	133^2
	$\boldsymbol{\mathcal{S}}^{6,6}_{4,4} \times \mathcal{S}^{5,5}_{4,4}$	0.5300	0.5650	-0.1189360	2.067730	128^2	1/128	153931	(136242+17689)	261^2
	Botella [20]	0.5308	0.5652	-0.1189249	2.067396		1/48			$\mathrm{N} = 48$
	Botella [20]	0.5308	0.5652	-0.1189366	2.067750		1/96			$\mathrm{N} = 96$
	Botella [20]	0.5308	0.5652	-0.1189366	2.067753		1/160			$\mathrm{N} = 160$
	Ghia [65]	0.5313	0.5625	-0.1179290	2.049680		1/128			129^2
	[144]	0.5300	0.5650	-0.1185110		256^2	1/256	66564		258^2

Table 3.1: Location, stream function and vorticity of the primary vortex for Re 100, 400 and 1000. N is used to characterize the $\mathrm{N}+1 \times \mathrm{N}+1$ Gauss-Lobatto grid used in the Chebyshev Collocation method utilized by Botella. In the case of the Isogeometric discretizations we carried our computations upon, the element meshes are uniformly spaced and "grid points" refers to the number of basis functions (degrees of freedom) of the respective discrete approximation space for one velocity component. $\mathrm{N_{dof}}$ and $\mathrm{N_{el}}$ represent the number of degrees of freedom and the number of elements, respectively.

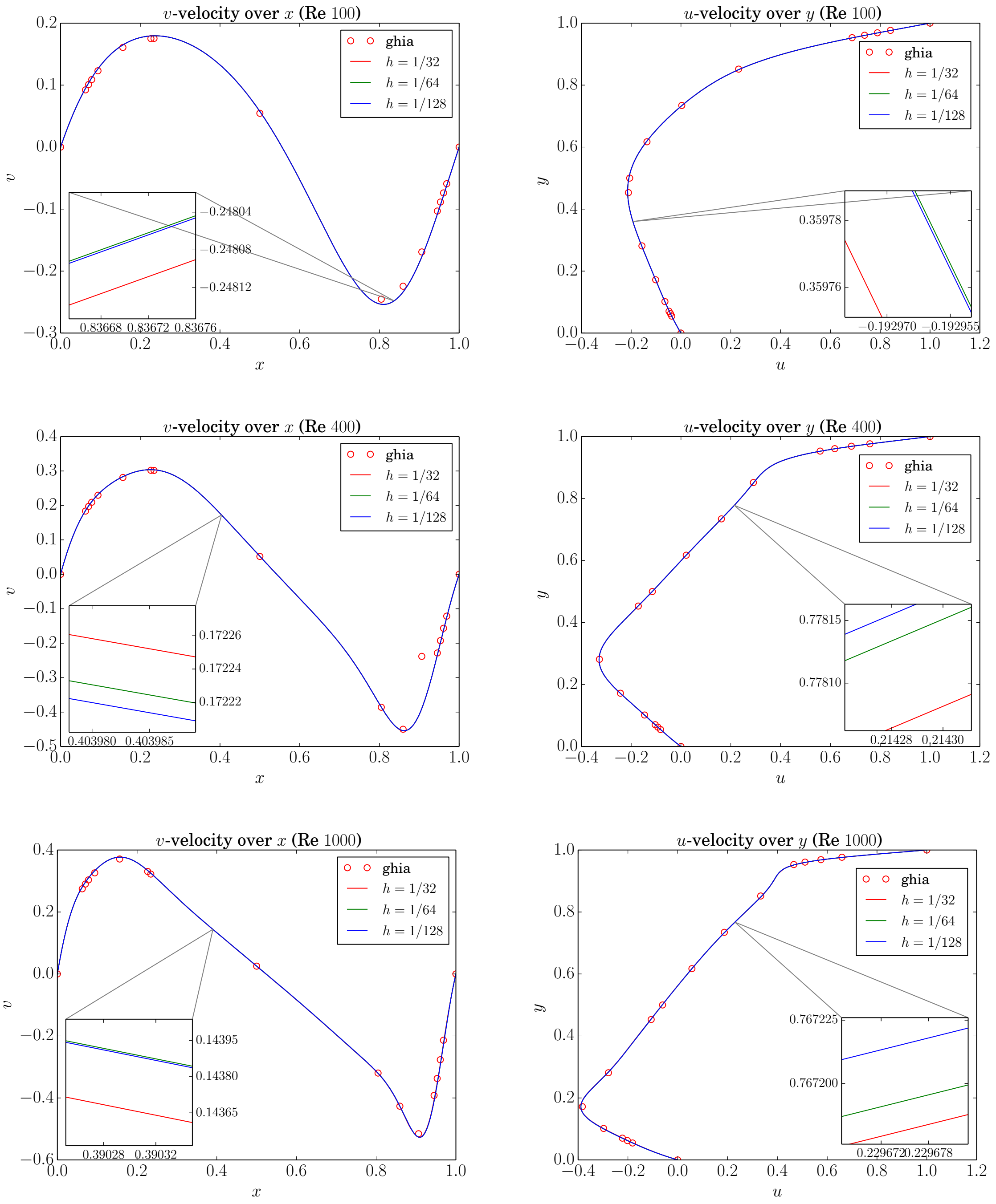

Figure 3.8: Profiles of v- and u-velocity components over horizontal and vertical lines through geometric center of the cavity for Re 100, 400 and 1000. Discretization: $\boldsymbol{\mathcal{S}}_{0,0}^{2,2} \times \mathcal{S}_{0,0}^{1,1}$; See Table 3.1 for the number of degrees of freedom.

$p = 0$, and compute the global quantities KINETIC ENERGY (E) and ENSTROPHY (Z)

$$E = \frac{1}{2} \int_{\Omega} \|\mathbf{u}\|^2 \, \mathrm{d}x, \qquad Z = \frac{1}{2} \int_{\Omega} \omega^2 \, \mathrm{d}x, \tag{3.89}$$

Re	Center line	Property	$\boldsymbol{\mathcal{S}}^{2,2}_{0,0} \times \mathcal{S}^{1,1}_{0,0} (h = 1/128)$	Botella [20]	Ghia [65]	[54] $(h = 1/128)$	[144] $(h = 1/256, p = 2)$
100	Vertical	u_{min}	$-0.214\,04$	$-0.214\,04$	$-0.210\,90$	$-0.214\,14$	$-0.214\,02$
	$(x = 0.5)$	y-coord	0.4578	0.4581	0.4531		0.4600
	Horizontal	v_{min}	$-0.253\,80$	$-0.253\,80$	$-0.245\,33$	$-0.253\,87$	$-0.253\,71$
	$(y = 0.5)$	x-coord	0.8112	0.8104	0.8047		0.8100
		v_{max}	$0.179\,57$	$0.179\,57$	$0.175\,27$	$0.179\,66$	$0.179\,53$
		x-coord	0.2369	0.2370	0.2344		0.2350
400	Vertical	u_{min}	$-0.328\,72$		$-0.327\,26$	$-0.329\,89$	$-0.328\,80$
	$(x = 0.5)$	y-coord	0.2811		0.2813		0.2800
	Horizontal	v_{min}	$-0.454\,02$		$-0.449\,93$	$-0.454\,70$	$-0.453\,86$
	$(y = 0.5)$	x-coord	0.8635		0.8594		0.8600
		v_{max}	$0.303\,83$		$0.302\,03$	$0.304\,71$	$0.303\,93$
		x-coord	0.2249		0.2266		0.2250
1000	Vertical	u_{min}	$-0.388\,57$	$-0.388\,53$	$-0.382\,89$	$-0.390\,21$	$-0.387\,54$
	$(x = 0.5)$	y-coord	0.1727	0.1717	0.1719		0.1700
	Horizontal	v_{min}	$-0.526\,92$	$-0.527\,07$	$-0.515\,50$	$-0.528\,84$	$-0.525\,82$
	$(y = 0.5)$	x-coord	0.9076	0.9092	0.9063		0.9100
		v_{max}	$0.376\,94$	$0.376\,94$	$0.370\,95$	$0.378\,56$	$0.375\,72$
		x-coord	0.1566	0.1578	0.1563		0.1600

Table 3.2: Extrema of the velocity components w.r.t vertical and horizontal lines through the geometric center of the cavity for Re $100, 400$ and 1000.

where $\omega = \frac{\partial v}{\partial x} - \frac{\partial u}{\partial y}$ denotes the scalar vorticity in 2D. In Table 3.3 we compare our results for Reynolds number 1000, computed on unstretched meshes, to the results of Bruneau [25] using finite differences and a [15] Q_2P_1 finite element discretization, published in [112]. All three isogeometric

Scheme	Kinetic energy	Enstrophy	$\mathrm{N_{el}}$	h	$\mathrm{N_{dof}}$	$\mathrm{N_{dof(vel.\ +\ pres.)}}$	Grid points
$\boldsymbol{\mathcal{S}}^{2,2}_{0,0} \times \mathcal{S}^{1,1}_{0,0}$	0.022909	4.80747	32^2	1/32	9539	(8450+1089)	65^2
	0.022778	4.82950	64^2	1/64	37507	(33282+4225)	129^2
	0.022767	4.83041	128^2	1/128	148739	(132098+16641)	257^2
	0.022767	4.83043	256^2	1/256	592387	(526338+66049)	513^2
$\boldsymbol{\mathcal{S}}^{3,3}_{0,0} \times \mathcal{S}^{2,2}_{0,0}$	0.022905	4.81717	16^2	1/16	5891	(4802+1089)	49^2
	0.022773	4.83079	32^2	1/32	23043	(18818+4225)	97^2
	0.022767	4.83047	64^2	1/64	91139	(74498+16641)	193^2
	0.022767	4.83042	128^2	1/128	362499	(296450+66049)	385^2
$\boldsymbol{\mathcal{S}}^{3,3}_{1,1} \times \mathcal{S}^{2,2}_{1,1}$	0.022777	4.82954	32^2	1/32	9868	(8712+1156)	66^2
	0.022767	4.83048	64^2	1/64	38156	(33800+4356)	130^2
	0.022767	4.83046	128^2	1/128	150028	(133128+16900)	258^2
Ref. [25] (Bruneau)	0.021564	4.6458					64^2
	0.022315	4.7711					128^2
	0.022542	4.8123					256^2
	0.022607	4.8243					512^2
Ref. [112] (Q_2P_1 FE)	0.022778	4.82954	64^2	1/64			
	0.022768	4.83040	128^2	1/128			
	0.022766	4.83050	256^2	1/256			

Table 3.3: Kinetic energy and enstrophy of the regularized cavity flow for Reynolds 1000. In the case of Isogeometric discretizations, "grid points" refers to the number of basis functions (degrees of freedom) of the respective discrete approximation space for one velocity component.

---

[15] Velocity: Biquadratic, continuous; Pressure: Linear (value and two partial derivatives), discontinuous

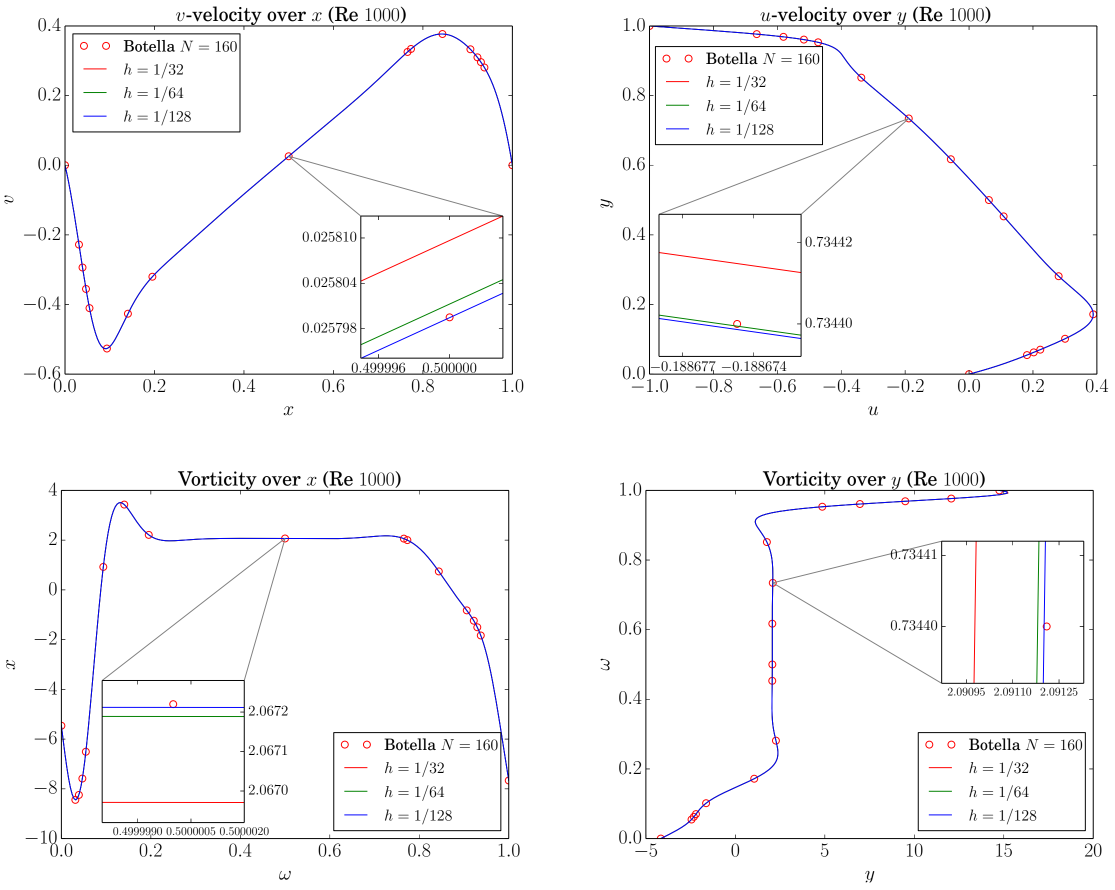

Figure 3.9: Profiles of v- and u-velocity components and vorticity over horizontal and vertical lines through geometric center of the cavity for Re 1000. Discretization: $\boldsymbol{\mathcal{S}}^{6,6}_{4,4} \times \mathcal{S}^{5,5}_{4,4}$; See Table 3.1 for the number of degrees of freedom.

finite element pairs in charge produce very satisfying results for kinetic energy and enstrophy obviously well integrating with references. Selecting the isogeometric finite element pair with the lowest degree $\boldsymbol{\mathcal{S}}^{2,2}_{0,0} \times \mathcal{S}^{1,1}_{0,0}$, we compare in Table 3.4 the approximated kinetic energy for three mesh refinement levels with data [112] obtained from three different finite element discretizations, namely[16], $\tilde{Q}_1 Q_0$, $Q_2 P_1$, and[17] W-LSFE Q_2, all available in the FeatFlow[18] package. As can be deduced from the tabulated data, our results are characterized by both a high accuracy and a satisfactory convergence for all considered Reynolds numbers.

3.5.4 Flow around cylinder

Flow around an obstacle in a channel is a prominent benchmark model for the assessment of flow affiliated attributes, produced by a numerical technique in charge with the analysis. Following the lines of [44, 45, 111, 129], we choose as flow scenarios a steady Re 20 and a transient Re 100 2D

---

[16] Velocity: Bilinear, rotated; Pressure: Constant.

[17] Biquadratic Least-Square finite elements.

[18] www.featflow.de.

Re	h	$\boldsymbol{\mathcal{S}}_{0,0}^{2,2} \times \mathcal{S}_{0,0}^{1,1}$	$\tilde{Q}_1 Q_0$ FE	$Q_2 P_1$ FE	W-LSFE Q_2 [112]
1	1/64	1.862439e-02	1.860621e-02	1.862439e-02	1.862353e-02
	1/128	1.862438e-02	1.861982e-02	1.862438e-02	1.862432e-02
	1/256	1.862438e-02	1.862324e-02	1.862438e-02	1.862438e-02
400	1/64	2.131703e-02	2.148649e-02	2.131707e-02	2.133053e-02
	1/128	2.131547e-02	2.136484e-02	2.131547e-02	2.131581e-02
	1/256	2.131537e-02	2.132812e-02	2.131529e-02	2.131537e-02
1000	1/64	2.277788e-02	2.409799e-02	2.277778e-02	2.552796e-02
	1/128	2.276761e-02	2.305179e-02	2.276761e-02	2.287704e-02
	1/256	2.276692e-02	2.282649e-02	2.276582e-02	2.277389e-02

Table 3.4: Convergence of approximated kinetic energy for the regularized cavity flow problem.

channel flow the details of which are presented in sections 3.5.4.1 and 3.5.4.2, respectively. The underlying geometry for both cases is depicted in Figure 3.10 and is defined as a pipe where a circular cylinder of radius $r = 0.05$ has been cut out, that is, $\Omega = (0, 2.2) \times (0, 0.41) \setminus B_r(0.2, 0.2)$[19]. The cylinder is centered around $(x, y) = (0.2, 0.2)$.

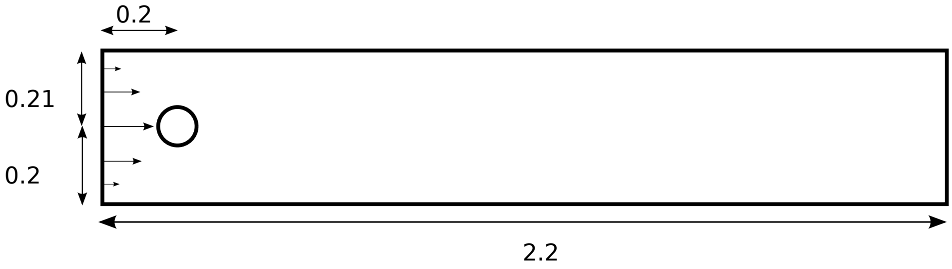

Figure 3.10: Computational domain for flow around cylinder.

3.5.4.1 DFG benchmark 2D-1

In DFG BENCHMARK 2D-1 the fluid density and kinematic viscosity are taken as $\rho = 1$ and $\nu = 0.001$. We require no-slip boundary conditions for the lower and upper walls $\Gamma_1 = (0, 2.2) \times \{0\}$ and $\Gamma_3 = (0, 2.2) \times \{0.41\}$, as well as for the boundary $S = \partial B_r(0.2, 0.2)$: $u_{|\Gamma_1} = u_{|\Gamma_3} = u_{|S} = 0$. On the left edge $\Gamma_4 = \{0\} \times (0, 0.41)$, a parabolic inflow profile is prescribed, $u(0, y) = \left(\frac{4Uy(0.41-y)}{0.41^2}, 0\right)$, with a maximum velocity $U = 0.3$. On the right edge $\Gamma_2 = \{2.2\} \times (0, 0.41)$, "do-nothing" boundary conditions, $-p\boldsymbol{n} + \nu(\boldsymbol{n} \cdot \nabla)\boldsymbol{v} = \boldsymbol{0}$, define the outflow, with $\boldsymbol{n}$ denoting the outer normal vector. For a maximum velocity of $U = 0.3$, the parabolic profile results in a mean velocity $\bar{U} = \frac{2}{3} \cdot 0.3 = 0.2$. The flow configurations characteristic length $D = 2 \cdot 0.05 = 0.1$ is the diameter of the object perpendicular to the flow direction. This particular problem configuration yields Reynolds number $\text{Re} = \frac{\bar{U}D}{\nu} = \frac{0.2 \cdot 0.1}{0.001} = 20$ for which the flow is considered stationary.

Following the above setup for $\text{Re} = 20$, we present the results of the application of Isogeometric Analysis, with particular emphasis on the approximated drag and lift values related to the entire

---

[19] The presented measures for the domain definition are in meters.

obstacle boundary.

With S dubbing the surface of the obstacle, $\boldsymbol{n}_S$ its inward pointing unit normal vector w.r.t. the computational domain Ω, tangent vector $\boldsymbol{\tau} := (n_y, -n_x)^T$ and $\boldsymbol{u}_\tau := \boldsymbol{u} \cdot \boldsymbol{\tau}$, the drag and lift forces are given by

$$\begin{aligned}
F_D &= \int_S \left(\rho\nu \frac{\partial \boldsymbol{v}_\tau}{\partial \boldsymbol{n}_S} n_y - p n_x \right) ds, \qquad F_L = -\int_S \left(\rho\nu \frac{\partial \boldsymbol{v}_\tau}{\partial \boldsymbol{n}_S} n_x + p n_y \right) ds, \\
\frac{\partial \boldsymbol{v}_\tau}{\partial \boldsymbol{n}_S} &= \frac{\partial \left(v_x n_y - v_y n_x \right)}{\partial \boldsymbol{n}_S} = \left(\frac{\partial v_x}{\partial x} n_x n_y + \frac{\partial v_x}{\partial y} n_y^2 - \frac{\partial v_y}{\partial x} n_x^2 - \frac{\partial v_y}{\partial y} n_x n_y \right), \\
C_D &= \frac{2}{\rho \bar{U}^2 D} F_D, \qquad C_L = \frac{2}{\rho \bar{U}^2 D} F_L,
\end{aligned} \tag{3.90}$$

where C_D and C_L are the drag and lift coefficients, and $\boldsymbol{u}$ and p represent velocity and pressure, respectively [93, 129]. We follow, however, the alternative approach of [93, 150] and evaluate a volume integral for the approximations of the drag and lift coefficients. Given filter functions

$$\boldsymbol{v}_{d|S} = (1,0)^T, \boldsymbol{v}_{d|\bar{\Omega}-S} = \mathbf{0} \qquad \boldsymbol{v}_{l|S} = (0,1)^T, \boldsymbol{v}_{l|\bar{\Omega}-S} = \mathbf{0}, \tag{3.91}$$

the corresponding volume integral expressions read

$$\begin{aligned}
C_D &= -\frac{2}{\rho \bar{U}^2 D} \left[(\nu \nabla \boldsymbol{u}, \nabla \boldsymbol{v_d}) - (p, \nabla \cdot \boldsymbol{v_d}) \right] \\
C_L &= -\frac{2}{\rho \bar{U}^2 D} \left[(\nu \nabla \boldsymbol{u}, \nabla \boldsymbol{v_l}) - (p, \nabla \cdot \boldsymbol{v_l}) \right],
\end{aligned} \tag{3.92}$$

with $(\cdot,\cdot)$ denoting the $L^2(\Omega)$ inner product. Note that in the discrete setting, we use the respective interpolants of the discontinuous filter functions $\boldsymbol{v}_d$ and $\boldsymbol{v}_l$.

We model the computational domain as a multi-patch NURBS mesh (see Fig. 3.11), due to the fact that the parametric space of a multi-variate NURBS patch exhibits a tensor product structure, and thus is not mappable to any other topology than a cube in the respective N-dimensional space. However, the multi-patch setup yields a perfect mathematical representation of the circular boundary and in particular avoids its approximation with straight line segments. Note that each quarter of the "obstacle circle" can be modeled exactly with a NURBS curve of degree 2 and just 3 control points. Since the ability to exactly represent conical sections is restricted to rational B-splines only, a NURBS mesh comes in handy for the modeling of the computational domain. In order to impose

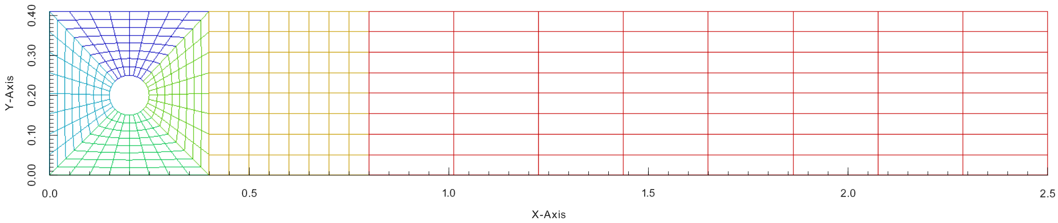

Figure 3.11: Multi-patch NURBS mesh for flow around cylinder at refinement level 3. Each uniquely colored initial 1×1 element patch has been refined three times, giving rise to 8×8 elements in each patch, eventually.

the parabolic inflow condition, we perform a finite element L^2-projection

$$\int_{\Gamma_4} (f - P_h f)\, w \,\mathrm{d}\Gamma_4 = 0, \quad \forall w \in \mathcal{W}_h \tag{3.93}$$

of the inflow profile f on the control points associated with the left boundary (Γ_4) in Fig. 3.11, whereby $\mathcal{W}_h$ denotes a suitable discrete space of weighting/test functions.

For the approximation of drag, lift, and pressure drop we use two different isogeometric discretizations, namely, $\boldsymbol{\mathcal{S}}^{3,3}_{0,0} \times \mathcal{S}^{2,2}_{0,0}$ and $\boldsymbol{\mathcal{S}}^{3,3}_{1,1} \times \mathcal{S}^{2,2}_{1,1}$, and compare their results for different mesh refinement levels with a reference solution computed with high order spectral methods [111]. The choice of these two isogeometric discretizations is explained by the fact that we require the discrete pressure approximation space to have the same degrees and regularities as the geometry. Since modeling one quarter of the obstacle circle requires a NURBS curve of at least degree 2, the degrees of the discrete pressure approximation space reflect this setting. The degrees and regularities of the discrete velocity approximation space eventually follow from the constraints defined by Taylor-Hood elements (see e.g. [29]). In fact, given an initial discrete pressure space, we use k-refinement [37] followed by knot insertion to setup a desired Taylor-Hood space of higher degree and possibly lower regularity.

We refer to table 3.5 for a compilation of the approximated forces for different mesh refinement levels. Our results exhibit high accuracy on the highest mesh refinement level (L8), since a comparison with the reference data reveals 4, 6, and 7 matching decimal digits for drag, lift, and pressure drop, respectively. Moreover, starting with mesh refinement level 6, the approximated drag and lift coefficients of both isogeometric discretizations are, except for one irregularity, identical with respect to the displayed number of decimal digits. This result is remarkable and advocates the usage of the discretization with higher continuity, since the number of degrees of freedoms it requires to reach the same accuracy on refinement level 7 is approximately 42% of its $\mathcal{C}^0$ counterpart. The development of this "gain" is illustrated in Figure 3.12 for mesh refinement levels one to eight. Comparing the presented $\mathcal{C}^0$- and $\mathcal{C}^1$-based isogeometric discretizations, one observes in the former case an increased amount of degrees of freedom on the same number of elements. This is due to the fact that the discretization with the lower continuity exhibits an increased internal knot multiplicity which in turn implies a larger number of basis functions. This leads on mesh refinement levels

Scheme	C_D	C_L	Δp	$\mathrm{N}_{\mathrm{dof}}$	N_{el}	Level (L)
$\boldsymbol{\mathcal{S}}^{3,3}_{0,0} \times \mathcal{S}^{2,2}_{0,0}$	5.645768	0.0067650	0.11675114	8832	384	L3
$\boldsymbol{\mathcal{S}}^{3,3}_{0,0} \times \mathcal{S}^{2,2}_{0,0}$	5.594618	0.0095045	0.11733243	34560	1536	L4
$\boldsymbol{\mathcal{S}}^{3,3}_{0,0} \times \mathcal{S}^{2,2}_{0,0}$	5.582119	0.0104074	0.11749107	136704	6144	L5
$\boldsymbol{\mathcal{S}}^{3,3}_{0,0} \times \mathcal{S}^{2,2}_{0,0}$	5.579918	0.0105860	0.11751658	543744	24576	L6
$\boldsymbol{\mathcal{S}}^{3,3}_{0,0} \times \mathcal{S}^{2,2}_{0,0}$	5.579588	0.0106143	0.11751977	2168832	98304	L7
$\boldsymbol{\mathcal{S}}^{3,3}_{0,0} \times \mathcal{S}^{2,2}_{0,0}$	5.579543	0.0106183	0.11752012	8663040	393216	L8
$\boldsymbol{\mathcal{S}}^{3,3}_{1,1} \times \mathcal{S}^{2,2}_{1,1}$	5.647333	0.0066836	0.11633509	4212	384	L3
$\boldsymbol{\mathcal{S}}^{3,3}_{1,1} \times \mathcal{S}^{2,2}_{1,1}$	5.594742	0.0095065	0.11723232	15300	1536	L4
$\boldsymbol{\mathcal{S}}^{3,3}_{1,1} \times \mathcal{S}^{2,2}_{1,1}$	5.582148	0.0104082	0.11749043	58212	6144	L5
$\boldsymbol{\mathcal{S}}^{3,3}_{1,1} \times \mathcal{S}^{2,2}_{1,1}$	5.579918	0.0105861	0.11751770	226980	24576	L6
$\boldsymbol{\mathcal{S}}^{3,3}_{1,1} \times \mathcal{S}^{2,2}_{1,1}$	5.579588	0.0106143	0.11751993	896292	98304	L7
$\boldsymbol{\mathcal{S}}^{3,3}_{1,1} \times \mathcal{S}^{2,2}_{1,1}$	5.579543	0.0106183	0.11752014	3562020	393216	L8
Ref. [44, 111]	5.57953523384	0.010618948146	0.11752016697			

Table 3.5: Approximation results for drag, lift and pressure drop (Δp).

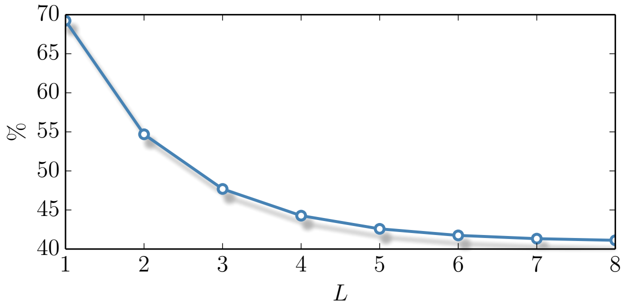

Figure 3.12: Percentage ratio $(\mathrm{DOFs}(\boldsymbol{\mathcal{S}}^{3,3}_{1,1} \times \mathcal{S}^{2,2}_{1,1}, \mathrm{L})/\mathrm{DOFs}(\boldsymbol{\mathcal{S}}^{3,3}_{0,0} \times \mathcal{S}^{2,2}_{0,0}, \mathrm{L}) \times 100)$ of the number of degrees of freedom of the $\mathcal{C}^1$ discretization and the $\mathcal{C}^0$ discretization for each mesh refinement level L of the flow around cylinder mesh. Table 3.5 lists the number of degrees of freedom for each L.

≥ 1 to numbers of degrees of freedom which are not well comparable between the two IGA-based discretizations. However, a linear interpolation of the the drag and lift percent errors, as depicted in Figure 3.13, bears testimony to the accuracy-wise superiority of the high continuity $\mathcal{C}^1$ approach. The semantics of superiority is in terms of gained accuracy with respect to the number of degrees

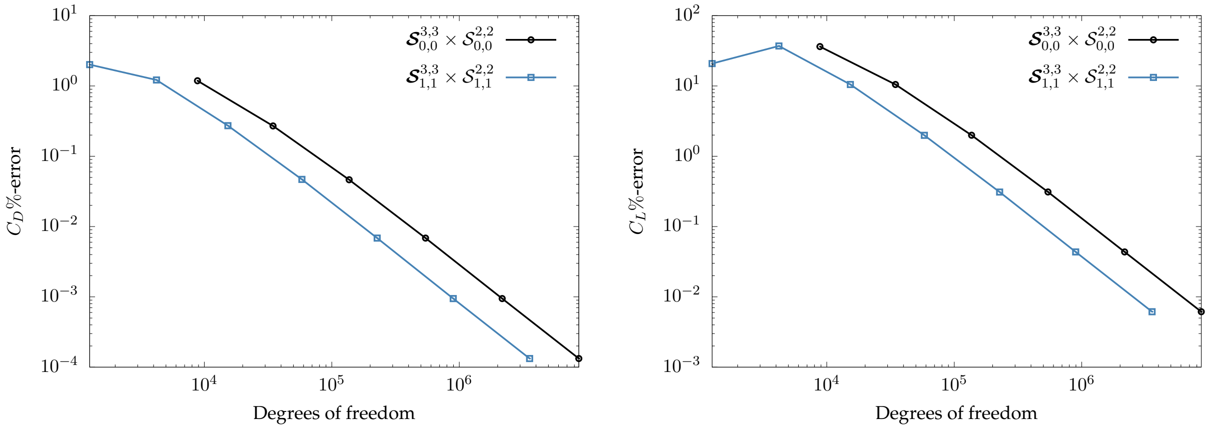

Figure 3.13: Sectional view of drag and lift percent errors. Discretizations: $\boldsymbol{\mathcal{S}}^{3,3}_{0,0} \times \mathcal{S}^{2,2}_{0,0}$; $\boldsymbol{\mathcal{S}}^{3,3}_{1,1} \times \mathcal{S}^{2,2}_{1,1}$.

of freedom invested.

Remark 3.5.2. *We point out that, regardless of the regularity, the support of univariate B-spline and NURBS basis functions of degree* p *is always* $p+1$ *knot spans. In* $1D$*, the number of functions that any given function shares support with (including itself) is* $2p+1$*, and the maximum bandwidth of a stiffness matrix produced with IGA in a Galerkin framework, is always* $2p+1$ *regardless of the smoothness of the basis functions* ($\mathcal{C}^0$ *or* $\mathcal{C}^{p-1}$ *continuous).*

Generally, it should be noted that the solutions we obtained with the $\mathcal{C}^{>0}$ approaches still reduce to $\mathcal{C}^0$ at patch boundaries. There exist means to overcome this deficiency [37], none of which have been considered in this study, though. Besides, for all simulations performed, we utilized standard quadrature rules (#cub.pts $= p+1$), certainly not the most efficient rules at Isogeometric Analysis' disposal. Finally, for the nonlinear iteration the same stopping criterion as in the lid-driven cavity case is used, that is, it is halted as soon as the euclidean norm of the residual of equation (3.74) is below 10^{-10}.

3.5.4.2 DFG benchmark 2D-2

In the following we turn our attention to the DFG benchmark 2D-2 [45, 129] defining an unsteady configuration for the flow around cylinder scenario on the same computational domain as in the DFG benchmark 2D-1 case. The setup aims to simulate the time-periodic behavior of a fluid in a 2D pipe with a circular obstacle. The attention is turned in particular to the resulting drag, lift, and pressure drop profiles which are shown to have an oscillating and periodic structure. These profiles are analyzed with respect to their frequency, amplitude, minimum, maximum, and mean values.

In this benchmark, the maximum velocity of the parabolic inflow profile amounts to $U = 1.5$, yielding Re $= \frac{\bar{U}D}{\nu} = \frac{\frac{2}{3}\cdot\frac{3}{2}\cdot 0.1}{0.001} = 100$. In order to obtain a time profile for the drag, lift, and pressure drop coefficients, we use again the NURBS mesh shown in Figure 3.11 and apply Isogeometric Analysis to the unsteady incompressible Navier-Stokes equations (3.79), using the Taylor-Hood B-spline spaces $\hat{Q}_h^{TH} = \mathcal{S}_{0,0}^{2,2}$ and $\hat{\mathbf{V}}_h^{TH} = \boldsymbol{\mathcal{S}}_{0,0}^{3,3}$ for pressure and velocity, respectively. Treating equation (3.79) as is, i.e. without the application of any operator splitting techniques, corresponds to solving in a fully coupled manner since we solve for all unknown functions simultaneously.

For the time discretization, the one-step θ-scheme with $\theta = 0.5$ is used, leading to the 2nd order accurate implicit Crank-Nicolson scheme [147]. Together with the space discretization, the following nonlinear block system has to be solved in every time step

$$\begin{pmatrix} \frac{1}{\Delta t}\mathbf{M} + \theta(\mathbf{D} + \mathbf{C}(v^{n+1})) & \mathbf{G} \\ \mathbf{G}^T & \mathbf{0} \end{pmatrix} \begin{pmatrix} \mathbf{v}^{n+1} \\ \mathbf{p}^{n+1} \end{pmatrix} = \begin{pmatrix} \frac{1}{\Delta t}\mathbf{M} - (1-\theta)(\mathbf{D} + \mathbf{C}(v^{n})) & \mathbf{0} \\ \mathbf{0} & \mathbf{0} \end{pmatrix} \begin{pmatrix} \mathbf{v}^{n} \\ \mathbf{p}^{n} \end{pmatrix} + \theta\mathbf{f}^{n+1} + (1-\theta)\mathbf{f}^{n}. \tag{3.94}$$

In the above system, $\mathbf{M}, \mathbf{D}, \mathbf{C}, \mathbf{G}$, and $\mathbf{G^T}$ denote the mass, diffusion, advection, gradient, and divergence matrices, respectively. The body forces are discretized into $\mathbf{f}$. As far as the treatment of nonlinearity is concerned, for every time step, the nonlinear iteration is advanced until the nonlinear residual of equation (3.94) is reduced to 10^{-3} of its initial value.

For all mesh levels we performed an intermediate computation with a very coarse time step ($\Delta t = 1/10$) for a total time of 35 simulation seconds. This yielded a profile which we took as an initial solution for the final computation with a finer time step, scheduled for 30 simulation seconds.

Exemplary sectional views of the approximated drag, lift and pressure drop time profiles for three consecutive mesh refinement levels and a time step size of $\Delta t = 1/400$ are presented in Figure 3.16. Note that the depicted time interval is chosen arbitrarily after the drag and lift profiles were considered fully developed. In addition, the curves have been shifted in time in order to facilitate comparison.

Tables 3.6 and 3.7 supply minimum, maximum, mean, and amplitude values for the approximated drag and lift coefficients of different mesh refinement levels.

Our results are shown to converge to the most accurate available results of an alternative numerical simulation [45] using Q_2P_1 finite elements (without stabilization) for space discretization and Crank-Nicolson scheme for time discretization. Note that the absolute error of the lift coefficient is at level $L4$ already one order of magnitude smaller than that of the drag coefficient. However, the

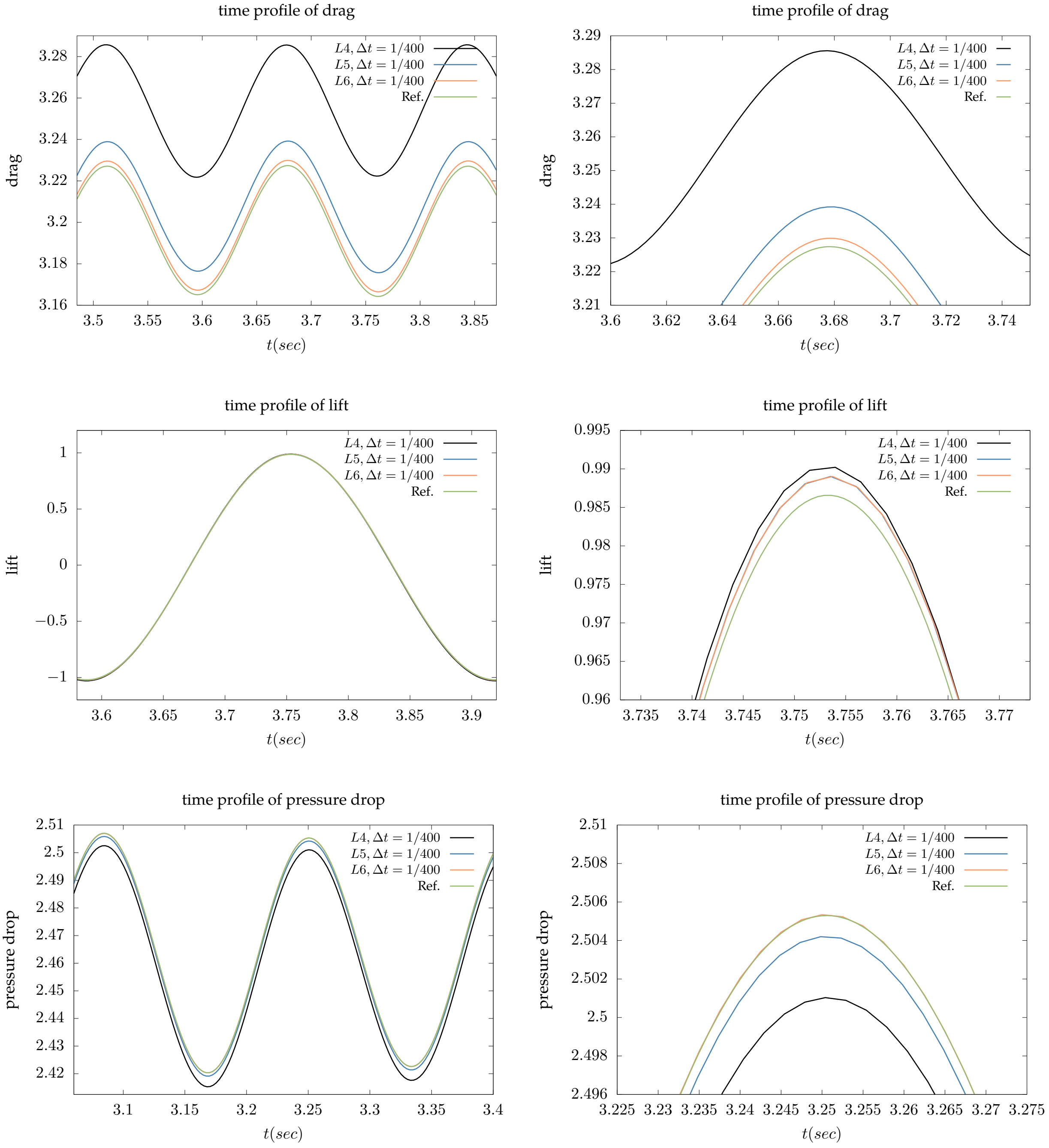

Figure 3.14: Sectional views of drag, lift, and pressure drop coefficient time profiles for Re 100 computed with a $\boldsymbol{\mathcal{S}}_{0,0}^{3,3} \times \mathcal{S}_{0,0}^{2,2}$ discretization and a time step of $\Delta t = 1/400$. These profiles are shown to converge to $Q_2 P_1$ FE based reference [45] results. The numbers of degrees of freedom are given in Table 3.5.

Level	Δt	min-C_D(Abs-Err,%-Err)	max-C_D(Abs-Err,%-Err)	mean-C_D(Abs-Err,%-Err)	amp-C_D(Abs-Err,%-Err)
L4	1/400	3.2216 (0.0573, 1.81)	3.2857 (0.0583, 1.81)	3.2536 (0.0578, 1.81)	0.0642 (0.0011, 1.62)
L5	1/400	3.1755 (0.0112, 0.35)	3.2392 (0.0118, 0.37)	3.2074 (0.0116, 0.36)	0.0637 (0.0006, 0.94)
L6	1/400	3.1665 (0.0022, 0.07)	3.2300 (0.0026, 0.08)	3.1983 (0.0025, 0.08)	0.0635 (0.0004, 0.58)
Ref. [45]		3.1643	3.2274	3.1958	0.0631

Table 3.6: min, max, mean, and amplitude of the drag coefficient values (including their absolute and percent errors) for different mesh levels.

Level	Δt	min-C_L(Abs-Err,%-Err)	max-C_L(Abs-Err,%-Err)	mean-C_L(Abs-Err,%-Err)	amp-C_L(Abs-Err,%-Err)
L4	1/400	-1.0302 (0.0089, 0.87)	0.9903 (0.0037, 0.38)	-0.01995 (0.00259, 14.92)	2.0206 (0.0127, 0.63)
L5	1/400	-1.0249 (0.0036, 0.35)	0.9890 (0.0024, 0.25)	-0.01794 (0.00058, 3.34)	2.0139 (0.0060, 0.30)
L6	1/400	-1.0242 (0.0029, 0.28)	0.9893 (0.0027, 0.27)	-0.01747 (0.00011, 0.63)	2.0135 (0.0056, 0.28)
Ref. [45]		-1.0213	0.9866	-0.01736	2.0079

Table 3.7: min, max, mean, and amplitude of the lift coefficient values (including their absolute and percent errors) for different mesh levels.

min/max values of the drag coefficient exhibit a significantly faster convergence than those of the lift coefficient.

In addition to min/max drag and lift coefficients, further quantities of interest are the lift profile frequency (f) and Strouhal number ($\mathrm{St} = \frac{Df}{U}$) which we provide values for in Table 3.8.

Level	Δt	$1/f$	St
L4	1/400	0.33250	0.30075
L5	1/400	0.33250	0.30075
L6	1/400	0.33000	0.30303
Ref. [45]		0.33125	0.30189

Table 3.8: Frequency and Strouhal numbers for different mesh levels.

On a general note, different aspects of the approximated drag and lift profiles, such as their minimum, maximum, mean, frequency, and amplitude values are demonstrated to be converged and in good agreement with the results of a reference simulation.

3.5.5 Drag and Lift force computation revisited

The content of the previous sections of this chapter including the computed drag and lift forces are part of a published and therefore sealed article [81]. Using a revised formula for the computation of hydrodynamic forces quite a long time after the publication of the above reference, we obtained improved drag and lift data that we present and compare in this section to previously obtained ones.

A fluid flowing past the surface S of a body (cf. Figure 3.10) exerts a force on it. Lift is the component of this force that is perpendicular to the oncoming flow direction. It contrasts with the drag force which is the component of the surface force parallel to the flow direction. The surface integrals (line integral in 2D) presented in equation (3.90) can readily be taken to compute the drag and lift forces (F_D, F_L) and coefficients (C_D, C_L).

However, following the spirit of [93, 150], we used an alternative approach and evaluated the volume integral (3.92) for the approximations of the drag and lift coefficients – so far. The constituents of the this volume integral obviously reflect the isotropic $(-p\,\delta_{ij})$ and non-isotropic, deviatoric stress tensor (s_{ij}) compartments of the fluid Cauchy stress tensor

$$\begin{aligned} \boldsymbol{\sigma} &= -p\boldsymbol{I} + \mu[\nabla\boldsymbol{v} + (\nabla\boldsymbol{v})^T], \\ \sigma_{ij} &= -p\,\delta_{ij} + s_{ij}. \end{aligned}$$

Furthermore, in the discrete setting, we used the respective interpolants of the discontinuous filter functions $\boldsymbol{v}_d$ and $\boldsymbol{v}_l$ (cf. equation (3.91)) and eventually computed the drag and lift coefficients as

$$\begin{aligned} C_D &= -\frac{2}{\rho\bar{U}^2 D}\,[\mathbf{D}_u \cdot \mathbf{v}_u + \mathbf{G}_u \cdot \mathbf{p}] \cdot \mathbf{v}_d, \text{ and} \\ C_L &= -\frac{2}{\rho\bar{U}^2 D}\,[\mathbf{D}_v \cdot \mathbf{v}_v + \mathbf{G}_v \cdot \mathbf{p}] \cdot \mathbf{v}_l, \end{aligned} \tag{3.95}$$

where the constituents of (3.95) – being the blocks $(\mathbf{D}_u, \mathbf{D}_v, \mathbf{G}_u, \mathbf{G}_v)$ of the system matrix, vector of unknowns $(\mathbf{v}_u, \mathbf{v}_v, \mathbf{p})$ and filter vectors $(\mathbf{v}_d, \mathbf{v}_l)$ – are organized as follows:

$$\begin{pmatrix} \mathbf{D}_u & & \mathbf{G}_u \\ & \mathbf{D}_v & \mathbf{G}_v \\ \mathbf{G}_u^T & \mathbf{G}_v^T & \end{pmatrix}, \begin{pmatrix} \mathbf{v}_u \\ \mathbf{v}_v \\ \mathbf{p} \end{pmatrix}, \begin{pmatrix} \mathbf{v}_d \\ \mathbf{v}_l \\ \end{pmatrix}.$$

Choosing the volume integral over the surface integral is for the most part motivated by the fact that when it comes to the computation of drag and lift forces, all ingredients of equation (3.95) are already at hand and the computation reduces to a few matrix-vector multiplications. We want to point out at this point though that in contrast to [93] the only bilinear forms appearing in equation (3.92) are those related to the viscous and pressure gradient terms of the Navier-Stokes equations. In fact, the advective and body force terms of the momentum equation are not included. This corresponds to the standard approach for the computation of hydrodynamic forces in the FeatFlow[18] FEA package and may be motivated by the low Reynolds number of the steady flow around cylinder test case and the absence of body forces therein.

However, John [93] proposes to test the full steady Navier-Stokes momentum equation (3.74a) with the corresponding filter functions $\boldsymbol{v}_d$ or $\boldsymbol{v}_l$, and to perform integration by parts in order to obtain the following volume integral:

$$\begin{aligned} C_D &= -\frac{2}{\rho\bar{U}^2 D}\left[(\nu\nabla\boldsymbol{v}, \nabla\boldsymbol{v_d}) + ((\boldsymbol{v}\cdot\nabla)\boldsymbol{v}, \boldsymbol{v_d}) - (p, \nabla\cdot\boldsymbol{v_d}) - (\boldsymbol{f}, \boldsymbol{v_d})\right] \\ C_L &= -\frac{2}{\rho\bar{U}^2 D}\left[(\nu\nabla\boldsymbol{v}, \nabla\boldsymbol{v_l}) + ((\boldsymbol{v}\cdot\nabla)\boldsymbol{v}, \boldsymbol{v_l}) - (p, \nabla\cdot\boldsymbol{v_l}) - (\boldsymbol{f}, \boldsymbol{v_l})\right]. \end{aligned} \tag{3.96}$$

Using the volume integral (3.96) for the computation of the hydrodynamic forces, we provide in the sequel new values for the drag and lift coefficients exhibiting a higher accuracy and an increased error convergence rate compared to those we published beforehand. As will be shown later in the text, the gain in accuracy and error convergence rates is quite significant. For the sake of a better comprehension of the observed improvements and the role of the obstacle boundary shape S, the investigations were extended to the FLOW AROUND SQUARE and REGULARIZED LID-DRIVEN CAVITY FLOW test cases, both involving straight line boundaries. Postponing the discussions of these two cases, we start off with the DFG benchmark 2D-1 and refer to Tables 3.9 and 3.10 for a compilation of the corresponding drag and lift coefficients, where the volume integral (3.96) and a NURBS-based Isogeometric $\boldsymbol{\mathcal{S}}_{0,0}^{3,3} \times \mathcal{S}_{0,0}^{2,2}$ discretization came to fruition. Moreover, in order to analyze the contribution of the various forms involved in (3.96), we have provided figures for the contribution of each to the drag and lift coefficients.

L	N$_{\text{el}}$	N$_{\text{dof}}$	C_D	$(\nu\nabla \boldsymbol{v}, \nabla \boldsymbol{v_d})$	$((\boldsymbol{v}\cdot\nabla)\boldsymbol{v}, \boldsymbol{v_d})$	$(p, \nabla\cdot\boldsymbol{v_d})$	EOC(C_D)
2	96	2304	5.50188978312	1.49652269632	-2.143488095257e-01	4.21971589632	
3	384	8832	5.57653244247	1.70621334607	-6.923565647967e-02	3.93955475287	2.34626
4	1536	34560	5.57950083360	1.82617889075	-1.511713701918e-02	3.76843907988	3.22387
5	6144	136704	5.57953507811	1.88748157260	-2.584123983265e-03	3.69463762950	3.89363
6	24576	543744	5.57953542609	1.91780462378	-3.820642157074e-04	3.66211286653	-0.151986
Ref. [44, 111]			5.57953523384				

Table 3.9: Flow around cylinder drag coefficient C_D computed with equation (3.96) and splitted into its respective components.

L	N$_{\text{el}}$	N$_{\text{dof}}$	C_L	$(\nu\nabla \boldsymbol{v}, \nabla \boldsymbol{v_l})$	$((\boldsymbol{v}\cdot\nabla)\boldsymbol{v}, \boldsymbol{v_l})$	$(p, \nabla\cdot\boldsymbol{v_l})$	EOC(C_L)
2	96	2304	0.023932136579	-3.52575833782e-03	1.33671206037e-02	1.40907743127e-02	
3	384	8832	0.011266417131	-2.07572674679e-03	4.50139922571e-03	8.84074465164e-03	2.18095
4	1536	34560	0.010633643977	3.39581050305e-04	1.12910258103e-03	9.16496034528e-03	2.73067
5	6144	136704	0.010619145366	2.00892070099e-03	2.11700526699e-04	8.39852413835e-03	3.10973
6	24576	543744	0.010618839082	2.89773460867e-03	3.28213672772e-05	7.68828310599e-03	0.427315
Ref. [44, 111]			0.010618948146				

Table 3.10: Flow around cylinder lift coefficient C_L computed with equation (3.96) and splitted into its respective components.

Remark 3.5.3. *The estimated order of convergence EOC is computed as follows: Let $h = 1/N_{el}$ define the element size, where N_{el} is the number of elements and let E_i be the error corresponding to h_i. Assuming $E_i = Ch_i^r$ for unknown constants C and r, we can compare two consecutive experiments, $E_i = Ch_i^r$ and $E_{i-1} = Ch_{i-1}^r$, and solve for r:*

$$r = \frac{\ln(E_i/E_{i-1})}{\ln(h_i/h_{i-1})} \tag{3.97}$$

The r values should approach the expected convergence order degree$+1$ as i increases.

For a contrasting juxtaposition, we refer to Figure 3.15 that provides a concise view of our previously published results [81] alongside those of Tables 3.9 and 3.10. Given the fact that in Table 3.9 the contribution of the advective term is one to four orders of magnitude smaller than that of the viscous and pressure gradient terms, its impact on the accuracy of the results is nonetheless quite remarkable. Tests with classical finite elements of type [15]Q_2P_1 and [20]$\tilde{Q}_1Q_0$ confirm the observed tendency of a decreasing contribution of the advective term as the mesh refinement level increases. However, the inclusion of the advective term, surprisingly, does not yield any noteworthy difference for the above mentioned classical finite elements, whereas the effect is very noticeable in the Isogeometric discretization.

For a better comprehension of the different behaviors observed, and the role of curvilinear or straight boundaries to compute the hydrodynamic forces on, the analysis has been extended to FLOW AROUND SQUARE and the classical REGULARIZED LID-DRIVEN CAVITY benchmark having been presented in detail in Section 3.5.3. In the former case, the same multi-patch domain partition as in Figure

---

[20] Velocity: Bilinear, rotated; Pressure: Constant.

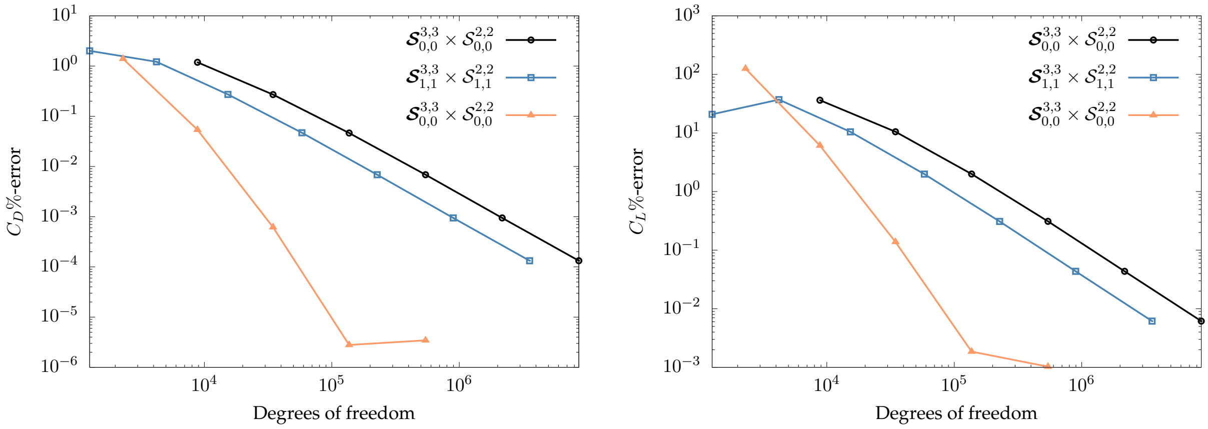

Figure 3.15: Sectional view of drag and lift percent errors for flow around cylinder. The black and blue lines refer to drag and lift coefficients computed with volume integral (3.92), while data plotted in orange refers to the new results computed with volume integral (3.96).

3.11 is used, where the control points of the NURBS patches touching the obstacle are modified accordingly to form a square. In the latter case, the drag and lift forces are computed on the lid's bottom boundary and the following velocity profile function is prescribed on the lid's top boundary:

$$\mathbf{u}_{lid} = [16x^2(1-x)^2, 0]. \tag{3.98}$$

Common to both cases is a straight line boundary on which the drag and lift coefficients are computed and the computations are required to reveal whether the inclusion of the advective term proves to be beneficial here as well. Beginning with FLOW AROUND SQUARE, we present in Tables 3.11 and 3.12 the drag and lift coefficients computed with volume integrals (3.92) and (3.96), respectively. The lack of a reference solution for this setup, renders a comparison of corresponding error

L	N$_{\text{el}}$	N$_{\text{dof}}$	C_D	C_L
2	96	984	7.3079515320	6.7913592300e-02
3	384	3696	7.1338241262	7.5366111312e-02
4	1536	14304	7.0069523272	8.3010116426e-02
5	6144	56256	6.9598040231	8.5339113567e-02
6	24576	223104	6.9461736770	8.5994041680e-02

Table 3.11: Flow around square drag and lift coefficient C_D and C_L computed with equation (3.92). Discretization: NURBS-based Isogeometric $\boldsymbol{\mathcal{S}}^{2,2}_{0,0} \times \mathcal{S}^{1,1}_{0,0}$

convergence order and rates not amenable. Nevertheless, a closer look at the figures reveals that the inclusion of the advective term has a positive contribution on the accuracy, for the coefficients presented on the last row of table 3.11 are already "roughly" available on much lower mesh refinement levels of Table 3.12. Yet again, this behavior could not be observed with aforementioned classical finite elements and surprisingly appears to occur in Isogeometric discretizations only. However, the inclusion of the advective term does not yield any appreciable contribution for the REGULARIZED LID-DRIVEN CAVITY setup as can be deduced from Tables 3.13 and 3.14.

Last but not least, we revisit the DFG BENCHMARK 2D-2 [45, 129] setup, defining an unsteady configuration for the flow around cylinder scenario, and recompute the drag and lift forces accord-

L	$\mathrm{N_{el}}$	$\mathrm{N_{dof}}$	C_D	$(\nu\nabla\boldsymbol{v}, \nabla\boldsymbol{v_d})$	$((\boldsymbol{v}\cdot\nabla)\boldsymbol{v}, \boldsymbol{v_d})$	$(p, \nabla\cdot\boldsymbol{v_d})$
2	96	984	6.9442769459	1.4856249327	-3.6367458611e-01	5.8223265993
3	384	3696	6.9398107619	1.5241458005	-1.9401336430e-01	5.6096783257
4	1536	14304	6.9394652050	1.4381909943	-6.7487122234e-02	5.5687613329
5	6144	56256	6.9411119331	1.3281986297	-1.8692089970e-02	5.6316053933
6	24576	543744	6.9415335574	1.2363126559	-4.6401196174e-03	5.7098610210
			C_L	$(\nu\nabla\boldsymbol{v}, \nabla\boldsymbol{v_l})$	$((\boldsymbol{v}\cdot\nabla)\boldsymbol{v}, \boldsymbol{v_l})$	$(p, \nabla\cdot\boldsymbol{v_l})$
2	96	984	9.1491263272e-02	1.3677056354e-03	2.3577670973e-02	6.6545886664e-02
3	384	3696	8.6387954457e-02	4.2665391532e-03	1.1021843144e-02	7.1099572159e-02
4	1536	14304	8.7108643699e-02	5.9107042335e-03	4.0985272730e-03	7.7099412193e-02
5	6144	56256	8.6525032119e-02	6.0812787390e-03	1.1859185528e-03	7.9257834828e-02
6	24576	223104	8.6301991348e-02	5.3760113957e-03	3.0794966756e-04	8.0618030285e-02

Table 3.12: Flow around square drag and lift coefficient C_D and C_L computed with equation (3.96) and splitted into its respective components. Discretization: NURBS-based Isogeometric $\boldsymbol{\mathcal{S}}_{0,0}^{2,2} \times \mathcal{S}_{0,0}^{1,1}$

L	$\mathrm{N_{el}}$	$\mathrm{N_{dof}}$	C_D	C_L
2	16	187	-1.1996731151e-01	-2.4130100053e-01
3	64	659	-1.3203238789e-01	-1.5432215226e-01
4	256	2467	-1.3777250834e-01	-1.5168848064e-01
5	1024	9539	-1.4084770785e-01	-1.5162614654e-01
6	4096	37507	-1.4241699857e-01	-1.5162361204e-01

Table 3.13: Regularized lid-driven cavity drag and lift coefficient C_D and C_L computed with volume integral (3.92). Discretization: NURBS-based Isogeometric $\boldsymbol{\mathcal{S}}_{0,0}^{2,2} \times \mathcal{S}_{0,0}^{1,1}$

L	$\mathrm{N_{el}}$	$\mathrm{N_{dof}}$	C_D	$(\nu\nabla\boldsymbol{v}, \nabla\boldsymbol{v_d})$	$((\boldsymbol{v}\cdot\nabla)\boldsymbol{v}, \boldsymbol{v_d})$	$(p, \nabla\cdot\boldsymbol{v_d})$
2	16	187	-1.1999211483e-01	-1.1996731151e-01	-2.4803321315e-05	1.9515639105e-17
3	64	659	-1.3203266882e-01	-1.3203238789e-01	-2.8092194888e-07	5.3668007538e-18
4	256	2467	-1.3777251412e-01	-1.3777250834e-01	-5.7845400964e-09	4.3910187986e-18
5	1024	9539	-1.4084770794e-01	-1.4084770785e-01	-9.0569738105e-11	4.7569370318e-18
6	4096	37507	-1.4241699857e-01	-1.4241699857e-01	-8.7247860112e-14	1.0306696902e-17
			C_L	$(\nu\nabla\boldsymbol{v}, \nabla\boldsymbol{v_l})$	$((\boldsymbol{v}\cdot\nabla)\boldsymbol{v}, \boldsymbol{v_l})$	$(p, \nabla\cdot\boldsymbol{v_l})$
2	16	187	-2.4180171034e-01	1.5758878577e-16	-5.0070980778e-04	-2.41301000530e-01
3	64	659	-1.5435925530e-01	5.7876067220e-17	-3.7103038573e-05	-1.54322152263e-01
4	256	2467	-1.5169117937e-01	-1.0563468587e-15	-2.6987317644e-06	-1.51688480642e-01
5	1024	9539	-1.5162633146e-01	3.8988263759e-15	-1.8492734353e-07	-1.51626146538e-01
6	4096	37507	-1.5162362420e-01	2.2993425811e-14	-1.2161476833e-08	-1.51623612038e-01

Table 3.14: Regularized lid-driven cavity drag and lift coefficient C_D and C_L computed with volume integral (3.96) and splitted into its respective components. Discretization: NURBS-based Isogeometric $\boldsymbol{\mathcal{S}}_{0,0}^{2,2} \times \mathcal{S}_{0,0}^{1,1}$

ing to an alternative volume integral. For the inclusion of the advective and body force terms – as shown in volume integral (3.96) – corresponds to considering the full steady Navier-Stokes momentum equation residual, and (3.96) proved to be beneficial for the steady flow around cylinder case, it seems obvious to additionally include the temporal term in the unsteady case. Therefore, for the computation of hydrodynamic forces, we consider the case where beside the body force term only the advective term is additionally included and the case where both the advective and temporal term are included as presented in equations (3.96) and (3.99), respectively.

$$\begin{aligned} C_D &= -\frac{2}{\rho \bar{U}^2 D}\left[(\dot{\boldsymbol{v}}, \boldsymbol{v_d}) + (\nu\nabla\boldsymbol{v}, \nabla\boldsymbol{v_d}) + ((\boldsymbol{v}\cdot\nabla)\boldsymbol{v}, \boldsymbol{v_d}) - (p, \nabla\cdot\boldsymbol{v_d}) - (\boldsymbol{f}, \boldsymbol{v_d})\right] \\ C_L &= -\frac{2}{\rho \bar{U}^2 D}\left[(\dot{\boldsymbol{v}}, \boldsymbol{v_l}) + (\nu\nabla\boldsymbol{v}, \nabla\boldsymbol{v_l}) + ((\boldsymbol{v}\cdot\nabla)\boldsymbol{v}, \boldsymbol{v_l}) - (p, \nabla\cdot\boldsymbol{v_l}) - (\boldsymbol{f}, \boldsymbol{v_l})\right] \end{aligned} \tag{3.99}$$

We refer to Figure 3.16 for a visual comparison of our previous results (solid lines) with the new ones printed with dashed lines. To be more specific, the graphs plotted with magenta and red dashed lines are computed with equations (3.96) and (3.99), respectively. For the drag coefficient profile, already the inclusion of the advective term yields for mesh refinement level 4 and time step size $\Delta t = 1/400$ a significant improvement, and the additional inclusion of the temporal term does not make any noticeable difference. This improvement is unfortunately not seen in the lift coefficient profile showing an even slightly decreased accuracy.

3.6 Summary and conclusions

In this chapter, we have presented our numerical results of the application of Galerkin-based Isogeometric Analysis to both the steady and the unsteady incompressible Navier-Stokes equations in velocity-pressure formulation. The velocity and pressure functions were approximated with LBB stable B-spline spaces which can be regarded as smooth generalizations of Taylor-Hood pairs of finite element space.

The classical lid-driven cavity flow and flow around cylinder scenarios were considered in two dimensions as model problems in order to investigate the numerical traits and behavior of the isogeometric discretizations.

Starting off with the lid-driven cavity flow problem including its regularized version, we have shown that the approximated flow attributes are very well comparable with reference results partially obtained with a highly accurate spectral (Chebyshev Collocation) method [20]. Moreover, we have extended our view to global quantities such as kinetic energy and enstrophy, and have provided results which are in very good agreement with reference results obtained with other approaches such as a Q_2P_1 finite element discretization [112] and a high order finite difference scheme utilized in [25].

In addition to lid-driven cavity flow, we extended the application of Galerkin-based Isogeometric Analysis to the prominent flow around cylinder benchmark, as proposed in [129], and analyzed the approximated drag and lift quantities with respect to accuracy and convergence. The usage of a $\mathcal{C}^1$ B-spline element pair turned out to be superior to its $\mathcal{C}^0$ counterpart in terms of the number of degrees of freedom required to gain a certain accuracy. We eventually turned our attention to the unsteady Re-100 flow around cylinder case involving the transient form of the Navier-Stokes equations. The governing equations were discretized in time with a second order implicit time discretization scheme and finally solved in a fully coupled mode. The time profile of the approximated drag and lift coefficients were shown to converge to the results of a reference finite element

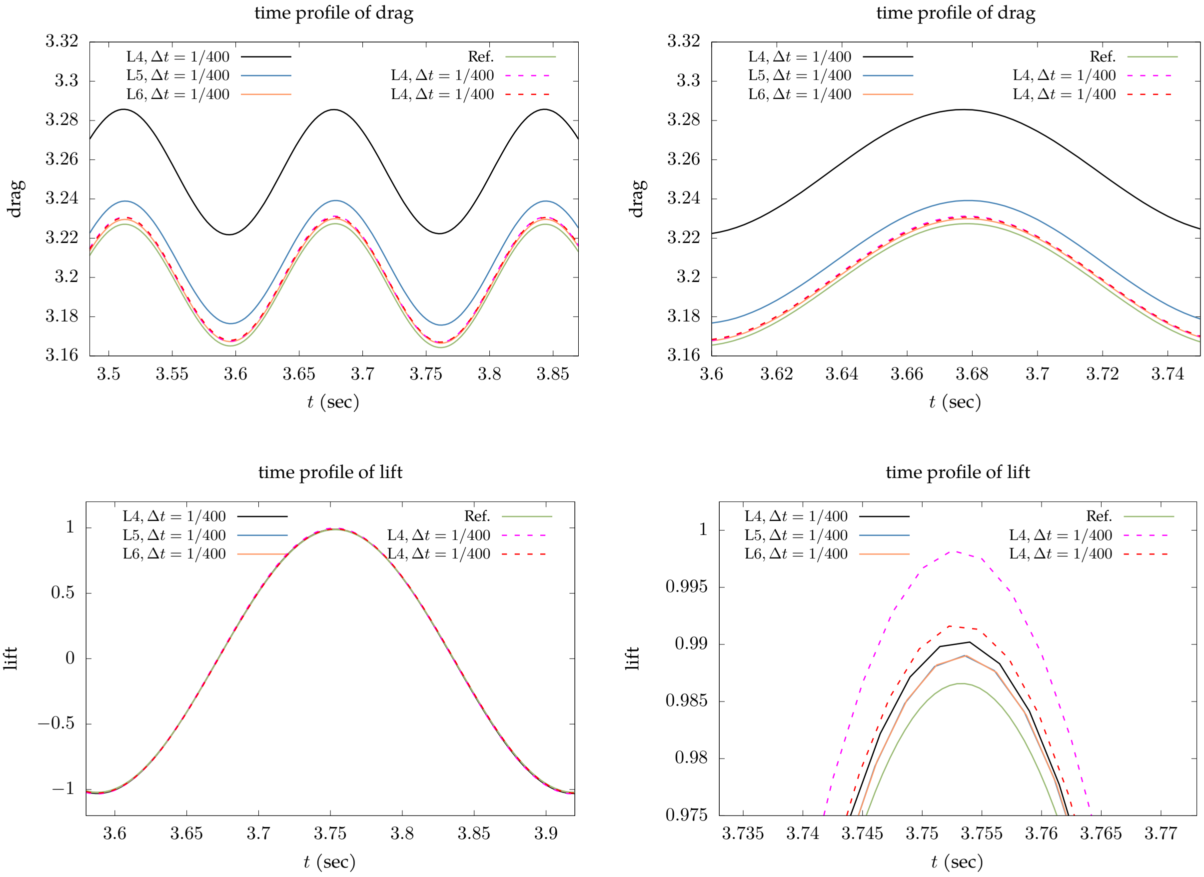

Figure 3.16: Sectional views of drag and lift coefficient time profiles of DFG benchmark 2D-2 (Re 100) computed with a $\boldsymbol{\mathcal{S}}^{3,3}_{0,0} \times \mathcal{S}^{2,2}_{0,0}$ discretization and a time step of $\Delta t = 1/400$. These profiles are shown to converge to Q_2P_1 FE based reference [45] results. Data plotted in magenta and red, have been computed with equations (3.96) and (3.99), respectively.

simulation.

The efficient solution of the arising linear equation systems with iterative techniques such as, for instance, multigrid were out of the scope of this study and will therefore be addressed in a forthcoming publication.

Isogeometric Analysis proved for us to be a robust and powerful technology showcasing unique features. For Taylor-Hood-like B-spline elements we carried our analysis upon, it turned out to be just a matter of changing settings in a configuration file to set up a desired B-spline element of a specific degree and continuity. This is without any doubt a huge benefit when compared to usual finite elements where one needs to provide an implementation for each element type. Moreover, for B-spline/NURBS geometries – already exactly representing a computational domain on the coarsest level – the process of meshing is straightforward. The mathematical definition of a B-spline/NURBS already defines a tensor product mesh eligible to NURBS-based refinement techniques such as h-, p-, or k-refinement [37, 119].

However, on a final note, the true virtue of the technology in the field of computational fluid dynamics can be better exploited in applications involving high order partial differential equations such as, for instance, the third order Navier-Stokes-Korteweg [76], or fourth order Cahn-Hilliard equations [75] in combination with complex geometries.

Chapter 4

Two-phase flow

4.1 Introduction

Multiphase flows of immiscible fluids, that is, flow of fluids which are incapable of mixing, such as e.g. oil and water are omnipresent in nature and industrial systems. By way of example we refer to the Deepwater Horizon oil spill in the gulf of Mexico and the respective industrial plant in charge with pumping an oil water mixture to the surface. In particular, in a multiphase flow context the dynamics of bubbles and droplets including their deformation, coalescence and breakup are intriguing processes which have gained a lot of attention in the scientific community, cf. [19, 32, 88, 94, 95]. In two-phase flows, being the most common multiphase flow configuration involving two distinct fluids, the fluids are segregated by a very thin interfacial region where surface tension effects and mass transfer due to chemical reactions may appear. The former is caused by molecular force imbalances in the vicinity of the fluid interface. The extension of the physical model to multiple fluids, with each fluid being allowed to have its own density and viscosity, comes at a cost of potentially sharp gradients of these quantities and pressure jumps across the phase separating interface. As for methodologies to address these issues, the sharp- and diffuse-interface methods are among the most widely used ones to model fluid interface dynamics. Traditionally, phase transition phenomena have been described with sharp interface models. This involves the tracking of the phase separating interface as it evolves over time. Among Eulerian interface tracking methods the volume-of-fluid [78] and the level-set [135] method constitute the most prominent sharp interface models and have been applied in a multitude of multiphase applications. However, especially in the realization of the latter method discontinuous functions are often regularized and artificially "smoothed" with regularized Heaviside or step functions. The regularization aids to circumvent problems with numerical integration when discontinuous coefficients and functions are involved. Henceforth, the level-set method can sometimes be regarded as a diffuse interface method as well, since it introduces a narrow transition region across which the regularization of discontinuous coefficients is realized.

In this work we use a phase field diffuse interface method based on the Cahn-Hilliard (CH) equation and apply Isogeometric Analysis for the discretization of the involved equations. Diffuse-interface models have been used in a wide spectrum of fields, ranging from material sciences to fracture mechanics. Moreover, in recent years they have been successfully used to describe the flow of two or more immiscible fluids for both numerical and theoretical studies. Particularly for two-phase flows, they have gained a lot of attention due to their ability to easily handle moving contact lines and topological transitions without any need for reinitialization or advective stabilization.

On a general note, diffuse interface models allow the modeling of interfacial forces as continuum forces with the effect that delta-function forces and discontinuities at the interface are smoothed by smearing them over thin yet numerically resolvable layers. The phase field method - also known as the diffuse interface model - is based on models of fluid free energy and offers a systematic physical approach by describing the interface in a physical rather than in a numerical sense. One principal advantage of diffuse interface models is their ability to describe topological transitions like droplet coalescence or break-up in a natural way. In the phase field framework, the interface is modeled by a function $\varphi(x,t)$ which represents the concentration of the fluids. The function $\varphi(x,t)$, also referred to as the order parameter, or the phase field, attains a distinct constant value in each phase and rapidly, but smoothly, changes in the interface region between the phases. For a binary fluid, a usual assumption is that φ takes values between -1 and 1, or 0 and 1. The relaxation of the order parameter is driven by local minimization of the fluid free energy subject to the phase field conservation. As a result, complex interface dynamics such as coalescence or segregation can be captured without any special procedures [13, 142].

The mathematical modeling of phase field-based two-phase incompressible flows dates at least back to the work of Gurtin et al. [74] and has originated a multitude of different models ever since. These models differ from each other by a group of quite diverse criteria, one of them being e.g. the treatment of the density, that is, considering it constant or variable. Moreover, not all models are based on a divergence-free velocity field and the modeling of extra contributions of additional forces to the stress tensor such as e.g. the surface tension induced capillary forces is quite varied across the models. While for some models no energy inequalities are known, others are shown to admit an energy law and to be thermodynamically consistent. For the latter to hold, some of the affected models are extended by additional terms. Each of these models has its own advantages and disadvantages in terms of suitability for particular flow scenarios, physical consistency and implementation simplicity. Following the agenda to assess Isogeometric Analysis-based approximations of various variable density two-phase flow problems with respect to reference "sharp interface"-based results, the identification of a reasonable model turned up to be a time consuming and tedious process. This is founded on the fact that there are quite a number of different models at one's disposal, each having a distinct set of traits determining its overall suitability. As an additional reason, we identify the lack of a consolidated inventory with emphasis on the most essential features and shortcomings of each model. In order to address this issue and to make this work self contained, we have decided to briefly present and screen the models in a dedicated section (see Section 4.2).

Using the numerical benchmark setups of Hysing et al. [88] for two-dimensional bubble dynamics, Aland et al. [6] compared three different phase field-based incompressible two-phase flow models utilizing a classical finite element discretization. More specifically, the results computed with the models of Ding, Boyer and Abels (see Section 4.2) are compared to both each other and to those of Hysing being based on a level-set sharp interface model. The performed numerical analysis indicates a good result-wise agreement among all three phase field models and in particular exhibits rather small differences between the models of Ding and Abels. Using this finding, we identify the model proposed by Ding as suitable for our purposes and apply Isogeometric Analysis to the above mentioned two-phase flow benchmark problems. To our best knowledge this is the first work aiming to recover Hysing's sharp interface based variable density and variable viscosity two-phase flow benchmark results applying Isogeometric Analysis to a NSCH model. Besides, the robustness of the Isogeometric discretization of the NSCH system is further underpinned by its application to other challenging two-phase flow scenarios such as for instance the "Rayleigh-Taylor instability".

We consider the combination of Isogeometric Analysis and the NSCH system for the numerical treatment of multiphase flow problems as very powerful. This is attributed on the one hand to the above mentioned benefits of phase field methods, and on the other hand to the ability to perform finite element type numerical analysis on complex geometries without the necessity to discretize it with straight line segments or flat faces. This has proven in a row of different context to yield gains in accuracy compared to alternative numerical methods [37]. Moreover, the Cahn-Hilliard equation in its primal formulation involves fourth order spatial derivatives requiring $\mathcal{C}^1$ continuous discrete approximation spaces which can easily be spanned with high regularity basis functions in Isogeometric Analysis.

As of writing of this chapter there are in all conscience two other works combining Isogeometric Analysis with the advective Cahn-Hilliard phase field model and fluid flow. The first article [104] uses the advective Cahn-Hilliard equation and presents an Isogeometric Analysis-based numerical study of spinodal decomposition of a binary fluid undergoing shear flow. In contrast to this work, however, they use a passive and externally provided velocity field and in particular do not solve a coupled NSCH system. The second work [53] on the other hand, aims to analyze the dynamics of liquid droplets in a liquid continuum. It does involve a NSCH system and utilizes divergence-free B-spline spaces to obtain a discrete pointwise divergence-free velocity field. The focus of that work is on the energy exchange analysis in droplet dynamics, or more specifically, on the analysis of the exchanges of the kinetic, potential, bulk and interfacial free energies as droplets start to merge. However, in contrast to this work, they use an NSCH model under the Boussinesq assumption to account for buoyancy effects. This imposes a severe constraint on the admitted density differences, in fact in their work they assume small density differences between the fluids while we go up to density ratio 1000.

The outline of this chapter is as follows: In Section 4.2 we follow the agenda to identify and select an adequate phase field-based two-phase flow model and provide therefore a concise traits-oriented characterization and comparison of the most significant models. The mathematical model used in this work is eventually described in Section 4.3 serving as a basis for Section 4.4 that is in turn dedicated to the discretization aspects of the mathematical model with Isogeometric Analysis. We present our numerical results in Section 4.5 and conclude the chapter with a short summary in Section 4.6.

4.2 Phase field-based two-phase flow models

When it comes to the coupling of phase segregation with hydrodynamics, the basic diffuse interface model for two incompressible, viscous Newtonian fluids is the so-called "Model H" [74, 79] which was derived in the framework of rational continuum mechanics and is shown to satisfy the second law of thermodynamics in a mechanical version based on local dissipation inequality. It leads to the coupled Navier-Stokes-Cahn-Hilliard (NSCH) system

$$\rho\partial_t \boldsymbol{v} + \rho\left(\boldsymbol{v}\cdot\nabla\right)\boldsymbol{v} - \operatorname{div}\left(2\mu(\varphi)\frac{1}{2}\left(\nabla\boldsymbol{v} + (\nabla\boldsymbol{v})^T\right)\right) + \nabla p = -\hat{\sigma}\varepsilon\operatorname{div}\left(\nabla\varphi\otimes\nabla\varphi\right), \tag{4.1a}$$

$$\operatorname{div}\boldsymbol{v} = 0, \tag{4.1b}$$

$$\partial_t\varphi + \boldsymbol{v}\cdot\nabla\varphi = \operatorname{div}\left(m\nabla\eta\right), \tag{4.1c}$$

$$\eta = \hat{\sigma}\varepsilon^{-1}\psi'(\varphi) - \hat{\sigma}\varepsilon\Delta\varphi, \tag{4.1d}$$

where $\rho, \mu(\varphi), \boldsymbol{v}$ and p denote the density, dynamic viscosity, mean velocity, and pressure, respectively and φ is the order parameter related to the concentration of the fluids (e.g. concentration of one component). Moreover, $\hat{\sigma}$ is the surface energy density coefficient, ε is a parameter related to the thickness of the interfacial region, ψ denotes the homogeneous free energy density function, $m = m(\varphi)$ is the mobility coefficient and μ is the chemical potential. The term $\hat{\sigma}\varepsilon\left(\nabla\varphi \otimes \nabla\varphi\right)$ on the right hand side of (4.1a) represents surface tension induced capillary forces and is modeled as an extra contribution in the stress tensor. The modeling assumption of constant density ρ in both components as well as in the transition region, unfortunately entails a severe constraint on the usability of this model and restricts its applicability to situations with negligible density differences. In order to nevertheless account for buoyancy effects in the treatment of problems with small density ratios, a customary practice is to use a Boussinesq approximation, that is, considering the density constant except when multiplying it with the gravitational force field $\boldsymbol{g}$.

In order to overcome the constant density constraint, the following thermodynamically consistent extension of Model H for different densities was derived by Lowengrub and Truskinovsky [105]

$$\rho\partial_t \boldsymbol{v} + \rho\left(\boldsymbol{v}\cdot\nabla\right)\boldsymbol{v} - \mathrm{div}\boldsymbol{S}\left(\varphi, \boldsymbol{D}(\boldsymbol{v})\right) + \nabla p = -\hat{\sigma}\varepsilon \mathrm{div}\left(\nabla\varphi\otimes\nabla\varphi\right), \tag{4.2a}$$

$$\partial_t\rho + \mathrm{div}(\rho\boldsymbol{v}) = 0, \tag{4.2b}$$

$$\rho\partial_t\varphi + \rho\boldsymbol{v}\cdot\nabla\varphi = \mathrm{div}\left(m(\varphi)\nabla\eta\right), \tag{4.2c}$$

$$\eta = -\rho^{-2}\frac{\partial\rho}{\partial\varphi}p + \frac{\hat{\sigma}}{\varepsilon}\psi'(\varphi) - \frac{\hat{\sigma}\varepsilon}{\rho}\mathrm{div}\left(\rho\nabla\varphi\right), \tag{4.2d}$$

where $\boldsymbol{D}(\boldsymbol{v}) = \frac{1}{2}\left(\nabla\boldsymbol{v} + (\nabla\boldsymbol{v})^T\right), \boldsymbol{S}\left(\varphi, \boldsymbol{D}(\boldsymbol{v})\right) = 2\mu(\varphi)\boldsymbol{D}(\boldsymbol{v}) + \lambda(\varphi)\,\mathrm{div}\,\boldsymbol{v}\,\boldsymbol{I}$ and $\lambda(\varphi)$ is the bulk viscosity coefficient. Equation (4.2) defines the mean velocity $\boldsymbol{v}$ as a mass averaged or barycentric velocity $\rho\boldsymbol{v} = \rho_1\boldsymbol{v}_1 + \rho_2\boldsymbol{v}_2$, where ρ_j and $\boldsymbol{v}_j$ with $j = 1, 2$ denote the densities and velocities of the individual fluids. It is necessary to point out though that this velocity is not divergence-free. In the above system the coupling of the Navier-Stokes (4.2a)-(4.2b) and the Cahn-Hilliard terms (4.2c)-(4.2d) is much stronger that in the classical Model H, since the fluid pressure p enters the equation of the chemical potential η and thus aggravates numerical simulations. An additional difficulty is introduced by the non-solenoidal velocity field for which no solution concept is available which avoids to determine the pressure p.

Despite the fact that simplifications of this model have successfully been used in numerical studies [99, 100], to the best of the author's knowledge, until recently there were no discrete schemes available being based on the full model (4.2a)-(4.2d). In recent years, however, different numerical schemes have been developed by the groups of Lowengrub and Giesselmann, cf. [71, 89].

Ding [46] and Boyer [21] each came up with alternative generalizations of Model H for different densities. Their starting point are the equations for the mass conservation of each phase

$$\frac{\partial\rho_j}{\partial t} + \mathrm{div}(\rho_j\boldsymbol{v}_j) = 0 \tag{4.3}$$

eventually yielding a divergence-free $\nabla\cdot\boldsymbol{v} = 0$ velocity field. Moreover, their definition of the mean velocity $\boldsymbol{v}$ of the mixture differs from that of Lowengrub and Truskinovsky inasmuch as it is defined to be the volume averaged velocity $\boldsymbol{v} = u_1\boldsymbol{v}_1 + u_2\boldsymbol{v}_2$ with u_j denoting the volume fraction of fluid j. The model proposed by Ding is basically a generalization of (4.1) for variable densities

$\rho(\varphi)$, while the more complicated model presented by Boyer

$$\rho(\varphi) = 1 + \frac{\varepsilon}{2}(\varphi - 1), \tag{4.4a}$$

$$\rho(\varphi)\left(\frac{\partial \boldsymbol{v}}{\partial t} + \boldsymbol{v}\cdot\nabla\boldsymbol{v}\right) - \frac{1}{Re}\mathrm{div}\left(2\mu(\varphi)\boldsymbol{D}(\boldsymbol{v})\right) + \nabla p = \mathcal{K}\eta\nabla\varphi + \varepsilon\mathcal{K}\frac{1-\varphi^2}{4}\nabla\left(\frac{\eta}{\rho(\varphi)}\right) + \rho(\varphi)\boldsymbol{g}, \tag{4.4b}$$

$$\mathrm{div}\,\boldsymbol{v} = 0, \tag{4.4c}$$

$$\frac{\partial\varphi}{\partial t} + \boldsymbol{v}\cdot\nabla\varphi - \frac{1}{Pe}\mathrm{div}\left(\frac{m(\varphi)}{\rho(\varphi)}\nabla\left(\frac{\eta}{\rho(\varphi)}\right)\right) = 0, \tag{4.4d}$$

$$\eta = \psi'(\varphi) - \alpha^2\Delta\varphi, \tag{4.4e}$$

differs from (4.1), amongst other things, by the usage of the continuum surface tension force in its potential form: $\eta\,\nabla\varphi$. In equation (4.4), $\varepsilon = (\rho_1 - \rho_2)/\max(\rho_1, \rho_2)$ denotes the density contrast, $\varphi \in [-1, 1]$ is an order parameter, α is a dimensionless parameter related to the interface thickness, $\mathcal{K}$ is the capillarity coefficient, $\boldsymbol{g}$ is the gravitational force field, Pe is the Peclet number and $m(\varphi) = (1-\varphi^2)^2/(8\xi(\varphi))$ is the mobility coefficient, whereby $\xi(\varphi)$ denotes the alloy composition dependent friction coefficient. However, it is noteworthy to straighten that, unfortunately, neither global nor local energy inequalities are known for the model presented in (4.4). The same holds true for the model presented in (4.1) when the density ρ is not constant, making it difficult to conduct mathematical analysis.

Shen et al. [136] derived the following physically consistent phase field model for two-phase incompressible flows with variable density $\rho(\varphi) = \frac{\rho_1-\rho_2}{2}\varphi + \frac{\rho_1+\rho_2}{2}\varphi$ and viscosity $\mu(\varphi) = \frac{\mu_1-\mu_2}{2}\varphi + \frac{\mu_1+\mu_2}{2}\varphi$

$$\sigma(\sigma\boldsymbol{v})_t + \frac{1}{2}\nabla\cdot(\rho\boldsymbol{v})\boldsymbol{v} + (\rho\boldsymbol{v}\cdot\nabla)\,\boldsymbol{v} - \nabla\cdot 2\mu\boldsymbol{D}(\boldsymbol{v}) + \nabla p = -\lambda\nabla\cdot(\nabla\varphi\otimes\nabla\varphi), \tag{4.5a}$$

$$\nabla\,\cdot\boldsymbol{v} = 0, \tag{4.5b}$$

$$\frac{\partial\varphi}{\partial t} + (\boldsymbol{v}\cdot\nabla)\,\varphi = -\gamma\Delta\left(\Delta\varphi - \psi'(\varphi)\right) \tag{4.5c}$$

admitting the following energy law:

$$\frac{d}{dt}\int_\Omega\left(\frac{1}{2}|\sigma\boldsymbol{v}|^2 + \frac{\lambda}{2}|\nabla\varphi|^2 + \lambda\psi(\varphi)\right)\,\mathrm{d}\boldsymbol{x} = -\int_\Omega\left(\mu|\boldsymbol{D}(\boldsymbol{u})|^2 + \lambda\gamma|\nabla(\Delta\varphi - \psi'(\varphi))|^2\right)\,\mathrm{d}\boldsymbol{x} \tag{4.6}$$

In equation. (4.5), λ denotes the mixing energy density, γ is a diffusion parameter and $\sigma = \sqrt{\rho}$.

Abels et al. [1] recently derived a thermodynamically consistent generalization of (4.1a)-(4.1d) for the case of variable density based on a solenoidal velocity field $\boldsymbol{v}$. Their model, expressed through (4.7), fulfills local and global dissipation inequalities and is frame indifferent. Using the method of matched asymptotic expansions, that is, matching asymptotic expansions in the bulk region with expansions in the interfacial regions, various sharp interface models are derived in the limit when the interfacial thickness tends to zero ($\varepsilon \to 0$).

$$\begin{aligned}\partial_t(\rho(\varphi)\boldsymbol{v}) + \operatorname{div}(\rho(\varphi)\boldsymbol{v}\otimes\boldsymbol{v}) - \operatorname{div}(2\mu(\varphi)\boldsymbol{D}(\boldsymbol{v})) &= -\nabla p - \hat{\sigma}\varepsilon\operatorname{div}(\nabla\varphi\otimes\nabla\varphi) \\ &\quad - \operatorname{div}\left(\boldsymbol{v}\otimes\frac{\rho_1-\rho_2}{2}m(\varphi)\nabla\eta\right), \qquad (4.7a)\\ \operatorname{div}\boldsymbol{v} &= 0, \qquad (4.7b)\\ \partial_t\varphi + \boldsymbol{v}\cdot\nabla\varphi &= \operatorname{div}(m(\varphi)\nabla\eta), \qquad (4.7c)\\ \eta &= \hat{\sigma}\varepsilon^{-1}\psi'(\varphi) - \hat{\sigma}\varepsilon\Delta\varphi \qquad (4.7d)\end{aligned}$$

We conclude this section with a consolidated listing (see Table 4.1) of the models alongside their peculiarities. In conformity with the motivation and justification to present and elaborate on the essential features and shortcomings of the available models, this section and in particular Table 4.1 may greatly facilitate and accelerate the process of identifying a suitable model.

	Variable density $\rho(\varphi)$	Thermodynamically consistent	Admitting energy law	Sharp interface limit identifiable when $\varepsilon \to 0$
Model H		✓	✓	✓
Lowengrub et al.	✓	✓	✓	✓
Ding et al.	✓			✓
Boyer	✓			
Shen et al.	✓	✓	✓	
Abels et al.	✓	✓	✓	✓

Table 4.1: Traits of different phase field models for two-phase incompressible flows.

4.3 Mathematical model

Let $\Omega = (\Omega_1 \cup \Omega_2) \subset \mathbb{R}^n$ be an arbitrary open domain, with $n = 2$ or 3 and let its boundary $\partial\Omega$ be sufficiently smooth (e.g. Lipschitz continuous[21]). Moreover, let Γ denote the interface between the different fluids or phases occupying the subdomains Ω_1 and Ω_2 and let $\boldsymbol{n}$ be the outward ($\Omega_1 \to \Omega_2$) unit normal at the interface. Classical two-phase flow systems being based on models of surface tension forces either apply a force balance boundary condition

$$[\![-p\boldsymbol{I} + \mu\left(\nabla\boldsymbol{v} + (\nabla\boldsymbol{v})^T\right)]\!]\big|_\Gamma \cdot \boldsymbol{n} = \sigma\kappa\boldsymbol{n} \qquad (4.8)$$

on the interface Γ or rewrite the internal force boundary condition as a volumetric surface tension force

$$\boldsymbol{f}_{st} = \sigma\kappa\boldsymbol{n}\delta(\Gamma, \boldsymbol{x}), \qquad (4.9)$$

where σ is the surface tension coefficient, κ is the interface curvature and $\delta(\Gamma, \boldsymbol{x})$ is a Dirac delta function localizing the surface tension force to the interface.

Phase field methods on the other hand, are based on models of fluid free energy. The simplest

---

[21] A Lipschitz-continuous boundary can be represented locally as a graph of a Lipschitz-continuous function with Ω being located on one side of this graph. We refer to [33] for more details.

free energy density model for isothermal fluids yielding two phases is

$$f(\varphi) = \frac{1}{2}\alpha|\nabla\varphi|^2 + \beta\psi(\varphi) \qquad \alpha > 0, \beta > 0 \tag{4.10}$$

and can be traced down to Van der Waals [153]. With φ denoting a measure of phase, the first term on the right hand side of (4.10) represents the interfacial (also known as “surface” or “gradient”) free-energy density with a positive constant α. Having been introduced in the theory of phase transitions to model capillary effects and penalizing large gradients, it accounts for the fact that gradients in the concentration field φ are energetically unfavorable. The second part of the above expression involves a homogeneous (or “bulk”) free-energy density function $\psi(\varphi)$ modeling the fluid components' immiscibility. It contains a term describing the entropy of mixing and a term taking into account the interaction between the two fluid components. The double-well function $\psi(\varphi)$ penalizes any mixing of the phases. A physically relevant expression for the potential ψ and $\varphi \in [-1, 1]$ is given by the logarithmic expression [21, 43]

$$\psi(\varphi) = T((1+\varphi)\log(1+\varphi) + (1-\varphi)\log(1-\varphi)) + T_c(1-\varphi^2), \tag{4.11}$$

where T and T_c are the temperature and the critical temperature of the mixture, respectively. For the phase separation phenomenon to occur, the relation between the temperatures need to satisfy $T < T_c$ such that $\psi(\varphi)$ is not convex and builds two minima corresponding to the two stable phases of the fluid (see Figure 4.1). In cases where T is close enough to T_c, expression (4.11) can be replaced

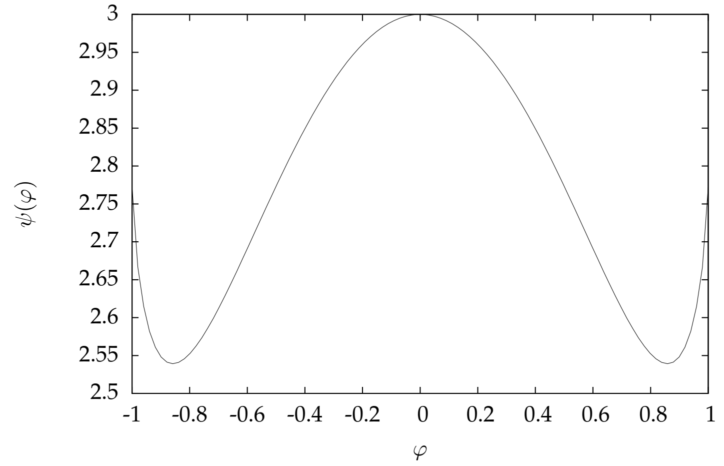

Figure 4.1: Homogeneous free energy density function (4.11) with $T = 2$ and $T_c = 3$.

by a polynomial approximation of the form $\psi(\varphi) = C_1\varphi^4 - C_2\varphi^2$. In fact all calculations in this paper were performed with

$$\psi(\varphi) = \frac{1}{4}(\varphi - 1)^2(\varphi + 1)^2, \tag{4.12}$$

where $\varphi \in [-1, 1]$ and $\varphi(x) = 1$ (respectively $\varphi(x) = -1$) if and only if fluid 1 (respectively fluid 2) is present at point x.

The theory of Cahn and Hilliard is based on Van der Waals' [153] hypothesis that equilibrium interface profiles are those that minimize a fluid free energy (Ginzburg-Landau free energy) functional

$$\mathcal{E}(\varphi) := \int_\Omega f \, \mathrm{d}\Omega = \int_\Omega \frac{1}{2}\alpha|\nabla\varphi|^2 + \beta\psi(\varphi) \, \mathrm{d}\Omega. \tag{4.13}$$

Variational calculus is used to determine the rate of change of the free energy functional $\mathcal{E}(\varphi)$ with respect to φ. More specifically, the variational derivative of $\mathcal{E}(\varphi)$ with respect to φ yields the chemical potential η being defined as

$$\eta = \frac{\delta\mathcal{E}}{\delta\varphi} = -\alpha\nabla^2\varphi + \beta\psi'(\varphi). \tag{4.14}$$

Equilibrium interface profiles satisfy

$$\beta\psi'(\varphi) - \alpha\nabla^2\varphi \equiv \eta = \text{const.}, \tag{4.15}$$

and setting α and β to respectively $O(\epsilon)$ and $O(1/\epsilon)$, produces phase field interfaces of thickness $O(\epsilon)$ and surface tension $O(1)$. Cahn and Hilliard generalized the problem to a mass diffusion equation in a binary system applying the principle of conservation of mass with a local diffusion mass flux $\boldsymbol{J}$ that is specified in terms of the chemical potential. The constitutive equation for the flux sets it proportional to the negative of the chemical potential, for the transport takes place from locations with a high chemical potential to those with a lower one. Therefore, we have the following definition for the flux

$$\boldsymbol{J} = -m(\varphi)\nabla\eta, \tag{4.16}$$

where $m(\varphi)$ is a concentration dependent mobility function[22] and is often replaced by a constant for simplification reasons. However, for all the calculations in this chapter we have used the following nonlinear mobility function

$$m(\varphi) = D(\varphi^2 - 1)^2, \tag{4.17}$$

where D represents a scaling parameter. In the absence of sources and sinks, mass conservation for φ requires

$$\frac{d\varphi}{dt} + \nabla\cdot\boldsymbol{J} = \frac{\partial\varphi}{\partial t} + \nabla\cdot(\boldsymbol{v}\varphi) + \nabla\cdot\boldsymbol{J} = 0. \tag{4.18}$$

Above, $\boldsymbol{v}$ denotes an advective velocity field. Requiring it to be solenoidal, that is, $\nabla\cdot\boldsymbol{v} = 0$ and substituting expressions (4.16) and (4.17) into (4.18), yields the fourth order advective Cahn-Hilliard equation

$$\frac{\partial\varphi}{\partial t} + \boldsymbol{v}\cdot\nabla\varphi = \nabla\cdot(m(\varphi)\nabla\eta) = \nabla\cdot\left(m(\varphi)\nabla\left(-\alpha\nabla^2\varphi + \beta\psi'(\varphi)\right)\right). \tag{4.19}$$

Ignoring the advective term $\boldsymbol{v}\cdot\nabla\varphi$, the pure Cahn-Hilliard equation approximates interfacial diffusion fluxes as being proportional to chemical potential gradients and governs the creation, movement and decomposition of diffusively controlled interfaces. Finally, the following boundary conditions are required at $\partial\Omega$ to complete the system

$$\begin{aligned} &\nabla\eta\cdot\boldsymbol{n} = 0, \quad \text{(no flux)} \\ &\nabla\varphi\cdot\boldsymbol{n} = \frac{1}{\epsilon\sqrt{2}}\cos(\theta)(1-\varphi^2), \quad \text{(contact angle)} \end{aligned} \tag{4.20}$$

where θ is an equilibrium contact angle[23] between the interface Γ and $\partial\Omega$. Note that $\theta = \pi/2$,

---

[22] In general tensor-valued mobility functions are consistent with the Cahn-Hilliard equation.

[23] For an interface in equilibrium, a contact angle condition $cos(\theta) = \frac{\sigma_{2S}-\sigma_{1S}}{\sigma}$ (Young's law) may be posed, where θ is the equilibrium contact angle and σ_{iS} is the interfacial energy between the solid and component i. The contact angle

implies $\nabla\varphi \cdot \boldsymbol{n} = 0$, and therefore an orthogonal relation between the interface and the boundary of the computational domain. Moreover, following the lines of [3] it holds

$$\frac{1}{\epsilon\sqrt{2}}(1-\varphi^2) = |\nabla\varphi|, \tag{4.21}$$

and therefore the contact angle boundary condition in eqn. (4.20) yields the correct angle condition

$$\boldsymbol{n} \cdot \frac{\nabla\varphi}{|\nabla\varphi|} = \cos(\theta). \tag{4.22}$$

Most of the computations in this chapter were performed with $\theta = \pi/2$, implying $\nabla\varphi \cdot \boldsymbol{n} = 0$, and hence an interface orthogonal to the boundary of the computational domain. Recalling equation (4.15) and using the free energy density function (4.12), the equilibrium interface profile is given by the solution of the equation

$$\eta(\varphi) = -\alpha\nabla^2\varphi + \beta\psi'(\varphi) = -\alpha\Delta\varphi + \beta\varphi(\varphi^2-1) = 0. \tag{4.23}$$

The solution is characterized by two stable minima at $\varphi \approx \pm 1$ standing for the two phases and a one-dimensional transition region given by

$$\varphi(x) = \tanh\left(\frac{x}{\sqrt{2}\sqrt{\alpha/\beta}}\right). \tag{4.24}$$

Following Jacqmin [90], the surface tension of the interface of an isothermal fluid system in equilibrium is equal to the integral of the free energy density through the interface. Therefore, recalling that the first term $(\alpha|\nabla\varphi|^2)$ of (4.10) is referred to the interfacial or surface free-energy density, the surface tension of a plane phase field interface is given by

$$\sigma = \alpha \int_{-\infty}^{\infty} \left(\frac{d\varphi}{dx}\right)^2 \mathrm{d}\boldsymbol{x} = \frac{2\sqrt{2}}{3}\sqrt{\alpha\beta}. \tag{4.25}$$

Since for general ψ, the surface tension and equilibrium interface thickness behave as $\sigma \propto \sqrt{\alpha\beta}$ and $\epsilon \propto \sqrt{\alpha/\beta}$, respectively [90], identity (4.25) is satisfied with the introduction of an auxiliary interface thickness $\xi = \sqrt{\alpha/\beta}$ and the following settings for the parameters α and β:

$$\alpha = \frac{3}{2\sqrt{2}}\sigma\xi, \qquad \beta = \frac{3}{2\sqrt{2}}\frac{\sigma}{\xi}. \tag{4.26}$$

The advective Cahn-Hilliard equation (4.19) is a stiff and nonlinear partial differential equation characterized by the presence of fourth-order spatial derivatives. Its finite element discretization in terms of primal variational formulation requires piecewise smooth and globally $\mathcal{C}^1$ continuous basis functions constituting high demands on discrete approximation spaces. In fact, the number of $\mathcal{C}^1$ finite elements being applicable to complex geometries is already very limited in two dimensions [75, 140]. Albeit Isogeometric Analysis easily allows the setup of high order discrete approximation spaces, we use the mixed formulation (4.27) of the Cahn–Hilliard equation, taking the chemical

---

characterizes the wettability of the surface with $\theta = 0$ denoting complete wetting.

potential η as an auxiliary variable.

$$\begin{aligned} \frac{\partial \varphi}{\partial t} + \boldsymbol{v} \cdot \nabla \varphi - \nabla \cdot (m(\varphi) \nabla \eta) = 0, \\ \eta - \beta \, \frac{d\psi(\varphi)}{d\varphi} + \alpha \, \nabla^2 \varphi = 0. \end{aligned} \tag{4.27}$$

Since the highest spatial derivatives appearing in the mixed formulation are reduced to order two, standard $\mathcal{C}^0$ discretizations may be used that avoid the costs associated with the usage of high-order and high-continuity basis functions. Besides, using (4.27) we avoid complications with the imposition of nonlinear boundary conditions arising from the discretization of the mass flux in the primal form.

The solution of the Cahn-Hilliard equation as presented above in (4.27) or in its unsplitted form (4.19) corresponds to the minimization of the Ginzburg-Landau free energy functional $\mathcal{E}(\varphi)$. We depict in Figure 4.2 the evolution of $\mathcal{E}(\varphi)$ for a randomly initialized phase field $\varphi \in [-1, 1]$. This randomly initialized field is shown in the left most tile of the top row of Figure 4.3 and is computed as $\varphi = \bar{\varphi} \pm \delta\varphi$, where $\bar{\varphi} = -1 + 0.63 \times 2$ is a median value and $\delta\varphi$ is a random number in the range $[0, 0.05]$. The remaining tiles of the top row illustrate the development of the phase field at later time stages. The evolution of the phase field is characterized by two processes. It starts with a fast segregation process driving the concentration (φ) to the binodal points - the two local minima of the homogeneous free energy density function $\psi(\varphi)$ (cf. Figure 4.1). The separation is driven by the minimization of the homogeneous free energy and is represented in Figure 4.2 by the fast decay of the Ginzburg-Landau free energy profile, especially between times $t \approx 2 \times 10^{-4}$ s

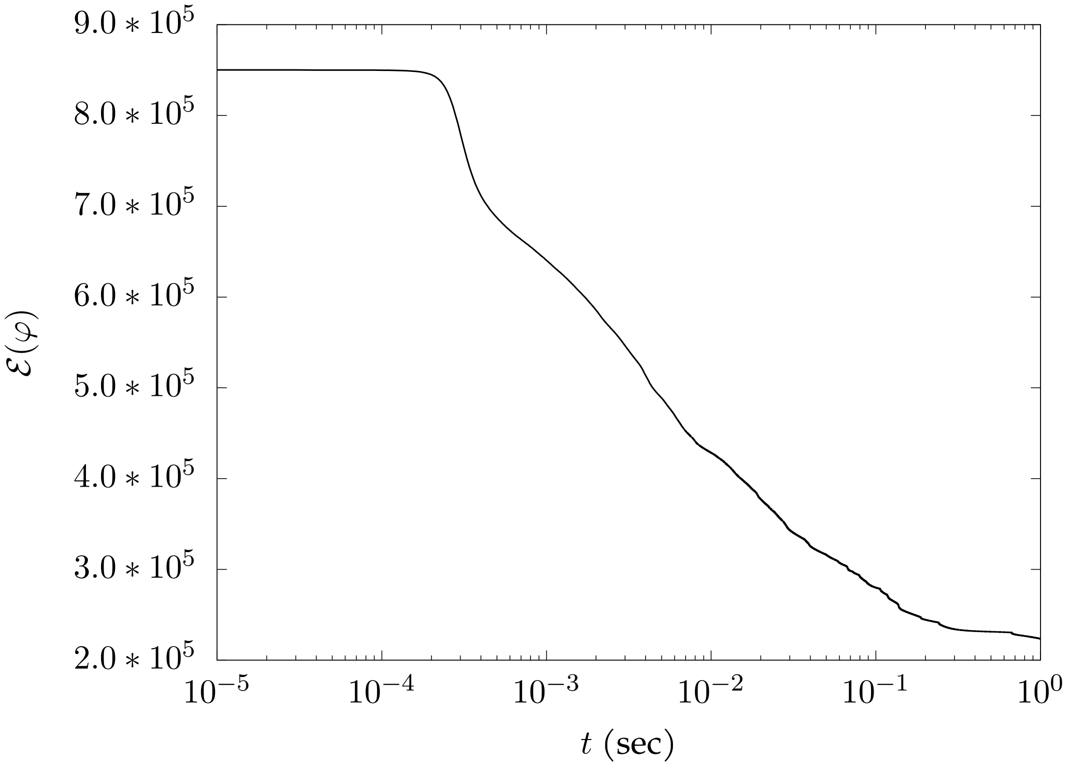

Figure 4.2: Evolution of the Ginzburg-Landau free energy.

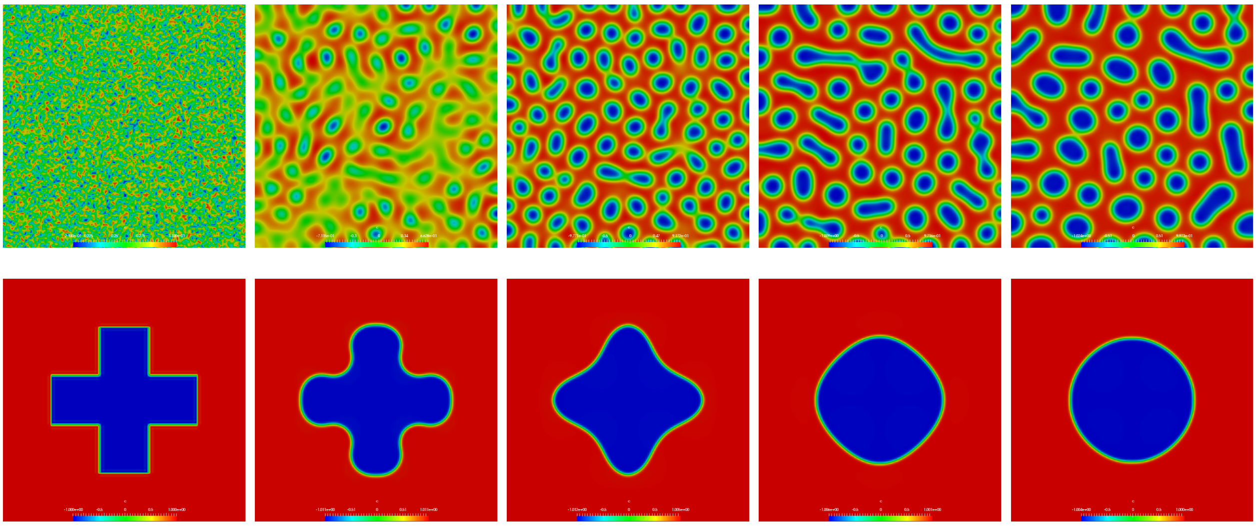

Figure 4.3: Minimization of the Ginzburg-Landau free energy.

and $t \approx 3 \times 10^{-4}\,\mathrm{s}$. Upon completion of the separation process, a so-called coarsening process starts that is driven by the minimization of the interfacial free energy. In the course of minimizing the length of fluid-fluid interfaces, it rearranges the interfaces with respect to this constraint and leads to the coalescence of enclosed areas (less total interface) and smoothening of areas with large curvatures along the interface. The latter is shown particularly well in the bottom row of Figure 4.2 demonstrating the deformation of a sharp-edged cross into a circle. The time scale of the coarsening stage is significantly larger than that of the separation stage.

In the sequel we focus on the coupling aspects of the diffuse interface model with a flow model for two incompressible, immiscible and isothermal fluids of different mass densities ρ_1, ρ_2 and viscosities μ_1, μ_2. We let the volume fraction of the first fluid in the mixture be defined as

$$\vartheta = \frac{dV_1}{dV}, \tag{4.28}$$

where dV_1 is the volume filled by fluid 1 and we use the following rescaling

$$\varphi = 2\vartheta - 1 \tag{4.29}$$

of the order parameter ϑ to the range $[-1, 1]$ to determine the composition of the two components in a volume element of the domain. Then, the total density and viscosity of the mixture is given as the volume averaged sum of each component's respective contribution, that is,

$$\begin{aligned} \rho(\varphi(x,y)) &= \rho_1(1+\varphi)/2 + \rho_2(1-\varphi)/2, \\ \mu(\varphi(x,y)) &= \mu_1(1+\varphi)/2 + \mu_2(1-\varphi)/2. \end{aligned} \tag{4.30}$$

Eventually, the Navier-Stokes-Cahn-Hilliard variable density, variable viscosity incompressible two-phase flow model (4.31) is obtained by the extension of the Navier-Stokes equations with a surface tension force term $\eta\nabla\varphi$, written in its potential form, and a fluid induced transport term $\boldsymbol{v} \cdot \nabla\varphi$ in the Cahn-Hilliard equation.

$$
\begin{aligned}
\rho(\varphi)\left(\frac{\partial \boldsymbol{v}}{\partial t} + (\boldsymbol{v}\cdot\nabla)\boldsymbol{v}\right) - \nabla\cdot\left(-p\boldsymbol{I} + \mu(\varphi)\left(\nabla\boldsymbol{v} + (\nabla\boldsymbol{v})^T\right)\right) &= \rho(\varphi)\boldsymbol{g} + \eta\nabla\varphi && \text{in } \Omega_T, && (4.31\text{a})\\
\nabla\cdot\boldsymbol{v} &= 0 && \text{in } \Omega_T, && (4.31\text{b})\\
\frac{\partial\varphi}{\partial t} + \boldsymbol{v}\cdot\nabla\varphi - \nabla\cdot(m(\varphi)\nabla\eta) &= 0 && \text{in } \Omega_T, && (4.31\text{c})\\
\eta - \beta\,\frac{d\psi(\varphi)}{d\varphi} + \alpha\,\nabla^2\varphi &= 0 && \text{in } \Omega_T, && (4.31\text{d})\\
\varphi(\boldsymbol{x},0) = \varphi_0(\boldsymbol{x}), \quad \boldsymbol{v}(\boldsymbol{x},0) &= \boldsymbol{v}_0(\boldsymbol{x}) && \text{in } \Omega, && (4.31\text{e})\\
\boldsymbol{v} &= \boldsymbol{v}_D && \text{on } (\partial\Omega_T)_D, && (4.31\text{f})\\
\nabla\varphi\cdot\boldsymbol{n} = \frac{1}{\epsilon\sqrt{2}}\cos(\theta)(1-\varphi^2), \quad \nabla\eta\cdot\boldsymbol{n} &= 0 && \text{on } (\partial\Omega_T)_N, && (4.31\text{g})\\
\left(-p\boldsymbol{I} + \mu(\varphi)\left(\nabla\boldsymbol{v} + (\nabla\boldsymbol{v})^T\right)\right)\cdot\boldsymbol{n} &= \boldsymbol{t} && \text{on } (\partial\Omega_T)_N && (4.31\text{h})
\end{aligned}
$$

Above, $\Omega_T = \Omega\times(0,T)$, $(\partial\Omega)_D$ is the Dirichlet part of the domain boundary, $\boldsymbol{t}$ is the prescribed traction force on the Neumann boundary $(\partial\Omega)_N$, $\boldsymbol{g}$ is the gravitational force field and p is the pressure variable acting as a Lagrange multiplier in the course of enforcing the incompressibility condition. This basically corresponds to the model presented by Ding et al. [46] which can be seen as a generalization of Model H (see equation (4.1)) for the case of different densities and viscosities. In contrast to Model H, a surface tension force term in potential form $\eta\nabla\varphi$ has replaced the divergence of the phase induced stress tensor $-\hat{\sigma}\varepsilon\,(\nabla\varphi\otimes\nabla\varphi)$. The latter, that is, $-\hat{\sigma}\varepsilon\,\mathrm{div}\,(\nabla\varphi\otimes\nabla\varphi)$, represents the phase induced force.

4.4 Discretization with Isogeometric finite elements

We use Isogeometric Analysis for the approximation of the solution of the coupled equation system (4.31). Inspired by operator splitting techniques, it is solved in two consecutive stages in order to alleviate numerical treatment. More specifically, given a flow field $\boldsymbol{v}$, we first solve the phase field equations (4.31c,4.31d) in order to update the phase φ and chemical potential information η. The second step eventually uses these information to compute the surface tension force and the phase dependent values of density $\rho(\varphi(\boldsymbol{x}))$ and viscosity $\mu(\varphi(\boldsymbol{x}))$ in the course of the solution of the Navier-Stokes equations (4.31a,4.31b). As time integrator for both systems, we use the one-step θ-scheme with $\theta = 1$ or $\theta = 0.5$ respectively yielding the 1st order implicit Euler or 2nd order Crank-Nicolson scheme. For the approximation of the velocity and pressure functions in the Navier-Stokes equations, we use LBB-stable Taylor-Hood-like NURBS[24] space pairs $\hat{\mathbf{V}}_h^{TH}/\hat{Q}_h^{TH}$ which are defined in the parametric spline domain $\hat{\Omega}$ as

$$
\begin{aligned}
\hat{\mathbf{V}}_h^{TH} &\equiv \hat{\mathbf{V}}_h^{TH}(\mathbf{p},\boldsymbol{\alpha}) = \boldsymbol{\mathcal{N}}_{\alpha,\alpha}^{p+1,p+1} = \mathcal{N}_{\alpha,\alpha}^{p+1,p+1}\times\mathcal{N}_{\alpha,\alpha}^{p+1,p+1},\\
\hat{Q}_h^{TH} &\equiv \hat{Q}_h^{TH}(\mathbf{p},\boldsymbol{\alpha}) = \mathcal{N}_{\alpha,\alpha}^{p,p}.
\end{aligned}
\tag{4.32}
$$

Above, $\mathcal{N}_{\alpha,\alpha}^{p+1,p+1}$ denotes a tensor product bivariate NURBS space of polynomial degrees $p+1$ and continuity α. We refer to Hosseini et al. [81] for a detailed description of the above spline spaces. In all performed computations we used a $\mathcal{C}^0$ $\boldsymbol{\mathcal{N}}_{0,0}^{2,2}/\mathcal{N}_{0,0}^{1,1}$ NURBS space pair for the approximation of the velocity and pressure functions. This corresponds to the Isogeometric counterpart of a Q_2Q_1

---

[24] Non-Uniform Rational B-splines (NURBS)

Taylor-Hood space well known from the finite element literature. The degree and continuity of the discrete spaces used for the approximation of the Navier-Stokes velocity and Cahn-Hilliard phase and chemical potential functions are set to be identical. In the sequel we picture the individual solution stages and outline the spatial and temporal discretization of the involved equations.

STEP 1 - CAHN-HILLIARD EQUATION:
For the treatment of nonlinearity in the advective Cahn-Hilliard equation, we seek for the current approximation of the solution $u^k = (\varphi^k, \eta^k)$ small perturbations $\delta u = (\delta\varphi, \delta\eta)$, such that

$$\begin{aligned} \varphi^{k+1} &= \varphi^k + \delta\varphi, \\ \eta^{k+1} &= \eta^k + \delta\eta \end{aligned} \tag{4.33}$$

satisfy the nonlinear partial differential equation (4.27). Under the premise that $\delta\varphi$ is sufficiently small, we linearize the nonlinear function $\psi'(\varphi)$ as:

$$\psi'(\varphi^{k+1}) = \psi'(\varphi^k) + \psi''(\varphi^k)\,\delta\varphi + \mathcal{O}((\delta\varphi)^2) \approx \psi'(\varphi^k) + \psi''(\varphi^k)\,\delta\varphi. \tag{4.34}$$

After the time discretization with the θ-scheme, we arrive at

$$\begin{aligned} \frac{\varphi^{n+1} - \varphi^n}{\Delta t} + \theta\left((\boldsymbol{v}\cdot\nabla)\varphi^{n+1} - \nabla\cdot m\,\nabla\eta^{n+1}\right) + (1-\theta)\left((\boldsymbol{v}\cdot\nabla)\varphi^n - \nabla\cdot m\,\nabla\eta^n\right) &= 0 \quad \text{in } \Omega_T, \\ \eta^{n+1} - \beta\,\psi'(\varphi^{n+1}) + \alpha\nabla^2\varphi^{n+1} &= 0 \quad \text{in } \Omega_T, \end{aligned} \tag{4.35}$$

where the boundary terms have not been displayed for the sake of lucidity. Above, in the spirit of Picard iteration, the nonlinear mobility function $m(\varphi)$ is evaluated with respect to the already available values of the phase field, that is, φ^n. This linearization allows it to be treated as a constant and simplifies the numerical treatment.

The variational form of the problem reads: Find $\varphi(\boldsymbol{x}, t)$ and $\eta(\boldsymbol{x}, t) \in \mathcal{H}^1(\Omega) \times (0, T)$, such that $\forall q, v \in \mathcal{H}^1_{0,\Gamma_D}(\Omega)$ it holds:

$$\begin{aligned} &\int_\Omega \frac{\varphi^{n+1} - \varphi^n}{\Delta t}\, q \,\mathrm{d}\boldsymbol{x} + \theta\left(\int_\Omega (\boldsymbol{v}\cdot\nabla)\varphi^{n+1}\, q + m\,\nabla\eta^{n+1}\cdot\nabla q \,\mathrm{d}\boldsymbol{x} - \int_{\partial\Omega} \boldsymbol{n}\cdot m\,\nabla\eta^{n+1}\, q \,\mathrm{d}s\right) \\ &\qquad + (1-\theta)\left(\int_\Omega (\boldsymbol{v}\cdot\nabla)\varphi^n\, q + m\,\nabla\eta^n\cdot\nabla q \,\mathrm{d}\boldsymbol{x} - \int_{\partial\Omega} \boldsymbol{n}\cdot m\,\nabla\eta^n\, q \,\mathrm{d}s\right) = 0, \\ &\int_\Omega \eta^{n+1}\, v \,\mathrm{d}\boldsymbol{x} - \int_\Omega \beta\,\frac{d\psi(\varphi^{n+1})}{d\varphi}\, v \,\mathrm{d}\boldsymbol{x} - \int_\Omega \alpha\,\nabla\varphi^{n+1}\cdot\nabla v \,\mathrm{d}\boldsymbol{x} + \int_{\partial\Omega} \boldsymbol{n}\cdot\alpha\nabla\varphi^{n+1} v \,\mathrm{d}s = 0. \end{aligned} \tag{4.36}$$

Recalling the contact angle b.c. in (4.20), we start with rewriting the corresponding weak form in (4.36) as

$$\begin{aligned} \int_{\partial\Omega} \boldsymbol{n}\cdot\alpha\nabla\varphi^{n+1}\, v \,\mathrm{d}s &= \int_{\partial\Omega} \alpha\frac{1}{\epsilon\sqrt{2}}\,\cos(\theta)(1-\varphi^2)\, v \,\mathrm{d}s \\ &= \int_{\partial\Omega} \alpha\frac{1}{\epsilon\sqrt{2}}\,\cos(\theta)\, q(\varphi)\, v \,\mathrm{d}s. \end{aligned} \tag{4.37}$$

Next, we linearize the nonlinear function $q : \mathbb{R} \to \mathbb{R}$ as

$$q(\varphi^{k+1}) = q(\varphi^k) + q'(\varphi^k)\delta\varphi + O\left((\delta\varphi)^2\right) \approx q(\varphi^k) + q'(\varphi^k)\delta\varphi, \tag{4.38}$$

and rewrite the right hand side of eqn. (4.37) as

$$\begin{aligned}
&\int_{\partial\Omega} \alpha \frac{1}{\epsilon\sqrt{2}} \cos(\theta) \left(q(\varphi^k) + q'(\varphi^k)\delta\varphi\right) v \,\mathrm{d}s = \int_{\partial\Omega} \alpha \frac{1}{\epsilon\sqrt{2}} \cos(\theta) \left(\left(1 - \left(\varphi^k\right)^2\right) - 2\varphi^k \delta\varphi\right) v \,\mathrm{d}s \\
&= \int_{\partial\Omega} \alpha \frac{1}{\epsilon\sqrt{2}} \cos(\theta) \left(-2\varphi^k \delta\varphi\right) v \,\mathrm{d}s + \int_{\partial\Omega} \alpha \frac{1}{\epsilon\sqrt{2}} \cos(\theta) \left(1 - \left(\varphi^k\right)^2\right) v \,\mathrm{d}s.
\end{aligned} \tag{4.39}$$

Eventually, the application of (4.33) and (4.34) on (4.36) yields:

$$\begin{aligned}
&\int_\Omega (\varphi^k + \delta\varphi - \varphi^n)\, q \,\mathrm{d}\boldsymbol{x} + \theta\Delta t \int_\Omega (\boldsymbol{v}\cdot\nabla)(\varphi^k + \delta\varphi)\, q + m\,\nabla(\eta^k + \delta\eta)\cdot\nabla q \,\mathrm{d}\boldsymbol{x} \\
&\qquad + (1-\theta)\Delta t \int_\Omega (\boldsymbol{v}\cdot\nabla)\varphi^n\, q + m\,\nabla\eta^n\cdot\nabla q \,\mathrm{d}\boldsymbol{x} = 0, \\
&\int_\Omega (\eta^k + \delta\eta)\, v \,\mathrm{d}\boldsymbol{x} - \int_\Omega \beta\left(\psi'(\varphi^k) + \psi''(\varphi^k)\,\delta\varphi\right) v \,\mathrm{d}\boldsymbol{x} - \int_\Omega \alpha\,\nabla(\varphi^k + \delta\varphi)\cdot\nabla v \,\mathrm{d}\boldsymbol{x} \\
&\qquad + \int_{\partial\Omega} \alpha \frac{1}{\epsilon\sqrt{2}} \cos(\theta) \left(-2\varphi^k\delta\varphi\right) v \,\mathrm{d}s + \int_{\partial\Omega} \alpha \frac{1}{\epsilon\sqrt{2}} \cos(\theta) \left(1 - \left(\varphi^k\right)^2\right) v \,\mathrm{d}s = 0.
\end{aligned} \tag{4.40}$$

In equation (4.40), the indices n and k refer to the solution from the last time step and the current Newton-iterate, respectively. $(\delta\varphi, \delta\eta)$ is associated to the Newton-update.

Gathering all terms with the unknowns $\delta\varphi$ and $\delta\eta$ on the left hand side, we obtain the following expressions

$$\begin{aligned}
&\int_\Omega \underbrace{\delta\varphi\, q}_{\mathbf{M}_1} + \theta\Delta t \left(\underbrace{(\boldsymbol{v}\cdot\nabla)\delta\varphi\, q}_{\mathbf{C}_1} + m\,\underbrace{\nabla\delta\eta\cdot\nabla q}_{\mathbf{D}_1} \right) \mathrm{d}\boldsymbol{x} = \\
&\int_\Omega -\underbrace{\varphi^k\, q}_{\mathbf{M}_2} - \theta\Delta t \left(\underbrace{(\boldsymbol{v}\cdot\nabla)\varphi^k\, q}_{\mathbf{C}_2} + m\,\underbrace{\nabla\eta^k\cdot\nabla q}_{\mathbf{D}_2} \right) \mathrm{d}\boldsymbol{x} \\
&+ \int_\Omega \underbrace{\varphi^n\, q}_{\mathbf{M}_3} - (1-\theta)\Delta t \left(\underbrace{(\boldsymbol{v}\cdot\nabla)\varphi^n\, q}_{\mathbf{C}_3} + m\,\underbrace{\nabla\eta^n\cdot\nabla q}_{\mathbf{D}_3} \right) \mathrm{d}\boldsymbol{x}, \\
&\int_\Omega \underbrace{\delta\eta\, v}_{\mathbf{M}_4} \,\mathrm{d}\boldsymbol{x} - \int_\Omega \beta\, \underbrace{\psi''(\varphi^k)\,\delta\varphi\, v}_{\mathbf{N}_1} \,\mathrm{d}\boldsymbol{x} - \int_\Omega \alpha\, \underbrace{\nabla\delta\varphi\cdot\nabla v}_{\mathbf{D}_4} \,\mathrm{d}\boldsymbol{x} \\
&+ \int_{\partial\Omega} \underbrace{\alpha \frac{1}{\epsilon\sqrt{2}} \cos(\theta) \left(-2\varphi^k\delta\varphi\right) v}_{\mathbf{N}_2} \,\mathrm{d}s = \\
&- \int_\Omega \underbrace{\eta^k\, v}_{\mathbf{M}_5} \,\mathrm{d}\boldsymbol{x} + \int_\Omega \beta\, \underbrace{\psi'(\varphi^k)\, v}_{\mathbf{n}_1} \,\mathrm{d}\boldsymbol{x} + \int_\Omega \alpha\, \underbrace{\nabla\varphi^k\cdot\nabla v}_{\mathbf{D}_5} \,\mathrm{d}\boldsymbol{x} \\
&- \int_{\partial\Omega} \underbrace{\alpha \frac{1}{\epsilon\sqrt{2}} \cos(\theta) \left(1 - \left(\varphi^k\right)^2\right) v \,\mathrm{d}s.}_{\mathbf{n}_2}
\end{aligned} \tag{4.41}$$

The corresponding discrete system for the Newton-Iteration may now be written in matrix form as

$$
\begin{aligned}
&\begin{array}{c} q \\ v \end{array} \underbrace{\begin{pmatrix} \mathbf{M}_1 + \theta \Delta t \mathbf{C}_1 & \theta \Delta t m \mathbf{D}_1 \\ -\alpha \mathbf{D}_4 - \beta \mathbf{N}_1 + \mathbf{N}_2 & \mathbf{M}_4 \end{pmatrix}}_{\mathbf{J}} \begin{pmatrix} \delta\varphi \\ \delta\eta \end{pmatrix} = \\
&\underbrace{\begin{pmatrix} -\mathbf{M}_2 - \theta \Delta t \mathbf{C}_2 & -\theta \Delta t m \mathbf{D}_2 \\ \alpha \mathbf{D}_5 & -\mathbf{M}_5 \end{pmatrix} \begin{pmatrix} \varphi^k \\ \eta^k \end{pmatrix} + \begin{pmatrix} \mathbf{0} \\ \beta \mathbf{n}_1 - \mathbf{n}_2 \end{pmatrix} + \begin{pmatrix} \mathbf{M}_3 - (1-\theta) \Delta t \mathbf{C}_3 & -(1-\theta) \Delta t m \mathbf{D}_3 \\ \mathbf{0} & \mathbf{0} \end{pmatrix} \begin{pmatrix} \varphi^n \\ \eta^n \end{pmatrix}}_{-\mathbf{F}}
\end{aligned}
\tag{4.42}
$$

and solved for δu in order to update the unknowns as $(\varphi^{k+1}, \eta^{k+1}) = (\varphi^k, \eta^k) + (\delta\varphi^k, \delta\eta^k)$.

Step 2 - Navier-Stokes equations: This step involves the numerical approximation of the solution of the unsteady variable density and variable viscosity Navier-Stokes equations extended by a surface tension force term. The initial condition is required to satisfy $\nabla \cdot \boldsymbol{v}_0 = 0$. With $\boldsymbol{b}$ denoting the body force term, the variational formulation of the problems (4.31a,4.31b) reads: Find $\boldsymbol{v}(\boldsymbol{x}, t) \in$ [25] $\left(\boldsymbol{\mathcal{H}}^1_{0,(\partial\Omega)_D}(\Omega) + \bar{\boldsymbol{v}}\right) \times (0, T)$ and $p(\boldsymbol{x}, t) \in \mathcal{L}_2(\Omega)/\mathbb{R} \times (0, T)$, such that for all $(\boldsymbol{w}, q) \in \boldsymbol{\mathcal{H}}^1_{0,(\partial\Omega)_D}(\Omega) \times \mathcal{L}_2(\Omega)/\mathbb{R}$ it holds

$$
\begin{cases}
(\boldsymbol{w}, \boldsymbol{v}_t) + a(\boldsymbol{w}, \boldsymbol{v}) + c(\boldsymbol{v}; \boldsymbol{w}, \boldsymbol{v}) + b(\boldsymbol{w}, p) = (\boldsymbol{w}, \boldsymbol{b}) + (\boldsymbol{w}, \boldsymbol{t})_{(\partial\Omega)_N} \\
b(q, \boldsymbol{v}) = 0.
\end{cases}
\tag{4.43}
$$

Replacement of the linear-, bilinear- and trilinear forms with their respective definitions and application of integration by parts yields

$$
\begin{aligned}
&\underbrace{\int_\Omega \rho(\varphi) \boldsymbol{w} \cdot \boldsymbol{v}_t \, \mathrm{d}\Omega}_{(\boldsymbol{w}, \boldsymbol{v}_t)} + \underbrace{\int_\Omega \mu(\varphi) \nabla \boldsymbol{w} \ : \ \left(\nabla \boldsymbol{v} + (\nabla \boldsymbol{v})^T\right) \, \mathrm{d}\Omega}_{a(\boldsymbol{w}, \boldsymbol{v})} + \underbrace{\int_\Omega \rho(\varphi) \boldsymbol{w} \cdot \boldsymbol{v} \cdot \nabla \boldsymbol{v} \, \mathrm{d}\Omega}_{c(\boldsymbol{v}; \boldsymbol{w}, \boldsymbol{v})} = \\
&\underbrace{\int_\Omega \nabla \cdot \boldsymbol{w} \, p \, \mathrm{d}\Omega}_{b(\boldsymbol{w}, p)} + \underbrace{\int_\Omega q \, \nabla \cdot \boldsymbol{v} \, \mathrm{d}\Omega}_{b(q, \boldsymbol{v})} + \underbrace{\int_\Omega \rho(\varphi) \boldsymbol{w} \cdot \boldsymbol{b} + \boldsymbol{w} \cdot \eta \nabla \varphi \, \mathrm{d}\Omega}_{(\boldsymbol{w}, \boldsymbol{b})} + \\
&\underbrace{\int_{(\partial\Omega)_N} \mu(\varphi) \, \boldsymbol{w} \cdot \left(\left(\nabla \boldsymbol{v} + (\nabla \boldsymbol{v})^T\right) \cdot \boldsymbol{n}\right) \, \mathrm{d}(\partial\Omega)_N - \int_{(\partial\Omega)_N} \boldsymbol{w} \cdot \boldsymbol{n} \, p \, \mathrm{d}(\partial\Omega)_N}_{(\boldsymbol{w}, \boldsymbol{t})_{(\partial\Omega)_N}} .
\end{aligned}
\tag{4.44}
$$

A downcast of the variational formulation (4.43) to the discrete level gives rise to the problem statement

$$
\begin{cases}
\text{Find } \ \boldsymbol{v}_h \in \left(\boldsymbol{\mathcal{H}}^1_{0,(\partial\Omega)_D}(\Omega) + \bar{\boldsymbol{v}}\right) \cap \mathbf{V}_h^{TH} \times (0, T) \ \text{ and } \ p_h \in \mathcal{L}_2(\Omega)/\mathbb{R} \cap Q_h^{TH} \times (0, T), \text{such that} \\
\forall (\boldsymbol{w}_h, q_h) \in \boldsymbol{\mathcal{H}}^1_{0,(\partial\Omega)_D}(\Omega) \cap \mathbf{V}_h^{TH} \times \mathcal{L}_2(\Omega)/\mathbb{R} \cap Q_h^{TH} \\
(\boldsymbol{w}_h, \partial_t \boldsymbol{v}_h) + a(\boldsymbol{w}_h, \boldsymbol{v}_h) + c(\boldsymbol{v}_h; \boldsymbol{w}_h, \boldsymbol{v}_h) + b(\boldsymbol{w}_h, p_h) = (\boldsymbol{w}_h, \boldsymbol{b}_h) + (\boldsymbol{w}_h, \boldsymbol{t}_h)_{(\partial\Omega)_N} \\
b(q_h, \boldsymbol{v}_h) = 0,
\end{cases}
\tag{4.45}
$$

with superscript h dubbing the mesh family index. Using Isogeometric Taylor-Hood finite elements

---

[25] $\bar{\boldsymbol{v}}$ denotes a Dirichlet lift function and for a definition of the space $\boldsymbol{\mathcal{H}}^1_{0,(\partial\Omega)_D}(\Omega)$ we refer to equation (3.76).

and the θ-scheme for the respective discretizations in space and time, the following discrete system

$$\begin{aligned}
&\underbrace{\begin{pmatrix} \frac{1}{\Delta t}\mathbf{M}(\varphi^{n+1}) + \theta(\mathbf{D}(\varphi^{n+1}) + \mathbf{C}(v^{n+1}, \varphi^{n+1})) & \mathbf{G} \\ \mathbf{G}^T & \mathbf{0} \end{pmatrix}}_{\mathbf{S}_l} \underbrace{\begin{pmatrix} \mathbf{v}^{n+1} \\ \mathbf{p}^{n+1} \end{pmatrix}}_{\mathbf{u}^{n+1}} = \\
&\underbrace{\begin{pmatrix} \frac{1}{\Delta t}\mathbf{M}(\varphi^{n}) - (1-\theta)(\mathbf{D}(\varphi^{n}) + \mathbf{C}(v^{n}, \varphi^{n})) & \mathbf{0} \\ \mathbf{0} & \mathbf{0} \end{pmatrix}}_{\mathbf{S}_r} \underbrace{\begin{pmatrix} \mathbf{v}^{n} \\ \mathbf{p}^{n} \end{pmatrix}}_{\mathbf{u}^{n}} + \underbrace{\theta\, \mathbf{f}^{n+1}(\eta^{n+1}, \varphi^{n+1})}_{\mathbf{b}^{n+1}} + \underbrace{(1-\theta)\mathbf{f}^{n}(\eta^{n}, \varphi^{n})}_{\mathbf{b}^{n}}
\end{aligned} \tag{4.46}$$

is obtained, where $\mathbf{M}, \mathbf{D}, \mathbf{C}, \mathbf{G}$, and $\mathbf{G^T}$ denote the mass, rate of deformation, advection, gradient, and divergence matrices, respectively. The body and the surface tension force terms are discretized altogether into $\mathbf{f}$. For the treatment of the nonlinearity in the Navier-Stokes equations (4.31a,4.31b), we use a Newton-Iteration

$$\mathbf{J}(\mathbf{u}^k, \varphi^k)\, \delta\mathbf{u} = -\mathbf{F}(\mathbf{u}^k, \mathbf{u}^n, \eta^k, \eta^n, \varphi^k, \varphi^n) \tag{4.47a}$$

$$\mathbf{u}^{k+1} = \mathbf{u}^k + \delta\mathbf{u}, \tag{4.47b}$$

whose right hand side is set to be the residual of equation (4.46), that is,

$$\mathbf{F}(\mathbf{u}^{n+1}, \mathbf{u}^n, \eta^{n+1}, \eta^n, \varphi^{n+1}, \varphi^n) = \mathbf{S}_l\, \mathbf{u}^{n+1} - \mathbf{S}_r\, \mathbf{u}^n - \mathbf{b}^{n+1} - \mathbf{b}^n. \tag{4.48}$$

For a detailed description of the setup of the Jacobian $\mathbf{J}$ in equation (4.47), we refer to [81].

4.5 Numerical results

Three numerical experiments are performed to assess the results obtained from the application of Isogeometric Analysis to two-phase flow problems. As aforementioned, the static bubble in equilibrium, the rising bubble and the Rayleigh-Taylor instability two-phase flow problems serve as model problems, each discussed in a separate section (4.5.1,4.5.2,4.5.3). Special emphasis is put on the rising bubble flow scenario whose setup follows an official two-phase flow benchmark problem and for which there exists an extensive set of results computed with different approximation methods by different research groups.

4.5.1 Static bubble

Being a simple setup, yet exhibiting prototypical behavior for multiphase flows, we consider a stationary bubble at equilibrium. This setup holds e.g. for the slow motion of a gas bubble in a viscoplastic fluid as described in [50]. With the bubble being at rest, the velocity field in the computational domain is expected to be zero. Nevertheless, numerical approximations of the velocity field unfortunately produce spurious currents, as for instance reported in [63, 137]. The computed pressure field is expected to satisfy the Laplace-Young law

$$p_i = p_o + \sigma/r, \tag{4.49}$$

where r is the bubble radius, σ is the surface tension coefficient and p_i and p_o denote the pressure inside $(x = 0.5, y = 0.5)$ and outside $(x = 1.0, y = 0.5)$ of the bubble, respectively. We set our computational domain Ω to be the unit square and partition it to two disjoint areas Ω_1 and Ω_2, such that $\Omega = \Omega_1 \cup \Omega_2$. Then, the static bubble is represented by the domain Ω_2 which is set up to be a circle of radius $r = 1/4$, centered at position $(1/2, 1/2)$. In order to setup the initial phase field profile, we perform a finite element L^2-projection

$$\int_\Omega (f - P_h f)\, w \,\mathrm{d}\boldsymbol{x} = 0, \quad \forall w \in \mathcal{W}_h \tag{4.50}$$

of the profile

$$f = \varphi_{\text{bubble}}(\boldsymbol{x}) = \begin{cases} +1, & \text{for } \boldsymbol{x} \in \Omega_1 \\ -1, & \text{for } \boldsymbol{x} \in \Omega_2 \end{cases} \tag{4.51}$$

on the NURBS-space degrees of freedom associated with the phase variable, whereby $\mathcal{W}_h$ denotes a suitable discrete space of weighting/test functions.

The gravitational force is neglected and the densities and viscosities of both fluids as well as the surface tension coefficient are set to 1. We use no-slip velocity boundary conditions in the entire domain and fix the value of the discrete pressure field at the lower left domain node with $p = 0$. Table 4.2 illustrates our pressure and velocity results for the above choice of parameters. Starting off with the pressure jump $[\![p]\!] = |p_i - p_o|$ across the interface, it is shown to converge to the value 4, corresponding to the output of the Laplace-Young law for the above parametrization. Moreover, the precision and convergence of both the spurious velocity errors and the pressure difference are in good agreement with the sharp interface model results at our disposal, as for instance [150]. We refer to Figure 4.4 for a graphical representation of the pressure and velocity profiles. The spurious velocities are shown to build pairwise counter rotating vortices at the phase boundary with the impression of attempting to tear the fluid-fluid interface. The pressure field expectedly exhibits a rapid, yet smooth transition in the interface layer. As illustrated in Figure 4.5 (left), a lateral view of the pressure profile for different mesh refinement levels and diffuse interface widths reveals the convergence of the shape to a reference cylinder with radius $r = 1/4$ and height $1/r$. We conclude the static bubble test case with the investigation of the pressure jumps for the following choice of bubble radii $r = 1/8,\ 1/4,\ 3/8,\ 7/16$, where the results - displayed to the right of Figure 4.5 - are shown to tightly integrate with the Laplace-Young law.

N$_{\text{el}}$	h	ξ	p_i	p_o	$\lvert\Delta p - (\frac{\sigma}{r})\rvert/(\frac{\sigma}{r})$	$\lvert p_i - p_o\rvert/(\frac{\sigma}{r})$	$\lVert p - p_h\rVert_{L^2}$	$\lVert \boldsymbol{v} - \boldsymbol{v_h}\rVert_{L^2}$
256	2^{-4}	0.0400	4.05234	-0.00431	0.01416	1.01416	0.539996	2.27e-04
1024	2^{-5}	0.0200	3.99563	-0.00233	0.00051	0.99949	0.379967	6.67e-05
4096	2^{-6}	0.0125	4.00642	-0.00139	0.00195	1.00195	0.296332	6.77e-05
16384	2^{-7}	0.007125	4.00067	-0.00074	0.00035	1.00035	0.222107	1.28e-04

Table 4.2: Pressure and velocity errors for surface tension coefficient $\sigma = 1$ and bubble radius $r = 1/4$.

4.5.2 Rising bubble

The rising bubble benchmark considers two initially quiescent fluids with different densities and viscosities in a rectangular domain $\Omega = \Omega_1 \cup \Omega_2 = (0, 1) \times (0, 2)$, where fluid i occupies the subdomain Ω_i. The lighter liquid (bubble) represented by the initially circular area Ω_2 with radius $r = 1/4$ and center $c = (1/2, 1/2)$ is subject to rising due to the effects of buoyancy. At the top and bottom boundaries we use the no-slip ($\boldsymbol{v} = 0$) boundary condition, whereas the free slip ($\boldsymbol{v} \cdot \boldsymbol{n} = 0, \boldsymbol{\tau} \cdot \left(\nabla \boldsymbol{u} + (\nabla \boldsymbol{u})^T\right) \cdot \boldsymbol{n} = 0, \boldsymbol{\tau} :=$ tangent vector) boundary condition is imposed on

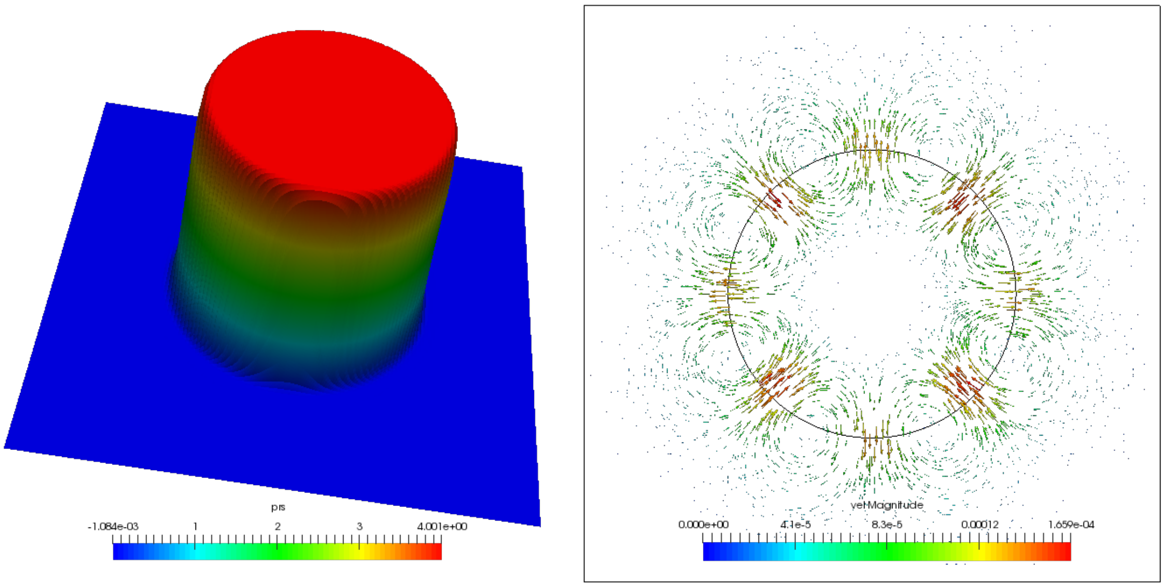

Figure 4.4: Pressure and velocity profiles for surface tension coefficient $\sigma = 1$ and bubble radius $r = 1/4$.

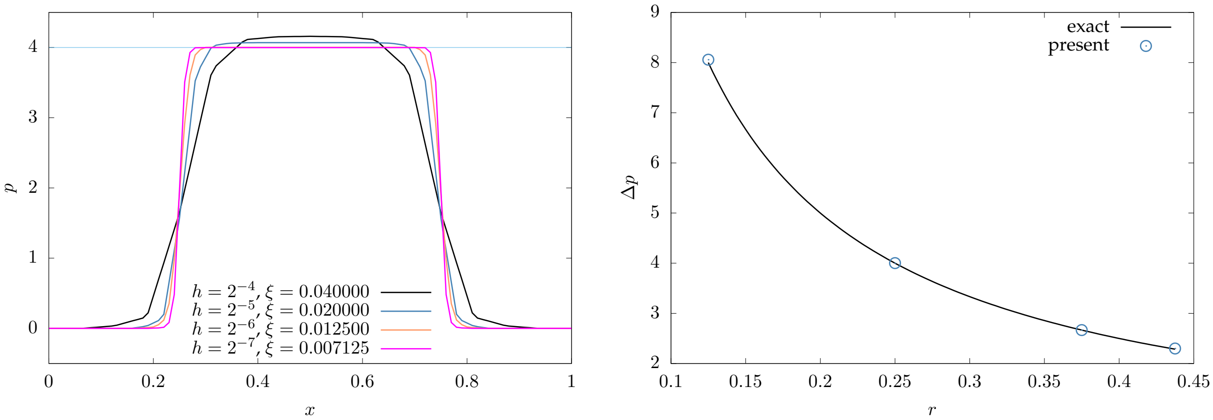

Figure 4.5: Left: Static bubble pressure profile development for surface tension coefficient $\sigma = 1$ and bubble radius $r = 1/4$. Right: Pressure differences Δp for a set of different bubble radii r compared to exact results based on the Laplace-Young law (4.49).

the vertical walls. This setup, graphically represented by Figure 4.6, corresponds to the FeatFlow[26] rising bubble benchmark [59, 88] for which different research groups[27] have provided extensive benchmark-relevant data. In particular, for the first rising bubble test case, we will consider the data provided by group 1 of [88] as reference.

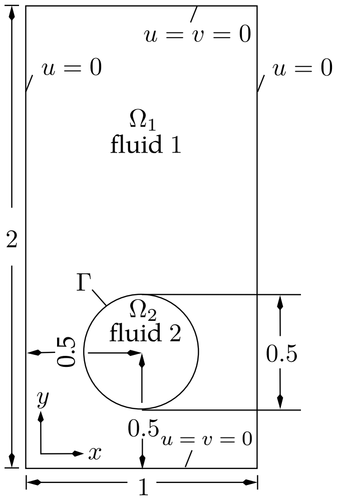

Figure 4.6: Configuration for the rising bubble test cases.

The rising bubble benchmark defines two test cases differing by their respective choice of the surface tension coefficient and the density and viscosity ratios of the fluids. We refer to Table 4.3 for a listing of the physical parameters of both test cases.

Test case	ρ_1	ρ_2	μ_1	μ_2	g	σ	Re	Eo	ρ_1/ρ_2	μ_1/μ_2
1	1000	100	10	1	0.98	24.5	49.5	9	10	10
2	1000	1	10	0.1	0.98	1.96	49.5	124.88	1000	100

Table 4.3: Physical parameters and dimensionless numbers defining the rising bubble test cases.

The problems are characterized by the dimensionless parameters density ratio ρ_1/ρ_2, viscosity ratio μ_1/μ_2, the Reynolds number $Re = \rho_1 \tilde{v} L/\mu_1$ and the Eötvös (or Bond) number $Eo = Bo = \Delta\rho g L^2/\sigma$, where we set the characteristic velocity to $\tilde{v} = \sqrt{g}$ and the characteristic length to $L = 2r$. Based on experimental findings, Clift et al. have published results (see Figure 2.5 in [34]) that render the bubble shape to be dependent on the combination of the Reynolds and Eötvös numbers. Albeit their results are for really three-dimensional bubbles, they can nonetheless be taken as a basis for qualitative comparisons. Based on their study, the combination shown for test case 1 is expected to produce an ellipsoidal shape, while due to the higher Eötvös number and thus smaller surface tension in test case 2, the bubble is expected to experience a more significant deformation. Therefore, in this case the bubble's shape is expected to be a blend between "skirted" and "dimpled ellipsoidal-cap" in Clift speak. In fact, our numerical bubble shapes presented in sections 4.5.2.1 and 4.5.2.2 are in good agreement with these experimental predictions.

---

[26] www.featflow.de

[27] TU Dortmund, Inst. of Applied Math: TP2D(FEM-Level Set),
EPFL Lausanne, Inst. of Analysis and Sci. Comp.: FreeLIFE (FEM-Level Set),
Uni. Magdeburg, Inst. of Analysis and Num. Math.: MooNMD (FEM-ALE).

For the quantification of the rising bubble dynamics, it is reasonable to compute a set of quantities such as the bubble's rise velocity V_b, center of mass Y_b and circularity $\not{c}$, being respectively defined as

$$\begin{aligned}
A_b &= \int_{\Omega_2} 1 \,\mathrm{d}\boldsymbol{x},\\
V_b &= \int_{\Omega_2} \boldsymbol{v}.y \,\mathrm{d}\boldsymbol{x}/A_b,\\
Y_b &= \int_{\Omega_2} \boldsymbol{x}.y \,\mathrm{d}\boldsymbol{x}/A_b,\\
\not{c} &= \frac{P_a}{P_b} = \frac{\text{perimeter of area-equivalent circle}}{\text{perimeter of bubble}} = \frac{2\pi\sqrt{A_b/\pi}}{P_b},
\end{aligned}$$

where A_b is both the area of the current bubble shape and the area of a circle with radius $r = \sqrt{A_b/\pi}$. For both rising bubble test cases we track the evolution of the bubble until the time $t_{\max} = 3$ and measure the temporal evolution of the above time dependent quantities with respect to the following relative error norms

$$\|e\|_1 = \frac{\sum_{t=1}^{N} |q_{t,\text{ref}} - q_t|}{\sum_{t=1}^{N} |q_{t,\text{ref}}|}, \quad \|e\|_2 = \left(\frac{\sum_{t=1}^{N} |q_{t,\text{ref}} - q_t|^2}{\sum_{t=1}^{N} |q_{t,\text{ref}}|^2} \right)^{1/2}, \quad \|e\|_\infty = \frac{\max_t |q_{t,\text{ref}} - q_t|}{\max_t |q_{t,\text{ref}}|},$$

where $\|e\|_1, \|e\|_2$ and $\|e\|_\infty$ respectively denote the l_1, l_2 and l_∞ relative error norms, $N = ((t_{\max} - t_1)/\Delta t) + 1$ is the number of time stepping sample points and q_t denotes the temporal evolution of quantity q. These relative error norms are eventually used to inspect the estimated order of convergence

$$\text{EOC} = \frac{\log(\|e_{i-1}\|/\|e_i\|)}{\log(h_{i-1}/h_i)}$$

of the quantities V_b, Y_b and $\not{c}$. Note that the reference solution $q_{t,\text{ref}}$ may possess a different time sampling concinnity than q_t. In such a situation interpolation is the means of choice to match the time steps.

4.5.2.1 Results for test case 1

The relatively low Eötvös number of this setup implies non-negligible surface tension forces, compared to body forces. The surface tension forces can be thought of to act towards preserving the bubble shape and topology, and as aforementioned the combination of the Reynolds and Eötvös numbers of case 1 is expected to yield an ellipsoidal bubble geometry. Figure 4.7 illustrates, at different time steps, the shapes of our rising bubble alongside those computed with a [28]Q_2P_1 finite element discretization. The temporal development of the initially circular bubble is characterized in the early time stages $0 \leq t \leq 1.5$ by an horizontal stretching and dimple development. However, the shapes of the subsequent time steps disclose the clear endeavor to develop an ellipsoidal shape being in good conformity with experimental predictions. At all time instances our bubble shapes are in very good agreement with the results obtained with standard Q_2P_1 FE. Moreover, at final time $t_{\max}$, our approximated bubble geometry is shown to have a remarkable geometrical congruency with that of the reference solution (TP2D), having been superimposed over our data. Mesh convergence of our results is demonstrated in Figure 4.8, where the bubble shapes associated to different mesh family indices h are shown to match each other with respect to an acceptable tol-

---

[28] Velocity: Biquadratic, continuous; Pressure: Linear (value and two partial derivatives), discontinuous

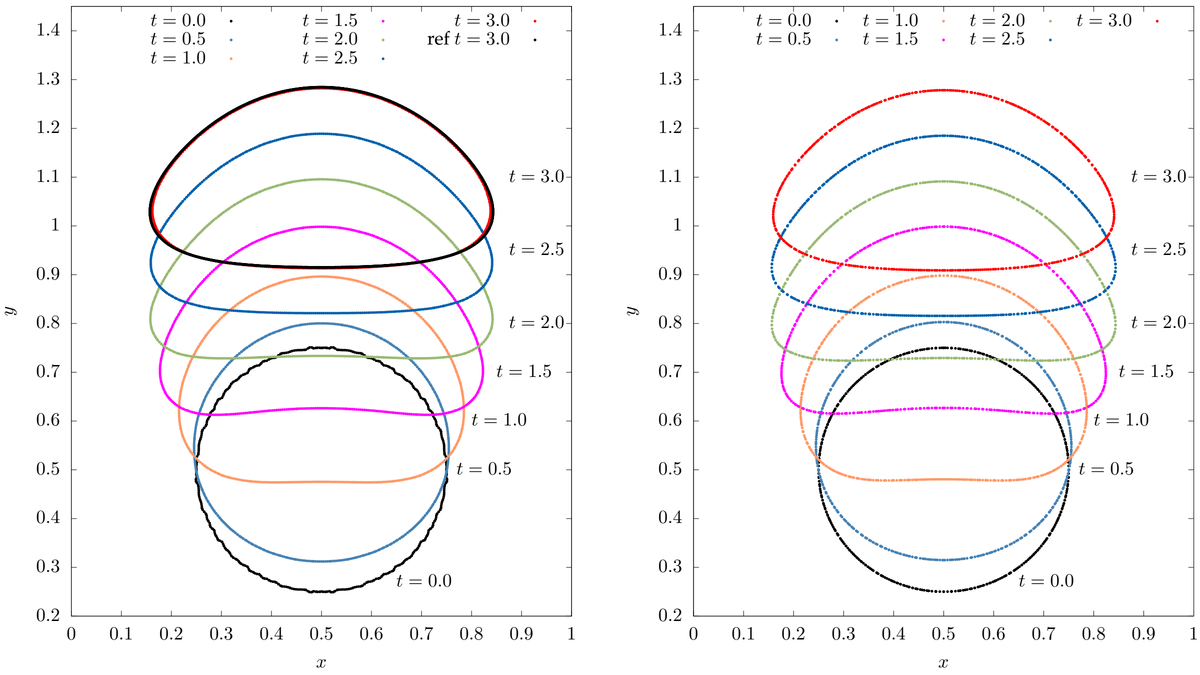

Figure 4.7: Shapes of the rising bubble at a set of time points. Left: Our results for $h = 2^{-6}$ and the TP2D reference shape at $t = t_{\max}$. Right: Level-set based sharp interface results computed with Q_2P_1 finite elements.

erance. The diffuse interface method, however, introduces a diffuse interface width ξ which can be varied as well. It is reasonable to set $\xi \propto h$ and, in fact, in all conducted computations for the first case of the rising bubble setup, the h, ξ and Δt settings of Table 4.4 together with mobility coefficient $D = 0.00004$ (cf. (4.17)) were used. The effect of modifying the diffuse interface width while keeping the mesh refinement level fixed is demonstrated in Figure 4.9. For three consecutive diffuse interface widths $\xi = 0.03,\ 0.02,\ 0.01$ on the exemplary chosen mesh refinement level 6, the results are shown to converge to the reference as ξ decreases. The choice of ξ needs to respect the size of h as without a "reasonable" amount of elements across the diffuse interface width, the numerics will fail to produce rational results due to undersampling effects.

h	ξ	Δt	$\not{c}_{\text{min}}$	$t\vert_{\not{c}=\not{c}_{\text{min}}}$	$V_{b,\max}$	$t\vert_{V_b=V_{b,\max}}$	$Y_b(t=3)$
2^{-4}	0.040	0.008	0.9425	2.1281	0.2384	1.2000	1.0665
2^{-5}	0.020	0.008	0.9151	1.9280	0.2423	0.9520	1.0778
2^{-6}	0.010	0.004	0.9044	1.9240	0.2422	0.9120	1.0792
2^{-7}	0.005	0.004	0.9013	1.9200	0.2420	0.9200	1.0794
ref			0.9013	1.9041	0.2417	0.9213	1.0813

Table 4.4: Minimum circularity and maximum rise velocity with corresponding incidence times and final position of the center of mass for test case 1.

Devoting our attention back to the previously defined benchmark quantities V_b, Y_b and $\not{c}$, we present in Figure 4.11 our results for their temporal evolution. For decreased h the profiles of all quantities converge to the reference. On the highest displayed refinement level, the congruency

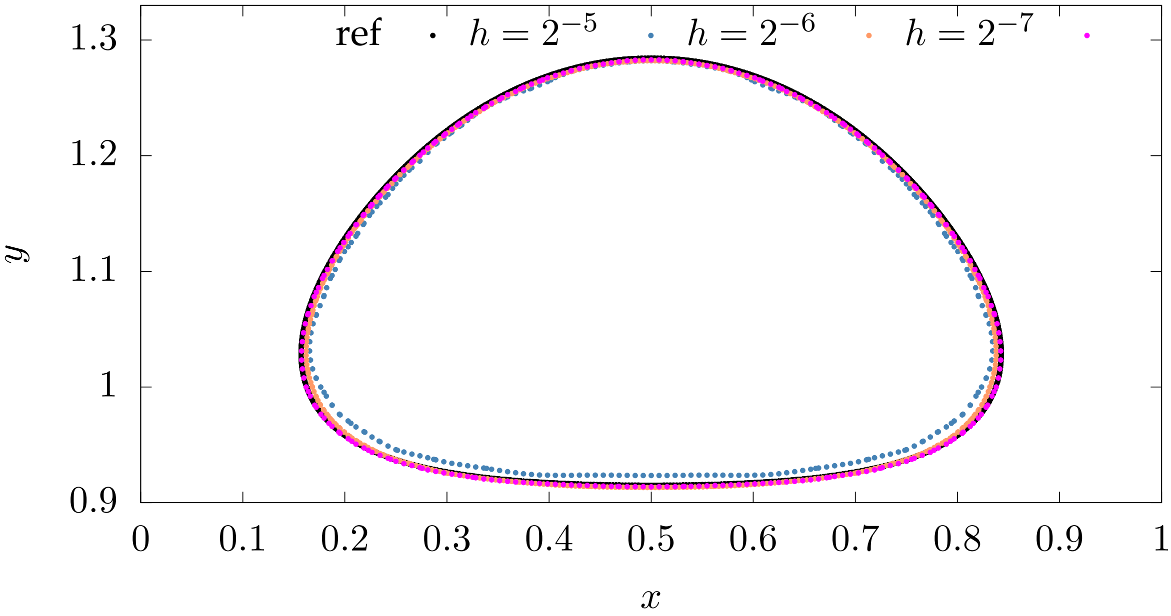

Figure 4.8: Shapes of the rising bubble at final time $t = 3$ for different h.

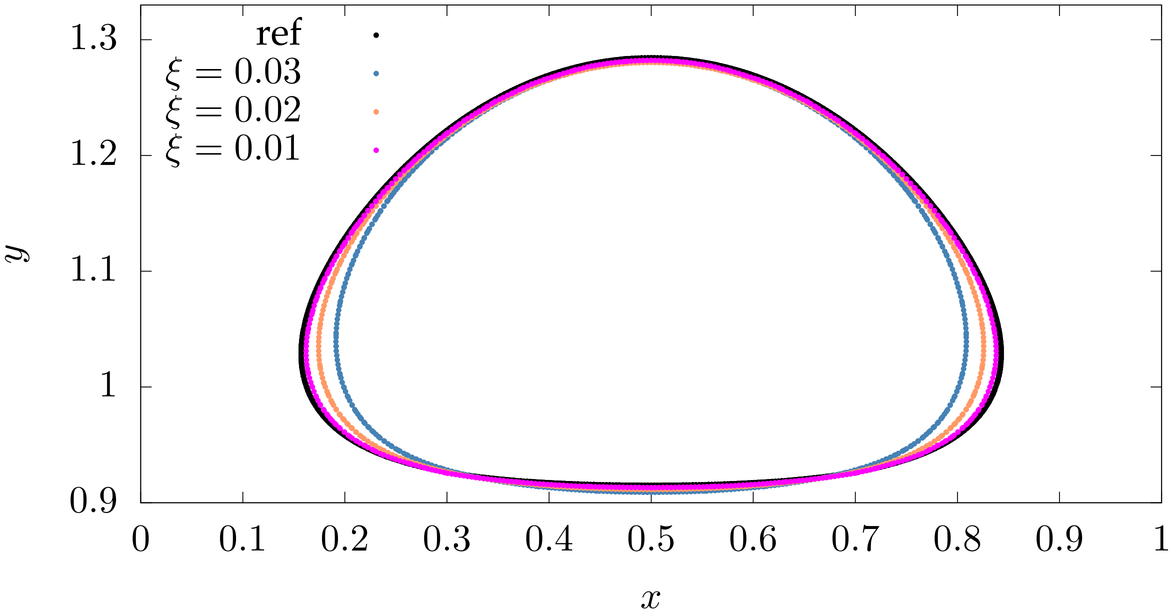

Figure 4.9: Shapes of the rising bubble at final time $t = 3$ for $h = 2^{-6}, \Delta t = 0.004$ and different diffuse interface widths.

of our profiles with the reference is remarkable. Extrema of these profiles, such as minimum circularity $\not{c}_{\min}$, maximum rise velocity $V_{b,\max}$ and final center of mass $Y_b(t = 3)$ together with their incidence times are tabulated in Table 4.4 for different mesh refinement levels. On levels 6 and 7, our approximations of $V_{b,\max}, Y_b(t = 3)$ and $\not{c}_{\min}$ respectively exhibit 3 and 2 matching decimal digits, when compared to each other. Besides, the quantities are shown to converge to the reference values. The relative error norms and the respective convergence orders of the quantities center of mass, rise velocity and circularity are illustrated in Table 4.5. For the quantities center of mass and rise velocity, the convergence orders of the l_1 and l_2 errors are around 1, while we approach quadratic convergence in case of circularity. For all quantities, the convergence order of the l_∞ error is as a matter of principle slightly lower than its counterparts. Note that the errors depicted in Table 4.5 are computed with respect to the sharp interface reference solution $q_{t,\text{ref}}$ published in [88]. Their computation of the l_1, l_2 and l_∞ errors consider their own solution on the finest grid to be the exact solution.

q	h	ξ	$\|e\|_1$	EOC$_1$	$\|e\|_2$	EOC$_2$	$\|e\|_\infty$	EOC$_\infty$
Y_b	2^{-4}	0.040	0.0171		0.0183		0.0217	
	2^{-5}	0.020	0.0053	1.7049	0.0057	1.6818	0.0078	1.4755
	2^{-6}	0.010	0.0019	1.4633	0.0020	1.5127	0.0026	1.5947
	2^{-7}	0.005	0.0013	0.5312	0.0013	0.5706	0.0014	0.8730
V_b	2^{-4}	0.040	0.0516		0.0559		0.0775	
	2^{-5}	0.020	0.0206	1.3263	0.0219	1.3518	0.0321	1.2714
	2^{-6}	0.010	0.0051	2.0064	0.0059	1.8934	0.0121	1.4112
	2^{-7}	0.005	0.0023	1.1755	0.0028	1.0575	0.0061	0.9790
$\not{c}$	2^{-4}	0.040	0.0267		0.0317		0.0431	
	2^{-5}	0.020	0.0095	1.4927	0.0111	1.5095	0.0152	1.5051
	2^{-6}	0.010	0.0023	2.0446	0.0027	2.0443	0.0040	1.9111
	2^{-7}	0.005	0.0005	2.1778	0.0007	2.0334	0.0013	1.6871

Table 4.5: Relative error norms and estimated orders of convergence of the benchmark quantities for test case 1. Errors have been computed w.r.t. the sharp interface reference solution.

For the sake of a fair comparison with diffuse interface models, we therefore extend our analysis to the same mode, that is, taking our finest grid solution as the reference. Doing so, clearly improves the convergence orders as illustrated in Table 4.6. Again, the convergence orders of the l_∞ errors are by trend smaller than those of the l_1 and l_2 errors. The latter mentioned are around 2 for all quantities. Finally, in order to inspect the influence of the diffuse interface width on the accuracy of the results, we have extended the analysis of the temporal development of the quantities to the situation where for each mesh refinement level, the diffuse interface width is varied. The results, depicted in Figure 4.10, disclose as expected an improvement of the results in terms of accuracy as the mesh refinement level and diffuse interface width approach a more favorable relation.

4.5.2.2 Results for test case 2

Compared to the first rising bubble setup, the second one is characterized by significantly higher density and viscosity ratios and a higher Eötvös number. This implies both a tremendous different amount of body forces acting on either side of the fluid-fluid interface and rather negligible surface tension forces, compared to body forces. As a consequence, the bubble is subject to significant de-

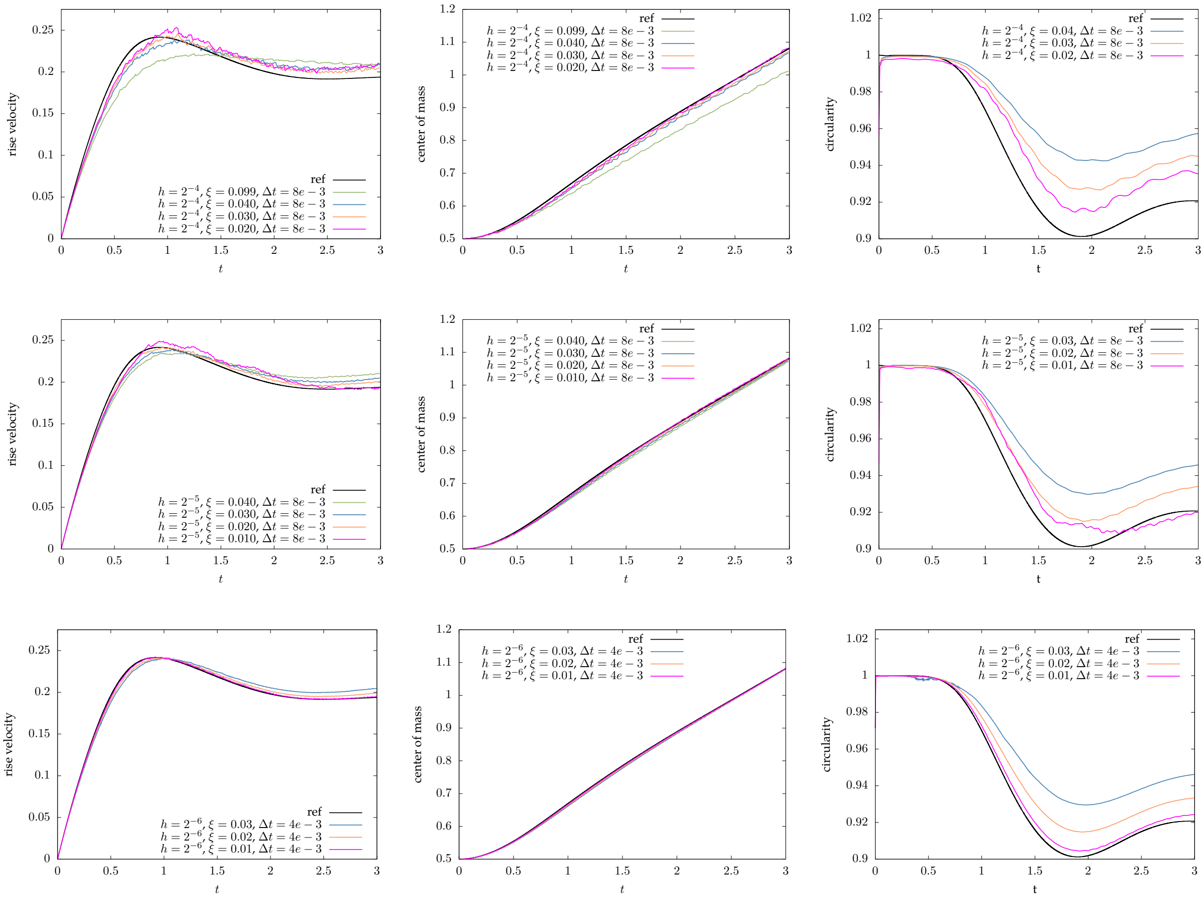

Figure 4.10: Rising bubble test case 1: Influence of the diffuse interface width ξ on the rise velocity and center of mass profiles for $h = 2^{-4}$, 2^{-5}, 2^{-6}.

q	h	ξ	$\|e\|_1$	EOC$_1$	$\|e\|_2$	EOC$_2$	$\|e\|_\infty$	EOC$_\infty$
Y_b	2^{-4}	0.040	0.0158		0.0170		0.0206	
	2^{-5}	0.020	0.0039	2.0024	0.0045	1.9263	0.0068	1.6026
	2^{-6}	0.010	0.0007	2.5718	0.0008	2.5136	0.0015	2.2132
V_b	2^{-4}	0.040	0.0505		0.0549		0.0748	
	2^{-5}	0.020	0.0193	1.3883	0.0209	1.3969	0.0323	1.2100
	2^{-6}	0.010	0.0037	2.3780	0.0042	2.3116	0.0076	2.0974
¢	2^{-4}	0.040	0.0261		0.0312		0.0428	
	2^{-5}	0.020	0.0090	1.5363	0.0107	1.5463	0.0198	1.1128
	2^{-6}	0.010	0.0018	2.3055	0.0022	2.2597	0.0063	1.6609

Table 4.6: Relative error norms and estimated convergence orders of the benchmark quantities for test case 1 assuming the finest grid solution as exact solution.

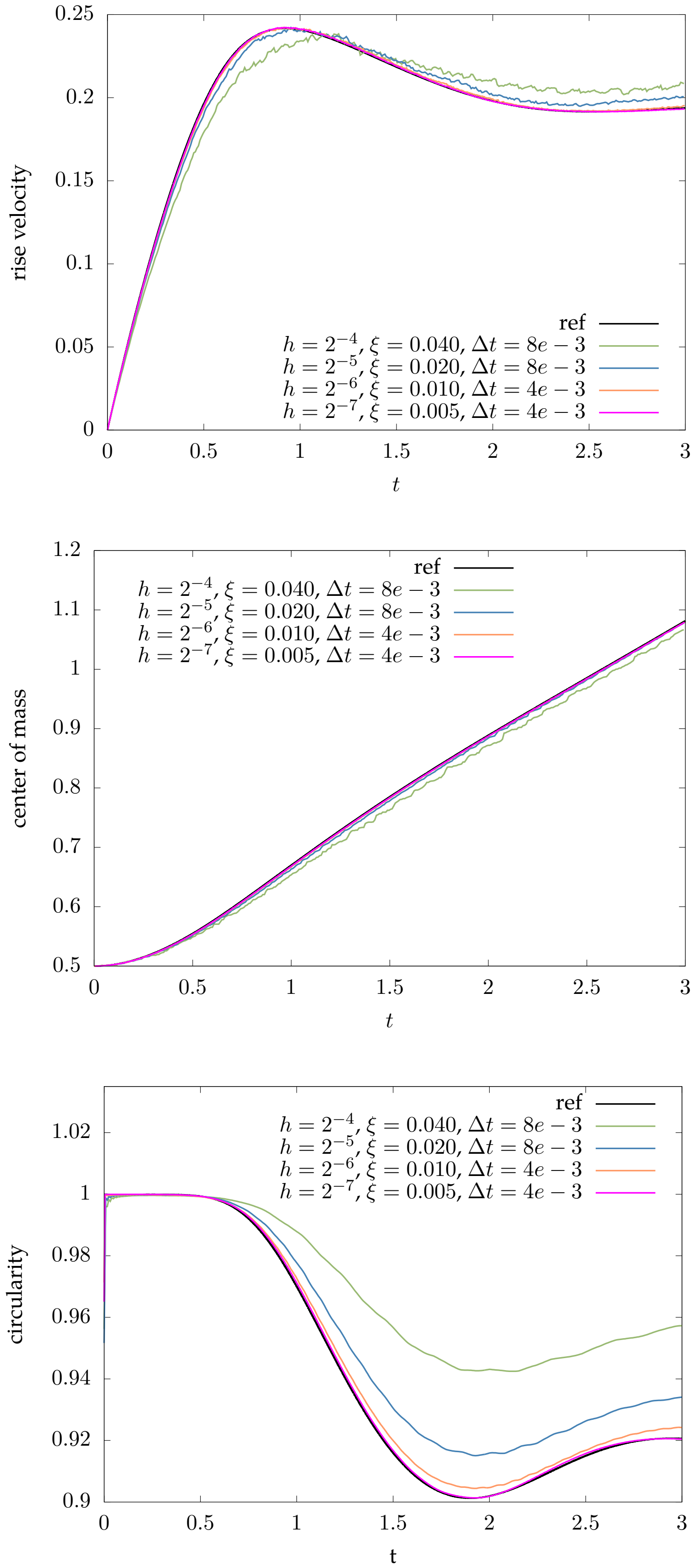

Figure 4.11: Rising bubble test case 1: Rise velocity, center of mass and circularity profiles (mobility coefficient $D = 0.00004$).

formations giving rise to the development of thin filaments at its lower left and right corners. As the bubble keeps rising due to buoyancy forces, these filaments experience elongation and develop an ever thinner getting region implying a break off in the limit. This problem involves large force gradients across the diffuse interface and is thus much harder to solve than the first rising bubble test case. As a matter of fact, the results produced by different numerical techniques in [88] are in no good agreement, particularly with regard to the second half of the computational time span. Moreover, it is not even clear whether break off is to occur. After all, according to experimental tests with three dimensional bubbles the shape is expected to be a blend between "skirted" and "dimpled ellipsoidal-cap". By analogy with the first test case, we analyze the benchmark quantities and the bubble shapes, however using now the simulation parameters of Table 4.7. We refer to Figure 4.12 for a depiction of the temporal evolution of the bubble shape at mesh refinement level 7. The initial circular shape is shown to gradually develop two filaments on its sides as it experiences an upward pushing force. The lower right image illustrates the final bubble shapes of three different "reference" groups. While the filaments computed with the diffuse interface method show a smooth and symmetric shape, those of the reference groups show less regularity. In fact, one of them even exhibits break off of the filaments and the formation of two satellite drops. In contrast to this, our results never showed break off at any tested mesh refinement level as demonstrated in Figure 4.13.

h	ξ	Δt	D
2^{-4}	0.040	0.008	0.000040
2^{-5}	0.020	0.004	0.000040
2^{-6}	0.010	0.002	0.000020
2^{-7}	0.005	0.001	0.000005

Table 4.7: Numerical parameters for the rising bubble test case 2.

It is, however, obvious that at higher mesh refinement levels the filaments tend to become thinner in their upper part which also imply narrower diffuse interfaces. Therefore, one may bring forward the argument that for $h \to 0$ and $\varepsilon \to 0$ with $\varepsilon \propto h$, the left and right boundaries of a filament at its narrowest region may come arbitrary close to each other, including the possibility to merge, that renders a break off inevitable.

The temporal evolution of the quantities V_b, Y_b and $\not{c}$ for different mesh refinement levels is depicted in Figure 4.14. In contrast to the reference rise velocity profile of the first rising bubble test case, we see two extrema roughly around times $t = 0.72$ and $t = 2.08$. The emergence of the second crest temporarily coincides with the development, elongation and the eventual shedding of the filaments. This in turn is believed to yield a more streamlined geometry which reduces the drag force and allows for a higher rise velocity. For our filaments are shown to never break off and to have an average thickness larger than those of the reference groups, the above described effect is expected to be less pronounced than in reference results. This is in fact reflected by the clear deviation of the phase field based rise velocity profiles around the second half of the simulation time span. Our profiles for the center of mass exhibit convergence and are in good correlation with the reference roughly until time $t = 2$. Following the arguments presented above, the missing or the rather smaller extra speed impulse results in a slightly shorter traveled distance. The sudden jump in the circularity profile of the reference happens around time $t = 2.4$ which happens to be nothing else but the break off moment. Therefore, it is reasonable to set this time instance as the upper bound when it comes to comparisons of the circularity profiles. Our approximations of the latter are shown to be converged and, except for a small deviation in the time interval $[1.6, 2.4]$, to

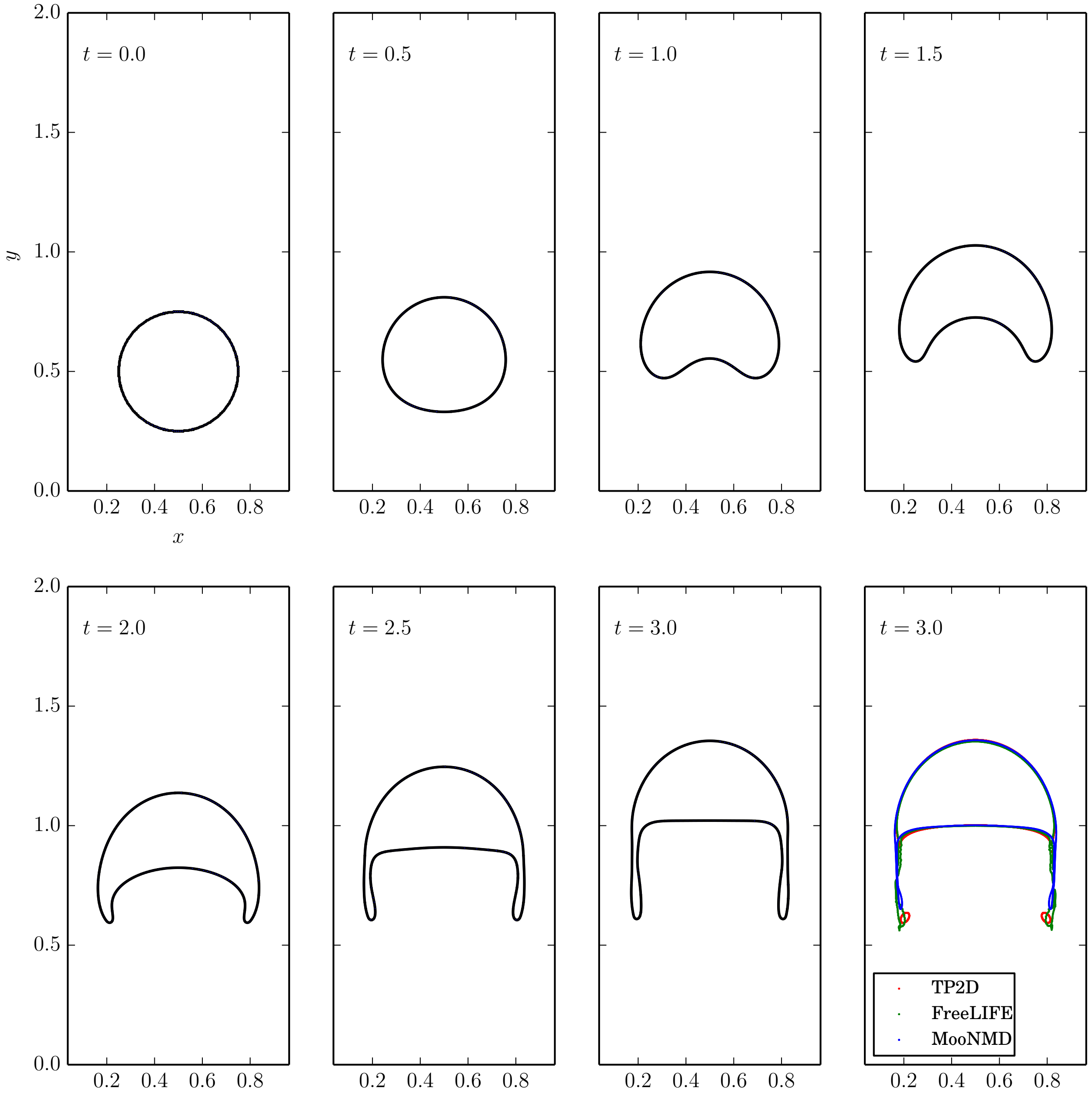

Figure 4.12: Shapes of the rising bubble at a set of time points for $h = 2^{-7}$.

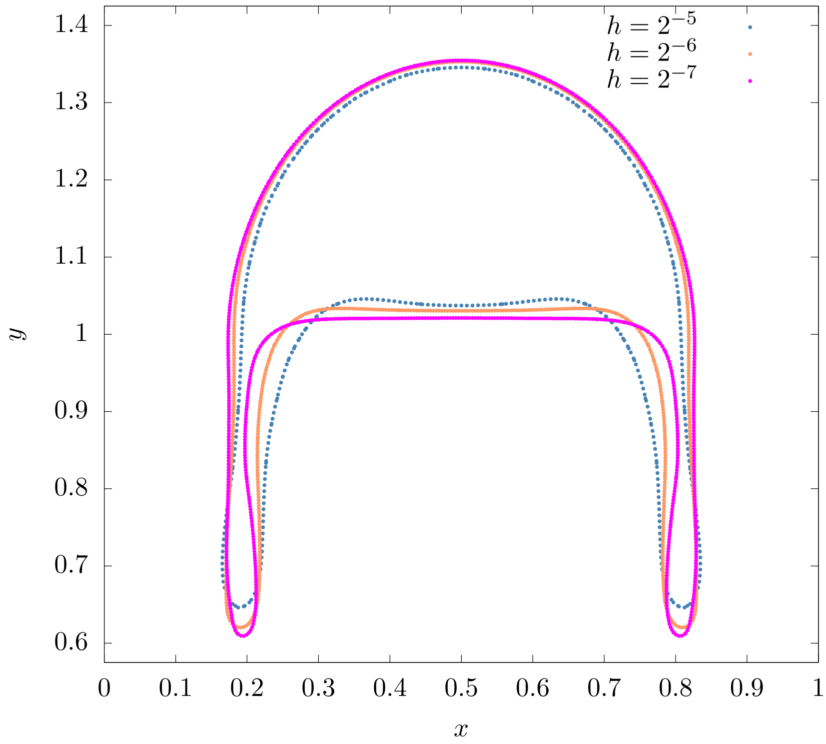

Figure 4.13: Shapes of the rising bubble at final time $t = 3$ for different h.

be in good consensus with the reference.

Again, for different mesh refinement levels, extrema of the benchmark quantities together with their incidence times are listed in Table 4.8. Due to the lack of an accepted reference, we have presented the "quasi"-reference results at our disposal to whom our results are compared. Bearing in mind that by virtue of the difficulties to solve this problem even the sharp interface-based quasi-reference results are in no satisfactory agreement, it would be presumptuous to expect the diffuse interface results to converge to one of these. Nevertheless, our approximations reflect the quasi-reference results and $\not{c}_{\text{min}}$ and $Y_b(t = 3)$ seem to converge to the figures of FreeLIFE.

h	ξ	Δt	$\not{c}_{\text{min}}$	$t\vert_{\not{c}=\not{c}_{\text{min}}}$	$V_{b,\text{max}}$	$t\vert_{V_b=V_{b,\text{max}}}$	$Y_b(t = 3)$
2^{-5}	0.020	0.004	0.5147	3	0.2520	0.6800	1.0952
2^{-6}	0.010	0.002	0.4952	3	0.2505	0.7680	1.1058
2^{-7}	0.005	0.001	0.4872	3	0.2498	0.7450	1.1137
TP2D			0.5869	2.4004	0.2524	0.7332	1.1380
FreeLIFE			0.4647	3	0.2514	0.7581	1.1249
MooNMD			0.5144	3	0.2502	0.7317	1.1376

Table 4.8: Minimum circularity and maximum rise velocity with corresponding incidence times and final position of the center of mass for test case 2.

Continuing the quantitative analysis, we present in Table 4.9 the relative error norms and the respective estimated convergence orders of the quantities center of mass, rise velocity and circularity. It's noteworthy to mention that for the computation of the l_1, l_2 and l_∞ errors and their convergence

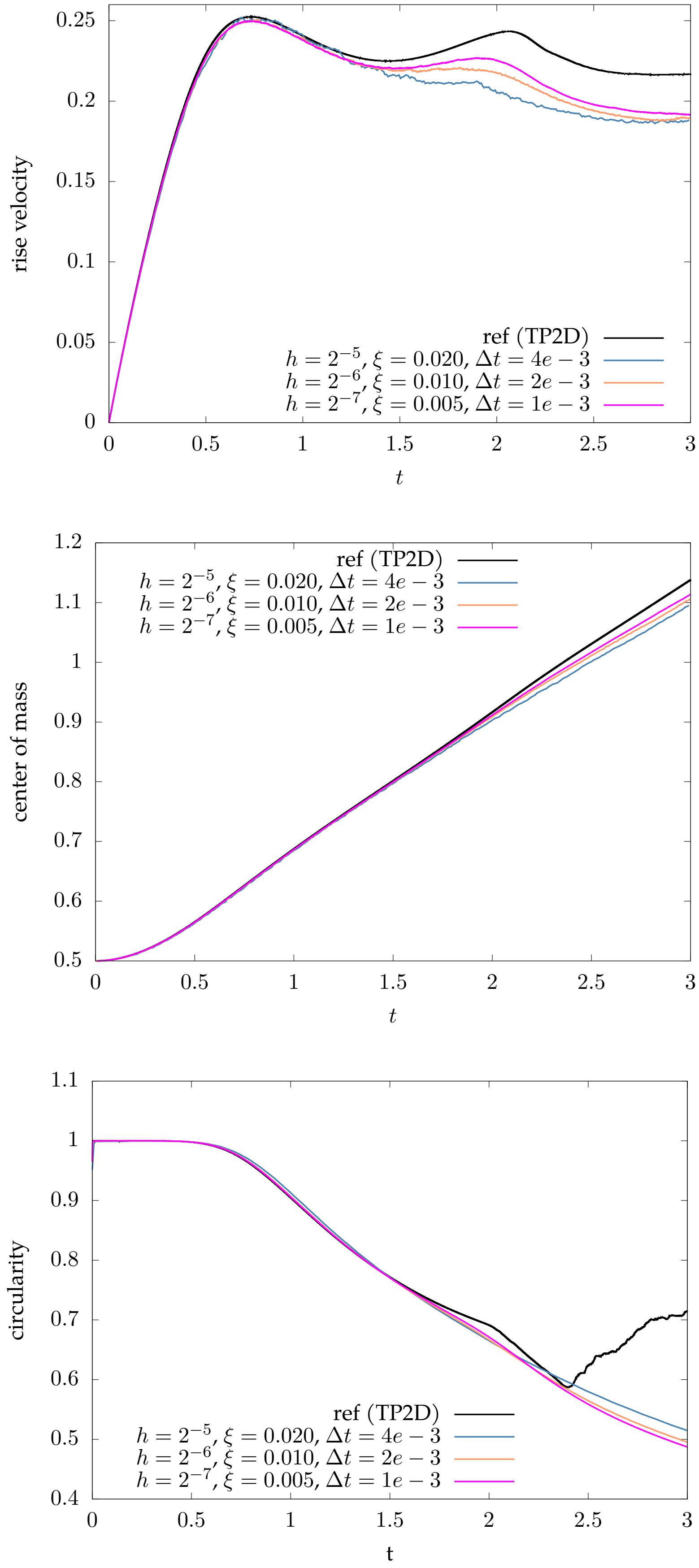

Figure 4.14: Rising bubble test case 2: Rise velocity, center of mass and circularity profiles.

q	h	ξ	$\|e\|_1$	EOC$_1$	$\|e\|_2$	EOC$_2$	$\|e\|_\infty$	EOC$_\infty$
Y_b	2^{-5}	0.020	0.0185		0.0208		0.0263	
	2^{-6}	0.010	0.0067	1.4620	0.0073	1.5072	0.0095	1.4755
	2^{-7}	0.005	0.0023	1.5358	0.0025	1.5600	0.0031	1.5947
V_b	2^{-5}	0.020	0.0458		0.0520		0.0775	
	2^{-6}	0.010	0.0185	1.3060	0.0201	1.3710	0.0321	1.2714
	2^{-7}	0.005	0.0063	1.5620	0.0068	1.5643	0.0121	1.4112
$\not{c}$	2^{-5}	0.020	0.0208		0.0277		0.0431	
	2^{-6}	0.010	0.0078	1.4147	0.0102	1.4478	0.0152	1.5051
	2^{-7}	0.005	0.0022	1.8389	0.0027	1.8880	0.0040	1.9111

Table 4.9: Relative error norms and estimated orders of convergence of the benchmark quantities for test case 2. Errors have been computed w.r.t. the TP2D sharp interface reference solution.

orders the considered time interval has been confined to $[0, 2]$, since for later times the reference solutions do not agree either. For all quantities the relative errors in all norms are shown to converge to 0 with a linear order of convergence. By analogy with the proceeding in the first rising bubble test case, we extend the study of the relative error convergence orders to the case where our solution on the finest mesh is taken as the exact value. This corresponds to the approach used in [88]. Measuring the errors with respect to this alternative reference, yields a considerable improvement and in fact shifts the convergence orders towards the quadratic region. (See Table 4.10.)

q	h	ξ	$\|e\|_1$	EOC$_1$	$\|e\|_2$	EOC$_2$	$\|e\|_\infty$	EOC$_\infty$
Y_b	2^{-4}	0.040	0.0158		0.0170		0.0206	
	2^{-5}	0.020	0.0039	2.0024	0.0045	1.9263	0.0068	1.6026
	2^{-6}	0.010	0.0007	2.5718	0.0008	2.5136	0.0015	2.2132
V_b	2^{-4}	0.040	0.0505		0.0549		0.0748	
	2^{-5}	0.020	0.0193	1.3883	0.0209	1.3969	0.0323	1.2100
	2^{-6}	0.010	0.0037	2.3780	0.0042	2.3116	0.0076	2.0974
$\not{c}$	2^{-4}	0.040	0.0261		0.0312		0.0428	
	2^{-5}	0.020	0.0090	1.5363	0.0107	1.5463	0.0198	1.1128
	2^{-6}	0.010	0.0018	2.3055	0.0022	2.2597	0.0063	1.6609

Table 4.10: Relative error norms and estimated convergence orders of the benchmark quantities for test case 2 assuming the finest grid solution as exact solution.

4.5.3 Rayleigh-Taylor instability

The Rayleigh-Taylor instability is a two-phase instability which occurs whenever two fluids of different density are accelerated against each other. Any perturbation along the interface between a heavy fluid (F_H) on top of a lighter fluid (F_L), both subject to a gravitational field, gives rise to the phenomenon of Rayleigh-Taylor instability. The initial perturbations progress from an initial linear growth phase into a nonlinear one, eventually developing “mushroom head” like structures moving upwards and thinning “spikes” falling downwards. Assuming negligible viscosity and surface tension, the instability is characterized by the density disparity, measured with the Atwood number $\mathcal{A} = (\rho_H - \rho_L)/(\rho_H + \rho_L)$. For the validation of our results, we will consider the works of Tryggvason [146] and Guermond et al. [70] as reference. The former investigated the initial growth and long-time evolution of the instability for incompressible and inviscid flows with zero surface tension at $\mathcal{A} = 0.5$. Guermond et al., on the other hand, studied this instability problem at the same Atwood number, however, taking viscous effects additionally into account.

The setup of the problem is described by a rectangular computational domain $[0, d] \times [0, 4d]$, where an initial wavy interface segregates a heavier fluid in the upper domain part from a lighter fluid on the lower part. The initial interface is described by the function

$$y(x) = 2d + 0.1d \cos(2\pi x/d)$$

representing a planar interface superimposed by a perturbation of wave number $k = 1$ and amplitude $0.1d$. Note that setting the surface tension coefficient σ to 0, effectively downgrades the Cahn-Hilliard equation (4.27) to a pure transport equation well known from the level-set context. This, in turn, implies to pass on both the physical benefits inherent to phase field models and to the automatic recreation of the smooth transition of the phase field in the interface region. In order to circumvent these issues, we chose to set the surface tension coefficient to the small, yet non-zero value 0.01. As for the remaining simulation parameters we set $d = 1, \rho_H = 3, \rho_L = 1, \mu_H = \mu_L = 0.0031316$ and $g = 9.80665$, giving rise to $\mathcal{A} = 0.5$ and $Re = \rho_H d^{3/2} g^{1/2}/\mu_H = 3000$. At the top and bottom boundaries we use the no-slip boundary condition, whereas the free slip boundary condition is imposed on the vertical walls. Figure 4.15 depicts our results for the temporal evolution of the interface computed in the time interval $[0, 1.5]$ with $\Delta t = 0.001, h = 2^{-7}, \varepsilon = 0.005$ and $D = 0.00004$. As anticipated, the heavier fluid on top starts to fall through the lighter fluid and gradually develops spikes which are subject to strong deformations. When it comes to the comparison of the vortex structure with the "inviscid" results of Tryggvason and the "viscous" results of Guermond et al., our viscous solution exhibits a satisfactory agreement with both, especially with the latter mentioned. Note that the data provided by the above references are computed with respect to individual scalings of the involved PDE variables in order to obtain nondimensional variables. Therefore, comparisons require the time scales of the respective simulations to be mapped to each other. Since, in contrast to the reference results, we did not perform any rescaling, our time t is mapped to Tryggvason's time $\tilde{t}$ via the relation $t = \sqrt{d/(\mathcal{A}\, g)}\, \tilde{t}$.

We continue the validation of our results with a quantitative analysis and conduct a comparison of the tip of the rising and falling fluids with the inviscid and viscous results provided by Tryggvason and Guermond et al., respectively. The results, depicted in Figure 4.16, correspond well with both references whose data have individually been translated along the y-axis to facilitate comparisons. The upper curve referring to the tip of the rising fluid shows a better correlation with the data provided by Tryggvason while our curve for the falling fluid seems to perfectly match the results of Guermond. The analysis is finally concluded with the examination of the interface structure at a randomly selected fixed time $t = 0.79031$ for three consecutive meshes of global mesh size $h = 2^{-5}$, 2^{-6}, 2^{-7} pointing to a refinement level index. As shown in Figure 4.17, the main difference between the figures is in the level of detail of the vortices. While there is only little roll-up in the coarse grid case, the vortices on the finest grid exhibit a tightly wound spiral. Besides, the y-coordinate of the tip of the rising and falling fluid slightly differ from one level to the other and are thus regarded as weakly resolution dependent. Apart from that no significant differences can be observed.

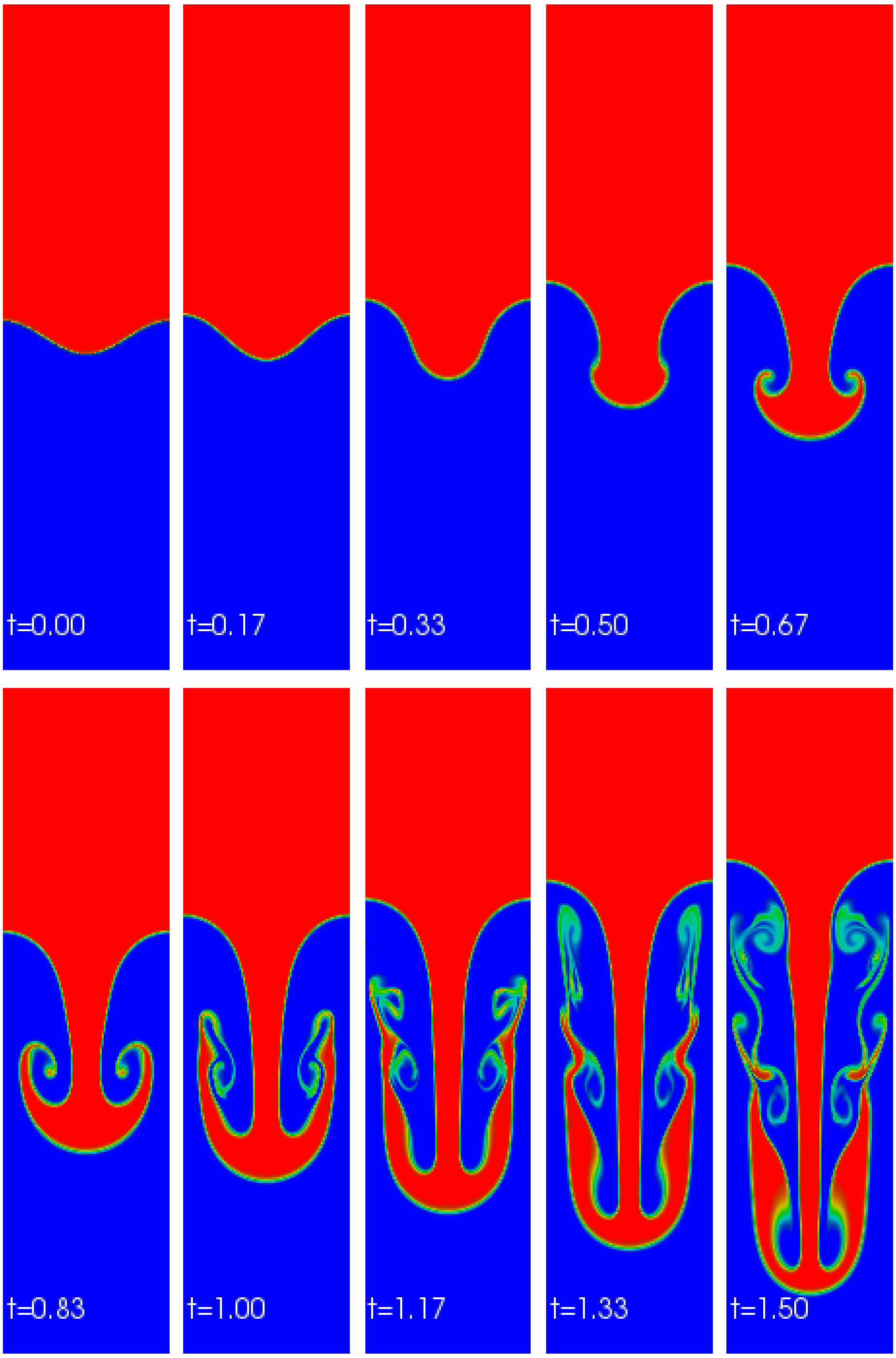

Figure 4.15: The evolution of a single wavelength initial condition in the Rayleigh-Taylor instability simulation.

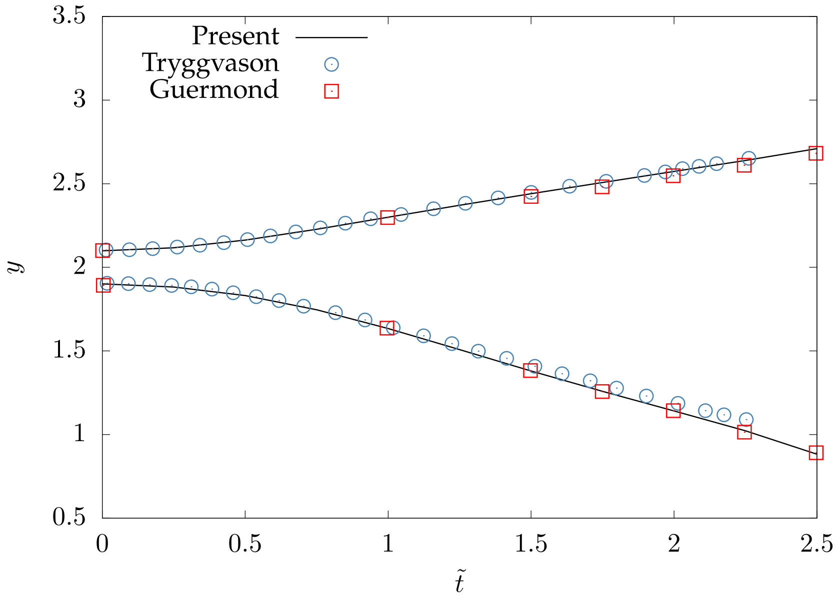

Figure 4.16: The y-coordinate of the tip of the rising and falling fluid versus time.

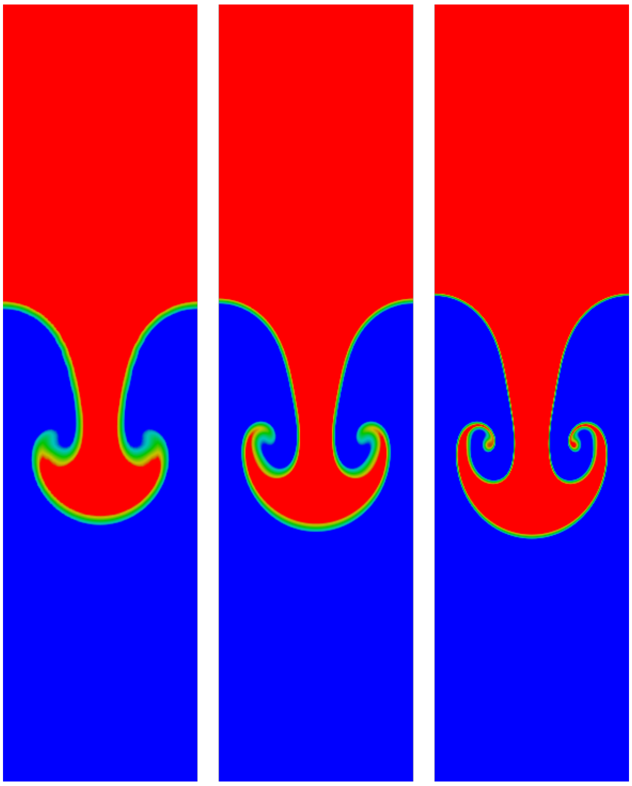

Figure 4.17: Rayleigh-Taylor instability simulation at time $t = 0.79031$ for three consecutive mesh refinement levels.

4.5.4 Sessile drop

We briefly demonstrate in this section the ability of the used NSCH model to impose the contact angle boundary condition (4.22). To this end we analyze the behavior of a sessile drop subject to the gravitational force. More specifically, we consider a small water drop with radius $r = 0.25\,\mathrm{cm}$ resting on a rigid solid's surface at the bottom of a rectangular domain $\Omega = (0, 1.5) \times (0, 0.5)\,\mathrm{cm}^2$ filled with air. We refer to Figure 4.18 for a sketch of this configuration. We adopt the densities of water ($998.21\,\mathrm{kg/m^3}$) and air ($1.2041\,\mathrm{kg/m^3}$) unaltered, however increase the dynamic viscosities of both fluids by factor 100 in order to reduce dynamic effects and to accelerate the computation of the equilibrium configuration. Therefore, we set $\mu_1 = 1.002 \times 10^{-1}\,\mathrm{Pa\,s}$ and $\mu_2 = 1.8208 \times 10^{-3}\,\mathrm{Pa\,s}$. Moreover, we set the surface tension to $\gamma = 0.073\,\mathrm{N/m}$, the diffuse interface width to [29] $\xi = 2h$, the mobility coefficient to $D = 10^{-7}\,\mathrm{m^2/s}$ and the gravitational acceleration to $g = 9.8\,\mathrm{m/s^2}$. We use a time step size of $\Delta t = 10^{-3}\,\mathrm{sec}$ and a uniform cell size NURBS-based computational mesh set up to initially have 3 cells in horizontal direction and 1 cell in the vertical direction - leading to cell size $h = dx = dy = w/3 \times 2^{-L}\,\mathrm{m}$ on mesh refinement level L.

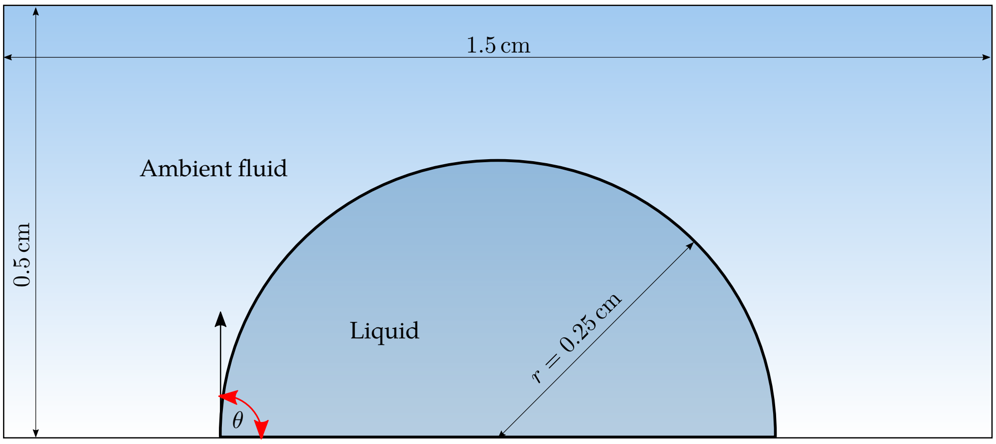

Figure 4.18: Sketch of the sessile drop with radius $r = 0.25\,\mathrm{cm}$ on a flat and rigid surface.

Given the initial contact angle $\theta = \pi/2$, we successively impose a series of different contact angles $\theta = 45°, 60°, 90°, 120°, 135°$ and compare the results with exact equilibrium solutions obtained from the solution of a set of ordinary differential equations as presented in [120]. Our equilibrium solutions of two-dimensional drops subject to the above mentioned contact angles are depicted in Figure 4.19 alongside analytical solutions and show excellent agreement with the latter. The ability to impose a contact angle will be an essential feature in our BFSI model presented in Chapter 6.

4.6 Summary and conclusions

In this chapter, we have presented our numerical results of the application of Galerkin-based Isogeometric Analysis to incompressible Navier-Stokes-Cahn-Hilliard equations in velocity-pressure-phase field-chemical potential formulation. In this formulation the fourth order Cahn-Hilliard

---

[29] In the sessile drop application we have linked the diffuse interface width ξ to the computational mesh cell size h. This leads for instance to $\xi = 2 \times 0.015/3 \times 2^{-\mathrm{L}}\,\mathrm{m} = 3.125 \times 10^{-4}\,\mathrm{m}$ on mesh refinement level L = 5.

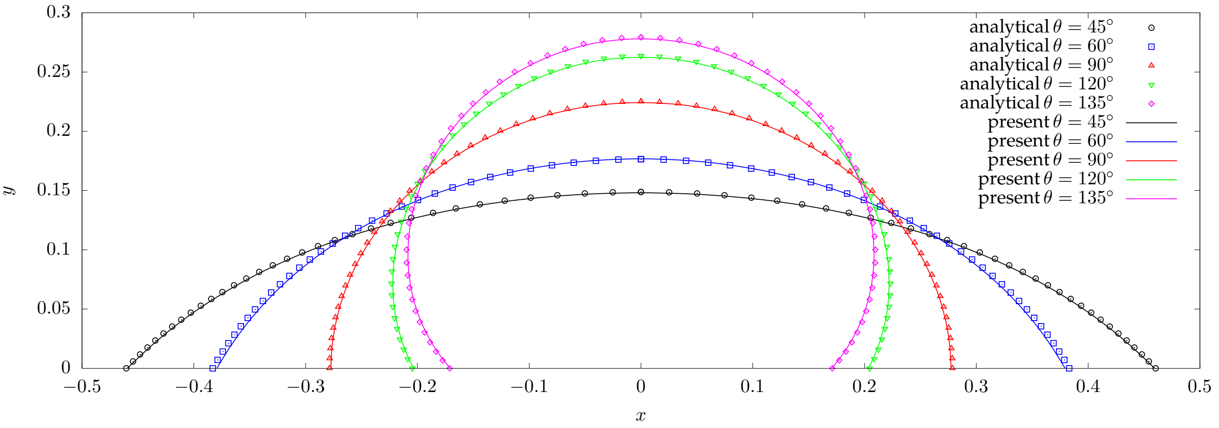

Figure 4.19: Sessile drops at different contact angles θ. Comparison of the numerical results with the analytical solution [120].

equation is split into two second order equations, effectively introducing the chemical potential η as a new variable. The reason we have preferred the splitted version over the original one is twofold: firstly depending on the way the surface tension force is modeled on top of the Navier-Stokes equations, the computation of the chemical potential may become a necessity and secondly we avoid complications with nonlinear boundary conditions arising from the discretization of the equation in its primal form. Nevertheless, Isogeometric Analysis easily allows to setup discrete approximation spaces with high continuity as for instance demonstrated in [81] for the case of one-phase flow.

The velocity and pressure functions were approximated with LBB stable non-uniform rational B-spline spaces which can be regarded as smooth generalizations of Taylor-Hood pairs of finite element space. The governing equations were discretized in time fully implicitly ($\theta >= 0.5$) with the one-step θ-scheme and finally solved blockwise, that is, solving the phase field system with the current velocity field and eventually using the phase field variables to solve the two-phase flow equations.

The static bubble, rising bubble and the Rayleigh-Taylor instability flow scenarios were considered in two dimensions as model problems in order to investigate the numerical traits and behavior of the Isogeometric discretization.

Starting off with the static bubble scenario, we have shown that the approximated velocity field is perturbed by spurious currents of order 10^{-4} down to 10^{-5} and the pressure jump across the interface behaves according to theoretical predictions. Moreover, the velocity and pressure fields were shown to be very well comparable with reference sharp interface model results, as for instance [150].

In addition to the static bubble, we extended the application of Galerkin-based Isogeometric Analysis to the prominent rising bubble benchmarks, as proposed in [59, 88], and analyzed the approximated benchmark quantities such as the bubble's rise velocity, center of mass and circularity with respect to accuracy and convergence. For the first rising bubble benchmark characterized by a relatively moderate density ratio, our results were shown to integrate very well with the reference data. In fact, with increased mesh refining the time profiles of the mentioned quantities exposed rapid convergence to the reference and were visually indistinguishable from it on the highest mesh refinement level. We extended the analysis to the inspection of the effect of different diffuse interface widths on a fixed mesh refinement level. The study, expectedly, rendered the accuracy to be sensitive to the ratio of the diffuse interface width and the mesh refinement level and to profit from reasonable settings. Moreover, the analysis was extended to inspect the convergence orders of l_1, l_2 and l_∞ relative errors of additional benchmark quantities, whereby the errors were computed with respect to both the reference results and our own results obtained on the mesh with the highest resolution. Referring to these two cases, the errors showed linear and quadratic convergence, respectively.

The second and more challenging rising bubble benchmark involves a large density ratio and a low surface tension which in turn implies large gradients of quantities such as e.g. pressure and severe shape deformations up to topological changes in the limit case. We point out that due to the difficulties to solve this problem, since at least the second half of the simulation time interval, the available references are in no good correspondence with each other. So are our approximations with regard to these references and it is in fact not even clear weather the elongated bubble filaments are to break off or not. The same analysis as in the first rising bubble test case was performed for the second test case as well with very similar results.

In order to demonstrate the robustness of the method, we included the Rayleigh-Taylor instability problem having become a popular test case for numerical methods intended to study multiphase or multimaterial problems. Using the setup and reference results of Tryggvason [146] and Guermond et al. [70], we analyzed the evolution of a single wavelength interface perturbation. Qualitative comparisons of the interface shapes and quantitative analysis of the positions of the tip of the rising and falling fluid rendered our approximations to be in good correlation with the above references. Moreover, we showed our results to be mesh converged, since the produced data associated to different mesh resolutions are well comparable except for the high resolution features such as the roll-up spirals emerging at higher mesh refinement levels.

The efficient solution of the arising linear equation systems with iterative techniques such as, for instance, multigrid were out of the scope of this study and will therefore be addressed in a forthcoming publication.

Isogeometric Analysis proved for us to be a robust and powerful technology showcasing well applicability to multiphase flow problems. Bearing in mind that, in contrast to the simple geometries involved in the considered benchmarks, simulations of real world multiphase flow problems need to cope with very complex geometries, the combination of Isogeometric Analysis and phase field based multiphase flow models may be a very good alternative to sharp interface models involving straight line segment approximation of curved domain boundaries. This is motivated by the fact that computations on exact geometries avoid any modification of the original computational domain and proved in a row of different contexts to be beneficial accuracy wise [37]. Moreover, Isogeometric Analysis is best suited for the numerical approximation of the fourth order Cahn-Hilliard equations in their primal formulation requiring a discrete approximation space with $\mathcal{C}^1$ regularity. The Cahn-Hilliard phase field model is equipped with the benefits to minimize interface energy, to be mass conservative and to avoid typical hassles involved with level-set methods such as for instance redistancing.

Chapter 5

Monolithic ALE Fluid-Structure Interaction

5.1 Introduction

In Chapters 3 and 4 we have successfully applied Isogeometric Analysis to solve "single-phase" and two-phase flow problems. In this chapter we extend the multiphysics nature of this work and additionally deal with Fluid-Structure Interaction[1] (FSI) problems which come along with a significantly increased complexity due to a mutual dependence between the fluid and solid (structural mechanics) parts of the continuum. At the fluid-solid contact interface, the solid experiences forces that are exerted by the fluid – forces that can significantly affect the solid's motion and deformation. The deformed solid and its motion in turn imply a modified fluid flow domain with obvious repercussions on the fluid's velocity and pressure and therefore on its stress. This completes the dependency cycle.

FSI problems are omnipresent in nature – just to name a few scenarios, we refer to the inflation of a balloon, the motion of a tree subject to wind, the fluttering of aircraft wings, the interaction of blood and heart valves in the heart, and wind induced deflection of wind-turbine blades. The aspect of omnipresency in nature and the desire to perform simulations "as realistic as it gets", render FSI a very relevant, attractive and active field of research.

As far as analytical methods are concerned, their application to non-toy fluid flow and structure deformation problems is already quite limited, let alone FSI problems. This is due to the time-dependent and inherently nonlinear nature of FSI. That being said, in recent decades a significant amount of attention has been put to the development of *computational* FSI methods with focus on robustness, efficiency and applicability to geometrically complex domains in 3D. As described more explicit in Section 5.3, there exist different solutions algorithms, each coming along with its own traits in terms on robustness, complexity and applicability. We have chosen to work with the very robust and widely applicable ALE monolithic approach that comes at the cost of a high implementation complexity. Besides, we apply Isogeometric Analysis for the discretization of the partial differential equations in space (see Section 5.3).

The rest of this chapter is organized as follows: In Section 5.2 we discuss the structural mechanics part of the FSI problem. The fluid dynamics part and the core part of the FSI discussion is in Section 5.3.

5.2 Structural mechanics problem

The theory of *Elasticity* deals with deformations and their description in elastic and continuous media. It builds – together with the theory of linear-viscous fluids – the basis for the classical material theory which in turn builds the foundation for theories of plasticity and viscoplasticity. Elasticity is the property of a body to change its shape under the influence of a force and to return to its original shape upon removal of that force. Throughout this work we restrict ourselves to homogeneous isotropic materials, that is, materials whose stress response function (to be introduced later) is both independent of a particular material point[30] $\boldsymbol{X} \in \Omega_{\boldsymbol{X}}$ and "the same in all directions". Moreover, we consider only "purely" elastic materials and therefore exclude thermoelasticity (inclusion of thermal effects), viscoelasticity (inclusion of time-dependent elastic behavior) and elastoplasticity (beyond a load threshold, elastic deformations are accompanied with plastic (irreversible) deformations). Finally, the creation of fractures and self penetration are also beyond the scope of this work and not covered here.

The point of departure for structural mechanics formulations are the *equations of equilibrium* and *the principle of virtual work in the deformed configuration*. Recalling Theorem 2.3.1, the axioms of force and moment balance imply that the Cauchy stress tensor field $\boldsymbol{\sigma}\colon \bar{\Omega} \to \mathbb{S}^3$ satisfies the following boundary value problem

$$\begin{aligned} -\nabla \cdot \boldsymbol{\sigma}(\boldsymbol{x}) &= \boldsymbol{f}(\boldsymbol{x}) && \forall \boldsymbol{x} \in \Omega, \\ \boldsymbol{\sigma}(\boldsymbol{x}) &= \boldsymbol{\sigma}(\boldsymbol{x})^T && \forall \boldsymbol{x} \in \Omega, \\ \boldsymbol{\sigma}(\boldsymbol{x})\, \boldsymbol{n} &= \boldsymbol{g}(\boldsymbol{x}) && \forall \boldsymbol{x} \in \Gamma_1, \end{aligned} \tag{5.1}$$

over the deformed configuration Ω, where $\Gamma_{0,\boldsymbol{x}} \equiv \Gamma_{D,\boldsymbol{x}}$ and $\Gamma_1 \equiv \Gamma_{N,\boldsymbol{x}}$ represent the Dirichlet and Neumann parts of its boundary $\Gamma = \partial\Omega$, respectively. The above equations are known as the equations of equilibrium in the deformed configuration. Throughout this work, the body force $\boldsymbol{f}$ and surface force $\boldsymbol{g}$ are for simplicity assumed to be dead loads, that is, loads that do not depend on the deformation $\boldsymbol{\varphi}$. Given smooth enough[31] vector fields $\boldsymbol{\theta}\colon \Omega \to \mathbb{R}^3$ that satisfy $\boldsymbol{\theta} = \boldsymbol{0}$ on $\Gamma_{0,\boldsymbol{x}} := \Gamma - \Gamma_1$, the above boundary value problem is formally equivalent to the following variational formulation

$$\int_{\Omega} \boldsymbol{\sigma} : \nabla\boldsymbol{\theta} \,\mathrm{d}\Omega = \int_{\Omega} \boldsymbol{f} \cdot \boldsymbol{\theta} \,\mathrm{d}\Omega + \int_{\Gamma_1} \boldsymbol{g} \cdot \boldsymbol{\theta} \,\mathrm{d}\Gamma_1 \tag{5.2}$$

which is also known as the principle of virtual work in the deformed configuration. A proof of this statement can be found in [33].

Note that the equations of equilibrium in the deformed configuration (5.1) are expressed in terms of the Euler variable $\boldsymbol{x} = \boldsymbol{\varphi}(\boldsymbol{X})$, being one of the unknowns. We recapitulate the problem we want to actually solve: Given an unstressed initial configuration of a body, which deformation $\boldsymbol{\varphi}$ does it undergo as we expose it to body and surface forces? Moreover, which stresses $\boldsymbol{\sigma}(\boldsymbol{x})$ arise in the material under these loads? In the spirit of this view, equations (5.1) may alternatively be rewritten in terms of the Lagrange variable $\boldsymbol{X}$ which is associated with the reference configuration and is in a sense already at hand. To this end we transform the ingredients of equation (5.1) to the reference configuration. Starting with the applied body force density $\boldsymbol{f}\colon \Omega \to \mathbb{R}^3$ per unit volume in the deformed configuration, we associate it with a vector field $\boldsymbol{f}_0\colon \Omega_{\boldsymbol{X}} \to \mathbb{R}^3$, such that it holds

$$\boldsymbol{f}_0(\boldsymbol{X}) \,\mathrm{d}V = \boldsymbol{f}(\boldsymbol{x}) \,\mathrm{d}v \quad \forall \boldsymbol{x} = \boldsymbol{\varphi}(\boldsymbol{X}) \in \Omega. \tag{5.3}$$

---

[30] Note that the domain symbols $\Omega_{\boldsymbol{X}}, \Omega_{\boldsymbol{X}}, \Omega_{\boldsymbol{x}}$ were already introduced in section 2.1 and therefore not repeated again.

[31] We use the phrase "smooth enough" to conveniently refer to a context, where in a given definition, theorem, proof, etc., the smoothness of the deformations involved is such that all arguments make sense.

Further, using relation (2.12), i.e., $\mathrm{d}v = \det \nabla_{\boldsymbol{X}} \boldsymbol{\varphi}(\boldsymbol{X})\, \mathrm{d}V = J\mathrm{d}V$, the above equation reduces to

$$\boldsymbol{f}_0(\boldsymbol{X}) = \det \nabla_{\boldsymbol{X}} \boldsymbol{\varphi}(\boldsymbol{X}) \boldsymbol{f}(\boldsymbol{x}) \quad \boldsymbol{x} = \boldsymbol{\varphi}(\boldsymbol{X}). \tag{5.4}$$

The vector field $\boldsymbol{f}_0$ measures the density of the applied body force per unit volume in the reference configuration.

Similar to the body force case, we associate the density of the applied surface force per unit area in the deformed configuration $\boldsymbol{g}\colon \Gamma_1 \to \mathbb{R}^3$ with a vector field $\boldsymbol{g}_0\colon \Gamma_{1,\boldsymbol{X}} \to \mathbb{R}^3$, such that it holds

$$\boldsymbol{g}_0(\boldsymbol{X})\, \mathrm{d}A = \boldsymbol{g}(\boldsymbol{x})\, \mathrm{d}a \quad \forall \boldsymbol{x} = \boldsymbol{\varphi}(\boldsymbol{X}) \in \Gamma_1. \tag{5.5}$$

Then from (2.15) or (2.34) it follows

$$\boldsymbol{g}_0(\boldsymbol{X}) = \det \nabla_{\boldsymbol{X}} \boldsymbol{\varphi}(\boldsymbol{X}) \left\| \nabla_{\boldsymbol{X}} \boldsymbol{\varphi}(\boldsymbol{X})^{-T} \boldsymbol{n}_0 \right\| \boldsymbol{g}(\boldsymbol{x}) = J \left\| \boldsymbol{F}^{-T} \boldsymbol{n}_0 \right\| \boldsymbol{g}(\boldsymbol{x}). \tag{5.6}$$

The vector field $\boldsymbol{g}_0$ measures the density of the applied surface force per unit area in the reference configuration.

With the above transformations of the body and surface forces and the usage of the first Piola-Kirchhoff stress tensor $\boldsymbol{P}(\boldsymbol{X}) = (\det \nabla_{\boldsymbol{X}} \boldsymbol{\varphi}(\boldsymbol{X}))\, \boldsymbol{\sigma}(\boldsymbol{x}) \nabla_{\boldsymbol{X}} \boldsymbol{\varphi}(\boldsymbol{X})^{-T}$ (cf. (2.35)), we obtain the equilibrium equations in the reference configuration[32]

$$\begin{aligned} -\nabla_{\boldsymbol{X}} \cdot \boldsymbol{P}(\boldsymbol{X}) &= \boldsymbol{f}_0(\boldsymbol{X}) && \forall \boldsymbol{X} \in \Omega_{\boldsymbol{X}}, \\ \boldsymbol{P}(\boldsymbol{X}) \nabla_{\boldsymbol{X}} \boldsymbol{\varphi}(\boldsymbol{X})^T &= \nabla_{\boldsymbol{X}} \boldsymbol{\varphi}(\boldsymbol{X}) \boldsymbol{P}(\boldsymbol{X})^T && \forall \boldsymbol{X} \in \Omega_{\boldsymbol{X}}, \\ \boldsymbol{P}(\boldsymbol{X})\, \boldsymbol{n}_0 &= \boldsymbol{g}_0(\boldsymbol{X}) && \forall \boldsymbol{X} \in \Gamma_{1,\boldsymbol{X}}, \end{aligned} \tag{5.7}$$

whose first and third equations are together equivalent to the following variational equation

$$\int_{\Omega_{\boldsymbol{X}}} \boldsymbol{P} : \nabla_{\boldsymbol{X}} \boldsymbol{\theta}_0 \, \mathrm{d}\Omega_{\boldsymbol{X}} = \int_{\Omega_{\boldsymbol{X}}} \boldsymbol{f}_0 \cdot \boldsymbol{\theta}_0 \, \mathrm{d}\Omega_{\boldsymbol{X}} + \int_{\Gamma_{1,\boldsymbol{X}}} \boldsymbol{g}_0 \cdot \boldsymbol{\theta}_0 \, \mathrm{d}\Gamma_{1,\boldsymbol{X}} \tag{5.8}$$

valid for all smooth enough vector fields $\boldsymbol{\theta}_0\colon \bar{\Omega}_{\boldsymbol{X}} \to \mathbb{R}^3$ that satisfy $\boldsymbol{\theta}_0 = \boldsymbol{0}$ on $\Gamma_{0,\boldsymbol{X}} := \Gamma_{\boldsymbol{X}} - \Gamma_{1,\boldsymbol{X}}$. For a corresponding proof, we refer to [33].

The definition of the second Piola-Kirchhoff stress tensor $\boldsymbol{S}(\boldsymbol{X}) = \boldsymbol{F}^{-1}\boldsymbol{P} = \nabla_{\boldsymbol{X}} \boldsymbol{\varphi}(\boldsymbol{X})^{-1} \boldsymbol{P}$ (cf. (2.40)), allows us to replace $\boldsymbol{P}$ with $\boldsymbol{F}\boldsymbol{S} = \nabla_{\boldsymbol{X}} \boldsymbol{\varphi}(\boldsymbol{X}) \boldsymbol{S}$, such that the equations of equilibrium in the reference configuration may now be expressed w.r.t. the symmetric tensor $\boldsymbol{S}$:

$$\begin{aligned} -\nabla_{\boldsymbol{X}} \cdot (\nabla_{\boldsymbol{X}} \boldsymbol{\varphi}(\boldsymbol{X}) \boldsymbol{S}(\boldsymbol{X})) &= \boldsymbol{f}_0(\boldsymbol{X}) && \forall \boldsymbol{X} \in \Omega_{\boldsymbol{X}}, \\ \boldsymbol{S}(\boldsymbol{X}) &= \boldsymbol{S}(\boldsymbol{X})^T && \forall \boldsymbol{X} \in \Omega_{\boldsymbol{X}}, \\ \nabla_{\boldsymbol{X}} \boldsymbol{\varphi}(\boldsymbol{X}) \boldsymbol{S}(\boldsymbol{X})\, \boldsymbol{n}_0 &= \boldsymbol{g}_0(\boldsymbol{X}) && \forall \boldsymbol{X} \in \Gamma_{1,\boldsymbol{X}}. \end{aligned} \tag{5.9}$$

Again, the first and third equations of (5.9) are together equivalent to the following variational equation

$$\int_{\Omega_{\boldsymbol{X}}} \nabla_{\boldsymbol{X}} \boldsymbol{\varphi}(\boldsymbol{X}) \boldsymbol{S} : \nabla_{\boldsymbol{X}} \boldsymbol{\theta}_0 \, \mathrm{d}\Omega_{\boldsymbol{X}} = \int_{\Omega_{\boldsymbol{X}}} \boldsymbol{f}_0 \cdot \boldsymbol{\theta}_0 \, \mathrm{d}\Omega_{\boldsymbol{X}} + \int_{\Gamma_{1,\boldsymbol{X}}} \boldsymbol{g}_0 \cdot \boldsymbol{\theta}_0 \, \mathrm{d}\Gamma_{1,\boldsymbol{X}}, \tag{5.10}$$

which describes the *principle of virtual work in the reference configuration* and is valid for all smooth enough vector fields $\boldsymbol{\theta}_0\colon \bar{\Omega}_{\boldsymbol{X}} \to \mathbb{R}^3$ that vanish on $\Gamma_{0,\boldsymbol{X}}$.

---

[32] The equations of equilibrium are considered together with Dirichlet boundary conditions.

The three equations of equilibrium over the reference configuration are valid regardless of the particular material under consideration (gas, liquid, solid) is made of. As is, these equations are by no means tied to a specific macroscopic continuum and therefore pose an abstract set of axioms at this stage. The equation system is in particular undetermined as we collocate nine unknowns, namely the three components of the deformation $\boldsymbol{\varphi}$ and the six[33] components of the first Piola-Kirchhoff stress tensor $\boldsymbol{P}$, with only three equations to determine these. The six missing equations are eventually deduced from assumptions concerning the nature of the constituting material under consideration and are therefore referred to as the constitutive equations. For given applied forces, the resulting deformations from a given reference configuration and the resulting internal stresses obviously differ if the body is made of rubber or steel. The constitutive equations are expected to determine the stress in such a way that does justice to the nature of the material. To give an example, in the simplest case, stress could be linearly dependent on strain. Besides, depending on the nature of the deformation problem to be solved, a strain measure may be used which is a simple linear function of displacement. These simplifications of the more general nonlinear theory of elasticity expressed by "exclusively linear relations" are for instance used in the context of *linearized elasticity* which is suitable for infinitesimal strains or "small" deformations only. However, the stress-strain relation may just as well be nonlinear and the problem may require strain measures which are nonlinear in displacement. In the sequel, we will characterize elastic and hyperelastic materials and present the governing equations obtained from the usage of these models in the context of the equilibrium equations.

5.2.1 Elastic materials

An elastic body exhibits the following macroscopic traits:

1. An initially unstressed body – subject to an arbitrary deformation by virtue of applied forces – returns to its original state upon removal of these forces.
2. The material response is independent of the deformation speed, i.e., the rate at which a deformation takes place has no influence on the resistance the body exerts to oppose the deformation.
3. For a given deformation, the reaction forces always have the same value regardless of the history.
4. In a uniaxial tensile test, loading and unloading always take place along the same path in the load-displacement diagram.

The following characterization of an elastic material in terms of the Cauchy stress tensor $\boldsymbol{\sigma}(\boldsymbol{x})$ is taken from [33]. A material is *elastic* if there exists a mapping

$$\hat{\boldsymbol{\sigma}}^D \colon (\boldsymbol{X}, \boldsymbol{F}) \in \bar{\Omega}_{\boldsymbol{X}} \times \mathbb{M}^3_+ \to \hat{\boldsymbol{\sigma}}^D(\boldsymbol{X}, \boldsymbol{F}) \in \mathbb{S}^3, \tag{5.11}$$

called the *response function of the Cauchy stress*, such that in any deformed[34] configuration that a body made of this material occupies, the Cauchy stress tensor $\boldsymbol{\sigma}(\boldsymbol{x})$ at any point $\boldsymbol{x} = \boldsymbol{\varphi}(\boldsymbol{X})$ of the

---

[33] The symmetry of the Cauchy stress tensor is taken into account.

[34] The superscript "D" of the response function $\hat{\boldsymbol{\sigma}}^D$ is used to emphasize that is used for the computation of a quantity in the deformed configuration.

deformed configuration is related to the deformation gradient $\boldsymbol{F} = \nabla_{\boldsymbol{X}}\boldsymbol{\varphi}(\boldsymbol{X})$ at the corresponding point $\boldsymbol{X}$ of the reference configuration by the equation

$$\boldsymbol{\sigma}(\boldsymbol{x}) = \hat{\boldsymbol{\sigma}}^D(\boldsymbol{X}, \nabla_{\boldsymbol{X}}\boldsymbol{\varphi}(\boldsymbol{X})), \quad \boldsymbol{x} = \boldsymbol{\varphi}(\boldsymbol{X}).$$

This relation is called the *constitutive equation* of the material. The quintessence of the presented characterization is the statement that in an elastic material the Cauchy stress is given by a stress response function, and this function solely depends on $\boldsymbol{X}$ and the deformation gradient $\nabla_{\boldsymbol{X}}\boldsymbol{\varphi}(\boldsymbol{X})$. In the characterization of the response functions we make use of the following definitions:

- $\mathbb{M}^n$: Set of all real square matrices of order n.
- $\mathbb{M}^n_+ = \{\boldsymbol{A} \in \mathbb{M}^n; \det \boldsymbol{A} > 0\}$.
- $\mathbb{O}^n = \{\boldsymbol{A} \in \mathbb{M}^n; \boldsymbol{A}\boldsymbol{A}^T = \boldsymbol{A}^T\boldsymbol{A} = \boldsymbol{I}\}$: Set of all orthogonal matrices of order n.
- $\mathbb{O}^n_+ = \{\boldsymbol{A} \in \mathbb{O}^n; \det \boldsymbol{A} = 1\}$: Set of all rotations in $\mathbb{R}^n$.
- $\mathbb{S}^n = \{\boldsymbol{A} \in \mathbb{M}^n; \boldsymbol{A} = \boldsymbol{A}^T\}$: Set of all symmetric matrices of order n.
- $\mathbb{S}^n_>$: Set of all symmetric positive definite matrices of order n.

As for an alternative characterization with respect to the first Piola-Kirchhoff tensor $\boldsymbol{P}(\boldsymbol{X}) = \boldsymbol{\sigma}(\boldsymbol{x})\, \mathbf{Cof}\, \nabla_{\boldsymbol{X}}\boldsymbol{\varphi}(\boldsymbol{X})$ and the second Piola-Kirchhoff tensor $\boldsymbol{S}(\boldsymbol{X}) = \nabla_{\boldsymbol{X}}\boldsymbol{\varphi}(\boldsymbol{X})^{-1}\boldsymbol{P}(\boldsymbol{X})$, let the mappings

$$\begin{aligned} \hat{\boldsymbol{P}}&\colon \bar{\Omega}_{\boldsymbol{X}} \times \mathbb{M}^3_+ \to \mathbb{M}^3, \text{ given by } & \hat{\boldsymbol{P}}(\boldsymbol{X}, \boldsymbol{F}) &= (\det \boldsymbol{F})\, \hat{\boldsymbol{\sigma}}^D(\boldsymbol{X}, \boldsymbol{F})\boldsymbol{F}^{-T}, \text{ and} \\ \hat{\boldsymbol{S}}&\colon \bar{\Omega}_{\boldsymbol{X}} \times \mathbb{M}^3_+ \to \mathbb{S}^3, \text{ given by } & \hat{\boldsymbol{S}}(\boldsymbol{X}, \boldsymbol{F}) &= (\det \boldsymbol{F})\, \boldsymbol{F}^{-1}\hat{\boldsymbol{\sigma}}^D(\boldsymbol{X}, \boldsymbol{F})\boldsymbol{F}^{-T}, \end{aligned}$$

denote elastic material characterizing *response functions for the first and second Piola-Kirchhoff stresses*, respectively. Then, a material is elastic if $\boldsymbol{P}(\boldsymbol{X})$ and $\boldsymbol{S}(\boldsymbol{X})$ are obtained from the respective response functions $\hat{\boldsymbol{P}}(\boldsymbol{X}, \boldsymbol{F})$ and $\hat{\boldsymbol{S}}(\boldsymbol{X}, \boldsymbol{F})$ (expressed solely in terms of $\boldsymbol{X}$ and $\nabla_{\boldsymbol{X}}\boldsymbol{\varphi}(\boldsymbol{X})$) in the context of *constitutive equations*:

$$\boldsymbol{P}(\boldsymbol{X}) = \hat{\boldsymbol{P}}(\boldsymbol{X}, \nabla_{\boldsymbol{X}}\boldsymbol{\varphi}(\boldsymbol{X})), \text{ and } \boldsymbol{S}(\boldsymbol{X}) = \hat{\boldsymbol{S}}(\boldsymbol{X}, \nabla_{\boldsymbol{X}}\boldsymbol{\varphi}(\boldsymbol{X})) \quad \forall \boldsymbol{X} \in \bar{\Omega}_{\boldsymbol{X}}. \tag{5.12}$$

As alluded in Section 5.2, a material in the reference configuration $\Omega_{\boldsymbol{X}}$ is called *homogeneous* if its response function is independent of the particular point $\boldsymbol{X} \in \bar{\Omega}_{\boldsymbol{X}}$ considered. In this case, the corresponding constitutive equation of (homogeneous) elastic material takes a simpler form

$$\boldsymbol{\sigma}(\boldsymbol{x}) = \hat{\boldsymbol{\sigma}}^D(\nabla_{\boldsymbol{X}}\boldsymbol{\varphi}(\boldsymbol{X})) \quad \forall \boldsymbol{x} = \boldsymbol{\varphi}(\boldsymbol{X}) \in \bar{\Omega}_{\boldsymbol{x}}.$$

Further restrictions on the possible constitutive relationships that describe material behavior (e.g. the constitutive relationship between the stresses and deformation), and therefore on stress response functions are imposed by the axiom of *material frame-indifference* (also known as *the axiom of invariance under a change of observer*, or the *axiom of objectivity*). The axiom requires that any so-called "observable quantity" (a quantity with an intrinsic character) that is computed through a constitutive equation must be independent of the particular basis in which it is computed. An example for a scalar quantity with an intrinsic character - or to put it differently - for a frame-indifferent scalar quantity is the distance between two material points, as two different observers measure the same value. Likewise, the vector connecting two material points is a frame-indifferent vector quantity. On the other hand, the speed of a material point is observer-dependent as different observers move in general relative to each other. Moreover, a material point's position and velocity vectors are observer-dependent as well, as they are expressed with regard to the underlying coordinate systems of the respective frames. In the present context, that is, the context of elastic materials, the "observable" quantity computed through the constitutive response of a material is the Cauchy stress vector. To clarify the idea, we consider a body in the current configuration and pick a stress vector at an arbitrary point of an arbitrary cut plane through the body. This stress vector being the answer of the elastic body to an applied load is required to be invariant with respect to a change of observer. Since an observer (a.k.a. frame) is basically a rigid body with a clock and in classical mechanics we may take the times of two different observers to be the same, instead of changing the frame we may just as well keep the basis fixed and apply a corresponding rigid body transformation[35] to the deformed body in the current configuration. The axiom - formalized in the following - basically says that when a deformed configuration is rotated around the origin, the Cauchy stress vector is transformed with the same rotation.

Axiom 5.2.1 (Material frame-indifference). *Let φ be a mapping from the reference to a deformed domain as presented in (2.1) and let $\bar{\Omega}^{\varphi}$ denote the deformed configuration. Moreover, let $\bar{\Omega}^{\psi}$ be another deformed configuration that is obtained from the application of a rotation to $\bar{\Omega}^{\varphi}$, that is, $\boldsymbol{\psi} = \boldsymbol{Q}\boldsymbol{\varphi}, \boldsymbol{Q} \in \mathbb{O}^3_+$. Then it holds*

$$\boldsymbol{t}^{\psi}(\boldsymbol{x}^{\psi}, \boldsymbol{Q}\boldsymbol{n}) = \boldsymbol{Q}\boldsymbol{t}^{\varphi}(\boldsymbol{x}^{\varphi}, \boldsymbol{n}) \quad \forall \boldsymbol{X} \in \Omega_{\boldsymbol{X}}, \boldsymbol{n} \in \boldsymbol{S}_1, \tag{5.13}$$

where $\boldsymbol{S}_1$ is defined as in (2.28), $\boldsymbol{x}^{\varphi} = \boldsymbol{\varphi}(\boldsymbol{X}), \boldsymbol{x}^{\psi} = \boldsymbol{\psi}(\boldsymbol{x}^{\varphi})$, and $\boldsymbol{t}^{\varphi} : \bar{\Omega}^{\varphi} \times \boldsymbol{S}_1 \to \mathbb{R}^3$ and $\boldsymbol{t}^{\psi} : \bar{\Omega}^{\psi} \times \boldsymbol{S}_1 \to \mathbb{R}^3$ denote the Cauchy stress fields in the deformed configurations $\bar{\Omega}^{\varphi}$ and $\bar{\Omega}^{\psi}$, respectively.

The following theorem defines the conditions for the Cauchy stress response function to satisfy the axiom of material frame-indifference.

Theorem 5.2.1. *The Cauchy stress response function $\hat{\boldsymbol{\sigma}}^D : \bar{\Omega}_{\boldsymbol{X}} \times \mathbb{M}^3_+ \to \mathbb{S}^3$ satisfies the axiom of material frame indifference if and only if for all $\boldsymbol{X} \in \bar{\Omega}_{\boldsymbol{X}}$ it holds*

$$\hat{\boldsymbol{\sigma}}^D(\boldsymbol{X}, \boldsymbol{Q}\boldsymbol{F}) = \boldsymbol{Q}\hat{\boldsymbol{\sigma}}^D(\boldsymbol{X}, \boldsymbol{F})\boldsymbol{Q}^T \quad \forall \boldsymbol{F} \in \mathbb{M}^3_+, \boldsymbol{F} \in \mathbb{O}^3_+; \tag{5.14}$$

or equivalently, if and only if there exists a mapping $\tilde{\boldsymbol{S}} : \bar{\Omega}_{\boldsymbol{X}} \times \mathbb{S}^3_> \to \mathbb{S}^3$, such that for all $\boldsymbol{X} \in \bar{\Omega}_{\boldsymbol{X}}$ it holds

$$\check{\boldsymbol{S}}(\boldsymbol{X}, \boldsymbol{F}) = \tilde{\boldsymbol{S}}(\boldsymbol{X}, \boldsymbol{F}^T\boldsymbol{F}) \quad \forall \boldsymbol{F} \in \mathbb{M}^3_+, \tag{5.15}$$

where $\check{\boldsymbol{S}} : \bar{\Omega}_{\boldsymbol{X}} \times \mathbb{M}^3_+ \to \mathbb{S}^3$ is the response function of the second Piola-Kirchhoff stress.

Proof. See [33], Theorem 3.3-1. □

Additional restrictions for the form of the response function are entailed by a material property called *isotropy*. In isotropic elastic materials the response function of the material "is the same in all directions". Thus, for a tensile specimen cut out of a block of an isotropic material, the stress-strain curve will be independent of the orientation of the specimen relative to the block of material. For a detailed mathematical description of material frame-indifference and isotropy, we refer to [33, 106].

Noticeably simple expressions of the response functions $\hat{\boldsymbol{\sigma}}^D$ and $\hat{\boldsymbol{S}}$ for the Cauchy stress and the second Piola-Kirchhoff stress of an isotropic elastic material satisfying the axiom of material frame-indifference are presented through the following theorem.

---

[35] The transformation is basically a rotation around the origin. Translations may be ignored since they have no effect on the deformation gradient.

Theorem 5.2.2. *Let an elastic material have a response function that is frame-indifferent and isotropic at a point* $\boldsymbol{X} \in \bar{\Omega}_{\boldsymbol{X}}$*, and let* $\boldsymbol{\varphi} \colon \bar{\Omega}_{\boldsymbol{X}} \to \mathbb{R}^3$ *denote a given arbitrary deformation. Then the Cauchy stress tensor at the point* $\boldsymbol{x} = \boldsymbol{\varphi}(\boldsymbol{X})$ *is given by*

$$\boldsymbol{\sigma}(\boldsymbol{x}) = \hat{\boldsymbol{\sigma}}^D(\boldsymbol{X}, \nabla_{\boldsymbol{X}}\boldsymbol{\varphi}(\boldsymbol{X})) = \bar{\boldsymbol{\sigma}}^D(\boldsymbol{X}, \nabla_{\boldsymbol{X}}\boldsymbol{\varphi}(\boldsymbol{X})\nabla_{\boldsymbol{X}}\boldsymbol{\varphi}(\boldsymbol{X})^T),$$

where the response function $\bar{\boldsymbol{\sigma}}^D(\boldsymbol{X}, \cdot) \colon \mathbb{S}^3_> \to \mathbb{S}^3$ *is of the form*

$$\bar{\boldsymbol{\sigma}}^D(\boldsymbol{X}, \boldsymbol{B}) = \beta_0(\boldsymbol{X}, \boldsymbol{\iota_B})\boldsymbol{I} + \beta_1(\boldsymbol{X}, \boldsymbol{\iota_B})\boldsymbol{B} + \beta_2(\boldsymbol{X}, \boldsymbol{\iota_B})\boldsymbol{B}^2, \quad \forall \boldsymbol{B} \in \mathbb{S}^3_>,$$

and $\beta_i(\boldsymbol{X}, \cdot), i = 0, 1, 2,$ *are real-valued functions of the principal invariants*[36] *of the left Cauchy-Green strain tensor* $\boldsymbol{B} = \nabla_{\boldsymbol{X}}\boldsymbol{\varphi}(\boldsymbol{X})\nabla_{\boldsymbol{X}}\boldsymbol{\varphi}(\boldsymbol{X})^T$*. Moreover, the second Piola-Kirchhoff stress tensor at the point* $\boldsymbol{X}$ *is given by*

$$\boldsymbol{S}(\boldsymbol{X}) = \hat{\boldsymbol{S}}(\boldsymbol{X}, \nabla_{\boldsymbol{X}}\boldsymbol{\varphi}(\boldsymbol{X})) = \tilde{\boldsymbol{S}}(\boldsymbol{X}, \nabla_{\boldsymbol{X}}\boldsymbol{\varphi}(\boldsymbol{X})^T\nabla_{\boldsymbol{X}}\boldsymbol{\varphi}(\boldsymbol{X})),$$

where the response function $\tilde{\boldsymbol{S}}(\boldsymbol{X}, \cdot) \colon \mathbb{S}^3_> \to \mathbb{S}^3$ *is of the form*

$$\tilde{\boldsymbol{S}}(\boldsymbol{X}, \boldsymbol{C}) = \gamma_0(\boldsymbol{X}, \boldsymbol{\iota_C})\boldsymbol{I} + \gamma_1(\boldsymbol{X}, \boldsymbol{\iota_C})\boldsymbol{C} + \gamma_2(\boldsymbol{X}, \boldsymbol{\iota_C})\boldsymbol{C}^2, \quad \forall \boldsymbol{C} \in \mathbb{S}^3_>, \tag{5.16}$$

and $\gamma_i(\boldsymbol{X}, \boldsymbol{\iota_C}), i = 0, 1, 2,$ *are real-valued functions of the principal invariants of the right Cauchy-Green strain tensor* $\boldsymbol{C} = \nabla_{\boldsymbol{X}}\boldsymbol{\varphi}(\boldsymbol{X})^T\nabla_{\boldsymbol{X}}\boldsymbol{\varphi}(\boldsymbol{X})$*. Contrariwise, if either one of the response functions* $\bar{\boldsymbol{\sigma}}^D$ *and* $\tilde{\boldsymbol{S}}$ *exhibits the above form, the axiom of material frame-indifference is satisfied and the material is isotropic at the point* $\boldsymbol{X}$*.*

Proof. See [33], Theorem 3.6-2. □

Note that the principal invariants of the right Cauchy-Green strain tensor used in equation (5.16), that is

$$\begin{aligned}
\iota_1(\boldsymbol{C}) &= \operatorname{tr}(\boldsymbol{C}) = \operatorname{tr}\left(\boldsymbol{F}^T \cdot \boldsymbol{F}\right) = \boldsymbol{F} \colon \boldsymbol{F} &&= \|\boldsymbol{F}\|_F^2, \\
\iota_2(\boldsymbol{C}) &= \operatorname{tr}(\mathbf{Cof}\,\boldsymbol{C}) = \operatorname{tr}\left(\mathbf{Cof}\,\boldsymbol{F}^T \cdot \mathbf{Cof}\,\boldsymbol{F}\right) &&= \|\mathbf{Cof}\,\boldsymbol{F}\|_F^2, \\
\iota_3(\boldsymbol{C}) &= \det \boldsymbol{C} = \det(\boldsymbol{F}^T \cdot \boldsymbol{F}) &&= \det(\boldsymbol{F})^2,
\end{aligned} \tag{5.17}$$

represent measures for changes in line elements, area elements and volume elements, respectively.

Based on the assumption that there exist *stress-free* states of a given body, a reference configuration $\bar{\Omega}_{\boldsymbol{X}}$ is considered as a *natural state* if the *residual stress tensor*

$$\boldsymbol{T}_R(\boldsymbol{X}) := \hat{\boldsymbol{\sigma}}^D(\boldsymbol{X}, \boldsymbol{I}) = \hat{\boldsymbol{S}}(\boldsymbol{X}, \boldsymbol{I}) = \tilde{\boldsymbol{S}}(\boldsymbol{X}, \boldsymbol{I})$$

vanishes at all points $\boldsymbol{X} \in \bar{\Omega}_{\boldsymbol{X}}$. A "deformed" configuration obtained from the application of a rigid deformation on a reference configuration in natural state is again in natural state if it is chosen

---

[36] The principal invariants $\boldsymbol{\iota_A} = (\iota_1(\boldsymbol{A}), \iota_2(\boldsymbol{A}), \iota_3(\boldsymbol{A}))$ of a matrix $\boldsymbol{A} \in \mathbb{M}^3$ are the coefficients in the characteristic polynomial of $\boldsymbol{A}$:

$$\det(\boldsymbol{A} - \lambda \boldsymbol{I}) = -\lambda^3 + \iota_1(\boldsymbol{A})\lambda^2 - \iota_2(\boldsymbol{A})\lambda + \iota_3(\boldsymbol{A}).$$

Moreover, letting $\lambda_i, i = 1, 2, 3$, denote the eigenvalues of the matrix $\boldsymbol{A}$, the following relations can be deduced from the above definition:

$$\begin{aligned}
\iota_1(\boldsymbol{A}) &= \operatorname{tr}(\boldsymbol{A}) = \lambda_1 + \lambda_2 + \lambda_3, \\
\iota_2(\boldsymbol{A}) &= \frac{1}{2}\{(\operatorname{tr}(\boldsymbol{A}))^2 - \operatorname{tr}\left(\boldsymbol{A}^2\right)\} = \operatorname{tr}(\mathbf{Cof}\,\boldsymbol{A}) = \lambda_1\lambda_2 + \lambda_2\lambda_3 + \lambda_3\lambda_1, \\
\iota_3(\boldsymbol{A}) &= \det \boldsymbol{A} = \frac{1}{6}\left\{(\operatorname{tr}(\boldsymbol{A}))^3 - 3\operatorname{tr}(\boldsymbol{A})\operatorname{tr}\left(\boldsymbol{A}^2\right) + 2\operatorname{tr}\left(\boldsymbol{A}^3\right)\right\} = \lambda_1\lambda_2\lambda_3.
\end{aligned}$$

as a new reference configuration.

We consider next the behavior of the constitutive equation of an elastic material "near" the reference configuration, i.e., for the case of moderate strains only - implying small values of $\|\boldsymbol{E}\|$. Since the Green-St. Venant strain tensor (cf. (2.22))

$$\boldsymbol{E} = \frac{1}{2}(\boldsymbol{C} - \boldsymbol{I}), \qquad \boldsymbol{C} = \nabla_{\boldsymbol{X}} \boldsymbol{\varphi}(\boldsymbol{X})^T \nabla_{\boldsymbol{X}} \boldsymbol{\varphi}(\boldsymbol{X}),$$

is in a sense a measure for the disparity between a given deformation $\boldsymbol{\varphi}$ and a rigid deformation for which it holds $\boldsymbol{C} = \boldsymbol{I}$, it seems reasonable to express the difference $\tilde{\boldsymbol{S}}(\boldsymbol{X}, \boldsymbol{I}+2\boldsymbol{E}) - \tilde{\boldsymbol{S}}(\boldsymbol{X}, \boldsymbol{I})$ in terms of the right Cauchy-Green strain tensor $\boldsymbol{C} = \boldsymbol{I} + 2\boldsymbol{E}$. Given a deformed configuration that is "near" the reference configuration, the corresponding response function for the second Piola Kirchhoff stress tensor may be approximated by a first order Taylor expansion around $\tilde{\boldsymbol{S}}(\boldsymbol{I})$:

$$\tilde{\boldsymbol{S}}(\boldsymbol{I} + 2\boldsymbol{E}) = \tilde{\boldsymbol{S}}(\boldsymbol{I}) + 2\frac{\partial \tilde{\boldsymbol{S}}}{\partial \boldsymbol{C}_{ij}}(\boldsymbol{I})\boldsymbol{E}_{ij} + o(\boldsymbol{E}) \in \mathbb{S}^3, \qquad \boldsymbol{I} + 2\boldsymbol{E} \in \mathbb{S}^3_>. \tag{5.18}$$

The first order term in (5.18) involves 36 constants $(\partial \tilde{S}_{ij}/\partial C_{ij})$, however, the stress response functions presented in Theorem 5.2.3 and its Corollary 5.2.4 (excluding the special parameter π) involve only two constants. This remarkable reduction is attributed to the Rivlin–Ericksen representation theorem [33] implying the stress response function $\tilde{\boldsymbol{S}}(\boldsymbol{C})$ to be of the form (5.16) and eventually allowing it to be casted to the forms presented in Theorems 5.2.3 and 5.2.4.

Theorem 5.2.3. *Let a given elastic material have a response function which is frame-indifferent and isotropic at a point* $\boldsymbol{X} \in \bar{\Omega}_{\boldsymbol{X}}$. *Besides, let the functions* $\gamma_i, i = 0, 1, 2,$ *(cf. Theorem 5.2.2) be differentiable at the point* $\boldsymbol{\iota}_{\boldsymbol{I}} = (3, 3, 1)$. *Then there exist constants* $\pi(\boldsymbol{X}), \lambda(\boldsymbol{X}), \mu(\boldsymbol{X}) \in \mathbb{R}$ *such that*

$$\tilde{\boldsymbol{S}}(\boldsymbol{C}) = -\pi(\boldsymbol{X})\boldsymbol{I} + \lambda(\boldsymbol{X}) \operatorname{tr}(\boldsymbol{E})\, \boldsymbol{I} + 2\mu(\boldsymbol{X})\boldsymbol{E} + o(\boldsymbol{E}; \boldsymbol{X}), \qquad \forall \boldsymbol{C} = \boldsymbol{I} + 2\boldsymbol{E}, \boldsymbol{F} \in \mathbb{S}^3_>. \tag{5.19}$$

For a proof of the above theorem, we refer to the proof of Theorem 3.7-1 in [33].

Theorem 5.2.4 ([33]). *Let a given elastic material be homogeneous and isotropic and let its reference configuration be a natural state. If the functions* $\gamma_i, i = 0, 1, 2,$ *(cf. Theorem 5.2.2) are differentiable at the point* $\boldsymbol{\iota}_{\boldsymbol{I}} = (3, 3, 1)$, *then there exist two constants* λ *and* μ *such that the response function* $\hat{\boldsymbol{S}} \colon \mathbb{M}^3_+ \to \mathbb{S}^3$ *is of the form*

$$\begin{aligned} &\hat{\boldsymbol{S}}(\boldsymbol{F}) = \tilde{\boldsymbol{S}}(\boldsymbol{C}) = \check{\boldsymbol{S}}(\boldsymbol{E}) = \lambda \operatorname{tr}(\boldsymbol{E})\, \boldsymbol{I} + 2\mu \boldsymbol{E} + o(\boldsymbol{E}), \\ &\boldsymbol{C} = \boldsymbol{F}^T \boldsymbol{F} = \boldsymbol{I} + 2\boldsymbol{E}, \boldsymbol{F} \in \mathbb{M}^3_+. \end{aligned} \tag{5.20}$$

Under the conditions of the above theorem, the constants λ and μ are referred to as the *Lamé constants* of a material. The constant μ is also known as the *shear modulus*[37] or *modulus of rigidity* and describes the material's response to shear stress (Ratio of shear stress to shear strain). It is one of the several quantities for measuring the stiffness of materials and quantifies in the context of elasticity the deformation of a solid when it is subject to a force parallel to its surface while its opposite face experiences an apposing force. In the context of fluid mechanics it is seen as the dynamic viscosity of a fluid. The parameters λ and μ together, yield the so-called *bulk modulus*[38] $K = \lambda + (2/3)\mu$ quantifying the resistance of the material to volume changes. Admissible numerical values for the

---

[37] The shear modulus is sometimes also denoted by G.

[38] The bulk modulus may also be expressed in terms of the Young's modulus E and the Poisson ratio ν: $K = E/(3(1 - 2\nu))$.

Lamé constants of an elastic material are obtained by "ideal" experiments involving simple tension, pure shear and equibiaxial tension or volumetric compression. These experiments imply the following constraints for the Lamé constants: $\mu > 0, \lambda > 0$. The properties of an elastic material can alternatively be specified in terms two other constants, namely the *Young's* (*elastic/tensile*) *modulus* E and the *Poisson ratio* ν. The Young's modulus E is the slope of the stress-strain curve in uniaxial tension and is a measure for the stiffness of the solid. It describes the material's strain response to uniaxial stress in the direction of this stress. The Poisson ratio ν represents the ratio of the lateral to longitudinal strain ($\nu := -\varepsilon_{\text{lateral}}/\varepsilon_{\text{longitudinal}}; \nu \in [-1, 1/2]$) in uniaxial tensile stress. In other words, it describes the material's strain response to uniaxial stress in the direction orthogonal to the uniaxial stress. The Poisson ratio is a measure for the compressibility of the solid. If $\nu = 1/2$, the solid is incompressible and its volume remains constant. This theoretical upper limit is obtained by relating the volumetric strain

$$\varepsilon_{\text{vol}} = \varepsilon_x + \varepsilon_y + \varepsilon_z \tag{5.21}$$

- being a measure for the change of the volume of an object under load - to the parameter ν. This is achieved by inserting the equations of the generalized Hooke's law

$$\varepsilon_x = \frac{1}{E}\left[\sigma_x - \nu(\sigma_y + \sigma_z)\right], \quad \varepsilon_y = \frac{1}{E}\left[\sigma_y - \nu(\sigma_x + \sigma_z)\right], \quad \varepsilon_z = \frac{1}{E}\left[\sigma_z - \nu(\sigma_x + \sigma_y)\right],$$

into (5.21), yielding the following expression for the volumetric strain which obviously vanishes for $\nu = 1/2$:

$$\varepsilon_{\text{vol}} = \frac{1-2\nu}{E}(\sigma_x + \sigma_y + \sigma_z).$$

The Lamé constants, the Poisson ratio, and the Young's modulus are related by the following equations:

$$\begin{aligned} \lambda &= \frac{E\nu}{(1+\nu)(1-2\nu)}, & E &= \frac{\mu(3\lambda + 2\mu)}{\lambda + \mu}, \\ \mu &= \frac{E}{2(1+\nu)}, & \nu &= \frac{\lambda}{2(\lambda+\mu)}. \end{aligned} \tag{5.22}$$

Moreover, it holds

$$\lambda > 0 \text{ and } \mu > 0 \iff 0 < \nu < \frac{1}{2} \text{ and } E > 0.$$

For *nearly incompressible materials* it holds $\lambda \gg \mu$, and therefore ν is very close to the incompressibility limit $1/2$.

A quite popular and the simplest among the nonlinear material models in the context of structural mechanics computations is given by the *St. Venant-Kirchhoff* material being a homogeneous, frame-indifferent and isotropic material with a natural state reference configuration. Its response function for the second Piola-Kirchhoff stress tensor is obtained by ignoring the higher-order terms in equation (5.20) and reads

$$\check{\boldsymbol{S}}(\boldsymbol{E}) = \tilde{\boldsymbol{S}}(\boldsymbol{I} + 2\boldsymbol{E}) = \lambda \operatorname{tr}(\boldsymbol{E})\, \boldsymbol{I} + 2\mu \boldsymbol{E}, \qquad \boldsymbol{I} + 2\boldsymbol{E} \in \mathbb{S}^3_>. \tag{5.23}$$

From the above relation we can deduce a linear relationship between the Green-St. Venant strain tensor $\boldsymbol{E}$ (cf. equation (2.22)) and the second Piola-Kirchhoff stress $\boldsymbol{S}$. However,

$$\boldsymbol{E} = \frac{1}{2}\left(\nabla_{\boldsymbol{X}}\boldsymbol{u} + (\nabla_{\boldsymbol{X}}\boldsymbol{u})^T + (\nabla_{\boldsymbol{X}}\boldsymbol{u})^T \nabla_{\boldsymbol{X}}\boldsymbol{u}\right)$$

itself is – due to the quadratic terms – a nonlinear function of the displacement $\boldsymbol{u}$, and therefore renders the material model nonlinear.

One of the shortcomings of the St. Venant-Kirchhoff material is the lack of any term in its associated stored energy density function (see Section 5.2.2) in charge with both the prevention of $\nabla_{\boldsymbol{X}}\boldsymbol{\varphi}(\boldsymbol{X})$ to approach zero and the enforcement of its positivity. St. Venant-Kirchhoff materials are often referred to as "large displacement-small strain" models and are at their best only adequate to be used in scenarios involving "small" strains $\boldsymbol{E}$. The physical validity of the St. Venant-Kirchhoff material model is only given for the case of small-strain regime as many materials deviate from a linear stress-strain relationship, even for very modest strain levels. Nonetheless, its performance can be expected to be superior to linearized elasticity models.

5.2.2 Hyperelasticity

Hyperelasticity provides means for the modeling of stress-strain behavior of materials for which linear elastic models do not accurately describe the actually observed material behavior. A prominent example of such a material exhibiting nonlinear elastic behavior is rubber which withstands large deformations and whose reaction can be modeled in a good approximation with hyperelasticity. Hyperelastic constitutive laws are utilized when it comes to the modeling of materials that respond elastically to very large strains. They take into account nonlinear material behavior as well as large shape changes.

A hyperelastic material is an elastic material that possesses all the macroscopic properties enumerated at the beginning of Section 5.2.1 and is additionally characterized by the traits described in the following. In a hyperelastic material, the applied deformation work is converted completely, i.e., without any dissipation, into strain energy and stored in the deformed body. Moreover, the deformation work is path-independent which is expressed by the fact that the deformation work depends only on the start and end point of the deformation path, but not on its course. For the special case of a closed deformation path (implying matching start and end points) it turns out that no work is carried out or energy is consumed. The deformation is reversible and until the return to the starting point of the deformation, the expended work is completely returned from the body. These traits render the material behavior *conservative*.

For a more formal view on the topic, we start with definitions for *conservative applied forces* and choose afterwards the equations of equilibrium in the reference configuration as point of departure for further discussions.

Definition 5.2.1 (Conservative applied body force). *Let* $\boldsymbol{f}_0\colon \Omega_{\boldsymbol{X}} \to \mathbb{R}^3$ *denote the density of an applied body force in the reference configuration. It is dubbed a conservative applied body force if the body force integral*

$$\int_{\Omega_{\boldsymbol{X}}} \boldsymbol{f}_0(\boldsymbol{X}) \cdot \boldsymbol{\theta}_0(\boldsymbol{X})\,\mathrm{d}\Omega_{\boldsymbol{X}} = \int_{\Omega_{\boldsymbol{X}}} \hat{\boldsymbol{f}}_0(\boldsymbol{X}, \boldsymbol{\varphi}(\boldsymbol{X})) \cdot \boldsymbol{\theta}_0(\boldsymbol{X})\,\mathrm{d}\Omega_{\boldsymbol{X}}$$

appearing in the principle of virtual work in the reference configuration, can be written as the Gâteaux derivative[39]

$$F'(\boldsymbol{\varphi})\boldsymbol{\theta}_0 = \int_{\Omega_{\boldsymbol{X}}} \hat{\boldsymbol{f}}_0(\boldsymbol{X}, \boldsymbol{\varphi}(\boldsymbol{X})) \cdot \boldsymbol{\theta}_0(\boldsymbol{X})\,\mathrm{d}\Omega_{\boldsymbol{X}} \quad \forall \boldsymbol{\varphi}, \boldsymbol{\theta}_0 : \bar{\Omega}_{\boldsymbol{X}} \to \mathbb{R}^3 \tag{5.24}$$

---

[39] The *Gâteaux* (*or directional*) *derivative* of a function f at the point $\boldsymbol{v}$ in the direction of the vector $\delta\boldsymbol{v}$ is defined as

$$f'(\boldsymbol{v})\delta\boldsymbol{v} = D_{\delta\boldsymbol{v}}[f](\boldsymbol{v}) \equiv D_{\delta\boldsymbol{v}}[f] = \lim_{\epsilon\to 0} \frac{f(\boldsymbol{v}+\epsilon\delta\boldsymbol{v}) - f(\boldsymbol{v})}{\epsilon} = \frac{d}{d\epsilon} f(\boldsymbol{v}+\epsilon\delta\boldsymbol{v})\Big|_{\epsilon=0}$$

of a functional F of the form

$$F\colon \{\boldsymbol{\psi}\colon \bar{\Omega}_{\boldsymbol{X}} \to \mathbb{R}^3\} \to F(\boldsymbol{\psi}) = \int_{\Omega_{\boldsymbol{X}}} \hat{F}(\boldsymbol{X}, \boldsymbol{\psi}(\boldsymbol{X}))\, \mathrm{d}\Omega_{\boldsymbol{X}},$$

where the function $\hat{F}\colon \Omega_{\boldsymbol{X}} \times \mathbb{R}^3 \to \mathbb{R}$ is called the potential of the applied body force.

Definition 5.2.2 (Conservative applied surface force). *Let $\boldsymbol{g}_0\colon \Gamma_{1,\boldsymbol{X}} \to \mathbb{R}^3$ denote the density of an applied surface force in the reference configuration. It is dubbed a conservative applied surface force if the body force integral*

$$\int_{\Gamma_{1,\boldsymbol{X}}} \boldsymbol{g}_0(\boldsymbol{X}) \cdot \boldsymbol{\theta}_0(\boldsymbol{X})\, \mathrm{d}\Gamma_{1,\boldsymbol{X}} = \int_{\Gamma_{1,\boldsymbol{X}}} \hat{\boldsymbol{g}}_0(\boldsymbol{X}, \nabla_{\boldsymbol{X}}\boldsymbol{\varphi}(\boldsymbol{X})) \cdot \boldsymbol{\theta}_0(\boldsymbol{X})\, \mathrm{d}\Gamma_{1,\boldsymbol{X}}$$

appearing in the principle of virtual work in the reference configuration, can be written as the Gâteaux derivative

$$G'(\boldsymbol{\varphi})\boldsymbol{\theta}_0 = \int_{\Gamma_{1,\boldsymbol{X}}} \hat{\boldsymbol{g}}_0(\boldsymbol{X}, \nabla_{\boldsymbol{X}}\boldsymbol{\varphi}(\boldsymbol{X})) \cdot \boldsymbol{\theta}_0(\boldsymbol{X})\, \mathrm{d}\Gamma_{1,\boldsymbol{X}} \quad \forall \boldsymbol{\varphi}, \boldsymbol{\theta}_0 : \bar{\Omega}_{\boldsymbol{X}} \to \mathbb{R}^3; \boldsymbol{\theta}_0 = \mathbf{0} \text{ on } \Gamma_{0,\boldsymbol{X}} \tag{5.25}$$

of a functional G of the form

$$G\colon \{\boldsymbol{\psi}\colon \bar{\Omega}_{\boldsymbol{X}} \to \mathbb{R}^3\} \to G(\boldsymbol{\psi}) = \int_{\Gamma_{1,\boldsymbol{X}}} \hat{G}(\boldsymbol{X}, \boldsymbol{\psi}(\boldsymbol{X}), \nabla_{\boldsymbol{X}}\boldsymbol{\psi}(\boldsymbol{X}))\, \mathrm{d}\Gamma_{1,\boldsymbol{X}},$$

where the function $\hat{G}\colon \Gamma_{1,\boldsymbol{X}} \times \mathbb{R}^3 \times \mathbb{M}^3_+ \to \mathbb{R}$ is called the potential of the applied surface force.

For the stress in elastic materials is obtained from a stress response function (cf. equation (5.12)), the equations of equilibrium in the reference configuration given by equation (5.7), may alternatively be expressed as

$$\begin{aligned} -\nabla_{\boldsymbol{X}} \cdot \hat{\boldsymbol{P}}(\boldsymbol{X}, \nabla_{\boldsymbol{X}}\boldsymbol{\varphi}(\boldsymbol{X})) &= \hat{\boldsymbol{f}}_0(\boldsymbol{X}, \boldsymbol{\varphi}(\boldsymbol{X})) && \forall \boldsymbol{X} \in \Omega_{\boldsymbol{X}}, \\ \hat{\boldsymbol{P}}(\boldsymbol{X}, \nabla_{\boldsymbol{X}}\boldsymbol{\varphi}(\boldsymbol{X}))\, \boldsymbol{n}_0 &= \hat{\boldsymbol{g}}_0(\boldsymbol{X}, \nabla_{\boldsymbol{X}}\boldsymbol{\varphi}(\boldsymbol{X})) && \forall \boldsymbol{X} \in \Gamma_{1,\boldsymbol{X}}, \\ \boldsymbol{\varphi}(\boldsymbol{X}) &= \boldsymbol{\varphi}_D(\boldsymbol{X}) && \forall \boldsymbol{X} \in \Gamma_{0,\boldsymbol{X}}, \end{aligned} \tag{5.26}$$

where the function $\boldsymbol{\varphi}_D\colon \Omega_{\boldsymbol{X}} \to \mathbb{R}^3$ provides Dirichlet boundary conditions and $\hat{\boldsymbol{f}}_0$ and $\hat{\boldsymbol{g}}_0$ denote functions for conservative applied body forces and conservative applied surface forces, respectively.

Accordingly, the principle of virtual work counterpart to equation (5.8), expressed in terms of the first Piola-Kirchhoff stress response function $\hat{\boldsymbol{P}}$, and the functions $\hat{\boldsymbol{f}}$ and $\hat{\boldsymbol{g}}$, reads

$$\begin{aligned} \int_{\Omega_{\boldsymbol{X}}} \hat{\boldsymbol{P}}(\boldsymbol{X}, \nabla_{\boldsymbol{X}}\boldsymbol{\varphi}(\boldsymbol{X})) : \nabla_{\boldsymbol{X}}\boldsymbol{\theta}_0(\boldsymbol{X})\, \mathrm{d}\Omega_{\boldsymbol{X}} = &\int_{\Omega_{\boldsymbol{X}}} \hat{\boldsymbol{f}}_0(\boldsymbol{X}, \boldsymbol{\varphi}(\boldsymbol{X})) \cdot \boldsymbol{\theta}_0(\boldsymbol{X})\, \mathrm{d}\Omega_{\boldsymbol{X}} \\ &+ \int_{\Gamma_{1,\boldsymbol{X}}} \hat{\boldsymbol{g}}_0(\boldsymbol{X}, \nabla_{\boldsymbol{X}}\boldsymbol{\varphi}(\boldsymbol{X})) \cdot \boldsymbol{\theta}_0(\boldsymbol{X})\, \mathrm{d}\Gamma_{1,\boldsymbol{X}} \end{aligned} \tag{5.27}$$

and is valid for all smooth enough vector fields $\boldsymbol{\theta}_0\colon \bar{\Omega}_{\boldsymbol{X}} \to \mathbb{R}^3$ that vanish on $\Gamma_{0,\boldsymbol{X}}$.

It is very appealing to cast the above equation into an energy minimization problem. To this end, the problem needs to be formulated in terms of a suitable functional which we then can try to minimize by seeking states for which its Gâteaux derivative vanishes. Since the applied forces were chosen to be conservative, using Definitions 5.2.1 and 5.2.2, the integrals in the right hand side of the above equation may be expressed as Gâteaux derivatives $F'(\boldsymbol{\varphi})\boldsymbol{\theta}_0$ and $G'(\boldsymbol{\varphi})\boldsymbol{\theta}_0$ (cf. equations (5.24) and (5.25)) of functionals F and G, respectively. It remains to rewrite the left hand side of the principle of virtual work in terms of the Gâteaux derivative of an appropriate functional W, that is

$$\int_{\Omega_{\boldsymbol{X}}} \hat{\boldsymbol{P}}(\boldsymbol{X}, \nabla_{\boldsymbol{X}}\boldsymbol{\varphi}(\boldsymbol{X})) : \nabla_{\boldsymbol{X}}\boldsymbol{\theta}_0(\boldsymbol{X})\,\mathrm{d}\Omega_{\boldsymbol{X}} = W'(\boldsymbol{\varphi})\boldsymbol{\theta}_0. \tag{5.28}$$

Above, the functional W, defined for any smooth enough mapping $\boldsymbol{\psi}$, is called *strain energy* and is defined as

$$W(\boldsymbol{\psi}) = \int_{\Omega_{\boldsymbol{X}}} \hat{W}(\boldsymbol{X}, \nabla_{\boldsymbol{X}}\boldsymbol{\psi}(\boldsymbol{X}))\,\mathrm{d}\Omega_{\boldsymbol{X}}, \tag{5.29}$$

where the function $\hat{W} : \bar{\Omega}_{\boldsymbol{X}} \times \mathbb{M}^3_+ \to \mathbb{R}$ is called the *stored energy density function* (a.k.a. *strain energy density function* or *elastic energy density function*).

With (5.24), (5.25) and (5.29), the principle of virtual work is equivalent to requiring the Gâteaux derivative of the functional $\{W - (F+G)\}$ to be zero for all "variations" that vanish on Γ_0.

We continue with a definition of hyperelastic material in terms of the stored energy density function $\hat{W}$ and use this definition in Theorem 5.2.5 in order to derive a representation for the equations of equilibrium which is formally equivalent to the minimization of the functional $\{W - (F+G)\}$.

Definition 5.2.3 (Hyperelastic material). *Let $\hat{\boldsymbol{P}} : \bar{\Omega}_{\boldsymbol{X}} \times \mathbb{M}^3_+ \to \mathbb{M}^3$ be the first Piola-Kirchhoff stress response function for an elastic material. This material is called hyperelastic if there exists a function $\hat{W} : \bar{\Omega}_{\boldsymbol{X}} \times \mathbb{M}^3_+ \to \mathbb{R}$, differentiable w.r.t. the deformation gradient $\boldsymbol{F} \in \mathbb{M}^3_+$, for each $\boldsymbol{X} \in \bar{\Omega}_{\boldsymbol{X}}$, such that,*

$$\hat{\boldsymbol{P}}(\boldsymbol{X}, \boldsymbol{F}) = \frac{\partial \hat{W}}{\partial \boldsymbol{F}}(\boldsymbol{X}, \boldsymbol{F}) \quad \forall \boldsymbol{X} \in \Omega_{\boldsymbol{X}}, \boldsymbol{F} \in \mathbb{M}^3_+.$$

Theorem 5.2.5. *Let the functional*

$$I(\boldsymbol{\psi}) = \int_{\Omega_{\boldsymbol{X}}} \hat{W}(\boldsymbol{X}, \nabla_{\boldsymbol{X}}\boldsymbol{\psi}(\boldsymbol{X}))\,\mathrm{d}\Omega_{\boldsymbol{X}} - (F(\boldsymbol{\psi}) + G(\boldsymbol{\psi})), \tag{5.30}$$

defined for smooth enough mappings $\boldsymbol{\psi} : \bar{\Omega}_{\boldsymbol{X}} \to \mathbb{R}^3$, be called the total energy and let a hyperelastic material body $\mathcal{B}$ be exposed to conservative body forces and conservative surface forces.

Then the reference configuration equations of equilibrium of the body $\mathcal{B}$ expressed in terms of the stored energy density function $\hat{W}$

$$\begin{aligned} -\nabla_{\boldsymbol{X}} \cdot \frac{\partial \hat{W}}{\partial \boldsymbol{F}}(\boldsymbol{X}, \nabla_{\boldsymbol{X}}\boldsymbol{\varphi}(\boldsymbol{X})) &= \hat{\boldsymbol{f}}_0(\boldsymbol{X}, \boldsymbol{\varphi}(\boldsymbol{X})) && \forall \boldsymbol{X} \in \Omega_{\boldsymbol{X}}, \\ \frac{\partial \hat{W}}{\partial \boldsymbol{F}}(\boldsymbol{X}, \nabla_{\boldsymbol{X}}\boldsymbol{\varphi}(\boldsymbol{X}))\,\boldsymbol{n}_0 &= \hat{\boldsymbol{g}}_0(\boldsymbol{X}, \nabla_{\boldsymbol{X}}\boldsymbol{\varphi}(\boldsymbol{X})) && \forall \boldsymbol{X} \in \Gamma_{1,\boldsymbol{X}}, \end{aligned}$$

are formally equivalent to requiring

$$I'(\boldsymbol{\psi})\boldsymbol{\theta}_0 = 0,$$

for all smooth enough maps $\boldsymbol{\theta}_0 : \bar{\Omega}_{\boldsymbol{X}} \to \mathbb{R}^3$ that vanish on $\Gamma_{0,\boldsymbol{X}}$.

Proof. A proof of this theorem is presented in [33], Theorem 4.1-1. □

We deduce from the above theorem that the boundary value problem

$$\begin{aligned}
-\nabla_{\boldsymbol{X}} \cdot \frac{\partial \hat{W}}{\partial \boldsymbol{F}}(\boldsymbol{X}, \nabla_{\boldsymbol{X}} \boldsymbol{\varphi}(\boldsymbol{X})) &= \boldsymbol{f}_0(\boldsymbol{X}, \boldsymbol{\varphi}(\boldsymbol{X})) && \forall \boldsymbol{X} \in \Omega_{\boldsymbol{X}}, \\
\frac{\partial \hat{W}}{\partial \boldsymbol{F}}(\boldsymbol{X}, \nabla_{\boldsymbol{X}} \boldsymbol{\varphi}(\boldsymbol{X}))\, \boldsymbol{n}_0 &= \boldsymbol{g}_0(\boldsymbol{X}, \nabla_{\boldsymbol{X}} \boldsymbol{\varphi}(\boldsymbol{X})) && \forall \boldsymbol{X} \in \Gamma_{1,\boldsymbol{X}}, \\
\boldsymbol{\varphi}(\boldsymbol{X}) &= \boldsymbol{\varphi}_D(\boldsymbol{X}) && \forall \boldsymbol{X} \in \Gamma_{0,\boldsymbol{X}},
\end{aligned} \tag{5.31}$$

forms the *Euler-Lagrange equations* associated with the total energy functional I. Any smooth enough minimizer $\boldsymbol{\varphi}$ of I over a set of admissible functions $\boldsymbol{\Phi}$ is a solution to the boundary value problem (5.31):

$$\begin{aligned}
&\boldsymbol{\varphi} \in \boldsymbol{\Phi} := \{\boldsymbol{\psi} \colon \bar{\Omega}_{\boldsymbol{X}} \to \mathbb{R}^3; \boldsymbol{\psi} = \boldsymbol{\varphi}_D \text{ on } \Gamma_0\}, \text{ and} \\
&I(\boldsymbol{\varphi}) = \inf_{\boldsymbol{\psi} \in \boldsymbol{\Phi}} I(\boldsymbol{\psi}).
\end{aligned} \tag{5.32}$$

We provided in Section 5.2.1 a characterization for elastic materials that relates the material's stress tensor to a stress response function. Besides, we presented stress response functions in terms of the deformation gradient $\boldsymbol{F}$, the right Cauchy-Green strain tensor $\boldsymbol{C}$ and the Green-St. Venant strain tensor $\boldsymbol{E}$, emerged from constraints given by material properties such as homogeneity and isotropy and the axiom of material frame-indifference. These material properties also have implications on the form of the stored energy density functions of hyperelastic materials as discussed in the following.

Theorem 5.2.6. *Let* $\hat{W} \colon \bar{\Omega}_{\boldsymbol{X}} \times \mathbb{M}^3_+ \to \mathbb{R}$ *denote the stored energy density function of a hyperelastic material.* $\hat{W}$ *satisfies the axiom of material frame-indifference if and only if at all points* $\boldsymbol{X} \in \bar{\Omega}_{\boldsymbol{X}}$ *it holds*

$$\hat{W}(\boldsymbol{X}, \boldsymbol{Q}\boldsymbol{F}) = \hat{W}(\boldsymbol{X}, \boldsymbol{F}) \quad \forall \boldsymbol{F} \in \mathbb{M}^3_+, \boldsymbol{Q} \in \mathbb{O}^3_+, \tag{5.33}$$

or equivalently, if and only if there exists a function[40] $\tilde{W} \colon \bar{\Omega}_{\boldsymbol{X}} \times \mathbb{S}^3_> \to \mathbb{R}$ *such that*

$$\hat{W}(\boldsymbol{X}, \boldsymbol{F}) = \tilde{W}(\boldsymbol{X}, \boldsymbol{F}^T\boldsymbol{F}) \quad \forall \boldsymbol{F} \in \mathbb{M}^3_+. \tag{5.34}$$

Proof. For a proof of this theorem we refer to [33], Theorem 4.2-1. □

Next, relation (5.34) is used in the following theorem expressing the response function of the second Piola-Kirchhoff stress tensor in terms of the stored energy density function $\tilde{W}$.

Theorem 5.2.7. *Let* $\hat{W} \colon \bar{\Omega}_{\boldsymbol{X}} \times \mathbb{M}^3_+ \to \mathbb{R}$ *denote a frame-indifferent stored energy density function of a hyperelastic material and let the function* $\tilde{W} \colon \bar{\Omega}_{\boldsymbol{X}} \times \mathbb{S}^3_> \to \mathbb{R}$ *be defined at each point* $\boldsymbol{X} \in \bar{\Omega}_{\boldsymbol{X}}$ *by*

$$\tilde{W}(\boldsymbol{X}, \boldsymbol{C}) = \hat{W}(\boldsymbol{X}, \boldsymbol{C}^{1/2}) \quad \forall \boldsymbol{C} \in \mathbb{S}^3_>.$$

Then under the assumption that $(\partial \tilde{W} / \partial \boldsymbol{C})(\boldsymbol{X}, \boldsymbol{C})$ *is a symmetric tensor, the second Piola-Kirchhoff stress response function is given by the relation*

$$\hat{\boldsymbol{S}}(\boldsymbol{X}, \boldsymbol{F}) = \tilde{\boldsymbol{S}}(\boldsymbol{X}, \boldsymbol{C}) = 2\frac{\partial \tilde{W}}{\partial \boldsymbol{C}}(\boldsymbol{X}, \boldsymbol{C}) \quad \forall \boldsymbol{F} \in \mathbb{M}^3_+, \tag{5.35}$$

or

$$\hat{\boldsymbol{S}}(\boldsymbol{X}, \boldsymbol{F}) = \check{\boldsymbol{S}}(\boldsymbol{X}, \boldsymbol{E}) = \frac{\partial \check{W}}{\partial \boldsymbol{E}}(\boldsymbol{X}, \boldsymbol{E}), \quad \forall \boldsymbol{F} \in \mathbb{M}^3_+, \tag{5.36}$$

---

[40] The function $\tilde{W} \colon \bar{\Omega}_{\boldsymbol{X}} \times \mathbb{S}^3_> \to \mathbb{R}$ will also be referred to as *stored energy density function*.

where $\breve{W}(\boldsymbol{X},\boldsymbol{E}) = \tilde{W}(\boldsymbol{X},\boldsymbol{C})$ *and* $\boldsymbol{I} + 2\boldsymbol{E} = \boldsymbol{C}$.

Contrarily, an elastic material is considered hyperelastic, if its second Piola-Kirchhoff stress response function $\hat{\boldsymbol{S}}$ *is of the form* (5.35) *and its stored energy density function is given by* (5.34).

Proof. See [33], Theorem 4.2-2. □

The form of the stored energy density function can be further reduced, if, at a point $\boldsymbol{X} \in \bar{\Omega}_{\boldsymbol{X}}$, in addition to the axiom of material frame-indifference, the hyperelastic material is required to be isotropic as well. In that case, there exists a function $\dot{W}(\boldsymbol{X},\cdot)\colon \boldsymbol{\iota}(\mathbb{S}^3_>) \to \mathbb{R}$ such that

$$\hat{W}(\boldsymbol{X},\boldsymbol{F}) = \tilde{W}(\boldsymbol{X},\boldsymbol{C}) = \dot{W}(\boldsymbol{X},\boldsymbol{\iota_C}) = \dot{W}(\boldsymbol{X},\boldsymbol{\iota_B}), \quad \forall \boldsymbol{F} \in \mathbb{M}^3_+. \tag{5.37}$$

Piola-Kirchhoff stress response functions in terms of the stored-energy function of the principal invariants of the right Cauchy-Green strain tensor $\boldsymbol{C}$ (cf. (5.17)), that is $\dot{W}(\boldsymbol{X},\boldsymbol{\iota_C})$, are presented in the following theorem.

Theorem 5.2.8. *Let at a point* $\boldsymbol{X} \in \bar{\Omega}_{\boldsymbol{X}}$ *the stored-energy function* $\hat{W}$ *be of the form*

$$\hat{W}(\boldsymbol{X},\boldsymbol{F}) = \dot{W}(\boldsymbol{X},\boldsymbol{\iota_C}), \qquad \boldsymbol{F} \in \mathbb{M}^3_+,$$

where the function $\dot{W}(\boldsymbol{X},\cdot)\colon \boldsymbol{\iota}(\mathbb{S}^3_>) \to \mathbb{R}$ *is required to be differentiable at* $\boldsymbol{\iota_C}$. *Then the associated first Piola-Kirchhoff stress response function is given by*

$$\hat{\boldsymbol{P}}(\boldsymbol{X},\boldsymbol{F}) = 2\left(\frac{\partial \dot{W}}{\partial \iota_1}\boldsymbol{F} + \frac{\partial \dot{W}}{\partial \iota_2}(\iota_1\boldsymbol{I} - \boldsymbol{F}\boldsymbol{F}^T)\boldsymbol{F} + \frac{\partial \dot{W}}{\partial \iota_3}\iota_3\boldsymbol{F}^{-T}\right),$$

and the associated second Piola-Kirchhoff stress response function is given by

$$\begin{aligned}\tilde{\boldsymbol{S}}(\boldsymbol{X},\boldsymbol{C}) &= 2\left(\frac{\partial \dot{W}}{\partial \iota_1}\boldsymbol{I} + \frac{\partial \dot{W}}{\partial \iota_2}(\iota_1\boldsymbol{I} - \boldsymbol{C}) + \frac{\partial \dot{W}}{\partial \iota_3}\iota_3\boldsymbol{C}^{-1}\right)\\ &= 2\left(\left(\frac{\partial \dot{W}}{\partial \iota_1} + \frac{\partial \dot{W}}{\partial \iota_2}\iota_1 + \frac{\partial \dot{W}}{\partial \iota_3}\iota_2\right)\boldsymbol{I} - \left(\frac{\partial \dot{W}}{\partial \iota_2} + \frac{\partial \dot{W}}{\partial \iota_3}\iota_1\right)\boldsymbol{C} + \frac{\partial \dot{W}}{\partial \iota_3}\boldsymbol{C}^2\right),\end{aligned}$$

where $\frac{\partial \dot{W}}{\partial \iota_i} := \frac{\partial \dot{W}}{\partial \iota_i}(\boldsymbol{X},\boldsymbol{\iota_C})$, *and* $\iota_i = \iota_i(\boldsymbol{C})$.

Proof. For a proof we refer to [33], Theorem 4.4-2. □

The following theorem presents the required conditions in terms of the material's response and a stored energy functions for a St. Venant-Kirchhoff material to be considered hyperelastic:

Theorem 5.2.9. *A St. Venant-Kirchhoff material with a response function*

$$\check{\boldsymbol{S}}(\boldsymbol{E}) = \lambda\,\mathrm{tr}\,(\boldsymbol{E})\,\boldsymbol{I} + 2\mu\boldsymbol{E} = \left(\frac{\lambda}{2}(\iota_1(\boldsymbol{C}) - 3) - \mu\right)\boldsymbol{I} + \mu\boldsymbol{C} = \tilde{\boldsymbol{S}}(\boldsymbol{C}) \tag{5.38}$$

is hyperelastic, with a stored energy density function given by

$$\breve{W}(\boldsymbol{E}) = \frac{\lambda}{2}\,\mathrm{tr}\,(\boldsymbol{E})^2 + \mu\,\mathrm{tr}\left(\boldsymbol{E}^2\right). \tag{5.39}$$

Proof. See [33], Theorem 4.4-3. □

We discuss next the behavior of the stored energy density function for small and large strains. In the former case, recalling the stress response function of a homogeneous, isotropic, elastic material "near" the reference configuration (cf. equation (5.20)), the "near a natural state" constitutive equation for the second Piola-Kirchhoff stress, reads

$$\boldsymbol{S} = \check{\boldsymbol{S}}(\boldsymbol{E}) = \lambda \operatorname{tr}(\boldsymbol{E})\, \boldsymbol{I} + 2\mu \boldsymbol{E} + o(\boldsymbol{E}).$$

The corresponding stored energy density function is presented in the following theorem.

Theorem 5.2.10. *Let*

$$\hat{W}(\boldsymbol{F}) = \dot{W}(\boldsymbol{\iota_C}) = \check{W}(\boldsymbol{E}), \qquad \boldsymbol{C} = \boldsymbol{I} + 2\boldsymbol{E}, \boldsymbol{F} \in \mathbb{M}^3_+,$$

denote the stored energy density function of a given homogeneous, isotropic, hyperelastic material, whose reference configuration is a natural state. Then, in case the function $\dot{W} \colon \boldsymbol{\iota}(\mathbb{S}^3_>) \to \mathbb{R}$ *is twice differentiable at the point* $\boldsymbol{\iota_I}$*, it holds*

$$\check{W}(\boldsymbol{E}) = \frac{\lambda}{2} \operatorname{tr}(\boldsymbol{E})^2 + \mu \operatorname{tr}\left(\boldsymbol{E}^2\right) + o(\|\boldsymbol{E}\|^2). \tag{5.40}$$

Proof. See [33], Theorem 4.5-1. □

Dropping the higher-order terms $o(\|\boldsymbol{E}\|^2)$ in (5.40), leads to the *stored energy density function of the St. Venant-Kirchhoff material* (5.39). Moreover since it holds

$$\check{\boldsymbol{S}}(\boldsymbol{E}) = \frac{\partial \check{W}}{\partial \boldsymbol{E}}(\boldsymbol{E}) = \lambda \operatorname{tr}(\boldsymbol{E})\, \boldsymbol{I} + 2\mu \boldsymbol{E},$$

it follows from Theorems 5.2.7 and 5.2.9 that the St. Venant-Kirchhoff material is hyperelastic. Accordingly this material's second and first Piola Kirchhoff stress tensors read

$$\boldsymbol{S} = \lambda \operatorname{tr}(\boldsymbol{E})\, \boldsymbol{I} + 2\mu \boldsymbol{E}, \text{ and} \tag{5.41a}$$

$$\boldsymbol{P} = \boldsymbol{F}\boldsymbol{S} = \lambda \operatorname{tr}(\boldsymbol{E})\, \boldsymbol{F} + 2\mu \boldsymbol{F}\boldsymbol{E}, \tag{5.41b}$$

respectively.

When it comes to *large strains*, a suitable stored energy density function needs to be designed according to the idea that "extreme strains go along with extreme stresses". An example for an extreme strain scenario pictures a material which is exposed to a compression, such that $\det \boldsymbol{F} \to 0$, and therefore, by the principle of causality, experiences an internal stress that approaches infinity. Therefore we can deduce that infinite energy is required in order to annihilate volumes. As for the design of a suitable stored energy density function, for hyperelastic materials, the stored energy density function $\hat{W}$ needs to approach $+\infty$, in case of emerging extreme strains. One possibility to measure the latter is when one of the eigenvalues $\lambda_i(\boldsymbol{C})$ of the right Cauchy-Green strain tensor $\boldsymbol{C}$ approaches 0 or $+\infty$.

Focusing on one of the eigenvalues, say $\lambda_i(\boldsymbol{C})$, while keeping the other two eigenvalues $\lambda_{i+1}(\boldsymbol{C})$ and $\lambda_{i+2}(\boldsymbol{C})$ in the compact interval $]0, +\infty[$, the following equivalence relations between $\lambda_i(\boldsymbol{C})$ and functions of the deformation gradient $\boldsymbol{F}$ can be expressed [33]:

$$\begin{aligned}
\lambda_i(\boldsymbol{C}) &\to 0^+ &&\iff \det \boldsymbol{F} \to 0^+,\\
\lambda_i(\boldsymbol{C}) &\to +\infty &&\iff \|\boldsymbol{F}\| \to +\infty,\\
\lambda_i(\boldsymbol{C}) &\to +\infty &&\iff \|\mathbf{Cof}\,\boldsymbol{F}\| \to +\infty,\\
\lambda_i(\boldsymbol{C}) &\to +\infty &&\iff \det \boldsymbol{F} \to +\infty.
\end{aligned}$$

The above expressions lead to the following assumptions on how the stored energy function $\hat{W}$ should behave in the presence of large strains:

$$\begin{aligned}
\det \boldsymbol{F} \to 0^+ &\implies \hat{W}(\boldsymbol{F}) \to +\infty, \qquad \boldsymbol{F} \in \mathbb{M}^3_+,\\
\|\boldsymbol{F}\| + \|\mathbf{Cof}\,\boldsymbol{F}\| + \det \boldsymbol{F} \to +\infty &\implies \hat{W}(\boldsymbol{F}) \to +\infty, \qquad \boldsymbol{F} \in \mathbb{M}^3_+.
\end{aligned} \tag{5.42}$$

The above material behavior requirements are now used in order to assess the suitability of the St. Venant-Kirchhoff material model for large strains. Since the stored energy density function of the St. Venant-Kirchhoff material model, given by equation (5.39), is not explicitly dependent on $\det \boldsymbol{F}$, the first requirement in equation (5.42) is not met. Moreover, the stored energy density function misses any terms that prevent $\det \boldsymbol{F} \to 0^+$, let alone to become negative. The usage of this model is therefore not considered to be reasonable in scenarios involving large strains.

A hyperelastic material satisfying the requirements expressed in equation (5.42), is the *Neo-Hookean material*. The stored energy density function of a variant of the compressible Neo-Hookean material that is frequently used in the literature [113], reads

$$\hat{W}(\boldsymbol{F}) = \frac{\mu}{2}(\mathrm{tr}\left(\boldsymbol{F}^T\boldsymbol{F}\right) - 3) - \mu \log(\det \boldsymbol{F}) + \frac{\lambda}{2}\log^2(\det \boldsymbol{F}) \tag{5.43}$$

and yields the following expression for the first Piola-Kirchhoff stress

$$\boldsymbol{P} = \mu(\boldsymbol{F} - \boldsymbol{F}^{-T}) + \lambda \log(\det \boldsymbol{F})\boldsymbol{F}^{-T}. \tag{5.44}$$

However, there exist [164] several alternative formulations for the stored energy density function of the compressible Neo-Hookean material, for example

$$\hat{W}(\boldsymbol{F}) = \frac{\mu}{2}(\mathrm{tr}\,(\boldsymbol{C}) - 3) - \mu \log(J) + \frac{\lambda}{4}(J^2 - 1) - \frac{\lambda}{2}\log(J) \tag{5.45}$$

which leads to the following forms of the first and second Piola-Kirchhoff stress tensor

$$\boldsymbol{P} = \mu(\boldsymbol{F} - \boldsymbol{F}^{-T}) + \frac{\lambda}{2}(J^2 - 1)\boldsymbol{F}^{-T}, \tag{5.46a}$$

$$\boldsymbol{S} = \boldsymbol{F}^{-1}\boldsymbol{P} = \mu(\boldsymbol{I} - \boldsymbol{C}^{-1}) + \frac{\lambda}{2}(J^2 - 1)\boldsymbol{C}^{-1}. \tag{5.46b}$$

Note that the logarithmic terms in equations (5.43) and (5.45) enforce the first requirement in (5.42). Moreover, the stress obviously vanishes in the reference configuration where it holds $\boldsymbol{F} = \boldsymbol{I}, \boldsymbol{C} = \boldsymbol{I}, J = 1$.

5.2.3 (Initial) boundary value problems of elasticity

In this section we present a set of (initial) boundary value problems of elasticity which are all based on the equations of equilibrium (cf. equations (5.1) and (5.7)) and basically differ by the stress measure used. The choice of the boundary value problem variant to work with, depends on the elastic deformation scenario. In case of transient problems, the boundary value problems contain terms that account for inertial forces. In all elastic deformation problems considered in this work, we consider only applied forces that are dead loads. Since instead of the deformation $\boldsymbol{\varphi}$, it is often more convenient to work with the *displacement* $\boldsymbol{u} : \bar{\Omega}_{\boldsymbol{X}} \to \mathbb{R}^3$ (with $\boldsymbol{u} = \boldsymbol{\varphi} - \mathbf{id}$) as the unknown, we recast the equations of equilibrium in terms of this unknown and obtain the governing equations of *Elastostatics*

$$\begin{aligned} -\nabla_{\boldsymbol{X}} \cdot \boldsymbol{P} &= J\rho\boldsymbol{b} && \text{in } \Omega_{\boldsymbol{X}}, \\ \boldsymbol{u} &= \boldsymbol{u}_D && \text{on } \Gamma_{D,\boldsymbol{X}}, \\ \boldsymbol{P}\,\boldsymbol{n}_0 &= \boldsymbol{g}_0 && \text{on } \Gamma_{N,\boldsymbol{X}}, \end{aligned} \tag{5.47}$$

and *Elastodynamics*

$$\begin{aligned} J\rho\frac{\partial^2 \boldsymbol{u}}{\partial t^2} - \nabla_{\boldsymbol{X}} \cdot \boldsymbol{P} &= J\rho\boldsymbol{b} && \text{in } \Omega_{\boldsymbol{X}} \times I, \\ \boldsymbol{u}(\cdot,0) = \mathring{\boldsymbol{u}}, \dot{\boldsymbol{u}}(\cdot,0) &= \overset{\circ}{\dot{\boldsymbol{u}}} && \text{in } \Omega_{\boldsymbol{X}}, \\ \boldsymbol{u} &= \boldsymbol{u}_D && \text{on } \Gamma_{D,\boldsymbol{X}} \times I, \\ \boldsymbol{P}\,\boldsymbol{n}_0 &= \boldsymbol{g}_0 && \text{on } \Gamma_{N,\boldsymbol{X}} \times I, \end{aligned} \tag{5.48}$$

where $\boldsymbol{g}_0$ is a reference configuration surface traction function (cf. (5.6)), and $J\rho\boldsymbol{b}$ denotes the body force density in the reference configuration, and can be obtained from relations (2.27) and (5.4). The above equations, expressed with respect to the unknown displacement field $\boldsymbol{u}$, serve as a basis for all (initial) boundary value problems presented in Sections 5.2.3.1 and 5.2.3.2. However, we will also present multi-field problem formulations, since classical single-field approaches can not correctly describe the response of quasi-incompressible materials. Materials that respond to volume changes with a significant increase of stored energy are called *nearly incompressible*. Further, if the material does not allow any volumetric changes whatsoever, that is, when the deformation $\boldsymbol{\varphi}$ of the material satisfies the incompressibility condition

$$J = \det \nabla_{\boldsymbol{X}}\boldsymbol{\varphi}(\boldsymbol{X}) = \det \boldsymbol{F} = 1, \quad \text{in } \bar{\Omega}_{\boldsymbol{X}},$$

it is called *incompressible*. By contrast, materials for which merely the orientation preservation restriction $\det \nabla_{\boldsymbol{X}}\boldsymbol{\varphi}(\boldsymbol{X}) > 0$ is required, are called *compressible*.

Analyzing the behavior of the stored energy functions (5.43), or alternatively (5.45) for the case when $\det \boldsymbol{F} \approx 1$, reveals that a volume change induced large energy increase is only possible when the *Lamé constant* λ is large. Therefore, the parameter λ can be considered as a measure for the incompressibility of a material, where increasing values of λ correlate with "less compressibility". Since in the incompressibility limit it holds $\nu = 1/2$, it follows (for fixed shear modulus μ) from equation (5.22) that

$$\nu \to 1/2 \iff \lambda \to \infty. \tag{5.49}$$

Approaching the incompressibility limit poses a problem for single-field (i.e. displacement only) formulations of boundary value problems of elasticity for they can not correctly describe the response of "quasi-incompressible" materials. The response turns out to be overly stiff, a phenomenon known as volumetric locking. One strategy for its circumvention, is the usage of a multi-field or mixed (e.g. displacement-pressure) formulation which we will refer to later.

We analyze next the behavior of the stored energy functions (5.43) and (5.45) for the case $\det \boldsymbol{F} = 1$. For in this scenario, it holds $J = 1$ and "$\lambda = \infty$", the stored energy functions collapse to

$$\hat{W}(\boldsymbol{F}) = \frac{\mu}{2}(\operatorname{tr}\left(\boldsymbol{F}^T\boldsymbol{F}\right) - 3), \tag{5.50}$$

and the expression for the second Piola-Kirchhoff stress tensor given by equation (5.46b) reduces to

$$\boldsymbol{S} = \mu(\boldsymbol{I} - \boldsymbol{C}^{-1}). \tag{5.51}$$

Due to the fact that equation (5.50) as well as equation (5.51) now lack any terms that enforce the constraint $J = 1$, it becomes necessary to carry out the computations with an additional variable that acts as a Lagrange multiplier in the course of enforcing the incompressibility constraint. This additional unknown in the equations systems to be solved can be interpreted as pressure.

The essential step for the derivation of mixed displacement-pressure $(\boldsymbol{u}, p)$ formulations of elasticity, is to outsource "suitable" parts of the respectively involved stress tensor into a pressure variable. We do this exemplary for the case of a Neo-Hookean material, whose second Piola-Kirchhoff stress tensor is given by the expression on the right hand side of equation (5.46b). Outsourcing those parts of it that are associated with compressibility into a new variable

$$p = -\frac{\lambda}{2}(J - \frac{1}{J}), \tag{5.52}$$

representing pressure, equations (5.46a) and (5.46b) can be expressed as

$$\boldsymbol{P} = \mu(\boldsymbol{F} - \boldsymbol{F}^{-T}) - pJ\boldsymbol{F}^{-T}, \text{ and} \tag{5.53a}$$

$$\boldsymbol{S} = \mu(\boldsymbol{I} - \boldsymbol{C}^{-1}) - pJ\boldsymbol{C}^{-1}, \tag{5.53b}$$

respectively. The above representation of the first Piola-Kirchhoff stress tensor in terms of the displacement $\boldsymbol{u}$ and pressure p will be used in the $(\boldsymbol{u}, p)$ formulations of the elasticity problem presented in Section 5.2.3.2.

5.2.3.1 Boundary value problems of linearized elasticity

As mentioned in Section 5.2, the theory of linearized elasticity is based on the linearization of all nonlinear relationships in (nonlinear) elasticity. We therefore need to come up with both a representation of strain as a linear function of displacement and a linear stress-strain relationship. The former is given by the infinitesimal strain tensor

$$\varepsilon(\boldsymbol{u}) = \frac{1}{2}\left(\nabla_{\boldsymbol{X}}\boldsymbol{u} + (\nabla_{\boldsymbol{X}}\boldsymbol{u})^T\right)$$

which is obtained from the Green-St. Venant strain tensor $\boldsymbol{E}$ (cf. (2.22)) by dropping its nonlinear terms. The latter is given by *Hooke's law* for isotropic material

$$\boldsymbol{\sigma} = 2\mu\varepsilon + \lambda \operatorname{tr}(\varepsilon)\boldsymbol{I} \tag{5.54}$$

which is obtained from the usage of the (linear) infinitesimal strain tensor ε in the St. Venant-Kirchhoff constitutive law (5.38). The symmetric tensor $\boldsymbol{\sigma}$ is a linearization of the second Piola-Kirchhoff stress tensor $\boldsymbol{S}$ (cf. 5.41a) and is an approximation for the real physical Cauchy stress occurring in the deformed body. Since for infinitesimal deformations the deviation of the deformation gradient $\boldsymbol{F}$ from identity is negligible, the governing equations may just as well be defined with respect to the current domain $\Omega_{\boldsymbol{x}} \equiv \Omega$ and the Cauchy stress $\boldsymbol{\sigma} = (\det \boldsymbol{F})^{-1}\boldsymbol{P}\boldsymbol{F}^T$ (cf. (2.35)). In this spirit, replacing in equation (5.47) the stress variable with the expression on the right hand side of equation (5.54), that is

$$\begin{aligned} -\nabla \cdot \boldsymbol{\sigma} &= -\nabla \cdot (2\mu\boldsymbol{\varepsilon} + \lambda \operatorname{tr}(\boldsymbol{\varepsilon})\, \boldsymbol{I}) \\ &= -2\mu\nabla \cdot \boldsymbol{\varepsilon} - \lambda\nabla \cdot (\operatorname{tr}(\boldsymbol{\varepsilon})\, \boldsymbol{I}) \\ &= -2\mu\nabla \cdot \boldsymbol{\varepsilon} - \lambda\nabla \cdot ((\nabla \cdot \boldsymbol{u})\boldsymbol{I}) \\ &= -2\mu\nabla \cdot \boldsymbol{\varepsilon} - \lambda\nabla(\nabla \cdot \boldsymbol{u}) \end{aligned} \tag{5.55}$$

yields the following elliptic differential equation for "linearized elastostatics" (also known as the *Lamé equation*) in displacement formulation:

$$\begin{aligned} -2\mu\nabla \cdot \boldsymbol{\varepsilon} - \lambda\nabla(\nabla \cdot \boldsymbol{u}) &= \boldsymbol{f} && \text{in } \Omega, \\ \boldsymbol{u} &= \boldsymbol{u}_D && \text{on } \Gamma_D, \\ \boldsymbol{\sigma}\,\boldsymbol{n} &= \boldsymbol{g} && \text{on } \Gamma_N. \end{aligned} \tag{5.56}$$

The continuous linear variational formulation of the above problem reads:

$$\begin{cases} \text{Find } \boldsymbol{u} + \boldsymbol{u}_D \in \boldsymbol{\mathcal{V}}, \text{ such that} \\ \forall \boldsymbol{\phi} \in \boldsymbol{\mathcal{V}} \\ a(\boldsymbol{u}, \boldsymbol{\phi}) = L(\boldsymbol{\phi}), \end{cases} \tag{5.57}$$

where $\boldsymbol{\mathcal{V}}$ denotes a Hilbert space and is defined as

$$\boldsymbol{\mathcal{V}} := \{\boldsymbol{v} \in \boldsymbol{\mathcal{H}}^1(\Omega) : \boldsymbol{v}\big|_{\boldsymbol{\Gamma_D}} = 0\},$$

$\boldsymbol{\mathcal{H}}^1$ and $\mathcal{L}^2$ are Sobolev spaces as defined in [2], and the bilinear form $a(\boldsymbol{u}, \boldsymbol{\phi})$ and linear form $L(\boldsymbol{\phi})$ are defined as

$$\begin{aligned} a(\boldsymbol{u}, \boldsymbol{\phi}) &:= 2\mu\, (\boldsymbol{\varepsilon}(\boldsymbol{\phi}), \boldsymbol{\varepsilon}(\boldsymbol{u}))_\Omega + \lambda\, ((\nabla \cdot \boldsymbol{u}), (\nabla \cdot \boldsymbol{\phi}))_\Omega\,, \\ L(\boldsymbol{\phi}) &:= (\boldsymbol{f}, \boldsymbol{\phi})_\Omega + (\boldsymbol{g}, \boldsymbol{\phi})_{\Gamma_N}. \end{aligned} \tag{5.58}$$

Above, $(\cdot,\cdot)_\Omega$ and $(\cdot,\cdot)_\Gamma$ are the usual $\mathcal{L}^2$ scalar products on Ω and Γ, respectively. With the definitions made in (5.58), the equation system to be solved in (5.57) eventually reads

$$\int_\Omega 2\mu\, \boldsymbol{\varepsilon}(\boldsymbol{\phi}) : \boldsymbol{\varepsilon}(\boldsymbol{u}) + \lambda(\nabla \cdot \boldsymbol{u})\, (\nabla \cdot \boldsymbol{\phi})\, \mathrm{d}\Omega = \int_\Omega \boldsymbol{\phi} \cdot \boldsymbol{f}\, \mathrm{d}\Omega + \int_{\Gamma_N} \boldsymbol{\phi} \cdot \boldsymbol{g}\, \mathrm{d}\Gamma_N. \tag{5.59}$$

The bilinear form $a(\cdot,\cdot)$ and the linear form $L(\cdot)$ are continuous (bounded), that is, there exist constants $c_1 > 0$ and $c_2 > 0$ such that

$$\begin{aligned} |a(\boldsymbol{u}, \boldsymbol{\phi})| &\leq c_1\, \|\boldsymbol{u}\|_1\, \|\boldsymbol{\phi}\|_1\,, \\ |L(\boldsymbol{\phi})| &\leq c_2\, \|\boldsymbol{\phi}\|_1\,. \end{aligned} \tag{5.60}$$

The Korn inequalities (see e.g. [22, 23]) are essential in establishing coerciveness of the differential operators of linear elastostatics and therefore form the basis for existence results in that theory. In fact these inequalities are used in [22, 23] to show that the the bilinear form $a(\cdot,\cdot)$ on $\boldsymbol{\mathcal{V}}$ is coercive or ($\boldsymbol{\mathcal{V}}$-elliptic), i.e.,

$$\exists\, \alpha > 0 \text{ such that } a(\boldsymbol{v}, \boldsymbol{v}) \geq \alpha\, \|\boldsymbol{v}\|_1^2 \qquad \forall \boldsymbol{v} \in \boldsymbol{\mathcal{V}}.$$

Then due to the continuity (boundedness) and coercivity of the bilinear form $a(\cdot,\cdot)$ on $\boldsymbol{\mathcal{V}}$, it holds

$$\exists\, \alpha, C > 0 : \alpha \left\|\boldsymbol{v}\right\|_1^2 \leq a(\boldsymbol{v},\boldsymbol{v}) \leq C \left\|\boldsymbol{v}\right\|_1^2 \qquad \forall \boldsymbol{v} \in \boldsymbol{\mathcal{V}},$$

and provided $measure(\Gamma_D) > 0$, it follows from the Lax-Milgram theorem [23, 138] that there exists a unique solution for the variational problem (5.57). This is formalized in the following theorem.

Theorem 5.2.11. *Let* $\boldsymbol{f} \in \boldsymbol{\mathcal{H}}^{-1}(\Omega), \boldsymbol{u}_D = \boldsymbol{z}|_{\Gamma_D}$, *where* $\boldsymbol{z} \in \boldsymbol{\mathcal{H}}^1(\Omega), \boldsymbol{g} \in \mathcal{L}^2(\Gamma_N)$, *and* $measure(\Gamma_D) > 0$. *Then the variational problem (5.57) has a unique solution.*

Proof. For a proof of this theorem we refer to [23], Theorem (11.2.28). □

We consider next a mixed displacement-pressure formulation of linearized elastostatics. With pressure being defined as

$$p := -\lambda \nabla \cdot \boldsymbol{u},$$

equation (5.56) can be rewritten as

$$\begin{aligned} -2\mu\nabla\cdot\boldsymbol{\varepsilon} + \nabla p &= \boldsymbol{f} && \text{in } \Omega, \\ -\nabla\cdot\boldsymbol{u} - \frac{1}{\lambda}p &= 0 && \text{in } \Omega, \\ \boldsymbol{u} &= \boldsymbol{u}_D && \text{on } \Gamma_D, \\ \boldsymbol{\sigma}\,\boldsymbol{n} &= \boldsymbol{g} && \text{on } \Gamma_N, \end{aligned} \tag{5.61}$$

which then together with the Hilbert space $\mathcal{Q} := \{q \mid q \in \mathcal{L}^2(\Omega)\}$ leads to the following continuous mixed linear variational formulation:

$$\begin{cases} \text{Find } (\boldsymbol{u} + \boldsymbol{u}_D, p) \in \boldsymbol{\mathcal{V}} \times \mathcal{Q}, \text{ such that} \\ \forall (\boldsymbol{\phi}, q) \in \boldsymbol{\mathcal{V}} \times \mathcal{Q} \\ a(\boldsymbol{u},\boldsymbol{\phi}) + b(\boldsymbol{\phi}, p) = L(\boldsymbol{\phi}) \\ b(\boldsymbol{u}, q) + c(p,q) = 0, \end{cases} \tag{5.62}$$

where the linear form $L(\cdot)$ is the same as in (5.58) and the bilinear forms $a(\cdot,\cdot), b(\cdot,\cdot)$ and $c(\cdot,\cdot)$ – partially obtained from the application of integration by parts – are defined as follows:

$$\begin{aligned} a(\boldsymbol{u},\boldsymbol{\phi}) &:= 2\mu(\boldsymbol{\varepsilon}(\boldsymbol{u}), \boldsymbol{\varepsilon}(\boldsymbol{\phi}))_\Omega, \\ b(\boldsymbol{\phi}, p) &:= -(\nabla\cdot\boldsymbol{\phi}, p)_\Omega, \\ c(p,q) &:= -\frac{1}{\lambda}(p,q)_\Omega. \end{aligned} \tag{5.63}$$

With the above definitions, the equation system to be solved in (5.62) eventually reads

$$\begin{aligned} \int_\Omega \boldsymbol{\varepsilon}(\boldsymbol{u}) : 2\mu\,\boldsymbol{\varepsilon}(\boldsymbol{\phi})\,\mathrm{d}\Omega - \int_\Omega p\cdot(\nabla\cdot\boldsymbol{\phi})\,\mathrm{d}\Omega &= \int_\Omega \boldsymbol{f}\cdot\boldsymbol{\phi}\,\mathrm{d}\Omega + \int_{\Gamma_N} \boldsymbol{g}\cdot\boldsymbol{\phi}\,\mathrm{d}\Gamma_N, \\ -\int_\Omega (\nabla\cdot\boldsymbol{u})\cdot q\,\mathrm{d}\Omega - \int_\Omega \frac{1}{\lambda}p\cdot q\,\mathrm{d}\Omega &= 0. \end{aligned} \tag{5.64}$$

The above equation system is fairly similar to the Stokes problem and exhibits the structure of a saddle point problem with a penalty term $\frac{1}{\lambda}$ since it holds

$$\lambda \to \infty \, (\text{or } \nu \to 1/2) \implies c(\cdot,\cdot) \to 0.$$

Recalling relation (5.49), the factor $\frac{1}{\lambda}$ in the bilinear form $c(\cdot,\cdot)$ can be replaced by the following positive constant

$$\varepsilon = \frac{1-2\nu}{\nu}, \tag{5.65}$$

where $\varepsilon = 0$ represents the incompressible case. In (5.62), we assume $\Gamma_D \neq \partial\Omega$. However, if $\Gamma_D = \partial\Omega$ and $\varepsilon = 0$, for the problem to have a unique solution, the pressure space needs to be replaced by

$$\bar{L}_0^2(\Omega) = \left\{ q \in \mathcal{L}^2(\Omega) \,\middle|\, \int_\Omega q = 0 \right\}.$$

Moreover, for the existence of a unique solution, the $\boldsymbol{\mathcal{V}}$-ellipticity of the bilinear form $a(\cdot,\cdot)$ is not sufficient anymore. The spaces $\boldsymbol{\mathcal{V}}$ and $\mathcal{Q}$ need to meet the following compatibility requirements, also known as the *Ladyzhenskaya-Babuška-Brezzi* (*LBB*) *conditions* [22]:

1. The bilinear form $a(\cdot,\cdot)$ is $\boldsymbol{\mathcal{V}}$-elliptic:

$$\exists\, \alpha > 0 : a(\boldsymbol{v},\boldsymbol{v}) \geq \alpha \left\|\boldsymbol{v}\right\|_1^2 \qquad \forall \boldsymbol{v} \in \boldsymbol{\mathcal{V}}.$$

2. The bilinear form $b(\cdot,\cdot)$ fulfills the inf-sup condition:

$$\exists\, \beta > 0 : \inf_{q\in\mathcal{Q}} \sup_{\boldsymbol{v}\in\boldsymbol{\mathcal{V}}} \frac{b(\boldsymbol{v},q)}{\left\|\boldsymbol{v}\right\|_1 \left\|q\right\|_0} \geq \beta.$$

In problem (5.62), the continuous bilinear forms $a(\cdot,\cdot)$ and $b(\cdot,\cdot)$ and the spaces $\boldsymbol{\mathcal{V}}$ and $\mathcal{Q}$ fulfill the above conditions. Moreover, the bilinear form $c(\cdot,\cdot)$ is continuous and it holds $c(q,q) \leq 0, q \in \mathcal{Q}$. Therefore, there exists a unique solution for the variational problem (5.62) (see [22], §4).

5.2.3.2 Boundary value problems of nonlinear elasticity

In this section we concisely present the strong as well as the weak forms of the partial differential equations that we solve in the context of the structural mechanics component of the FSI problem. The equations presented basically differ by the scenario they address (static or dynamic), by the problem formulation in terms of the involved unknowns, and by the material model used. We present by no means all possible combinations and restrict the presentation to the cases we have considered in this work.

5.2.3.2.1 Elastostatics in displacement formulation (St. Venant-Kirchhoff material)

Letting $\boldsymbol{P}$ represent the first Piola-Kirchhoff stress tensor of the St. Venant-Kirchhoff material (cf. (5.41b)), the governing equations of elastostatics (5.47) in displacement formulation read

$$\begin{aligned} -\nabla_{\boldsymbol{X}} \cdot (\lambda \operatorname{tr}(\boldsymbol{E})\,\boldsymbol{F} + 2\mu \boldsymbol{F}\boldsymbol{E}) &= J\rho\boldsymbol{b} && \text{in } \Omega_{\boldsymbol{X}}, \\ \boldsymbol{u} &= \boldsymbol{u}_D && \text{on } \Gamma_{D,\boldsymbol{X}}, \\ \boldsymbol{P}\,\boldsymbol{n}_0 &= \boldsymbol{g}_0 && \text{on } \Gamma_{N,\boldsymbol{X}}. \end{aligned} \tag{5.66}$$

Together with the trial and test spaces $\boldsymbol{\mathcal{T}}$ and $\boldsymbol{\mathcal{V}}$, respectively (re)defined as

$$\begin{aligned} \boldsymbol{\mathcal{T}} :=& \{\boldsymbol{v} \in \boldsymbol{\mathcal{H}}^1(\Omega_{\boldsymbol{X}}) \mid \boldsymbol{v} = \boldsymbol{v}_D \text{ on } \Gamma_{D,\boldsymbol{X}}\}, \\ \boldsymbol{\mathcal{V}} :=& \{\boldsymbol{v} \in \boldsymbol{\mathcal{H}}^1(\Omega_{\boldsymbol{X}}) \mid \boldsymbol{v} = 0 \text{ on } \Gamma_{D,\boldsymbol{X}}\}, \end{aligned} \tag{5.67}$$

the continuous nonlinear variational formulation of the above problem reads:

$$\begin{cases} \text{Find } \boldsymbol{u} \in \boldsymbol{\mathcal{T}} \text{ such that} \\ \mathcal{F}(\boldsymbol{u};\boldsymbol{\phi}) = 0 \quad \forall \boldsymbol{\phi} \in \boldsymbol{\mathcal{V}}, \end{cases} \tag{5.68}$$

where the semilinear form[41] $\mathcal{F} \colon \boldsymbol{\mathcal{T}} \times \boldsymbol{\mathcal{V}} \to \mathbb{R}$ is defined as

$$\mathcal{F}(\boldsymbol{u};\boldsymbol{\phi}) := \int_{\Omega_{\boldsymbol{X}}} (\lambda \operatorname{tr}(\boldsymbol{E})\, \boldsymbol{F} + 2\mu \boldsymbol{F}\boldsymbol{E}) : \nabla_{\boldsymbol{X}} \boldsymbol{\phi} \, \mathrm{d}\Omega_{\boldsymbol{X}} - \int_{\Omega_{\boldsymbol{X}}} J\rho \boldsymbol{b} \cdot \boldsymbol{\phi} \, \mathrm{d}\Omega_{\boldsymbol{X}} - \int_{\Gamma_{N,\boldsymbol{X}}} \boldsymbol{g}_0 \cdot \boldsymbol{\phi} \, \mathrm{d}\Gamma_{N,\boldsymbol{X}} \tag{5.69}$$

5.2.3.2.2 Elastostatics in displacement formulation (Neo-Hookean material)

When it comes to the Neo-Hookean material, we have presented with (5.44) and (5.46a) two popular and alternative expressions for the corresponding first Piola-Kirchhoff stress tensor. Either one of these expressions can be used and we randomly select the former one to be inserted into (5.47). This yields

$$\begin{aligned} -\nabla_{\boldsymbol{X}} \cdot \big(\mu(\boldsymbol{F} - \boldsymbol{F}^{-T}) + \lambda \log(\det \boldsymbol{F}) \boldsymbol{F}^{-T}\big) &= J\rho \boldsymbol{b} && \text{in } \Omega_{\boldsymbol{X}}, \\ \boldsymbol{u} &= \boldsymbol{u}_D && \text{on } \Gamma_{D,\boldsymbol{X}}, \\ \boldsymbol{P}\, \boldsymbol{n}_0 &= \boldsymbol{g}_0 && \text{on } \Gamma_{N,\boldsymbol{X}}. \end{aligned} \tag{5.70}$$

The continuous nonlinear variational formulation of this problem is given through (5.68), where the semilinear form is now given as

$$\begin{aligned} \mathcal{F}(\boldsymbol{u};\boldsymbol{\phi}) := & \int_{\Omega_{\boldsymbol{X}}} \big(\mu(\boldsymbol{F} - \boldsymbol{F}^{-T}) + \lambda \log(\det \boldsymbol{F}) \boldsymbol{F}^{-T}\big) : \nabla_{\boldsymbol{X}} \boldsymbol{\phi} \, \mathrm{d}\Omega_{\boldsymbol{X}} \\ & - \int_{\Omega_{\boldsymbol{X}}} J\rho \boldsymbol{b} \cdot \boldsymbol{\phi} \, \mathrm{d}\Omega_{\boldsymbol{X}} - \int_{\Gamma_{N,\boldsymbol{X}}} \boldsymbol{g}_0 \cdot \boldsymbol{\phi} \, \mathrm{d}\Gamma_{N,\boldsymbol{X}}. \end{aligned} \tag{5.71}$$

5.2.3.2.3 Elastostatics in displacement-pressure formulation (Neo-Hookean material)

The formulation of the elastostatics problem presented now differs from the previous one in two aspects: Firstly, we make use of a mixed displacement-pressure formulation, and secondly we use the alternative first Piola-Kirchhoff stress tensor expression (5.46a) for the the Neo-Hookean material. Defining the additionally required (pressure) variable as

$$p := -\frac{\lambda}{2}(J - \frac{1}{J}),$$

---

[41] A semilinear form is linear in the test function(s) - the argument(s) subsequent to the semicolon.

equation (5.47) can be rewritten as

$$\begin{aligned}
-\nabla_{\boldsymbol{X}} \cdot \left(\mu(\boldsymbol{F} - \boldsymbol{F}^{-T}) - pJ\boldsymbol{F}^{-T}\right) &= J\rho\boldsymbol{b} && \text{in } \Omega_{\boldsymbol{X}}, \\
-\frac{1}{2}(J - \frac{1}{J}) - \frac{1}{\lambda}p &= 0 && \text{in } \Omega_{\boldsymbol{X}}, \\
\boldsymbol{u} &= \boldsymbol{u}_D && \text{on } \Gamma_{D,\boldsymbol{X}}, \\
\boldsymbol{P}\,\boldsymbol{n}_0 &= \boldsymbol{g}_0 && \text{on } \Gamma_{N,\boldsymbol{X}}.
\end{aligned} \tag{5.72}$$

Letting the pressure space be now defined as $\mathcal{Q} := \{q \mid q \in \mathcal{L}^2(\Omega_{\boldsymbol{X}})\}$, the continuous mixed non-linear variational formulation of the above problem reads:

$$\begin{cases} \text{Find } \boldsymbol{u} \in \boldsymbol{\mathcal{T}} \text{ and } p \in \mathcal{Q}, \text{ such that} \\ \mathcal{F}\left((\boldsymbol{u}, p); (\boldsymbol{\phi}, q)\right) = 0 \quad \forall (\boldsymbol{\phi}, q) \in \boldsymbol{\mathcal{V}} \times \mathcal{Q}, \end{cases} \tag{5.73}$$

where the semilinear form of this problem formulation is given as

$$\begin{aligned}
\mathcal{F}\left((\boldsymbol{u}, p); (\boldsymbol{\phi}, q)\right) := &\int_{\Omega_{\boldsymbol{X}}} \left(\mu(\boldsymbol{F} - \boldsymbol{F}^{-T}) - pJ\boldsymbol{F}^{-T}\right) : \nabla_{\boldsymbol{X}}\boldsymbol{\phi}\, \mathrm{d}\Omega_{\boldsymbol{X}} \\
&- \int_{\Omega_{\boldsymbol{X}}} \left(\frac{1}{2}(J - \frac{1}{J}) - \frac{1}{\lambda}p\right) \cdot q\, \mathrm{d}\Omega_{\boldsymbol{X}} \\
&- \int_{\Omega_{\boldsymbol{X}}} J\rho\boldsymbol{b} \cdot \boldsymbol{\phi}\, \mathrm{d}\Omega_{\boldsymbol{X}} - \int_{\Gamma_{N,\boldsymbol{X}}} \boldsymbol{g}_0 \cdot \boldsymbol{\phi}\, \mathrm{d}\Gamma_{N,\boldsymbol{X}}.
\end{aligned}$$

5.2.3.2.4 Elastodynamics in displacement-velocity formulation (St. Venant-Kirchhoff material)

The governing equations of elastodynamics given by the PDE (5.48) involves an acceleration term. In order to avoid having to deal with the second derivative of displacement with respect to time, the introduction of an additional (velocity) variable – given by the first temporal derivative of displacement – allows the PDE to be reformulated in terms of a system of first order in time equations. For the St. Venant-Kirchhoff material (cf. (5.41b)) we obtain:

$$\begin{aligned}
J\rho\frac{\partial \boldsymbol{v}}{\partial t} - \nabla_{\boldsymbol{X}} \cdot \left(\lambda \operatorname{tr}(\boldsymbol{E})\, \boldsymbol{F} + 2\mu\boldsymbol{F}\boldsymbol{E}\right) &= J\rho\boldsymbol{b} && \text{in } \Omega_{\boldsymbol{X}} \times I, \\
\frac{\partial \boldsymbol{u}}{\partial t} - \boldsymbol{v} &= 0 && \text{in } \Omega_{\boldsymbol{X}} \times I, \\
\boldsymbol{u}(\cdot, 0) = \mathring{\boldsymbol{u}}, \boldsymbol{v}(\cdot, 0) &= \mathring{\boldsymbol{v}} && \text{in } \Omega_{\boldsymbol{X}}, \\
\boldsymbol{u} = \boldsymbol{u}_D, \boldsymbol{v} &= \boldsymbol{v}_D && \text{on } \Gamma_{D,\boldsymbol{X}} \times I, \\
\boldsymbol{P}\,\boldsymbol{n}_0 &= \boldsymbol{g}_0 && \text{on } \Gamma_{N,\boldsymbol{X}} \times I.
\end{aligned} \tag{5.74}$$

Similar to (5.68), the continuous mixed nonlinear variational formulation of the above problem requires to

$$\text{Find } \boldsymbol{u}(\boldsymbol{X},t) \in \boldsymbol{\mathcal{T}} \times \boldsymbol{I} \text{ and } \boldsymbol{v}(\boldsymbol{X},t) \in \boldsymbol{\mathcal{T}} \times \boldsymbol{I}, \text{ such that } \forall(\boldsymbol{\phi}^{\boldsymbol{u}}, \boldsymbol{\phi}^{\boldsymbol{v}}) \in \boldsymbol{\mathcal{V}}: \tag{5.75a}$$

$$\begin{aligned} &\int_0^T \int_{\Omega_{\boldsymbol{X}}} J\rho\, \dot{\boldsymbol{v}} \cdot \boldsymbol{\phi}^{\boldsymbol{u}} \, \mathrm{d}\Omega_{\boldsymbol{X}} \, \mathrm{d}t + \int_0^T \int_{\Omega_{\boldsymbol{X}}} (\lambda \operatorname{tr}(\boldsymbol{E})\, \boldsymbol{F} + 2\mu \boldsymbol{F}\boldsymbol{E}) : \nabla_{\boldsymbol{X}} \boldsymbol{\phi}^{\boldsymbol{u}} \, \mathrm{d}\Omega_{\boldsymbol{X}} \, \mathrm{d}t \\ = &\int_0^T \int_{\Omega_{\boldsymbol{X}}} J\rho \boldsymbol{b} \cdot \boldsymbol{\phi}^{\boldsymbol{u}} \, \mathrm{d}\Omega_{\boldsymbol{X}} \, \mathrm{d}t + \int_0^T \int_{\Gamma_{N,\boldsymbol{X}}} \boldsymbol{g}_0 \cdot \boldsymbol{\phi}^{\boldsymbol{u}} \, \mathrm{d}\Gamma_{N,\boldsymbol{X}} \, \mathrm{d}t, \quad \text{and} \\ &\int_0^T \int_{\Omega_{\boldsymbol{X}}} (\dot{\boldsymbol{u}} - \boldsymbol{v}) \cdot \boldsymbol{\phi}^{\boldsymbol{v}} \, \mathrm{d}\Omega_{\boldsymbol{X}} \, \mathrm{d}t = 0. \end{aligned} \tag{5.75b}$$

5.2.3.2.5 Elastodynamics in displacement-velocity formulation (Neo-Hookean material)

The governing equations of elastodynamics in combination with the first Piola-Kirchhoff stress tensor expression of the Neo-Hookean material according to (5.44), leads to

$$\begin{aligned} J\rho \frac{\partial \boldsymbol{v}}{\partial t} - \nabla_{\boldsymbol{X}} \cdot \big(\mu(\boldsymbol{F} - \boldsymbol{F}^{-T}) + \lambda \log(\det \boldsymbol{F}) \boldsymbol{F}^{-T}\big) &= J\rho \boldsymbol{b} && \text{in } \Omega_{\boldsymbol{X}} \times I, \\ \frac{\partial \boldsymbol{u}}{\partial t} - \boldsymbol{v} &= 0 && \text{in } \Omega_{\boldsymbol{X}} \times I, \\ \boldsymbol{u}(\cdot, 0) = \mathring{\boldsymbol{u}}, \boldsymbol{v}(\cdot, 0) &= \mathring{\boldsymbol{v}} && \text{in } \Omega_{\boldsymbol{X}}, \\ \boldsymbol{u} &= \boldsymbol{u}_D && \text{on } \Gamma_{D,\boldsymbol{X}} \times I, \\ \boldsymbol{P}\boldsymbol{n}_0 &= \boldsymbol{g}_0 && \text{on } \Gamma_{N,\boldsymbol{X}} \times I. \end{aligned} \tag{5.76}$$

Its continuous mixed nonlinear variational formulation of the above problem is as follows:

$$\text{Find } \boldsymbol{u}(\boldsymbol{X},t) \in \boldsymbol{\mathcal{T}} \times \boldsymbol{I} \text{ and } \boldsymbol{v}(\boldsymbol{X},t) \in \boldsymbol{\mathcal{T}} \times \boldsymbol{I}, \text{ such that } \forall(\boldsymbol{\phi}^{\boldsymbol{u}}, \boldsymbol{\phi}^{\boldsymbol{v}}) \in \boldsymbol{\mathcal{V}}: \tag{5.77a}$$

$$\begin{aligned} &\int_0^T \int_{\Omega_{\boldsymbol{X}}} J\rho\, \dot{\boldsymbol{v}} \cdot \boldsymbol{\phi}^{\boldsymbol{u}} \, \mathrm{d}\Omega_{\boldsymbol{X}} \, \mathrm{d}t + \int_0^T \int_{\Omega_{\boldsymbol{X}}} \big(\mu(\boldsymbol{F} - \boldsymbol{F}^{-T}) + \lambda \log(\det \boldsymbol{F}) \boldsymbol{F}^{-T}\big) : \nabla_{\boldsymbol{X}} \boldsymbol{\phi}^{\boldsymbol{u}} \, \mathrm{d}\Omega_{\boldsymbol{X}} \, \mathrm{d}t \\ = &\int_0^T \int_{\Omega_{\boldsymbol{X}}} J\rho \boldsymbol{b} \cdot \boldsymbol{\phi}^{\boldsymbol{u}} \, \mathrm{d}\Omega_{\boldsymbol{X}} \, \mathrm{d}t + \int_0^T \int_{\Gamma_{N,\boldsymbol{X}}} \boldsymbol{g}_0 \cdot \boldsymbol{\phi}^{\boldsymbol{u}} \, \mathrm{d}\Gamma_{N,\boldsymbol{X}} \, \mathrm{d}t, \quad \text{and} \\ &\int_0^T \int_{\Omega_{\boldsymbol{X}}} (\dot{\boldsymbol{u}} - \boldsymbol{v}) \cdot \boldsymbol{\phi}^{\boldsymbol{v}} \, \mathrm{d}\Omega_{\boldsymbol{X}} \, \mathrm{d}t = 0. \end{aligned} \tag{5.77b}$$

5.2.3.3 Treatment of nonlinearity

All variational formulations presented in Section 5.2.3.2 refer to stationary and transient nonlinear problems. Considering the more general case of a time dependent problem, one faces after temporal discretization in each single time step a nonlinear quasi-stationary problem

$$A(\boldsymbol{u}; \boldsymbol{\phi}) = F(\boldsymbol{\phi}) \quad \forall \boldsymbol{\phi} \in \boldsymbol{\mathcal{V}},$$

whose residual is given as

$$\mathcal{F} \equiv R(\boldsymbol{u}) = A(\boldsymbol{u}; \boldsymbol{\phi}) - F(\boldsymbol{\phi}).$$

We point out at this point that the above representation form suits just as well to a stationary problem. As shown in (5.68), the nonlinear residual is typically expressed in terms of a semilinear form $\mathcal{F}$ which is required to vanish for all test functions of the underlying test space. Newton's method is our method of choice for the treatment of nonlinearity. Exemplary choosing the semilinear form given by (5.69), Newton's method requires - until convergence ($\|\mathcal{F}\| \leq \epsilon_{tol}$) - the following problem to be solved in each iteration k:

$$\begin{aligned} &\text{Find } \delta \boldsymbol{u} \in \boldsymbol{\mathcal{T}}, \text{ such that} \\ &\mathcal{F}'(\boldsymbol{u}^k; \delta \boldsymbol{u}, \boldsymbol{\phi}) = -\mathcal{F}(\boldsymbol{u}^k; \boldsymbol{\phi}), \quad \forall \boldsymbol{\phi} \in \boldsymbol{\mathcal{V}} \\ &\boldsymbol{u}^{k+1} = \boldsymbol{u}^k + \omega\, \delta \boldsymbol{u}. \end{aligned} \tag{5.78}$$

Above, the bilinear form $\mathcal{F}'(\boldsymbol{u}^k; \delta\boldsymbol{u}, \boldsymbol{w})$ is the Gâteaux derivative (Jacobian) of $\mathcal{F}$ and is obtained from the linearization of $\mathcal{F}$ around a fixed $\boldsymbol{u} \equiv \boldsymbol{u}^k$. Note that for each fixed $\boldsymbol{u}^k$, $\mathcal{F}'(\boldsymbol{u}^k; \cdot, \cdot)$ is a bilinear form and $\mathcal{F}(\boldsymbol{u}^k; \cdot)$ is a linear form. The action of the latter yields a vector which is obtained from the evaluation of the partial differential equation operator with the most current already available values for $\boldsymbol{u}$, that is, $\boldsymbol{u}^k$.

For (5.78) we need to compute the directional derivative of a semilinear form $A(\boldsymbol{u}; \boldsymbol{\phi})$ at $\boldsymbol{u}$ in direction $\delta\boldsymbol{u}$ that is tested with $\boldsymbol{\phi}$:

$$A'(\boldsymbol{u}; \delta\boldsymbol{u}, \boldsymbol{\phi}) := \lim_{\epsilon \to 0} \frac{A(\boldsymbol{u} + \epsilon\delta\boldsymbol{u}; \boldsymbol{\phi}) - A(\boldsymbol{u}; \boldsymbol{\phi})}{\epsilon} = \frac{d}{d\epsilon} A(\boldsymbol{u} + \epsilon\delta\boldsymbol{u}; \boldsymbol{\phi})\Big|_{\epsilon=0}.$$

Since the semilinear form A involves invertible matrix-valued operators, we need to compute derivatives of these operators. Let $\boldsymbol{F}$ denote – for the time being – an invertible matrix-valued operator and let $J := \det \boldsymbol{F}$. Then, recalling the definition of the directional derivative presented on page 124 it holds

(i) $D_{\boldsymbol{\delta z}}[\boldsymbol{F}] = \nabla \boldsymbol{\delta z}$,

(ii) $D_{\boldsymbol{\delta z}}[\boldsymbol{F}^T] = (\nabla \boldsymbol{\delta z})^T$,

(iii) $D_{\boldsymbol{\delta z}}[\boldsymbol{F}^{-1}] = -\boldsymbol{F}^{-1}\, \nabla \boldsymbol{\delta z}\, \boldsymbol{F}^{-1}$,

(iv) $D_{\boldsymbol{\delta z}}[\boldsymbol{F}^{-T}] = -\boldsymbol{F}^{-T}\, (\nabla \boldsymbol{\delta z})^T\, \boldsymbol{F}^{-T}$,

(v) $D_{\boldsymbol{\delta z}}[J] = J\, \mathrm{tr}\left(\boldsymbol{F}^{-1}\, \nabla \boldsymbol{\delta z}\right) = J\, \boldsymbol{F}^{-T} : \nabla \boldsymbol{\delta z}$.

For a proof of these basic relations, we refer to [72, 123].

The nonlinear problems (5.69), (5.71), (5.93b), and (5.88b) stand for four different peculiarities of $\mathcal{F}$. It remains to specify their respective Jacobians so as to complete the requirements of Newton's method sketched in (5.78). In the sequel, we will successively present the analytically derived Jacobians of the nonlinear problems listed above.

5.2.3.3.1 Analytical Jacobian for elastostatics in displacement formulation (St. Venant-Kirchhoff material)

In (5.66) and accordingly (5.69) the first Piola-Kirchhoff stress tensor $\boldsymbol{P}$ is given through the following nonlinear function of the displacement $\boldsymbol{u}$:

$$\boldsymbol{P}(\boldsymbol{u}) := 2\mu \boldsymbol{F}(\boldsymbol{u})\boldsymbol{E}(\boldsymbol{u}) + \lambda\, \mathrm{tr}\left(\boldsymbol{E}(\boldsymbol{u})\right) \boldsymbol{F}(\boldsymbol{u}). \tag{5.79}$$

In order to setup the exact Jacobian, we need to compute the derivative of this expression with respect to the only unknown $\boldsymbol{u}$, for (5.66) is a displacement only formulation. In mixed formulations we need to also account for the other unknowns.

$$\begin{aligned}&\partial_{\delta \boldsymbol{U}}[\boldsymbol{P}]\\ =&D_{\delta \boldsymbol{u}}\left[2\mu \boldsymbol{F}\boldsymbol{E} + \lambda \operatorname{tr}(\boldsymbol{E})\boldsymbol{F}\right]\\ =&\underbrace{D_{\delta \boldsymbol{u}}\left[2\mu \boldsymbol{F}\boldsymbol{E}\right]}_{(1)} + \underbrace{D_{\delta \boldsymbol{u}}\left[\lambda \operatorname{tr}(\boldsymbol{E})\boldsymbol{F}\right].}_{(2)}\end{aligned} \tag{5.80a}$$

$$\begin{aligned}(1):&D_{\delta \boldsymbol{u}}\left[2\mu \boldsymbol{F}\boldsymbol{E}\right]\\ =&D_{\delta \boldsymbol{u}}\left[2\mu \boldsymbol{F}\right]\boldsymbol{E} + 2\mu \boldsymbol{F} D_{\delta \boldsymbol{u}}\left[\boldsymbol{E}\right]\\ =&2\mu(\nabla_{\boldsymbol{X}}\delta \boldsymbol{u})\boldsymbol{E} + 2\mu \boldsymbol{F} D_{\delta \boldsymbol{u}}\left[\frac{1}{2}\left(\boldsymbol{F}^T\boldsymbol{F} - \boldsymbol{I}\right)\right]\\ =&2\mu(\nabla_{\boldsymbol{X}}\delta \boldsymbol{u})\boldsymbol{E} + 2\mu \boldsymbol{F}\left(D_{\delta \boldsymbol{u}}\left[\frac{1}{2}\boldsymbol{F}^T\right]\boldsymbol{F} + \frac{1}{2}\boldsymbol{F}^T D_{\delta \boldsymbol{u}}\left[\boldsymbol{F}\right]\right)\\ =&2\mu(\nabla_{\boldsymbol{X}}\delta \boldsymbol{u})\boldsymbol{E} + 2\mu \boldsymbol{F}\left(\frac{1}{2}(\nabla_{\boldsymbol{X}}\delta \boldsymbol{u})^T\boldsymbol{F} + \frac{1}{2}\boldsymbol{F}^T\nabla_{\boldsymbol{X}}\delta \boldsymbol{u}\right)\\ =&2\mu\left((\nabla_{\boldsymbol{X}}\delta \boldsymbol{u})\boldsymbol{E} + \boldsymbol{F}\left(\frac{1}{2}(\nabla_{\boldsymbol{X}}\delta \boldsymbol{u})^T\boldsymbol{F} + \frac{1}{2}\boldsymbol{F}^T\nabla_{\boldsymbol{X}}\delta \boldsymbol{u}\right)\right).\end{aligned} \tag{5.80b}$$

$$\begin{aligned}(2):&D_{\delta \boldsymbol{u}}\left[\lambda \operatorname{tr}(\boldsymbol{E})\boldsymbol{F}\right]\\ =&D_{\delta \boldsymbol{u}}\left[\lambda \operatorname{tr}(\boldsymbol{E})\right]\boldsymbol{F} + \lambda \operatorname{tr}(\boldsymbol{E}) D_{\delta \boldsymbol{u}}\left[\boldsymbol{F}\right]\\ =&\lambda \operatorname{tr}\left(\frac{1}{2}\left((\nabla_{\boldsymbol{X}}\delta \boldsymbol{u})^T\boldsymbol{F} + \boldsymbol{F}^T\nabla_{\boldsymbol{X}}\delta \boldsymbol{u}\right)\right)\boldsymbol{F} + \lambda \operatorname{tr}(\boldsymbol{E})\nabla_{\boldsymbol{X}}\delta \boldsymbol{u}.\end{aligned} \tag{5.80c}$$

Putting all results together, the exact Jacobian of (5.69) can be assembled with the following bilinear form

$$\begin{aligned}&\mathcal{F}'(\boldsymbol{u}^k;\delta \boldsymbol{u},\boldsymbol{\phi}) :=\\ &\int_{\Omega_{\boldsymbol{X}}} 2\mu\left((\nabla_{\boldsymbol{X}}\delta \boldsymbol{u})\boldsymbol{E}(\boldsymbol{u}^k) + \boldsymbol{F}(\boldsymbol{u}^k)\left(\frac{1}{2}(\nabla_{\boldsymbol{X}}\delta \boldsymbol{u})^T\boldsymbol{F}(\boldsymbol{u}^k) + \frac{1}{2}\boldsymbol{F}(\boldsymbol{u}^k)^T\nabla_{\boldsymbol{X}}\delta \boldsymbol{u}\right)\right) : \nabla_{\boldsymbol{X}}\boldsymbol{\phi}\,\mathrm{d}\Omega_{\boldsymbol{X}}\\ +&\int_{\Omega_{\boldsymbol{X}}}\left(\lambda \operatorname{tr}\left(\frac{1}{2}\left((\nabla_{\boldsymbol{X}}\delta \boldsymbol{u})^T\boldsymbol{F}(\boldsymbol{u}^k) + \boldsymbol{F}(\boldsymbol{u}^k)^T\nabla_{\boldsymbol{X}}\delta \boldsymbol{u}\right)\right)\boldsymbol{F}(\boldsymbol{u}^k) + \lambda \operatorname{tr}\left(\boldsymbol{E}(\boldsymbol{u}^k)\right)\nabla_{\boldsymbol{X}}\delta \boldsymbol{u}\right) : \nabla_{\boldsymbol{X}}\boldsymbol{\phi}\,\mathrm{d}\Omega_{\boldsymbol{X}}.\end{aligned} \tag{5.81}$$

5.2.3.3.2 Analytical Jacobian for elastostatics in displacement formulation (Neo-Hookean material)

The nonlinearity in (5.70) and (5.71) is due to the following nonlinear expression for the first Piola-Kirchhoff stress tensor:

$$\boldsymbol{P}(\boldsymbol{u}) := \mu(\boldsymbol{F}(\boldsymbol{u}) - \boldsymbol{F}(\boldsymbol{u})^{-T}) + \lambda \log(\det \boldsymbol{F}(\boldsymbol{u}))\boldsymbol{F}(\boldsymbol{u})^{-T}. \tag{5.82}$$

We proceed with the computation of the derivative of this expression:

$$\begin{aligned}
&D_{\delta \boldsymbol{U}}[\boldsymbol{P}] \\
=&D_{\delta \boldsymbol{u}}\left[\mu(\boldsymbol{F}-\boldsymbol{F}^{-T})+\lambda \log(\det \boldsymbol{F})\boldsymbol{F}^{-T}\right] \\
=&\underbrace{D_{\delta \boldsymbol{u}}\left[\mu(\boldsymbol{F}-\boldsymbol{F}^{-T})\right]}_{(1)}+\underbrace{D_{\delta \boldsymbol{u}}\left[\lambda \log(\det \boldsymbol{F})\boldsymbol{F}^{-T}\right].}_{(2)}
\end{aligned} \tag{5.83a}$$

$$\begin{aligned}
&(1): D_{\delta \boldsymbol{u}}\left[\mu(\boldsymbol{F}-\boldsymbol{F}^{-T})\right] \\
&=\mu\left(\nabla_{\boldsymbol{X}}\delta \boldsymbol{u}-\left(-\boldsymbol{F}^{-T}(\nabla_{\boldsymbol{X}}\delta \boldsymbol{u})^T\boldsymbol{F}^{-T}\right)\right).
\end{aligned} \tag{5.83b}$$

$$\begin{aligned}
&(2): D_{\delta \boldsymbol{u}}\left[\lambda \log(\det \boldsymbol{F})\boldsymbol{F}^{-T}\right] \\
&=D_{\delta \boldsymbol{u}}\left[\lambda \log(\det \boldsymbol{F})\right]\boldsymbol{F}^{-T}+\lambda \log(\det \boldsymbol{F})D_{\delta \boldsymbol{u}}\left[\boldsymbol{F}^{-T}\right] \\
&=\lambda/(J\log(e))\,J\operatorname{tr}\left(\boldsymbol{F}^{-1}\nabla_{\boldsymbol{X}}\delta \boldsymbol{u}\right)\boldsymbol{F}^{-T}+\lambda\log(J)\left(-\boldsymbol{F}^{-T}(\nabla_{\boldsymbol{X}}\delta \boldsymbol{u})^T\boldsymbol{F}^{-T}\right) \\
&=\lambda\operatorname{tr}\left(\boldsymbol{F}^{-1}\nabla_{\boldsymbol{X}}\delta \boldsymbol{u}\right)\boldsymbol{F}^{-T}+\lambda\log(J)\left(-\boldsymbol{F}^{-T}(\nabla_{\boldsymbol{X}}\delta \boldsymbol{u})^T\boldsymbol{F}^{-T}\right).
\end{aligned} \tag{5.83c}$$

It follows from these results that the Jacobian of (5.71) can be obtained from the action of the following bilinear form

$$\begin{aligned}
&\mathcal{F}'(\boldsymbol{u}^k;\delta \boldsymbol{u},\boldsymbol{\phi}):= \\
&\int_{\Omega_{\boldsymbol{X}}}\mu\left(\nabla_{\boldsymbol{X}}\delta \boldsymbol{u}-\left(-\boldsymbol{F}(\boldsymbol{u}^k)^{-T}(\nabla_{\boldsymbol{X}}\delta \boldsymbol{u})^T\boldsymbol{F}(\boldsymbol{u}^k)^{-T}\right)\right):\nabla_{\boldsymbol{X}}\boldsymbol{\phi}\,\mathrm{d}\Omega_{\boldsymbol{X}} \\
+&\int_{\Omega_{\boldsymbol{X}}}\left(\lambda\operatorname{tr}\left(\boldsymbol{F}(\boldsymbol{u}^k)^{-1}\nabla_{\boldsymbol{X}}\delta \boldsymbol{u}\right)\boldsymbol{F}(\boldsymbol{u}^k)^{-T}+\lambda\log(J(\boldsymbol{u}^k))\left(-\boldsymbol{F}(\boldsymbol{u}^k)^{-T}(\nabla_{\boldsymbol{X}}\delta \boldsymbol{u})^T\boldsymbol{F}(\boldsymbol{u}^k)^{-T}\right)\right):\nabla_{\boldsymbol{X}}\boldsymbol{\phi}\,\mathrm{d}\Omega_{\boldsymbol{X}}.
\end{aligned} \tag{5.84}$$

5.2.3.3.3 Analytical Jacobian for elastodynamics in displacement-velocity formulation (St. Venant-Kirchhoff material)

The transient nature of the nonlinear problems (5.75) and (5.77) requires discretization in time, for which various approaches such as space-time Galerkin methods as well as classical "finite difference type" time integrators are at one's disposal.

Discretizing the time dependent problem (5.75) in time with the one-step θ-scheme, we arrive at the following nonlinear quasi-stationary problem which needs to be solved in every time step:

$$\begin{aligned}
&\text{Find } \boldsymbol{u}(\boldsymbol{X}) \in \boldsymbol{\mathcal{T}} \text{ and } \boldsymbol{v}(\boldsymbol{X}) \in \boldsymbol{\mathcal{T}}, \text{ such that } \forall(\boldsymbol{\phi}^{\boldsymbol{u}}, \boldsymbol{\phi}^{\boldsymbol{v}}) \in \boldsymbol{\mathcal{V}}: && (5.85\text{a})\\
&\int_{\Omega_{\boldsymbol{X}}} J\rho\,(\boldsymbol{v} - \boldsymbol{v}^n) \cdot \boldsymbol{\phi}^{\boldsymbol{u}} \,\mathrm{d}\Omega_{\boldsymbol{X}}\\
+&\int_{\Omega_{\boldsymbol{X}}} \Delta t\theta\,(\lambda\,\mathrm{tr}\,(\boldsymbol{E}(\boldsymbol{u}))\,\boldsymbol{F}(\boldsymbol{u}) + 2\mu\boldsymbol{F}(\boldsymbol{u})\boldsymbol{E}(\boldsymbol{u})) : \nabla_{\boldsymbol{X}}\boldsymbol{\phi}^{\boldsymbol{u}} \,\mathrm{d}\Omega_{\boldsymbol{X}}\\
+&\int_{\Omega_{\boldsymbol{X}}} \Delta t\,(1-\theta)\,(\lambda\,\mathrm{tr}\,(\boldsymbol{E}(\boldsymbol{u}^n))\,\boldsymbol{F}(\boldsymbol{u}^n) + 2\mu\boldsymbol{F}(\boldsymbol{u}^n)\boldsymbol{E}(\boldsymbol{u}^n)) : \nabla_{\boldsymbol{X}}\boldsymbol{\phi}^{\boldsymbol{u}} \,\mathrm{d}\Omega_{\boldsymbol{X}}\\
=&\int_{\Omega_{\boldsymbol{X}}} \Delta t\theta\, J\rho\boldsymbol{b}(\boldsymbol{u}) \cdot \boldsymbol{\phi}^{\boldsymbol{u}} \,\mathrm{d}\Omega_{\boldsymbol{X}} + \int_{\Gamma_{N,\boldsymbol{X}}} \Delta t\theta\,\boldsymbol{g}_0(\boldsymbol{u}) \cdot \boldsymbol{\phi}^{\boldsymbol{u}} \,\mathrm{d}\Gamma_{N,\boldsymbol{X}}\\
+&\int_{\Omega_{\boldsymbol{X}}} \Delta t\,(1-\theta)\, J\rho\boldsymbol{b}(\boldsymbol{u}^n) \cdot \boldsymbol{\phi}^{\boldsymbol{u}} \,\mathrm{d}\Omega_{\boldsymbol{X}} + \int_{\Gamma_{N,\boldsymbol{X}}} \Delta t\,(1-\theta)\,\boldsymbol{g}_0(\boldsymbol{u}^n) \cdot \boldsymbol{\phi}^{\boldsymbol{u}} \,\mathrm{d}\Gamma_{N,\boldsymbol{X}}, \quad \text{and}\\
&\int_{\Omega_{\boldsymbol{X}}} (\boldsymbol{u} - \boldsymbol{u}^n) \cdot \boldsymbol{\phi}^{\boldsymbol{v}} \,\mathrm{d}\Omega_{\boldsymbol{X}}\,\mathrm{d}t - \int_{\Omega_{\boldsymbol{X}}} \Delta t\theta\,\boldsymbol{v} \cdot \boldsymbol{\phi}^{\boldsymbol{v}} \,\mathrm{d}\Omega_{\boldsymbol{X}}\,\mathrm{d}t - \int_{\Omega_{\boldsymbol{X}}} \Delta t\,(1-\theta)\,\boldsymbol{v}^n \cdot \boldsymbol{\phi}^{\boldsymbol{v}} \,\mathrm{d}\Omega_{\boldsymbol{X}}\,\mathrm{d}t = 0, && (5.85\text{b})
\end{aligned}$$

where $\boldsymbol{u}^n$ and $\boldsymbol{v}^n$ denote the already known displacement and velocity functions of the previous time step n. Note that above we have refrained from explicitly specifying the time index of field variables at the new time step $n+1$, and therefore $\boldsymbol{u}^{n+1}$ is simply represented as $\boldsymbol{u}$ and likewise $\boldsymbol{v}^{n+1}$ as $\boldsymbol{v}$. This convention may be applied throughout this work in the context of finite difference expansions of temporal derivatives for the sake of a more compact notation.

The source of the nonlinearity in the above problem is already given in (5.79) and we presented the computation of its derivative in (5.80a). Therefore, with

$$\begin{aligned}
&D_{\delta\boldsymbol{U}}\,[J\rho\boldsymbol{v}]\\
=&D_{\delta\boldsymbol{u}}\,[J\rho\boldsymbol{v}] + D_{\delta\boldsymbol{v}}\,[J\rho\boldsymbol{v}] && (5.86\text{a})\\
=&J\mathrm{tr}\left(\boldsymbol{F}^{-1}\nabla_{\boldsymbol{X}}\delta\boldsymbol{u}\right)\rho\boldsymbol{v} + J\rho\,\delta\boldsymbol{v}, \quad \text{and}\\
&D_{\delta\boldsymbol{U}}\,[\boldsymbol{u} - \Delta t\theta\,\boldsymbol{v}]\\
=&D_{\delta\boldsymbol{u}}\,[\boldsymbol{u} - \Delta t\theta\,\boldsymbol{v}] + D_{\delta\boldsymbol{v}}\,[\boldsymbol{u} - \Delta t\theta\,\boldsymbol{v}] && (5.86\text{b})\\
=&\delta\boldsymbol{u} - \Delta t\theta\,\delta\boldsymbol{v},
\end{aligned}$$

the bilinear form whose action assembles the Jacobian of (5.93b) is basically given through (5.81) plus the terms that do not vanish in the computation of the derivative. It reads

$$\begin{aligned}
&\mathcal{F}'(\boldsymbol{u}^k; \delta\boldsymbol{u}, \delta\boldsymbol{v}, \boldsymbol{\phi}^{\boldsymbol{u}}, \boldsymbol{\phi}^{\boldsymbol{v}}) :=\\
&\int_{\Omega_{\boldsymbol{X}}} \left(J\mathrm{tr}\left(\boldsymbol{F}^{-1}\nabla_{\boldsymbol{X}}\delta\boldsymbol{u}\right)\rho\boldsymbol{v} + J\rho\,\delta\boldsymbol{v}\right) \cdot \boldsymbol{\phi}^{\boldsymbol{u}} \,\mathrm{d}\Omega_{\boldsymbol{X}}\\
+&\int_{\Omega_{\boldsymbol{X}}} \Delta t\theta 2\mu \left((\nabla_{\boldsymbol{X}}\delta\boldsymbol{u})\boldsymbol{E}(\boldsymbol{u}^k) + \boldsymbol{F}(\boldsymbol{u}^k)\left(\frac{1}{2}(\nabla_{\boldsymbol{X}}\delta\boldsymbol{u})^T\boldsymbol{F}(\boldsymbol{u}^k) + \frac{1}{2}\boldsymbol{F}(\boldsymbol{u}^k)^T\nabla_{\boldsymbol{X}}\delta\boldsymbol{u}\right)\right) : \nabla_{\boldsymbol{X}}\boldsymbol{\phi}^{\boldsymbol{u}} \,\mathrm{d}\Omega_{\boldsymbol{X}}\\
+&\int_{\Omega_{\boldsymbol{X}}} \Delta t\theta \left(\lambda\,\mathrm{tr}\left(\frac{1}{2}\left((\nabla_{\boldsymbol{X}}\delta\boldsymbol{u})^T\boldsymbol{F}(\boldsymbol{u}^k) + \boldsymbol{F}(\boldsymbol{u}^k)^T\nabla_{\boldsymbol{X}}\delta\boldsymbol{u}\right)\right)\boldsymbol{F}(\boldsymbol{u}^k) + \lambda\,\mathrm{tr}\left(\boldsymbol{E}(\boldsymbol{u}^k)\right)\nabla_{\boldsymbol{X}}\delta\boldsymbol{u}\right) : \nabla_{\boldsymbol{X}}\boldsymbol{\phi}^{\boldsymbol{u}} \,\mathrm{d}\Omega_{\boldsymbol{X}}\\
+&\int_{\Omega_{\boldsymbol{X}}} \delta\boldsymbol{u} \cdot \boldsymbol{\phi}^{\boldsymbol{v}} \,\mathrm{d}\Omega_{\boldsymbol{X}} - \int_{\Omega_{\boldsymbol{X}}} \Delta t\theta\,\delta\boldsymbol{v} \cdot \boldsymbol{\phi}^{\boldsymbol{v}} \,\mathrm{d}\Omega_{\boldsymbol{X}}. && (5.87)
\end{aligned}$$

5.2.3.3.4 Analytical Jacobian for elastodynamics in displacement-velocity formulation (Neo-Hookean material)

Similar to the previous section, the time-discretization of equation (5.77) with the one-step θ-scheme, yields the following problem:

$$\text{Find } \boldsymbol{u}(\boldsymbol{X}) \in \boldsymbol{\mathcal{T}} \text{ and } \boldsymbol{v}(\boldsymbol{X}) \in \boldsymbol{\mathcal{T}}, \text{ such that } \forall(\boldsymbol{\phi}^{\boldsymbol{u}}, \boldsymbol{\phi}^{\boldsymbol{v}}) \in \boldsymbol{\mathcal{V}}: \tag{5.88a}$$

$$\begin{aligned}
&\int_{\Omega_{\boldsymbol{X}}} J\rho\,(\boldsymbol{v}-\boldsymbol{v}^n)\cdot\boldsymbol{\phi}^{\boldsymbol{u}}\,\mathrm{d}\Omega_{\boldsymbol{X}}\\
&+\int_{\Omega_{\boldsymbol{X}}} \Delta t\theta\left(\mu\left(\boldsymbol{F}(\boldsymbol{u})-\boldsymbol{F}(\boldsymbol{u})^{-T}\right)+\lambda\log(\det\boldsymbol{F}(\boldsymbol{u}))\boldsymbol{F}(\boldsymbol{u})^{-T}\right):\nabla_{\boldsymbol{X}}\boldsymbol{\phi}^{\boldsymbol{u}}\,\mathrm{d}\Omega_{\boldsymbol{X}}\\
&+\int_{\Omega_{\boldsymbol{X}}} \Delta t\,(1-\theta)\left(\mu\left(\boldsymbol{F}(\boldsymbol{u}^n)-\boldsymbol{F}(\boldsymbol{u}^n)^{-T}\right)+\lambda\log(\det\boldsymbol{F}(\boldsymbol{u}^n))\boldsymbol{F}(\boldsymbol{u}^n)^{-T}\right):\nabla_{\boldsymbol{X}}\boldsymbol{\phi}^{\boldsymbol{u}}\,\mathrm{d}\Omega_{\boldsymbol{X}}\\
&=\int_{\Omega_{\boldsymbol{X}}} \Delta t\theta\,J\rho\boldsymbol{b}(\boldsymbol{u})\cdot\boldsymbol{\phi}^{\boldsymbol{u}}\,\mathrm{d}\Omega_{\boldsymbol{X}}+\int_{\Gamma_{N,\boldsymbol{X}}}\Delta t\theta\,\boldsymbol{g}_0(\boldsymbol{u})\cdot\boldsymbol{\phi}^{\boldsymbol{u}}\,\mathrm{d}\Gamma_{N,\boldsymbol{X}}\\
&+\int_{\Omega_{\boldsymbol{X}}} \Delta t\,(1-\theta)\,J\rho\boldsymbol{b}(\boldsymbol{u}^n)\cdot\boldsymbol{\phi}^{\boldsymbol{u}}\,\mathrm{d}\Omega_{\boldsymbol{X}}+\int_{\Gamma_{N,\boldsymbol{X}}}\Delta t\,(1-\theta)\,\boldsymbol{g}_0(\boldsymbol{u}^n)\cdot\boldsymbol{\phi}^{\boldsymbol{u}}\,\mathrm{d}\Gamma_{N,\boldsymbol{X}},\quad\text{and}\\
&\int_{\Omega_{\boldsymbol{X}}}(\boldsymbol{u}-\boldsymbol{u}^n)\cdot\boldsymbol{\phi}^{\boldsymbol{v}}\,\mathrm{d}\Omega_{\boldsymbol{X}}\,\mathrm{d}t-\int_{\Omega_{\boldsymbol{X}}}\Delta t\theta\,\boldsymbol{v}\cdot\boldsymbol{\phi}^{\boldsymbol{v}}\,\mathrm{d}\Omega_{\boldsymbol{X}}\,\mathrm{d}t-\int_{\Omega_{\boldsymbol{X}}}\Delta t\,(1-\theta)\,\boldsymbol{v}^n\cdot\boldsymbol{\phi}^{\boldsymbol{v}}\,\mathrm{d}\Omega_{\boldsymbol{X}}\,\mathrm{d}t=0.
\end{aligned}\tag{5.88b}$$

The source of the nonlinearity in the above problem is already given in (5.82) and we presented the computation of its derivative in (5.83a). Therefore the bilinear form whose action assembles the Jacobian of (5.88b) is basically given through (5.84) plus the terms that do not vanish in the computation of the derivative. It reads

$$\begin{aligned}
&\mathcal{F}'(\boldsymbol{u}^k;\delta\boldsymbol{u},\delta\boldsymbol{v},\boldsymbol{\phi}^{\boldsymbol{u}},\boldsymbol{\phi}^{\boldsymbol{v}}):=\\
&\int_{\Omega_{\boldsymbol{X}}}\left(J\mathrm{tr}\left(\boldsymbol{F}^{-1}\nabla_{\boldsymbol{X}}\delta\boldsymbol{u}\right)\rho\boldsymbol{v}+J\rho\,\delta\boldsymbol{v}\right)\cdot\boldsymbol{\phi}^{\boldsymbol{u}}\,\mathrm{d}\Omega_{\boldsymbol{X}}\\
&\int_{\Omega_{\boldsymbol{X}}}\Delta t\theta\mu\left(\nabla_{\boldsymbol{X}}\delta\boldsymbol{u}-\left(-\boldsymbol{F}(\boldsymbol{u}^k)^{-T}(\nabla_{\boldsymbol{X}}\delta\boldsymbol{u})^T\boldsymbol{F}(\boldsymbol{u}^k)^{-T}\right)\right):\nabla_{\boldsymbol{X}}\boldsymbol{\phi}^{\boldsymbol{u}}\,\mathrm{d}\Omega_{\boldsymbol{X}}\\
&+\int_{\Omega_{\boldsymbol{X}}}\Delta t\theta\left(\lambda\,\mathrm{tr}\left(\boldsymbol{F}(\boldsymbol{u}^k)^{-1}\nabla_{\boldsymbol{X}}\delta\boldsymbol{u}\right)\boldsymbol{F}(\boldsymbol{u}^k)^{-T}+\lambda\log(J(\boldsymbol{u}^k))\left(-\boldsymbol{F}(\boldsymbol{u}^k)^{-T}(\nabla_{\boldsymbol{X}}\delta\boldsymbol{u})^T\boldsymbol{F}(\boldsymbol{u}^k)^{-T}\right)\right):\nabla_{\boldsymbol{X}}\boldsymbol{\phi}^{\boldsymbol{u}}\,\mathrm{d}\Omega_{\boldsymbol{X}}\\
&+\int_{\Omega_{\boldsymbol{X}}}\delta\boldsymbol{u}\cdot\boldsymbol{\phi}^{\boldsymbol{v}}\,\mathrm{d}\Omega_{\boldsymbol{X}}-\int_{\Omega_{\boldsymbol{X}}}\Delta t\theta\,\delta\boldsymbol{v}\cdot\boldsymbol{\phi}^{\boldsymbol{v}}\,\mathrm{d}\Omega_{\boldsymbol{X}}.
\end{aligned}\tag{5.89}$$

5.2.4 Application to the Turek-Hron structural mechanics benchmark problems

For the validation of the nonlinear elasticity component of our IGA-based fluid-structure interaction solver, we adopt the *Computational Structural Mechanics* (*CSM*) tests of the FSI benchmark proposed in [58, 148]. These tests consider an elastic bar (cantilever beam) that is anchored at one end to a fixed support and is subject to an applied body force such as the gravitational force. The geometrical setup of the CSM tests is depicted in Figure 5.1. The elastic bar of length $l = 0.35$ and thickness $h = 0.02$ is attached to a rigid cylinder with center $C = (0.2, 0.2)$ and radius $r = 0.05$. The quantity of interest in all CSM benchmark tests is the displacement (u_1, u_2) of a reference point (at $t = 0$)

$A = (0.6, 0.2)$. All specified parameters are in si units (e.g. the distances are given in meters).

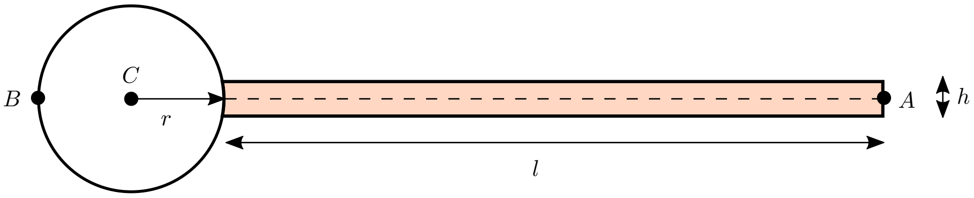

Figure 5.1: Elastic bar clamped to a rigid cylinder.

The CSM tests comprise three tests whose parameters are presented in table 5.1.

Parameter	Description	Unit	CSM 1	CSM 2	CSM 3
ρ^s	Density	$[\mathrm{kg/m^3}]$	1000	1000	1000
ν^s	Poisson's ratio		0.4	0.4	0.4
μ^s	Lamé constant	$[\mathrm{kg/(m\,s^2)}]$	0.5×10^6	2×10^6	0.5×10^6
E^s	Young's modulus	$[\mathrm{kg/(m\,s^2)}]$	1.4×10^6	5.6×10^6	1.4×10^6
g	Gravitational acceleration	$[\mathrm{m/s^2}]$	2	2	2

Table 5.1: Parameter settings for the CSM tests.

CSM 1 and CSM 2 present steady state cases while CSM 3 is computed as a time dependent case starting from the undeformed configuration. The numerical treatment of the dynamics involving CSM 3 case is discussed in Section 5.2.4.1. For the steady state problems CSM 1 and CSM 2 we use Isogeometric Analysis to solve the elastostatics equation for both St. Venant-Kirchhoff and Neo-Hookean materials (cf. equations (5.66) and (5.70)). As for a discrete spline-based approximation space, we use a $\mathcal{C}^0$ $\boldsymbol{\mathcal{N}}^{2,2}_{0,0}$ NURBS space for the approximation of the displacement function $\boldsymbol{u}$ in all CSM tests, and for the approximation of the velocity function $\boldsymbol{v}$ in the CSM 3 test.

The discrete nonlinear variational formulation of the problem (5.68) is then simply obtained by confining the trial and test spaces to their finite dimensional counterparts, that is

$$\begin{cases} \text{Find } \boldsymbol{u}_h \in \boldsymbol{\mathcal{T}} \cap \boldsymbol{\mathcal{N}}^{2,2}_{0,0} \text{ such that} \\ \mathcal{F}(\boldsymbol{u}_h; \boldsymbol{\phi}_h) = 0, \quad \forall \boldsymbol{\phi}_h \in \boldsymbol{\mathcal{V}} \cap \boldsymbol{\mathcal{N}}^{2,2}_{0,0}, \end{cases} \tag{5.90}$$

with $\mathcal{F}\colon (\boldsymbol{\mathcal{T}} \cap \boldsymbol{\mathcal{N}}^{2,2}_{0,0}) \times (\boldsymbol{\mathcal{V}} \cap \boldsymbol{\mathcal{N}}^{2,2}_{0,0}) \to \mathbb{R}$ being now

$$\begin{aligned} \mathcal{F}(\boldsymbol{u}_h; \boldsymbol{\phi}_h) := &\int_{\Omega_{\boldsymbol{X}}} \left(\lambda \operatorname{tr}(\boldsymbol{E}(\boldsymbol{u}_h))\, \boldsymbol{F}(\boldsymbol{u}_h) + 2\mu \boldsymbol{F}(\boldsymbol{u}_h)\boldsymbol{E}(\boldsymbol{u}_h)\right) : \nabla_{\boldsymbol{X}} \boldsymbol{\phi}_h \,\mathrm{d}\Omega_{\boldsymbol{X}} \\ &+ \int_{\Omega_{\boldsymbol{X}}} J\rho \boldsymbol{b} \cdot \boldsymbol{\phi}_h \,\mathrm{d}\Omega_{\boldsymbol{X}} + \int_{\Gamma_{N,\boldsymbol{X}}} \boldsymbol{g}_0 \cdot \boldsymbol{\phi}_h \,\mathrm{d}\Gamma_{N,\boldsymbol{X}} \end{aligned} \tag{5.91}$$

in the St. Venant-Kirchhoff case, and

$$\begin{aligned} \mathcal{F}(\boldsymbol{u}_h; \boldsymbol{\phi}_h) := &\int_{\Omega_{\boldsymbol{X}}} \left(\mu(\boldsymbol{F}(\boldsymbol{u}_h) - \boldsymbol{F}(\boldsymbol{u}_h)^{-T}) + \lambda \log(\det \boldsymbol{F}(\boldsymbol{u}_h)) \boldsymbol{F}(\boldsymbol{u}_h)^{-T}\right) : \nabla_{\boldsymbol{X}} \boldsymbol{\phi}_h \,\mathrm{d}\Omega_{\boldsymbol{X}} \\ &+ \int_{\Omega_{\boldsymbol{X}}} J\rho \boldsymbol{b} \cdot \boldsymbol{\phi}_h \,\mathrm{d}\Omega_{\boldsymbol{X}} + \int_{\Gamma_{N,\boldsymbol{X}}} \boldsymbol{\phi}_h \cdot \boldsymbol{g}_0 \,\mathrm{d}\Gamma_{N,\boldsymbol{X}} \end{aligned} \tag{5.92}$$

in the Neo-Hookean case.

For the solution of the nonlinear problem (5.90), we apply Newton's method as presented in (5.78). For discrete trial and test spaces and a fixed $\boldsymbol{u}^{h,k}$ the corresponding respective linear forms are given by (5.91) and (5.92) and the respective bilinear forms in charge with the assembly of the Jacobian are the discrete counterparts of (5.81) and (5.84).

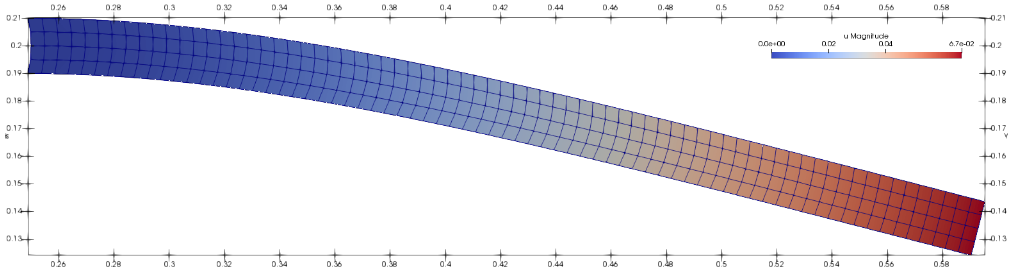

Figure 5.2: Displacement of the elastic bar in CSM 1.

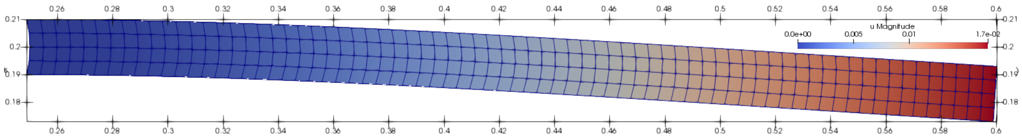

Figure 5.3: Displacement of the elastic bar in CSM 2.

Figures 5.2 and 5.3 depict the displacement of the elastic bar for CMS 1 and CSM 2. Moreover, Tables 5.2, 5.3 and Figures 5.4, 5.5 respectively present in a tabular as well as a visual way the development of the CSM 1 and CSM 2 displacement component profiles under mesh refinement. We provide data for both St. Venant-Kirchhoff and Neo-Hookean materials. Since the reference provides data for the St. Venant-Kirchhoff material only, we refrain from comparing the Neo-Hookean data to the reference results. Focusing on the St. Venant-Kirchhoff case only, our results are evidently in excellent agreement with the reference in terms of accuracy.

	Level	N$_{\text{el}}$	N$_{\text{dof}}$	St. Venant-Kirchhoff		Neo-Hookean	
				u_1 of A $[\times 10^{-3}]$	u_2 of A $[\times 10^{-3}]$	u_1 of A $[\times 10^{-3}]$	u_2 of A $[\times 10^{-3}]$
	0	18	120	-6.72316	-63.9386	-6.69894	-63.9484
	1	72	560	-7.12375	-65.7917	-7.09714	-65.7986
	2	288	2304	-7.17519	-66.0386	-7.14828	-66.0453
	3	1152	9248	-7.18434	-66.0850	-7.15737	-66.0915
	4	4608	36960	-7.18662	-66.0968	-7.15963	-66.1033
	5	18432	147680	-7.18739	-66.1008	-7.16040	-66.1073
	6	73728	590304	-7.18767	-66.1023	-7.16068	-66.1088
Ref.	$5+0$	22772	435776	-7.18767	-66.1023		

Table 5.2: Approximation results for displacement (u_1, u_2) in CSM 1.

The displacement of the elastic bar for CSM 2 is depicted in Figure 5.3. Analogous to CSM 1, Table 5.3 and Figure 5.5 provide data for the development of the displacement component profiles under mesh refinement.

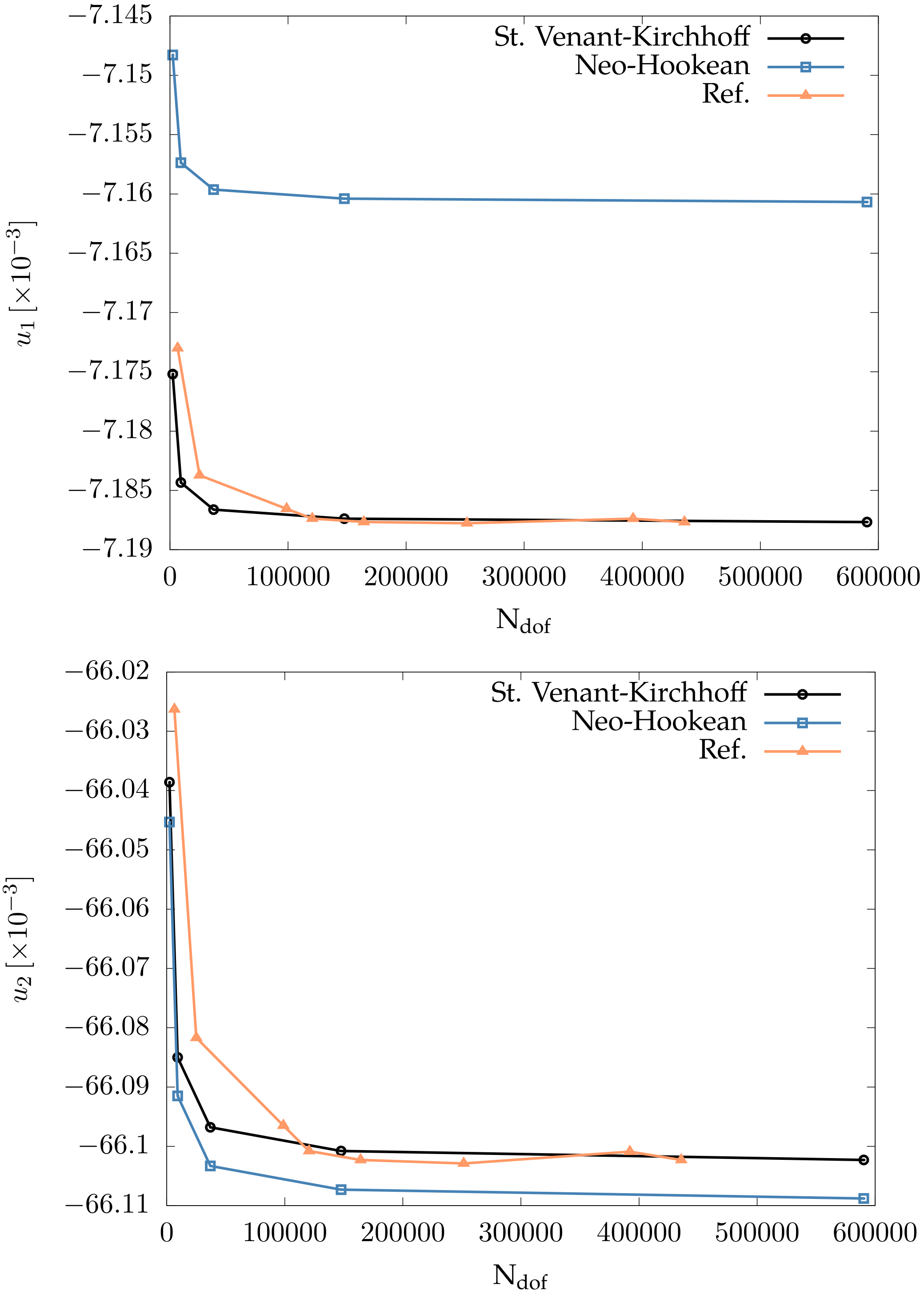

Figure 5.4: Comparison of the displacement profiles in CSM 1.

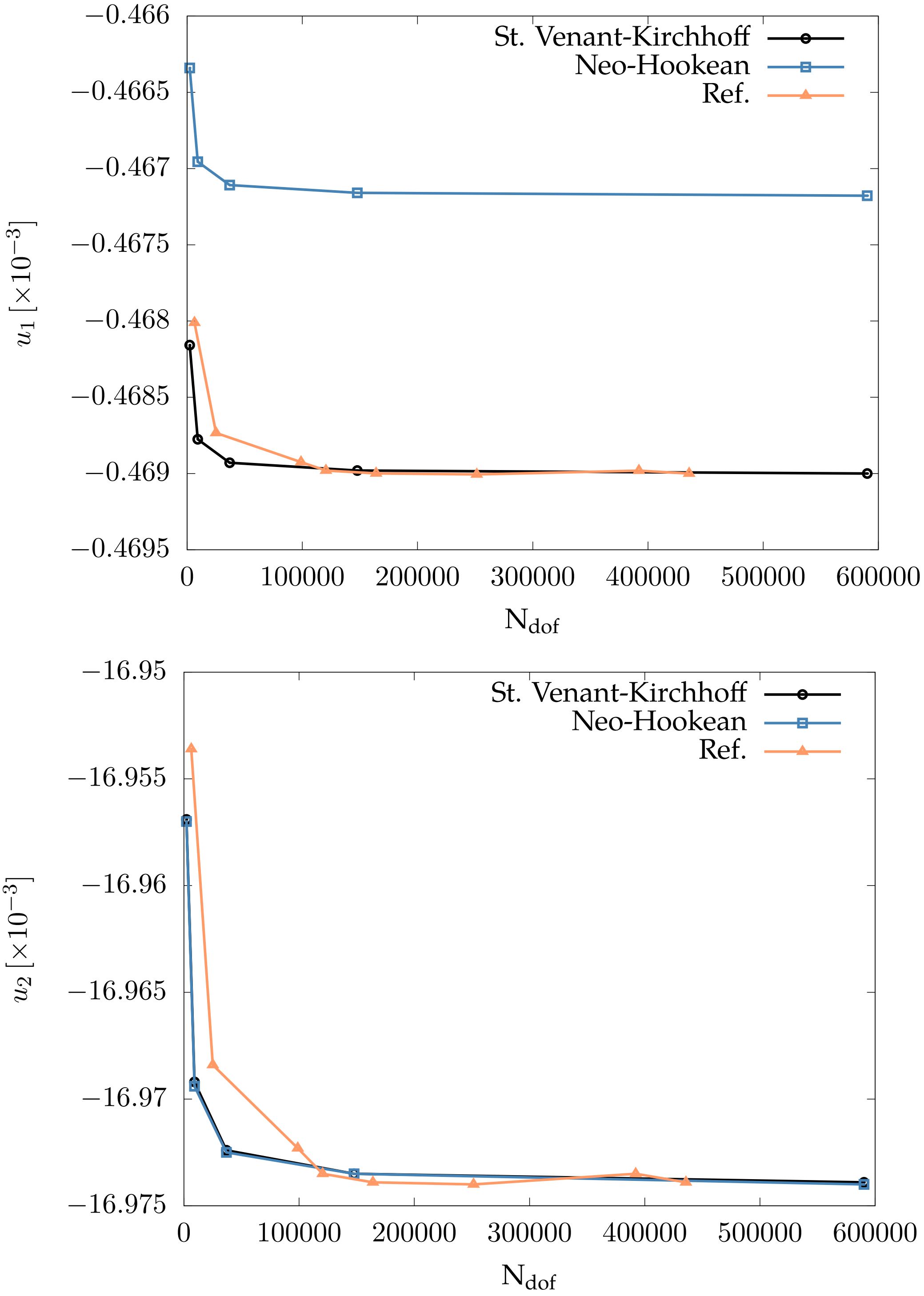

Figure 5.5: Comparison of the displacement profiles in CSM 2.

Level	N$_{\text{el}}$	N$_{\text{dof}}$	St. Venant-Kirchhoff		Neo-Hookean	
			u_1 of A $[\times 10^{-3}]$	u_2 of A $[\times 10^{-3}]$	u_1 of A $[\times 10^{-3}]$	u_2 of A $[\times 10^{-3}]$
0	18	120	-0.437858	-16.3971	-0.436168	-16.3973
1	72	560	-0.464688	-16.8908	-0.462887	-16.8909
2	288	2304	-0.468158	-16.9569	-0.466340	-16.9570
3	1152	9248	-0.468775	-16.9692	-0.466955	-16.9694
4	4608	36960	-0.468929	-16.9724	-0.467108	-16.9725
5	18432	147680	-0.468980	-16.9735	-0.467159	-16.9735
6	73728	590304	-0.469000	-16.9739	-0.467178	-16.9740
Ref. $5+0$	22772	435776	-0.469000	-16.9739		

Table 5.3: Approximation results for displacement (u_1, u_2) in CSM 2.

5.2.4.1 CSM 3

The dynamic nature of the CSM 3 test case requires to solve the elastodynamics equations (5.48). Since we consider now only the St. Venant-Kirchhoff material, the equations to be solved are the discrete version of (5.75). After time discretization with the one-step θ-scheme a discrete version of (5.85), reads

$$\text{Find } \boldsymbol{u}_h(\boldsymbol{X}), \boldsymbol{v}_h(\boldsymbol{X}) \in \boldsymbol{\mathcal{T}} \cap \boldsymbol{\mathcal{N}}_{0,0}^{2,2} \text{ such that } \forall(\boldsymbol{\phi}_h^{\boldsymbol{u}}, \boldsymbol{\phi}_h^{\boldsymbol{v}}) \in \boldsymbol{\mathcal{V}} \cap \boldsymbol{\mathcal{N}}_{0,0}^{2,2} : \tag{5.93a}$$

$$\begin{aligned}
&\int_{\Omega_{\boldsymbol{X}}} J\rho\,(\boldsymbol{v}_h - \boldsymbol{v}_h^n)\cdot\boldsymbol{\phi}_h^{\boldsymbol{u}}\,\mathrm{d}\Omega_{\boldsymbol{X}} \\
&+\int_{\Omega_{\boldsymbol{X}}} \Delta t\theta\,(\lambda\,\mathrm{tr}\,(\boldsymbol{E}(\boldsymbol{u}_h))\,\boldsymbol{F}(\boldsymbol{u}_h) + 2\mu\boldsymbol{F}(\boldsymbol{u}_h)\boldsymbol{E}(\boldsymbol{u}_h)) : \nabla_{\boldsymbol{X}}\boldsymbol{\phi}_h^{\boldsymbol{u}}\,\mathrm{d}\Omega_{\boldsymbol{X}} \\
&+\int_{\Omega_{\boldsymbol{X}}} \Delta t\,(1-\theta)\,(\lambda\,\mathrm{tr}\,(\boldsymbol{E}(\boldsymbol{u}_h^n))\,\boldsymbol{F}(\boldsymbol{u}_h^n) + 2\mu\boldsymbol{F}(\boldsymbol{u}_h^n)\boldsymbol{E}(\boldsymbol{u}_h^n)) : \nabla_{\boldsymbol{X}}\boldsymbol{\phi}_h^{\boldsymbol{u}}\,\mathrm{d}\Omega_{\boldsymbol{X}} \\
&=\int_{\Omega_{\boldsymbol{X}}} \Delta t\theta\,J\rho\boldsymbol{b}(\boldsymbol{u}_h)\cdot\boldsymbol{\phi}_h^{\boldsymbol{u}}\,\mathrm{d}\Omega_{\boldsymbol{X}} + \int_{\Gamma_{N,\boldsymbol{X}}} \Delta t\theta\,\boldsymbol{g}_0(\boldsymbol{u}_h)\cdot\boldsymbol{\phi}_h^{\boldsymbol{u}}\,\mathrm{d}\Gamma_{N,\boldsymbol{X}} \\
&+\int_{\Omega_{\boldsymbol{X}}} \Delta t\,(1-\theta)\,J\rho\boldsymbol{b}(\boldsymbol{u}_h^n)\cdot\boldsymbol{\phi}_h^{\boldsymbol{u}}\,\mathrm{d}\Omega_{\boldsymbol{X}} + \int_{\Gamma_{N,\boldsymbol{X}}} \Delta t\,(1-\theta)\,\boldsymbol{g}_0(\boldsymbol{u}_h^n)\cdot\boldsymbol{\phi}_h^{\boldsymbol{u}}\,\mathrm{d}\Gamma_{N,\boldsymbol{X}}, \qquad \text{and} \\
&\int_{\Omega_{\boldsymbol{X}}} (\boldsymbol{u}_h - \boldsymbol{u}_h^n)\cdot\boldsymbol{\phi}_h^{\boldsymbol{v}}\,\mathrm{d}\Omega_{\boldsymbol{X}}\,\mathrm{d}t - \int_{\Omega_{\boldsymbol{X}}} \Delta t\theta\,\boldsymbol{v}_h\cdot\boldsymbol{\phi}_h^{\boldsymbol{v}}\,\mathrm{d}\Omega_{\boldsymbol{X}}\,\mathrm{d}t - \int_{\Omega_{\boldsymbol{X}}} \Delta t\,(1-\theta)\,\boldsymbol{v}_h^n\cdot\boldsymbol{\phi}_h^{\boldsymbol{v}}\,\mathrm{d}\Omega_{\boldsymbol{X}}\,\mathrm{d}t = 0,
\end{aligned} \tag{5.93b}$$

where the superscript n denotes the already known field values from the previous time step. For the solution of the above nonlinear problem, we apply in every time step Newton's method as presented in (5.78). For discrete trial and test spaces and a fixed $\boldsymbol{u}^{h,k}$ the bilinear form in charge with the assembly of the Jacobian is then just the discrete counterpart of (5.87).

Figure 5.6 presents a few snapshots from the solution of the above problem. For $\theta = 0.5$ – leading to the 2-nd order accurate implicit Crank-Nicolson scheme – and under the absence of damping terms in the equations of elastodynamics, the elastic bar exhibits undamped oscillations as shown in Figure 5.7. The profiles shown in this figure are computed for three consecutive mesh refinement and time step size levels and testify mesh and time converged results. The corresponding numbers – listed in Table 5.4 – show as in the first two CSM cases very good consensus with the reference.

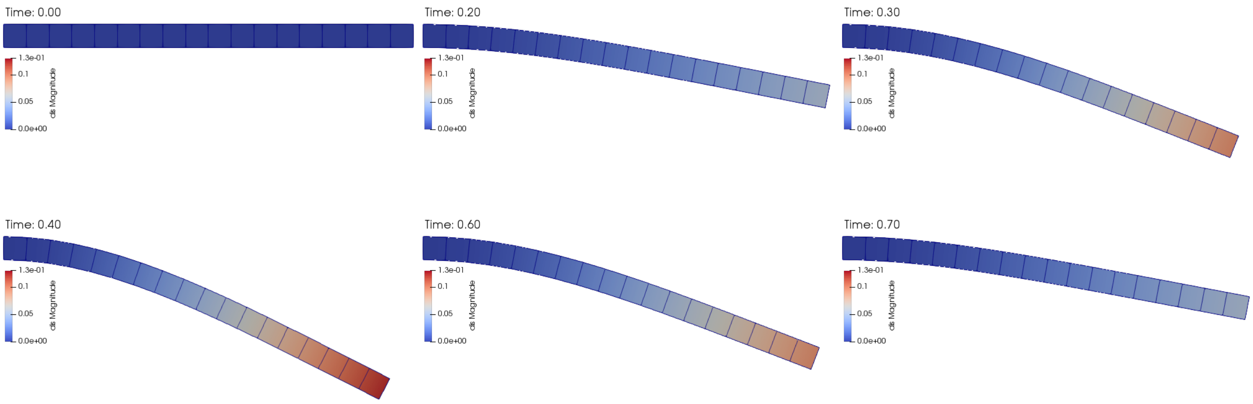

Figure 5.6: Displacement of the elastic bar at a few selected time steps in CSM 3.

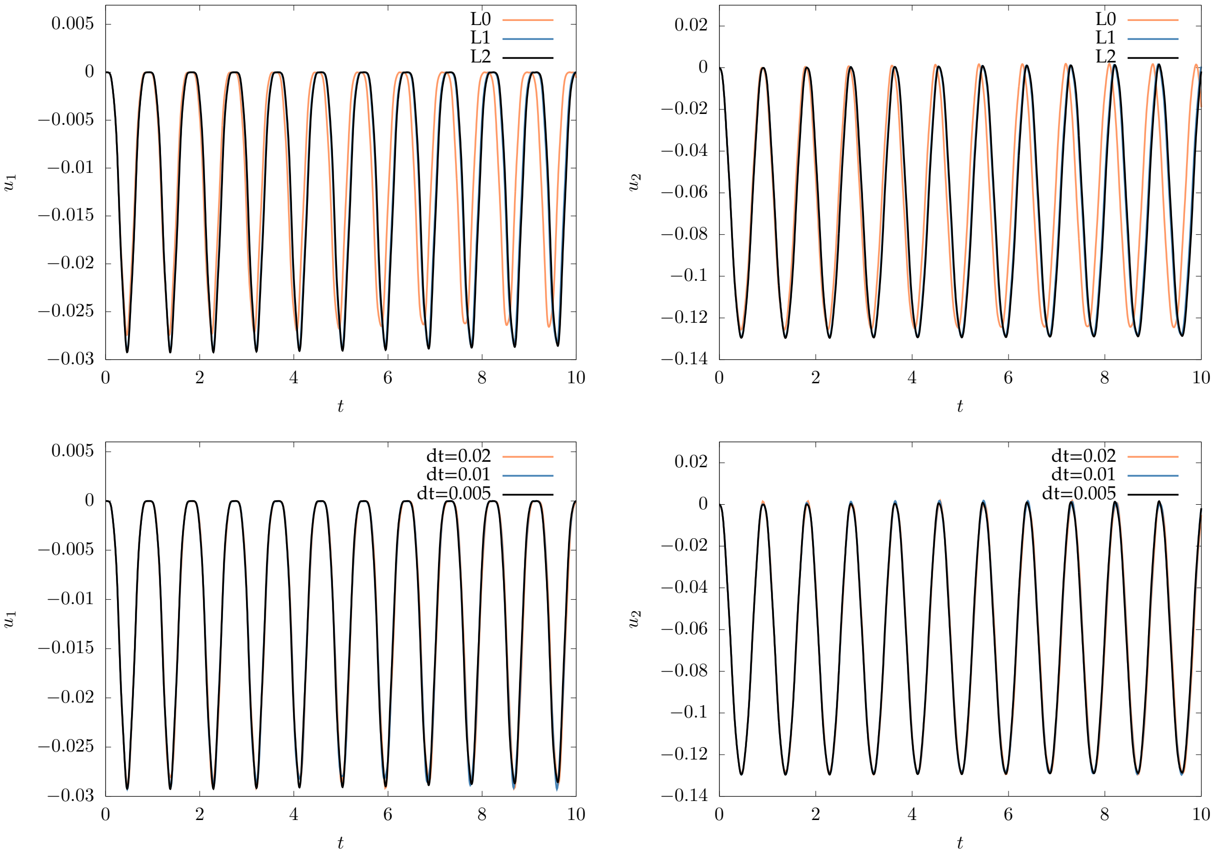

Figure 5.7: CSM 3. Top row: Displacement time profiles under h-refinement for $\Delta t = 0.005$. Bottom row: Displacement time profiles under t-refinement for $L = 2$.

	Level	$\mathrm{N}_{\mathrm{dof}}$	Δt	$u_1(A)[\times 10^{-3}]$ [f]	$u_2(A)[\times 10^{-3}]$ [f]
	0	240	0.02	$-13.686 \pm 13.698[1.1100]$	$-61.870 \pm 63.697[1.1100]$
	1	1120		$-14.511 \pm 14.522[1.0940]$	$-63.642 \pm 65.524[1.0940]$
	2	4608		$-14.602 \pm 14.613[1.0920]$	$-63.807 \pm 65.753[1.0920]$
	3	18496		$-14.592 \pm 14.602[1.0920]$	$-63.805 \pm 65.768[1.0920]$
	4	73920		$-14.605 \pm 14.615[1.0920]$	$-63.813 \pm 65.779[1.0920]$
	0	240	0.01	$-13.722 \pm 13.723[1.1120]$	$-61.976 \pm 63.771[1.1110]$
	1	1120		$-14.525 \pm 14.532[1.0960]$	$-63.669 \pm 65.518[1.0960]$
	2	4608		$-14.635 \pm 14.642[1.0940]$	$-63.900 \pm 65.771[1.0930]$
	3	18496		$-14.646 \pm 14.652[1.0940]$	$-63.944 \pm 65.792[1.0940]$
	4	73920		$-14.650 \pm 14.657[1.0930]$	$-63.953 \pm 65.805[1.0930]$
	0	240	0.005	$-13.715 \pm 13.716[1.1118]$	$-61.867 \pm 63.820[1.1118]$
	1	1120		$-14.527 \pm 14.527[1.0963]$	$-63.750 \pm 65.417[1.0958]$
	2	4608		$-14.626 \pm 14.627[1.0943]$	$-64.033 \pm 65.590[1.0938]$
	3	18496		$-14.645 \pm 14.646[1.0938]$	$-64.074 \pm 65.632[1.0933]$
	4	73920		$-14.650 \pm 14.651[1.0938]$	$-64.087 \pm 65.640[1.0933]$
HronTurek	$4+0$	98820	0.005	$-14.305 \pm 14.305[1.0995]$	$-63.607 \pm 65.160[1.0995]$
FEEL++		68662	0.005	$-14.650 \pm 14.651[1.0966]$	$-64.095 \pm 65.640[1.0951]$

Table 5.4: Approximation results for displacement (median ± amp [freq]) in CSM 3.

5.3 Fluid-Structure Interaction problem

FSI problems require the coupling of the governing equations of fluids and solids with appropriate interface conditions. As the coupling takes place at the interface between the fluid and solid domains, FSI problems belong to the set of surface-coupled multiphysics problems.

Numerical methods for FSI comprise methods with fixed meshes, methods with moving meshes and – for the sake of completeness – quasi mesh-free methods such as the Material Point Method [85] and the mesh-free Lattice Boltzmann method [55, 56, 97].

In the category of fixed mesh methods fall the Immersed Boundary Method (IBM) [116–118], the Fictitious Domain Method (FDM) [7, 67, 68], the Level-Set Method [35, 36, 66], the so-called Eulerian FSI methods [51, 124, 162], and the deforming composite grids [14, 15, 102]. Fixed mesh methods – as the name already proposes – share the property to utilize a fixed fluid mesh, yet the way they implement the presence of the structure is fairly different. By way of example, in the Immersed Boundary Method, the fluid perceives the solid by means of external forces acting on it, with the coupling between the fixed background fluid mesh and the immersed (Lagrangian) solid mesh being realized via (smoothed) Dirac Delta functions. The Fictitious Domain Method, on the other hand, realizes the coupling between the fluid and solid via Lagrange Multipliers that for instance either impose the continuity of velocity or the no-slip condition. This approach has been applied to rigid as well deformable solids with the Lagrange Multipliers being located along the structure surface. Fixed mesh methods such as e.g. IBM and FDM do not require the fluid and solid domains to be boundary-fitted with respect to each other and are therefore quite attractive in problems involving large deformations of the solid boundary. However, the drawback of this same trait is the loss of accuracy near the interface, rendering the applicability of these approaches limited when a high accuracy in the computation of the stresses at the interface is important. For a "reasonable" accuracy in the computation of the hydrodynamic forces acting on the structure, these methods need to employ adaptive mesh refinement around the fluid-solid interface.

In the boundary-fitted approach in which the fluid and solid domains are perfectly fitted to each other, the fluid domain is attached to the solid domain and therefore follows its movement. The fluid problem is then typically expressed with respect to an ALE coordinate system to account for the mesh movement. More specifically, the motion of the fluid mesh is steered by means of an ALE mapping that is calculated based on the current location of the solid (e.g., as a harmonic extension of the current interface position onto the fluid domain). The explicit representation of the interface is very appealing when it comes to the imposition of coupling conditions and in the computation of the stresses at the interface. However, the ALE method faces problems whenever large deformations or even topological changes of the interface lead to a degeneration of the computational mesh. In the former case an expensive remeshing can take remedial action in order to maintain mesh quality and solution accuracy. For the FSI simulations done in this work we use a boundary-fitted approach with an ALE-based formulation of the governing equations of fluid dynamics.

ALE-based FSI methods maybe further subdivided into partitioned and monolithic approaches. Roughly summarized, partitioned FSI techniques solve the involved subproblems one at a time. For instance, as shown in Figure 5.8, they may start with first solving the fluid problem in order to obtain updated velocity and pressure fields yielding a new fluid induced interface stress. The updated interface stress is in turn used as an applied surface force when solving the elasticity equations for displacement in the solid domain. Eventually, the updated solid displacement field at the fluid-solid interface is used as a Dirichlet boundary condition when solving for the mesh (regularization) equation (introduced later in the text). One speaks of weak coupling when inside a time step $t^n \to t^{n+1}$ this workflow path is taken only once, and of strong coupling when the workflow path is repeated until the relative displacement increment in the k-th iteration is below a certain stopping tolerance ϵ:

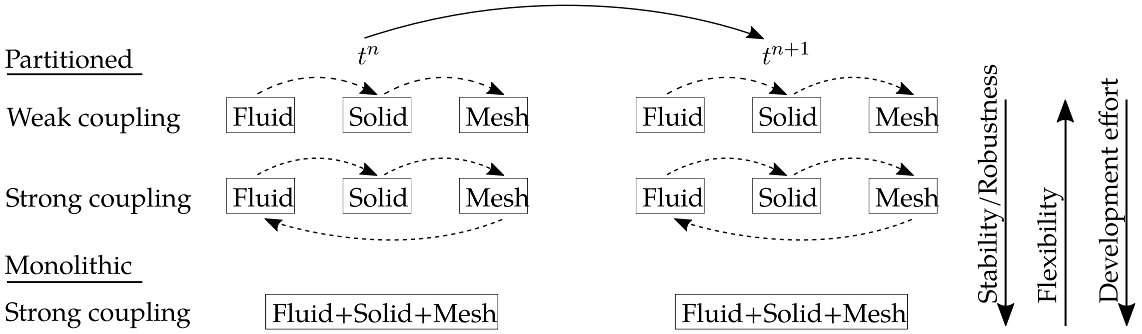

Figure 5.8: FSI coupling strategies.

$$\frac{\|\boldsymbol{u}_{k+1} - \boldsymbol{u}_k\|}{\|\boldsymbol{u}\|_k} < \epsilon.$$

The attractivity of partitioned approaches is basically founded on the fact that well tested pre-existing solvers for each subproblem may be connected via a "thin coupling layer" in order to have an FSI solver. Furthermore, the sequential solving of the subproblems has a smaller resource requirements footprint than monolithic methods. However, partitioned approaches face instabilities when the mass density of the fluid becomes comparable or greater than the mass density of the solid body. In those cases the added-mass effect [31, 156] becomes not negligible and leads to an increased number of subiterations k in order to achieve a desired force balance accuracy at the interface.

In the light of the fact that in biomechanical contexts such as in the case of blood flow inside an artery, it holds $\rho_f/\rho_s \approx 1$, the deficiencies of the partitioned approach are avoided by an implicit and monolithic solution approach that takes the full fluid-structure interaction problem as one coupled unity, without partitioning. When modeling the coupled dynamics of FSI, one is confronted with the dilemma that the fluid model is naturally based on an Eulerian perspective while it is very natural to express the solid problem in Lagrangian formulation. The fluid and the solid problems are essentially momentum conservation equations. When left in their natural frameworks, they cannot be combined into one conservation equation due to the different underlying frames of reference. In order to overcome this problem one of the subproblems needs to be rewritten with respect to the framework of the complementary problem. In this work, we leave the solid equations in their natural framework and rewrite the fluid equations in a "structure-appropriate" framework. This means a pull back reformulation of the fluid equations with respect to a fixed reference domain. Since the common interface between the fluid and solid domains is affected by the motion of the solid, the fluid domain has no other choice but to follow this motion. This motion, described by a domain deformation function, and the above addressed reformulation of the fluid problem are all handled in an Arbitrary Lagrangian-Eulerian (ALE) framework which we will discuss further below in the text (page 155). Such approaches are generally referred to as "interface tracking" methods.

The monolithic approach we take, uses a fully coupled ALE variational formulation of the FSI problem (cf. [84]) and applies Galerkin-based Isogeometric Analysis for the discretization of the partial differential equations involved. This approach – introduced in the sequel – solves the difficulty of a common variational description and facilitates a consistent Galerkin discretization of the FSI problem.

In this work we deal with the interaction of incompressible newtonian fluid flows and compressible hyperelastic solids. We consider a continuum body that is composed of a fluid part $\mathcal{F}$ and a solid part $\mathcal{S}$. The current domain $\Omega_{\boldsymbol{x}}$ of the joint body correspondingly admits the decomposition

$$\Omega_{\boldsymbol{x}} = \Omega_{\boldsymbol{x}}^{\mathcal{F}} \cup \Omega_{\boldsymbol{x}}^{\mathcal{S}}, \qquad \emptyset = \Omega_{\boldsymbol{x}}^{\mathcal{F}} \cap \Omega_{\boldsymbol{x}}^{\mathcal{S}},$$

where $\Omega_{\boldsymbol{x}}^{\mathcal{F}}$ and $\Omega_{\boldsymbol{x}}^{\mathcal{S}}$ represent the subdomains occupied by the fluid and solid, respectively.

Besides, we let the boundary $\Gamma_{\boldsymbol{x}} = \partial\Omega_{\boldsymbol{x}}$ be composed of the union of the four non-overlapping partitions

$$\Gamma_{\boldsymbol{x}} = \Gamma_{N,\boldsymbol{x}}^{\mathcal{F}} \cup \Gamma_{D,\boldsymbol{x}}^{\mathcal{F}} \cup \Gamma_{N,\boldsymbol{x}}^{\mathcal{S}} \cup \Gamma_{D,\boldsymbol{x}}^{\mathcal{S}},$$

where $\Gamma_{N,\boldsymbol{x}}^{\mathcal{F}}$ and $\Gamma_{D,\boldsymbol{x}}^{\mathcal{F}}$ denote the Neumann and Dirichlet parts of the fluid domain boundary, respectively. Likewise, $\Gamma_{N,\boldsymbol{x}}^{\mathcal{S}}$ and $\Gamma_{D,\boldsymbol{x}}^{\mathcal{S}}$ represent the Neumann and Dirichlet parts of the solid domain boundary, respectively. Moreover, we let the fluid-solid interface in the current domain be denoted by $\Gamma_{\boldsymbol{x}}^{\mathcal{I}}$. This interface is a common boundary part of both problem subdomains in the sense that the respective subdomains never detach from each other. We refer to Figure 5.9 for a depiction of the described setup. From the point of view of the fundamental conservation laws to be enforced, FSI requires in general the enforcement of both the balance of linear momentum and the conservation of mass in the fluid as well as the solid part of the joint continuum body. In the above order, these fundamental conservation laws may be expressed in local form as

$$\begin{aligned} \frac{D(\rho \boldsymbol{v})}{Dt} - \nabla \cdot \boldsymbol{\sigma} &= \rho \boldsymbol{b}, \\ \frac{D\rho}{Dt} &= 0. \end{aligned} \tag{5.94}$$

So far, both parts of the continuum body are governed by the same governing equations (5.94).

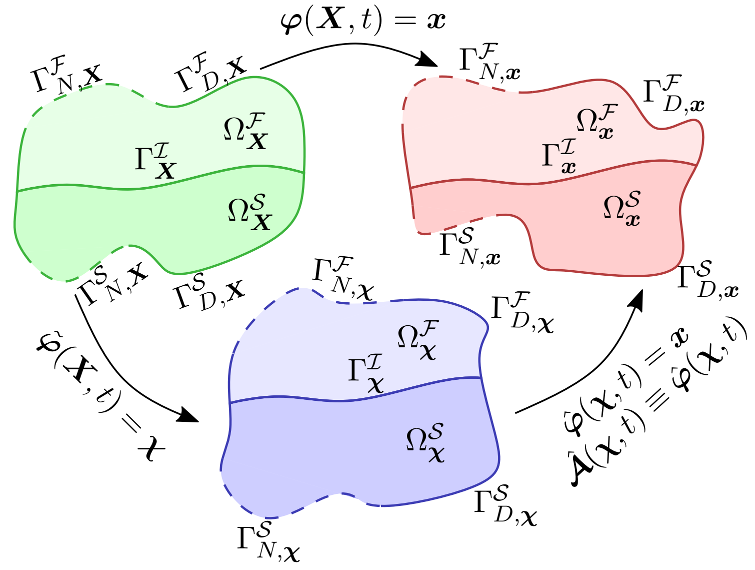

Figure 5.9: Depiction of the fluid-structure interaction problem setting.

In fact, they start to branch from this common departure point by the respective stress response functions. In the fluid subdomain the stress response is viscous, whereas it is elastic in the solid subdomain. This leads to different constitutive equations in each subdomain and eventually requires to solve the Navier-Stokes equations of incompressible flows in the fluid subdomain and the elastodynamics equations in the solid subdomain. In the latter case, mass conservation is not enforced since we consider compressible materials for which mass conservation is automatically satisfied in the Lagrangian framework.

Since the fluid and solid subdomains are attached to each other, the motion of the solid (together with its domain) induces a motion of the fluid domain. This makes it necessary to solve the flow problem in a moving fluid domain $\Omega^{\mathcal{F}}_{\boldsymbol{x}} \subset \mathbb{R}^d$, as described in the sequel:

5.3.1 Flow problem in a moving domain

The Navier-Stokes equations in a moving fluid domain [42]$\Omega^{\mathcal{F}}_{\boldsymbol{x}}(t)$ read:

$$\begin{aligned}
\rho\left(\left.\frac{\partial \boldsymbol{v}}{\partial t}\right|_{\boldsymbol{x}} + (\boldsymbol{v}\cdot\nabla)\boldsymbol{v}\right) &= \nabla\cdot\boldsymbol{\sigma} + \rho\boldsymbol{b} && \text{in } \Omega^{\mathcal{F}}_{\boldsymbol{x}}(t), t\in I,\\
\nabla\cdot\boldsymbol{v} &= 0 && \text{in } \Omega^{\mathcal{F}}_{\boldsymbol{x}}(t), t\in I,\\
p(\cdot,0)=\mathring{p}, \boldsymbol{v}(\cdot,0) &= \mathring{\boldsymbol{v}} && \text{in } \Omega^{\mathcal{F}}_{\boldsymbol{x}}(0),\\
\boldsymbol{v} &= \boldsymbol{v}_D && \text{on } \Gamma^{\mathcal{F}}_{D,\boldsymbol{x}}(t), t\in I,\\
\boldsymbol{\sigma}\cdot\boldsymbol{n} &= \boldsymbol{g} && \text{on } \Gamma^{\mathcal{F}}_{N,\boldsymbol{x}}(t), t\in I,
\end{aligned} \tag{5.95}$$

where the constitutive relation for the Cauchy stress tensor in the case of an incompressible newtonian fluid is

$$\boldsymbol{\sigma} := -p\boldsymbol{I} + \mu\left(\nabla\boldsymbol{v} + (\nabla\boldsymbol{v})^T\right). \tag{5.96}$$

---

[42] For the sake of a compact notation, in this section, we may denote the moving fluid domain $\Omega^{\mathcal{F}}_{\boldsymbol{x}}(t)$ with $\Omega^{\mathcal{F}}_{\boldsymbol{x}}$, that is, $\Omega^{\mathcal{F}}_{\boldsymbol{x}}(t) \equiv \Omega^{\mathcal{F}}_{\boldsymbol{x}}$.

Angular momentum is automatically conserved[43] for incompressible newtonian fluid flows. Based on this the conservation equations for momentum and mass decouple from the energy conservation equation. We will not need the temperature or the specific internal energy-density state variables, hence we omit the energy conservation equation. Thus we only consider the conservation equations for (linear) momentum and mass (respectively):

For the derivation of the weak formulation of (5.95), we multiply its ingredients with suitable velocity and pressure test functions ($\boldsymbol{\phi}^{\boldsymbol{v}}$ and ϕ^p) and take then the integrals:

Problem 5.3.1 (Incompressible fluid problem in a moving domain). *Let* $\boldsymbol{v}_D \in \mathcal{H}^1(\Omega^{\mathcal{F}}_{\boldsymbol{x}}(t))^d$ *be an extension of the Dirichlet data on* $\Gamma^{\mathcal{F}}_{D,\boldsymbol{x}}(t)$ *into the domain* $\Omega^{\mathcal{F}}_{\boldsymbol{x}}(t)$ *and let* $\boldsymbol{\mathcal{S}}_v := \boldsymbol{\mathcal{H}}^1_{0,\Gamma^{\mathcal{F}}_{D,\boldsymbol{x}}(t)}(\Omega^{\mathcal{F}}_{\boldsymbol{x}}(t))$, *and* $\mathcal{S}_p := \mathcal{L}^2(\Omega^{\mathcal{F}}_{\boldsymbol{x}}(t))$. *Then the weak formulation of* (5.95) *requires to find* $\{\boldsymbol{v}, p\} \in \{(\boldsymbol{\mathcal{S}}_v + \boldsymbol{v}_D) \times$[44]$\mathcal{S}_p\}$ *such that* $\boldsymbol{v}|_{t=0} = \boldsymbol{v}^0$, *and for almost all time steps* $t \in I$ *it holds:*

$$
\begin{aligned}
\rho\left(\frac{\partial \boldsymbol{v}}{\partial t}\Big|_{\boldsymbol{x}} + (\boldsymbol{v}\cdot\nabla)\boldsymbol{v}, \boldsymbol{\phi}^{\boldsymbol{v}}\right)_{\Omega^{\mathcal{F}}_{\boldsymbol{x}}(t)} + \left(\boldsymbol{\sigma}^{\mathcal{F}}, \nabla\boldsymbol{\phi}^{\boldsymbol{v}}\right)_{\Omega^{\mathcal{F}}_{\boldsymbol{x}}(t)} &= \rho\,(\boldsymbol{b}_{\mathcal{F}}, \boldsymbol{\phi}^{\boldsymbol{v}})_{\Omega^{\mathcal{F}}_{\boldsymbol{x}}(t)} + (\boldsymbol{g}, \boldsymbol{\phi}^{\boldsymbol{v}})_{\Gamma^{\mathcal{F}}_{N,\boldsymbol{x}}(t)} && \forall \boldsymbol{\phi}^{\boldsymbol{v}} \in \boldsymbol{\mathcal{S}}_v,\\
(\nabla\cdot\boldsymbol{v}, \phi^p)_{\Omega^{\mathcal{F}}_{\boldsymbol{x}}(t)} &= 0 && \forall \phi^p \in \mathcal{S}_p.
\end{aligned}
\tag{5.97}
$$

By now the fluid and the solid problems – being essentially momentum conservation problems – are left in their natural frameworks (Lagrangian, Eulerian), and in addition, the fluid domain is in motion. Considering the fact that one is willing to solve both problems simultaneously, the discrepancy induced by the respective reference frames, poses a problem. Prior to proceeding to shed light on a possible way to overcome this problem, we want to mention – for the sake of completeness – that there exists a mixed or hybrid version of (5.95) involving a referential time derivative and (Eulerian) spatial derivatives (cf. equation (2.120)):

$$
\begin{aligned}
\rho\left(\frac{\partial \boldsymbol{v}}{\partial t}\Big|_{\boldsymbol{\chi}} + \nabla\boldsymbol{v}\cdot(\boldsymbol{v} - \hat{\boldsymbol{v}})\right) &= \nabla\cdot\boldsymbol{\sigma} + \rho\boldsymbol{b} && \text{in } \Omega^{\mathcal{F}}_{\boldsymbol{x}}(t), t \in I,\\
\nabla\cdot\boldsymbol{v} &= 0 && \text{in } \Omega^{\mathcal{F}}_{\boldsymbol{x}}(t), t \in I,\\
p(\cdot,0) = \mathring{p}, \boldsymbol{v}(\cdot,0) &= \mathring{\boldsymbol{v}} && \text{in } \Omega^{\mathcal{F}}_{\boldsymbol{x}}(0),\\
\boldsymbol{v} &= \boldsymbol{v}_D && \text{on } \Gamma^{\mathcal{F}}_{D,\boldsymbol{x}}(t), t \in I,\\
\boldsymbol{\sigma}\cdot\boldsymbol{n} &= \boldsymbol{g} && \text{on } \Gamma^{\mathcal{F}}_{N,\boldsymbol{x}}(t), t \in I.
\end{aligned}
\tag{5.98}
$$

The weak formulation of (5.98) is presented in Problem 5.3.2 for which we define the following function spaces on a moving domain $\Omega_{\boldsymbol{x}}(t)$:

$$
\begin{aligned}
\boldsymbol{\mathcal{V}} \equiv \boldsymbol{\mathcal{V}}_{\Omega_{\boldsymbol{x}}(t)} &:= \{\boldsymbol{v} : \Omega_{\boldsymbol{x}} \times I \to \mathbb{R}^d : \boldsymbol{v} \circ \hat{\boldsymbol{\mathcal{A}}} = \boldsymbol{v}_{\boldsymbol{\chi}}, \boldsymbol{v}_{\boldsymbol{\chi}} \in [\mathcal{H}^1(\Omega_{\boldsymbol{\chi}})]^d\},\\
\mathcal{L} \equiv \mathcal{L}_{\Omega_{\boldsymbol{x}}(t)} &:= \{p : \Omega_{\boldsymbol{x}} \times I \to \mathbb{R}^d : p \circ \hat{\boldsymbol{\mathcal{A}}} = p_{\boldsymbol{\chi}}, p_{\boldsymbol{\chi}} \in [\mathcal{L}^2(\Omega_{\boldsymbol{\chi}})]\}.
\end{aligned}
$$

Above, $\hat{\boldsymbol{\mathcal{A}}} : \Omega_{\boldsymbol{\chi}} \to \Omega_{\boldsymbol{x}}(t)$ denotes an ALE transformation that is explained below.

Problem 5.3.2 (ALE formulation of the incompressible fluid problem in a moving domain). *Let* $\boldsymbol{v}_D \in \mathcal{H}^1(\Omega^{\mathcal{F}}_{\boldsymbol{x}}(t))^d$ *be an extension of the Dirichlet data on* $\Gamma^{\mathcal{F}}_{D,\boldsymbol{x}}(t)$ *into the domain* $\Omega^{\mathcal{F}}_{\boldsymbol{x}}(t)$. *Then the weak*

---

[43] It can be shown that the angular momentum conservation follows from linear momentum conservation (expressed by the Euler/Navier-Stokes equations) combined with the symmetry of the stress tensor.

[44] In the case of purely Dirichlet boundary conditions, the pressure is defined only up to a constant. Therefore its value must be prescribed at a given point of the domain. In such a case the pressure space is to be normalized: $\mathcal{L}_\Omega := \mathcal{L}^2(\Omega)/\mathbb{R}$.

formulation of (5.98) requires to find $\{\boldsymbol{v}, p\} \in \{(\boldsymbol{\mathcal{V}}^{\mathcal{F}} + \boldsymbol{v}_D) \times \mathcal{L}^{\mathcal{F}}\}$ *such that* $\boldsymbol{v}|_{t=0} = \boldsymbol{v}^0$*, and for almost all time steps* $t \in I$ *it holds:*

$$\begin{aligned} \rho \left(\frac{\partial \boldsymbol{v}}{\partial t}\Big|_{\boldsymbol{\chi}} + \nabla \boldsymbol{v} \cdot (\boldsymbol{v} - \hat{\boldsymbol{v}}), \boldsymbol{\phi}^{\boldsymbol{v}} \right)_{\Omega^{\mathcal{F}}_{\boldsymbol{x}}(t)} + \left(\boldsymbol{\sigma}^{\mathcal{F}}, \nabla \boldsymbol{\phi}^{\boldsymbol{v}}\right)_{\Omega^{\mathcal{F}}_{\boldsymbol{x}}(t)} &= \rho \left(\boldsymbol{b}_{\mathcal{F}}, \boldsymbol{\phi}^{\boldsymbol{v}}\right)_{\Omega^{\mathcal{F}}_{\boldsymbol{x}}(t)} + \left(\boldsymbol{g}, \boldsymbol{\phi}^{\boldsymbol{v}}\right)_{\Gamma^{\mathcal{F}}_{N,\boldsymbol{x}}(t)} \quad && \forall \boldsymbol{\phi}^{\boldsymbol{v}} \in \boldsymbol{\mathcal{V}}, \\ \left(\nabla \cdot \boldsymbol{v}, \phi^p\right)_{\Omega^{\mathcal{F}}_{\boldsymbol{x}}(t)} &= 0 && \forall \phi^p \in \mathcal{L}. \end{aligned} \tag{5.99}$$

The two problem formulations introduced above hide the transformations encoded in the deformation tensor $\hat{\boldsymbol{F}}$ and its determinant $\hat{J}$. Yet they are required since the terms are integrated in the moving domain $\Omega^{\mathcal{F}}_{\boldsymbol{x}}(t)$ whose motion/deformation depends on $\hat{\boldsymbol{F}}$ and $\hat{J}$. These formulations are convenient for stability and error estimates but are not very practicable from an implementation point of view.

One way to address the above described discrepancy issue, is to rewrite the fluid problem in a "structure-appropriate" framework. Bearing in mind that the solid deformation problem is expressed with respect to an initial/undeformed reference domain, it is very appealing to have the fluid equations expressed with respect to such a fixed reference domain as well. One of the benefits of this approach is that one always works on the well known initial domain coming along with a clean and a priori known delineation of the fluid-solid interface including the orientation of the interface normals. The nature of the given problem proposes the usage of the ALE framework in which we rewrite the fluid equations with respect to an arbitrary reference frame which then may be mapped to the Eulerian frame of reference with a bijective map

$$\begin{aligned} \hat{\boldsymbol{\mathcal{A}}}(\boldsymbol{\chi}, t) \colon \overline{\Omega}^{\mathcal{F}}_{\boldsymbol{\chi}} \times I &\longrightarrow \overline{\Omega}^{\mathcal{F}}_{\boldsymbol{x}} \times I \\ (\boldsymbol{\chi}, t) &\longmapsto \hat{\boldsymbol{\mathcal{A}}}(\boldsymbol{\chi}, t) = (\boldsymbol{x}, t), \end{aligned} \tag{5.100}$$

also-called the ALE map (cf. the referential to Eulerian map given by (2.72)). This arbitrary reference domain is typically the initial (undeformed) computational domain, that is, it holds $\overline{\Omega}^{\mathcal{F}}_{\boldsymbol{\chi}} = \overline{\Omega}^{\mathcal{F}}_{\boldsymbol{X}} = \overline{\Omega}^{\mathcal{F}}_{\boldsymbol{x}}(0)$. The motion of the domain is then given by the invertible ALE map from a fixed reference domain $\Omega^{\mathcal{F}}_{\boldsymbol{\chi}} \subset \mathbb{R}^d$.

For the time being, the mapping (5.100) is assumed to be part of the problem data, such that properties such as regularity and invertibility can be prescribed. However, as shown later in the text, the computation of the above mapping will be a part of the unknown solution of the FSI problem. The temporal derivative of the above mapping yields a velocity which we denote as domain or mesh velocity $\hat{\boldsymbol{v}}$, cf. equation (2.75). This velocity is not to be confused with the flow velocity $\boldsymbol{v}$ and in general it holds: $\partial_t \hat{\boldsymbol{\mathcal{A}}}(\boldsymbol{\chi}) = \hat{\boldsymbol{v}} \neq \boldsymbol{v}$.

The solid deformation equations are already defined in a Lagrangian sense, that is, with respect to a fixed reference domain $\Omega^{\mathcal{S}}_{\boldsymbol{X}}$. Note that according to (2.66), the choice $\tilde{\boldsymbol{\varphi}}^{-1} = \boldsymbol{I}$ renders the Lagrangian and referential coordinates identical, that is, $\boldsymbol{X} \equiv \boldsymbol{\chi}$ (See Figure 2.3).

Under the premise that the mapping $\hat{\boldsymbol{\mathcal{A}}}$ is a $\mathcal{C}^1$-diffeomorphism, the Navier-Stokes equations may be transformed onto the referential domain $\Omega^{\mathcal{F}}_{\boldsymbol{\chi}}$. Thanks to the derivations of the mass and momentum conservation equations with respect to the ALE frame of reference in section 2.6.2, all ingredients are already at hand. It holds:

$$\rho\left(\left.\frac{\partial \boldsymbol{v}}{\partial t}\right|_{\boldsymbol{x}} + (\boldsymbol{v}\cdot\nabla)\boldsymbol{v}, \boldsymbol{\phi}^{\boldsymbol{v}}\right)_{\Omega^{\mathcal{F}}_{\boldsymbol{x}}} = \left(\hat{J}\rho\left(\left.\frac{\partial \boldsymbol{v}}{\partial t}\right|_{\boldsymbol{\chi}} + \nabla_{\boldsymbol{\chi}}\boldsymbol{v}\left(\hat{\boldsymbol{F}}^{-1}(\boldsymbol{v}-\partial_t\hat{\boldsymbol{\mathcal{A}}})\right)\right), \boldsymbol{\phi}^{\boldsymbol{v}}\right)_{\Omega^{\mathcal{F}}_{\boldsymbol{\chi}}}, \tag{5.101a}$$

$$(\boldsymbol{\sigma}, \nabla\boldsymbol{\phi}^{\boldsymbol{v}})_{\Omega^{\mathcal{F}}_{\boldsymbol{x}}} = \left(\hat{J}\boldsymbol{\sigma}\hat{\boldsymbol{F}}^{-T}, \nabla_{\boldsymbol{\chi}}\boldsymbol{\phi}^{\boldsymbol{v}}\right)_{\Omega^{\mathcal{F}}_{\boldsymbol{\chi}}}, \tag{5.101b}$$

$$(\nabla\cdot\boldsymbol{v}, \phi^{p})_{\Omega^{\mathcal{F}}_{\boldsymbol{x}}} = \left(\nabla_{\boldsymbol{\chi}}\cdot\left(\hat{J}\hat{\boldsymbol{F}}^{-1}\boldsymbol{v}\right), \phi^{p}\right)_{\Omega^{\mathcal{F}}_{\boldsymbol{\chi}}}, \tag{5.101c}$$

$$(\rho\boldsymbol{b}, \boldsymbol{\phi}^{\boldsymbol{v}})_{\Omega^{\mathcal{F}}_{\boldsymbol{x}}} = \left(\hat{J}\rho\boldsymbol{b}, \boldsymbol{\phi}^{\boldsymbol{v}}\right)_{\Omega^{\mathcal{F}}_{\boldsymbol{\chi}}}. \tag{5.101d}$$

Note that the right hand sides of (5.101a) and (5.101b) follow from the non-conservative (advective) form of the linear momentum conservation equation in the referential domain $\Omega_{\boldsymbol{\chi}}$, as presented in (2.116). Moreover, transforming the velocity gradients in the Cauchy stress tensor (5.96) from the current domain to the referential domain with the "referential-current" equivalent of (2.48), the right hand side of (5.101b) may be further expanded to

$$\begin{aligned}\hat{J}\boldsymbol{\sigma}\hat{\boldsymbol{F}}^{-T} :=& \hat{J}\left(-p\boldsymbol{I} + \mu\left(\nabla\boldsymbol{v} + (\nabla\boldsymbol{v})^{T}\right)\right)\hat{\boldsymbol{F}}^{-T}\\ =& \hat{J}\left(-p\boldsymbol{I} + \mu\left(\nabla_{\boldsymbol{\chi}}\boldsymbol{v}\hat{\boldsymbol{F}}^{-1} + \hat{\boldsymbol{F}}^{-T}(\nabla_{\boldsymbol{\chi}}\boldsymbol{v})^{T}\right)\right)\hat{\boldsymbol{F}}^{-T}\end{aligned} \tag{5.102}$$

The right hand side of (5.101c) is obtained from the non-conservative (advective) form of the mass conservation equation in the referential domain, as presented in (2.105). Note that all terms involving a derivative of the density ρ have vanished due to the incompressibility constraint. Eventually the right hand side of (5.101d) is simply a consequence of the *Transformationssatz* (2.41).

In (5.101) and (5.102) we rewrote the ingredients of the Navier-Stokes equations with respect to the ALE frame. These expressions are now used to pose the ALE formulation of the incompressible Navier-Stokes equations in the fixed referential domain $\Omega^{\mathcal{F}}_{\boldsymbol{\chi}}$:

$$\begin{aligned}\hat{J}\rho\left(\left.\frac{\partial \boldsymbol{v}}{\partial t}\right|_{\boldsymbol{\chi}} + \nabla_{\boldsymbol{\chi}}\boldsymbol{v}\left(\hat{\boldsymbol{F}}^{-1}(\boldsymbol{v}-\partial_t\hat{\boldsymbol{\mathcal{A}}})\right)\right)&\\ -\nabla_{\boldsymbol{\chi}}\cdot\left(\hat{J}\left(-p\boldsymbol{I} + \mu\left(\nabla_{\boldsymbol{\chi}}\boldsymbol{v}\hat{\boldsymbol{F}}^{-1} + \hat{\boldsymbol{F}}^{-T}(\nabla_{\boldsymbol{\chi}}\boldsymbol{v})^{T}\right)\right)\hat{\boldsymbol{F}}^{-T}\right) &= \hat{J}\rho\boldsymbol{b} && \text{in } \Omega^{\mathcal{F}}_{\boldsymbol{\chi}}\times(0,T),\\ \nabla_{\boldsymbol{\chi}}\cdot\left(\hat{J}\hat{\boldsymbol{F}}^{-1}\boldsymbol{v}\right) &= 0 && \text{in } \Omega^{\mathcal{F}}_{\boldsymbol{\chi}}\times[0,T),\\ p(\cdot,0) = \mathring{p}, \boldsymbol{v}(\cdot,0) &= \mathring{\boldsymbol{v}} && \text{in } \Omega^{\mathcal{F}}_{\boldsymbol{\chi}},\\ \boldsymbol{v} &= \boldsymbol{v}_D && \text{on } \Gamma^{\mathcal{F}}_{D,\boldsymbol{\chi}}\times(0,T),\\ \left(\hat{J}\boldsymbol{\sigma}\hat{\boldsymbol{F}}^{-T}\right)\boldsymbol{n}_0 &= \boldsymbol{g}_0 && \text{on } \Gamma^{\mathcal{F}}_{N,\boldsymbol{\chi}}\times(0,T),\end{aligned} \tag{5.103}$$

Since we have chosen to set the arbitrary referential domain to the initial (undeformed) domain ($\overline{\Omega}^{\mathcal{F}}_{\boldsymbol{\chi}} = \overline{\Omega}^{\mathcal{F}}_{\boldsymbol{X}}$) , in (5.103) we refer with $\boldsymbol{g}_0$ to the density of the applied surface forces per unit area in the referential configuration, and let $\boldsymbol{n}_0$ denote the outward unit normal vector in the referential configuration. The above formulation introduces additional geometric nonlinearities expressed in terms of the deformation gradient $\hat{\boldsymbol{F}}$ and its determinant $\hat{J}$. Both are functions of the displacement $\boldsymbol{u}$ which is an unknown in the FSI problem. We proceed with the presentation of the variational form of (5.103) in Problem 5.3.3 for which it is necessary to introduce the following function spaces on a fixed referential domain $\Omega_{\boldsymbol{\chi}}$:

$$
\begin{aligned}
&\boldsymbol{\mathcal{V}}_{\boldsymbol{\chi}} \equiv \boldsymbol{\mathcal{V}}_{\Omega_{\boldsymbol{\chi}}} := \{\boldsymbol{v} \in \boldsymbol{\mathcal{H}}^1(\Omega_{\boldsymbol{\chi}}) = [\mathcal{H}^1(\Omega_{\boldsymbol{\chi}})]^d \,|\, \boldsymbol{v} = \boldsymbol{v}_D \text{ on } \partial\Omega_{D,\boldsymbol{\chi}}\},\\
&\boldsymbol{\mathcal{V}}_{0,\boldsymbol{\chi}} \equiv \boldsymbol{\mathcal{V}}_{0,\Omega_{\boldsymbol{\chi}}} := \boldsymbol{\mathcal{H}}^1_0(\Omega_{\boldsymbol{\chi}}, \partial\Omega_{D,\boldsymbol{\chi}}) = \{\boldsymbol{v} \in \boldsymbol{\mathcal{H}}^1(\Omega_{\boldsymbol{\chi}}) \,|\, \boldsymbol{v} = 0 \text{ on } \partial\Omega_{D,\boldsymbol{\chi}}\},\\
&\mathcal{L}_{\boldsymbol{\chi}} \equiv \mathcal{L}_{\Omega_{\boldsymbol{\chi}}} := \mathcal{L}^2(\Omega_{\boldsymbol{\chi}})/\mathbb{R}.
\end{aligned}
\tag{5.104}
$$

Problem 5.3.3 (ALE formulation of the incompressible fluid problem in a fixed domain). *Let* $\boldsymbol{v}_D \in \mathcal{H}^1(\Omega^{\mathcal{F}}_{\boldsymbol{\chi}})^d$ *be an extension of the Dirichlet data on* $\Gamma^{\mathcal{F}}_{D,\boldsymbol{\chi}}$ *into the domain* $\Omega^{\mathcal{F}}_{\boldsymbol{\chi}}$. *Then the weak formulation of (5.103) requires to find* $\{\boldsymbol{v}, p\} \in \{\boldsymbol{\mathcal{V}}_{\Omega^{\mathcal{F}}_{\boldsymbol{\chi}}} \times \mathcal{L}_{\Omega^{\mathcal{F}}_{\boldsymbol{\chi}}}\}$ *such that* $\boldsymbol{v}|_{t=0} = \boldsymbol{v}^0$, *and for almost all time steps* $t \in I$ *it holds:*

$$
\begin{aligned}
&\left(\hat{J}\rho\left(\frac{\partial \boldsymbol{v}}{\partial t}\Big|_{\boldsymbol{\chi}} + \nabla_{\boldsymbol{\chi}}\boldsymbol{v}\left(\hat{\boldsymbol{F}}^{-1}(\boldsymbol{v} - \partial_t\hat{\boldsymbol{\mathcal{A}}})\right)\right), \boldsymbol{\phi}^{\boldsymbol{v}}\right)_{\Omega^{\mathcal{F}}_{\boldsymbol{\chi}}}\\
&+ \left(\hat{J}\left(-p\boldsymbol{I} + \mu\left(\nabla_{\boldsymbol{\chi}}\boldsymbol{v}\hat{\boldsymbol{F}}^{-1} + \hat{\boldsymbol{F}}^{-T}(\nabla_{\boldsymbol{\chi}}\boldsymbol{v})^T\right)\right)\hat{\boldsymbol{F}}^{-T}, \nabla\boldsymbol{\phi}^{\boldsymbol{v}}\right)_{\Omega^{\mathcal{F}}_{\boldsymbol{\chi}}}\\
&\qquad - \left(\hat{J}\rho\boldsymbol{b}, \boldsymbol{\phi}^{\boldsymbol{v}}\right)_{\Omega^{\mathcal{F}}_{\boldsymbol{\chi}}} - (\boldsymbol{g}_0, \boldsymbol{\phi}^{\boldsymbol{v}})_{\Gamma^{\mathcal{F}}_{N,\boldsymbol{\chi}}} = 0 \qquad \forall \boldsymbol{\phi}^{\boldsymbol{v}} \in \boldsymbol{\mathcal{V}}_{0,\Omega^{\mathcal{F}}_{\boldsymbol{\chi}}},\\
&\qquad \left(\nabla_{\boldsymbol{\chi}} \cdot \left(\hat{J}\hat{\boldsymbol{F}}^{-1}\boldsymbol{v}\right), \phi^p\right)_{\Omega^{\mathcal{F}}_{\boldsymbol{\chi}}} = 0 \qquad \forall \phi^p \in \mathcal{L}_{\Omega^{\mathcal{F}}_{\boldsymbol{\chi}}}.
\end{aligned}
\tag{5.105}
$$

With (5.97) and (5.105) we have presented two different variational formulations of the Navier-Stokes equations in Eulerian and ALE coordinates. The following statements on the equivalence of these representations are based on [123] and the references cited therein. The equivalence of the Eulerian and the ALE formulation of the Navier-Stokes equations strictly depends on the regularity of the mapping $\hat{\boldsymbol{\mathcal{A}}}$. The equivalence does not any longer hold if this mapping looses its regularity. However, if $\{\boldsymbol{v}(t), p(t)\} \in \{(\boldsymbol{\mathcal{V}} + \boldsymbol{v}_D) \times \mathcal{L}\}$ is a unique solution of the Eulerian formulation of the Navier-Stokes equations, then for suitable mappings $\hat{\boldsymbol{\mathcal{A}}}$, the ALE formulation will have a corresponding unique solution $\{\boldsymbol{v}_{\boldsymbol{\chi}}, p_{\boldsymbol{\chi}}\} \in \{\boldsymbol{\mathcal{V}}_{\Omega^{\mathcal{F}}_{\boldsymbol{\chi}}} \times \mathcal{L}_{\Omega^{\mathcal{F}}_{\boldsymbol{\chi}}}\}$ and it holds

$$
\begin{aligned}
&c(\hat{\boldsymbol{\mathcal{A}}}(t))^{-1}\left\{\|\nabla\boldsymbol{v}(t)\|_{\boldsymbol{\mathcal{V}}_{\Omega^{\mathcal{F}}_{\boldsymbol{x}}(t)}} + \|p(t)\|_{\mathcal{L}_{\Omega^{\mathcal{F}}_{\boldsymbol{x}}(t)}}\right\}\\
&\qquad \le \|\nabla_{\boldsymbol{\chi}}\boldsymbol{v}_{\boldsymbol{\chi}}\|_{\boldsymbol{\mathcal{V}}_{\Omega^{\mathcal{F}}_{\boldsymbol{\chi}}}} + \|p_{\boldsymbol{\chi}}\|_{\mathcal{L}_{\Omega^{\mathcal{F}}_{\boldsymbol{\chi}}}} \le\\
&c(\hat{\boldsymbol{\mathcal{A}}}(t))\left\{\|\nabla\boldsymbol{v}(t)\|_{\boldsymbol{\mathcal{V}}_{\Omega^{\mathcal{F}}_{\boldsymbol{x}}(t)}} + \|p(t)\|_{\mathcal{L}_{\Omega^{\mathcal{F}}_{\boldsymbol{x}}(t)}}\right\}.
\end{aligned}
\tag{5.106}
$$

The constant $c(\hat{\boldsymbol{\mathcal{A}}}(t))$ is deformation dependent and may go to infinity, $c(\hat{\boldsymbol{\mathcal{A}}}(t)) \to \infty$, if the mapping $\hat{\boldsymbol{\mathcal{A}}}$ looses its regularity.

5.3.2 FSI coupling conditions

We recall that the computational domain is subdivided into a fluid and solid part which share a common moving interface boundary $\Gamma^{\mathcal{I}}_{\boldsymbol{x}}(t)$. Since each problem is solved in its own subdomain, the only way of interaction is through exchange of information over the common boundary, justifying the name "surface coupled multiphysics problem". The fluid and solid problem are coupled at the common interface through the following interface boundary conditions:

- *Geometric coupling condition*: The fluid, and solid domains need to always match at the interface, neither holes nor overlappings are allowed at the interface. The moving fluid domain follows the motion of the interface, it holds[45]

$$\hat{\boldsymbol{u}}^{\mathcal{F}} = \boldsymbol{u}^{\mathcal{S}} \qquad \text{on } \Gamma^{\mathcal{I}}_{\boldsymbol{\chi}}. \tag{5.107}$$

The solid displacement field $\boldsymbol{u}^{\mathcal{S}}$ has a physical meaning in the sense that it is linked to the solid material particle velocity $\boldsymbol{v}^{\mathcal{S}}$ via the relation $\boldsymbol{u}^{\mathcal{S}} = \boldsymbol{v}^{\mathcal{S}}\Delta t$. However, in the interior of the fluid domain the fluid displacement degree of freedom $\boldsymbol{u}^{\mathcal{F}}$ is deliberately linked to the displacement of a "virtual fluid mesh particle" $\hat{\boldsymbol{u}}^{\mathcal{F}}$ and not to the displacement of a fluid material particle, and in general the following relation does not hold: $\hat{\boldsymbol{u}}^{\mathcal{F}} \neq \boldsymbol{v}^{\mathcal{F}}\Delta t$. The fluid mesh displacement is typically computed under the constraint of minimizing mesh distortions and has therefore no physical connection to the fluid material particle velocity. We will discuss this in more detail in Section 5.3.3.

- *Continuity of velocity condition*: The velocity must be continuous on the interface. This condition is a simple extension of the no-slip boundary condition for viscous fluids which says that at a solid boundary, the fluid will have zero velocity relative to the boundary. Therefore the fluid velocity at all fluid-solid boundaries is equal to that of the solid boundary:

  $$\boldsymbol{v}^{\mathcal{F}} = \hat{\boldsymbol{v}}^{\mathcal{F}} = \boldsymbol{v}^{\mathcal{S}} \qquad \text{on } \Gamma^{\mathcal{I}}_{\boldsymbol{\chi}}. \tag{5.108}$$

  Under the prerequisite of sufficient regularity of the solid velocity, the continuity of velocity condition may be seen as a Dirichlet-like boundary condition prescribed to the fluid problem.

- *Continuity of normal stresses condition*: The normal stresses of fluid and solid are continuous on the interface. This condition reflects Newton's third law of action and reaction, and requires the normal stresses, that is, the (normal to the interface) forces per area acting on the interface to be in equilibrium:

  $$\boldsymbol{\sigma}^{\mathcal{F}} \cdot \boldsymbol{n}^{\mathcal{F}}_{\boldsymbol{x}} = -\boldsymbol{\sigma}^{\mathcal{S}} \cdot \boldsymbol{n}^{\mathcal{S}}_{\boldsymbol{x}} \qquad \text{on } \Gamma^{\mathcal{I}}_{\boldsymbol{x}}(t). \tag{5.109}$$

  Above, $\boldsymbol{n}^{\mathcal{F}}_{\boldsymbol{x}}$ and $\boldsymbol{n}^{\mathcal{S}}_{\boldsymbol{x}}$ represent the normal vectors at the fluid and solid domain boundaries and it holds $\boldsymbol{n}^{\mathcal{F}}_{\boldsymbol{x}} = -\boldsymbol{n}^{\mathcal{S}}_{\boldsymbol{x}}$. Rewriting (5.109) with respect to the referential domain, yields

  $$\begin{aligned} &\hat{J}\boldsymbol{\sigma}^{\mathcal{F}}\hat{\boldsymbol{F}}^{-T}\boldsymbol{n}^{\mathcal{F}}_0 + \hat{J}\boldsymbol{\sigma}^{\mathcal{S}}\hat{\boldsymbol{F}}^{-T}\boldsymbol{n}^{\mathcal{S}}_0 \\ =&\hat{J}\boldsymbol{\sigma}^{\mathcal{F}}\hat{\boldsymbol{F}}^{-T}\boldsymbol{n}^{\mathcal{F}}_0 + \hat{\boldsymbol{P}}^{\mathcal{S}}\boldsymbol{n}^{\mathcal{S}}_0 \\ =&\hat{J}\boldsymbol{\sigma}^{\mathcal{F}}\hat{\boldsymbol{F}}^{-T}\boldsymbol{n}^{\mathcal{F}}_0 + \hat{\boldsymbol{F}}\hat{\boldsymbol{S}}^{\mathcal{S}}\boldsymbol{n}^{\mathcal{S}}_0 \\ =&0 \qquad \text{on } \Gamma^{\mathcal{I}}_{\boldsymbol{\chi}}, \end{aligned} \tag{5.110}$$

  where $\hat{\boldsymbol{P}}$ and $\hat{\boldsymbol{S}}$ represent the first and second Piola-Kirchhoff stresses, respectively (cf. equations (2.35) and (2.40)). This condition corresponds to a Neumann-like boundary condition prescribed to the solid problem.

5.3.3 Construction of the ALE map

As a consequence of the geometric coupling condition presented in Section 5.3.2, the fluid and solid domains remain attached to each other at their joint interface. Since the solid responses to applied forces with corresponding deformations affecting its domain, by the principle of causality the fluid

---

[45] To differentiate the fluid and solid values we have added a respective $\mathcal{F}$ or $\mathcal{S}$ upper suffix.

domain (attached to the solid domain) follows the solid domain motion. The fluid and solid problems are naturally formulated with respect to the Eulerian and Lagrangian frameworks. In the course of coupling both problems a discrepancy arises which is caused by mismatch in the fluid and solid coordinate systems. In order to address this discrepancy, we decided to rewrite the fluid problem in a "structure-appropriate" framework to facilitate a coupled formulation. To this end we switched to an ALE formulation of the fluid problem where the governing equations are expressed with respect to a referential domain. A straight forward choice for this referential domain is the initial (undeformed) fluid domain, i.e., $\Omega_{\boldsymbol{\chi}}^{\mathcal{F}} = \Omega_{\boldsymbol{x}}^{\mathcal{F}}(0)$, while other choices are also admissible. The ALE formulation of the Navier-Stokes equations requires suitable (smooth enough and bijective) (ALE-)maps which allow a mapping between referential coordinates $\boldsymbol{\chi}$ and Eulerian coordinates $\boldsymbol{x}$, cf. (5.100). The motion of the fluid-solid interface induced by the solid domain motion causes on the one hand distortions in the fluid mesh cells and may on the other hand push (interface) mesh nodes even inside mesh cells further away from the interface, leading to overlapping mesh cells. Since the former mentioned may lead to massively squeezed or stretched mesh cells and the latter mentioned even destroys the one-to-one relation required in the ALE-map, the fluid mesh needs to be "treated" so as to prevent these issues. To be more specific, it is necessary to find a fluid mesh node displacement field $\hat{\boldsymbol{u}}^{\mathcal{F}}$ that lets the fluid mesh nodes follow the solid domain deformation such that the fluid mesh motion can be described in terms of a suitable ALE-map and the element distortion is kept at bay. We can construct the mapping by

$$\hat{\boldsymbol{\mathcal{A}}}(\boldsymbol{\chi}, t) := \boldsymbol{\chi} + \hat{\boldsymbol{u}}^{\mathcal{F}}(\boldsymbol{\chi}, t), \tag{5.111}$$

where it has been assumed that the motion of the fluid domain boundary $\partial\Omega_{\boldsymbol{x}}^{\mathcal{F}}(t)$ is known. In general the displacement field $\hat{\boldsymbol{u}}^{\mathcal{F}}$ is obtained as the solution of an auxiliary partial differential equation which takes the prescribed fluid domain boundary values as Dirichlet data.

We proceed with the presentation and discussion of three mesh motion models, each providing a distinct mesh node displacement field $\hat{\boldsymbol{u}}^{\mathcal{F}}$ for the construction of the ALE-map as described in (5.111). The regularity of $\hat{\boldsymbol{u}}^{\mathcal{F}}$ turns out to be a very significant aspect, for the regularity of the ALE-mapping $\hat{\boldsymbol{\mathcal{A}}}$ directly depends on it. Recalling at this point the high regularity requirements for the equivalence between the Eulerian, and ALE formulations of the Navier-Stokes equations, the mesh motion models are basically assessed by their ability to produce suitable mappings with as high as possible regularities.

Harmonic mesh motion model

The simplest mesh motion model is based on the harmonic extension of the solid displacement into the fluid domain and is obtained from the solution of the following partial differential equation

$$\begin{aligned} -\nabla_{\boldsymbol{\chi}} \cdot (\boldsymbol{\sigma}_{\text{mesh}}) &= 0 && \text{in } \Omega_{\boldsymbol{\chi}}^{\mathcal{F}}, \\ \boldsymbol{u}^{\mathcal{F}} &= \boldsymbol{u}^{\mathcal{S}} && \text{on } \Gamma_{\boldsymbol{\chi}}^{\mathcal{I}}, \\ \boldsymbol{u}^{\mathcal{F}} &= 0 && \text{on } \partial\Omega_{\boldsymbol{\chi}}^{\mathcal{F}} \setminus \Gamma_{\boldsymbol{\chi}}^{\mathcal{I}}, \end{aligned} \tag{5.112}$$

with

$$\boldsymbol{\sigma}_{\text{mesh}} = D\nabla_{\boldsymbol{\chi}}\boldsymbol{u}. \tag{5.113}$$

Above, $D(\boldsymbol{\chi}) : \Omega_{\boldsymbol{\chi}}^{\mathcal{F}} \to \mathbb{R}_+$ denotes a mesh node diffusion function which needs to be constructed with the objective of counteracting mesh cell distortions (e.g. squeezed cells). As (5.112) combined with (5.113) forms nothing but the Laplace equation, the solution $\boldsymbol{u}$ is a harmonic function of whom we know [132] that its value at an arbitrary domain point coincides with its average value in a neighborhood of that point. Therefore, the smoothing action of the Laplace operator – amplified by the conductivity parameter D – in a sense counteracts an uneven distribution of mesh cell nodes which is for example given in the case of a highly squeezed cell.

Since the degree of mesh cell distortions is significantly higher in the vicinity of the fluid-solid interface, the function $D(\boldsymbol{\chi})$ may for example be designed to exponentially decay with increasing distance to the interface. An alternative strategy (see [139, 145]), is to model the mesh node diffusion function as

$$D(\boldsymbol{\chi}) = \alpha_u \hat{J}^{-1}, \tag{5.114}$$

where $\alpha_u \geq 0$ is a tweakable parameter. For cells subject to squeezing (typically happening in the vicinity of the interface) it holds $\hat{J} \to 0$. Therefore using (5.114) the diffusion coefficient is correspondingly amplified in those mesh locations.

At this point we reflect the regularity statements presented in [123]. Inside the fluid domain qualitative regularity is given by the smoothing property of the Laplace operator. However, at the fluid-solid interface the regularity of the solid displacement field $\boldsymbol{u}^{\mathcal{S}}$ limits the regularity of the fluid displacement field $\boldsymbol{u}^{\mathcal{F}}$. The regularity of the fluid displacement field may be further limited by the shape of the fluid domain boundary. $\boldsymbol{u}^{\mathcal{F}} \in \boldsymbol{\mathcal{H}}^2(\Omega_{\boldsymbol{X}})$ is the highest regularity one may expect in convex domains, and in concave domains even this regularity is lost.

Linear elastic mesh motion model

The ALE map may alternatively be constructed by means of a pseudo-elasticity problem. To this end one may solve the equations of linearized elasticity

$$\begin{aligned} -\nabla_{\boldsymbol{\chi}} \cdot (\boldsymbol{\sigma}_{\text{mesh}}) &= 0 && \text{in } \Omega^{\mathcal{F}}_{\boldsymbol{\chi}}, \\ \boldsymbol{u}^{\mathcal{F}} &= \boldsymbol{u}^{\mathcal{S}} && \text{on } \Gamma^{\mathcal{I}}_{\boldsymbol{\chi}}, \\ \boldsymbol{u}^{\mathcal{F}} &= 0 && \text{on } \partial\Omega^{\mathcal{F}}_{\boldsymbol{\chi}} \setminus \Gamma^{\mathcal{I}}_{\boldsymbol{\chi}}, \end{aligned} \tag{5.115}$$

with

$$\boldsymbol{\sigma}_{\text{mesh}} = 2\alpha_\mu \boldsymbol{\varepsilon} + \alpha_\lambda \operatorname{tr}(\boldsymbol{\varepsilon})\, \boldsymbol{I}. \tag{5.116}$$

For the derivation of the partial differential equation (5.115), we refer to equations (5.55) and (5.56). Motivated by the arguments that the largest deformations take place in the vicinity of the interface and stiffer cells are harder to deform, the mesh Lamé parameters $\alpha_\mu := \alpha_\mu(\boldsymbol{\chi})$ and $\alpha_\lambda := \alpha_\lambda(\boldsymbol{\chi})$ may be chosen so as to render cells in the vicinity of the fluid-solid interface stiffer than those further away from it.

Biharmonic mesh motion model

Yet another alternative for the construction of the ALE map is the biharmonic mesh motion model which can be used when the deformation should be as “smooth” as possible. It requires to solve the biharmonic equation

$$\begin{aligned} \nabla^4_{\boldsymbol{\chi}} \boldsymbol{u} = \nabla^2_{\boldsymbol{\chi}} \nabla^2_{\boldsymbol{\chi}} \boldsymbol{u} = \Delta^2_{\boldsymbol{\chi}} \boldsymbol{u} &= 0 && \text{in } \Omega^{\mathcal{F}}_{\boldsymbol{\chi}}, \\ \boldsymbol{u}^{\mathcal{F}} = \boldsymbol{u}^{\mathcal{S}}, \partial_{\boldsymbol{n}} \boldsymbol{u}^{\mathcal{F}} &= \partial_{\boldsymbol{n}} \boldsymbol{u}^{\mathcal{S}} && \text{on } \Gamma^{\mathcal{I}}_{\boldsymbol{\chi}}, \\ \boldsymbol{u}^{\mathcal{F}} = 0, \partial_{\boldsymbol{n}} \boldsymbol{u}^{\mathcal{F}} &= 0 && \text{on } \partial\Omega^{\mathcal{F}}_{\boldsymbol{\chi}} \setminus \Gamma^{\mathcal{I}}_{\boldsymbol{\chi}}. \end{aligned} \tag{5.117}$$

The biharmonic equation is a fourth-order partial differential equation which requires $\mathcal{C}^1$ finite elements. Using Isogeometric Analysis, it is easy to setup a (single patch) discrete approximation space with corresponding regularity requirements. The alternative is to reformulate the fourth order equation in terms of two second order equations

$$\Delta_{\boldsymbol{\chi}} \boldsymbol{\eta} = 0 \qquad \text{and} \qquad \boldsymbol{\eta} = \Delta_{\boldsymbol{\chi}} \boldsymbol{u}, \tag{5.118}$$

such that function spaces with lower regularity requirements can be used. Either way, the computational effort to solve the biharmonic equation is quite large. The formulation presented in (5.117) requires the computation of high order derivatives which renders it computationally expensive. The mixed formulation (5.118) comes at the cost of an extra unknown which adds to the global complexity of the system to be solved.

5.3.4 Interface regularity, and existence and uniqueness theory for FSI

In this section we will briefly review the theoretical results published in the literature on aspects of interface regularity as well as on existence and uniqueness theory for FSI.

Our discussion on interface regularity – presented in the sequel – draws on the results and arguments that are published in [109, 123, 160]. We start the discussion with the following thought: *Since the solid velocity $\boldsymbol{v}^{\mathcal{S}}$ can be considered to be a Dirichlet condition for the fluid velocity (Continuity of velocity condition), can we expect it to have enough regularity so as to satisfy the fluid problem?*

We consider the velocity field[46]

$$\boldsymbol{v}^{\mathcal{F}} \in \boldsymbol{\mathcal{L}}^2(I; \boldsymbol{\mathcal{H}}^1(\Omega^{\mathcal{F}}_{\boldsymbol{\chi}})) \tag{5.119}$$

of a solution of the Navier-Stokes equations with right hand side

$$\boldsymbol{f}^{\mathcal{F}} \in \boldsymbol{\mathcal{L}}^2(I; \boldsymbol{\mathcal{H}}^{-1}(\Omega^{\mathcal{F}}_{\boldsymbol{\chi}})) \tag{5.120}$$

solved with initial data $\boldsymbol{v}^{\mathcal{F}}(0) = \boldsymbol{v}^{\mathcal{F},0} \in \boldsymbol{\mathcal{L}}^2(\Omega^{\mathcal{F}}_{\boldsymbol{\chi}})$ in a fixed domain. This velocity field has traces

$$\boldsymbol{v}^{\mathcal{F}}\Big|_{\Gamma^{\mathcal{F}}_{\boldsymbol{\chi}}} \in \boldsymbol{\mathcal{H}}^{1/2}(\Gamma^{\mathcal{F}}_{\boldsymbol{\chi}}). \tag{5.121}$$

Then it follows from the *continuity of velocity condition* (5.108) that the solid velocity field needs to have traces in $\boldsymbol{\mathcal{H}}^{1/2}(\Gamma^{\mathcal{S}}_{\boldsymbol{\chi}})$ as well,

$$\boldsymbol{v}^{\mathcal{F}}\Big|_{\Gamma^{\mathcal{I}}_{\boldsymbol{\chi}}} = \boldsymbol{v}^{\mathcal{S}}\Big|_{\Gamma^{\mathcal{I}}_{\boldsymbol{\chi}}} \implies \boldsymbol{v}^{\mathcal{S}}\Big|_{\Gamma^{\mathcal{S}}_{\boldsymbol{\chi}}} = d_t \boldsymbol{u}^{\mathcal{S}}\Big|_{\Gamma^{\mathcal{S}}_{\boldsymbol{\chi}}} \in \boldsymbol{\mathcal{H}}^{1/2}(\Gamma^{\mathcal{S}}_{\boldsymbol{\chi}}) \tag{5.122}$$

which is given for the solid velocity field

$$\boldsymbol{v}^{\mathcal{S}} = d_t \boldsymbol{u}^{\mathcal{S}} \in \boldsymbol{\mathcal{H}}^1(\Omega^{\mathcal{S}}_{\boldsymbol{\chi}}). \tag{5.123}$$

We refer at this point to recent results provided by Mitrea and Monniaux [109] concerning the regularity of the non-stationary Navier-Lamé problem

$$\rho \frac{\partial^2 \boldsymbol{u}^{\mathcal{S}}}{\partial t^2} - \nabla \cdot \boldsymbol{\sigma} = \rho \boldsymbol{b}, \quad \boldsymbol{u}^{\mathcal{S}}(0) = \boldsymbol{u}^{\mathcal{S},0}, \quad \partial_t \boldsymbol{u}^{\mathcal{S}}(0) = \boldsymbol{v}^{\mathcal{S},0} \tag{5.124}$$

---

[46] For time-dependent functions in Bochner spaces we refer to [163].

with homogeneous Dirichlet data. The authors in principle show that for a sufficiently regular domain boundary (Lipschitz continuous), the solution of the non-stationary Navier-Lamé problem with zero initial, and Dirichlet data satisfies

$$\boldsymbol{u}^{\mathcal{S}} \in \boldsymbol{\mathcal{H}}^1(I; \boldsymbol{\mathcal{L}}^2(\Omega^{\mathcal{S}})) \tag{5.125}$$

for every right hand side $\boldsymbol{f} \in \boldsymbol{\mathcal{L}}^2(I, \boldsymbol{\mathcal{L}}^2(\Omega^{\mathcal{S}}))$ [123]. Then it follows from (5.125) that

$$\boldsymbol{v}^{\mathcal{S}} = \partial_t \boldsymbol{u}^{\mathcal{S}} \in \boldsymbol{\mathcal{L}}^2(I; \boldsymbol{\mathcal{L}}^2(\Omega^{\mathcal{S}})) \tag{5.126}$$

and this is not sufficient to define a $\boldsymbol{\mathcal{H}}^{1/2}$-trace on the fluid-solid interface. In general, one can unfortunately only expect (the insufficient regularity) $\boldsymbol{u}^{\mathcal{S}} \in \boldsymbol{\mathcal{H}}^1(\Omega^{\mathcal{S}})$ and $\boldsymbol{v}^{\mathcal{S}} \in \boldsymbol{\mathcal{L}}^2(\Omega^{\mathcal{S}})$ [109, 132]. This lack of regularity poses an issue when it comes to the imposition of the *continuity of velocity condition* (5.108). In fact, using standard fluid and solid equations, the solid velocity does not provide enough regularity on the interface to be coupled with the fluid equations. We present two approaches to overcome this lack of regularity. The first approach simply adds some (smoothing/stabilizing) diffusion terms acting on the velocity variable to the solid equations. Considering a formulation in terms of displacement and velocity, it is enough to replace

$$\boldsymbol{v}^{\mathcal{S}} = d_t \boldsymbol{u}^{\mathcal{S}}, \tag{5.127}$$

with

$$\boldsymbol{v}^{\mathcal{S}} - \alpha^{\mathcal{S}} \Delta \boldsymbol{v}^{\mathcal{S}} = d_t \boldsymbol{u}^{\mathcal{S}}, \tag{5.128}$$

in order to obtain sufficient regularity. The consistency error made above can be controlled with the parameter $\alpha^{\mathcal{S}}$ and as shown in [61], for a small enough $\alpha^{\mathcal{S}}$ the overall accuracy is not deteriorated.

The second and alternative approach is to add damping terms to (linear) "solid" equations. This approach draws on the results provided by Gazzola and Squassina [64] where the authors study the behavior of local solutions of the (hyperbolic) wave equation[47] with (possibly strong) linear damping

$$\begin{cases} u_{tt} - \Delta u - \omega \Delta u_t + \mu u_t = f & \text{in } [0,T] \times \Omega, \\ u(0,x) = u_0(x) & \text{in } \Omega, \\ u_t(0,x) = u_1(x) & \text{in } \Omega, \\ u(t,x) = 0 & \text{on } [0,T] \times \partial\Omega. \end{cases} \tag{5.129}$$

Above, the right hand side function f is sufficient regular, Ω is an open and bounded Lipschitz subset of $\mathbb{R}^n (n \geq 1), T > 0, u_0 \in \mathcal{H}_0^1(\Omega), u_1 \in \mathcal{L}^2(\Omega), \omega \geq 0, \mu > -\omega\lambda_1$, and λ_1 is the first eigenvalue of the operator $-\Delta$ under homogeneous Dirichlet boundary conditions. The authors show that this problem has a unique solution satisfying

$$u \in \mathcal{C}^0\left([0,T], \mathcal{H}_0^1(\Omega)\right) \cap \mathcal{C}^1\left([0,T], \mathcal{L}^2(\Omega)\right) \cap \mathcal{C}^2\left([0,T], \mathcal{H}^{-1}(\Omega)\right), \tag{5.130}$$

with

$$v = u_t \in \mathcal{L}^2\left([0,T], \mathcal{H}_0^1(\Omega)\right) \tag{5.131}$$

whenever $\omega > 0$. Due to the high regularity provided by the linear strong damping, we can assume $v \in \mathcal{H}^{1/2}(\partial\Omega)$ such that the *continuity of velocity condition* (5.108) holds true when the linear equation (5.129) is used as the governing equation for the solid problem.

---

[47] The presentation form used in (5.129) deliberately follows that of Gazzola and Squassina, but the main result presented in (5.131) can be perfectly used in the course of our FSI interface regularity discussion.

In the spirit of the above approach, however without theoretical assertions on the solution regularity, one may come up with the idea to add damping terms to the equations of elastodynamics (5.48). Doing so (cf. [160]), we obtain:

$$\begin{aligned}
J\rho \frac{\partial \boldsymbol{v}^{\mathcal{S}}}{\partial t} - \nabla_{\boldsymbol{X}} \cdot \boldsymbol{P} + \gamma_w \frac{\partial \boldsymbol{u}^{\mathcal{S}}}{\partial t} - \gamma_s \partial_t \nabla_{\boldsymbol{X}} \cdot \boldsymbol{\epsilon}(\boldsymbol{u}^{\mathcal{S}}) &= J\rho \boldsymbol{b} && \text{in } \Omega_{\boldsymbol{X}} \times I, \\
\frac{\partial \boldsymbol{u}^{\mathcal{S}}}{\partial t} - \boldsymbol{v}^{\mathcal{S}} &= 0 && \text{in } \Omega_{\boldsymbol{X}} \times I, \\
\boldsymbol{u}^{\mathcal{S}}(\cdot, 0) = \mathring{\boldsymbol{u}}, \boldsymbol{v}^{\mathcal{S}}(\cdot, 0) &= \mathring{\boldsymbol{v}} && \text{in } \Omega_{\boldsymbol{X}}, \\
\boldsymbol{u}^{\mathcal{S}} &= \boldsymbol{u}_D^{\mathcal{S}} && \text{on } \Gamma_{D,\boldsymbol{X}} \times I, \\
\boldsymbol{P}\boldsymbol{n}_0 &= \boldsymbol{g}_0 && \text{on } \Gamma_{N,\boldsymbol{X}} \times I.
\end{aligned} \tag{5.132}$$

Above, the terms containing the parameters γ_w and γ_s denote the weak, and (linear) strong damping terms, respectively and $\boldsymbol{\epsilon}(\boldsymbol{w}) := \frac{1}{2}\left(\nabla \boldsymbol{w} + (\nabla \boldsymbol{w})^T\right)$. Under the premise that spatial and temporal differentiation can be exchanged, it holds

$$-\gamma_s \partial_t \nabla_{\boldsymbol{X}} \cdot \boldsymbol{\epsilon}(\boldsymbol{u}^{\mathcal{S}}) = -\gamma_s \nabla_{\boldsymbol{X}} \cdot \boldsymbol{\epsilon}(\partial_t \boldsymbol{u}^{\mathcal{S}}) = -\gamma_s \nabla_{\boldsymbol{X}} \cdot \boldsymbol{\epsilon}(\boldsymbol{v}^{\mathcal{S}}) \tag{5.133}$$

and the first equation in (5.132) can be replaced with

$$J\rho \frac{\partial \boldsymbol{v}^{\mathcal{S}}}{\partial t} - \nabla_{\boldsymbol{X}} \cdot \boldsymbol{P} + \gamma_w \boldsymbol{v}^{\mathcal{S}} - \gamma_s \nabla_{\boldsymbol{X}} \cdot \boldsymbol{\epsilon}(\boldsymbol{v}^{\mathcal{S}}) = J\rho \boldsymbol{b}. \tag{5.134}$$

We proceed with a concise literature review of existence and uniqueness theory for FSI. Given the fact that we still lack a fully developed theory providing general results on existence and uniqueness of solutions of the incompressible Navier-Stokes equations in two and three dimensions, the question emerges how we can expect such a general theory to exist for the significantly more complicated FSI problem in the first place. The coupled FSI problem is afflicted by additional problems, one of them being the motion of the fluid and solid domains that is steered be the problem solution (displacement $\boldsymbol{u}$) itself. Since the solid displacement $\boldsymbol{u}^{\mathcal{S}}$ affects the deformation of the solid domain including the fluid-solid interface, low regularity of $\boldsymbol{u}^{\mathcal{S}}$ implies low regularity of both subdomains which then in turn may limit the regularities of the two subproblem solution functions. Another complicating factor is the coupling of partial differential equations of potentially different types. Therefore, it comes as no surprise that theoretical results on coupled fluid-solid interaction are not abundant.

For the case of steady state FSI problems, we refer to the results published by Grandmont [69], where the author uses a St. Venant Kirchhoff model for the elastic structure and sets the equations of viscous fluid motion in an unknown domain depending on the structure displacement. The equations for the fluid and solid problems in steady state configuration are governed by elliptic operators. The author shows the existence of a solution to this problem for small enough applied exterior forces. However, apart from small right hand side and boundary data, uniqueness cannot be assured by the argument that have been used to show existence [160]. Various other articles prove existence (and uniqueness) for certain *special* configurations.

In the case of transient FSI problems, the equations governing the fluid problem are of parabolic character, whereas the solid problem is governed by equations of hyperbolic type. The different behaviors of the involved equations lead to a lack of regularity at the fluid-solid interface which we have addressed above. A linearized and therefore greatly simplified FSI problem is given by the combination of the (linear) incompressible Stokes flow equations being of parabolic type and the hyperbolic (linear) Navier-Lamé equations on fixed fluid and solid domains. For results on existence and regularity of solutions of this coupled problem we refer to [9–12, 48, 49]. Coutand and Shkoller investigated the motion of an elastic solid inside an incompressible elastic fluid and proved existence and uniqueness of such motions, when the elastic solid is the linear Kirchhoff elastic material. Coupling the time-dependent Navier-Stokes equations set in Lagrangian variables and the linear equations of elastodynamics, they proved the existence of a unique weak solution for which they also provided corresponding regularity statements [39]. The same authors proved in [40] the existence and uniqueness (locally in time) of strong solutions in Sobolev spaces for quasilinear elastodynamics coupled to the incompressible Navier-Stokes equations. However they impose very high regularity requirements on the initial data as well as on the computational domain and the fluid-solid interface.

5.3.5 Coupled ALE formulation

Combining the results obtained so far, the strong form of the monolithic FSI problem in ALE formulation using the harmonic mesh motion model, reads:

$$
\begin{aligned}
&\hat{J}\rho^{\mathcal{F}}\left(\frac{\partial \boldsymbol{v}^{\mathcal{F}}}{\partial t}\Big|_{\boldsymbol{\chi}} + \nabla_{\boldsymbol{\chi}}\boldsymbol{v}^{\mathcal{F}}\left(\hat{\boldsymbol{F}}^{-1}(\boldsymbol{v}^{\mathcal{F}} - \partial_t\hat{\boldsymbol{\mathcal{A}}})\right)\right) && \\
-\nabla_{\boldsymbol{\chi}}\cdot\left(\hat{J}\left(-p^{\mathcal{F}}\boldsymbol{I} + \mu^{\mathcal{F}}\left(\nabla_{\boldsymbol{\chi}}\boldsymbol{v}^{\mathcal{F}}\hat{\boldsymbol{F}}^{-1} + \hat{\boldsymbol{F}}^{-T}(\nabla_{\boldsymbol{\chi}}\boldsymbol{v}^{\mathcal{F}})^{T}\right)\right)\hat{\boldsymbol{F}}^{-T}\right) &= \hat{J}\rho^{\mathcal{F}}\boldsymbol{b}^{\mathcal{F}} && \text{in } \Omega^{\mathcal{F}}_{\boldsymbol{\chi}}\times(0,T),\\
\nabla_{\boldsymbol{\chi}}\cdot\left(\hat{J}\hat{\boldsymbol{F}}^{-1}\boldsymbol{v}^{\mathcal{F}}\right) &= 0 && \text{in } \Omega^{\mathcal{F}}_{\boldsymbol{\chi}}\times[0,T),\\
p^{\mathcal{F}}(\cdot,0) = \mathring{p}^{\mathcal{F}}, \boldsymbol{u}^{\mathcal{F}}(\cdot,0) = \mathring{\boldsymbol{u}}^{\mathcal{F}}, \boldsymbol{v}^{\mathcal{F}}(\cdot,0) &= \mathring{\boldsymbol{v}}^{\mathcal{F}} && \text{in } \Omega^{\mathcal{F}}_{\boldsymbol{\chi}},\\
\boldsymbol{u}^{\mathcal{F}} = \boldsymbol{u}^{\mathcal{F}}_{D}, \boldsymbol{v}^{\mathcal{F}} &= \boldsymbol{v}^{\mathcal{F}}_{D} && \text{on } \Gamma^{\mathcal{F}}_{D,\boldsymbol{\chi}}\times(0,T),\\
\left(\hat{J}\boldsymbol{\sigma}^{\mathcal{F}}\hat{\boldsymbol{F}}^{-T}\right)\boldsymbol{n}^{\mathcal{F}}_{0} &= \boldsymbol{g}^{\mathcal{F}}_{0} && \text{on } \Gamma^{\mathcal{F}}_{N,\boldsymbol{\chi}}\times(0,T).\\
\hat{J}\rho^{\mathcal{S}}\frac{\partial \boldsymbol{v}^{\mathcal{S}}}{\partial t}\Big|_{\boldsymbol{\chi}} - \nabla_{\boldsymbol{\chi}}\cdot\hat{\boldsymbol{P}}^{\mathcal{S}} &= \hat{J}\rho^{\mathcal{S}}\boldsymbol{b}^{\mathcal{S}} && \text{in } \Omega^{\mathcal{S}}_{\boldsymbol{\chi}}\times(0,T),\\
\frac{\partial \boldsymbol{u}^{\mathcal{S}}}{\partial t} - \boldsymbol{v}^{\mathcal{S}} &= 0 && \text{in } \Omega^{\mathcal{S}}_{\boldsymbol{\chi}}\times(0,T),\\
\boldsymbol{u}^{\mathcal{S}}(\cdot,0) = \mathring{\boldsymbol{u}}^{\mathcal{S}}, \boldsymbol{v}^{\mathcal{S}}(\cdot,0) &= \mathring{\boldsymbol{v}}^{\mathcal{S}} && \text{in } \Omega^{\mathcal{S}}_{\boldsymbol{\chi}},\\
\boldsymbol{u}^{\mathcal{S}} = \boldsymbol{u}^{\mathcal{S}}_{D}, \boldsymbol{v}^{\mathcal{S}} &= \boldsymbol{v}^{\mathcal{S}}_{D} && \text{on } \Gamma^{\mathcal{S}}_{D,\boldsymbol{\chi}}\times(0,T),\\
\hat{\boldsymbol{P}}^{\mathcal{S}}\boldsymbol{n}^{\mathcal{S}}_{0} &= \boldsymbol{g}^{\mathcal{S}}_{0} && \text{on } \Gamma^{\mathcal{S}}_{N,\boldsymbol{\chi}}\times(0,T).\\
\nabla_{\boldsymbol{\chi}}\cdot\left(\alpha_u\hat{J}^{-1}\nabla_{\boldsymbol{\chi}}\boldsymbol{u}^{\mathcal{F}}\right) &= 0 && \text{in } \Omega^{\mathcal{F}}_{\boldsymbol{\chi}}\times(0,T),\\
\boldsymbol{u}^{\mathcal{F}} = \boldsymbol{u}^{\mathcal{S}}, \boldsymbol{v}^{\mathcal{F}} &= \boldsymbol{v}^{\mathcal{S}}, && \text{on } \Gamma^{\mathcal{I}}_{\boldsymbol{\chi}}\times(0,T).
\end{aligned}
\tag{5.135}
$$

Above, the first Piola-Kirchhoff stress tensor of the solid may be chosen with respect to different materials, such as e.g. the St. Venant-Kirchhoff

$$
\hat{\boldsymbol{P}}^{\mathcal{S}} := \lambda\,\mathrm{tr}\left(\hat{\boldsymbol{E}}\right)\hat{\boldsymbol{F}} + 2\mu\hat{\boldsymbol{F}}\hat{\boldsymbol{E}}, \tag{5.136}
$$

or the Neo-Hookean material

$$
\hat{\boldsymbol{P}}^{\mathcal{S}} := \mu(\hat{\boldsymbol{F}} - \hat{\boldsymbol{F}}^{-T}) + \lambda\log(\det\hat{\boldsymbol{F}})\hat{\boldsymbol{F}}^{-T}. \tag{5.137}
$$

Moreover, it is easily possible to modify (5.135) so as to work with an alternative mesh motion model. For the variational formulation of (5.135) it is necessary to define a set of trial and test spaces in the fluid and solid domains which is presented in the sequel.

With regard to the spaces in the (fixed referential) domain, we

- let the displacement trial and test spaces in the fluid domain be defined as

$$\begin{aligned}\boldsymbol{\mathcal{T}}^{\boldsymbol{u},\mathcal{F}} &:= \{\boldsymbol{u}^{\mathcal{F}} \in \boldsymbol{\mathcal{H}}^1(\Omega^{\mathcal{F}}_{\boldsymbol{\mathcal{X}}}) \,|\, \boldsymbol{u}^{\mathcal{F}} = \boldsymbol{u}^{\mathcal{S}} \text{ on } \Gamma^{\mathcal{I}}_{\chi}, \boldsymbol{u}^{\mathcal{F}} = \boldsymbol{u}^{\mathcal{F}}_{D} \text{ on } \Gamma^{\mathcal{F}}_{D,\boldsymbol{\mathcal{X}}}\},\\ \boldsymbol{\mathcal{W}}^{\boldsymbol{u},\mathcal{F}} &:= \{\boldsymbol{\phi}^{\boldsymbol{u},\mathcal{F}} \in \boldsymbol{\mathcal{H}}^1_0(\Omega^{\mathcal{F}}_{\boldsymbol{\mathcal{X}}};\Gamma^{\mathcal{F}}_{D,\boldsymbol{\mathcal{X}}}) \,|\, \boldsymbol{\phi}^{\boldsymbol{u},\mathcal{F}} = \boldsymbol{\phi}^{\boldsymbol{u},\mathcal{S}} \text{ on } \Gamma^{\mathcal{I}}_{\chi}\},\end{aligned} \tag{5.138}$$

- let the velocity trial and test spaces in the fluid domain be defined as

$$\begin{aligned}\boldsymbol{\mathcal{T}}^{\boldsymbol{v},\mathcal{F}} &:= \{\boldsymbol{v}^{\mathcal{F}} \in \boldsymbol{\mathcal{H}}^1(\Omega^{\mathcal{F}}_{\boldsymbol{\mathcal{X}}}) \,|\, \boldsymbol{v}^{\mathcal{F}} = \boldsymbol{v}^{\mathcal{S}} \text{ on } \Gamma^{\mathcal{I}}_{\chi}, \boldsymbol{v}^{\mathcal{F}} = \boldsymbol{v}^{\mathcal{F}}_{D} \text{ on } \Gamma^{\mathcal{F}}_{D,\boldsymbol{\mathcal{X}}}\},\\ \boldsymbol{\mathcal{W}}^{\boldsymbol{v},\mathcal{F}} &:= \{\boldsymbol{\phi}^{\boldsymbol{v},\mathcal{F}} \in \boldsymbol{\mathcal{H}}^1_0(\Omega^{\mathcal{F}}_{\boldsymbol{\mathcal{X}}};\Gamma^{\mathcal{F}}_{D,\boldsymbol{\mathcal{X}}}) \,|\, \boldsymbol{\phi}^{\boldsymbol{v},\mathcal{F}} = \boldsymbol{\phi}^{\boldsymbol{v},\mathcal{S}} \text{ on } \Gamma^{\mathcal{I}}_{\chi}\},\end{aligned} \tag{5.139}$$

- and let the pressure trial and test spaces in the fluid domain be defined as

$$\mathcal{L}^{\mathcal{F}} := \mathcal{L}^2(\Omega^{\mathcal{F}}_{\boldsymbol{\mathcal{X}}})/\mathbb{R}. \tag{5.140}$$

It remains to specify the trial and test spaces in the solid domain. We let

- the displacement trial and test space in the solid domain be defined as

$$\begin{aligned}\boldsymbol{\mathcal{T}}^{\boldsymbol{u},\mathcal{S}} &:= \{\boldsymbol{u}^{\mathcal{S}} \in \boldsymbol{\mathcal{H}}^1(\Omega^{\mathcal{S}}_{\boldsymbol{\mathcal{X}}}) \,|\, \boldsymbol{u}^{\mathcal{S}} = \boldsymbol{u}^{\mathcal{S}}_{D} \text{ on } \Gamma^{\mathcal{S}}_{D,\boldsymbol{\mathcal{X}}}\},\\ \boldsymbol{\mathcal{W}}^{\boldsymbol{u},\mathcal{S}} &:= \boldsymbol{\mathcal{H}}^1_0(\Omega^{\mathcal{S}}_{\boldsymbol{\mathcal{X}}};\Gamma^{\mathcal{S}}_{D,\boldsymbol{\mathcal{X}}}),\end{aligned} \tag{5.141}$$

- the velocity trial and test space in the solid domain be defined as

$$\begin{aligned}\boldsymbol{\mathcal{T}}^{\boldsymbol{v},\mathcal{S}} &:= \{\boldsymbol{v}^{\mathcal{S}} \in \boldsymbol{\mathcal{H}}^1(\Omega^{\mathcal{S}}_{\boldsymbol{\mathcal{X}}}) \,|\, \boldsymbol{v}^{\mathcal{S}} = \boldsymbol{v}^{\mathcal{S}}_{D} \text{ on } \Gamma^{\mathcal{S}}_{D,\boldsymbol{\mathcal{X}}}\},\\ \boldsymbol{\mathcal{W}}^{\boldsymbol{v},\mathcal{S}} &:= \boldsymbol{\mathcal{H}}^1_0(\Omega^{\mathcal{S}}_{\boldsymbol{\mathcal{X}}};\Gamma^{\mathcal{S}}_{D,\boldsymbol{\mathcal{X}}}),\end{aligned} \tag{5.142}$$

- and let the pressure trial and test spaces in the solid domain be defined as

$$\mathcal{L}^{\mathcal{S}} := \mathcal{L}^2(\Omega^{\mathcal{S}}_{\boldsymbol{\mathcal{X}}})/\mathbb{R}. \tag{5.143}$$

Problem 5.3.4 (Variational formulation of the FSI problem in ALE coordinates with harmonic mesh motion). *Let* $\boldsymbol{\mathcal{T}} := \{\boldsymbol{\mathcal{T}}^{\boldsymbol{v},\mathcal{F}} \times \boldsymbol{\mathcal{T}}^{\boldsymbol{v},\mathcal{S}} \times \boldsymbol{\mathcal{T}}^{\boldsymbol{u},\mathcal{F}} \times \boldsymbol{\mathcal{T}}^{\boldsymbol{u},\mathcal{S}} \times \mathcal{L}^{\mathcal{F}} \times \mathcal{L}^{\mathcal{S}}\}$ *and* $\boldsymbol{\mathcal{W}} := \{\boldsymbol{\mathcal{W}}^{\boldsymbol{v},\mathcal{F}} \times \boldsymbol{\mathcal{V}}^{\boldsymbol{v},\mathcal{S}} \times \boldsymbol{\mathcal{W}}^{\boldsymbol{u},\mathcal{F}} \times \boldsymbol{\mathcal{V}}^{\boldsymbol{u},\mathcal{S}} \times \mathcal{L}^{\mathcal{F}} \times \mathcal{L}^{\mathcal{S}}\}$*. Find* $\boldsymbol{U} = \{\boldsymbol{v}^{\mathcal{F}}, \boldsymbol{v}^{\mathcal{S}}, \boldsymbol{u}^{\mathcal{F}}, \boldsymbol{u}^{\mathcal{S}}, p^{\mathcal{F}}, p^{\mathcal{S}}\} \in \boldsymbol{\mathcal{T}} \times I$*, such that* $\boldsymbol{u}^{\mathcal{F}}(0) = \mathring{\boldsymbol{u}}^{\mathcal{F}}, \boldsymbol{v}^{\mathcal{F}}(0) =$

$\mathring{\boldsymbol{v}}^{\mathcal{F}}$, $\boldsymbol{u}^{\mathcal{S}}(0) = \mathring{\boldsymbol{u}}^{\mathcal{S}}$ *and* $\boldsymbol{v}^{\mathcal{S}}(0) = \mathring{\boldsymbol{v}}^{\mathcal{S}}$ *are satisfied, and it holds:*

$$
\begin{aligned}
&\int_0^T \int_{\Omega_{\boldsymbol{\chi}}^{\mathcal{F}}} \hat{J}\rho^{\mathcal{F}} \left(\frac{\partial \boldsymbol{v}^{\mathcal{F}}}{\partial t}\Big|_{\boldsymbol{\chi}} + \nabla_{\boldsymbol{\chi}} \boldsymbol{v}^{\mathcal{F}} \left(\hat{\boldsymbol{F}}^{-1} (\boldsymbol{v}^{\mathcal{F}} - \partial_t \hat{\boldsymbol{\mathcal{A}}}) \right) \right) \cdot \boldsymbol{\phi}^{\boldsymbol{v},\mathcal{F}} \, \mathrm{d}\Omega_{\boldsymbol{\chi}}^{\mathcal{F}} \, \mathrm{d}t \\
&+ \int_0^T \int_{\Omega_{\boldsymbol{\chi}}^{\mathcal{F}}} \hat{J} \left(-p^{\mathcal{F}} \boldsymbol{I} + \mu^{\mathcal{F}} \left(\nabla_{\boldsymbol{\chi}} \boldsymbol{v}^{\mathcal{F}} \hat{\boldsymbol{F}}^{-1} + \hat{\boldsymbol{F}}^{-T} (\nabla_{\boldsymbol{\chi}} \boldsymbol{v}^{\mathcal{F}})^T \right) \right) \hat{\boldsymbol{F}}^{-T} : \nabla_{\boldsymbol{\chi}} \boldsymbol{\phi}^{\boldsymbol{v},\mathcal{F}} \, \mathrm{d}\Omega_{\boldsymbol{\chi}}^{\mathcal{F}} \, \mathrm{d}t \\
&- \int_0^T \int_{\Omega_{\boldsymbol{\chi}}^{\mathcal{F}}} \hat{J}\rho^{\mathcal{F}} \boldsymbol{f}^{\mathcal{F}} \cdot \boldsymbol{\phi}^{\boldsymbol{v},\mathcal{F}} \, \mathrm{d}\Omega_{\boldsymbol{\chi}}^{\mathcal{F}} \, \mathrm{d}t - \int_0^T \int_{\Gamma_{N,\boldsymbol{\chi}}^{\mathcal{F}}} \boldsymbol{g}_0^{\mathcal{F}} \cdot \boldsymbol{\phi}^{\boldsymbol{v},\mathcal{F}} \, \mathrm{d}\Gamma_{N,\boldsymbol{\chi}}^{\mathcal{F}} \, \mathrm{d}t = 0 && \forall \boldsymbol{\phi}^{\boldsymbol{v},\mathcal{F}} \in \boldsymbol{\mathcal{W}}^{\boldsymbol{v},\mathcal{F}}, \\
&\int_0^T \int_{\Omega_{\boldsymbol{\chi}}^{\mathcal{F}}} \nabla_{\boldsymbol{\chi}} \cdot \left(\hat{J} \hat{\boldsymbol{F}}^{-1} \boldsymbol{v}^{\mathcal{F}} \right) \cdot \phi^{p,\mathcal{F}} \, \mathrm{d}\Omega_{\boldsymbol{\chi}}^{\mathcal{F}} \, \mathrm{d}t = 0 && \forall \phi^{p,\mathcal{F}} \in \mathcal{L}^{\mathcal{F}}, \\
&\int_0^T \int_{\Omega_{\boldsymbol{\chi}}^{\mathcal{S}}} \hat{J}\rho^{\mathcal{S}} \frac{\partial \boldsymbol{v}^{\mathcal{S}}}{\partial t}\Big|_{\boldsymbol{\chi}} \cdot \boldsymbol{\phi}^{\boldsymbol{v},\mathcal{S}} \, \mathrm{d}\Omega_{\boldsymbol{\chi}}^{\mathcal{S}} \, \mathrm{d}t + \int_0^T \int_{\Omega_{\boldsymbol{\chi}}^{\mathcal{S}}} \hat{\boldsymbol{P}}^{\mathcal{S}} : \nabla_{\boldsymbol{\chi}} \boldsymbol{\phi}^{\boldsymbol{v},\mathcal{S}} \, \mathrm{d}\Omega_{\boldsymbol{\chi}}^{\mathcal{S}} \, \mathrm{d}t \\
&- \int_0^T \int_{\Omega_{\boldsymbol{\chi}}^{\mathcal{S}}} \hat{J}\rho^{\mathcal{S}} \boldsymbol{b}^{\mathcal{S}} \cdot \boldsymbol{\phi}^{\boldsymbol{v},\mathcal{S}} \, \mathrm{d}\Omega_{\boldsymbol{\chi}}^{\mathcal{S}} \, \mathrm{d}t - \int_0^T \int_{\Gamma_{N,\boldsymbol{\chi}}^{\mathcal{S}}} \boldsymbol{g}_0^{\mathcal{S}} \cdot \boldsymbol{\phi}^{\boldsymbol{v},\mathcal{S}} \, \mathrm{d}\Gamma_{N,\boldsymbol{\chi}}^{\mathcal{S}} \, \mathrm{d}t = 0 && \forall \boldsymbol{\phi}^{\boldsymbol{v},\mathcal{S}} \in \boldsymbol{\mathcal{W}}^{\boldsymbol{v},\mathcal{S}}, \\
&\int_0^T \int_{\Omega_{\boldsymbol{\chi}}^{\mathcal{S}}} \left(\frac{\partial \boldsymbol{u}^{\mathcal{S}}}{\partial t}\Big|_{\boldsymbol{\chi}} - \boldsymbol{v}^{\mathcal{S}} \right) \cdot \boldsymbol{\phi}^{\boldsymbol{u},\mathcal{S}} \, \mathrm{d}\Omega_{\boldsymbol{\chi}}^{\mathcal{S}} \, \mathrm{d}t = 0 && \forall \boldsymbol{\phi}^{\boldsymbol{u},\mathcal{S}} \in \boldsymbol{\mathcal{W}}^{\boldsymbol{u},\mathcal{S}}, \\
&\int_0^T \int_{\Omega_{\boldsymbol{\chi}}^{\mathcal{S}}} p^{\mathcal{S}} \cdot \phi^{p,\mathcal{S}} \, \mathrm{d}\Omega_{\boldsymbol{\chi}}^{\mathcal{S}} \, \mathrm{d}t = 0 && \forall \phi^{p,\mathcal{S}} \in \mathcal{L}^{\mathcal{S}}, \\
&\int_0^T \int_{\Omega_{\boldsymbol{\chi}}^{\mathcal{F}}} \alpha_u \hat{J}^{-1} \nabla_{\boldsymbol{\chi}} \boldsymbol{u}^{\mathcal{F}} : \nabla_{\boldsymbol{\chi}} \boldsymbol{\phi}^{\boldsymbol{u}} \, \mathrm{d}\Omega_{\boldsymbol{\chi}}^{\mathcal{F}} \, \mathrm{d}t = 0 && \forall \boldsymbol{\phi}^{\boldsymbol{u},\mathcal{F}} \in \boldsymbol{\mathcal{W}}^{\boldsymbol{u},\mathcal{F}}.
\end{aligned}
\tag{5.144}
$$

In terms of a variational formulation, the *continuity of normal stresses condition*

$$
\hat{J} \boldsymbol{\sigma}^{\mathcal{F}} \hat{\boldsymbol{F}}^{-T} \boldsymbol{n}_0^{\mathcal{F}} + \hat{J} \boldsymbol{\sigma}^{\mathcal{S}} \hat{\boldsymbol{F}}^{-T} \boldsymbol{n}_0^{\mathcal{S}} = 0 \qquad \text{on } \Gamma_{\boldsymbol{\chi}}^{\mathcal{I}}, \tag{5.145}
$$

may in principle be presented in the form of a jump of the first Piola-Kirchhoff normal stress of both systems, that is

$$
\left(\hat{J} \boldsymbol{\sigma}^{\mathcal{F}} \hat{\boldsymbol{F}}^{-T} \boldsymbol{n}_0^{\mathcal{F}}, \boldsymbol{\phi}^{\boldsymbol{v},\mathcal{F}} \right)_{\Gamma_{\boldsymbol{\chi}}^{\mathcal{I}}} + \left(\hat{J} \boldsymbol{\sigma}^{\mathcal{S}} \hat{\boldsymbol{F}}^{-T} \boldsymbol{n}_0^{\mathcal{S}}, \boldsymbol{\phi}^{\boldsymbol{v},\mathcal{S}} \right)_{\Gamma_{\boldsymbol{\chi}}^{\mathcal{I}}}. \tag{5.146}
$$

However, by omitting the above boundary integral jump, the (weak) continuity of the normal stress becomes an implicit condition of the combined variational formulation (6.16) [52].

Remark 5.3.1. *Trying to explicitly enforce (5.146) turned up to be problematic in our tests. Since we use a monolithic method with matching test functions along the fluid-solid interface, the continuity of normal stresses condition is satisfied in a weak sense automatically. Trying to explicitly enforce this condition could arguably be interpreted as the attempt to impose too many conditions on the interface.*

5.3.5.1 Discretization and treatment of nonlinearity

The solution of the monolithically coupled highly nonlinear FSI problem (6.16) requires a discretization in space and time. For the temporal discretization we use finite differences and present two quasi-stationary counterparts of (6.16) obtained with the one-step θ-scheme and fractional-step θ-scheme. We apply Galerkin-based Isogeometric Analysis for the spatial discretization. The system at hand after the spatial and temporal discretization is still highly nonlinear. For the treatment of the nonlinearity of the discretized monolithically coupled FSI system, we will apply Newton's method. In this regard, we will present in the spirit of the examples presented in [52, 57, 122, 124, 160, 161] how the corresponding Jacobian matrix can be derived analytically.

We start with the aspect of temporal discretization for which we partition the time interval $I = [0, T]$ into subintervals $I_n = [t_{n-1}, t_n]$ of time step size $\delta t := t_n - t_{n-1}$ with $0 = t_0 < \ldots < t_N = T$. Moreover, with $\Phi = \{\boldsymbol{\phi}^{v,\mathcal{F}}, \boldsymbol{\phi}^{v,\mathcal{S}}, \boldsymbol{\phi}^{u,\mathcal{F}}, \boldsymbol{\phi}^{u,\mathcal{S}}, \phi^{p,\mathcal{F}}, \phi^{p,\mathcal{S}}\}$, we let (6.16) be represented in an abstract form as

$$\int_0^T A(\boldsymbol{U}; \Phi)\,\mathrm{d}t = \int_0^T F(\Phi)\,\mathrm{d}t \quad \forall \Phi \in \boldsymbol{\mathcal{W}},$$

where the linear form $F(\Phi)$ is defined as

$$F(\Phi) := \left(\hat{J}\rho^{\mathcal{F}}\boldsymbol{b}^{\mathcal{F}}, \boldsymbol{\phi}^{\boldsymbol{v}}\right)_{\Omega^{\mathcal{F}}_{\boldsymbol{\chi}}} + \left(\hat{J}\rho^{\mathcal{S}}\boldsymbol{b}^{\mathcal{S}}, \boldsymbol{\phi}^{\boldsymbol{v}}\right)_{\Omega^{\mathcal{S}}_{\boldsymbol{\chi}}}, \tag{5.147}$$

and the semilinear form $A(\boldsymbol{U}; \Phi)$ is defined with the following partition

$$A(\boldsymbol{U}; \Phi) := A_{\mathrm{I}}(\boldsymbol{U}; \Phi) + A_{\mathrm{II}}(\boldsymbol{U}; \Phi) + A_{\mathrm{III}}(\boldsymbol{U}; \Phi) + A_{\mathrm{IV}}(\boldsymbol{U}; \Phi), \tag{5.148}$$

where

$$\begin{aligned}
A_{\mathrm{I}}(\boldsymbol{U}; \Phi) &= \left(\hat{J}\rho^{\mathcal{F}}\frac{\partial \boldsymbol{v}^{\mathcal{F}}}{\partial t}\Big|_{\boldsymbol{\chi}}, \boldsymbol{\phi}^{\boldsymbol{v},\mathcal{F}}\right)_{\Omega^{\mathcal{F}}_{\boldsymbol{\chi}}} - \left(\hat{J}\rho^{\mathcal{F}}\nabla_{\boldsymbol{\chi}}\boldsymbol{v}^{\mathcal{F}}\hat{\boldsymbol{F}}^{-1}\hat{\boldsymbol{v}}^{\mathcal{F}}, \boldsymbol{\phi}^{\boldsymbol{v},\mathcal{F}}\right)_{\Omega^{\mathcal{F}}_{\boldsymbol{\chi}}} \\
&\quad + \left(\hat{J}\rho^{\mathcal{S}}\,\frac{\partial \boldsymbol{v}^{\mathcal{S}}}{\partial t}\Big|_{\boldsymbol{\chi}}, \boldsymbol{\phi}^{\boldsymbol{v},\mathcal{S}}\right)_{\Omega^{\mathcal{S}}_{\boldsymbol{\chi}}} + \left(\rho^{\mathcal{S}}\,\frac{\partial \boldsymbol{u}^{\mathcal{S}}}{\partial t}\Big|_{\boldsymbol{\chi}}, \boldsymbol{\phi}^{\boldsymbol{u},\mathcal{S}}\right)_{\Omega^{\mathcal{S}}_{\boldsymbol{\chi}}} \\
A_{\mathrm{II}}(\boldsymbol{U}; \Phi) &= \left(\alpha_u\hat{J}^{-1}\nabla_{\boldsymbol{\chi}}\boldsymbol{u}^{\mathcal{F}}, \nabla_{\boldsymbol{\chi}}\boldsymbol{\phi}^{\boldsymbol{u},\mathcal{F}}\right)_{\Omega^{\mathcal{F}}_{\boldsymbol{\chi}}} + \left(\nabla_{\boldsymbol{\chi}}\cdot\left(\hat{J}\hat{\boldsymbol{F}}^{-1}\boldsymbol{v}^{\mathcal{F}}\right), \phi^{p,\mathcal{F}}\right)_{\Omega^{\mathcal{F}}_{\boldsymbol{\chi}}} + \left(p^{\mathcal{S}}, \phi^{p,\mathcal{S}}\right)_{\Omega^{\mathcal{S}}_{\boldsymbol{\chi}}} \\
A_{\mathrm{III}}(\boldsymbol{U}; \Phi) &= \left(\hat{J}\rho^{\mathcal{F}}\left(\nabla_{\boldsymbol{\chi}}\boldsymbol{v}^{\mathcal{F}}\hat{\boldsymbol{F}}^{-1}\boldsymbol{v}^{\mathcal{F}}\right), \boldsymbol{\phi}^{\boldsymbol{v},\mathcal{F}}\right)_{\Omega^{\mathcal{F}}_{\boldsymbol{\chi}}} \\
&\quad + \left(\hat{J}\mu^{\mathcal{F}}\left(\nabla_{\boldsymbol{\chi}}\boldsymbol{v}^{\mathcal{F}}\hat{\boldsymbol{F}}^{-1} + \hat{\boldsymbol{F}}^{-T}(\nabla_{\boldsymbol{\chi}}\boldsymbol{v}^{\mathcal{F}})^T\right)\hat{\boldsymbol{F}}^{-T}, \nabla_{\boldsymbol{\chi}}\boldsymbol{\phi}^{\boldsymbol{v},\mathcal{F}}\right)_{\Omega^{\mathcal{F}}_{\boldsymbol{\chi}}} \\
&\quad + \left(\hat{\boldsymbol{P}}^{\mathcal{S}}, \nabla_{\boldsymbol{\chi}}\boldsymbol{\phi}^{\boldsymbol{v},\mathcal{F}}\right)_{\Omega^{\mathcal{S}}_{\boldsymbol{\chi}}} - \left(\boldsymbol{v}^{\mathcal{S}}, \boldsymbol{\phi}^{\boldsymbol{u},\mathcal{S}}\right)_{\Omega^{\mathcal{S}}_{\boldsymbol{\chi}}} \\
A_{\mathrm{IV}}(\boldsymbol{U}; \Phi) &= \left(\hat{J}(-p^{\mathcal{F}}\boldsymbol{I})\hat{\boldsymbol{F}}^{-T}, \nabla\boldsymbol{\phi}^{\boldsymbol{v},\mathcal{F}}\right)_{\Omega^{\mathcal{F}}_{\boldsymbol{\chi}}}.
\end{aligned}$$

The above partition is the common departure point for the time discretized equations obtained with the one-step and fractional-step θ-schemes. As presented in the text below, these equations are obtained by different weighted combinations of $A_{\mathrm{I}}, \ldots, A_{\mathrm{IV}}$. For temporal discretization, let at time step $n+1$ corresponding to time $t_{n+1} \in I, n = 0, \ldots, N (N \in \mathbb{N})$, $A_{\mathrm{I}}(\boldsymbol{U}; \Phi)$ be approximated by $A_{\mathrm{I}}(\boldsymbol{U}^{n+1,\delta t}; \Phi)$

$$A_{\mathrm{I}}(\boldsymbol{U}; \Phi) \approx A_{\mathrm{I}}(\boldsymbol{U}^{n+1,\delta t}; \Phi),$$

where

$$\begin{aligned}
A_{\mathrm{I}}(\boldsymbol{U}^{n+1,\delta t}; \Phi) &= \frac{1}{\delta t}\left(\hat{J}^{\theta}\rho^{\mathcal{F}}(\boldsymbol{v}^{\mathcal{F}} - \boldsymbol{v}^{\mathcal{F},n}), \boldsymbol{\phi}^{\boldsymbol{v}}\right)_{\Omega^{\mathcal{F}}_{\boldsymbol{\chi}}} - \frac{1}{\delta t}\left(\hat{J}\rho^{\mathcal{F}}\nabla_{\boldsymbol{\chi}}\boldsymbol{v}^{\mathcal{F}}\hat{\boldsymbol{F}}^{-1}(\hat{\boldsymbol{u}}^{\mathcal{F}} - \hat{\boldsymbol{u}}^{\mathcal{F},n}), \boldsymbol{\phi}^{\boldsymbol{v}}\right)_{\Omega^{\mathcal{F}}_{\boldsymbol{\chi}}} \\
&\quad + \frac{1}{\delta t}\left(\hat{J}\rho^{\mathcal{S}}(\boldsymbol{v}^{\mathcal{S}} - \boldsymbol{v}^{\mathcal{S},n}), \boldsymbol{\phi}^{\boldsymbol{v}}\right)_{\Omega^{\mathcal{S}}_{\boldsymbol{\chi}}} + \frac{1}{\delta t}\left(\rho^{\mathcal{S}}\,(\boldsymbol{u}^{\mathcal{S}} - \boldsymbol{u}^{\mathcal{S},n}), \boldsymbol{\phi}^{\boldsymbol{u}}\right)_{\Omega^{\mathcal{S}}_{\boldsymbol{\chi}}},
\end{aligned} \tag{5.149}$$

is obtained from $A_{\mathrm{I}}(\boldsymbol{U}; \Phi)$ via the replacements of the temporal derivatives with finite differences

$(d_t(\cdot)^{n+1} := (((\cdot)^{n+1} - (\cdot)^n))/\delta t)$, and $\boldsymbol{U}^{n+1,\delta t} \equiv \boldsymbol{U}^{n+1} = \{\boldsymbol{v}^{n+1,\mathcal{F}}, \boldsymbol{v}^{n+1,\mathcal{S}}, \boldsymbol{u}^{n+1,\mathcal{F}}, \boldsymbol{u}^{n+1,\mathcal{S}}, p^{n+1,\mathcal{F}}, p^{n+1,\mathcal{S}}\} \in \boldsymbol{\mathcal{T}}$. Here we use the notational convention to represent the solution at the current/new time step with $\boldsymbol{u}^i := \boldsymbol{u}^{n+1,i} = \boldsymbol{u}^i(t_{n+1}), \boldsymbol{v}^i := \boldsymbol{v}^{n+1,i} = \boldsymbol{v}^i(t_{n+1}), i = \mathcal{F}, \mathcal{S}$, and the solution at the previous time step with $\boldsymbol{u}^{n,i} \equiv \boldsymbol{u}^{0,i} = \boldsymbol{u}^i(t_n), \boldsymbol{v}^{n,i} \equiv \boldsymbol{v}^{0,i} = \boldsymbol{v}^i(t_n)$. Likewise for time step $n+1$ we express the time-discrete version of the partitioned semilinear form (5.148) as

$$A(\boldsymbol{U}^{n+1}; \Phi) := A_{\text{I}}(\boldsymbol{U}^{n+1,\delta t}; \Phi) + A_{\text{II}}(\boldsymbol{U}^{n+1}; \Phi) + A_{\text{III}}(\boldsymbol{U}^{n+1}; \Phi) + A_{\text{IV}}(\boldsymbol{U}^{n+1}; \Phi)$$

and accordingly the linear form (5.147) as

$$F^{n+1}(\Phi) = \left(\hat{J}\rho^{\mathcal{F}}\boldsymbol{b}^{\mathcal{F},n+1}, \boldsymbol{\phi}^{\boldsymbol{v}}\right)_{\Omega^{\mathcal{F}}_{\boldsymbol{\chi}}} + \left(\hat{J}\rho^{\mathcal{S}}\boldsymbol{b}^{\mathcal{S},n+1}, \boldsymbol{\phi}^{\boldsymbol{v}}\right)_{\Omega^{\mathcal{S}}_{\boldsymbol{\chi}}}.$$

After the temporal discretization the following quasi-stationary problem is to be solved

$$A(\boldsymbol{U}^{n+1}; \Phi) = F(\Phi) \quad \forall \Phi \in \boldsymbol{\mathcal{W}}, \tag{5.150}$$

where the composition of the right and left hand sides depends on the respective scheme.

The one-step θ-scheme

Given the solution of the previous time step $\boldsymbol{U}^n = \{\boldsymbol{v}^{n,\mathcal{F}}, \boldsymbol{v}^{n,\mathcal{S}}, \boldsymbol{u}^{n,\mathcal{F}}, \boldsymbol{u}^{n,\mathcal{S}}, p^{n,\mathcal{F}}, p^{n,\mathcal{S}}\}$ the one-step θ-scheme requires to find $\boldsymbol{U}^{n+1} \equiv \boldsymbol{U} = \{\boldsymbol{v}^{\mathcal{F}}, \boldsymbol{v}^{\mathcal{S}}, \boldsymbol{u}^{\mathcal{F}}, \boldsymbol{u}^{\mathcal{S}}, p^{\mathcal{F}}, p^{\mathcal{S}}\}$, such that $\forall \Phi \in \boldsymbol{\mathcal{W}}$:

$$\begin{aligned} &A_{\text{I}}(\boldsymbol{U}^{n+1,\delta t}; \Phi) + \theta A_{\text{III}}(\boldsymbol{U}^{n+1}; \Phi) + A_{\text{IV}}(\boldsymbol{U}^{n+1}; \Phi) + A_{\text{II}}(\boldsymbol{U}^{n+1}; \Phi) \\ &\quad = -(1-\theta) A_{\text{III}}(\boldsymbol{U}^n; \Phi) + \theta F^{n+1}(\Phi) + (1-\theta) F^n(\Phi). \end{aligned} \tag{5.151}$$

Above, the choices $\theta = 1$ and $\theta = \frac{1}{2}$ leads to the Backward Euler and Crank-Nicolson schemes, respectively. The particular choice $\theta = \frac{1}{2} + O(\delta t)$ yields the so-called *shifted* Crank-Nicolson scheme [123].

The fractional-step θ-scheme

For the fractional-step θ-scheme, let $\theta = 1 - \frac{\sqrt{2}}{2}, \theta' = 1 - 2\theta, \alpha = \frac{1-2\theta}{1-\theta}, \beta = 1 - \alpha$, and let again the solution of the previous time step be given by $\boldsymbol{U}^n = \{\boldsymbol{v}^{n,\mathcal{F}}, \boldsymbol{v}^{n,\mathcal{S}}, \boldsymbol{u}^{n,\mathcal{F}}, \boldsymbol{u}^{n,\mathcal{S}}, p^{n,\mathcal{F}}, p^{n,\mathcal{S}}\}$. This three-stage scheme splitting one time step into three consecutive sub steps $((1): t_n \to t_{n+\theta}, (2): t_{n+\theta} \to t_{n+1-\theta}, (3): t_{n+1-\theta} \to t_{n+1})$ requires to find $\boldsymbol{U}^{n+1} \equiv \boldsymbol{U} = \{\boldsymbol{v}^{\mathcal{F}}, \boldsymbol{v}^{\mathcal{S}}, \boldsymbol{u}^{\mathcal{F}}, \boldsymbol{u}^{\mathcal{S}}, p^{\mathcal{F}}, p^{\mathcal{S}}\}$, such that $\forall \Phi \in \boldsymbol{\mathcal{W}}$:

$$\begin{aligned} (1): A_{\text{I}}(\boldsymbol{U}^{n+\theta,\delta t}; \Phi) + \alpha\theta A_{\text{III}}(\boldsymbol{U}^{n+\theta}; \Phi) + \theta A_{\text{IV}}(\boldsymbol{U}^{n+\theta}; \Phi) + A_{\text{II}}(\boldsymbol{U}^{n+\theta}; \Phi) & \\ = -\beta\theta A_{\text{III}}(\boldsymbol{U}^n; \Phi) + \theta F^n(\Phi), & \\ (2): A_{\text{I}}(\boldsymbol{U}^{n+1-\theta,\delta t}; \Phi) + \alpha\theta A_{\text{III}}(\boldsymbol{U}^{n+1-\theta}; \Phi) + \theta' A_{\text{IV}}(\boldsymbol{U}^{n+1-\theta}; \Phi) + A_{\text{II}}(\boldsymbol{U}^{n+1-\theta}; \Phi) & \\ = -\alpha\theta' A_{\text{III}}(\boldsymbol{U}^{n+\theta}; \Phi) + \theta' F^{n+1-\theta}(\Phi), & \\ (3): A_{\text{I}}(\boldsymbol{U}^{n+1,\delta t}; \Phi) + \alpha\theta A_{\text{III}}(\boldsymbol{U}^{n+1}; \Phi) + \theta A_{\text{IV}}(\boldsymbol{U}^{n+1}; \Phi) + A_{\text{II}}(\boldsymbol{U}^{n+1}; \Phi) & \\ = -\beta\theta A_{\text{III}}(\boldsymbol{U}^n; \Phi) + \theta F^{n+1-\theta}(\Phi). & \end{aligned} \tag{5.152}$$

5.3.5.1.1 Treatment of nonlinearity

The quasi-stationary system (5.150) to be solved at each time step is highly nonlinear. For the treatment of its nonlinearity, we apply Newton's method which we briefly sketch here again for ease of readability. The method requires – until convergence ($\|\mathcal{F}\| \leq \epsilon_{tol}$) – the following problem to be solved in each nonlinear iteration k:

$$\begin{aligned}
&\text{Find } \delta \boldsymbol{U} \in \boldsymbol{\mathcal{T}}, \text{ such that} \\
&\mathcal{F}'(\boldsymbol{U}^k; \delta \boldsymbol{U}, \boldsymbol{\Phi}) = -\mathcal{F}(\boldsymbol{U}^k; \boldsymbol{\Phi}), \qquad \forall \boldsymbol{\Phi} \in \boldsymbol{\mathcal{W}} \\
&\boldsymbol{U}^{k+1} = \boldsymbol{U}^k + \omega\, \delta \boldsymbol{U}.
\end{aligned} \tag{5.153}$$

Above, $\mathcal{F} \equiv R(\boldsymbol{U}) = A(\boldsymbol{U}; \boldsymbol{\Phi}) - F(\boldsymbol{\Phi})$ represents the nonlinear residual. It is typically expressed in terms of a semilinear form that is required to vanish for all test functions of the underlying test space. The bilinear form $\mathcal{F}'(\boldsymbol{U}^k; \delta \boldsymbol{U}, \boldsymbol{\Phi})$ is the Fréchet derivative (Jacobian) of $\mathcal{F}$ and is obtained from the linearization of $\mathcal{F}$ around a fixed $\boldsymbol{U} \equiv \boldsymbol{U}^k$. Note that for each fixed $\boldsymbol{U}^k$, $\mathcal{F}'(\boldsymbol{U}^k; \cdot, \cdot)$ is a bilinear form and $\mathcal{F}(\boldsymbol{U}^k; \cdot)$ is a linear form. It remains to specify $\mathcal{F}$ and $\mathcal{F}'(\boldsymbol{U}^k; \cdot, \cdot)$.

We begin with the specification of $\mathcal{F}$ and exemplary choose (due to its simplicity) the one-step θ-scheme as our time discretization scheme. We let $\mathcal{F}$ be given by the semilinear forms of the following nonlinear quasi-stationary problem that is obtained from the temporal discretization of the time dependent problem (6.16) with the one-step θ-scheme:

$$
\begin{aligned}
&\text{Find } \boldsymbol{U} \in \boldsymbol{\mathcal{T}} \text{ such that :} && \\
&\left(\rho^{\mathcal{F}} \hat{J}^{\theta} \left(\boldsymbol{v}^{\mathcal{F}} - \boldsymbol{v}^{n,\mathcal{F}}\right), \boldsymbol{\phi}^{\boldsymbol{v},\mathcal{F}}\right)_{\Omega^{\mathcal{F}}_{\boldsymbol{\chi}}} + \left(\Delta t \theta \rho^{\mathcal{F}} \hat{J} \nabla_{\boldsymbol{\chi}} \boldsymbol{v}^{\mathcal{F}} \hat{\boldsymbol{F}}^{-1} \boldsymbol{v}^{\mathcal{F}}, \boldsymbol{\phi}^{\boldsymbol{v},\mathcal{F}}\right)_{\Omega^{\mathcal{F}}_{\boldsymbol{\chi}}} && \\
&+ \left(\Delta t (1-\theta)\, \rho^{\mathcal{F}} \hat{J}^{n} \nabla_{\boldsymbol{\chi}} \boldsymbol{v}^{n,\mathcal{F}} \left(\hat{\boldsymbol{F}}^{n}\right)^{-1} \boldsymbol{v}^{n,\mathcal{F}}, \boldsymbol{\phi}^{\boldsymbol{v},\mathcal{F}}\right)_{\Omega^{\mathcal{F}}_{\boldsymbol{\chi}}} && \\
&- \left(\rho^{\mathcal{F}} \hat{J} \nabla_{\boldsymbol{\chi}} \boldsymbol{v}^{\mathcal{F}} \hat{\boldsymbol{F}}^{-1} \cdot \left(\boldsymbol{u}^{\mathcal{F}} - \boldsymbol{u}^{n,\mathcal{F}}\right), \boldsymbol{\phi}^{\boldsymbol{v},\mathcal{F}}\right)_{\Omega^{\mathcal{F}}_{\boldsymbol{\chi}}} && \\
&+ \left(\Delta t \theta \hat{J} \mu^{\mathcal{F}} \left(\nabla_{\boldsymbol{\chi}} \boldsymbol{v}^{\mathcal{F}} \hat{\boldsymbol{F}}^{-1} + \hat{\boldsymbol{F}}^{-T} \cdot \left(\nabla_{\boldsymbol{\chi}} \boldsymbol{v}^{\mathcal{F}}\right)^{T}\right) \hat{\boldsymbol{F}}^{-T}, \nabla_{\boldsymbol{\chi}} \boldsymbol{\phi}^{\boldsymbol{v},\mathcal{F}}\right)_{\Omega^{\mathcal{F}}_{\boldsymbol{\chi}}} && \\
&+ \left(\Delta t (1-\theta)\, \hat{J}^{n}\, \mu^{\mathcal{F}} \left(\nabla_{\boldsymbol{\chi}} \boldsymbol{v}^{n,\mathcal{F}} \left(\hat{\boldsymbol{F}}^{n}\right)^{-1} + (\hat{\boldsymbol{F}}^{n})^{-T} \cdot (\nabla_{\boldsymbol{\chi}} \boldsymbol{v}^{n,\mathcal{F}})^{T}\right) \left(\hat{\boldsymbol{F}}^{n}\right)^{-T}, \nabla_{\boldsymbol{\chi}} \boldsymbol{\phi}^{\boldsymbol{v},\mathcal{F}}\right)_{\Omega^{\mathcal{F}}_{\boldsymbol{\chi}}} && \\
&+ \left(\Delta t \hat{J} \left(-p^{\mathcal{F}} \boldsymbol{I}\right) \hat{\boldsymbol{F}}^{-T}, \nabla_{\boldsymbol{\chi}} \boldsymbol{\phi}^{\boldsymbol{v},\mathcal{F}}\right)_{\Omega^{\mathcal{F}}_{\boldsymbol{\chi}}} - \left(\rho^{\mathcal{F}}\, \Delta t \hat{J}^{\theta} \boldsymbol{b}^{\mathcal{F}}, \boldsymbol{\phi}^{\boldsymbol{v},\mathcal{F}}\right)_{\Omega^{\mathcal{F}}_{\boldsymbol{\chi}}} - \left(\Delta t \boldsymbol{g}^{\mathcal{F}}_{0}, \boldsymbol{\phi}^{\boldsymbol{v},\mathcal{F}}\right)_{\Gamma^{\mathcal{F}}_{N,\boldsymbol{\chi}}} = 0 && \forall \boldsymbol{\phi}^{\boldsymbol{v},\mathcal{F}} \in \boldsymbol{\mathcal{W}}^{\boldsymbol{v},\mathcal{F}}, \\
&\left(\hat{J} \hat{\boldsymbol{F}}^{-1} : \left(\nabla_{\boldsymbol{\chi}} \boldsymbol{v}^{\mathcal{F}}\right)^{T}, \phi^{p,\mathcal{F}}\right)_{\Omega^{\mathcal{F}}_{\boldsymbol{\chi}}} = 0 && \forall \phi^{p,\mathcal{F}} \in \mathcal{L}^{\mathcal{F}}, \\
&\left(\hat{J} \rho^{\mathcal{S}} \left(\boldsymbol{v}^{\mathcal{S}} - \boldsymbol{v}^{n,\mathcal{S}}\right), \boldsymbol{\phi}^{\boldsymbol{v},\mathcal{S}}\right)_{\Omega^{\mathcal{S}}_{\boldsymbol{\chi}}} && \\
&+ \left(\Delta t \theta\, \hat{\boldsymbol{P}} \left(\boldsymbol{u}^{\mathcal{S}}\right), \nabla_{\boldsymbol{\chi}} \boldsymbol{\phi}^{\boldsymbol{v},\mathcal{S}}\right)_{\Omega^{\mathcal{S}}_{\boldsymbol{\chi}}} + \left(\Delta t (1-\theta)\, \hat{\boldsymbol{P}} \left(\boldsymbol{u}^{n,\mathcal{S}}\right), \nabla_{\boldsymbol{\chi}} \boldsymbol{\phi}^{\boldsymbol{v},\mathcal{S}}\right)_{\Omega^{\mathcal{S}}_{\boldsymbol{\chi}}} && \\
&- \left(\Delta t \theta\, \hat{J}^{\theta} \rho^{\mathcal{S}} \boldsymbol{b}^{\mathcal{S}}, \boldsymbol{\phi}^{\boldsymbol{v},\mathcal{S}}\right)_{\Omega^{\mathcal{S}}_{\boldsymbol{\chi}}} - \left(\Delta t \boldsymbol{g}^{\mathcal{S}}_{0}, \boldsymbol{\phi}^{\boldsymbol{v},\mathcal{S}}\right)_{\Gamma^{\mathcal{S}}_{N,\boldsymbol{\chi}}} = 0 && \forall \boldsymbol{\phi}^{\boldsymbol{v},\mathcal{S}} \in \boldsymbol{\mathcal{W}}^{\boldsymbol{v},\mathcal{S}}, \\
&\left(\boldsymbol{u}^{\mathcal{S}} - \boldsymbol{u}^{n,\mathcal{S}}, \boldsymbol{\phi}^{\boldsymbol{u},\mathcal{S}}\right)_{\Omega^{\mathcal{S}}_{\boldsymbol{\chi}}} - \left(\Delta t \theta\, \boldsymbol{v}^{\mathcal{S}}, \boldsymbol{\phi}^{\boldsymbol{u},\mathcal{S}}\right)_{\Omega^{\mathcal{S}}_{\boldsymbol{\chi}}} - \left(\Delta t (1-\theta)\, \boldsymbol{v}^{n,\mathcal{S}}, \boldsymbol{\phi}^{\boldsymbol{u},\mathcal{S}}\right)_{\Omega^{\mathcal{S}}_{\boldsymbol{\chi}}} = 0 && \forall \boldsymbol{\phi}^{\boldsymbol{u},\mathcal{S}} \in \boldsymbol{\mathcal{W}}^{\boldsymbol{u},\mathcal{S}}, \\
&\left(p^{\mathcal{S}}, \phi^{p,\mathcal{S}}\right)_{\Omega^{\mathcal{S}}_{\boldsymbol{\chi}}} = 0 && \forall \phi^{p,\mathcal{S}} \in \mathcal{L}^{\mathcal{S}}, \\
&\left(\alpha_u \hat{J}^{-1} \nabla_{\boldsymbol{\chi}} \boldsymbol{u}^{\mathcal{F}}, \nabla_{\boldsymbol{\chi}} \boldsymbol{\phi}^{\boldsymbol{u}}\right)_{\Omega^{\mathcal{F}}_{\boldsymbol{\chi}}} = 0 && \forall \boldsymbol{\phi}^{\boldsymbol{u},\mathcal{F}} \in \boldsymbol{\mathcal{W}}^{\boldsymbol{u},\mathcal{F}},
\end{aligned}
\tag{5.154}
$$

where

$$\hat{J}^{\theta} := \theta \hat{J} + (1-\theta) \hat{J}^{n} = \theta \hat{J}(\boldsymbol{u}) + (1-\theta) \hat{J}(\boldsymbol{u}^{n}). \tag{5.155}$$

With a presentation of $\mathcal{F}$ at hand, we continue to present its analytically derived Jacobian.

Remark 5.3.2. *As explicitly stated in the explanation of the geometric coupling condition on page 158, inside the fluid domain, the "fluid displacement" variable $\boldsymbol{u}^{\mathcal{F}}$ is by no means physically related to the physically meaningful fluid material velocity $\boldsymbol{v}^{\mathcal{F}}$. This variable is (mis)used to actually hold the fluid mesh displacement field $\hat{\boldsymbol{u}}^{\mathcal{F}}$ and not the fluid material displacement field. With $\boldsymbol{u}^{\mathcal{F}}$ being linked to $\hat{\boldsymbol{u}}^{\mathcal{F}}$ in the above sense, we have decided to drop the "hat" symbol over $\boldsymbol{u}^{\mathcal{F}}$ in equation (5.154) and in the rest of the text in order to ease notation. Note for instance that this symbol was explicitly specified in (5.149).*

Derivative of the fluid mesh motion term

We derive the derivative of the harmonic mesh motion term

$$\left(\alpha_u \hat{J}^{-1} \nabla_{\boldsymbol{\chi}} \boldsymbol{u}^{\mathcal{F}}, \nabla_{\boldsymbol{\chi}} \boldsymbol{\phi}^{\boldsymbol{u},\mathcal{F}}\right)_{\Omega^{\mathcal{F}}_{\boldsymbol{\chi}}}$$

of equation (5.154).

$$\begin{aligned}
&D_{\delta \boldsymbol{u}}\left[\alpha_u \hat{J}^{-1} \nabla_{\boldsymbol{\chi}} \boldsymbol{u}^{\mathcal{F}}\right] \\
=&D_{\delta \boldsymbol{u}}\left[\alpha_u \hat{J}^{-1}\right] \nabla_{\boldsymbol{\chi}} \boldsymbol{u}^{\mathcal{F}}+\alpha_u \hat{J}^{-1} D_{\delta \boldsymbol{u}}\left[\nabla_{\boldsymbol{\chi}} \boldsymbol{u}^{\mathcal{F}}\right] \\
=&-\alpha_u \hat{J}^{-1} \operatorname{tr}\left(\hat{\boldsymbol{F}}^{-1} \nabla_{\boldsymbol{\chi}} \delta \boldsymbol{u}^{\mathcal{F}}\right) \nabla_{\boldsymbol{\chi}} \boldsymbol{u}^{\mathcal{F}}+\alpha_u \hat{J}^{-1} \nabla_{\boldsymbol{\chi}} \delta \boldsymbol{u}^{\mathcal{F}} .
\end{aligned} \tag{5.156}$$

Derivative of the fluid velocity time derivative term

We derive the derivative of the fluid velocity time derivative term

$$\left(\rho^{\mathcal{F}} \hat{J}^{\theta}\left(\boldsymbol{v}^{\mathcal{F}}-\boldsymbol{v}^{n, \mathcal{F}}\right), \boldsymbol{\phi}^{\boldsymbol{v}, \mathcal{F}}\right)_{\Omega_{\boldsymbol{\chi}}^{\mathcal{F}}}$$

of equation (5.154).

$$\begin{aligned}
&D_{\delta \boldsymbol{U}}\left[\rho^{\mathcal{F}} \hat{J}^{\theta}\left(\boldsymbol{v}^{\mathcal{F}}-\boldsymbol{v}^{n, \mathcal{F}}\right)\right] \\
=&D_{\delta \boldsymbol{u}}\left[\rho^{\mathcal{F}}\left(\theta \hat{J}(\boldsymbol{u})+(1-\theta) \hat{J}\left(\boldsymbol{u}^n\right)\right)\left(\boldsymbol{v}^{\mathcal{F}}-\boldsymbol{v}^{n, \mathcal{F}}\right)\right]+D_{\delta \boldsymbol{v}}\left[\rho^{\mathcal{F}} \hat{J}^{\theta}\left(\boldsymbol{v}^{\mathcal{F}}-\boldsymbol{v}^{n, \mathcal{F}}\right)\right] \\
=&\rho^{\mathcal{F}} \theta \hat{J} \operatorname{tr}\left(\hat{\boldsymbol{F}}^{-1} \nabla_{\boldsymbol{\chi}} \delta \boldsymbol{u}^{\mathcal{F}}\right)\left(\boldsymbol{v}^{\mathcal{F}}-\boldsymbol{v}^{n, \mathcal{F}}\right)+\rho^{\mathcal{F}} \hat{J}^{\theta} \delta \boldsymbol{v}^{\mathcal{F}} .
\end{aligned} \tag{5.157}$$

Derivative of the fluid ALE advection term

We derive the derivative of the following nonlinear parts of the fluid advection term

$$\left(\Delta t \theta \rho^{\mathcal{F}} \hat{J} \nabla_{\boldsymbol{\chi}} \boldsymbol{v}^{\mathcal{F}} \hat{\boldsymbol{F}}^{-1} \boldsymbol{v}^{\mathcal{F}}, \boldsymbol{\phi}^{\boldsymbol{v}, \mathcal{F}}\right)_{\Omega_{\boldsymbol{\chi}}^{\mathcal{F}}}-\left(\rho^{\mathcal{F}} \hat{J} \nabla_{\boldsymbol{\chi}} \boldsymbol{v}^{\mathcal{F}} \hat{\boldsymbol{F}}^{-1} \cdot\left(\boldsymbol{u}^{\mathcal{F}}-\boldsymbol{u}^{n, \mathcal{F}}\right), \boldsymbol{\phi}^{\boldsymbol{v}, \mathcal{F}}\right)_{\Omega_{\boldsymbol{\chi}}^{\mathcal{F}}}$$

of equation (5.154).

$$\begin{aligned}
&D_{\delta \boldsymbol{U}}\left[\Delta t \theta \rho^{\mathcal{F}} \hat{J} \nabla_{\boldsymbol{\chi}} \boldsymbol{v}^{\mathcal{F}} \hat{\boldsymbol{F}}^{-1} \boldsymbol{v}^{\mathcal{F}}\right] \\
=&D_{\delta \boldsymbol{u}}\left[\Delta t \theta \rho^{\mathcal{F}} \hat{J} \nabla_{\boldsymbol{\chi}} \boldsymbol{v}^{\mathcal{F}} \hat{\boldsymbol{F}}^{-1} \boldsymbol{v}^{\mathcal{F}}\right]+D_{\delta \boldsymbol{v}}\left[\Delta t \theta \rho^{\mathcal{F}} \hat{J} \nabla_{\boldsymbol{\chi}} \boldsymbol{v}^{\mathcal{F}} \hat{\boldsymbol{F}}^{-1} \boldsymbol{v}^{\mathcal{F}}\right] .
\end{aligned} \tag{5.158}$$

$$\begin{aligned}
&D_{\delta \boldsymbol{u}}\left[\Delta t \theta \rho^{\mathcal{F}} \hat{J} \nabla_{\boldsymbol{\chi}} \boldsymbol{v}^{\mathcal{F}} \hat{\boldsymbol{F}}^{-1} \boldsymbol{v}^{\mathcal{F}}\right] \\
=&D_{\delta \boldsymbol{u}}\left[\Delta t \theta \rho^{\mathcal{F}} \hat{J}\right] \nabla_{\boldsymbol{\chi}} \boldsymbol{v}^{\mathcal{F}} \hat{\boldsymbol{F}}^{-1} \boldsymbol{v}^{\mathcal{F}}+\Delta t \theta \rho^{\mathcal{F}} \hat{J} D_{\delta \boldsymbol{u}}\left[\nabla_{\boldsymbol{\chi}} \boldsymbol{v}^{\mathcal{F}} \hat{\boldsymbol{F}}^{-1} \boldsymbol{v}^{\mathcal{F}}\right] \\
=&\Delta t \theta \rho^{\mathcal{F}}\left(\hat{J} \operatorname{tr}\left(\hat{\boldsymbol{F}}^{-1} \nabla_{\boldsymbol{\chi}} \delta \boldsymbol{u}^{\mathcal{F}}\right) \nabla_{\boldsymbol{\chi}} \boldsymbol{v}^{\mathcal{F}} \hat{\boldsymbol{F}}^{-1} \boldsymbol{v}^{\mathcal{F}}+\hat{J} \nabla_{\boldsymbol{\chi}} \boldsymbol{v}^{\mathcal{F}}\left(-\hat{\boldsymbol{F}}^{-1} \nabla_{\boldsymbol{\chi}} \delta \boldsymbol{u}^{\mathcal{F}} \hat{\boldsymbol{F}}^{-1}\right) \boldsymbol{v}^{\mathcal{F}}\right) .
\end{aligned} \tag{5.159}$$

$$\begin{aligned}
&D_{\delta \boldsymbol{v}}\left[\Delta t \theta \rho^{\mathcal{F}} \hat{J} \nabla_{\boldsymbol{\chi}} \boldsymbol{v}^{\mathcal{F}} \hat{\boldsymbol{F}}^{-1} \boldsymbol{v}^{\mathcal{F}}\right] \\
=&D_{\delta \boldsymbol{v}}\left[\Delta t \theta \rho^{\mathcal{F}} \hat{J} \nabla_{\boldsymbol{\chi}} \boldsymbol{v}^{\mathcal{F}}\right] \hat{\boldsymbol{F}}^{-1} \boldsymbol{v}^{\mathcal{F}}+\Delta t \theta \rho^{\mathcal{F}} \hat{J} \nabla_{\boldsymbol{\chi}} \boldsymbol{v}^{\mathcal{F}} D_{\delta \boldsymbol{v}}\left[\hat{\boldsymbol{F}}^{-1} \boldsymbol{v}^{\mathcal{F}}\right] \\
=&\Delta t \theta \rho^{\mathcal{F}} \hat{J}\left(\nabla_{\boldsymbol{\chi}} \delta \boldsymbol{v}^{\mathcal{F}} \hat{\boldsymbol{F}}^{-1} \boldsymbol{v}^{\mathcal{F}}+\nabla_{\boldsymbol{\chi}} \boldsymbol{v}^{\mathcal{F}} \hat{\boldsymbol{F}}^{-1} \delta \boldsymbol{v}^{\mathcal{F}}\right) .
\end{aligned} \tag{5.160}$$

$$
\begin{aligned}
&D_{\delta \boldsymbol{U}}\left[-\rho^{\mathcal{F}}\hat{J}\nabla_{\boldsymbol{\chi}}\boldsymbol{v}^{\mathcal{F}}\hat{\boldsymbol{F}}^{-1}\cdot\left(\boldsymbol{u}^{\mathcal{F}}-\boldsymbol{u}^{n,\mathcal{F}}\right)\right]\\
=&D_{\delta \boldsymbol{u}}\left[-\rho^{\mathcal{F}}\hat{J}\nabla_{\boldsymbol{\chi}}\boldsymbol{v}^{\mathcal{F}}\hat{\boldsymbol{F}}^{-1}\cdot\left(\boldsymbol{u}^{\mathcal{F}}-\boldsymbol{u}^{n,\mathcal{F}}\right)\right]+D_{\delta \boldsymbol{v}}\left[-\rho^{\mathcal{F}}\hat{J}\nabla_{\boldsymbol{\chi}}\boldsymbol{v}^{\mathcal{F}}\hat{\boldsymbol{F}}^{-1}\cdot\left(\boldsymbol{u}^{\mathcal{F}}-\boldsymbol{u}^{n,\mathcal{F}}\right)\right].
\end{aligned}
\tag{5.161}
$$

$$
\begin{aligned}
&D_{\delta \boldsymbol{u}}\left[-\rho^{\mathcal{F}}\hat{J}\nabla_{\boldsymbol{\chi}}\boldsymbol{v}^{\mathcal{F}}\hat{\boldsymbol{F}}^{-1}\cdot\left(\boldsymbol{u}^{\mathcal{F}}-\boldsymbol{u}^{n,\mathcal{F}}\right)\right]\\
=&D_{\delta \boldsymbol{u}}\left[-\rho^{\mathcal{F}}\hat{J}\right]\nabla_{\boldsymbol{\chi}}\boldsymbol{v}^{\mathcal{F}}\hat{\boldsymbol{F}}^{-1}\cdot\left(\boldsymbol{u}^{\mathcal{F}}-\boldsymbol{u}^{n,\mathcal{F}}\right)-\rho^{\mathcal{F}}\hat{J}D_{\delta \boldsymbol{u}}\left[\nabla_{\boldsymbol{\chi}}\boldsymbol{v}^{\mathcal{F}}\hat{\boldsymbol{F}}^{-1}\cdot\left(\boldsymbol{u}^{\mathcal{F}}-\boldsymbol{u}^{n,\mathcal{F}}\right)\right]\\
=&-\rho^{\mathcal{F}}\hat{J}\operatorname{tr}\left(\hat{\boldsymbol{F}}^{-1}\nabla_{\boldsymbol{\chi}}\delta\boldsymbol{u}^{\mathcal{F}}\right)\nabla_{\boldsymbol{\chi}}\boldsymbol{v}^{\mathcal{F}}\hat{\boldsymbol{F}}^{-1}\cdot\left(\boldsymbol{u}^{\mathcal{F}}-\boldsymbol{u}^{n,\mathcal{F}}\right)\\
&-\rho^{\mathcal{F}}\hat{J}\left(D_{\delta \boldsymbol{u}}\left[\nabla_{\boldsymbol{\chi}}\boldsymbol{v}^{\mathcal{F}}\hat{\boldsymbol{F}}^{-1}\right]\left(\boldsymbol{u}^{\mathcal{F}}-\boldsymbol{u}^{n,\mathcal{F}}\right)+\nabla_{\boldsymbol{\chi}}\boldsymbol{v}^{\mathcal{F}}\hat{\boldsymbol{F}}^{-1}D_{\delta \boldsymbol{u}}\left[\boldsymbol{u}^{\mathcal{F}}-\boldsymbol{u}^{n,\mathcal{F}}\right]\right)\\
=&-\rho^{\mathcal{F}}\hat{J}\operatorname{tr}\left(\hat{\boldsymbol{F}}^{-1}\nabla_{\boldsymbol{\chi}}\delta\boldsymbol{u}^{\mathcal{F}}\right)\nabla_{\boldsymbol{\chi}}\boldsymbol{v}^{\mathcal{F}}\hat{\boldsymbol{F}}^{-1}\cdot\left(\boldsymbol{u}^{\mathcal{F}}-\boldsymbol{u}^{n,\mathcal{F}}\right)\\
&-\rho^{\mathcal{F}}\hat{J}\left(\nabla_{\boldsymbol{\chi}}\boldsymbol{v}^{\mathcal{F}}\left(-\hat{\boldsymbol{F}}^{-1}\nabla_{\boldsymbol{\chi}}\delta\boldsymbol{u}^{\mathcal{F}}\hat{\boldsymbol{F}}^{-1}\right)\left(\boldsymbol{u}^{\mathcal{F}}-\boldsymbol{u}^{n,\mathcal{F}}\right)+\nabla_{\boldsymbol{\chi}}\boldsymbol{v}^{\mathcal{F}}\hat{\boldsymbol{F}}^{-1}\delta\boldsymbol{u}^{\mathcal{F}}\right).
\end{aligned}
\tag{5.162}
$$

$$
D_{\delta \boldsymbol{v}}\left[-\rho^{\mathcal{F}}\hat{J}\nabla_{\boldsymbol{\chi}}\boldsymbol{v}^{\mathcal{F}}\hat{\boldsymbol{F}}^{-1}\cdot\left(\boldsymbol{u}^{\mathcal{F}}-\boldsymbol{u}^{0,\mathcal{F}}\right)\right]=-\rho^{\mathcal{F}}\hat{J}\nabla_{\boldsymbol{\chi}}\delta\boldsymbol{v}^{\mathcal{F}}\hat{\boldsymbol{F}}^{-1}\cdot\left(\boldsymbol{u}^{\mathcal{F}}-\boldsymbol{u}^{n,\mathcal{F}}\right).
\tag{5.163}
$$

It follows from the partial contributions

$$
\begin{aligned}
&D_{\delta \boldsymbol{U}}\left[\Delta t\theta\rho^{\mathcal{F}}\hat{J}\nabla_{\boldsymbol{\chi}}\boldsymbol{v}^{\mathcal{F}}\hat{\boldsymbol{F}}^{-1}\boldsymbol{v}^{\mathcal{F}}\right]\\
=&\Delta t\theta\rho^{\mathcal{F}}\left(\hat{J}\operatorname{tr}\left(\hat{\boldsymbol{F}}^{-1}\nabla_{\boldsymbol{\chi}}\delta\boldsymbol{u}^{\mathcal{F}}\right)\nabla_{\boldsymbol{\chi}}\boldsymbol{v}^{\mathcal{F}}\hat{\boldsymbol{F}}^{-1}\boldsymbol{v}^{\mathcal{F}}+\hat{J}\nabla_{\boldsymbol{\chi}}\boldsymbol{v}^{\mathcal{F}}\left(-\hat{\boldsymbol{F}}^{-1}\nabla_{\boldsymbol{\chi}}\delta\boldsymbol{u}^{\mathcal{F}}\hat{\boldsymbol{F}}^{-1}\right)\boldsymbol{v}^{\mathcal{F}}\right)\\
&+\Delta t\theta\rho^{\mathcal{F}}\hat{J}\left(\nabla_{\boldsymbol{\chi}}\delta\boldsymbol{v}^{\mathcal{F}}\hat{\boldsymbol{F}}^{-1}\boldsymbol{v}^{\mathcal{F}}+\nabla_{\boldsymbol{\chi}}\boldsymbol{v}^{\mathcal{F}}\hat{\boldsymbol{F}}^{-1}\delta\boldsymbol{v}^{\mathcal{F}}\right)\\
&-\rho^{\mathcal{F}}\hat{J}\operatorname{tr}\left(\hat{\boldsymbol{F}}^{-1}\nabla_{\boldsymbol{\chi}}\delta\boldsymbol{u}^{\mathcal{F}}\right)\nabla_{\boldsymbol{\chi}}\boldsymbol{v}^{\mathcal{F}}\hat{\boldsymbol{F}}^{-1}\cdot\left(\boldsymbol{u}^{\mathcal{F}}-\boldsymbol{u}^{n,\mathcal{F}}\right)\\
&-\rho^{\mathcal{F}}\hat{J}\left(\nabla_{\boldsymbol{\chi}}\boldsymbol{v}^{\mathcal{F}}\left(-\hat{\boldsymbol{F}}^{-1}\nabla_{\boldsymbol{\chi}}\delta\boldsymbol{u}^{\mathcal{F}}\hat{\boldsymbol{F}}^{-1}\right)\left(\boldsymbol{u}^{\mathcal{F}}-\boldsymbol{u}^{n,\mathcal{F}}\right)+\nabla_{\boldsymbol{\chi}}\boldsymbol{v}^{\mathcal{F}}\hat{\boldsymbol{F}}^{-1}\delta\boldsymbol{u}^{\mathcal{F}}\right)\\
&-\rho^{\mathcal{F}}\hat{J}\nabla_{\boldsymbol{\chi}}\delta\boldsymbol{v}^{\mathcal{F}}\hat{\boldsymbol{F}}^{-1}\cdot\left(\boldsymbol{u}^{\mathcal{F}}-\boldsymbol{u}^{n,\mathcal{F}}\right).
\end{aligned}
\tag{5.164}
$$

Derivative of the fluid Cauchy stress term

We derive the derivative of the fluid Cauchy stress term

$$
\left(\Delta t\theta\hat{J}\mu^{\mathcal{F}}\left(\nabla_{\boldsymbol{\chi}}\boldsymbol{v}^{\mathcal{F}}\hat{\boldsymbol{F}}^{-1}+\hat{\boldsymbol{F}}^{-T}\cdot\left(\nabla_{\boldsymbol{\chi}}\boldsymbol{v}^{\mathcal{F}}\right)^{T}\right)\hat{\boldsymbol{F}}^{-T},\nabla_{\boldsymbol{\chi}}\boldsymbol{\phi}^{\boldsymbol{v},\mathcal{F}}\right)_{\Omega_{\boldsymbol{\chi}}^{\mathcal{F}}}+\left(\Delta t\hat{J}\left(-p^{\mathcal{F}}\boldsymbol{I}\right)\hat{\boldsymbol{F}}^{-T},\nabla_{\boldsymbol{\chi}}\boldsymbol{\phi}^{\boldsymbol{v},\mathcal{F}}\right)_{\Omega_{\boldsymbol{\chi}}^{\mathcal{F}}}
$$

of equation (5.154). Let the fluid Cauchy stress in the referential domain

$$
\boldsymbol{\sigma}^{\mathcal{F}}:=-p^{\mathcal{F}}\boldsymbol{I}+\mu^{\mathcal{F}}\left(\nabla_{\boldsymbol{\chi}}\boldsymbol{v}^{\mathcal{F}}\hat{\boldsymbol{F}}^{-1}+\hat{\boldsymbol{F}}^{-T}(\nabla_{\boldsymbol{\chi}}\boldsymbol{v}^{\mathcal{F}})^{T}\right)
$$

be splitted into an isotropic part

$$
\boldsymbol{\sigma}_{p}^{\mathcal{F}}:=-p^{\mathcal{F}}\boldsymbol{I}
$$

and a deviatoric part

$$\boldsymbol{\sigma}_{uv}^{\mathcal{F}} := \mu^{\mathcal{F}} \left(\nabla_{\boldsymbol{\chi}} \boldsymbol{v}^{\mathcal{F}} \hat{\boldsymbol{F}}^{-1} + \hat{\boldsymbol{F}}^{-T} (\nabla_{\boldsymbol{\chi}} \boldsymbol{v}^{\mathcal{F}})^T \right),$$

which we derive separately.

$$\begin{aligned} & D_{\delta \boldsymbol{U}} \left[\hat{J} \boldsymbol{\sigma}_{uv}^{\mathcal{F}} \hat{\boldsymbol{F}}^{-T} \right] \\ =& D_{\delta \boldsymbol{u}} \left[\hat{J} \boldsymbol{\sigma}_{uv}^{\mathcal{F}} \hat{\boldsymbol{F}}^{-T} \right] + D_{\delta \boldsymbol{v}} \left[\hat{J} \boldsymbol{\sigma}_{uv}^{\mathcal{F}} \hat{\boldsymbol{F}}^{-T} \right]. \end{aligned} \tag{5.165}$$

$$\begin{aligned} & D_{\delta \boldsymbol{u}} \left[\hat{J} \boldsymbol{\sigma}_{uv}^{\mathcal{F}} \hat{\boldsymbol{F}}^{-T} \right] \\ =& \boldsymbol{\sigma}_{uv}^{\mathcal{F}} D_{\delta \boldsymbol{u}} \left[\hat{J} \hat{\boldsymbol{F}}^{-T} \right] + D_{\delta \boldsymbol{u}} \left[\boldsymbol{\sigma}_{uv}^{\mathcal{F}} \right] \hat{J} \hat{\boldsymbol{F}}^{-T} \\ =& \boldsymbol{\sigma}_{uv}^{\mathcal{F}} D_{\delta \boldsymbol{u}} \left[\hat{J} \frac{1}{\hat{J}} \begin{pmatrix} 1 + \partial u_2/\partial y & -\partial u_2/\partial x \\ -\partial u_1/\partial y & 1 + \partial u_1/\partial x \end{pmatrix} \right] + D_{\delta \boldsymbol{u}} \left[\boldsymbol{\sigma}_{uv}^{\mathcal{F}} \right] \hat{J} \hat{\boldsymbol{F}}^{-T} \\ =& \boldsymbol{\sigma}_{uv}^{\mathcal{F}} \boldsymbol{G}(\delta \boldsymbol{u}) + D_{\delta \boldsymbol{u}} \left[\boldsymbol{\sigma}_{uv}^{\mathcal{F}} \right] \hat{J} \hat{\boldsymbol{F}}^{-T}, \end{aligned} \tag{5.166}$$

where we define $\boldsymbol{G}(\delta \boldsymbol{u}) := \begin{pmatrix} \partial \delta u_2/\partial y & -\partial \delta u_2/\partial x \\ -\partial \delta u_1/\partial y & \partial \delta u_1/\partial x \end{pmatrix}$ in order to ease the notation.

$$\begin{aligned} & D_{\delta \boldsymbol{u}} \left[\boldsymbol{\sigma}_{uv}^{\mathcal{F}} \right] \hat{J} \hat{\boldsymbol{F}}^{-T} \\ =& D_{\delta \boldsymbol{u}} \left[\mu \left(\nabla_{\boldsymbol{\chi}} \boldsymbol{v}^{\mathcal{F}} \hat{\boldsymbol{F}}^{-1} + \hat{\boldsymbol{F}}^{-T} (\nabla_{\boldsymbol{\chi}} \boldsymbol{v}^{\mathcal{F}})^T \right) \right] \hat{J} \hat{\boldsymbol{F}}^{-T} \\ =& \mu \left(\nabla_{\boldsymbol{\chi}} \boldsymbol{v}^{\mathcal{F}} \left(-\hat{\boldsymbol{F}}^{-1} \nabla_{\boldsymbol{\chi}} \delta \boldsymbol{u}^{\mathcal{F}} \hat{\boldsymbol{F}}^{-1} \right) + \left(-\hat{\boldsymbol{F}}^{-T} \cdot (\nabla_{\boldsymbol{\chi}} \delta \boldsymbol{u}^{\mathcal{F}})^T \hat{\boldsymbol{F}}^{-T} \right) (\nabla_{\boldsymbol{\chi}} \boldsymbol{v}^{\mathcal{F}})^T \right) \hat{J} \hat{\boldsymbol{F}}^{-T}. \end{aligned} \tag{5.167}$$

$$\begin{aligned} & D_{\delta \boldsymbol{v}} \left[\hat{J} \boldsymbol{\sigma}_{uv}^{\mathcal{F}} \hat{\boldsymbol{F}}^{-T} \right] \\ =& D_{\delta \boldsymbol{v}} \left[\boldsymbol{\sigma}_{uv}^{\mathcal{F}} \right] \hat{J} \hat{\boldsymbol{F}}^{-T} + \boldsymbol{\sigma}_{uv}^{\mathcal{F}} D_{\delta \boldsymbol{v}} \left[\hat{J} \hat{\boldsymbol{F}}^{-T} \right] \\ =& \mu \left(\nabla_{\boldsymbol{\chi}} \delta \boldsymbol{v}^{\mathcal{F}} \hat{\boldsymbol{F}}^{-1} + \hat{\boldsymbol{F}}^{-T} (\nabla_{\boldsymbol{\chi}} \delta \boldsymbol{v}^{\mathcal{F}})^T \right) \hat{J} \hat{\boldsymbol{F}}^{-T}. \end{aligned} \tag{5.168}$$

$$\begin{aligned} & D_{\delta \boldsymbol{U}} \left[\hat{J} \boldsymbol{\sigma}_{p}^{\mathcal{F}} \hat{\boldsymbol{F}}^{-T} \right] \\ =& D_{\delta \boldsymbol{u}} \left[\hat{J} \boldsymbol{\sigma}_{p}^{\mathcal{F}} \hat{\boldsymbol{F}}^{-T} \right] + D_{\delta p} \left[\hat{J} \boldsymbol{\sigma}_{p}^{\mathcal{F}} \hat{\boldsymbol{F}}^{-T} \right] \\ =& D_{\delta \boldsymbol{u}} \left[(-pI) \hat{J} \hat{\boldsymbol{F}}^{-T} \right] + D_{\delta p} \left[(-pI) \hat{J} \hat{\boldsymbol{F}}^{-T} \right] \\ =& D_{\delta \boldsymbol{u}} \left[-(pI) \hat{J} \frac{1}{\hat{J}} \begin{pmatrix} 1 + \partial u_2/\partial y & -\partial u_2/\partial x \\ -\partial u_1/\partial y & 1 + \partial u_1/\partial x \end{pmatrix} \right] - (\delta p \, \boldsymbol{I}) \hat{J} \hat{\boldsymbol{F}}^{-T} \\ =& -(pI) \boldsymbol{G}(\delta \boldsymbol{u}) - (\delta p \, \boldsymbol{I}) \hat{J} \hat{\boldsymbol{F}}^{-T}. \end{aligned} \tag{5.169}$$

$$D_{\delta p} \left[\Delta t \hat{J} \left(-p^{\mathcal{F}} \boldsymbol{I} \right) \hat{\boldsymbol{F}}^{-T} \right] = -\left(\delta p^{\mathcal{F}} \boldsymbol{I} \right) \hat{J} \hat{\boldsymbol{F}}^{-T}. \tag{5.170}$$

Gathering all contributions, it holds

$$\begin{aligned}
&D_{\delta \boldsymbol{U}}\left[\hat{J}\boldsymbol{\sigma}^{\mathcal{F}}\hat{\boldsymbol{F}}^{-T}\right]\\
=&D_{\delta \boldsymbol{U}}\left[\hat{J}\boldsymbol{\sigma}_{uv}^{\mathcal{F}}\hat{\boldsymbol{F}}^{-T}\right]+D_{\delta \boldsymbol{U}}\left[\hat{J}\boldsymbol{\sigma}_{p}^{\mathcal{F}}\hat{\boldsymbol{F}}^{-T}\right]\\
=&\boldsymbol{\sigma}_{uv}^{\mathcal{F}}\boldsymbol{G}(\delta\boldsymbol{u})\\
+&\mu\left(\nabla_{\boldsymbol{\chi}}\boldsymbol{v}^{\mathcal{F}}\left(-\hat{\boldsymbol{F}}^{-1}\nabla_{\boldsymbol{\chi}}\delta\boldsymbol{u}^{\mathcal{F}}\hat{\boldsymbol{F}}^{-1}\right)+\left(-\hat{\boldsymbol{F}}^{-T}\cdot(\nabla_{\boldsymbol{\chi}}\delta\boldsymbol{u}^{\mathcal{F}})^{T}\hat{\boldsymbol{F}}^{-T}\right)(\nabla_{\boldsymbol{\chi}}\boldsymbol{v}^{\mathcal{F}})^{T}\right)\hat{J}\hat{\boldsymbol{F}}^{-T}\\
+&\mu\left(\nabla_{\boldsymbol{\chi}}\delta\boldsymbol{v}^{\mathcal{F}}\hat{\boldsymbol{F}}^{-1}+\hat{\boldsymbol{F}}^{-T}(\nabla_{\boldsymbol{\chi}}\delta\boldsymbol{v}^{\mathcal{F}})^{T}\right)\hat{J}\hat{\boldsymbol{F}}^{-T}\\
-&(pI)\boldsymbol{G}(\delta\boldsymbol{u})-(\delta p\,\boldsymbol{I})\hat{J}\hat{\boldsymbol{F}}^{-T}-\left(\delta p^{\mathcal{F}}\boldsymbol{I}\right)\hat{J}\hat{\boldsymbol{F}}^{-T}.
\end{aligned} \tag{5.171}$$

Derivative of the fluid incompressibility condition term

We derive the derivative of the fluid incompressibility condition term

$$\left(\nabla_{\boldsymbol{\chi}}\cdot\left(\hat{J}\hat{\boldsymbol{F}}^{-1}\boldsymbol{v}^{\mathcal{F}}\right),\phi^{p,\mathcal{F}}\right)_{\Omega_{\boldsymbol{\chi}}^{\mathcal{F}}}$$

of equation (5.154).

$$\begin{aligned}
&D_{\delta \boldsymbol{U}}\left[\nabla_{\boldsymbol{\chi}}\cdot\left(\hat{J}\hat{\boldsymbol{F}}^{-1}\boldsymbol{v}^{\mathcal{F}}\right)\right]\\
=&D_{\delta \boldsymbol{U}}\left[\hat{J}\operatorname{tr}\left(\nabla_{\boldsymbol{\chi}}\boldsymbol{v}^{\mathcal{F}}\hat{\boldsymbol{F}}^{-1}\right)\right]\\
=&D_{\delta \boldsymbol{u}}\left[\hat{J}\operatorname{tr}\left(\nabla_{\boldsymbol{\chi}}\boldsymbol{v}^{\mathcal{F}}\hat{\boldsymbol{F}}^{-1}\right)\right]+D_{\delta \boldsymbol{v}}\left[\hat{J}\operatorname{tr}\left(\nabla_{\boldsymbol{\chi}}\boldsymbol{v}^{\mathcal{F}}\hat{\boldsymbol{F}}^{-1}\right)\right].
\end{aligned} \tag{5.172}$$

$$\begin{aligned}
&D_{\delta \boldsymbol{u}}\left[\hat{J}\operatorname{tr}\left(\nabla_{\boldsymbol{\chi}}\boldsymbol{v}^{\mathcal{F}}\hat{\boldsymbol{F}}^{-1}\right)\right]\\
=&D_{\delta \boldsymbol{u}}\left[\hat{J}\right]\operatorname{tr}\left(\nabla_{\boldsymbol{\chi}}\boldsymbol{v}^{\mathcal{F}}\hat{\boldsymbol{F}}^{-1}\right)+\hat{J}D_{\delta \boldsymbol{u}}\left[\operatorname{tr}\left(\nabla_{\boldsymbol{\chi}}\boldsymbol{v}^{\mathcal{F}}\hat{\boldsymbol{F}}^{-1}\right)\right]\\
=&\hat{J}\operatorname{tr}\left(\hat{\boldsymbol{F}}^{-1}\nabla_{\boldsymbol{\chi}}\delta\boldsymbol{u}^{\mathcal{F}}\right)\operatorname{tr}\left(\nabla_{\boldsymbol{\chi}}\boldsymbol{v}^{\mathcal{F}}\hat{\boldsymbol{F}}^{-1}\right)+\hat{J}\operatorname{tr}\left(\nabla_{\boldsymbol{\chi}}\boldsymbol{v}^{\mathcal{F}}\left(-\hat{\boldsymbol{F}}^{-1}\nabla_{\boldsymbol{\chi}}\delta\boldsymbol{u}^{\mathcal{F}}\hat{\boldsymbol{F}}^{-1}\right)\right).
\end{aligned} \tag{5.173}$$

$$D_{\delta \boldsymbol{v}}\left[\hat{J}\operatorname{tr}\left(\nabla_{\boldsymbol{\chi}}\boldsymbol{v}^{\mathcal{F}}\hat{\boldsymbol{F}}^{-1}\right)\right]=\hat{J}\operatorname{tr}\left(\nabla_{\boldsymbol{\chi}}\delta\boldsymbol{v}^{\mathcal{F}}\hat{\boldsymbol{F}}^{-1}\right). \tag{5.174}$$

Derivative of the solid terms

For the solid part of the FSI problem, we may choose different material models. Two models discussed in this work are the St. Venant-Kirchhoff and the Neo-Hookean materials for which we have already presented the bilinear forms (cf. (5.87) and (5.89)) whose respective action assembles the Jacobian required in Newton's method.

Analytically derived Jacobian of the FSI problem

The combination of the derivatives of all fluid and solid terms, where the solid stress is given by the St. Venant-Kirchhoff material model, is presented in the bilinear form (5.175). Its action yields the

Jacobian of the FSI problem and therefore provides the last missing ingredient for the application of Newton's method.

$$
\begin{aligned}
&\mathcal{F}'(\boldsymbol{U}^k;\delta\boldsymbol{U},\boldsymbol{\Phi}) := \\
&\int_{\Omega^{\mathcal{F}}_{\boldsymbol{\chi}}} \left(\rho^{\mathcal{F}}\theta\hat{J}\,\mathrm{tr}\left(\hat{\boldsymbol{F}}^{-1}\nabla_{\boldsymbol{\chi}}\delta\boldsymbol{u}^{\mathcal{F}}\right)\left(\boldsymbol{v}^{k,\mathcal{F}}-\boldsymbol{v}^{n,\mathcal{F}}\right)+\rho^{\mathcal{F}}\hat{J}^{\theta}\delta\boldsymbol{v}^{\mathcal{F}}\right)\cdot\boldsymbol{\phi}^{\boldsymbol{v},\mathcal{F}}\,\mathrm{d}\Omega^{\mathcal{F}}_{\boldsymbol{\chi}} \\
&+\int_{\Omega^{\mathcal{F}}_{\boldsymbol{\chi}}} \Bigg(\Delta t\theta\rho^{\mathcal{F}}\left(\hat{J}\,\mathrm{tr}\left(\hat{\boldsymbol{F}}^{-1}\nabla_{\boldsymbol{\chi}}\delta\boldsymbol{u}^{\mathcal{F}}\right)\nabla_{\boldsymbol{\chi}}\boldsymbol{v}^{k,\mathcal{F}}\hat{\boldsymbol{F}}^{-1}\boldsymbol{v}^{k,\mathcal{F}}+\hat{J}\nabla_{\boldsymbol{\chi}}\boldsymbol{v}^{k,\mathcal{F}}\left(-\hat{\boldsymbol{F}}^{-1}\nabla_{\boldsymbol{\chi}}\delta\boldsymbol{u}^{\mathcal{F}}\hat{\boldsymbol{F}}^{-1}\right)\boldsymbol{v}^{k,\mathcal{F}}\right) \\
&\quad+\Delta t\theta\rho^{\mathcal{F}}\hat{J}\left(\nabla_{\boldsymbol{\chi}}\delta\boldsymbol{v}^{\mathcal{F}}\hat{\boldsymbol{F}}^{-1}\boldsymbol{v}^{k,\mathcal{F}}+\nabla_{\boldsymbol{\chi}}\boldsymbol{v}^{k,\mathcal{F}}\hat{\boldsymbol{F}}^{-1}\delta\boldsymbol{v}^{\mathcal{F}}\right) \\
&\quad-\rho^{\mathcal{F}}\hat{J}\,\mathrm{tr}\left(\hat{\boldsymbol{F}}^{-1}\nabla_{\boldsymbol{\chi}}\delta\boldsymbol{u}^{\mathcal{F}}\right)\nabla_{\boldsymbol{\chi}}\boldsymbol{v}^{k,\mathcal{F}}\hat{\boldsymbol{F}}^{-1}\cdot\left(\boldsymbol{u}^{k,\mathcal{F}}-\boldsymbol{u}^{n,\mathcal{F}}\right) \\
&\quad-\rho^{\mathcal{F}}\hat{J}\left(\nabla_{\boldsymbol{\chi}}\boldsymbol{v}^{k,\mathcal{F}}\left(-\hat{\boldsymbol{F}}^{-1}\nabla_{\boldsymbol{\chi}}\delta\boldsymbol{u}^{\mathcal{F}}\hat{\boldsymbol{F}}^{-1}\right)\left(\boldsymbol{u}^{k,\mathcal{F}}-\boldsymbol{u}^{n,\mathcal{F}}\right)+\nabla_{\boldsymbol{\chi}}\boldsymbol{v}^{k,\mathcal{F}}\hat{\boldsymbol{F}}^{-1}\delta\boldsymbol{u}^{\mathcal{F}}\right) \\
&\quad-\rho^{\mathcal{F}}\hat{J}\nabla_{\boldsymbol{\chi}}\delta\boldsymbol{v}^{\mathcal{F}}\hat{\boldsymbol{F}}^{-1}\cdot\left(\boldsymbol{u}^{k,\mathcal{F}}-\boldsymbol{u}^{n,\mathcal{F}}\right)\Bigg)\cdot\boldsymbol{\phi}^{\boldsymbol{v},\mathcal{F}}\,\mathrm{d}\Omega^{\mathcal{F}}_{\boldsymbol{\chi}} \\
&+\int_{\Omega^{\mathcal{F}}_{\boldsymbol{\chi}}} \Bigg(\boldsymbol{\sigma}^{\mathcal{F}}_{uv}\boldsymbol{G}(\delta\boldsymbol{u})+\mu^{\mathcal{F}}\left(\nabla_{\boldsymbol{\chi}}\boldsymbol{v}^{k,\mathcal{F}}\left(-\hat{\boldsymbol{F}}^{-1}\nabla_{\boldsymbol{\chi}}\delta\boldsymbol{u}^{\mathcal{F}}\hat{\boldsymbol{F}}^{-1}\right)+\left(-\hat{\boldsymbol{F}}^{-T}\cdot(\nabla_{\boldsymbol{\chi}}\delta\boldsymbol{u}^{\mathcal{F}})^T\hat{\boldsymbol{F}}^{-T}\right)(\nabla_{\boldsymbol{\chi}}\boldsymbol{v}^{k,\mathcal{F}})^T\right)\hat{J}\hat{\boldsymbol{F}}^{-T} \\
&\quad+\mu^{\mathcal{F}}\left(\nabla_{\boldsymbol{\chi}}\delta\boldsymbol{v}^{\mathcal{F}}\hat{\boldsymbol{F}}^{-1}+\hat{\boldsymbol{F}}^{-T}(\nabla_{\boldsymbol{\chi}}\delta\boldsymbol{v}^{\mathcal{F}})^T\right)\hat{J}\hat{\boldsymbol{F}}^{-T} \\
&\quad-(p^{\mathcal{F}}\boldsymbol{I})\boldsymbol{G}(\delta\boldsymbol{u})-(\delta p^{\mathcal{F}}\boldsymbol{I})\hat{J}\hat{\boldsymbol{F}}^{-T}-\left(\delta p^{\mathcal{F}}\boldsymbol{I}\right)\hat{J}\hat{\boldsymbol{F}}^{-T}\Bigg):\nabla_{\boldsymbol{\chi}}\boldsymbol{\phi}^{\boldsymbol{v},\mathcal{F}}\,\mathrm{d}\Omega^{\mathcal{F}}_{\boldsymbol{\chi}} \\
&+\int_{\Omega^{\mathcal{F}}_{\boldsymbol{\chi}}} \Bigg(\hat{J}\,\mathrm{tr}\left(\hat{\boldsymbol{F}}^{-1}\nabla_{\boldsymbol{\chi}}\delta\boldsymbol{u}^{\mathcal{F}}\right)\mathrm{tr}\left(\nabla_{\boldsymbol{\chi}}\boldsymbol{v}^{k,\mathcal{F}}\hat{\boldsymbol{F}}^{-1}\right) \\
&\quad+\hat{J}\,\mathrm{tr}\left(\nabla_{\boldsymbol{\chi}}\boldsymbol{v}^{k,\mathcal{F}}\left(-\hat{\boldsymbol{F}}^{-1}\nabla_{\boldsymbol{\chi}}\delta\boldsymbol{u}^{\mathcal{F}}\hat{\boldsymbol{F}}^{-1}\right)\right)+\hat{J}\,\mathrm{tr}\left(\nabla_{\boldsymbol{\chi}}\delta\boldsymbol{v}^{\mathcal{F}}\hat{\boldsymbol{F}}^{-1}\right)\Bigg)\cdot\phi^{p,\mathcal{F}}\,\mathrm{d}\Omega^{\mathcal{F}}_{\boldsymbol{\chi}} \\
&+\int_{\Omega^{\mathcal{F}}_{\boldsymbol{\chi}}} \left(-\alpha_u\hat{J}^{-1}\mathrm{tr}\left(\hat{\boldsymbol{F}}^{-1}\nabla_{\boldsymbol{\chi}}\delta\boldsymbol{u}^{\mathcal{F}}\right)\nabla_{\boldsymbol{\chi}}\boldsymbol{u}^{k,\mathcal{F}}+\alpha_u\hat{J}^{-1}\nabla_{\boldsymbol{\chi}}\delta\boldsymbol{u}^{\mathcal{F}}\right):\nabla_{\boldsymbol{\chi}}\boldsymbol{\phi}^{\boldsymbol{u},\mathcal{F}}\,\mathrm{d}\Omega^{\mathcal{F}}_{\boldsymbol{\chi}} \\
&+\int_{\Omega^{\mathcal{S}}_{\boldsymbol{\chi}}} \rho^{\mathcal{S}}\,\delta\boldsymbol{v}\cdot\boldsymbol{\phi}^{\boldsymbol{v},\mathcal{S}}\,\mathrm{d}\Omega^{\mathcal{S}}_{\boldsymbol{\chi}} \\
&+\int_{\Omega^{\mathcal{S}}_{\boldsymbol{\chi}}} \Delta t\theta 2\mu^{\mathcal{S}}\left((\nabla_{\boldsymbol{\chi}}\delta\boldsymbol{u})\hat{\boldsymbol{E}}+\hat{\boldsymbol{F}}\left(\frac{1}{2}(\nabla_{\boldsymbol{\chi}}\delta\boldsymbol{u})^T\hat{\boldsymbol{F}}+\frac{1}{2}\hat{\boldsymbol{F}}^T\nabla_{\boldsymbol{\chi}}\delta\boldsymbol{u}\right)\right):\nabla_{\boldsymbol{\chi}}\boldsymbol{\phi}^{\boldsymbol{v},\mathcal{S}}\,\mathrm{d}\Omega^{\mathcal{S}}_{\boldsymbol{\chi}} \\
&+\int_{\Omega^{\mathcal{S}}_{\boldsymbol{\chi}}} \Delta t\theta\lambda^{\mathcal{S}}\,\mathrm{tr}\left(\frac{1}{2}\left((\nabla_{\boldsymbol{\chi}}\delta\boldsymbol{u})^T\hat{\boldsymbol{F}}+\hat{\boldsymbol{F}}^T\nabla_{\boldsymbol{\chi}}\delta\boldsymbol{u}\right)\right)\hat{\boldsymbol{F}}:\nabla_{\boldsymbol{\chi}}\boldsymbol{\phi}^{\boldsymbol{v},\mathcal{S}}\,\mathrm{d}\Omega^{\mathcal{S}}_{\boldsymbol{\chi}} \\
&+\int_{\Omega^{\mathcal{S}}_{\boldsymbol{\chi}}} \delta\boldsymbol{u}\cdot\boldsymbol{\phi}^{\boldsymbol{u},\mathcal{S}}\,\mathrm{d}\Omega^{\mathcal{S}}_{\boldsymbol{\chi}}-\int_{\Omega^{\mathcal{S}}_{\boldsymbol{\chi}}} \Delta t\theta\,\delta\boldsymbol{v}\cdot\boldsymbol{\phi}^{\boldsymbol{u},\mathcal{S}}\,\mathrm{d}\Omega^{\mathcal{S}}_{\boldsymbol{\chi}}.
\end{aligned}
\tag{5.175}
$$

Above, $\mu^{\mathcal{S}}$ and $\lambda^{\mathcal{S}}$ are the Lamé constants of the elasticity problem, $\boldsymbol{U}^k$ represents the values of the field variables at the current nonlinear iteration k, and $\delta\boldsymbol{U}$ and $\boldsymbol{\Phi}$ denote the set of trial and test functions, respectively. Moreover, we have used above the following compact notation $\boldsymbol{F} := \boldsymbol{F}(\boldsymbol{u}^k), \boldsymbol{F}^{-1} := \boldsymbol{F}^{-1}(\boldsymbol{u}^k), \boldsymbol{F}^{-T} := \boldsymbol{F}^{-T}(\boldsymbol{u}^k), \boldsymbol{E} := \boldsymbol{E}(\boldsymbol{u}^k)$.

5.3.6 Numerical results

In this section we present numerical results obtained from the application of Isogeometric Analysis to fluid-structure interaction problems that are treated in a fully coupled monolithic manner. The numerical experiments performed serve the purpose to assess and validate this combination of solution algorithms and numerical techniques that we have chosen to work with.

5.3.6.1 Application to the Turek-Hron FSI benchmark problems

For validation purposes we adopt the "Turek-Hron FSI benchmark" that is based on the classical flow around cylinder benchmark [129] for incompressible laminar flow and on the setup described in [157]. The problem setup is shown in Figure 5.10. It basically adopts all settings of the flow around cylinder benchmark and extends the fixed, rigid cylinder at its right end by a 2D elastic beam. The elastic beam is allowed to be compressible and will undergo large deformations that are induced by the stress of the surrounding fluid in motion. Since the deforming beam modifies in turn the flow channel geometry, the fluid responses with corresponding changes in velocity and pressure. This coupling will cause a waving motion of the elastic beam, in a sense similar to the vortex shedding patterns one observes in the flow part. The fluid flow is modeled to be Newtonian, laminar and incompressible. Its balance equations are the Navier-Stokes equations

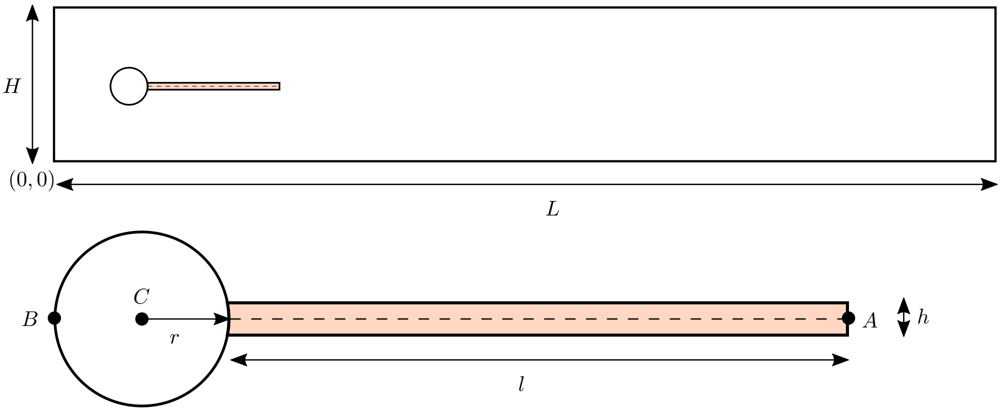

Figure 5.10: Computational domains (fluid+solid) for the 2D flow past an elastic beam FSI benchmark. The computational domain has length $L = 2.5$ and height $H = 0.41$. Measured from the bottom left corner of the channel, the circle is centered at $C = (0.2, 0.2)$ and has radius $r = 0.05$. The elastic beam has length $l = 0.35$ and height $h = 0.02$ and is fully attached to the cylinder at its left circular arc shaped boundary. Its bottom right corner has the position $(0.6, 0.19)$. The control point $A(t)$ is fixed to the structure and has the initial position $A(0) = (0.6, 0.2)$. $B = (0.15, 0.2)$ is another control point. All specified parameters are in si units (e.g. the distances are given in meters).

$$\begin{aligned} \rho^{\mathcal{F}} \left(\frac{\partial \boldsymbol{v}^{\mathcal{F}}}{\partial t} + (\boldsymbol{v}^{\mathcal{F}} \cdot \nabla) \boldsymbol{v}^{\mathcal{F}} \right) - \nabla \cdot \boldsymbol{\sigma}^{\mathcal{F}} &= \rho^{\mathcal{F}} \boldsymbol{f}, \\ \nabla \cdot \boldsymbol{v}^{\mathcal{F}} &= 0, \end{aligned} \tag{5.176}$$

where the fluid stress is described by the following constitutive equation

$$\boldsymbol{\sigma}^{\mathcal{F}} = -p\boldsymbol{I} + \rho^{\mathcal{F}} \nu^{\mathcal{F}} (\nabla \boldsymbol{v}^{\mathcal{F}} + (\nabla \boldsymbol{v}^{\mathcal{F}})^T). \tag{5.177}$$

Above, $\rho^{\mathcal{F}}$ and $\nu^{\mathcal{F}}$ denote the density and kinematic viscosity of the fluid. The response of the elastic beam to external stimuli is modeled with the constitutive equation for the St. Venant-Kirchhoff material where the second Piola-Kirchhoff stress of the solid material reads

$$\boldsymbol{S}^{\mathcal{S}} = \lambda \operatorname{tr}(\boldsymbol{E})\, \boldsymbol{I} + 2\mu \boldsymbol{E}. \tag{5.178}$$

Accordingly with the relation given in (2.40) the Cauchy stress of the material is

$$\boldsymbol{\sigma}^{\mathcal{S}} = J^{-1}\boldsymbol{F}\boldsymbol{S}^{\mathcal{S}}\boldsymbol{F}^{T} = J^{-1}\boldsymbol{F}(\lambda \operatorname{tr}(\boldsymbol{E})\, \boldsymbol{I} + 2\mu \boldsymbol{E})\boldsymbol{F}^{T}. \tag{5.179}$$

We continue with the presentation of the problem's geometry parameters and point out at this point that all parameters given are in meters. The flow domain has length $L = 2.5$ and height $H = 0.41$. This domain defining a cartesian coordinate system at its lower left corner is the frame of reference of all position specifications given in the sequel. The cylinder with radius $r = 0.05$ is centered at $C = (0.2, 0.2)$. To its right end is the fully attached elastic beam[48] with length $l = 0.35$ and height $h = 0.02$. The lower right corner of the beam is at position $(0.6, 0.19)$. For the comparison of the elastic beam's time dependent deflection, a reference point $A(t)$ at the right end of the beam is selected which is initially at $A(0) = (0.6, 0.2)$.

The flow in the transient tests is driven by a smoothly increasing parabolic velocity profile that is parametrized with time and is prescribed in the Dirichlet sense at the left boundary of the channel. The flow profile is given by the function

$$v^{\mathcal{F}}(t, 0, y) = \begin{cases} v^{\mathcal{F}}(0, y)[1 - \cos(\pi t/2)]/2 & \text{if } t < 2, \\ v^{\mathcal{F}}(0, y) \quad \text{otherwise}, \end{cases} \tag{5.180}$$

where

$$v^{\mathcal{F}}(0, y) = U\frac{y(H-y)}{(H/2)^2} = \frac{3}{2}\bar{U}\frac{y(H-y)}{(H/2)^2}, \tag{5.181}$$

and U and $\bar{U}$ denote the maximum and mean velocity in the parabolic inflow profile. The outflow condition prescribed to the right end of the channel may be set to the no-stress or do-nothing conditions. The outflow condition effectively prescribes values for the pressure variable [149]. The benchmark proposes to set a zero mean pressure value at the outflow boundary. The *no-slip* boundary condition is prescribed at all other boundary parts, that is, on the top and bottom walls of the channel, on the cylinder, and on the fluid-solid interface. Since the fluid-solid interface is subject to motion, the *no-slip* condition is satisfied through

$$\boldsymbol{v}^{\mathcal{F}} = \boldsymbol{v}^{\mathcal{S}}. \tag{5.182}$$

In addition to the just specified *continuity of velocity condition* (cf. equation (5.108)), the balance of forces expressed through

$$\boldsymbol{\sigma}^{\mathcal{F}}\boldsymbol{n} = \boldsymbol{\sigma}^{\mathcal{S}}\boldsymbol{n}, \tag{5.183}$$

is another crucial condition that needs to be satisfied on the joint interface (with unit normal vector $\boldsymbol{n}$).

The benchmark considers three test scenarios whose parameters are given in Table 5.5. The tests basically differ by their respective inflow speeds ($Re = 20, Re = 100, Re = 200$) and the

---

[48] When it comes to meshing, it is important to model the left end of the elastic beam with a circular arc. Modeling this end with a straight line is already sufficient to deteriorate the accuracy of results.

Parameter	Description	Unit	FSI 1	FSI 2	FSI 3
$\rho^{\mathcal{S}}$	Solid density	$[\mathrm{kg/m^3}]$	1000	10000	1000
$\nu^{\mathcal{S}}$	Solid Poisson's ratio		0.4	0.4	0.4
$\mu^{\mathcal{S}}$	Solid Lamé constant	$[\mathrm{kg/(m\,s^2)}]$	0.5×10^6	0.5×10^6	2×10^6
$\rho^{\mathcal{F}}$	Fluid density	$[\mathrm{kg/m^3}]$	1000	1000	1000
$\nu^{\mathcal{F}}$	Fluid kinematic viscosity	$[\mathrm{m^2/s}]$	0.001	0.001	0.001
$\bar{U}$	Average inflow velocity	$[\mathrm{m/s}]$	0.2	1	2
$\beta = \frac{\rho^{\mathcal{S}}}{\rho^{\mathcal{F}}}$	Fluid-solid density ratio		1	10	1
$Re = \frac{\bar{U}d}{\nu^{\mathcal{F}}}$	Reynold's number		20	100	200

Table 5.5: Parameter settings for the FSI tests.

elasticity (or stiffness) settings of the elastic beam. The parameter settings of FSI 1 yield a steady state solution, whereas those of FSI 2 and FSI 3 result in periodic solutions. However, we treat FSI 1 as a transient problem and iterate the solution in time until a steady state solution is obtained. FSI 1 and FSI 3 have a fluid-solid density ratio of 1 which – due to the *added mass effect* [123] – may be considered as particularly challenging for partitioned FSI approaches.

Prior to presenting the results obtained for the three FSI test cases, a discussion on the quantities used for comparisons is in order. In the transient FSI cases we observe periodic oscillations in the flow as well as in the solid. Once the flow is fully developed we measure the following quantities for comparisons:

1. The displacements $u_1(t)$ and $u_2(t)$ of the reference point $A(t)$in the x, and y directions.
2. Drag and lift forces

$$(F_D, F_L)^T = \int_S \boldsymbol{\sigma}^{\mathcal{F}} \boldsymbol{n} \,\mathrm{d}S = \int_{S_1} \boldsymbol{\sigma}^{\mathcal{F}} \boldsymbol{n} \,\mathrm{d}S_1 + \int_{S_2} \boldsymbol{\sigma}^{\mathcal{F}} \boldsymbol{n} \,\mathrm{d}S_2 \tag{5.184}$$

exerted by the fluid on the whole submerged body $S = S_1 \cup S_2$, where S_1 denotes the surface of the rigid cylinder (modulo the part shared with the beam), S_2 represents the surface of the elastic beam (modulo the part shared with the cylinder), and $\boldsymbol{n}$ is the outer unit normal vector on S pointing into the fluid domain.

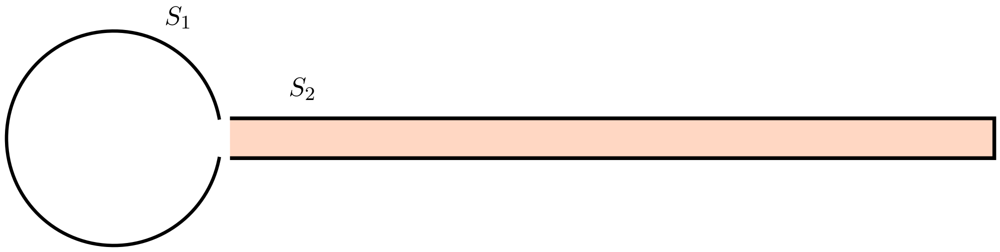

Figure 5.11: Integration path $S = S_1 \cup S_2$ for the force calculation.

For time dependent quantities we consider their mean value, amplitude and frequency. When it comes to the computation of the mean value and the amplitude of a quantity, we consider the last oscillation period and measure the maximum and minimum value of the quantity under inspection. From these values the mean value is derived as follows:

$$\begin{aligned} \text{mean} =& \frac{1}{2}(\max + \min), \\ \text{amplitude} =& \frac{1}{2}(\max - \min). \end{aligned} \tag{5.185}$$

The oscillation frequency can be either computed as

$$f = \frac{1}{T},$$

where T denotes the oscillation period time, or determined via a Fourier analysis of the periodic data, where we pick the lowest significant frequency in the spectrum. The latter approach is used for all the frequency data we present for FSI 1-3.

In order to obtain solution data for FSI 1-3, we aim to solve the transient and nonlinear problem given by equation (6.16). This requires a proper treatment of nonlinearity alongside discretization in time and space. We recall that we have already shown in Section 5.3.5.1.1 a time-discrete version of the above problem in the context of Newton's method. Therefore, all we need to present now is the corresponding spatial discretization for which we use Isogeometric Analysis. The multi-patch NURBS mesh we use for the modeling of our computational domain is depicted in Figure 5.12. This mesh – exhibiting a significant number of elements with a large aspect ratio – is far from optimal and is of a rather prototypical character. Therefore, results with a higher accuracy may be expected for better meshes. For the approximation of the velocity and pressure functions in the Navier-Stokes and Elasticity equations, we use LBB-stable Taylor-Hood-like B-spline/NURBS space pairs $\mathbf{V}_h^{TH}/Q_h^{TH}$ which has already been introduced in (3.73). Moreover, we let the displacement function $\boldsymbol{u}$ have the same degree and regularity as the velocity function $\boldsymbol{v}$. In all performed computations we used a $\mathcal{C}^0$ $\boldsymbol{\mathcal{N}}_{0,0}^{3,3}/\mathcal{N}_{0,0}^{2,2}$ NURBS space pair for the approximation of the velocity and pressure functions. This corresponds to the Isogeometric counterpart of a Q_2Q_1 Taylor-Hood space well known from the finite element literature.

Figure 5.12: Multi-patch NURBS mesh (coarsest level) used for FSI tests 1-3. The elastic bar is resolved with 11 elements along the x-axis.

Remark 5.3.3. *We would like to explicitly point out that the multi-patch NURBS mesh we use is "watertight" and "compatible" in the following sense: Two NURBS patches touching at a common boundary need to have the same degrees and regularities on the common boundary curve. Moreover, the choice of the B-spline/NURBS knot vectors of the adjacent sides of two patches results in a partition of the patches such that the NURBS segments (elements) to the left and right of the joint boundary geometrically match along the common patch boundary. Furthermore, the position of the NURBS control points of the touching sides of two patches is chosen such that they coincide geometrically. Then, under the premise that a multi-patch NURBS mesh fulfills the above requirements, we literally glue together geometrically matching control points by assigning them the same degree of freedom for each finite element function we want to be represented on the* *mesh. Note that this significantly simplifies the implementation of the geometric coupling condition (5.107) and the continuity of velocity condition (5.108).*

With the above spatial discretization, a reformulation of our sketch of Newton's method in terms of the discrete trial space

$$\begin{aligned}\mathcal{T}_h := \{\, &(\boldsymbol{\mathcal{T}}^{\boldsymbol{v},\mathcal{F}} \cap \mathbf{V}_h^{TH}) \times (\boldsymbol{\mathcal{T}}^{\boldsymbol{v},\mathcal{S}} \cap \mathbf{V}_h^{TH}) \times (\boldsymbol{\mathcal{T}}^{\boldsymbol{u},\mathcal{F}} \cap \mathbf{V}_h^{TH}) \times (\boldsymbol{\mathcal{T}}^{\boldsymbol{u},\mathcal{S}} \cap \mathbf{V}_h^{TH}) \\ &\times (\mathcal{L}^{\mathcal{F}} \cap Q_h^{TH}) \times (\mathcal{L}^{\mathcal{S}} \cap Q_h^{TH})\},\end{aligned} \tag{5.186}$$

the discrete test space

$$\begin{aligned}\mathcal{W}_h := \{\, &(\boldsymbol{\mathcal{W}}^{\boldsymbol{v},\mathcal{F}} \cap \mathbf{V}_h^{TH}) \times (\boldsymbol{\mathcal{W}}^{\boldsymbol{v},\mathcal{S}} \cap \mathbf{V}_h^{TH}) \times (\boldsymbol{\mathcal{W}}^{\boldsymbol{u},\mathcal{F}} \cap \mathbf{V}_h^{TH}) \times (\boldsymbol{\mathcal{W}}^{\boldsymbol{u},\mathcal{S}} \cap \mathbf{V}_h^{TH}) \\ &\times (\mathcal{L}^{\mathcal{F}} \cap Q_h^{TH}) \times (\mathcal{L}^{\mathcal{S}} \cap Q_h^{TH})\},\end{aligned} \tag{5.187}$$

and discrete functions

$$\begin{aligned}\delta \boldsymbol{U}_h &= \{\delta \boldsymbol{v}_h^{\mathcal{F}}, \delta \boldsymbol{v}_h^{\mathcal{S}}, \delta \boldsymbol{u}_h^{\mathcal{F}}, \delta \boldsymbol{u}_h^{\mathcal{S}}, \delta p_h^{\mathcal{F}}, \delta p_h^{\mathcal{S}}\}, \\ \boldsymbol{U}_h &= \{\boldsymbol{v}_h^{\mathcal{F}}, \boldsymbol{v}_h^{\mathcal{S}}, \boldsymbol{u}_h^{\mathcal{F}}, \boldsymbol{u}_h^{\mathcal{S}}, p_h^{\mathcal{F}}, p_h^{\mathcal{S}}\}, \\ \boldsymbol{\Phi}_h &= \{\boldsymbol{\phi}_h^{v,\mathcal{F}}, \boldsymbol{\phi}_h^{v,\mathcal{S}}, \boldsymbol{\phi}_h^{u,\mathcal{F}}, \boldsymbol{\phi}_h^{u,\mathcal{S}}, \phi_h^{p,\mathcal{F}}, \phi_h^{p,\mathcal{S}}\},\end{aligned} \tag{5.188}$$

reads

```
while $\|\mathcal{F}(\boldsymbol{U}_h^k; \boldsymbol{\Phi}_h)\| \leq \epsilon_{tol}$ and $k < k^{max}$ do
    Find $\delta \boldsymbol{U}_h \in \mathcal{T}_h$, such that
    $\mathcal{F}'(\boldsymbol{U}_h^k; \delta \boldsymbol{U}_h, \boldsymbol{\Phi}_h) = -\mathcal{F}(\boldsymbol{U}_h^k; \boldsymbol{\Phi}_h), \quad \forall \boldsymbol{\Phi}_h \in \mathcal{W}_h$    (5.189)
    $\boldsymbol{U}_h^{k+1} = \boldsymbol{U}_h^k + \omega\, \delta \boldsymbol{U}_h$,
end
```

where $\mathcal{F}(\boldsymbol{U}_h^k; \boldsymbol{\Phi}_h)$ and $\mathcal{F}'(\boldsymbol{U}_h^k; \delta \boldsymbol{U}_h, \boldsymbol{\Phi}_h)$ are simply the discrete versions of (5.154) and (5.175).

So far we have presented a description of the benchmark tests, and designated Isogeometric Analysis as spatial discretization technique. For the latter, we presented a multi-patch NURBS mesh on which we span NURBS-based discrete approximation spaces. With the presentation of Newton's method for the time and space discretized FSI problem (6.16), we have delivered all necessary ingredients to solve the FSI 1-3 problems and to reproduce the data we have obtained from computations. For comparison purposes, we take the results of Hron and Turek [58, 83, 148, 149] as reference. In [149], Turek and Hron list their results for a contrasting juxtaposition alongside those provided by other benchmark participants (M. Schäfer, R. Rannacher, M. Breuer, M. Krafczyk, E. Rank, W.A. Wall, K.-U. Bletzinger). We adopt this practice for the sake of the valuable insights it provides and compare our results not only to the reference but also to other published results whenever available. Our data are presented and discussed in the sequel.

5.3.6.1.1 FSI 1

The FSI 1 problem features a very low Reynolds number (20). This yields a laminar flow pattern and the solution tends to a "steady state" as $t \to \infty$. In such cases one may in principle use a computationally much more efficient 'stationary' FSI problem formulation which by definition is free of time marching. In this work, however, we treat FSI 1-3 cases as transient problems and use the formulation given in Problem 5.3.4. Our FSI 1 solutions depicted in Table 5.6 and Figures 5.13 and 5.14 are iterated 25 steps "into the steady state limit" with the Backward Euler time stepping scheme

($\theta = 1$) using a fixed time step size $\Delta t = 1$. From Table 5.6 we deduce that our data blends very well with the data provided by the sources on the bottom half of the table. Especially for u_1, F_D and F_L we can see that our solution converges to the reference. For u_1 and F_D the percentual error (w.r.t. the reference) almost halves from mesh level i to $i+1$. However, for the quantity u_2 our solution does not march towards that of Turek/Hron and rather follows the data of Rannacher. We mention at this point that for the sake of keeping the table concise, we have merely shown the final results provided by the external sources and have refrained from showing the convergence histories. For the latter we refer to [149] where the convergence histories of u_2 provided by Rannacher, Krafczyk/Rank and Wall show a clearly decreasing trend. This circumstance and the fact that almost all values provided by Rannacher for u_2 are smaller than that of Hron/Turek and even smaller than our values, make it at least questionable what the reference value for u_2 really is.

	N_{dof}	$u_1(A)[\times 10^{-5}]$ (%-Err)	$u_2(A)[\times 10^{-4}]$ (%-Err)	F_D (%-Err)	F_L (%-Err)
Present	5067	2.240935(1.30)	8.455798(3.01)	14.28377(0.073)	0.774193(1.368)
	25209	2.261569(0.39)	8.201354(0.09)	14.28930(0.035)	0.765377(0.214)
	111573	2.266417(0.18)	8.196860(0.15)	14.29256(0.012)	0.764979(0.161)
	468621	2.268144(0.10)	8.194405(0.18)	14.29334(0.006)	0.764847(0.144)
	1919997	2.268989(0.07)	8.191383(0.21)	14.29367(0.004)	0.764798(0.138)
1) Schäfer	322338			14.2890	0.76900
2b) Rannacher	351720	2.2695	8.1556	14.2603	0.76388
3) Turek/Hron[149]	19320832	2.270493	8.208773	14.29426	0.76374
5) Krafczyk/Rank	14155776	2.2160	8.2010	14.3815	0.75170
6) Wall	164262	2.2680	8.2310	14.2940	0.76487
7) Bletzinger	217500	2.2640	8.2800	14.3510	0.76351

Table 5.6: Results for the FSI 1 case.

The temporal developments of the quantities under inspection are illustrated in Figures 5.13 and 5.14 for five consequent mesh refinement levels (L0 - L4). The data plots show that the solutions become stationary after at most 10 seconds simulation time. Moreover the traces of the curves of level 1 to level 4 show very little deviation from each other and are therefore barely distinguishable in the plot. We conclude the FSI 1 section with the presentation of the computed velocity, displace-

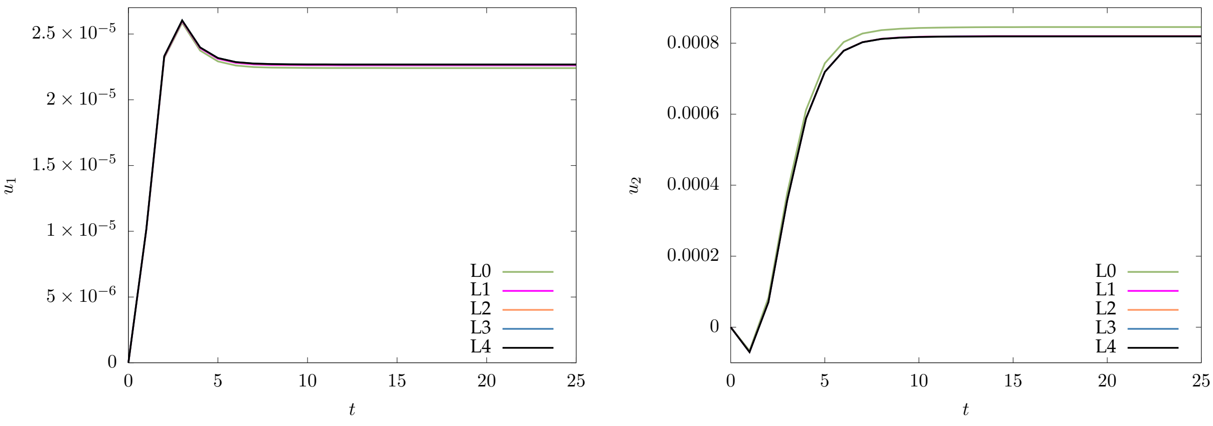

Figure 5.13: FSI 1 displacement (u_1, u_2) for $\theta = 1, \Delta t = 1$, $u_1^{\text{ref}} : 2.270493e-5$, $u_2^{\text{ref}} : 8.208773e-4$.

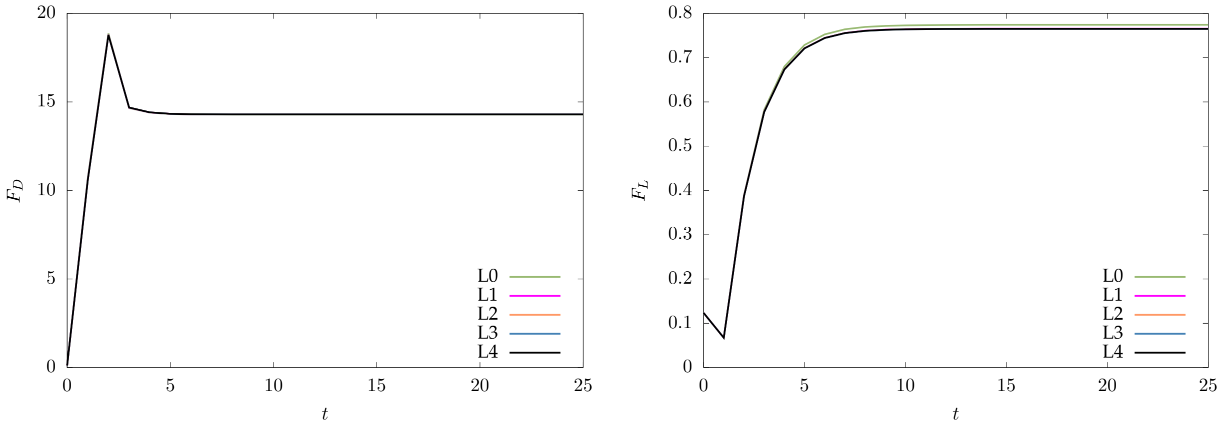

Figure 5.14: FSI 1 drag and lift forces (F_D, F_L) for $\theta = 1, \Delta t = 1$, $F_D^{\text{ref}} : 14.29426$, $F_L^{\text{ref}} : 0.7637460$.

ment and pressure functions on the computational domain (see Figures 5.15 and 5.16). We want to point out that the pressure in the interior of the solid domain neither has a meaning nor a contribution in the computations as the formulation we presently use for the elasticity equations does not involve a pressure variable. However, since we may switch to an alternative formulation with an explicit pressure variable, from the implementation point of view, there is a pressure degree of freedom in the solid patch which needs to be assigned with values for the plot. These values are for the time being all zero.

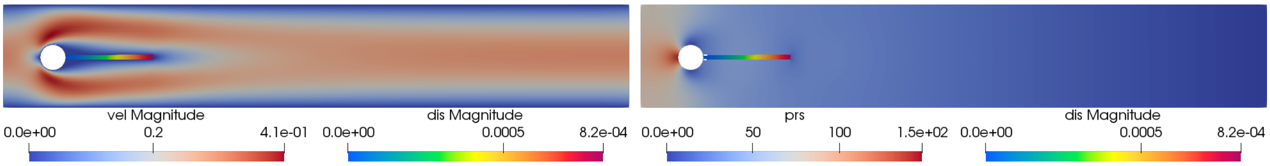

Figure 5.15: FSI 1: Illustration of the displacement of the elastic beam alongside the velocity (left) and pressure fields (right) of the flow in the entire flow channel.

5.3.6.1.2 FSI 2

Our results for FSI 2 for two different time step sizes and three consecutive mesh refinement levels are presented in Table 5.7. The format of the data of the last four columns is: mean value ± amplitude[frequency], cf. (5.185). Except the data provided by Turek and Hron we have in this case – unlike the FSI 1 and FSI 3 cases – no additional sources to which we can compare our data. The stable temporal evolution of the quantities u_1, u_2, F_D and F_L are illustrated in the top row of the Figures 5.17, 5.18, 5.19 and 5.20. As far as stability is concerned, we would like to point out that in long term FSI computations such as in FSI 2 and FSI 3, the standard Crank-Nicolson (CN) time stepping scheme $(\theta = 0.5)$ leads to unstable behavior. The solutions literally blow up even after a long stable sequence. In fact, stable results such as those shown in the above mentioned figures are simply out of reach for the same time step size with the standard CN scheme. In order to address

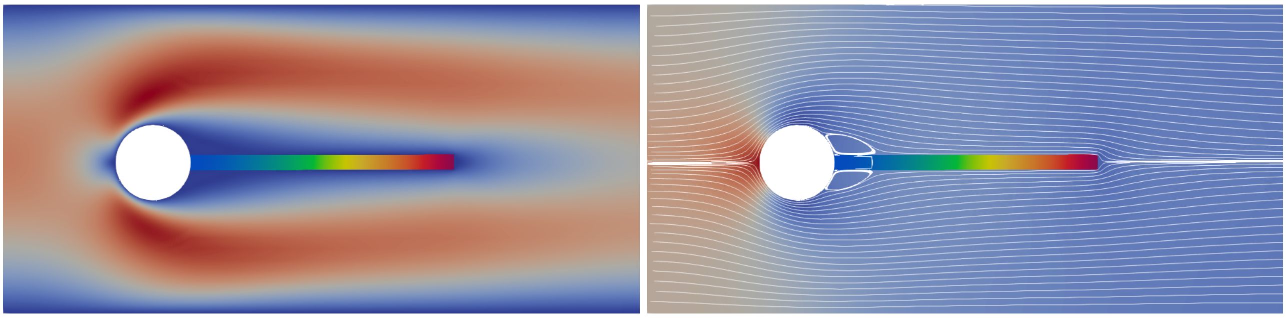

Figure 5.16: FSI 1: Magnified view of the displacement of the elastic beam alongside the velocity (left) and pressure fields (right) of the flow. The pressure field is overlayed with velocity streamlines.

	Δt	Level	$\mathrm{N_{dof}}$	$u_1(A)[\times 10^{-3}]$ [f]	$u_2(A)[\times 10^{-3}]$ [f]	F_D [f]	F_L [f]
	1×10^{-2}	1	25209	$-15.22 \pm 13.34[3.85]$	$1.23 \pm 82.1[1.92]$	$211.43 \pm 77.41[3.84]$	$1.1 \pm 237.6[1.92]$
		2	111573	$-15.14 \pm 13.28[3.85]$	$1.21 \pm 82.1[1.92]$	$214.53 \pm 78.80[3.84]$	$1.3 \pm 236.0[1.92]$
		3	468621	$-15.22 \pm 13.33[3.85]$	$1.27 \pm 82.4[1.92]$	$217.48 \pm 80.30[3.84]$	$1.2 \pm 236.9[1.93]$
	5×10^{-3}	1	25209	$-15.23 \pm 13.13[3.85]$	$1.23 \pm 82.4[1.92]$	$210.70 \pm 77.66[3.84]$	$0.9 \pm 243.0[1.93]$
		2	111573	$-15.21 \pm 13.10[3.86]$	$1.20 \pm 82.5[1.92]$	$213.91 \pm 79.13[3.85]$	$1.2 \pm 241.9[1.93]$
		3	468621	$-15.29 \pm 13.15[3.86]$	$1.26 \pm 82.8[1.92]$	$216.80 \pm 80.63[3.85]$	$0.9 \pm 242.8[1.93]$
Turek/Hron[58]	5×10^{-4}	$4+0$	304128	$-14.85 \pm 12.70[3.86]$	$1.30 \pm 81.6[1.93]$	$215.06 \pm 77.65[3.86]$	$0.6 \pm 237.8[1.93]$

Table 5.7: Results for the FSI 2 case.

this issue, we used the so-called *Shifted Crank-Nicolson scheme* which is obtained by the implicit shift

$$\theta = \frac{1}{2} + O(\Delta t), \tag{5.190}$$

and has better stability properties than the standard CN scheme. The resulting method is still second order accurate, but has a slightly larger stability region [123]. In the bottom row of the above mentioned figures, we depict a magnified view of the profiles for three consecutive mesh refinement levels (L1-L3) for fixed time step size $\Delta t = 0.005$. The profiles shown basically differ by a slight phase shift and are considered mesh converged. The time convergence of our results are shown in the bottom row of the Figures 5.21 and 5.22 depicting a magnified view of the profiles for two time step sizes ($\Delta t = 0.01, \Delta t = 0.005$). Again, the profiles basically differ by the level of detail of the features resolved and a slight phase shift[49].

The elastic beam of the FSI 2 case is significantly less stiff than that of FSI 3. This results in a very pronounced deflection of the beam which poses quite some challenges on the mesh regularization PDE we solve for the ALE mapping. Figure 5.23 depicts for some randomly selected instants of time the results we have obtained from the nonlinear harmonic mesh motion PDE we solve in all FSI test cases. Figures 5.24 and 5.25 illustrate the computed velocity and pressure field in addition to the

---

[49] Since the profiles displayed for FSI 2 and FSI 3 (See Figures 5.17, 5.18, 5.19 and 5.20, 5.21, 5.22, 5.28, 5.29, 5.30 and 5.31 5.32, 5.33) exhibit a periodic character, their start time and start phase is irrelevant. Important is only the fully developed state which however happens to be slightly phase shifted for different mesh and time step refinement levels. In order to facilitate comparisons, we have shifted the coarse level profiles along the time axis so as to overlap with the profile on the highest level.

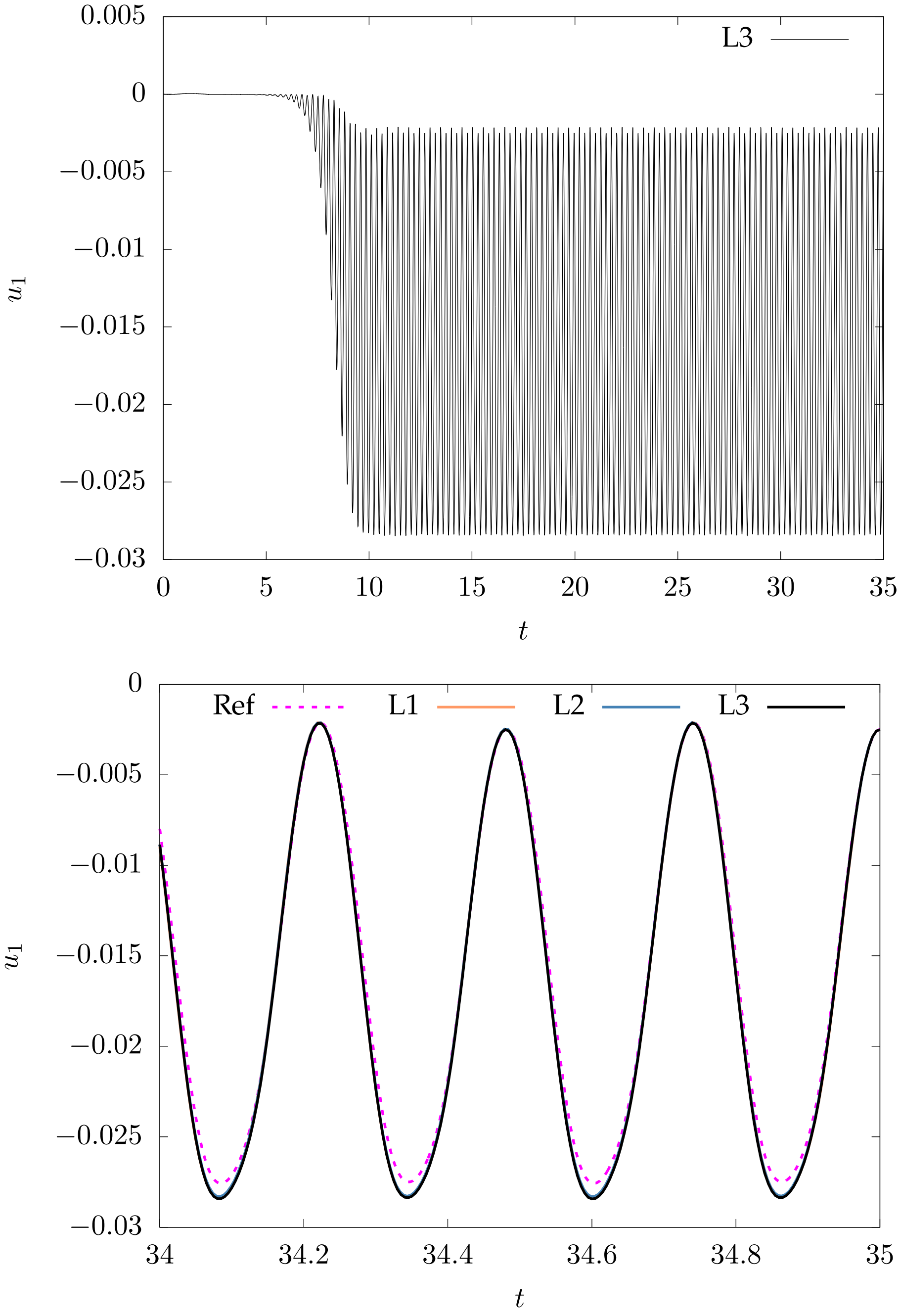

Figure 5.17: FSI 2, Displacement x (u_1), $\Delta t = 0.005$, $\theta = 0.5 + \Delta t$.

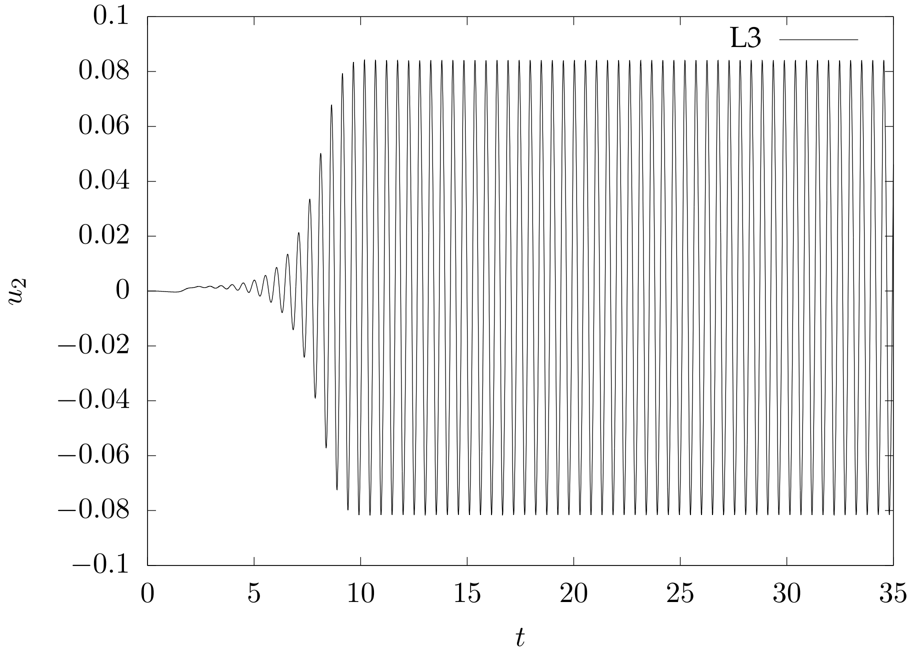

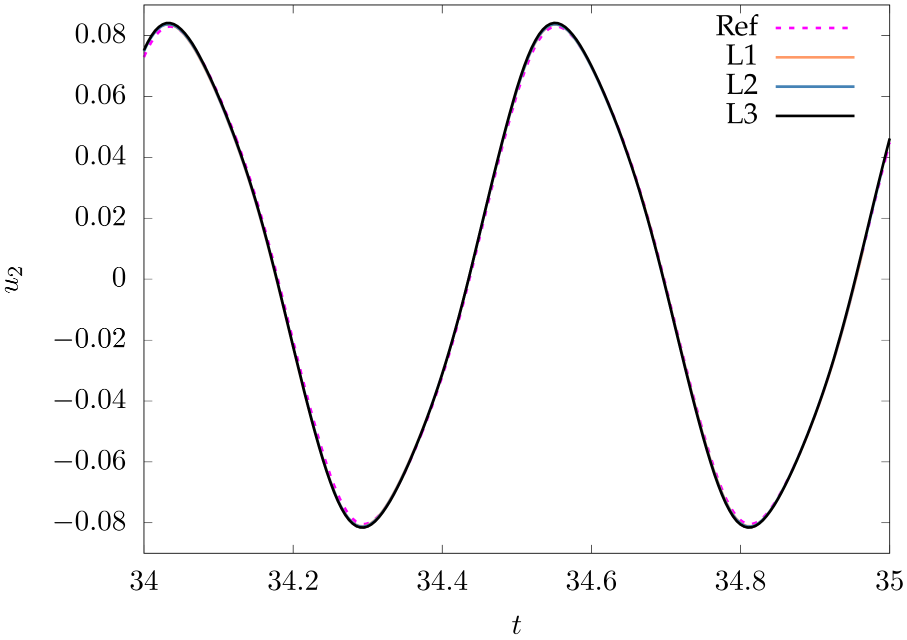

Figure 5.18: FSI 2, Displacement y (u_2), $\Delta t = 0.005$, $\theta = 0.5 + \Delta t$. Top: Stable temporal evolution of the y-displacement profile until the end of the simulation time. Bottom: Magnified view of the y-displacement profiles of three consecutive mesh refinement levels.

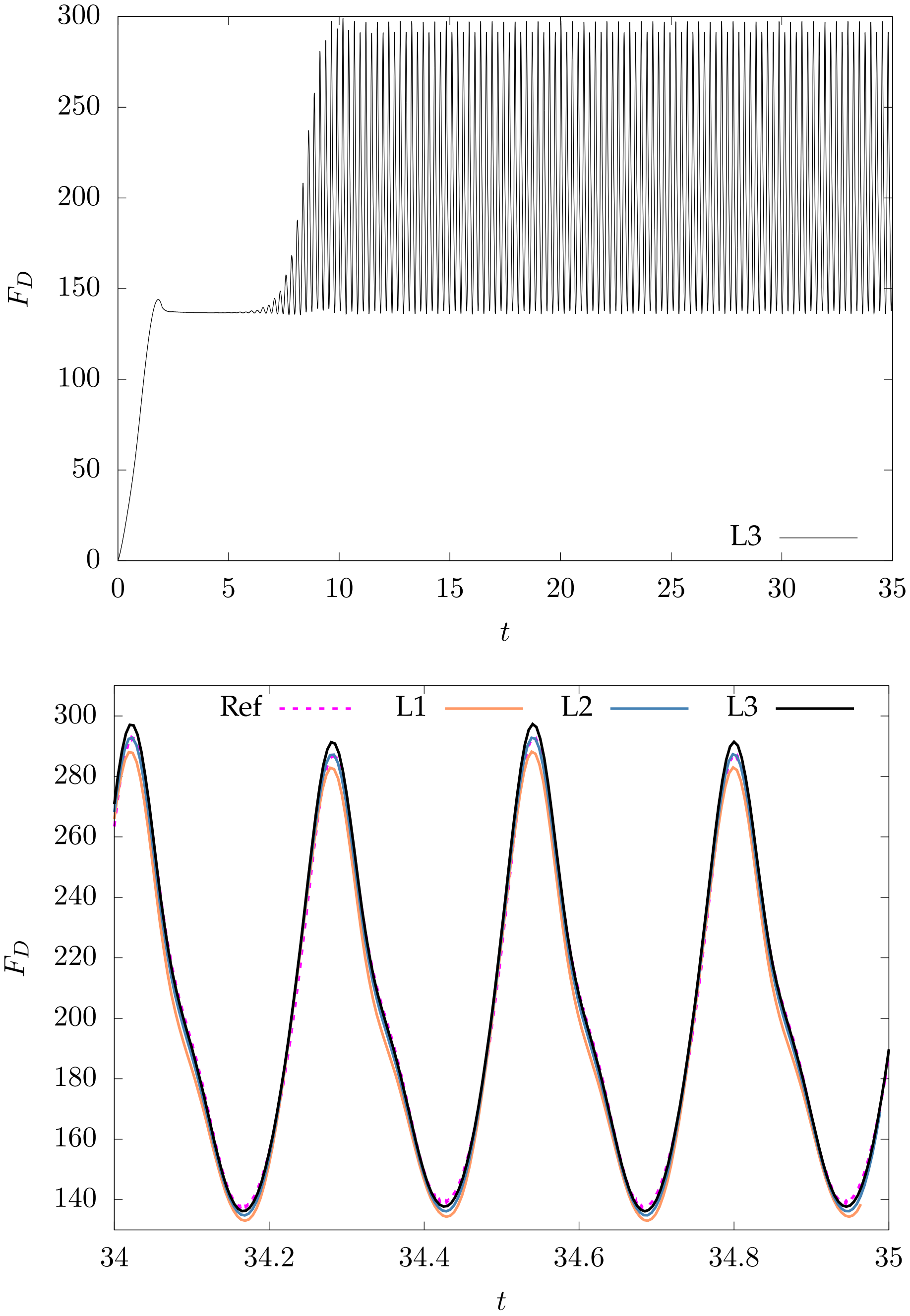

Figure 5.19: FSI 2, Drag force (F_D), $\Delta t = 0.005$, $\theta = 0.5 + \Delta t$. Top: Stable temporal evolution of the drag force profile until the end of the simulation time. Bottom: Magnified view of the drag force profiles of three consecutive mesh refinement levels.

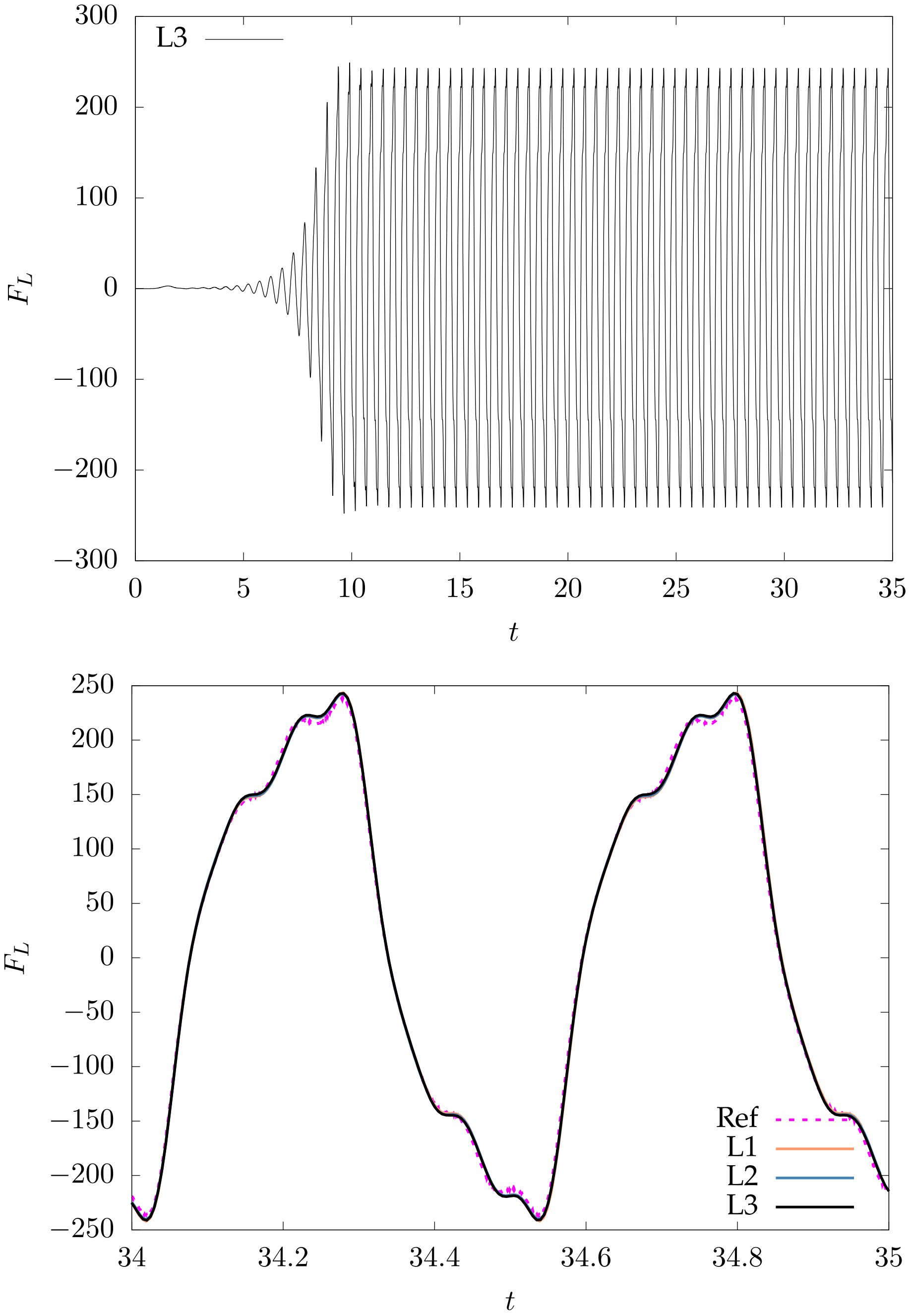

Figure 5.20: FSI 2, Lift force (F_D), $\Delta t = 0.005$, $\theta = 0.5 + \Delta t$. Top: Stable temporal evolution of the lift force profile until the end of the simulation time. Bottom: Magnified view of the lift force profiles of three consecutive mesh refinement levels.

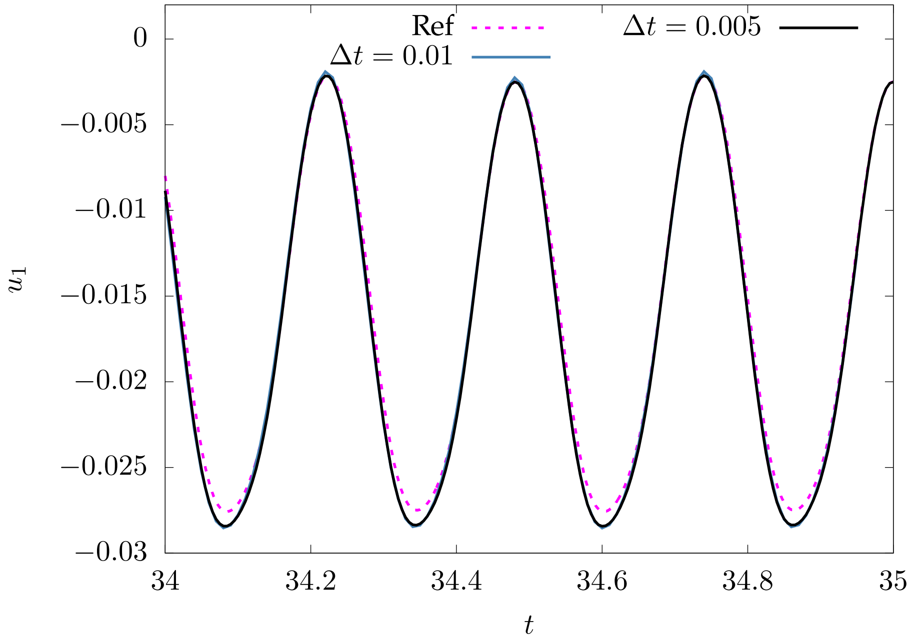

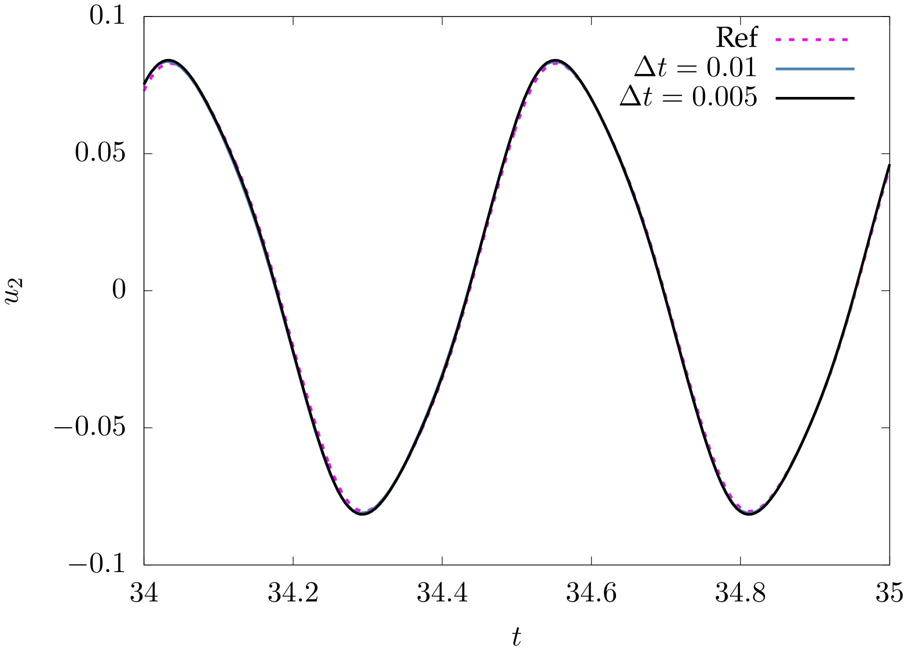

Figure 5.21: FSI 2, Displacement profiles obtained with time step sizes $\Delta t = 0.01$ and $\Delta t = 0.005$ for mesh refinement level L3.

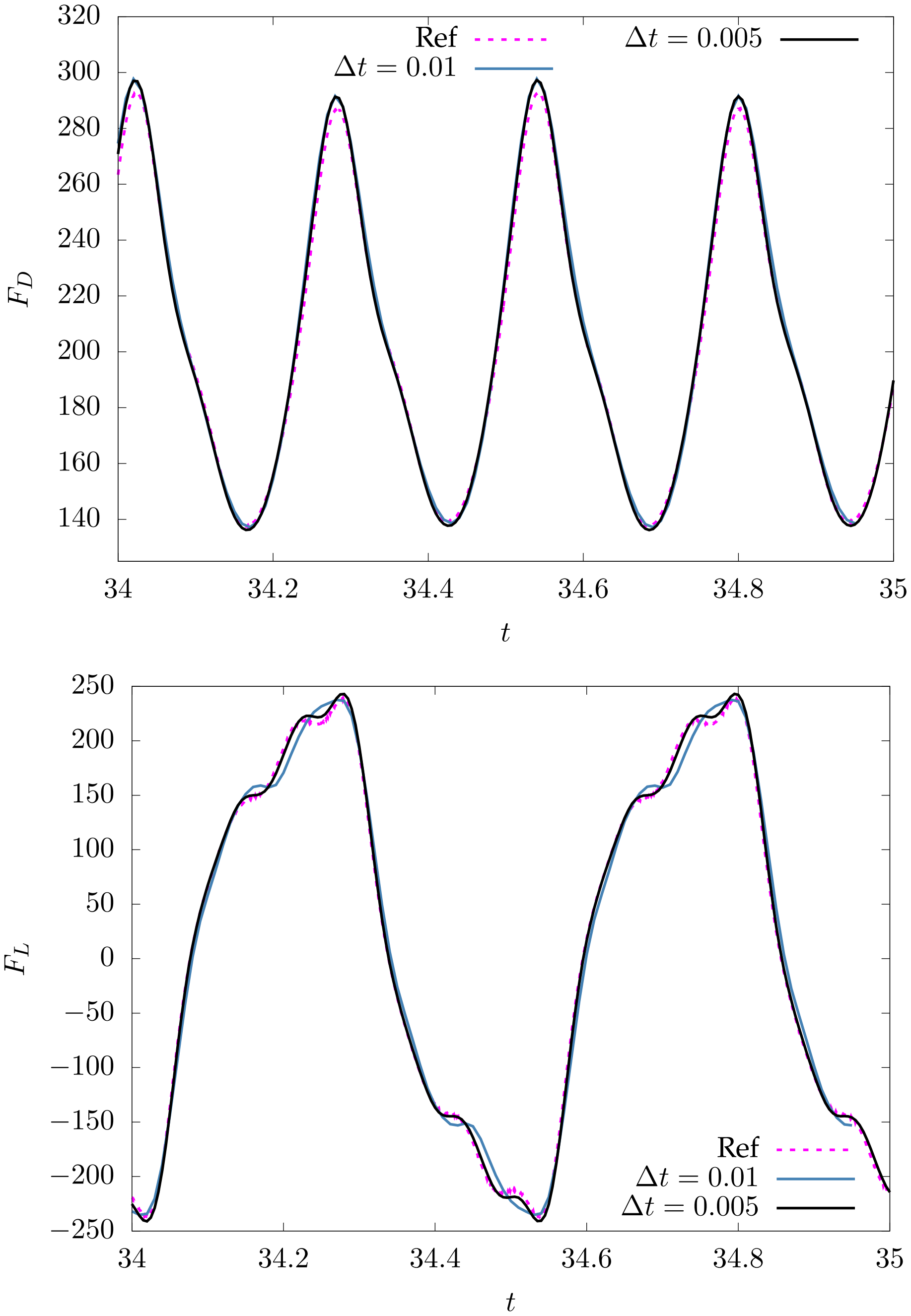

Figure 5.22: FSI 2, Drag and Lift profiles obtained with time step sizes $\Delta t = 0.01$ and $\Delta t = 0.005$ for mesh refinement level L3.

deflection of the elastic beam for some randomly selected instants of time. The overall conclusion we draw is that our results are time and mesh converged and are compliant with the reference.

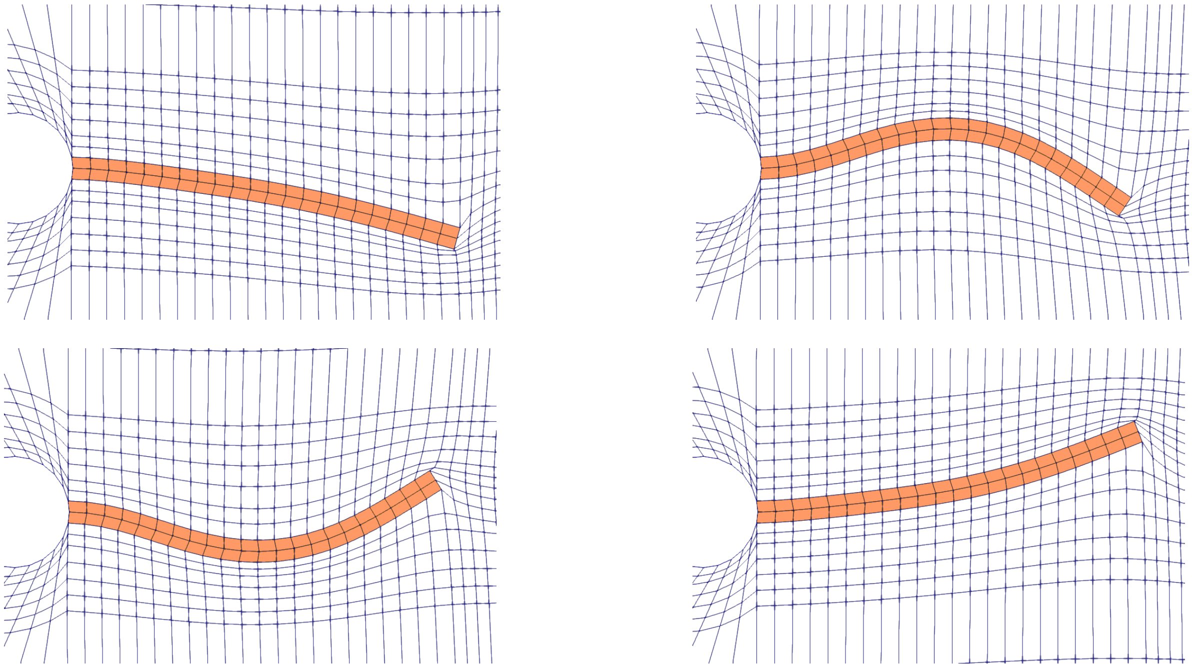

Figure 5.23: Illustration of the mesh distortion at some random instants of time using the nonlinear mesh motion PDE: $-\nabla_{\chi} \cdot (\alpha/\hat{J}\nabla_{\chi} u) = 0$.

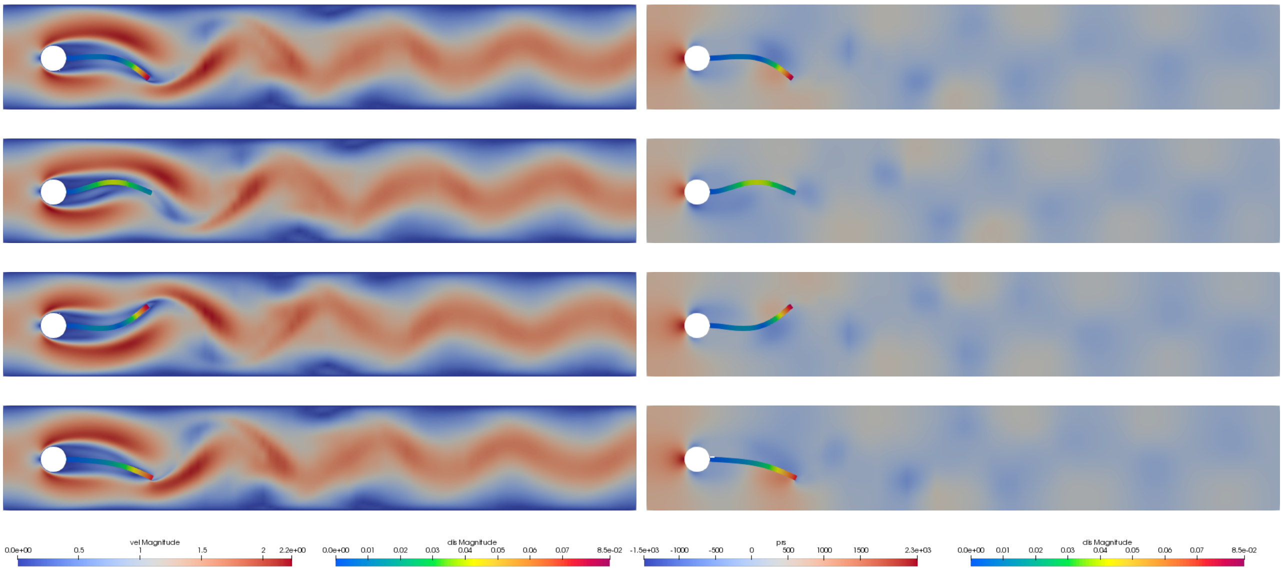

Figure 5.24: FSI 2: Illustration of the displacement of the elastic beam alongside the velocity (left) and pressure fields (right) of the flow in the entire flow channel. Times shown are at 14.6, 14.725, 14.875, and 15.075 s.

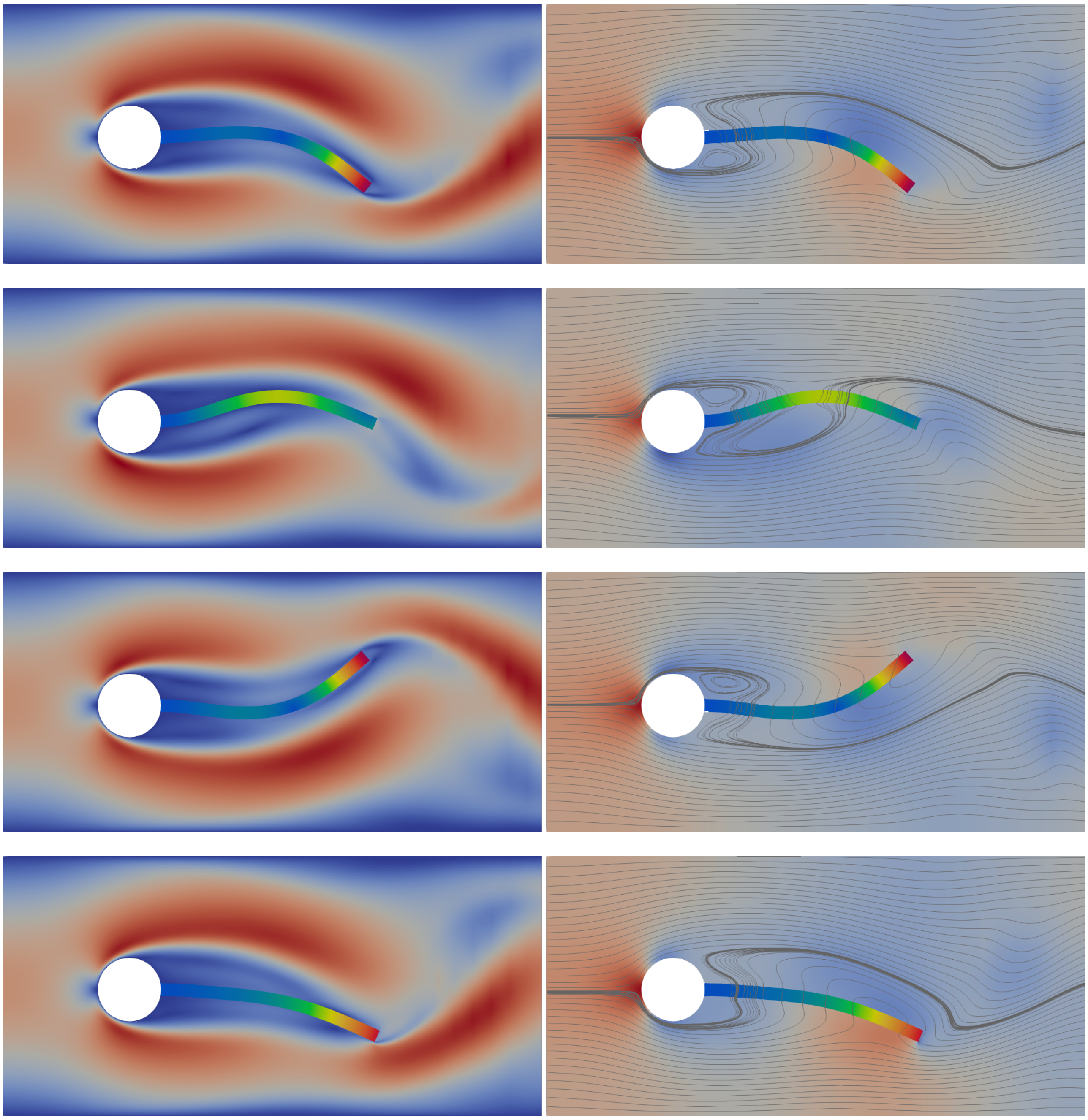

Figure 5.25: FSI 2: Magnified view of the displacement of the elastic beam alongside the velocity (left) and pressure fields (right) of the flow. The pressure field is overlayed with velocity streamlines. Times shown are at 14.6, 14.725, 14.875, and 15.075 s.

5.3.6.1.3 FSI 3

Among the three FSI test cases, the FSI 3 setup is characterized by the stiffest elastic beam and fastest flow. This results in a significantly higher oscillation frequency, where the oscillation amplitude, however, is lower than that of FSI 2. Like in the FSI 1 case, we are here in the convenient situation to be able to compare our data to a multitude of results provided by several research groups, cf. [149]. These data are listed in Table 5.8. Since the shear amount of data displayed in this table makes comparisons a bit cumbersome, we figured, it would be easier to display for each data set a bar whose center represents the mean value of a quantity and whose extension to either direction represents the quantities amplitude. That said, Figures 5.26 and 5.27 provide a very comprehensible overview of the data of Table 5.8, making it extremely easy to compare the results and put them into perspective. For all quantities under inspection we provide data for three consecutive mesh refinement levels, dubbed L1, L2, and L3. The stable temporal evolution of the inspected quantities are displayed in Figures 5.28, 5.29, 5.30, and 5.31. Like in the FSI 2 case, the standard Crank-Nicolson scheme leads to a blow-up of the solution and does not allow the computation to complete. A remedy to this problem is the usage of the fractional-step θ-scheme or the Shifted Crank-Nicolson scheme which we have used.

	Δt	$\mathrm{N}_{\mathrm{dof}}$	$u_1(A)[\times 10^{-3}]$ [f]	$u_2(A)[\times 10^{-3}]$ [f]	F_D [f]	F_L [f]
Present	1.0e−3	25209	$-3.26 \pm 3.08[10.90]$	$1.48 \pm 37.21[5.46]$	$457.6 \pm 31.59[10.88]$	$1.29 \pm 169.74[5.43]$
		111573	$-2.85 \pm 2.69[10.92]$	$1.38 \pm 34.78[5.47]$	$458.1 \pm 27.65[10.90]$	$2.06 \pm 158.95[5.44]$
		468621	$-2.92 \pm 2.76[10.93]$	$1.45 \pm 35.25[5.47]$	$459.5 \pm 28.32[10.97]$	$2.15 \pm 159.57[5.51]$
Present	5.0e−4	111573	$-2.89 \pm 2.72[10.88]$	$1.49 \pm 34.99[5.44]$	$458.6 \pm 27.19[10.86]$	$2.43 \pm 159.59[5.42]$
	5.0e−4	468621	$-3.01 \pm 2.83[10.89]$	$1.39 \pm 35.85[5.45]$	$460.8 \pm 28.62[10.87]$	$2.20 \pm 158.86[5.42]$
1) Schäfer	1.0e−3	941158	$-2.91 \pm 2.77[11.63]$	$1.47 \pm 35.26[4.98]$	459.9 ± 27.92	1.84 ± 157.70
2b) Rannacher	5.0e−4	72696	$-2.84 \pm 2.67[10.84]$	$1.28 \pm 34.61[5.42]$	452.4 ± 26.19	2.36 ± 152.70
3) Turek/Hron[149]	2.5e−4	304128	$-2.88 \pm 2.72[10.93]$	$1.47 \pm 34.99[5.46]$	460.5 ± 27.74	2.50 ± 153.91
4) Münsch/Breuer[110]	2.0e−5	324480	$-4.54 \pm 4.34[10.12]$	$1.50 \pm 42.50[5.05]$	467.5 ± 39.50	16.2 ± 188.70
5) Krafczyk/Rank	5.1e−5	2480814	$-2.88 \pm 2.71[11.00]$	$1.48 \pm 35.10[5.50]$	463.0 ± 31.30	1.81 ± 154.00
6) Wall	5.0e−4	27147	$-2.00 \pm 1.89[10.60]$	$1.45 \pm 29.00[5.30]$	434.0 ± 17.50	2.53 ± 88.60
7) Bletzinger	5.0e−4	271740	$-3.04 \pm 2.87[10.99]$	$1.55 \pm 36.63[5.51]$	474.9 ± 28.12	3.86 ± 165.90
Gallinger[62]					474.9 ± 28.10	3.90 ± 165.90
Sandboge[128]			$-2.83 \pm 2.78[10.8]$	$1.35 \pm 34.75[5.4]$	458.5 ± 24.00	2.50 ± 147.50
Breuer[24]					464.5 ± 40.50	6.00 ± 166.00

Table 5.8: Results for the FSI 3 case.

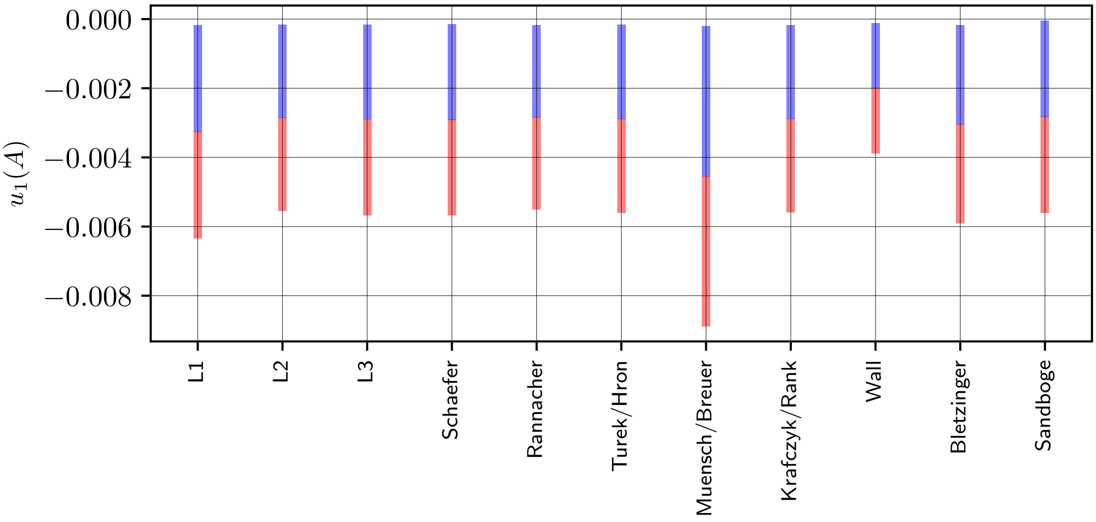

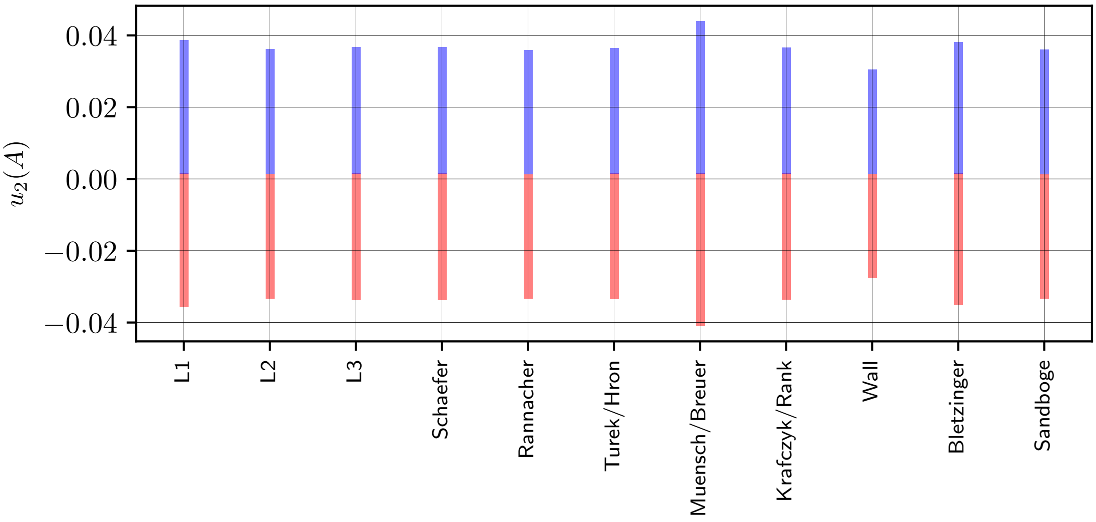

Figure 5.26: FSI 3 min/max/mean displacement comparison. Present results for $\Delta t = 0.001$ and three consecutive mesh refinement levels (L1,L2,L3) are compared with results provided by other groups.

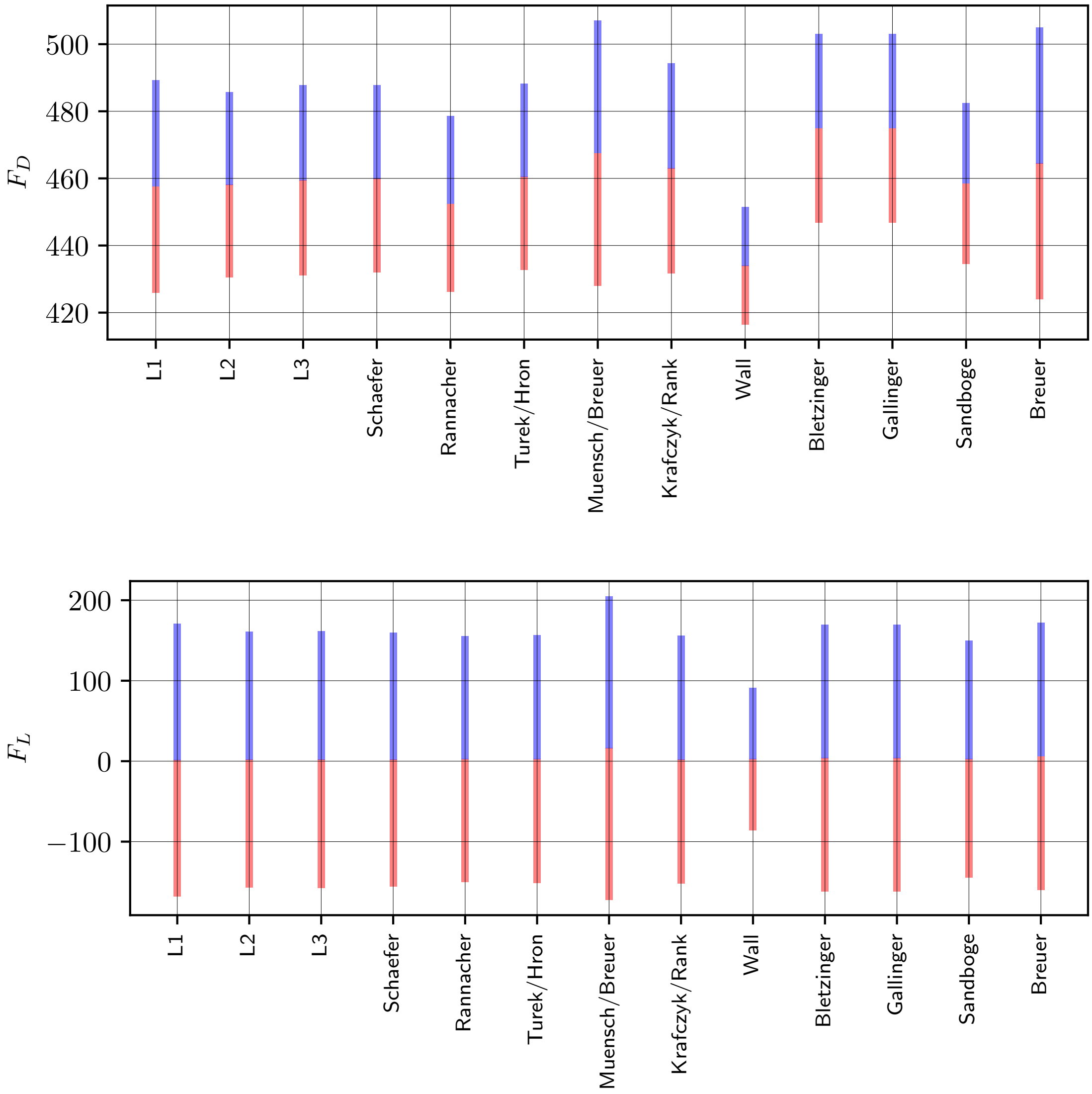

Figure 5.27: FSI 3 min/max/mean F_D, F_L comparison. Present results for $\Delta t = 0.001$ and three consecutive mesh refinement levels (L1,L2,L3) are compared with results provided by other groups.

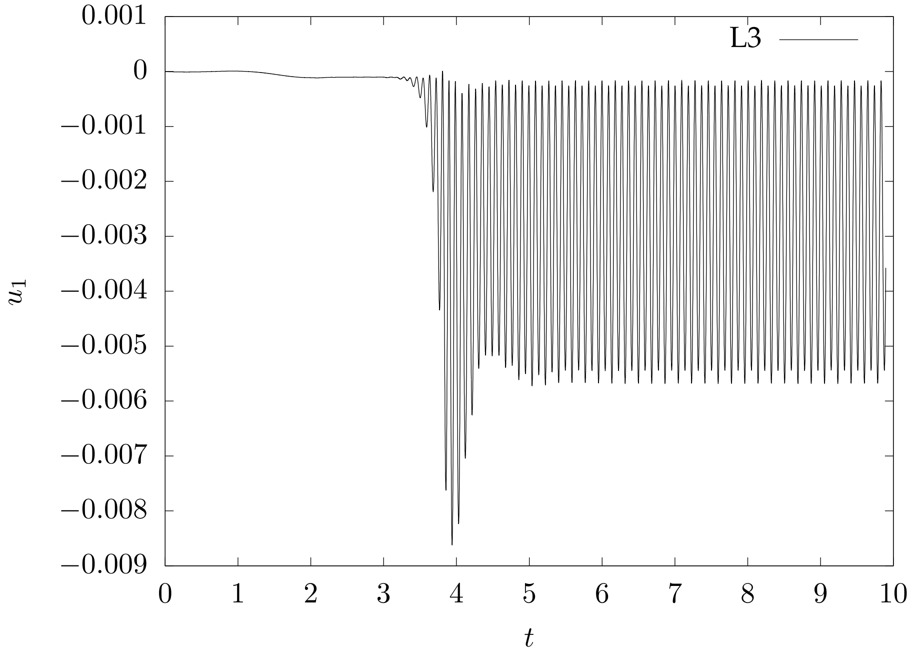

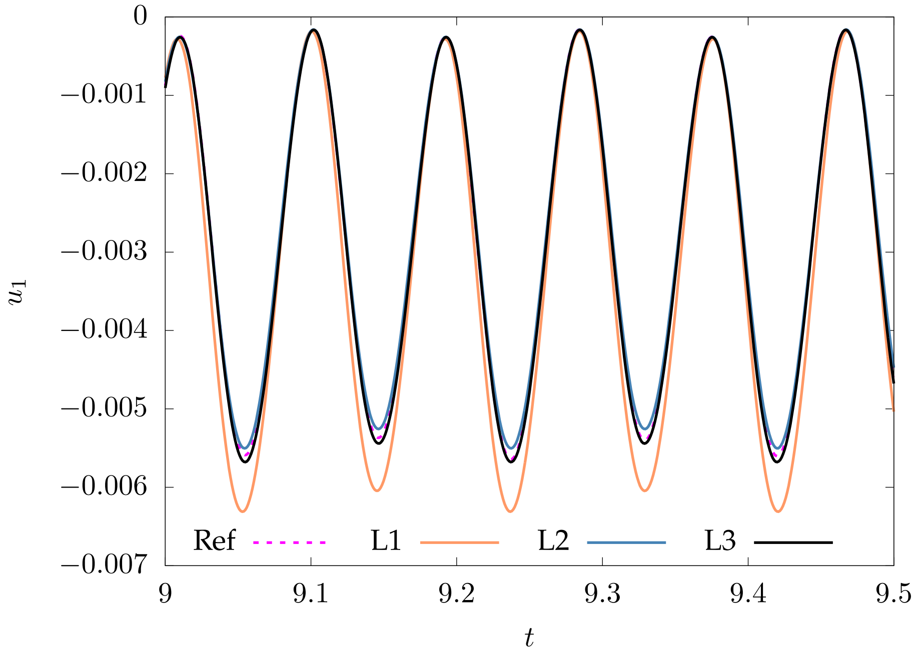

Figure 5.28: FSI 3, Displacement x (u_1), $\Delta t = 0.001$, $\theta = 0.5 + \Delta t$. Top: Stable temporal evolution of the x-displacement profile until the end of the simulation time. Bottom: Magnified view of the x-displacement profiles of three consecutive mesh refinement levels.

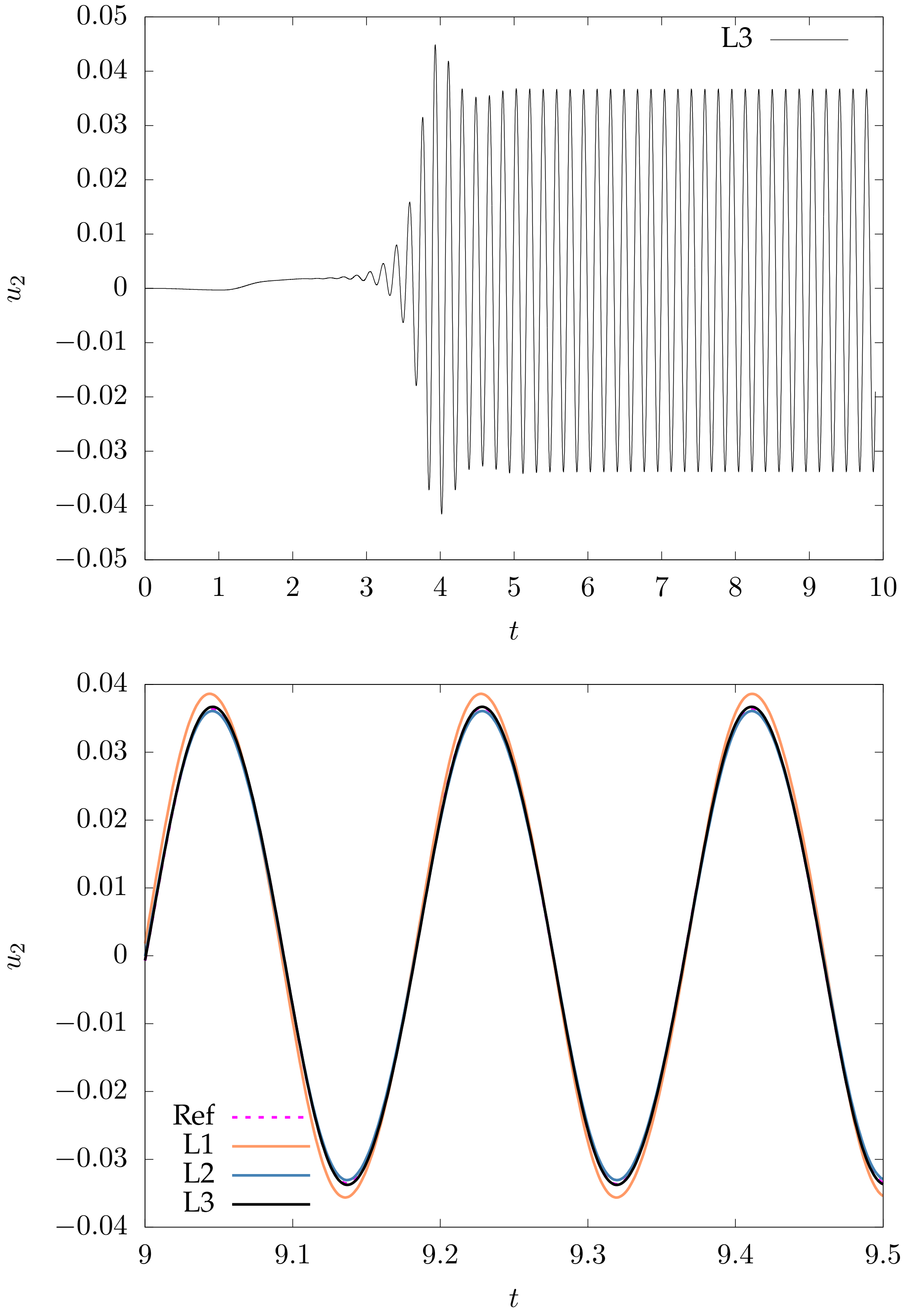

Figure 5.29: FSI 3, Displacement y (u_2), $\Delta t = 0.001$, $\theta = 0.5 + \Delta t$. Top: Stable temporal evolution of the y-displacement profile until the end of the simulation time. Bottom: Magnified view of the y-displacement profiles of three consecutive mesh refinement levels.

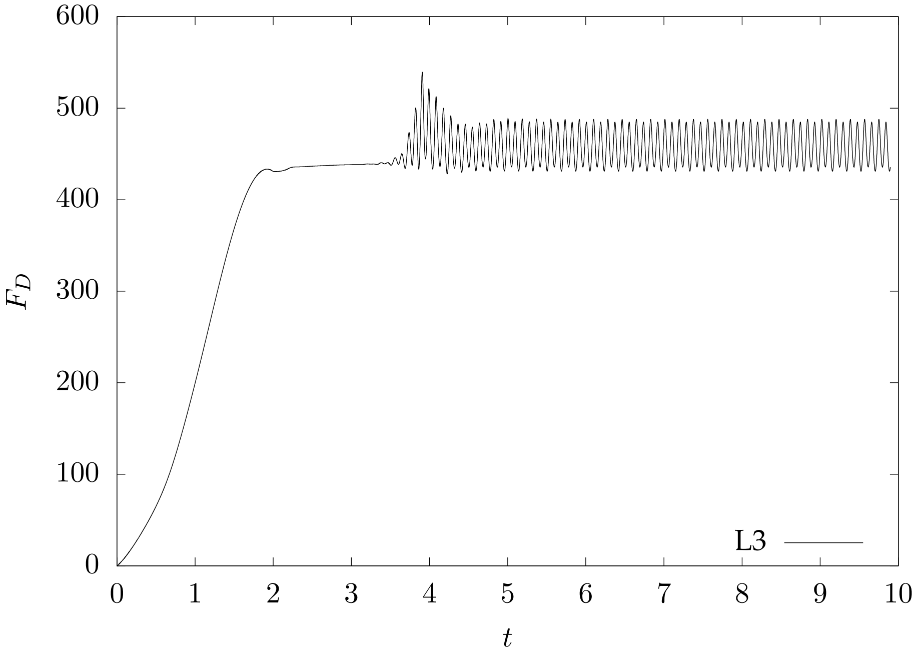

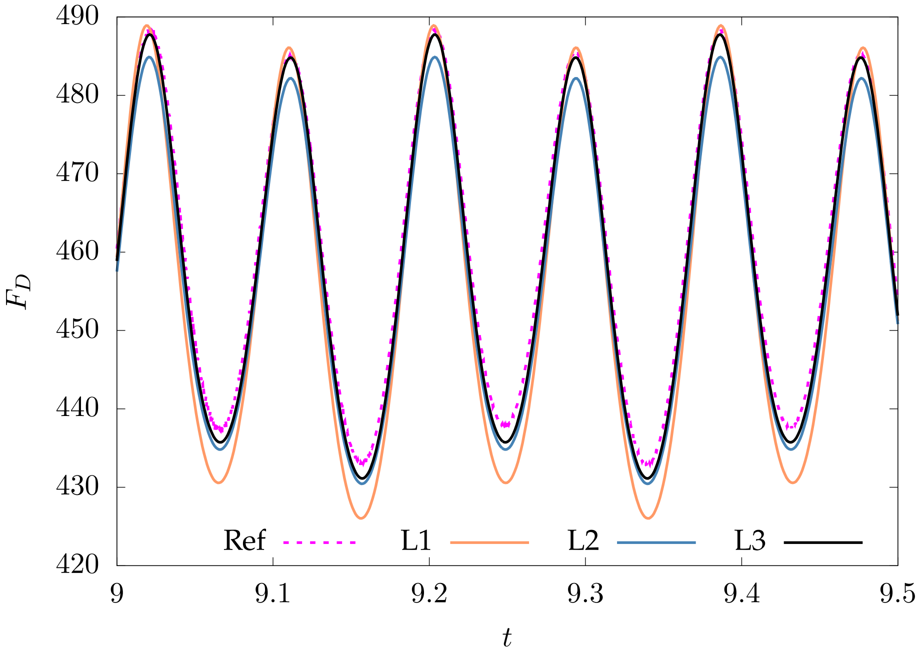

Figure 5.30: FSI 3, Drag force (F_D), $\Delta t = 0.001$, $\theta = 0.5 + \Delta t$. Top: Stable temporal evolution of the drag force profile until the end of the simulation time. Bottom: Magnified view of the drag force profiles of three consecutive mesh refinement levels.

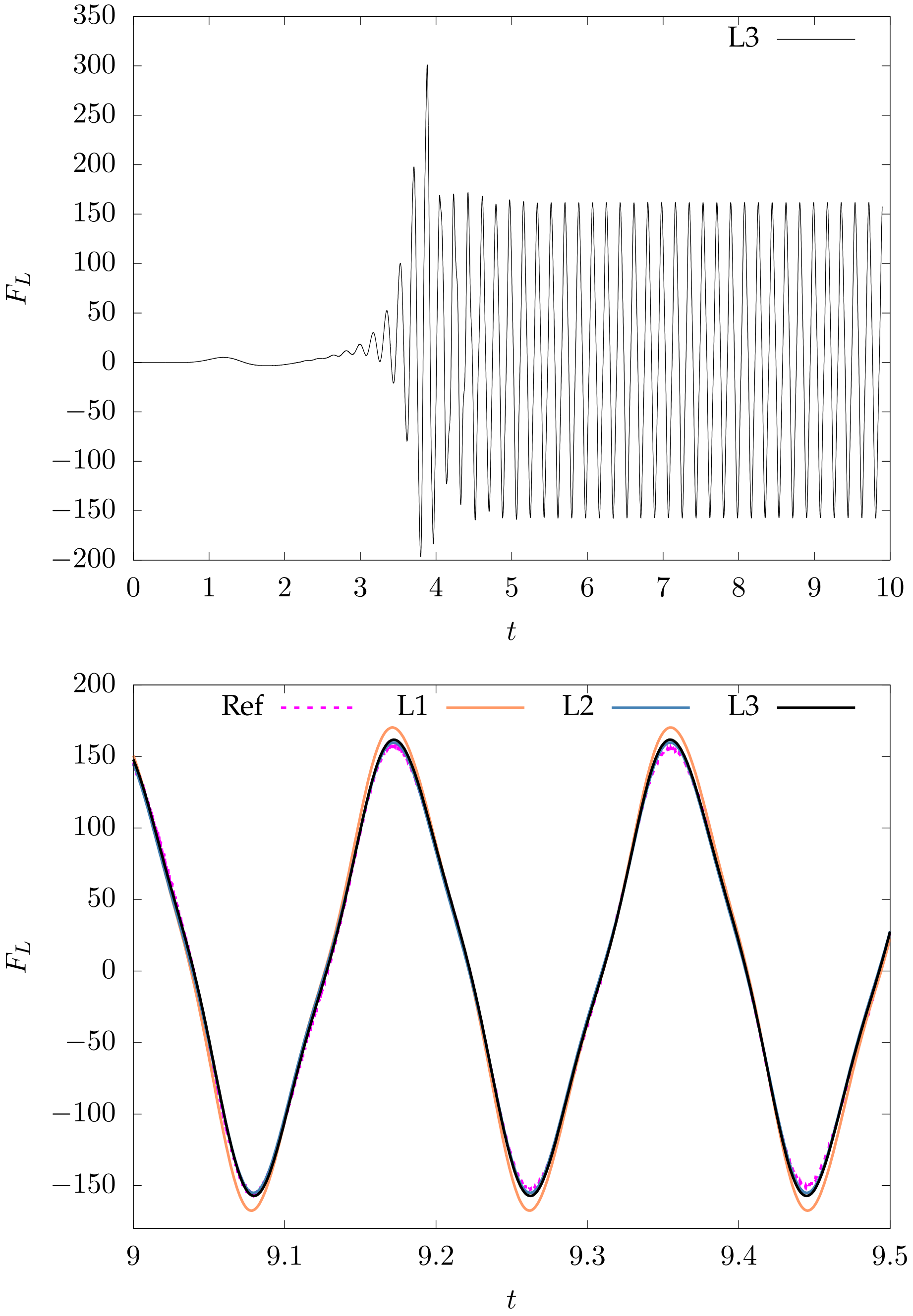

Figure 5.31: FSI 3, Lift force (F_D), $\Delta t = 0.001$, $\theta = 0.5 + \Delta t$. Top: Stable temporal evolution of the lift force profile until the end of the simulation time. Bottom: Magnified view of the lift force profiles of three consecutive mesh refinement levels.

The mesh deformation in the FSI 3 is less pronounced than that of FSI 2 due to the higher stiffness of elastic beam used. Therefore the mesh moving technique (Solving a nonlinear harmonic mesh motion PDE) that already performed fairly well in the FSI 2 case has been used here as well. We refer to Figures 5.34 and 5.35 for the illustration of the computed velocity and pressure fields in addition to the deflection of the elastic beam for some randomly selected instants of time.

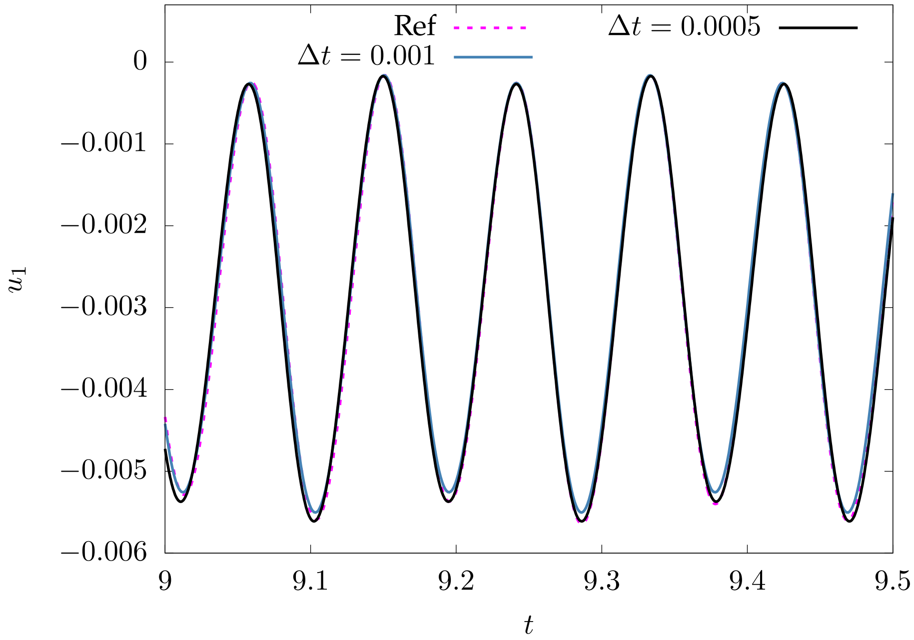

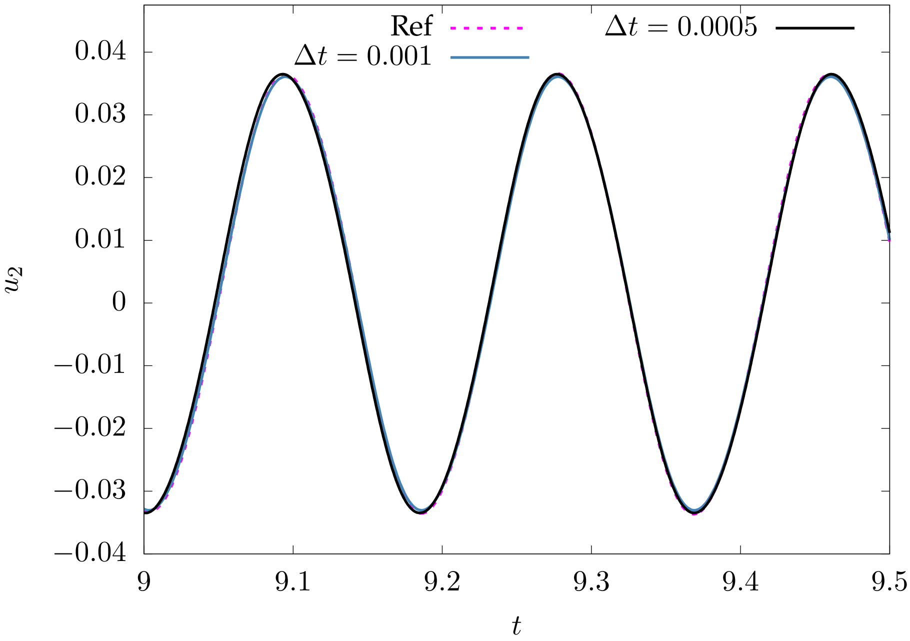

Figure 5.32: FSI 3, Displacement profiles obtained with time step sizes $\Delta t = 0.001$ and $\Delta t = 0.0005$ for mesh refinement level L2.

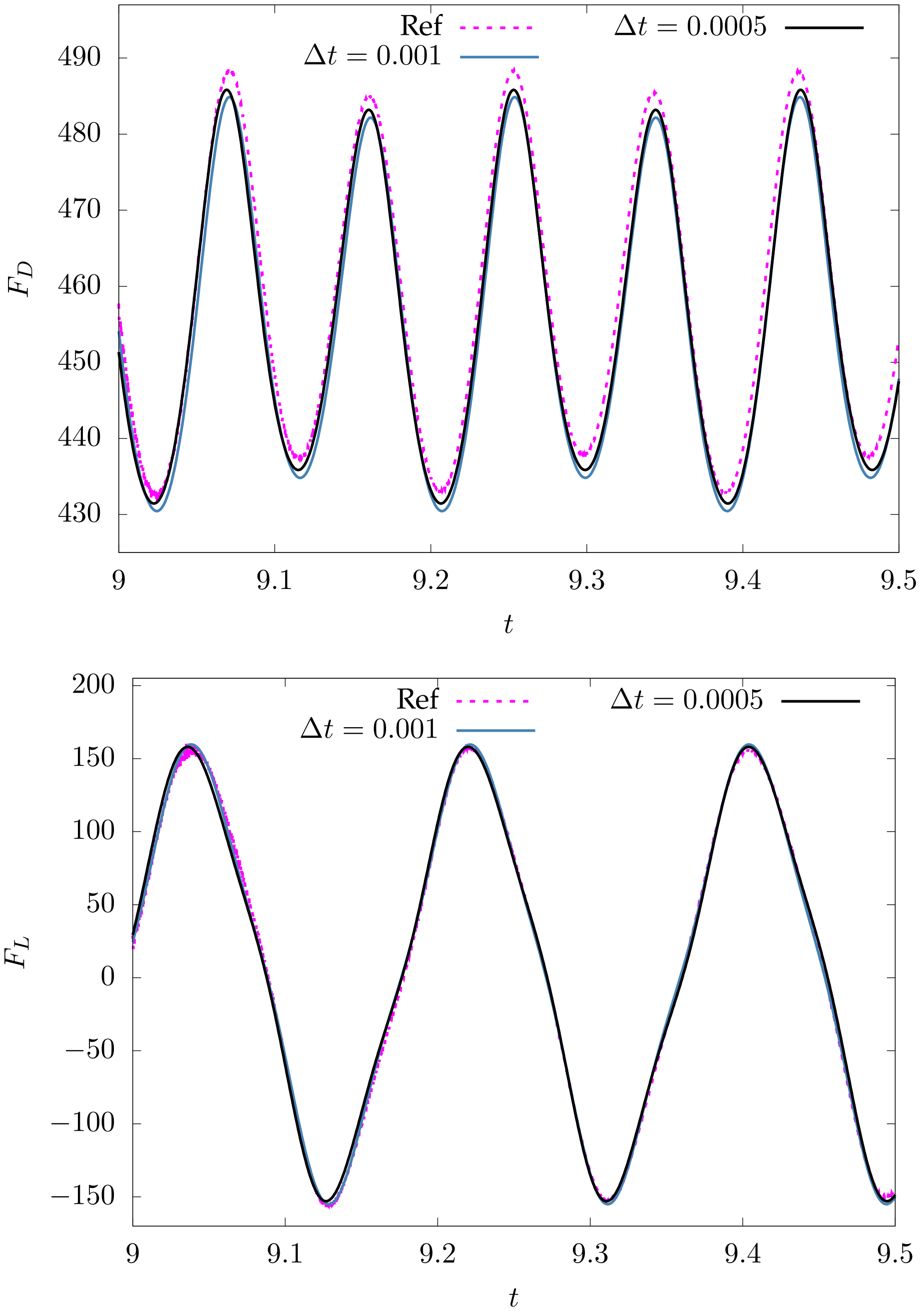

Figure 5.33: FSI 3, Drag and Lift profiles obtained with time step sizes $\Delta t = 0.001$ and $\Delta t = 0.0005$ for mesh refinement level L2.

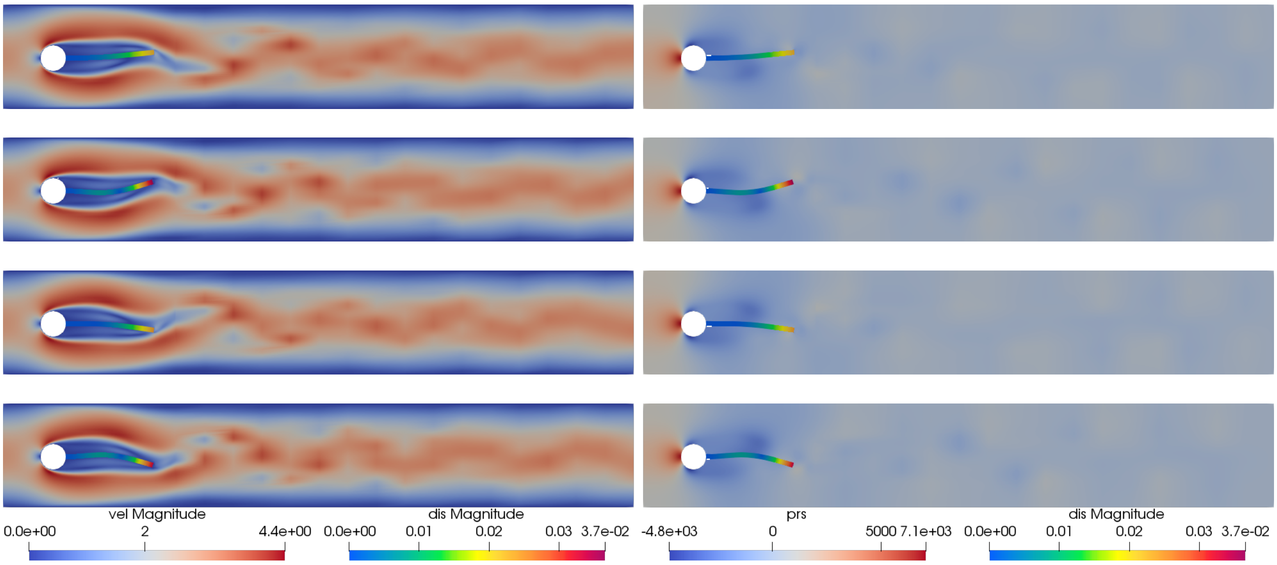

Figure 5.34: FSI 3: Illustration of the displacement of the elastic beam alongside the velocity (left) and pressure fields (right) of the flow in the entire flow channel. Times shown are at 9.02, 9.052, 9.116, and 9.141 s.

The conclusion we draw for the FSI 3 case is that our results fit quite well in the row of data provided by other sources. In particular, our results for mesh refinement levels L2 and L3 show little fluctuations and resemble most the data provided by Turek and Hron. Comparing the temporal evolution curves of our quantities of interest at different refinement levels, we observe a certain phase shift, while the amplitude and frequency seem to be less exposed to changes. This observation applies to the FSI 2 case as well. The data visualization and comparison method we have used in Figure 5.26 and Figure 5.27 discloses to some extent the difficulty of the FSI computations. In fact, considering the data provided by all sources including the present work, a certain fluctuation in the data of u_1 and F_D is simply undeniable. In this light, we consider our results to be of high quality since they are in very good agreement with the “reference” provided by Turek and Hron.

5.4 Summary and conclusions

In this chapter we have presented and discussed the next building block in the context of the complex multiphysics problem we aim to solve in this work. This building block consists of the fluid-structure interaction problem which as the name already suggests, consists of a fluid mechanics and a structural mechanics problem. Since we have devoted two chapters (3, 4) to single, and two-phase flows, we have put our focus in this chapter to the structural mechanics problem and the interaction of fluids with solids. To this end we found it necessary to begin with a digest of the theoretical background of the structural mechanics problem. We presented next a selection of problem formulations for elastostatics and elastodynamics that are relevant for the bigger FSI problem. For the variational problems addressed, we showed how to efficiently treat their inherent nonlinearities with Newton’s method. The structural mechanics part was rounded with the presentation of numerical results obtained with Isogeometric Analysis. The results presented, validated the correctness of our approach and let us proceed to the encompassing FSI problem of whom the

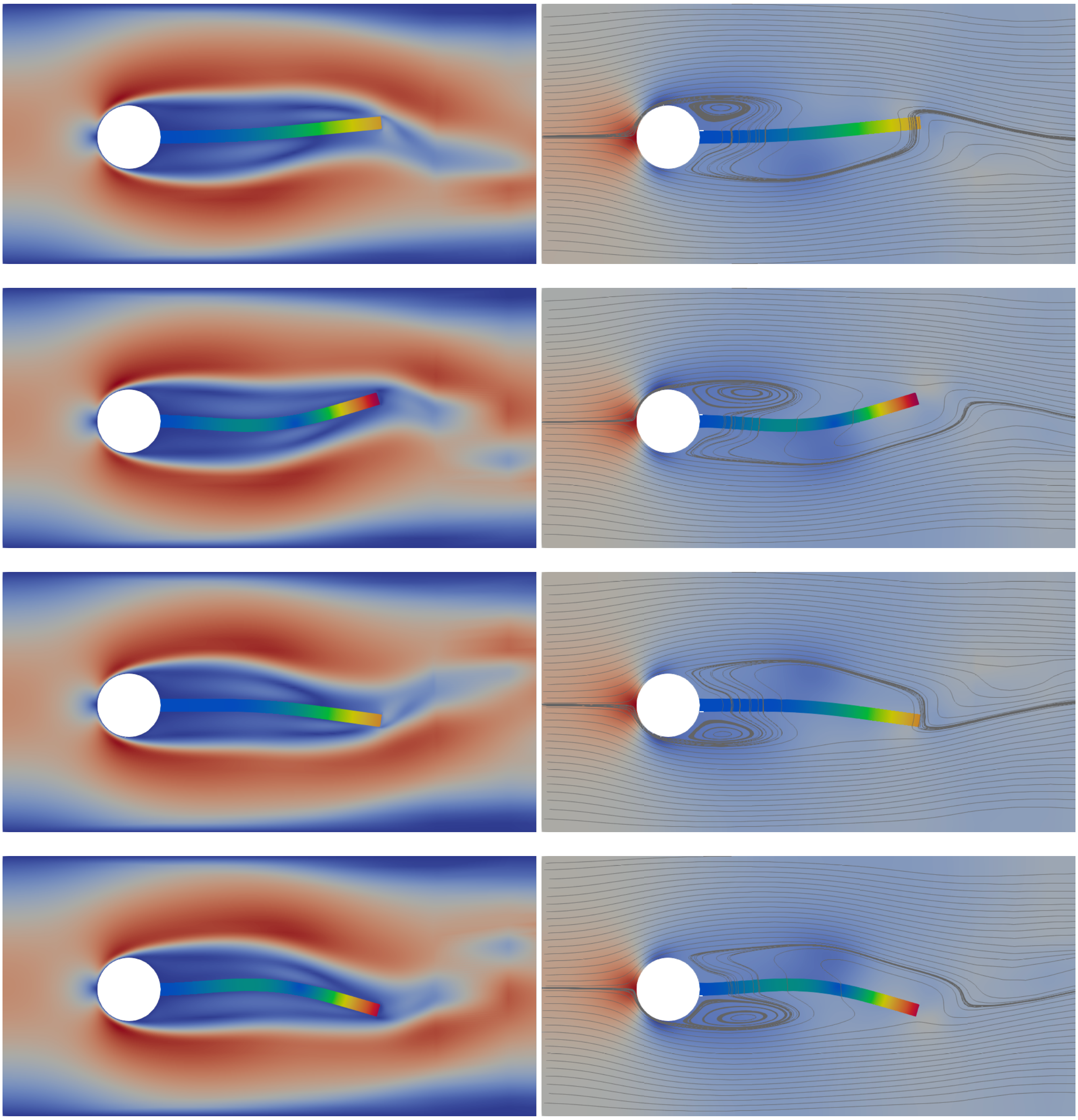

Figure 5.35: FSI 3: Magnified view of the displacement of the elastic beam alongside the velocity (left) and pressure fields (right) of the flow. The pressure field is overlayed with velocity streamlines. Times shown are at 9.02, 9.052, 9.116, and 9.141 s.

structural mechanics problem was only a constituent part.

Next, we briefly discussed the FSI problem and the aspects that render it difficult and delicate. This includes the dilemma that the fluid model is naturally based on an Eulerian perspective while it is very natural to express the solid problem in Lagrangian formulation. In order to naturally address this problem and not having to bother with the *added mass effect*, we opted for a monolithic approach based on an ALE formulation, literally requiring to pull back the fluid equations to a frame of reference that is compatible with the structural mechanics problem. This, however, couples the unknown velocity and pressure variables of the fluid problem to the unknown displacement variable of the solid problem, and therefore renders almost all terms in the Navier-Stokes problem nonlinear. This dramatically aggravates its nonlinearity and requires efficient means to address this and the remaining structural mechanics and mesh regularization problems which are all solved at once, that is in a monolithic manner. We showed how to efficiently treat the nonlinearities in the coupled FSI problem using Newton's method and used the FSI benchmark proposed by Turek and Hron for validation purposes. The numerical results that were obtained using Isogeometric Analysis were shown to be of high quality and to be in very good agreement with the reference(s).

The results and experiences gained from this benchmark setting provided invaluable experience and data that will be used for both the tackling of further problems as well as the development of a large scale 3D simulation model.

Chapter 6

ALE Binary-Fluid-Structure Interaction

6.1 Introduction

In Chapters 4 and 5 we have successfully applied Isogeometric Analysis to solve incompressible two-phase flow problems (with the Cahn-Hilliard phase field model) and fluid-structure interaction problems. In this final chapter integrating all previous results, we extend once again the multiphysics nature of this work and combine Cahn-Hilliard phase field based incompressible two-phase flow with fluid-structure interaction. This means nothing less than considering the highly complex interaction of two immiscible and incompressible fluids with both, each other, and an elastic solid.

Starting off with the former, the notion two-phase flow refers to the simultaneous flow of two materials with different thermodynamic phases (e.g. gas, liquid, etc.), or materials with different chemical properties in the same phase, such as oil and water. In two-phase flows, being the most common multiphase flow configuration involving two distinct fluids, the fluids are segregated by a very thin interfacial region (fluid-fluid interface) where surface tension effects and mass transfer (due to chemical reactions) may appear. Closely related to this and emerging later in the text is the term *capillarity* standing for the study of interfaces segregating two immiscible liquids, or the interfaces between liquids and gases. The interfaces under consideration are free to deform – they may for instance change their shape in order to minimize their surface energy. The two-phase flow models and scenarios considered in Chapter 4 and in this chapter are restricted to the case of two immiscible and incompressible liquids with distinct densities and viscosities which we refer to as "binary fluids". The (fluid-fluid) surface tension in binary fluids is associated with the surface energy of the fluid-fluid interface.

While multiphase and multicomponent flow[50] problems and classical (single fluid) fluid-structure interaction problems have seen a vast amount of research, the complex mechanical interaction of multiple fluids with deformable solids has essentially remained unexplored until recently [28, 86, 121, 151, 152]. The latter mentioned falls under the umbrella of the fascinating phenomenon of *Elasto-capillarity*, where capillary forces at the fluid-fluid interface may deform elastic solids. When it comes to the interaction of a binary fluid with a deformable solid, one needs to additionally take into account the fluid-solid surface energy that is distinct for the two components of the binary fluid and therefore yields two distinct fluid-solid surface tensions[51]. The consideration of forces

---

[50] Flow of different chemical species that are mixed at the molecular level and generally share the same velocity and temperature. The chemical species involved may interact through chemical reactions giving rise to multicomponent reactive flows.

[51] In solids, the surface energy and surface stress are related by the Shuttleworth relation [141].

in association with both the fluid-fluid interface and the fluid-solid interface gives rise to *wetting* phenomena [41, 42, 91, 134, 165] which we concisely recapitulate in Section 6.2.

In terms of mechanics, we observe in Elasto-capillarity phenomena a competition between bulk's elastic strain energy and the energy of the surfaces/interfaces. At small scales, that is mm to nm scale, the interaction of multiple fluids and a solid tends to become increasingly dominated by capillary forces as the length L of a structure keeps decreasing. With reference to scaling laws, capillary forces are proportional to L, whereas elastic forces or pressure forces (e.g. wind drag) are proportional to L^2, and volume forces scale proportionally to L^3 [126]. Therefore, downscaling a given structure implies a much faster decay of pressure and body forces in comparison to capillary forces, rendering the latter dominant after a certain size threshold. Elasto-capillarity related phenomena are ubiquitous in nature as well as high-tech (micro-/nanodevice manufacturing) industry. Examples for capillary interactions include the cohesion of sandcastles, the bending of slender structures that induces the bundling of fiber arrays (e.g. assembly of wet hair into bundles), and thin sheets that may partially wrap liquid droplets (e.g. capillary origami). Another example with biophysical background is the complete or partial collapse of pulmonary alveoli due to capillary forces with possibly fatal consequences. Elasto-capillarity is also of high relevance in high-tech micro and nano technologies. In fact, small scale devices such as e.g. microelectromechanical systems exhibit slender internal structures that are often created by wet lithography. This process involves selectively etching a layer of photosensitive resin into a given micostructure and rinsing the removed material in a solvent. During the drying process, capillary bridges may attract, deform or break slender flexible parts leading to severe damage ("stiction" phenomenon in design of micostructures) [126].

The motivation for the work presented in this chapter was to develop a computational model and simulation technique capable of capturing the physics behind the intriguing phenomena of Elasto-capillarity. A sophisticated enough numerical method may provide useful insights in its complex dynamics and eventually leverage better designs of submillimetric technology.

The structure of this chapter is as follows. Section 6.2 is devoted to the provision of a concise survey of the wetting of rigid and soft solids. We present our mathematical model for binary-fluid-structure interaction in Section 6.3 and discuss its variational formulation including aspects of its discretization in Section 6.4. Section 6.5 eventually presents the numerical results obtained from the application of our model to binary-fluid-structure interaction problems.

6.2 Wetting of rigid and soft solids in a nutshell

This section is dedicated to a very brief and therefore incomprehensive overview over the fascinating *wetting* phenomena of rigid and soft solids. We considered it necessary to present at least a concise summary of the main aspects of the wetting process in order to facilitate reading this chapter and putting the presented results into perspective. Besides, this recap is limited to those aspects of wetting that are relevant for the problems considered in the present chapter.

The notion *wetting* refers to the study of the behavior (spreading) of a liquid that is in contact with the surface of a solid (or another liquid). The wetting "degree", or to put it differently, the amount of wetting a surface experiences through the contact with a liquid, depends on the fluid(s) involved, and on the material (e.g. glass, plastic,..) making up the solid surface together with its properties such as roughness. To give an example, a drop of water placed on a very clean glass shows a significantly larger degree of spreading than the same drop of water on plastic. On the other hand, taking the same solid (e.g. glass), there is a difference between the spreading of water and mercury drops.

Figure 6.1 exemplarily shows the wetting behavior of three different sessile droplets on a rigid and flat interface. The wetting is shown to increase with a decrease of the contact angle θ. The spread of the liquid droplet across the surface is driven by adhesive[52] forces between the liquid and the solid. The opposite of this, that is, the contraction of the droplet towards a ball shape is driven by cohesive[53] forces within the liquid. Given a configuration where the latter mentioned forces start to dominate, the droplet will in a sense try to minimize its contact with the surface accordingly. Hence, a balance between adhesive and cohesive forces determines wettability, that is, the degree of wetting a (solid) surface experiences by the presence of an adjacent liquid. Considering the case of a liquid droplet (Phase 1) which is embedded in an ambient fluid (Phase 3) and is in touch with a flat rigid solid (Phase 2), as depicted in Figure 6.1, the value of the equilibrium contact angle θ_E is given by the Young-Dupré equation

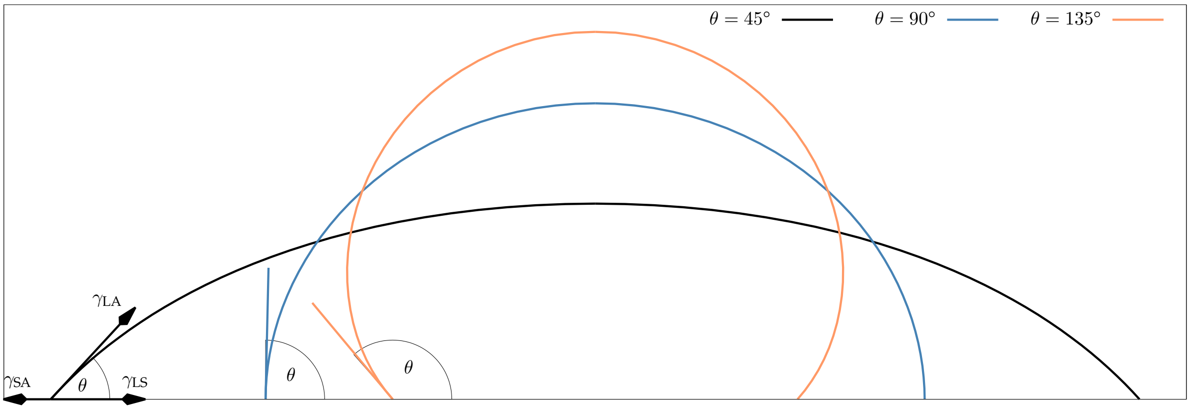

Figure 6.1: Exemplary sketch of the unequal wetting behavior of three sessile droplets with differing properties: The droplet with the smallest contact angle $\theta = 45°$ shows the highest wetting.

$$\gamma_{SA} = \gamma_{LS} + \cos\theta_E\,\gamma_{LA}, \tag{6.1}$$

encoding the balance of horizontal forces. In equation (6.1) the coefficients $\gamma_{LA}, \gamma_{LS}, \gamma_{SA} \in \mathbb{R}$ denote the interfacial tensions (stresses) of the fluid-fluid (a.k.a. liquid-ambient fluid interface), the liquid-solid, and the solid-ambient fluid interfaces, respectively. We may alternatively refer to these coefficients through subscript indices reflecting the involved phases and therefore set: $\gamma_{LA} \equiv \gamma_{13}, \gamma_{LS} \equiv \gamma_{12}$, and $\gamma_{SA} \equiv \gamma_{23}$. These tensions are visualized in Figure 6.1 for one of the droplets and can be thought of to pull along the respective interfaces. Given a non-zero vector sum of these tensions and excluding chemical and topographical inhomogeneities, the contact angle θ will adjust so as to satisfy Young's equilibrium equation (6.1). This affects the droplet's spread and therefore the contact line position.

The static wetting law given by the Young-Dupré equation requires a rigid and flat interface, however, solid interfaces exhibit a broad range of rigidity. For instance, larger amounts of energy are required to deform/break solid materials such as metals, glasses and ceramic, than soft biological tissues or soft gels. Since very soft solids may significantly deform in response to the forces exerted by the adjacent fluids, the question arises whether Young-Dupré law is a valid model in case of the

---

[52] Adhesive forces: Forces of attraction acting between molecules of different types.

[53] Cohesive forces: Forces of attraction acting between molecules of the same type.

involvement of very soft substrates. This is motivated by the observation that equation (6.1) must have been modeled with respect to the assumption of an infinitely rigid solid, and therefore involves only the balance of the tangential force on the contact line, ignoring the normal component.

At this point we recall a second classical law for static wetting involving three immiscible liquids – the Neumann's law. For its description we consider a liquid drop (Phase 1) floating on a bath of another liquid (Phase 2) and being otherwise surrounded by a third liquid (Phase 3). This configuration – illustrated in Figure 6.2 – yields a three phase contact line and for equilibrium the net force per unit length acting along this three phase boundary line is required to be zero, that is,

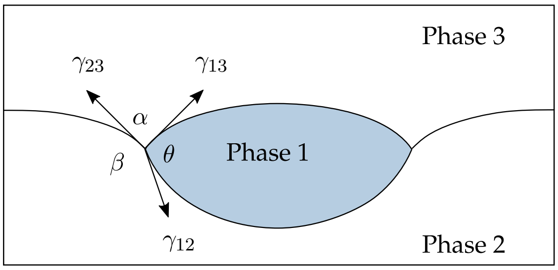

Figure 6.2: Exemplary sketch of the static equilibrium of three fluid phases in mutual contact. α, β, θ denote the angles between the indicated phase interfaces at the contact line.

$$\gamma_{12}\,\boldsymbol{t}_{12} + \gamma_{13}\,\boldsymbol{t}_{13} + \gamma_{23}\,\boldsymbol{t}_{23} = \mathbf{0}. \tag{6.2}$$

In the above equation, known as Neumann's equation, $\boldsymbol{t}_{ij}$ denotes the unit vector tangent to the $i - j$ interface at the contact line, and the angles $\alpha, \beta,$ and θ between the interfaces at the contact line are given by the orientation of these vectors. The complete (vector) force balance of Neumann's equation contrasts with Young-Dupré's equation which as stated above is based on the implicit assumption of a flat and rigid surface and therefore ignores force components normal to the surface. Note that setting the angle $\beta = \pi$, leaves only one angle (θ) to be determined as $\alpha = \pi - \theta$, and in fact it can be shown that equation (6.1) is obtained from a reduction of equation (6.2) to the case of planar geometry. This renders the validity of the Young-Dupré law questionable for the case of very soft and therefore easy to deform solid materials. For further discussions on the validity of Young-Dupré's law for the wetting of soft substrates, we refer the reader to [101, 107, 127, 158, 159].

After the recapitulation of static wetting laws of Young-Dupré and Neumann, we proceed with the presentation of the expected wetting behavior of soft solids. Given a droplet deposited on a sufficiently soft solid as sketched in Figure 6.3, the surface tension of the droplet deforms the solid at the three-phase contact line [92, 103, 107, 115, 141, 154]. At the contact line, the solid develops a cusp like feature – often denoted as the *wetting ridge* – whose shape is determined by the balance of interfacial tensions. More specifically, at the contact line, the liquid-ambient fluid surface tension force has a component normal to the solid surface. This force is concentrated to the neighborhood of the contact line (typically within the molecular width of the contact line) and exerts a highly localized pull on the solid eventually leading to the above described cusp like elevation. Besides, the excess Laplace pressure in the interior of the droplet leads to a dimple in the soft substrate section wetted by the droplet. The overall deformation in the elastic solid is the result of the competition between surface forces and bulk elastic stresses. In accordance with [141], at the contact line, capillarity dominates bulk elasticity for feature sizes $\ll O(\gamma_{LS}, \gamma_{SA})$ and therefore contributes the most to the shape of the wetting ridge. This, however, does not rule out elastic behavior at the contact

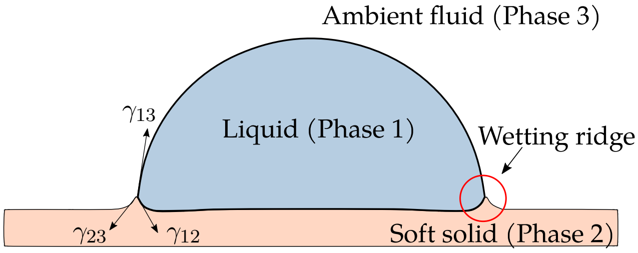

Figure 6.3: Exemplary sketch of a liquid droplet deposited on a soft substrate. Near the three phase contact line, the surface tension of the droplet is shown to deform the soft substrate – leading to a wetting ridge.

line and the solid remains elastic. The above described competition of forces is formalized through the elastocapillary length scale

$$L_{EC} = \gamma_{LA}/E \tag{6.3}$$

of an elastic material expressed as the ratio between the liquid-ambient fluid surface tension γ_{LA} and the Young's modulus[54] E. This quantity is immeasurably small for typical liquid surface tensions (e.g. water-air interface: $72.75\,\mathrm{mN\,m^{-1}}$) on most solids. To give an example, for a water droplet on glass, L_{EC} is below the nanometer scale and therefore practically irrelevant. However, for a sufficiently small droplet and a sufficiently compliant solid (e.g. biological tissue, gels, etc.) the elastocapillary length scale may become comparable to the droplet radius.

For a comprehensive experimental study on the wetting behavior of tiny droplets on soft substrates, we refer to [141] and summarize in the sequel some of its most significant statements: In regimes where the droplet radius shrinks so as to become comparable to the elastocapillary length scale, Young's law is reported to be violated as the macroscopic contact angle θ turns out to exhibit a dependence on the droplet radius R. More specifically, the angle θ – measured between the liquid-ambient fluid interface and the undeformed substrate – is shown to decrease for shrinking droplet radii R. Besides, while the wetting behavior of droplets with radius $R \gg O(\gamma_{LA}/E)$ is properly described by Young's law, Neumann's law is proposed as a more appropriate model for the case $R \ll O(\gamma_{LA}/E)$ and yields a smaller value for the contact angle θ. As of approaching the elastocapillary length γ_{LA}/E, there is a smooth transition between the contact angles predicted by these two models.

6.3 Mathematical model for Binary-Fluid-Structure Interaction

In this work we deal with the interaction of incompressible newtonian binary-fluids (composed of two constituents) and compressible hyperelastic solids. We consider a continuum body that is composed of a solid part $\mathcal{S}$ and a binary-fluid part $\mathcal{F} = \bigcup_{i=1}^{2} \mathcal{F}^i$, where i represents the i-th constituent of the binary-fluid.

The current domain[55] $\Omega_{\boldsymbol{x}}$ of the joint body correspondingly admits the decomposition

$$\Omega_{\boldsymbol{x}} = \Omega_{\boldsymbol{x}}^{\mathcal{F}} \cup \Omega_{\boldsymbol{x}}^{\mathcal{S}}, \qquad \Omega_{\boldsymbol{x}}^{\mathcal{F}} \cap \Omega_{\boldsymbol{x}}^{\mathcal{S}} = \emptyset,$$

where $\Omega_{\boldsymbol{x}}^{\mathcal{S}}$ and $\Omega_{\boldsymbol{x}}^{\mathcal{F}}$ represent the subdomains occupied by the solid and the binary-fluid, respec-

---

[54] The Young's modulus was introduced on page 122

[55] The domain symbols $\Omega_{\boldsymbol{X}}, \Omega_{\mathbf{X}}, \Omega_{\boldsymbol{x}}$ were already introduced in section 2.1.

tively. The latter allows itself a partition into corresponding fluid constituent subdomains $\Omega_{\boldsymbol{x}}^{\mathcal{F}^i}$, that is,

$$\Omega_{\boldsymbol{x}}^{\mathcal{F}} = \Omega_{\boldsymbol{x}}^{\mathcal{F}^1} \cup \Omega_{\boldsymbol{x}}^{\mathcal{F}^2}, \quad \Omega_{\boldsymbol{x}}^{\mathcal{F}^1} \cap \Omega_{\boldsymbol{x}}^{\mathcal{F}^2} = \emptyset.$$

Moreover, we let the boundary $\Gamma_{\boldsymbol{x}} = \partial\Omega_{\boldsymbol{x}}$ be composed of the union of the four non-overlapping partitions

$$\Gamma_{\boldsymbol{x}} = \Gamma_{N,\boldsymbol{x}}^{\mathcal{F}} \cup \Gamma_{D,\boldsymbol{x}}^{\mathcal{F}} \cup \Gamma_{N,\boldsymbol{x}}^{\mathcal{S}} \cup \Gamma_{D,\boldsymbol{x}}^{\mathcal{S}},$$

where the subscripts N and D represent the Neumann and Dirichlet parts of the particular $(\mathcal{F}, \mathcal{S})$ domain boundaries, respectively. The fluid-solid interface – denoted in the current domain by $\Gamma_{\boldsymbol{x}}^{\mathcal{FS}}$ – is a joint boundary part of fluid and solid problem subdomains in the sense that the respective subdomains never detach from each other. Finally, we represent the fluid-fluid interface in the current domain with $\Gamma_{\boldsymbol{x}}^{\mathcal{FF}}$.

The binary-fluid-structure interaction (BFSI) model used in this work is a natural extension of the monolithic "unary"-fluid-structure interaction (FSI) model presented in Chapter 5. It inherits from our (standard) monolithic FSI model the characteristic of being a boundary-fitted approach with a sharp fluid-solid interface. The fluid-fluid transition region on the other hand is represented by a diffuse interface, given that we use a NSCH phase field-based two-phase incompressible flow model (cf. Chapter 4). The model can therefore be seen to be of hybrid nature, combining a sharp interface and a phase field diffuse interface method for the treatment of the individual problems.

Binary-fluid-structure interaction requires the following problems to be solved:

(i) "Phase problem" on a moving domain.
This step requires the solution of a PDE which governs the creation, movement and decomposition of fluid-fluid interfaces and provides for every position in the computational domain information on the local fluid composition (concentration of each fluid constituent).

(ii) Two-phase flow problem on a moving domain.
This step requires the solution of the Navier-Stokes equations with phase dependent density and viscosity, and additionally equipped with a surface tension stress or force term.

(iii) Solid deformation problem.
This step requires the solution of the equations of Hyperelasticity.

(iv) Mesh motion problem.
Since the fluid domain is attached to the moving solid domain, it becomes necessary to move the fluid mesh as well and reposition its internal nodes in order to minimize mesh cell distortion. This step typically requires the solution of an additional possibly nonlinear PDE – for instance the partial differential equation of Elasticity, Nonlinear Laplace, or the Biharmonic problem.

Depending on the choice which of the above listed problems to solve at the same time and which ones in one or multiple successor steps, one may come up with a variety of different BFSI models, each with its own advantages and disadvantages w.r.t. different metrics. For instance, in [28, 151, 152] the two-phase flow problems (i) and (ii) are solved at the same time, while the solid deformation problem (iii) is solved separately. This corresponds evidently to a segregated or partitioned FSI approach. In biomechanical contexts such as in the case of blood flow inside an artery, it holds $\rho_f/\rho_s \approx 1$. Partitioned FSI techniques often face instabilities when the solid density ρ_s approaches the fluid density ρ_f (Added mass effect). Besides, for the convergence of a partitioned FSI problem, typically a few rounds of iteration are necessary, where in each round the respective problems are solved one at a time. In fact, the results in [151] indicate severe non-robustness of partitioned methods for elasto-capillary FSI.

These deficiencies are avoided by an implicit and monolithic solution approach that takes the full fluid-structure interaction problem as one coupled unity, without partitioning. When modeling the coupled dynamics of FSI, one is confronted with the dilemma that the fluid model is naturally based on an Eulerian perspective while it is very natural to express the solid problem in Lagrangian formulation. We take a monolithic approach which uses a fully coupled Arbitrary Lagrangian-Eulerian (ALE) variational formulation of the FSI problem (cf. [84]) and applies Galerkin-based Isogeometric Analysis for the discretization of the partial differential equations involved. This approach solves the difficulty of a common variational description and facilitates a consistent Galerkin discretization of the FSI problem.

However, the superiority of monolithic methods over segregated methods in terms of accuracy and robustness comes at a high price already in standard fluid-structure interaction, let alone binary-fluid-structure interaction. This is attributed to considering all involved field variables simultaneously in the computations. Since our BFSI model is a two-phase fluid extension of the monolithic FSI model described in Chapter 5, we inherit the property of having to rewrite the fluid equations w.r.t. a "structure appropriate" frame of reference. This alone yields a coupling between the displacement ($\boldsymbol{u}$), velocity ($\boldsymbol{v}$), and pressure (p) fields and renders almost all terms in the monolithic FSI problem (5.135) nonlinear. The simultaneous consideration of a large number of (nonlinearly combined) field variables takes its toll on the derivation of the Fréchet derivative (Jacobian) of the problem and on the bandwidth of the matrices obtained from the discretized partial differential equations involved. Given that solving the Navier-Stokes-Cahn-Hilliard equations in a partitioned or monolithic manner did not make any difference for us in terms of robustness and stability, we opted for the following approach:

```
while $t < T$ do
    1. Solve the Cahn-Hilliard phase field problem.
    2. Solve the
        • two-phase flow,
        • solid deformation, and
        • mesh motion
       problems monolithically.
end
```

Algorithm 1: BFSI solution approach

This relieves from the necessity and burden of having to consider the phase (φ) and chemical potential (η) fields as additional unknowns when solving for the fluid-structure interaction problem, since they are already available and therefore considered constant. The explicit treatment of the phase field variables weakens to a certain degree the actually monolithic nature of this approach and makes us consider it "quasi monolithic".

In the sequel we will elaborate on the details of Algorithm 1.
The Navier-Stokes-Cahn-Hilliard equations variant that we need to solve for BFSI is a slight modification of equation (4.31) and incorporates the surface tension stress term $-\hat{\sigma}\varepsilon \nabla \cdot (\nabla\varphi \otimes \nabla\varphi)$ instead of the surface tension force term $\eta\nabla\varphi$. While the latter variant was just fine for pure two-

phase flow computations, the NSCH variant using the surface tension stress term is necessary in BFSI, for it is responsible for a low pressure regime inside the fluid-fluid interface (cf. Figure 6.5) that turns out to play a significant role in elastocapillarity. In fact, it is this low pressure region at the three-phase interface that exerts a traction on the solid in a direction tangential to the fluid-fluid interface.

Without further ado, our NSCH variant of choice suitable for BFSI is obtained by the extension of the variable density and viscosity Navier-Stokes equations with a phase field-based surface tension stress term $-\nabla \cdot (-\hat{\sigma}\varepsilon\, \nabla\varphi \otimes \nabla\varphi)$, and a fluid induced transport term $\boldsymbol{v} \cdot \nabla\varphi$ in the Cahn-Hilliard equations. It reads:

$$\begin{aligned}
\rho(\varphi)\left(\frac{\partial \boldsymbol{v}}{\partial t} + (\boldsymbol{v}\cdot\nabla)\boldsymbol{v}\right) - \nabla\cdot\left(-p\boldsymbol{I} + \mu(\varphi)\left(\nabla\boldsymbol{v} + (\nabla\boldsymbol{v})^T\right)\right)& \\
-\nabla\cdot(-\hat{\sigma}\varepsilon\,\nabla\varphi\otimes\nabla\varphi) = \rho(\varphi)\boldsymbol{g} &\quad \text{in } \Omega_T, \qquad (6.4a)\\
\nabla\cdot\boldsymbol{v} = 0 &\quad \text{in } \Omega_T, \qquad (6.4b)\\
\frac{\partial\varphi}{\partial t} + \boldsymbol{v}\cdot\nabla\varphi - \nabla\cdot(m(\varphi)\nabla\eta) = 0 &\quad \text{in } \Omega_T, \qquad (6.4c)\\
\eta - \frac{d\psi(\varphi)}{d\varphi} + \varepsilon^2\,\nabla^2\varphi = 0 &\quad \text{in } \Omega_T, \qquad (6.4d)\\
\varphi(\boldsymbol{x},0) = \varphi_0(\boldsymbol{x}), \quad \boldsymbol{v}(\boldsymbol{x},0) = \boldsymbol{v}_0(\boldsymbol{x}) &\quad \text{in } \Omega, \qquad (6.4e)\\
\boldsymbol{v} = \boldsymbol{v}_D &\quad \text{on } (\partial\Omega_T)_D, \qquad (6.4f)\\
\nabla\varphi\cdot\boldsymbol{n} = \frac{1}{\epsilon\sqrt{2}}\cos(\theta)(1-\varphi^2), \quad \nabla\eta\cdot\boldsymbol{n} = 0 &\quad \text{on } (\partial\Omega_T)_N, \qquad (6.4g)\\
\boldsymbol{\sigma}\cdot\boldsymbol{n} = \boldsymbol{t} &\quad \text{on } (\partial\Omega_T)_N. \qquad (6.4h)
\end{aligned}$$

Above, $\Omega_T = \Omega \times (0,T)$, $(\partial\Omega)_D$ is the Dirichlet part of the domain boundary, $\boldsymbol{\sigma} = -p\boldsymbol{I} + \mu(\varphi)\left(\nabla\boldsymbol{v} + (\nabla\boldsymbol{v})^T\right) - \hat{\sigma}\varepsilon\,\nabla\varphi\otimes\nabla\varphi$ is the (extended) fluid Cauchy stress, $\boldsymbol{t}$ is the prescribed traction force on the Neumann boundary $(\partial\Omega)_N$, $\boldsymbol{g}$ is the gravitational force field and p is the pressure variable acting as a Lagrange multiplier in the course of enforcing the incompressibility condition. The parameter $\hat{\sigma}$ denotes a scaled surface tension and is related to the physical surface tension by the relation $\hat{\sigma} = \sigma\frac{3}{2\sqrt{2}}$.

With reference to the discrepancy caused by the respective frameworks (Lagrangian, Eulerian) in which the fluid and solid problems are naturally expressed (cf. Problems 5.3.1 and 5.3.2), we briefly recall our strategy to address this issue in our monolithic FSI model. It required to reformulate the fluid problem with respect to a "structure-appropriate" framework, that is, expressing it – in analogy to the solid deformation equations – in terms of the initial/undeformed reference domain. The result of this endeavor is equation system (5.135) which is however merely suitable for unary-fluid-structure interaction.

Our binary-fluid-structure interaction model additionally requires the corresponding reformulation of both the Cahn-Hilliard equations ((6.4c), (6.4d)), and surface tension stress or force terms that are expressed as a function of the phase field and chemical potential variables.

Combining the results obtained so far, the strong form of the monolithic BFSI problem in ALE formulation using the nonlinear harmonic mesh motion model, reads:

$$
\begin{aligned}
\hat{J}\left(\left.\frac{\partial\varphi}{\partial t}\right|_{\boldsymbol{\chi}} + \nabla_{\boldsymbol{\chi}}\varphi\left(\hat{\boldsymbol{F}}^{-1}(\boldsymbol{v}^{\mathcal{F}} - \partial_t\hat{\boldsymbol{\mathcal{A}}})\right) - \nabla_{\boldsymbol{\chi}}\cdot\left(\hat{J}\hat{\boldsymbol{F}}^{-1}m(\varphi)\nabla_{\boldsymbol{\chi}}\eta\right)\right) &= 0 && \text{in } \Omega^{\mathcal{F}}_{\boldsymbol{\chi}}\times(0,T),\\
\hat{J}\left(\eta - \frac{d\psi(\varphi)}{d\varphi} + \varepsilon^2\,\nabla_{\boldsymbol{\chi}}\cdot\left(\hat{J}\hat{\boldsymbol{F}}^{-1}\nabla_{\boldsymbol{\chi}}\varphi\right)\right) &= 0 && \text{in } \Omega^{\mathcal{F}}_{\boldsymbol{\chi}}\times(0,T),\\
\text{“contact angle b.c.”},\qquad \nabla_{\boldsymbol{\chi}}\eta\cdot\boldsymbol{n}_0 &= 0 && \text{on } \Gamma^{\mathcal{F}}_{N,\boldsymbol{\chi}}\times(0,T),\\
\hat{J}\rho^{\mathcal{F}}(\varphi)\left(\left.\frac{\partial\boldsymbol{v}^{\mathcal{F}}}{\partial t}\right|_{\boldsymbol{\chi}} + \nabla_{\boldsymbol{\chi}}\boldsymbol{v}^{\mathcal{F}}\left(\hat{\boldsymbol{F}}^{-1}(\boldsymbol{v}^{\mathcal{F}} - \partial_t\hat{\boldsymbol{\mathcal{A}}})\right)\right)&\\
-\nabla_{\boldsymbol{\chi}}\cdot\left(-\hat{\sigma}\varepsilon\,\hat{\boldsymbol{F}}^{-T}\nabla_{\boldsymbol{\chi}}\varphi\otimes\hat{\boldsymbol{F}}^{-T}\nabla_{\boldsymbol{\chi}}\varphi\right)&\\
-\nabla_{\boldsymbol{\chi}}\cdot\left(\hat{J}\left(-p^{\mathcal{F}}\boldsymbol{I} + \mu^{\mathcal{F}}(\varphi)\left(\nabla_{\boldsymbol{\chi}}\boldsymbol{v}^{\mathcal{F}}\hat{\boldsymbol{F}}^{-1} + \hat{\boldsymbol{F}}^{-T}(\nabla_{\boldsymbol{\chi}}\boldsymbol{v}^{\mathcal{F}})^T\right)\right)\hat{\boldsymbol{F}}^{-T}\right) &= \hat{J}\rho^{\mathcal{F}}(\varphi)\boldsymbol{b}^{\mathcal{F}} && \text{in } \Omega^{\mathcal{F}}_{\boldsymbol{\chi}}\times(0,T),\\
\nabla_{\boldsymbol{\chi}}\cdot\left(\hat{J}\hat{\boldsymbol{F}}^{-1}\boldsymbol{v}^{\mathcal{F}}\right) &= 0 && \text{in } \Omega^{\mathcal{F}}_{\boldsymbol{\chi}}\times[0,T),\\
\varphi(\cdot,0) = \mathring{\varphi}, p^{\mathcal{F}}(\cdot,0) = \mathring{p}^{\mathcal{F}}, \boldsymbol{u}^{\mathcal{F}}(\cdot,0) = \mathring{\boldsymbol{u}}^{\mathcal{F}}, \boldsymbol{v}^{\mathcal{F}}(\cdot,0) &= \mathring{\boldsymbol{v}}^{\mathcal{S}} && \text{in } \Omega^{\mathcal{F}}_{\boldsymbol{\chi}},\\
\boldsymbol{u}^{\mathcal{F}} = \boldsymbol{u}^{\mathcal{F}}_D, \boldsymbol{v}^{\mathcal{F}} &= \boldsymbol{v}^{\mathcal{F}}_D && \text{on } \Gamma^{\mathcal{F}}_{D,\boldsymbol{\chi}}\times(0,T),\\
\left(\hat{J}\boldsymbol{\sigma}^{\mathcal{F}}\hat{\boldsymbol{F}}^{-T}\right)\boldsymbol{n}^{\mathcal{F}}_0 &= \boldsymbol{g}^{\mathcal{F}}_0 && \text{on } \Gamma^{\mathcal{F}}_{N,\boldsymbol{\chi}}\times(0,T),\\
\hat{J}\rho^{\mathcal{S}}\left.\frac{\partial\boldsymbol{v}^{\mathcal{S}}}{\partial t}\right|_{\boldsymbol{\chi}} - \nabla_{\boldsymbol{\chi}}\cdot\hat{\boldsymbol{P}}^{\mathcal{S}} &= \hat{J}\rho^{\mathcal{S}}\boldsymbol{b}^{\mathcal{S}} && \text{in } \Omega^{\mathcal{S}}_{\boldsymbol{\chi}}\times(0,T),\\
\frac{\partial\boldsymbol{u}^{\mathcal{S}}}{\partial t} - \boldsymbol{v}^{\mathcal{S}} &= 0 && \text{in } \Omega^{\mathcal{S}}_{\boldsymbol{\chi}}\times(0,T),\\
\boldsymbol{u}^{\mathcal{S}}(\cdot,0) = \mathring{\boldsymbol{u}}^{\mathcal{S}}, \boldsymbol{v}^{\mathcal{S}}(\cdot,0) &= \mathring{\boldsymbol{v}}^{\mathcal{S}} && \text{in } \Omega^{\mathcal{S}}_{\boldsymbol{\chi}},\\
\boldsymbol{u}^{\mathcal{S}} = \boldsymbol{u}^{\mathcal{S}}_D, \boldsymbol{v}^{\mathcal{S}} &= \boldsymbol{v}^{\mathcal{S}}_D && \text{on } \Gamma^{\mathcal{S}}_{D,\boldsymbol{\chi}}\times(0,T),\\
\hat{\boldsymbol{P}}^{\mathcal{S}}\,\boldsymbol{n}^{\mathcal{S}}_0 &= \boldsymbol{g}^{\mathcal{S}}_0 && \text{on } \Gamma^{\mathcal{S}}_{N,\boldsymbol{\chi}}\times(0,T),\\
\nabla_{\boldsymbol{\chi}}\cdot\left(\alpha_u\hat{J}^{-1}\nabla_{\boldsymbol{\chi}}\boldsymbol{u}^{\mathcal{F}}\right) &= 0 && \text{in } \Omega^{\mathcal{F}}_{\boldsymbol{\chi}}\times(0,T),\\
\boldsymbol{u}^{\mathcal{F}} = \boldsymbol{u}^{\mathcal{S}}, \boldsymbol{v}^{\mathcal{F}} &= \boldsymbol{v}^{\mathcal{S}}, && \text{on } \Gamma^{\mathcal{I}}_{\boldsymbol{\chi}}\times(0,T).
\end{aligned}
\tag{6.5}
$$

Above, the first Piola-Kirchhoff stress tensor of the solid may be chosen with respect to different materials, such as e.g. the St. Venant-Kirchhoff

$$\hat{\boldsymbol{P}}^{\mathcal{S}} := \lambda\,\mathrm{tr}\left(\hat{\boldsymbol{E}}\right)\hat{\boldsymbol{F}} + 2\mu\hat{\boldsymbol{F}}\hat{\boldsymbol{E}}, \tag{6.6}$$

or the Neo-Hookean material

$$\hat{\boldsymbol{P}}^{\mathcal{S}} := \mu(\hat{\boldsymbol{F}} - \hat{\boldsymbol{F}}^{-T}) + \lambda\log(\det\hat{\boldsymbol{F}})\hat{\boldsymbol{F}}^{-T}. \tag{6.7}$$

Moreover, it is easily possible to modify equation (6.5) so as to work with an alternative mesh motion model.

Remark 6.3.1. *Note that the handling of the FSI coupling conditions (cf. Section 5.3.2) is inherited from our monolithic FSI model. Therefore, the continuity of normal stresses condition is expected to be automatically satisfied in a weak sense by the choice of matching test functions along the fluid-solid interface - analogously to the single fluid monolithic FSI case.*

A bona fide monolithic solution approach for the proposed BFSI model requires the simultaneous solution of the highly nonlinear multi-field problem (6.5). The fields to consider are the phase field φ, chemical potential η, displacement $\boldsymbol{u}$, velocity $\boldsymbol{v}$, and pressure p. This large number of problem variables and their combinations in various terms negatively affects the bandwidth of the system matrices obtained from the discretization process and may pose a problem in high resolution large scale 3D BFSI simulations. Additional difficulties with regard to the existence of unique solutions and stability - albeit already present in standard FSI (cf. Section 5.3.4) - arise from the different natures (parabolic, hyperbolic) of the partial differential equations involved. However, it is the aspect of nonlinearity that poses one of biggest computational challenges in our quasi monolithic BFSI model. We briefly recall its sources in the sequel: Starting off with the elasticity problem, we remind of using a model that is not limited to infinitesimal strains or "small" deformations. Accordingly, the stress-strain relation used is nonlinear and the model is expressed in terms of a strain measure which is nonlinear in displacement. We continue with the fluid flow problem whose governing equations (Navier-Stokes) were reformulated with respect to a frame of reference that is compatible with the structural mechanics problem. This formulation introduces additional geometric nonlinearities expressed in terms of the deformation gradient $\hat{\boldsymbol{F}}$ and its determinant $\hat{J}$. Both are functions of the displacement $\boldsymbol{u}$ which is an unknown in the FSI problem. The formulation couples the unknown velocity and pressure variables of the fluid problem to the unknown displacement variable of the solid problem, and therefore renders almost all terms in the Navier-Stokes problem nonlinear. In addition to these two problems, we solve a nonlinear mesh motion model that is expressed in terms of the unknown $\hat{J}$. Our BFSI model additionally requires the solution of the nonlinear Cahn-Hilliard phase field problem which we also reformulate with respect to a frame of reference that is compatible with the structural mechanics problem. Just as in the pulled back Navier-Stokes problem, this measure effectively couples the unknowns of the solid deformation problem to the unknowns of the phase field problem and aggravates its nonlinearity if the Cahn-Hilliard equations and the rest of the involved PDEs are solved simultaneously. The delicate point of departure we are facing requires efficient means to address the inherent nonlinearity of our BFSI model. The measures we take to address some of the above mentioned aspects are as follows: On the one hand we use Newton's method for algorithmically efficient treatment of the nonlinearity and on the other hand we solve the phase field problem separated from the rest (cf. Algorithm 1).

Remark 6.3.2. *Adopting the Cahn-Hilliard phase field model in our BFSI model, we are rewarded with the ability to impose a contact angle and therefore gain the ability to control wetting on a flat and rigid surface as showcased in Figure 4.19. This corresponds to the wetting law of Young-Dupré (cf. Equation (6.1)). With that being said, given a flat and hard enough surface, and a sufficiently large droplet (cf. Elastocapillary length scale), the contact angle boundary condition in Equation (4.20) is in fact very appealing as it merely requires an angle to be specified. In particular, it does not require the specification of the three surface tensions* γ_{LS}, γ_{LA}, *and* γ_{SA} *(cf. Figures 6.1) whose values might be difficult to determine. This flexibility, however, raises reasonable doubt concerning the unrestrained physical validity of this approach. For instance, one might ponder, in how far one is free to simply specify a certain contact angle without changing other material parameters of the involved fluids. After all, there is a reason why a certain combination of two fluids have a distinct surface tension.*

As far as alternatives, we presented in Section 6.2 an alternative wetting model involving three immiscible liquids (Neumann's law) and referred to research works that question the validity of the classical wetting law of Young-Dupré for very small droplet sizes. When it comes to the deformation of a compliant solid by a binary-fluid the wetting law of Young-Dupré might be considered as inappropriate as an initially flat fluid-solid interface might cease to stay flat. This violates in a strict sense the precondition of this law. Neumann's law may be conceived to appear as a more appropriate model in the case of the wetting of soft solids, however it requires the specification of three surface tensions that might wind up difficult to determine.

Despite its potential shortcomings, we incorporated - for the time being - the classical contact angle boundary condition as described by the wetting law of Young-Dupré. This part of our BFSI model is however treated as exchangeable and is likely to be replaced in future work. In order to emphasize this aspect we refrained from specifying the corresponding equation and deliberately used a "textual placeholder" in Equation (6.5) *and its descendants.*

6.4 Variational formulation

This section presents the variational formulation of our binary-fluid-structure interaction model, a discussion on the treatment of its nonlinearity, and details on the time and space discretizations of the corresponding equations, where Isogeometric Analysis is used for the latter.

We begin with the variational formulation of our BFSI problem for which it is necessary to define trial and test spaces in the (fixed referential) fluid and solid domains. At this point let it be briefly reminded that the structure deformation problem is solved in the solid domain, whereas the fluid flow, the phase field, and the mesh deformation problems are solved in the fluid domain. In analogy to the standard monolithic FSI problem we define – in the fluid domain – the displacement trial ($\boldsymbol{\mathcal{T}}^{\boldsymbol{u},\mathcal{F}}$) and test ($\boldsymbol{\mathcal{W}}^{\boldsymbol{u},\mathcal{F}}$) spaces as

$$\begin{aligned}\boldsymbol{\mathcal{T}}^{\boldsymbol{u},\mathcal{F}} &:= \{\boldsymbol{u}^{\mathcal{F}} \in \boldsymbol{\mathcal{H}}^1(\Omega^{\mathcal{F}}_{\boldsymbol{\chi}}) \,|\, \boldsymbol{u}^{\mathcal{F}} = \boldsymbol{u}^{\mathcal{S}} \text{ on } \Gamma^{\mathcal{I}}_{\chi}, \boldsymbol{u}^{\mathcal{F}} = \boldsymbol{u}^{\mathcal{F}}_D \text{ on } \Gamma^{\mathcal{F}}_{D,\boldsymbol{\chi}}\},\\ \boldsymbol{\mathcal{W}}^{\boldsymbol{u},\mathcal{F}} &:= \{\boldsymbol{\phi}^{\boldsymbol{u},\mathcal{F}} \in \boldsymbol{\mathcal{H}}^1_0(\Omega^{\mathcal{F}}_{\boldsymbol{\chi}}; \Gamma^{\mathcal{F}}_{D,\boldsymbol{\chi}}) \,|\, \boldsymbol{\phi}^{\boldsymbol{u},\mathcal{F}} = \boldsymbol{\phi}^{\boldsymbol{u},\mathcal{S}} \text{ on } \Gamma^{\mathcal{I}}_{\chi}\},\end{aligned} \tag{6.8}$$

and the velocity trial ($\boldsymbol{\mathcal{T}}^{\boldsymbol{v},\mathcal{F}}$) and test ($\boldsymbol{\mathcal{W}}^{\boldsymbol{v},\mathcal{F}}$) spaces as

$$\begin{aligned}\boldsymbol{\mathcal{T}}^{\boldsymbol{v},\mathcal{F}} &:= \{\boldsymbol{v}^{\mathcal{F}} \in \boldsymbol{\mathcal{H}}^1(\Omega^{\mathcal{F}}_{\boldsymbol{\chi}}) \,|\, \boldsymbol{v}^{\mathcal{F}} = \boldsymbol{v}^{\mathcal{S}} \text{ on } \Gamma^{\mathcal{I}}_{\chi}, \boldsymbol{v}^{\mathcal{F}} = \boldsymbol{v}^{\mathcal{F}}_D \text{ on } \Gamma^{\mathcal{F}}_{D,\boldsymbol{\chi}}\},\\ \boldsymbol{\mathcal{W}}^{\boldsymbol{v},\mathcal{F}} &:= \{\boldsymbol{\phi}^{\boldsymbol{v},\mathcal{F}} \in \boldsymbol{\mathcal{H}}^1_0(\Omega^{\mathcal{F}}_{\boldsymbol{\chi}}; \Gamma^{\mathcal{F}}_{D,\boldsymbol{\chi}}) \,|\, \boldsymbol{\phi}^{\boldsymbol{v},\mathcal{F}} = \boldsymbol{\phi}^{\boldsymbol{v},\mathcal{S}} \text{ on } \Gamma^{\mathcal{I}}_{\chi}\}.\end{aligned} \tag{6.9}$$

Furthermore, we let the pressure trial and test spaces in the fluid domain be defined as

$$\mathcal{L}^{\mathcal{F}} := \mathcal{L}^2(\Omega^{\mathcal{F}}_{\boldsymbol{\chi}})/\mathbb{R}, \tag{6.10}$$

and eventually set the search space for trial and test functions of the phase field problem to

$$\mathcal{Y}^{\mathcal{F}} := \mathcal{H}^1(\Omega^{\mathcal{F}}_{\boldsymbol{\chi}}). \tag{6.11}$$

Continuing with the specification of the approximation spaces in the solid domain, we let the displacement trial and test spaces in this domain be defined as

$$\boldsymbol{\mathcal{T}}^{\boldsymbol{u},\mathcal{S}} := \{\boldsymbol{u}^{\mathcal{S}} \in \boldsymbol{\mathcal{H}}^1(\Omega^{\mathcal{S}}_{\boldsymbol{\chi}}) \,|\, \boldsymbol{u}^{\mathcal{S}} = \boldsymbol{u}^{\mathcal{S}}_D \text{ on } \Gamma^{\mathcal{S}}_{D,\boldsymbol{\chi}}\}, \quad \boldsymbol{\mathcal{W}}^{\boldsymbol{u},\mathcal{S}} := \boldsymbol{\mathcal{H}}^1_0(\Omega^{\mathcal{S}}_{\boldsymbol{\chi}}; \Gamma^{\mathcal{S}}_{D,\boldsymbol{\chi}}), \tag{6.12}$$

respectively. We proceed with the velocity trial ($\boldsymbol{\mathcal{T}}^{\boldsymbol{v},\mathcal{S}}$) and test ($\boldsymbol{\mathcal{W}}^{\boldsymbol{v},\mathcal{S}}$) spaces in the solid domain and define them as

$$\boldsymbol{\mathcal{T}}^{\boldsymbol{v},\mathcal{S}} := \{\boldsymbol{v}^{\mathcal{S}} \in \boldsymbol{\mathcal{H}}^1(\Omega^{\mathcal{S}}_{\boldsymbol{\chi}}) \,|\, \boldsymbol{v}^{\mathcal{S}} = \boldsymbol{v}^{\mathcal{S}}_D \text{ on } \Gamma^{\mathcal{S}}_{D,\boldsymbol{\chi}}\}, \quad \boldsymbol{\mathcal{W}}^{\boldsymbol{v},\mathcal{S}} := \boldsymbol{\mathcal{H}}^1_0(\Omega^{\mathcal{S}}_{\boldsymbol{\chi}}; \Gamma^{\mathcal{S}}_{D,\boldsymbol{\chi}}), \tag{6.13}$$

We conclude the specification of approximation spaces with the following definition of pressure trial and test spaces in the solid domain

$$\mathcal{L}^{\mathcal{S}} := \mathcal{L}^2(\Omega^{\mathcal{S}}_{\boldsymbol{\chi}})/\mathbb{R}. \tag{6.14}$$

With the above definitions at hand, we are now able to pose the weak formulation of the ALE binary-fluid-structure interaction problem.

Problem 6.4.1 (Variational formulation of the BFSI problem in ALE coordinates). *Let* $\mathcal{T}_1 := \{\mathcal{Y}^{\mathcal{F}} \times \mathcal{Y}^{\mathcal{F}}\}, \mathcal{W}_1 := \{\mathcal{Y}^{\mathcal{F}} \times \mathcal{Y}^{\mathcal{F}}\}, \boldsymbol{\mathcal{T}}_2 := \{\boldsymbol{\mathcal{T}}^{\boldsymbol{v},\mathcal{F}} \times \boldsymbol{\mathcal{T}}^{\boldsymbol{v},\mathcal{S}} \times \boldsymbol{\mathcal{T}}^{\boldsymbol{u},\mathcal{F}} \times \boldsymbol{\mathcal{T}}^{\boldsymbol{u},\mathcal{S}} \times \mathcal{L}^{\mathcal{F}} \times \mathcal{L}^{\mathcal{S}}\}$*, and* $\boldsymbol{\mathcal{W}}_2 := \{\boldsymbol{\mathcal{W}}^{\boldsymbol{v},\mathcal{F}} \times \boldsymbol{\mathcal{V}}^{\boldsymbol{v},\mathcal{S}} \times \boldsymbol{\mathcal{W}}^{\boldsymbol{u},\mathcal{F}} \times \boldsymbol{\mathcal{V}}^{\boldsymbol{u},\mathcal{S}} \times \mathcal{L}^{\mathcal{F}} \times \mathcal{L}^{\mathcal{S}}\}$.
Step 1: Solve problem 6.4.2
Step 2: Solve problem 6.4.3

Problem 6.4.2 (Variational formulation of the mixed Cahn-Hilliard phase field problem in ALE coordinates, Step 1). *Find* $U_1 = \{\varphi, \eta\} \in \mathcal{T}_1 \times I$*, such that it holds:*

$$
\begin{aligned}
&\int_0^T \int_{\Omega_{\boldsymbol{\chi}}^{\mathcal{F}}} \hat{J}\left(\frac{\partial \varphi}{\partial t}\Big|_{\boldsymbol{\chi}} + \nabla_{\boldsymbol{\chi}}\varphi\left(\hat{\boldsymbol{F}}^{-1}(\boldsymbol{v}^{\mathcal{F}} - \partial_t \hat{\boldsymbol{\mathcal{A}}})\right)\right) \cdot \phi^{\varphi} + \hat{J}\left(\hat{J}\hat{\boldsymbol{F}}^{-1} m(\varphi)\nabla_{\boldsymbol{\chi}}\eta\right) : \nabla_{\boldsymbol{\chi}}\phi^{\varphi}\,\mathrm{d}\Omega_{\boldsymbol{\chi}}^{\mathcal{F}}\,\mathrm{d}t = 0 \quad \forall \phi^{\varphi} \in \mathcal{Y}^{\mathcal{F}},\\
&\int_0^T \int_{\Omega_{\boldsymbol{\chi}}^{\mathcal{F}}} \hat{J}\left(\eta - \frac{d\psi(\varphi)}{d\varphi}\right) \cdot \phi^{\eta} - \hat{J}\varepsilon^2\left(\hat{J}\hat{\boldsymbol{F}}^{-1}\nabla_{\boldsymbol{\chi}}\varphi\right) : \nabla_{\boldsymbol{\chi}}\phi^{\eta}\,\mathrm{d}\Omega_{\boldsymbol{\chi}}^{\mathcal{F}}\,\mathrm{d}t = 0 \quad \forall \phi^{\eta} \in \mathcal{Y}^{\mathcal{F}},\\
&+ \text{“contact angle b.c.”}.
\end{aligned}
\tag{6.15}
$$

Problem 6.4.3 (Variational formulation of the BFSI problem in ALE coordinates, Step 2). *Find* $\boldsymbol{U}_2 = \{\boldsymbol{v}^{\mathcal{F}}, \boldsymbol{v}^{\mathcal{S}}, \boldsymbol{u}^{\mathcal{F}}, \boldsymbol{u}^{\mathcal{S}}, p^{\mathcal{F}}, p^{\mathcal{S}}\} \in \boldsymbol{\mathcal{T}}_2 \times I$*, such that* $\boldsymbol{u}^{\mathcal{F}}(0) = \mathring{\boldsymbol{u}}^{\mathcal{F}}, \boldsymbol{v}^{\mathcal{F}}(0) = \mathring{\boldsymbol{v}}^{\mathcal{F}}, \boldsymbol{u}^{\mathcal{S}}(0) = \mathring{\boldsymbol{u}}^{\mathcal{S}}$ *and* $\boldsymbol{v}^{\mathcal{S}}(0) = \mathring{\boldsymbol{v}}^{\mathcal{S}}$ *are satisfied, and it holds:*

$$
\begin{aligned}
&\int_0^T \int_{\Omega_{\boldsymbol{\chi}}^{\mathcal{F}}} \hat{J}\rho^{\mathcal{F}}(\varphi)\left(\frac{\partial \boldsymbol{v}^{\mathcal{F}}}{\partial t}\Big|_{\boldsymbol{\chi}} + \nabla_{\boldsymbol{\chi}}\boldsymbol{v}^{\mathcal{F}}\left(\hat{\boldsymbol{F}}^{-1}(\boldsymbol{v}^{\mathcal{F}} - \partial_t\hat{\boldsymbol{\mathcal{A}}})\right)\right) \cdot \boldsymbol{\phi}^{\boldsymbol{v},\mathcal{F}}\,\mathrm{d}\Omega_{\boldsymbol{\chi}}^{\mathcal{F}}\,\mathrm{d}t\\
&+\int_0^T \int_{\Omega_{\boldsymbol{\chi}}^{\mathcal{F}}} \hat{J}\left(-p^{\mathcal{F}}\boldsymbol{I} + \mu^{\mathcal{F}}(\varphi)\left(\nabla_{\boldsymbol{\chi}}\boldsymbol{v}^{\mathcal{F}}\hat{\boldsymbol{F}}^{-1} + \hat{\boldsymbol{F}}^{-T}(\nabla_{\boldsymbol{\chi}}\boldsymbol{v}^{\mathcal{F}})^T\right)\right)\hat{\boldsymbol{F}}^{-T} : \nabla_{\boldsymbol{\chi}}\boldsymbol{\phi}^{\boldsymbol{v},\mathcal{F}}\,\mathrm{d}\Omega_{\boldsymbol{\chi}}^{\mathcal{F}}\,\mathrm{d}t\\
&+\int_0^T \int_{\Omega_{\boldsymbol{\chi}}^{\mathcal{F}}} \left(\hat{\sigma}\varepsilon\,\hat{\boldsymbol{F}}^{-T}\nabla_{\boldsymbol{\chi}}\varphi \otimes \hat{\boldsymbol{F}}^{-T}\nabla_{\boldsymbol{\chi}}\varphi\right) : \nabla_{\boldsymbol{\chi}}\boldsymbol{\phi}^{\boldsymbol{v},\mathcal{F}}\,\mathrm{d}\Omega_{\boldsymbol{\chi}}^{\mathcal{F}}\,\mathrm{d}t\\
&-\int_0^T \int_{\Omega_{\boldsymbol{\chi}}^{\mathcal{F}}} \hat{J}\rho^{\mathcal{F}}(\varphi)\boldsymbol{f}^{\mathcal{F}} \cdot \boldsymbol{\phi}^{\boldsymbol{v},\mathcal{F}}\,\mathrm{d}\Omega_{\boldsymbol{\chi}}^{\mathcal{F}}\,\mathrm{d}t - \int_0^T \int_{\Gamma_{N,\boldsymbol{\chi}}^{\mathcal{F}}} \boldsymbol{g}_0^{\mathcal{F}} \cdot \boldsymbol{\phi}^{\boldsymbol{v},\mathcal{F}}\,\mathrm{d}\Gamma_{N,\boldsymbol{\chi}}^{\mathcal{F}}\,\mathrm{d}t = 0 && \forall \boldsymbol{\phi}^{\boldsymbol{v},\mathcal{F}} \in \boldsymbol{\mathcal{W}}^{\boldsymbol{v},\mathcal{F}},\\
&\int_0^T \int_{\Omega_{\boldsymbol{\chi}}^{\mathcal{F}}} \nabla_{\boldsymbol{\chi}} \cdot \left(\hat{J}\hat{\boldsymbol{F}}^{-1}\boldsymbol{v}^{\mathcal{F}}\right) \cdot \phi^{p,\mathcal{F}}\,\mathrm{d}\Omega_{\boldsymbol{\chi}}^{\mathcal{F}}\,\mathrm{d}t = 0 && \forall \phi^{p,\mathcal{F}} \in \mathcal{L}^{\mathcal{F}},\\
&\int_0^T \int_{\Omega_{\boldsymbol{\chi}}^{\mathcal{S}}} \hat{J}\rho^{\mathcal{S}}\frac{\partial \boldsymbol{v}^{\mathcal{S}}}{\partial t}\Big|_{\boldsymbol{\chi}} \cdot \boldsymbol{\phi}^{\boldsymbol{v},\mathcal{S}}\,\mathrm{d}\Omega_{\boldsymbol{\chi}}^{\mathcal{S}}\,\mathrm{d}t + \int_0^T \int_{\Omega_{\boldsymbol{\chi}}^{\mathcal{S}}} \hat{\boldsymbol{P}}^{\mathcal{S}} : \nabla_{\boldsymbol{\chi}}\boldsymbol{\phi}^{\boldsymbol{v},\mathcal{S}}\,\mathrm{d}\Omega_{\boldsymbol{\chi}}^{\mathcal{S}}\,\mathrm{d}t\\
&-\int_0^T \int_{\Omega_{\boldsymbol{\chi}}^{\mathcal{S}}} \hat{J}\rho^{\mathcal{S}}\boldsymbol{b}^{\mathcal{S}} \cdot \boldsymbol{\phi}^{\boldsymbol{v},\mathcal{S}}\,\mathrm{d}\Omega_{\boldsymbol{\chi}}^{\mathcal{S}}\,\mathrm{d}t - \int_0^T \int_{\Gamma_{N,\boldsymbol{\chi}}^{\mathcal{S}}} \boldsymbol{g}_0^{\mathcal{S}} \cdot \boldsymbol{\phi}^{\boldsymbol{v},\mathcal{S}}\,\mathrm{d}\Gamma_{N,\boldsymbol{\chi}}^{\mathcal{S}}\,\mathrm{d}t = 0 && \forall \boldsymbol{\phi}^{\boldsymbol{v},\mathcal{S}} \in \boldsymbol{\mathcal{W}}^{\boldsymbol{v},\mathcal{S}},\\
&\int_0^T \int_{\Omega_{\boldsymbol{\chi}}^{\mathcal{S}}} \left(\frac{\partial \boldsymbol{u}^{\mathcal{S}}}{\partial t}\Big|_{\boldsymbol{\chi}} - \boldsymbol{v}^{\mathcal{S}}\right) \cdot \boldsymbol{\phi}^{\boldsymbol{u},\mathcal{S}}\,\mathrm{d}\Omega_{\boldsymbol{\chi}}^{\mathcal{S}}\,\mathrm{d}t = 0 && \forall \boldsymbol{\phi}^{\boldsymbol{u},\mathcal{S}} \in \boldsymbol{\mathcal{W}}^{\boldsymbol{u},\mathcal{S}},\\
&\int_0^T \int_{\Omega_{\boldsymbol{\chi}}^{\mathcal{S}}} p^{\mathcal{S}} \cdot \phi^{p,\mathcal{S}}\,\mathrm{d}\Omega_{\boldsymbol{\chi}}^{\mathcal{S}}\,\mathrm{d}t = 0 && \forall \phi^{p,\mathcal{S}} \in \mathcal{L}^{\mathcal{S}},\\
&\int_0^T \int_{\Omega_{\boldsymbol{\chi}}^{\mathcal{F}}} \alpha_u \hat{J}^{-1}\nabla_{\boldsymbol{\chi}}\boldsymbol{u}^{\mathcal{F}} : \nabla_{\boldsymbol{\chi}}\boldsymbol{\phi}^{\boldsymbol{u}}\,\mathrm{d}\Omega_{\boldsymbol{\chi}}^{\mathcal{F}}\,\mathrm{d}t = 0 && \forall \boldsymbol{\phi}^{\boldsymbol{u},\mathcal{F}} \in \boldsymbol{\mathcal{W}}^{\boldsymbol{u},\mathcal{F}}.
\end{aligned}
\tag{6.16}
$$

Note that in equations (6.5) and (6.15) we have refrained from specifying the actual terms for the contact angle boundary condition. This is due to the fact that as of writing of this work, it has not been finally clarified in detail yet, how to correctly rewrite the contact angle boundary condition integral in the sense of a pull back to the referential domain. In the context of our standalone two-phase flow computations the left hand side of the contact angle boundary condition in equation (4.20) was naturally obtained from the application of integration by parts

$$\begin{aligned}\int_\Omega C\nabla^2\varphi\,\phi^\eta\,\mathrm{d}\boldsymbol{x} &= -\int_\Omega C\,\nabla\varphi\cdot\nabla\phi^\eta\,\mathrm{d}\boldsymbol{x} + \int_{\partial\Omega}\boldsymbol{n}\cdot C\nabla\varphi\,\phi^\eta\,ds \\ &\overset{(4.37)}{=} -\int_\Omega C\,\nabla\varphi\cdot\nabla\phi^\eta\,\mathrm{d}\boldsymbol{x} + \underbrace{\int_{\partial\Omega} C\frac{1}{\epsilon\sqrt{2}}\cos(\theta)(1-\varphi^2)\,\phi^\eta\,\mathrm{d}s}_{\text{contact angle boundary integral}}\end{aligned} \tag{6.17}$$

on the Laplacian of the phase field φ (scaled with constant C) in the Cahn-Hilliard equations (4.27), cf. equations (4.35) and (4.36). The situation turns out to be a bit more involved in binary-fluid-structure interaction. Until that has been finally clarified, we have decided to basically apply the contact angle boundary integral as presented in (6.17) without further modifications. This expression is most likely not complete yet and for the time being we consider its application as a provisional and temporary measure.

6.4.1 Discretization and treatment of nonlinearity

In this section we present the space and time discretization of our choice for the highly nonlinear problem (6.4.1) and our strategy to address its inherent nonlinearity. A brief recap of the steps taken so far is in order. Facing a large number of combined field variables, we decided to trade to a certain degree the monolithic character of our BFSI model for the sake of an easier numerical treatment. More specifically, we decided to separately solve the phase field problem and use its results in an explicit sense in the remaining set of problems to be solved. This segregation lead us to the subproblems 6.4.2 and 6.4.3 – presented in variational formulation. Their spatial and temporal discretization is discussed in the sequel.

For temporal discretization, let the set $P_{\delta t} = \{t_n\}_{n=0}^N$ be a quasi-uniform partition of the time interval $[0, T]$ with time step size $\delta t := T/N$, where this partition could also be given by varying time step sizes (adaptive time stepping). We perform the time integration of both problems implicitly with the one-step θ-scheme, yielding the 1st order implicit Euler and 2nd order Crank-Nicolson schemes for the choices $\theta = 1$, and $\theta = 0.5$, respectively. Consequently, in the time discretized equations the temporal derivatives are replaced with their finite difference counterpart $d_t v^{n+1} := (v^{n+1} - v^n)/\delta t$, where the upper index denotes the time step number.

Likewise, for both problems we use Newton's method for algorithmically efficient treatment of nonlinearity and apply Galerkin-based Isogeometric Analysis for the space discretization of the involved partial differential equations. For the approximation of the velocity and pressure functions in the Navier-Stokes equations, we use LBB-stable Taylor-Hood-like B-spline space pairs $\mathbf{V}_h^{TH}/Q_h^{TH}$ that have already been presented in Section 3.3. For all computations presented in this chapter, we used a $\mathcal{C}^0$ $\boldsymbol{\mathcal{S}}_{0,0}^{2,2}/\mathcal{S}_{0,0}^{1,1}$ B-spline space pair for the approximation of the velocity and pressure functions. This corresponds to the Isogeometric counterpart of a Q_2Q_1 Taylor-Hood space well known from the finite element literature. The degree and continuity of the discrete spline spaces used for the approximation of the displacement ($\boldsymbol{u}$), velocity ($\boldsymbol{v}$), phase field (φ), and chemical potential (η) functions are set to be identical.

6.4.1.1 Discrete phase field problem

In this section we will present the space and time discretized version of Problem 6.4.2, where in each time step Newton's method is applied for the treatment of the nonlinearity of the quasi-stationary systems obtained from the time discretization. We briefly recall that the application of Newton's method – in view of the sketch in (5.189) applied to the current problem – requires the specification of a semilinear[56] form $\mathcal{F}_{\text{CH}}$ that is obtained from the difference of the left $(A_{\text{CH}}(U_{h,\text{CH}}, \Phi_h))$ and right $(F_{\text{CH}}(\Phi_h))$ hand sides of the nonlinear partial differential equation under consideration. With this in mind, the space and time discretized version of Problem 6.4.2 may be reformulated as follows:

Let $\mathcal{T}_1^h := \{(\mathcal{Y}^{\mathcal{F}} \cap V_h^{TH}) \times (\mathcal{Y}^{\mathcal{F}} \cap V_h^{TH})\}, \mathcal{W}_1^h := \{(\mathcal{Y}^{\mathcal{F}} \cap V_h^{TH}) \times (\mathcal{Y}^{\mathcal{F}} \cap V_h^{TH})\}$, and $\Phi_h = \{\phi_h^{\varphi}, \phi_h^{\eta}\} \in \mathcal{W}_1^h$. Find $U_{h,\text{CH}} = \{\varphi_h, \eta_h\} \in \mathcal{T}_1^h \times I$, such that $\varphi_h(0) = \mathring{\varphi}^h$ and $\eta_h(0) = \mathring{\eta}^h$ are satisfied, and it holds

$$\mathcal{F}_{\text{CH}}(U_{h,\text{CH}}, \Phi_h) = A_{\text{CH}}(U_{h,\text{CH}}, \Phi_h) - F_{\text{CH}}(\Phi_h) = 0, \quad \forall \Phi_h \in \mathcal{W}_1^h, \tag{6.18}$$

where the semilinear form $\mathcal{F}_{\text{CH}}(U_{h,\text{CH}}, \Phi_h)$ is defined as

$$\begin{aligned} \mathcal{F}_{\text{CH}}(U_{h,\text{CH}}, \Phi_h) &:= \left(\hat{J}_h \frac{\varphi_h - \varphi_h^n}{\Delta t}, \phi_h^{\varphi} \right)_{\Omega_{\boldsymbol{\chi}}^{\mathcal{F}}} \\ &+ \left(\hat{J}_h \theta \nabla_{\boldsymbol{\chi}} \varphi_h \cdot \left(\hat{\boldsymbol{F}}_h^{-1} (\boldsymbol{v}_h^{\mathcal{F}} - \partial_t \hat{\boldsymbol{\mathcal{A}}}) \right), \phi_h^{\varphi} \right)_{\Omega_{\boldsymbol{\chi}}^{\mathcal{F}}} + \left(\hat{J}_h \theta \hat{J}_h \hat{\boldsymbol{F}}_h^{-1} m(\varphi_h) \nabla_{\boldsymbol{\chi}} \eta_h, \nabla_{\boldsymbol{\chi}} \phi_h^{\varphi} \right)_{\Omega_{\boldsymbol{\chi}}^{\mathcal{F}}} \\ &+ \left(\hat{J}_h (1-\theta) \nabla_{\boldsymbol{\chi}} \varphi_h^n \cdot \left(\hat{\boldsymbol{F}}_h^{-1} (\boldsymbol{v}_h^{\mathcal{F}} - \partial_t \hat{\boldsymbol{\mathcal{A}}}) \right), \phi_h^{\varphi} \right)_{\Omega_{\boldsymbol{\chi}}^{\mathcal{F}}} + \left(\hat{J}_h (1-\theta) \hat{J}_h \hat{\boldsymbol{F}}_h^{-1} m(\varphi_h^n) \nabla_{\boldsymbol{\chi}} \eta_h^n, \nabla_{\boldsymbol{\chi}} \phi_h^{\varphi} \right)_{\Omega_{\boldsymbol{\chi}}^{\mathcal{F}}} \\ &+ \left(\hat{J}_h \left(\eta_h - \frac{d\psi(\varphi_h)}{d\varphi} \right), \phi_h^{\eta} \right)_{\Omega_{\boldsymbol{\chi}}^{\mathcal{F}}} - \left(\hat{J}_h \varepsilon^2 \, \hat{J}_h \hat{\boldsymbol{F}}_h^{-1} \nabla_{\boldsymbol{\chi}} \varphi_h, \nabla_{\boldsymbol{\chi}} \phi_h^{\eta} \right)_{\Omega_{\boldsymbol{\chi}}^{\mathcal{F}}} + \text{“contact angle b.c.”}. \end{aligned} \tag{6.19}$$

With a view to (5.189) applied to the present problem, the bilinear form $\mathcal{F}'_{\text{CH}}(U^{h,k}; \delta U_{h,\text{CH}}, \Phi_h)$ is the Fréchet derivative (Jacobian) of $\mathcal{F}_{\text{CH}}$ and is obtained from the linearization of $\mathcal{F}_{\text{CH}}$ around a fixed $U_{\text{CH}} \equiv U_{\text{CH}}^k$. We remind that for each fixed U_{CH}^k, $\mathcal{F}'_{\text{CH}}(U_{\text{CH}}^k; \cdot, \cdot)$ is a bilinear form and $\mathcal{F}_{\text{CH}}(U_{\text{CH}}^k; \cdot)$ is a linear form. Since the latter is simply obtained from the evaluation of the respective partial differential operator with the last available U, that is, U^k, it merely remains to specify $\mathcal{F}'_{\text{CH}}(U_{\text{CH}}^k; \cdot, \cdot)$.

The above presented expression (6.19) – basically corresponding to (4.36) – is nonlinear in φ by way of the definition of the mobility function $m(\varphi)$ (cf. equation (4.17)) and the homogeneous free energy density function $\psi(\varphi)$ (cf. equation (4.11) or (4.12)). At this point we want to point out that thanks to the two stage binary-fluid-structure interaction solution approach, where the phase field problem is solved separately, the velocity field $\boldsymbol{v}$ and functions of the displacement field $\boldsymbol{u}$, that is, $\hat{J}, \hat{\boldsymbol{F}}^{-1}$, and $\partial_t \hat{\boldsymbol{\mathcal{A}}}$, turn into "explicitly" given constants and do not add to the system's nonlinearity. This significantly simplifies the nonlinearity treatment of the "pulled back" phase field problem and is one of the reasons we opted to solve the corresponding equations separately. This circumstance also allows us to easily deduce $\mathcal{F}'_{\text{CH}}(U_{\text{CH}}^k; \cdot, \cdot)$ from the derivations done in the

---

[56] Linear with respect to the test functions, but not in the trial functions

two-phase flow Chapter 4, cf. equation (4.41). We define

$$\begin{aligned}\mathcal{F}'_{\mathrm{CH}}(U^k_{h,\mathrm{CH}}; \delta U^k_{h,\mathrm{CH}}, \Phi_h) := {} & \left(\hat{J}_h \delta\varphi_h, \phi^{\varphi}_h\right)_{\Omega^{\mathcal{F}}_{\boldsymbol{\chi}}} + \left(\hat{J}_h \theta \Delta t \, \left(\hat{\boldsymbol{F}}_h^{-1} (\boldsymbol{v}^{\mathcal{F}}_h - \partial_t \hat{\boldsymbol{\mathcal{A}}}) \cdot \nabla_{\boldsymbol{\chi}}\right) \delta\varphi_h, \phi^{\varphi}_h\right)_{\Omega^{\mathcal{F}}_{\boldsymbol{\chi}}} \\ & + \left(\hat{J}_h \theta \Delta t \, m(\varphi^n_h) \hat{J}_h \hat{\boldsymbol{F}}_h^{-1} \nabla_{\boldsymbol{\chi}} \delta\eta_h, \nabla_{\boldsymbol{\chi}} \phi^{\varphi}_h\right)_{\Omega^{\mathcal{F}}_{\boldsymbol{\chi}}} - \left(\hat{J}_h \varepsilon^2 \, \hat{J}_h \hat{\boldsymbol{F}}_h^{-1} \nabla_{\boldsymbol{\chi}} \delta\varphi_h, \nabla_{\boldsymbol{\chi}} \phi^{\eta}_h\right)_{\Omega^{\mathcal{F}}_{\boldsymbol{\chi}}} \\ & - \left(\hat{J}_h \psi''(\varphi^k_h) \, \delta\varphi_h, \phi^{\eta}_h\right)_{\Omega^{\mathcal{F}}_{\boldsymbol{\chi}}} + \left(\hat{J}_h \delta\eta_h, \phi^{\eta}_h\right)_{\Omega^{\mathcal{F}}_{\boldsymbol{\chi}}} + \text{“contact angle b.c. der.”}. \end{aligned} \tag{6.20}$$

Above, $\delta U_{h,\mathrm{CH}} = \{\delta\varphi_h, \delta\eta_h\} \in \mathcal{T}^h_1$ denotes the set of phase field and chemical potential trial functions and the indices n and k refer to the solution from the last time step and the current Newton-iterate, respectively. Note that in the evaluation of both, the linear form $\mathcal{F}_{\mathrm{CH}}(U^k_{\mathrm{CH}}; \cdot)$, and the bilinear form (6.20) we evaluate – in the spirit of Picard iteration – the nonlinear mobility function $m(\varphi)$ with respect to the values of the phase field from the previous time step, that is, φ^n. This linearization allows it to be treated as a constant and simplifies the numerical treatment.

6.4.1.2 Discrete BFSI problem

In analogy to the content and structure of Section 6.4.1.1, we present in this section a discrete version of the nonlinear Problem 6.4.3. As shown multiple times throughout this work, for the treatment of nonlinearity, it comes in handy to represent the discretized yet still nonlinear problem under consideration through a semilinear form which evaluated with respect to the last available values of the unknowns, turns into a linear form – representing the residual of the problem. Eventually specifying the derivative of the PDE operator completes the list of ingredients for Newton's method. In the light of the above, we reformulate a space and time discretized version of Problem 6.4.3 as follows:

Let the discrete trial and test spaces $\boldsymbol{\mathcal{T}}_{h,2}$ and $\boldsymbol{\mathcal{W}}_{h,2}$ be defined as presented in (5.186) and (5.187), respectively, and let the corresponding set of trial ($\boldsymbol{U}_{h,\mathrm{FSI}}$) and test ($\boldsymbol{\Phi}_h$) functions be defined as presented in (5.188). Find $\boldsymbol{U}_{h,\mathrm{FSI}} \in \boldsymbol{\mathcal{T}}_{h,2} \times I$, such that $\boldsymbol{u}^{\mathcal{F}}_h(0) = \mathring{\boldsymbol{u}}^{\mathcal{F}}_h, \boldsymbol{v}^{\mathcal{F}}_h(0) = \mathring{\boldsymbol{v}}^{\mathcal{F}}_h, \boldsymbol{u}^{\mathcal{S}}_h(0) = \mathring{\boldsymbol{u}}^{\mathcal{S}}_h$ and $\boldsymbol{v}^{\mathcal{S}}_h(0) = \mathring{\boldsymbol{v}}^{\mathcal{S}}_h$ are satisfied, and it holds

$$\mathcal{F}_{\mathrm{FSI}}(\boldsymbol{U}_h, \boldsymbol{\Phi}_h) = 0 \quad \forall \Phi_h \in \boldsymbol{\mathcal{W}}_{h,2}, \tag{6.21}$$

where the semilinear form $\mathcal{F}_{\text{FSI}}(\boldsymbol{U}_h, \boldsymbol{\Phi}_h)$ is defined as

$$
\begin{aligned}
&\mathcal{F}_{\text{FSI}}(\boldsymbol{U}_h, \Phi_h) := \\
&\quad \left(\rho^{\mathcal{F}}(\varphi_h)\hat{J}_h^{\theta}\left(\boldsymbol{v}_h^{\mathcal{F}} - \boldsymbol{v}_h^{n,\mathcal{F}}\right), \boldsymbol{\phi}_h^{\boldsymbol{v},\mathcal{F}}\right)_{\Omega_{\boldsymbol{\chi}}^{\mathcal{F}}} + \left(\Delta t\theta\rho^{\mathcal{F}}(\varphi_h)\hat{J}_h\nabla_{\boldsymbol{\chi}}\boldsymbol{v}_h^{\mathcal{F}}\hat{\boldsymbol{F}}_h^{-1}\boldsymbol{v}_h^{\mathcal{F}}, \boldsymbol{\phi}_h^{\boldsymbol{v},\mathcal{F}}\right)_{\Omega_{\boldsymbol{\chi}}^{\mathcal{F}}} \\
&\quad + \left(\Delta t(1-\theta)\,\rho^{\mathcal{F}}(\varphi_h)\hat{J}_h^{n}\nabla_{\boldsymbol{\chi}}\boldsymbol{v}_h^{n,\mathcal{F}}\left(\hat{\boldsymbol{F}}_h^{n}\right)^{-1}\boldsymbol{v}_h^{n,\mathcal{F}}, \boldsymbol{\phi}_h^{\boldsymbol{v},\mathcal{F}}\right)_{\Omega_{\boldsymbol{\chi}}^{\mathcal{F}}} \\
&\quad - \left(\rho^{\mathcal{F}}(\varphi_h)\hat{J}_h\nabla_{\boldsymbol{\chi}}\boldsymbol{v}_h^{\mathcal{F}}\hat{\boldsymbol{F}}_h^{-1}\cdot\left(\boldsymbol{u}_h^{\mathcal{F}} - \boldsymbol{u}_h^{n,\mathcal{F}}\right), \boldsymbol{\phi}_h^{\boldsymbol{v},\mathcal{F}}\right)_{\Omega_{\boldsymbol{\chi}}^{\mathcal{F}}} \\
&\quad + \left(\Delta t\theta\hat{J}_h\mu^{\mathcal{F}}(\varphi_h)\left(\nabla_{\boldsymbol{\chi}}\boldsymbol{v}_h^{\mathcal{F}}\hat{\boldsymbol{F}}_h^{-1} + \hat{\boldsymbol{F}}_h^{-T}\cdot\left(\nabla_{\boldsymbol{\chi}}\boldsymbol{v}_h^{\mathcal{F}}\right)^{T}\right)\hat{\boldsymbol{F}}_h^{-T}, \nabla_{\boldsymbol{\chi}}\boldsymbol{\phi}_h^{\boldsymbol{v},\mathcal{F}}\right)_{\Omega_{\boldsymbol{\chi}}^{\mathcal{F}}} \\
&\quad + \left(\Delta t(1-\theta)\,\hat{J}_h^{n}\,\mu^{\mathcal{F}}(\varphi_h)\left(\nabla_{\boldsymbol{\chi}}\boldsymbol{v}_h^{n,\mathcal{F}}\left(\hat{\boldsymbol{F}}_h^{n}\right)^{-1} + (\hat{\boldsymbol{F}}_h^{n})^{-T}\cdot(\nabla_{\boldsymbol{\chi}}\boldsymbol{v}_h^{n,\mathcal{F}})^{T}\right)\left(\hat{\boldsymbol{F}}_h^{n}\right)^{-T}, \nabla_{\boldsymbol{\chi}}\boldsymbol{\phi}_h^{\boldsymbol{v},\mathcal{F}}\right)_{\Omega_{\boldsymbol{\chi}}^{\mathcal{F}}} \\
&\quad - \left(\Delta t\,\hat{\sigma}\varepsilon\,(\hat{\boldsymbol{F}}_h^{n})^{-T}\nabla_{\boldsymbol{\chi}}\varphi_h^{n}\otimes(\hat{\boldsymbol{F}}_h^{n})^{-T}\nabla_{\boldsymbol{\chi}}\varphi_h^{n}, \nabla_{\boldsymbol{\chi}}\boldsymbol{\phi}_h^{\boldsymbol{v},\mathcal{F}}\right)_{\Omega_{\boldsymbol{\chi}}^{\mathcal{F}}} \\
&\quad + \left(\Delta t\hat{J}_h\left(-p_h^{\mathcal{F}}\boldsymbol{I}\right)\hat{\boldsymbol{F}}_h^{-T}, \nabla_{\boldsymbol{\chi}}\boldsymbol{\phi}_h^{\boldsymbol{v},\mathcal{F}}\right)_{\Omega_{\boldsymbol{\chi}}^{\mathcal{F}}} - \left(\rho^{\mathcal{F}}(\varphi_h)\,\Delta t\hat{J}_h^{\theta}\boldsymbol{b}^{\mathcal{F}}, \boldsymbol{\phi}_h^{\boldsymbol{v},\mathcal{F}}\right)_{\Omega_{\boldsymbol{\chi}}^{\mathcal{F}}} - \left(\Delta t\boldsymbol{g}_0^{\mathcal{F}}, \boldsymbol{\phi}_h^{\boldsymbol{v},\mathcal{F}}\right)_{\Gamma_{N,\boldsymbol{\chi}}^{\mathcal{F}}} \\
&\quad + \left(\hat{J}_h\hat{\boldsymbol{F}}_h^{-1} : \left(\nabla_{\boldsymbol{\chi}}\boldsymbol{v}_h^{\mathcal{F}}\right)^{T}, \phi_h^{p,\mathcal{F}}\right)_{\Omega_{\boldsymbol{\chi}}^{\mathcal{F}}} \\
&\quad + \left(\hat{J}_h\rho^{\mathcal{S}}\left(\boldsymbol{v}_h^{\mathcal{S}} - \boldsymbol{v}_h^{n,\mathcal{S}}\right), \boldsymbol{\phi}_h^{\boldsymbol{v},\mathcal{S}}\right)_{\Omega_{\boldsymbol{\chi}}^{\mathcal{S}}} \\
&\quad + \left(\Delta t\theta\,\hat{\boldsymbol{P}}\left(\boldsymbol{u}_h^{\mathcal{S}}\right), \nabla_{\boldsymbol{\chi}}\boldsymbol{\phi}_h^{\boldsymbol{v},\mathcal{S}}\right)_{\Omega_{\boldsymbol{\chi}}^{\mathcal{S}}} + \left(\Delta t(1-\theta)\,\hat{\boldsymbol{P}}\left(\boldsymbol{u}_h^{n,\mathcal{S}}\right), \nabla_{\boldsymbol{\chi}}\boldsymbol{\phi}_h^{\boldsymbol{v},\mathcal{S}}\right)_{\Omega_{\boldsymbol{\chi}}^{\mathcal{S}}} \\
&\quad - \left(\Delta t\theta\,\hat{J}_h^{\theta}\rho^{\mathcal{S}}\boldsymbol{b}^{\mathcal{S}}, \boldsymbol{\phi}_h^{\boldsymbol{v},\mathcal{S}}\right)_{\Omega_{\boldsymbol{\chi}}^{\mathcal{S}}} - \left(\Delta t\boldsymbol{g}_0^{\mathcal{S}}, \boldsymbol{\phi}_h^{\boldsymbol{v},\mathcal{S}}\right)_{\Gamma_{N,\boldsymbol{\chi}}^{\mathcal{S}}} \\
&\quad + \left(\boldsymbol{u}_h^{\mathcal{S}} - \boldsymbol{u}_h^{n,\mathcal{S}}, \boldsymbol{\phi}_h^{\boldsymbol{u},\mathcal{S}}\right)_{\Omega_{\boldsymbol{\chi}}^{\mathcal{S}}} - \left(\Delta t\theta\,\boldsymbol{v}_h^{\mathcal{S}}, \boldsymbol{\phi}_h^{\boldsymbol{u},\mathcal{S}}\right)_{\Omega_{\boldsymbol{\chi}}^{\mathcal{S}}} - \left(\Delta t(1-\theta)\,\boldsymbol{v}_h^{n,\mathcal{S}}, \boldsymbol{\phi}_h^{\boldsymbol{u},\mathcal{S}}\right)_{\Omega_{\boldsymbol{\chi}}^{\mathcal{S}}} \\
&\quad + \left(p^{\mathcal{S}}, \phi_h^{p,\mathcal{S}}\right)_{\Omega_{\boldsymbol{\chi}}^{\mathcal{S}}} \\
&\quad + \left(\alpha_u\hat{J}_h^{-1}\nabla_{\boldsymbol{\chi}}\boldsymbol{u}_h^{\mathcal{F}}, \nabla_{\boldsymbol{\chi}}\boldsymbol{\phi}_h^{\boldsymbol{u}}\right)_{\Omega_{\boldsymbol{\chi}}^{\mathcal{F}}}.
\end{aligned}
\tag{6.22}
$$

Note that the above expression is a natural extension of (5.154) in the sense that the fluid density $\rho^{\mathcal{F}}$ and viscosity $\mu^{\mathcal{F}}$ now depend on the phase field φ and we additionally consider a "pulled back" phase field-based surface tension stress term

$$
\left(-\Delta t\,\hat{\sigma}\varepsilon\,(\hat{\boldsymbol{F}}^{n})^{-T}\nabla_{\boldsymbol{\chi}}\varphi^{n}\otimes(\hat{\boldsymbol{F}}^{n})^{-T}\nabla_{\boldsymbol{\chi}}\varphi^{n}, \nabla_{\boldsymbol{\chi}}\boldsymbol{\phi}^{\boldsymbol{v},\mathcal{F}}\right)_{\Omega_{\boldsymbol{\chi}}^{\mathcal{F}}}. \tag{6.23}
$$

However, this term does not add to the nonlinearity of the system by virtue of the fact that we solve the phase field problem separately, and therefore each occurrence of the phase field φ and chemical potential η in (6.22) takes place in an "explicit" sense. This effectively renders them as constants therein. Moreover, in the evaluation of (6.23) we use the already available displacement field $\boldsymbol{u}^{n}$ from the last time step n - likewise turning the inverse transpose of the deformation gradient into a given constant. Since compared to (5.154) the only additional term to consider in (6.22) is linear, the Jacobian matrix of the present problem can be obtained by the action of the already derived bilinear form (5.175). This concludes the discussion of this section.

6.5 Numerical experiments

In this section we present our numerical results obtained from the application of the quasi monolithic binary-fluid-structure interaction model (6.5) to a selected set of scenarios involving the complex interaction of two immiscible and incompressible fluids with each other and with an elastic solid. The results presented are intended to give valuable insights in the assessment of the predictive capabilities of our BFSI model, and its overall stability and robustness. The BFSI-scenarios considered comprise the *deformation of a soft substrate by a sessile micro droplet*, and a *dam break with elastic obstacle*. For the first application there exist comprehensive experimental data that we use in a benchmark sense for validation of our results. The latter mentioned application is merely intended to showcase the ability of the present model to tackle problems from the class of free-surface fluid-structure interaction. We devote Sections 6.5.1 and 6.5.2 to the presentation of the respective problem statements and numerical results.

6.5.1 Deformation of a soft substrate by a sessile micro droplet

The setup described in this section involves a droplet resting upon a soft substrate. From a topological point of view, the sessile droplet is enclosed by the solid on its bottom side and by the "ambient fluid" (e.g. air) on the remaining parts of its boundary. Such a configuration yields a three-phase[57] contact line at which the surface tension of the droplet deforms the solid substrate [141]. Using confocal microscopy and laser surface profilometry the authors of the cited reference have provided a large database of experimentally obtained measurement data for the deformation of a soft solid substrate beneath a sessile droplet. More specifically, the experiments were conducted with a solid substrate modeled through a thin sheet of silicone gel, and droplets of different radii ($26.8, 74.5, 176.7,$ and $225.5\,\mu$m) and materials (glycerol and fluorinated oil). From these set of parameters we have randomly chosen one configuration and have tried to reproduce the corresponding experimentally obtained data with numerical simulation. The specifics of the chosen experiment is pictured in the sequel.

We consider the test case of a glycerol droplet of radius $r = 225.5\,\mu\text{m}$ deposited on a $50\,\mu\text{m}$ thick silicon gel modeling the soft solid substrate. A sketch of this setup is presented in Figure 6.4. We adopt the values of surface tensions as reported in [141], i.e., the surface tensions of the fluid-fluid interface (γ_{LA}) (a.k.a. liquid-ambient fluid interface), the liquid-solid interface (γ_{SL}), and the solid-ambient fluid interface (γ_{SA}) are set to $\gamma_{LA} = 46\,\text{mN/m}$, $\gamma_{LS} = 31\,\text{mN/m}$, and $\gamma_{SA} = 36\,\text{mN/m}$, respectively. For the density (ρ) and dynamic viscosity (μ) of the liquid droplet we use the material parameters of glycerol, that is, $\rho_L = 1261\,\text{kg/m}^3$ and $\mu_L = 1.412\,\text{Ns/m}^2$. Note that choosing the ambient fluid to represent air, it holds $\rho_{\text{air}} = 1.2041\,\text{kg/m}^3$ and $\mu_{\text{air}} = 1.8208 \times 10^{-5}\,\text{Ns/m}^2$, and the respective densities and dynamic viscosities of the involved fluids roughly differ by three and five orders of magnitude. Since such a disparity/discontinuity across the fluid-fluid interface is known to be challenging in two-phase flow simulations (cf. Chapter 4), we have artificially increased the dynamic viscosity of the ambient fluid and therefore set $\rho_A = 1.2041\,\text{kg/m}^3$ and $\mu_A = 1.8208 \times 10^{-2}\,\text{Ns/m}^2$. We consider this modification as tolerable as we are essentially interested in steady state solutions of the present problem and neglect its dynamics. For the Cahn-Hilliard phase field model we made the call to set the diffuse interface width ϵ proportional to the minimum mesh cell width h. This choice differs from the typical practice of setting the diffuse interface width to a fixed size of $2\,\mu\text{m}$ [28, 151] and comes with the trait of automatically adjusting the diffuse interface width as the computational mesh is refined. On the other hand, it evidently requires a "fine enough"

---

[57] Phase 1: Liquid droplet (L), Phase 2: Ambient fluid (A), Phase 3: Solid (S)

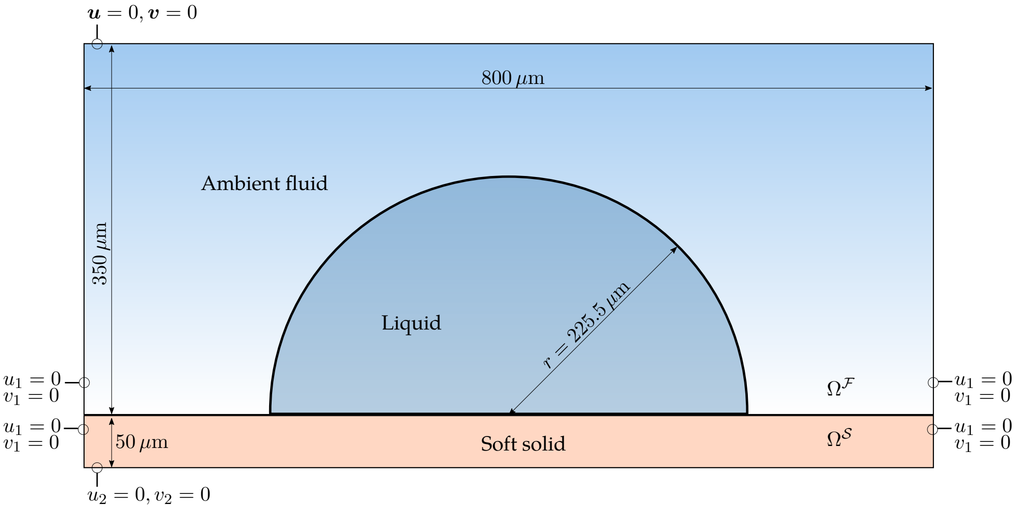

Figure 6.4: Sketch of the sessile droplet on soft substrate problem. A droplet of radius $r = 225.5\,\mu\text{m}$ is placed on a $50\,\mu\text{m}$ thick soft solid substrate such that it is adjacent to the solid on its bottom boundary and is surrounded otherwise by the ambient fluid.

computational mesh such that the fluid-fluid interface is always reasonably resolved. For the results presented in this section, we have set the mobility coefficient (cf. eqn. (4.17)) to $D = 10^{-8}\,\text{m}^2/\text{s}$ and the diffuse interface width to $\epsilon = 4/5\,h$. This choice for the diffuse interface width may be far from optimal and it might even be advantageous to work with a fixed diffuse interface width as specified above. The Cahn-Hilliard equations are solved with a contact angle of $\theta = 96.24°$ – obtained from the the Young-Dupré equation and the above specified surface tensions. The solid material parameters correspond to that of a nearly incompressible silicone gel with solid density $\rho_S = 12600\,\text{kg/m}^3$, Young's modulus $E = 3\,\text{kPa}$ and Poisson ratio $\nu = 0.499$. For the constitutive behavior of the solid we have chosen to use the *St. Venant-Kirchhoff* material model.

The computational domain for the present problem is a rectangular domain $\Omega = (\Omega^{\mathcal{F}} \cup \Omega^{\mathcal{S}}) \subset \mathbb{R}^2$ $(\Omega^{\mathcal{F}} \cap \Omega^{\mathcal{S}} = \emptyset)$ of width $w = 800\,\mu\text{m}$ and height $h = 400\,\mu\text{m}$. The fluid and solid subdomains $\Omega^{\mathcal{F}}$ and $\Omega^{\mathcal{S}}$ are vertically stacked and have the individual heights of $50\,\mu\text{m}$ and $350\,\mu\text{m}$, respectively (see Figure 6.4). For convenience we have horizontally centered the computational domain around the origin such that it holds $\Omega = (-400, 400) \times (0, 400)$. We model the computational domain with a two-patch NURBS mesh with a fluid and solid patch for the respective subdomains of Ω. The continuity across these two patches is $\mathcal{C}^0$, whereas the degree and regularity inside each patch follows that of the discrete approximation space used (cf. Section 6.4.1). We proceed with the specification of boundary conditions and require $u_i = 0$ and $v_i = 0$ on the top boundary of Ω, where the subscript $i = 1, 2$ denotes the components of the respective vectors. Moreover, we require $u_1 = 0$ and $v_1 = 0$ on the left and right boundaries of Ω, and $u_2 = 0$ and $v_2 = 0$ on its bottom boundary. We set the pressure at the upper left corner of the fluid domain $\Omega^{\mathcal{F}}$ to zero and enforce the *contact angle* and *no flux of chemical potential* boundary conditions (cf. eqn. (4.20)) on all boundaries of $\Omega^{\mathcal{F}}$. We use time step sizes (Δt) between $10^{-6}\,\text{s}$ and $10^{-5}\,\text{s}$ and use a uniform mesh that on the coarsest level (L0) exhibits 16×1 and 16×7 cells in the solid and fluid domains, respectively. This yields an initial mesh cell size of $h_0 = dx = dy = 5 \times 10^{-5}\,\text{m}$. Such a uniform partition of the computational domain obviously leaves plenty of room for optimization as the refinement required to reasonably resolve a "thin-enough" fluid-fluid interface propagates throughout the computational domain. This aspect may easily turn into a limiting factor for both the accuracy obtained and the computational effort one is ready to invest. The reason we left this aspect unoptimized as of writing this work is twofold:

First, our IGA-based computational framework is based on ("standard") B-splines/NURBS and therefore doesn't allow for reasonably locally confined mesh refinement due to the tensor product structure of these geometry representations. The computational framework is however already scheduled to be extended by Truncated Hierarchical B-splines or similar technologies – allowing us to get rid of this limitation. Second, any non-uniform partition of the computational NURBS mesh yields by definition grid cells whose aspect ratios are numerically less favorable than the perfect ones we obtain from uniform partitioning.

We proceed with the presentation and discussion of our computational results for three consecutive mesh refinement levels (L2, L3, L4). The number of degrees of freedom ($\mathrm{N}_{\mathrm{dof}}$) alongside the time step size (Δt) and diffuse interface width (ϵ) used at each level are listed in Table 6.1. Our computational results (with respect to level 4 of Table 6.1) picturing the displacement field $\boldsymbol{u}$, the pressure field p and the phase field φ at time $t = 21\,\mathrm{ms}$ are displayed in Figure 6.5. In the top row picture (a) the droplet's contour is shown to be cleanly delineated by a thin transition layer smoothly interpolating the inside ($\varphi = 1$) and outside ($\varphi = -1$) phase field values. Moreover, at the three-phase contact line, i.e. at the locations the fluid-fluid interface touches the solid, the vertical displacement field of the substrate shows its maximum value. This resonates well with the expected behavior of a soft substrate being wetted by a liquid droplet as presented in Section 6.2. A magnification of the computed wetting ridge together with the corresponding mesh deformation in the fluid and solid domains is displayed in the bottom row picture (c). The middle row picture (b) illustrates a low pressure region coinciding with the droplet's diffuse interface. At the three-phase contact line it can be thought of to exert a pull tangential to the fluid-fluid interface giving rise to the development of the wetting ridge. At this point it is noteworthy to mention that in order to obtain this low pressure rim, it is necessary to use the surface tension stress term $-\nabla \cdot (-\hat{\sigma}\varepsilon\, \nabla\varphi \otimes \nabla\varphi)$ as presented in equation (6.4a). The surface tension force term $\eta\nabla\varphi$ we have used in our pure two-phase flow computations (cf. equation (4.31a)) turns out to be inappropriate in this context as it yields a scaled pressure inside the diffuse interface region. The middle row picture (b) additionally shows two randomly chosen pressure values $p_i \approx -165.32$ and $p_o \approx -370.47$ sampled from the inside and outside (in the ambient fluid) of the liquid droplet. They yield a computationally obtained pressure difference of $(\Delta p)_c = p_i - p_o = 205.15$. Given the fluid-fluid surface tension $\gamma_{LA} = 46\,\mathrm{mN/m}$ and droplet radius $r = 225.5\,\mu\mathrm{m}$, the theoretical pressure difference between the interior and exterior of the droplet can be obtained from the Laplace-Young law (4.49) and amounts to $(\Delta p)_e = (46\,\mathrm{mN/m})/(225.5\,\mu\mathrm{m}) \approx 204.44\,\mathrm{N/m}^2\,(1\mathrm{Pa} = 1\mathrm{N/m}^2)$. This results in a 0.35% error between the theoretically predicted ($(\Delta p)_e$) and computationally obtained ($(\Delta p)_c$) pressure differences. For a more quantitative analysis, we have depicted in Figure 6.6 the temporal evolution of the droplet's wetting ridge for three consecutive mesh refinement levels (L2, L3, L4). In order to facilitate a contrasting juxtaposition, we have plotted for each mesh refinement level our computationally obtained soft substrate deformation profiles alongside the experimentally obtained data printed with black dots. Starting as an initially horizontal line, the profiles are shown to develop a cusp like shape around the three-phase contact located at a distance of $225.5\,\mu\mathrm{m}$ from

L	$\mathrm{N}_{\mathrm{dof}}^{\boldsymbol{uv}p}$	$\mathrm{N}_{\mathrm{dof}}^{\varphi\eta}$	$\mathrm{N}_{\mathrm{el}} : (16 \times 2^L) \times (8 \times 2^L)$	$h\,[\mathrm{m}]$	$\Delta t\,[\mathrm{s}]$	$\epsilon\,[\mathrm{m}]$
2	35685	14706	2048	1.250×10^{-5}	10^{-5}	1.0×10^{-5}
3	140997	58082	8192	6.250×10^{-6}	10^{-5}	5.0×10^{-6}
4	560517	230850	32768	3.125×10^{-6}	10^{-6}	2.5×10^{-6}

Table 6.1: Simulation parameters for the BFSI test case: Sessile glycerol droplet on a silicone deposit.

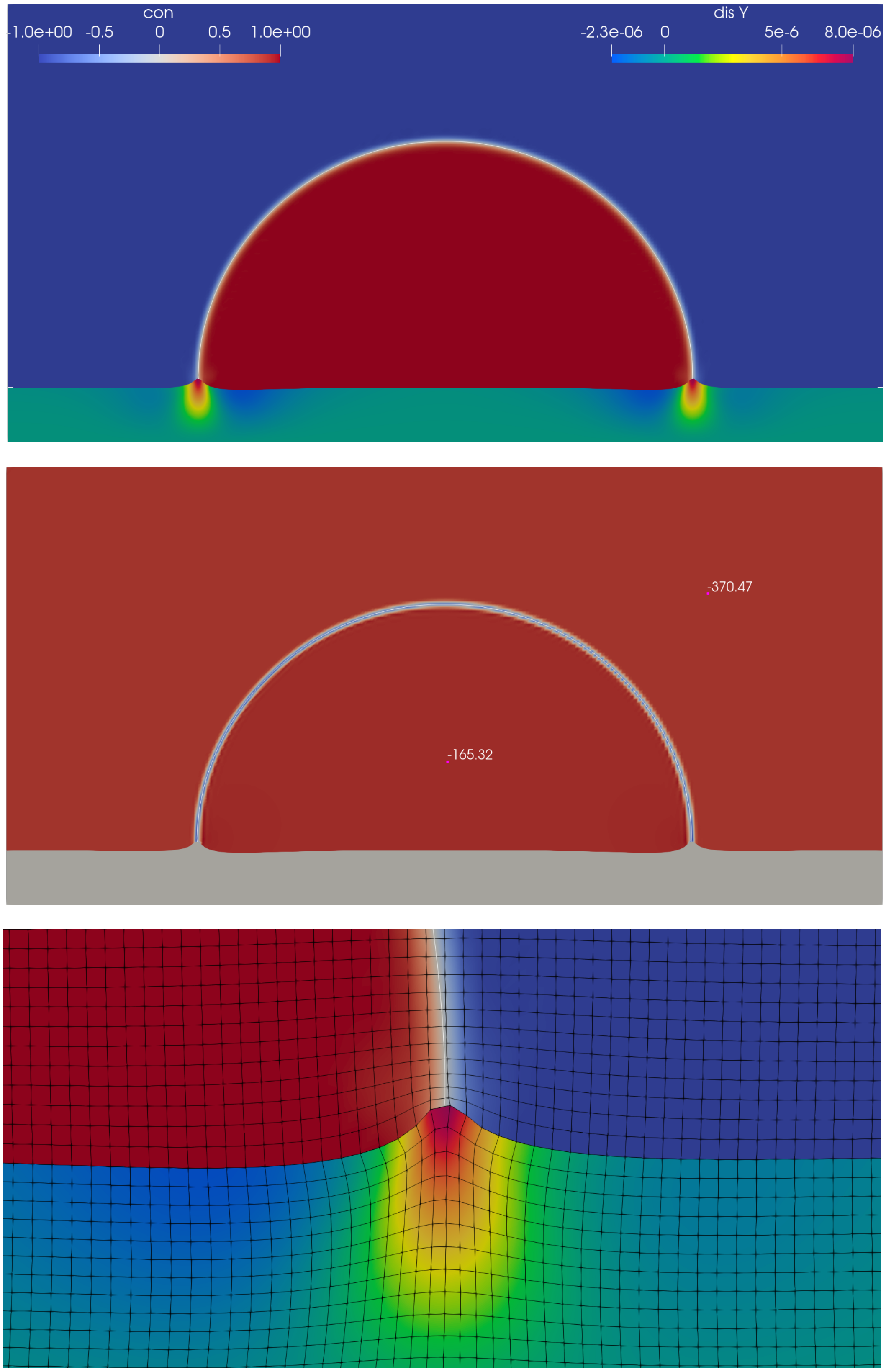

Figure 6.5: Sessile glycerol droplet on a silicone deposit at time $t = 21\,\mathrm{ms}$. Top row (a): Illustration of the displacement in the solid domain, and the phase field in the fluid domain. Middle row (b): Depiction of the low pressure rim along the droplet boundary and two randomly picked pressure values on either sides of the droplet. Bottom row (c): Enlarged view of the right end of the droplet for the portrayal of both the wetting ridge and mesh deformation.

the center of the droplet. As time progresses, so does the height of the wetting ridge and reaches by the end of simulation time at $t = 21\,\mathrm{ms}$ for levels L3 and L4 a height of approximately $8\,\mu\mathrm{m}$. The experimentally determined height for the tip of the wetting ridge exceeds this value and is approximately $9.5\,\mu\mathrm{m}$. The shapes of the wetting ridge profiles belonging to times $t = 0.04\,\mathrm{ms}$ (light blue), $t = 0.3\,\mathrm{ms}$ (orange), $t = 1.5\,\mathrm{ms}$ (magenta), $t = 3\,\mathrm{ms}$ (green), $t = 9\,\mathrm{ms}$ (blue), and $t = 21\,\mathrm{ms}$ (red) disclose a nonuniform increasing rate of the wetting ridge height. Starting very rapidly, the gains in height decay with increased simulation duration. Our results overestimate the dimple shape in the vicinity of the wetting ridge's left leg. The overshooting, however, seems to decay with increased mesh refinement. On a general note, the computations necessary to solve the present problem, fascinating as it is, turned out to be extremely tricky and challenging.

In particular, the approximation of the soft substrate's deformation, especially that of the wetting ridge's shape reacts quite sensitive to various simulation aspects, at least in the realm of our quasi monolithic BFSI model. For the reproduction of this or similar works we want to mention three aspects that need special care. First of all, for a decent approximation of the location, shape and height of the wetting ridge, it is indispensable to use the phase induced surface tension stress term in the Navier-Stokes equations (cf. page 223). Second, the diffuse fluid-fluid interface needs to be both thin enough and well enough resolved giving rise to the question what is the optimal number of elements across the diffuse interface with respect to accuracy and computational costs. Our choice for the relation between the diffuse interface width and mesh cell size h, namely $\epsilon = 4/5\,h$, has not seen any optimization. Besides, our uniform cell size NURBS mesh doesn't allow for highly localized refinement along the fluid-fluid interface – helping to improve the accuracy and to keep the number of degrees of freedom at bay.

Last but not least, for the *sessile droplet on soft substrate* application, we found it unexpectedly difficult to decide when the nonlinear iteration should be considered converged.

We briefly recall the stopping criterion $\|\mathcal{F}\| \leq \epsilon_{tol}$ in the nonlinear residual $(\mathcal{F})$ minimization loop (cf. algorithm 5.189) and present the threshold value used for all the results presented in this section: $\epsilon_{tol} = 10^{-10}$. Note that choosing a different threshold makes a non-negligible difference in the final wetting ridge shape leading to the conclusion that it reacts very sensitively to the nonlinear iteration threshold. This may be related to the fact that we are simulating changes in μm scale (height of the wetting ridge) where the implications of doing or not doing one or two more nonlinear iterations have a certain impact in the scale of the wetting ridge. In close relation to this aspect is the observation that even by the end of simulation the shape of the wetting ridge still showed tiniest changes – raising the question what can be considered a steady state solution of the present application. On that note, the soft substrate deformation profiles presented so far are still considered as intermediate results of a work in progress.

6.5.2 Dam break with elastic obstacle

Binary-fluid-structure interaction models such as the one presented in this work may be used for the modeling of FSI with free surfaces, involving totally or partially submerged solids. Such scenarios are typically of interest in mechanical, civil and offshore engineering – to name a few application fields. Recalling the force exchange between the fluid and solid in standard FSI, in BFSI the fluid-solid interface may be subject to abruptly changing interface loads caused by possibly large density and viscosity ratios of the involved fluids. Moreover, the motion of the fluid-fluid interface causes the load disparity to sweep along large portions of the fluid-solid interface and adds to the complexity of the overall dynamics. For a qualitative assessment of our BFSI method, we analyze the problem of a collapsing water column that hits an elastic wall as sketched in Figure 6.8. This prob-

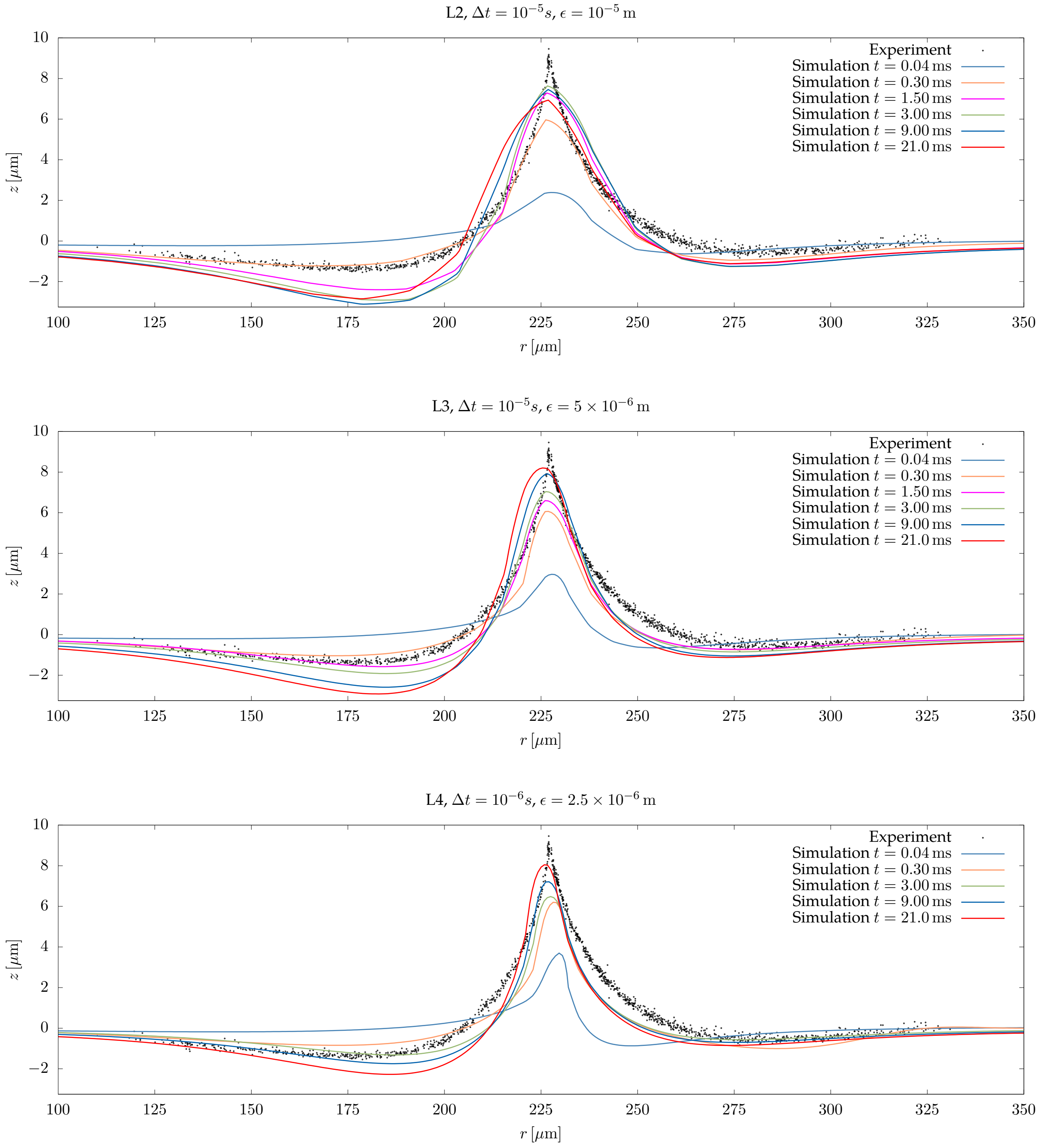

Figure 6.6: Development of the wetting ridge for a sessile droplet of radius $r = 225.5\,\mu$m.

lem has been previously analyzed with different numerical methods, see for instance [77, 155]. The details of the problem setup are as follows: A water column of width $0.146\,\mathrm{m}$ and height $0.292\,\mathrm{m}$ is placed on the lower left corner of a tank of width $0.584\,\mathrm{m}$ and height $0.365\,\mathrm{m}$. The water column is embedded in a matrix (or ambient) fluid that in the original setup [155] is modeled to be air. Facing a few yet untreated stability issues, we decreased for the time being the density and dynamic viscosity ratios of the involved fluids, and use the following fluid densities $\rho_L = 1000\,\mathrm{kg/m^3}$, $\rho_A = 10\,\mathrm{kg/m^3}$ and dynamic fluid viscosities $\mu_L = 1\,\mathrm{Ns/m^2}$, $\mu_A = 10^{-1}\,\mathrm{Ns/m^2}$ instead of the values for water and air[58]. As for phase field parameters, we use the following diffuse interface width $\epsilon = 5.959 \times 10^{-3}\,\mathrm{m}$ and mobility coefficient $D = 4 \times 10^{-5}\,\mathrm{m^2/s}$. Furthermore, we ignore surface tension effects as the large scales in this example render it for our considerations neglectable. For the constitutive behavior of the elastic wall we choose the St. Venant-Kirchhoff material model and set the solid density to $\rho_S = 2500\,\mathrm{kg/m^3}$, the Young's modulus to $E = 10^6\,\mathrm{Pa}$, and the Poisson ratio to $\nu = 0$. Our setup additionally deviates from the original configuration: We use a gravitational acceleration of $g = 9.81\,\mathrm{m/s^2}$, and require the normal component of the velocity function to be zero on on all domain boundaries, that is, on the bottom, right, top, and left domain boundaries. In accordance to the reference, we require zero pressure along the entire upper domain boundary.

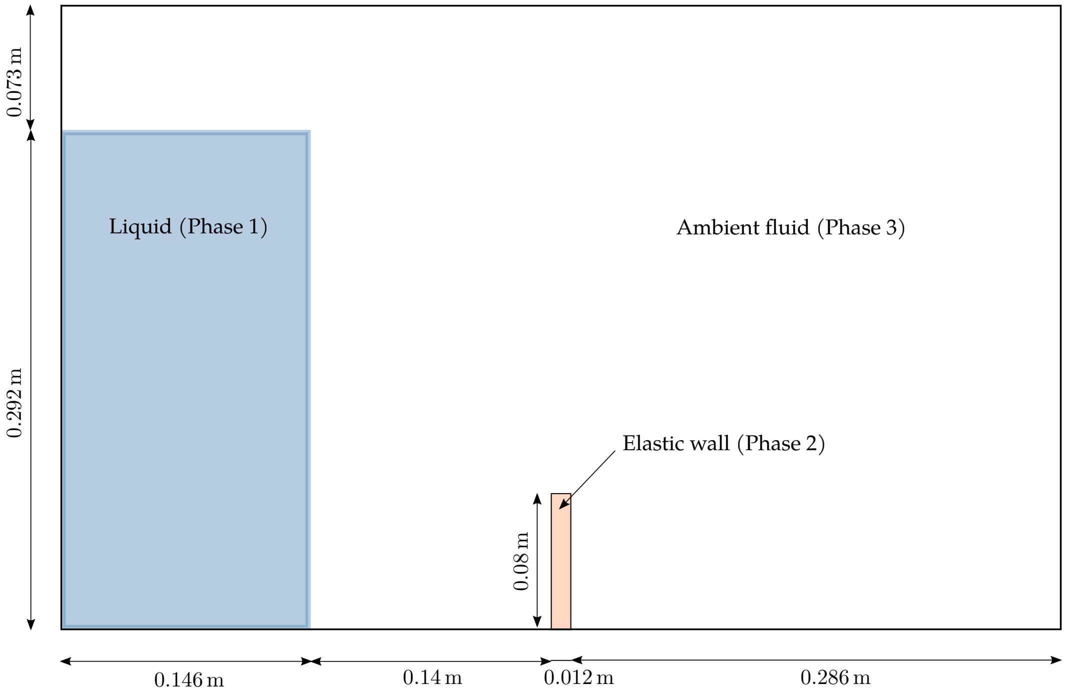

Figure 6.7: Sketch of the dam break with elastic obstacle problem.

In Figure 6.8, the advancing front along with the elastic deformation of the wall is shown for various time steps. The computational results shown, were performed with a $\mathcal{C}^0$ $\boldsymbol{\mathcal{N}}^{2,2}_{0,0}/\mathcal{N}^{1,1}_{0,0}$ NURBS space pair for the approximation of the velocity ($\boldsymbol{v}$) and pressure (p) functions on a uniform cell-size (cf. Figure 6.9) multi-patch NURBS mesh. For the approximation of the displacement ($\boldsymbol{u}$), phase field (φ), and chemical potential (η) functions, we used NURBS spaces whose degrees and continuities match that of the velocity space. For the time integration we used the 2nd order

---

[58] Density and dynamic viscosity of water and air (20 °C): $\rho_{\text{water}} = 998.21\,\mathrm{kg/m^3}$, $\rho_{\text{air}} = 1.2041\,\mathrm{kg/m^3}$, $\mu_{\text{water}} = 1.002 \times 10^{-3}\,\mathrm{Ns/m^2}$, $\mu_{\text{air}} = 1.8208 \times 10^{-5}\,\mathrm{Ns/m^2}$.

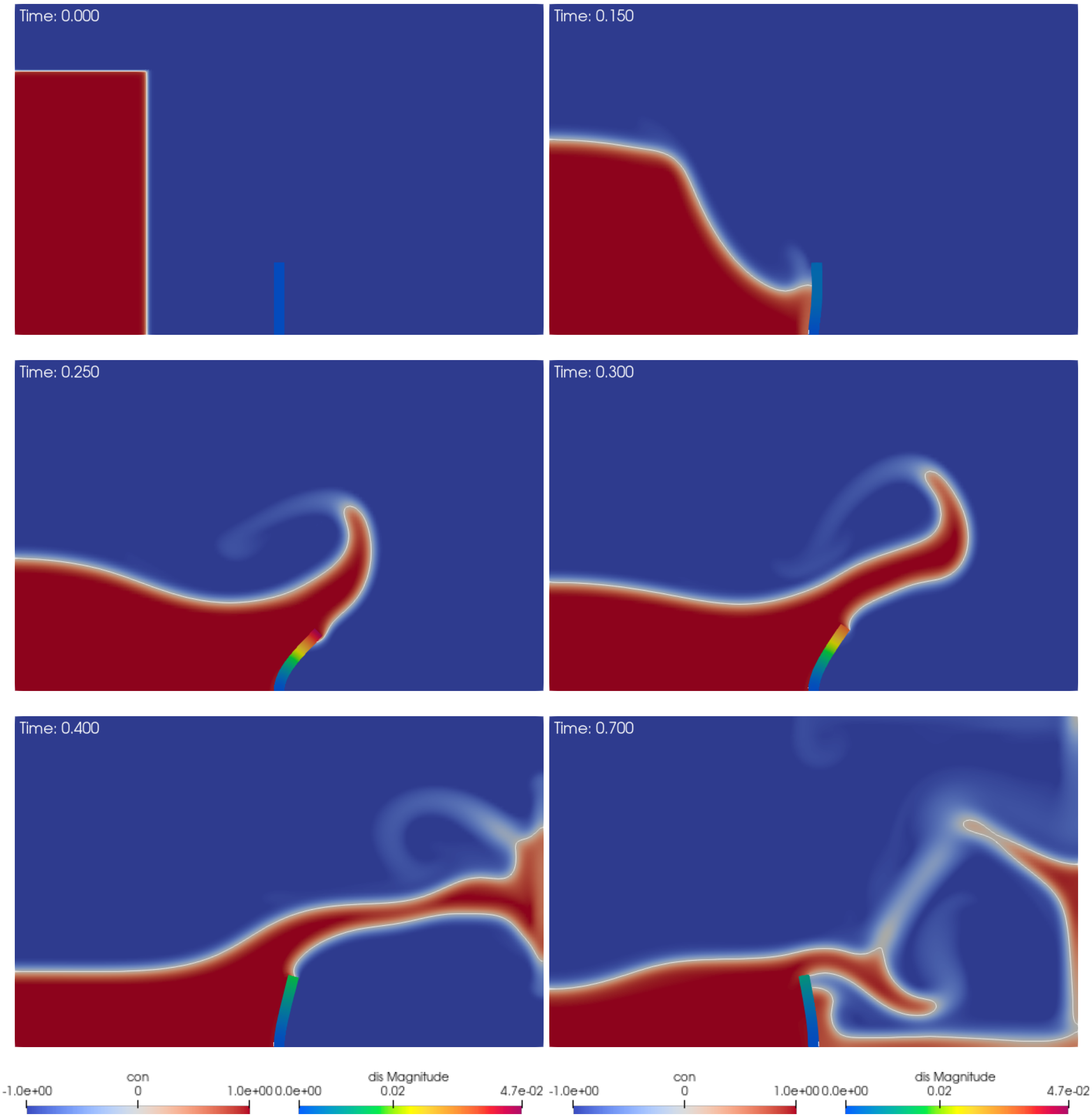

Figure 6.8: Wave interaction with the elastic wall at various time steps.

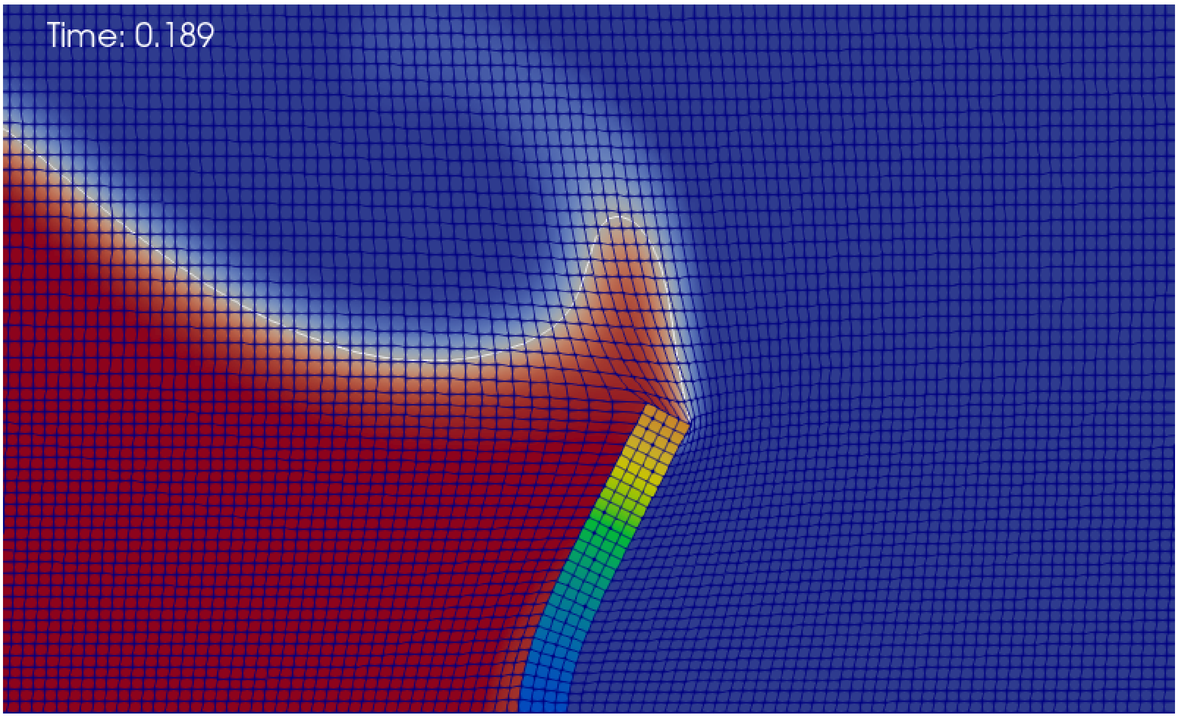

Figure 6.9: Dam break with elastic obstacle: Uniform cell-size mesh whose motion is controlled by the nonlinear harmonic mesh motion PDE (5.112) in combination with (5.114).

accurate implicit Crank-Nicolson scheme with a time step size of $\Delta t = 10^{-3}\,\mathrm{s}$. The results depicted in Figure 6.8 were computed on mesh refinement level 2 of our initial NURBS mesh yielding $\mathrm{N}_{el} = 18816$ elements. With regard to the chosen discrete approximation spaces, this amounts to the following numbers of degrees of freedom: $\mathrm{N}^{\boldsymbol{u}}_{dof} = 151698, \mathrm{N}^{\boldsymbol{v}}_{dof} = 151698, \mathrm{N}^{p}_{dof} = 19109$, and $\mathrm{N}^{\varphi}_{dof}, \mathrm{N}^{\eta}_{dof} = 75457$. Note that the velocity and displacement functions are defined on fluid and solid subdomains, while the phase field and chemical potential functions are defined only on the fluid part of the domain.

In [155] the temporal evolution of the displacement of the elastic wall's upper left corner is specified that in principle allows a more quantitative analysis to be performed. However, the relaxations we had to make for the fluid density and dynamic viscosity ratios, unfortunately render it infeasible to perform a comparison with [155], as we literally consider a different binary-fluid. The difficulties we presently face with the material settings of water and air, and a uniform cell-size mesh, may be alleviated by means of local refinement (e.g. with Truncated Hierarchical B-splines) around the elastic wall. Moreover, as shown in Figure 6.9, using the present fluid densities and viscosities settings and working with the nonlinear harmonic mesh motion model[59] leads to a few highly squeezed elements in the vicinity of the upper right corner of the elastic wall. The distortion is evidently caused by the bending of the elastic wall. This issue is likely to be aggravated by a higher fluid density ratio such as that of water and air that is expected to yield a higher momentum to the collapsing fluid column with the causal consequence of a larger bending of the elastic wall. An alternative mesh motion model such as the Linear Elastic or the Biharmonic mesh motion model may yield better results for this application.

---

[59] with $\alpha_u = 10^{-8}$ in Equation (5.114)

6.6 Summary and conclusions

The main objective of the work presented in this thesis was the development of a computational model and simulation technique capable of capturing the complex physics behind the intriguing phenomena of elasto-capillarity. This multiphysics problem has an inherently high complexity as it combines two-phase flow with fluid-structure interaction and poses an enormous challenge for corresponding computational simulations. Our approach to tackle this problem was to systematically decompose the overall problem into smaller and independent units or building blocks (cf. Figure 1.2) and to address each of them individually before ultimately integrating all partial results for the final objective. We devoted dedicated chapters to the *single-phase flow*, *two-phase flow* and *fluid-structure interaction* building blocks, where in each block we presented the respective problem formulation, followed by a proposed mathematical model alongside a numerical solution approach, and eventually rounded with extensive numerical tests for validation purposes.

For the design of a computational model for binary-fluid-structure interaction we weighed up different two-phase flow modeling approaches (e.g. volume-of-fluid, front tracking, immersed boundary, level-set and phase field (a.k.a. diffuse interface) methods) in terms of their overall suitability and decided to adopt the Cahn-Hilliard phase field model as an essential component in our BFSI model. Our primary motivation for working with the phase field approach was given by virtue of the fact that the phase field method has a solid theoretical foundation in thermodynamics and statistical mechanics. It may therefore be perceived as a physically motivated extension of the level-set or volume-of-fluid methods. The Cahn-Hilliard phase field model is based on the minimization of a fluid free energy functional and globally conserves the phase field variable φ. Diffuse interface models allow the modeling of interfacial forces as continuum forces with the effect that delta-function forces and discontinuities at the interface are smoothed by smearing them over thin yet numerically resolvable layers. Moreover, they describe the surface tension as the excess free energy per unit surface area concentrated at the interface. Note that in conventional sharp interface methods the surface tension must be explicitly accounted for. Moreover, when it comes to topological changes and moving contact-line problems, conventional sharp interface two-phase flow models with no-slip boundary condition typically suffer from a singularity at the contact line. The solid physical background of the Cahn-Hilliard phase field method, its approach to handle interfacial forces, its natural support for the imposition of a contact angle, and its ability to easily handle moving contact lines and topological transitions like droplet coalescence or break-up without any need for reinitialization (e.g. redistancing in the level-set method), led us to the decision to adopt this phase field model in this work. Besides, the firm thermodynamic structure of phase field models facilitates model extensions. For instance, the fluid free energy functional may be modified with respect to the constitutive equations for more complex rheologies (e.g. viscoelasticity). Committing ourselves to a phase field-based two-phase flow model, immediately raised the question which of the many Navier-Stokes-Cahn-Hilliard models to use. These models differ from each other by a group of quite diverse criteria, one of them being e.g. the treatment of the density, that is, considering it constant or variable. Moreover, not all models are based on a divergence-free velocity field and the modeling of extra contributions of additional forces to the stress tensor such as e.g. the surface tension induced capillary forces is quite varied across the models. While for some models no energy inequalities are known, others are shown to admit an energy law and to be thermodynamically consistent. For the latter to hold, some of the affected models are extended by additional terms. Each of these models has its own advantages and disadvantages in terms of suitability for particular flow scenarios, physical consistency and implementation simplicity. That said, the identification of a reasonable model in the context of this work turned up to be a time consuming and tedious process. In this thesis we have provided a comparison of these models which can be seen as a consolidated inventory with emphasis on the most essential features and shortcomings of each model and its overall suitability for our BFSI model. The availability of such an analysis would have been very useful for ourselves in the stage of entering the field of phase field-based two-phase flow modeling. Moreover, we have provided in this work a very detailed description of the numerical treatment of a selected NSCH model that provides all layers of information that are necessary for the reproduction of this work. This work also provides extensive numerical two-phase flow tests that on the one hand are used to validate the achieved results, and on the other hand show the dependence of the results on sensitive model parameters such as mobility and diffuse interface width. We showed that despite the hassle of having to deal with these two tunable parameters, the NSCH model is very well suited for the modeling of challenging two-phase flow problems and has all the prerequisites to mix in its merits into a binary-fluid-structure interaction model.

The next subproblem considered in this work was fluid-structure interaction. Since from a numerical analysis point of view, partitioned FSI approaches are known to suffer from non-robustness and exhibit poor convergence properties, the FSI component of our BFSI model was required to be of monolithic type, that is, required to solve the fluid and structural dynamics equations simultaneously. In FSI one is confronted with the dilemma, that the fluid part of the problem formulation is based on an Eulerian description of motion, whereas it is very natural and common to employ a Lagrangian description of motion for the derivation of the structural dynamics equations. Considering the fact that one is willing to solve both problems simultaneously, the discrepancy induced by the respective reference frames, poses a problem. Moreover, the solid domain is subject to deformation and motion as a natural consequence of the load applied to the solid body. This, however, implies a deformation and motion of the fluid domain as well, since these two domains need to stay attached to each other. In order to address these issues we re-expressed the fluid problem (Navier-Stokes equations) in Arbitrary-Lagrangian-Eulerian formulation (set in the undeformed configuration) and used a nonlinear harmonic mesh motion model for the motion of the fluid domain. The reformulation of the Navier-Stokes equations with respect to a "structure-appropriate" framework massively added to its nonlinearity, as almost all of its terms turned nonlinear due to the resulting couplings to unknowns from the solid deformation problem. We have provided in this thesis a very detailed description of the mathematical model and numerical treatment of this problem including the treatment of its inherent nonlinearity. In analogy to the two-phase flow part, we performed extensive numerical tests for the validation of the corresponding FSI results. We showed that the monolithic FSI part of our BFSI model is very robust and yields results of very high accuracy.

Ultimately, we presented in this thesis a "quasi-monolithic" computational model for binary-fluid-structure interaction based on an Arbitrary-Lagrangian-Eulerian formulation of the Navier-Stokes-Cahn-Hilliard equations combined with the equations of nonlinear Elastodynamics, and an additional PDE for mesh motion. In the course of designing the BFSI computational model, we made the call to separately solve the phase field problem from the rest of the involved partial differential equations. The remaining problems, that is, the variable fluid density and viscosity fluid-structure interaction and the mesh motion problems are then solved monolithically. This evidently weakens to a certain degree the monolithic nature of our approach, but yields a set of benefits that rendered it attractive and worthy to follow. However, the proposed computational model is not tied to separately solving the phase field problem and can be adapted to operate in a bona fide monolithic manner. The handling of the FSI coupling conditions in our BFSI model is inherited from our monolithic FSI model. Note that in our monolithic FSI model the continuity of normal stresses condition is automatically satisfied in a weak sense by the choice of matching test functions along the fluid-solid interface. In terms of difference to standard FSI, we deal in BFSI with a two-phase flow system that additionally requires the consideration of the two-phase flow surface tension force contribution. These contributions are, however, accounted for by the inclusion of a phase field-based surface tension stress term in the Navier-Stokes-Cahn-Hilliard equations. From our experience with monolithic FSI methods that involve matching test functions along the fluid-solid interface, trying to explicitly enforce the continuity of normal stresses along the fluid-solid interface with additional equations is problematic as one would then have too many conditions at the interface. We assessed our BFSI model based on an elasto-capillary fluid-structure interaction scenario that has been experimentally investigated and for which a comprehensive set of measurement data is available. We presented for this setup mesh converged results that are – according to our classification – acceptable, but leave space for improvements. We believe this is attributed to the following two aspects: Firstly, as of submitting this work, the proposed BFSI model is not entirely complete. More specifically, we consider the pull back reformulation of the contact angle boundary condition to a "structure-appropriate" framework as not complete yet. The presently used expression may have a negative impact on the quality of the results. Secondly, we employ an equidistant cell size mesh that is far from optimal in terms of high resolution of local features through refinement around the three phase interface region. We expect significant improvements of the results with local mesh refinement along the fluid-fluid and fluid-solid interfaces with technologies such as Truncated Hierarchical B-splines, for instance. We also showcased that our model may in principle be used for the modeling of FSI with free surfaces. We draw the conclusion that the BFSI model presented in this work is a very robust and well suited framework for the simulation of elasto-capillarity phenomena. Moreover, as far as techniques for the numerical treatment of partial differential equations are concerned, Isogeometric Analysis has been the foundation for the numerical analysis of all problems tackled in this work. This technology proved to be very robust and powerful for our purposes. Besides, featuring very interesting traits like support for the setup of discrete approximation spaces of possibly high degrees and continuities, the ability to perform computations directly on representations of exact geometries (NURBS, etc.), and the intrinsic support for complex computational geometries, rendered this approach very attractive for this work and future works. All numerical results presented in this work have been computed with an Isogeometric Finite Element Analysis kernel that the author has developed from scratch in the context of this thesis.

Bibliography

[1] H. Abels, H. Garcke, and G. Grün. Thermodynamically Consistent, Frame Indifferent Diffuse Interface Models For Incompressible Two-Phase Flows With Different Densities. *Mathematical Models and Methods in Applied Sciences*, 22(03):1150013, 2012.

[2] R. A. Adams and J. J. F. Fournier. *Sobolev Spaces*. Pure and Applied Mathematics. Elsevier Science, 2003.

[3] S. Aland. *Modelling of two-phase flow with surface active particles*. PhD thesis, Technische Universität Dresden, May 2012.

[4] S. Aland. Time integration for diffuse interface models for two-phase flow. *Journal of Computational Physics*, 262:58 – 71, 2014.

[5] S. Aland. Phase field models for two-phase flow with surfactants and biomembranes. In *Transport Processes at Fluidic Interfaces*, pages 271–290. Springer, 2017.

[6] S. Aland and A. Voigt. Benchmark computations of diffuse interface models for two-dimensional bubble dynamics. *International Journal for Numerical Methods in Fluids*, 69(3):747–761, 2012.

[7] S. V. Apte, M. Martin, and N. A. Patankar. A numerical method for fully resolved simulation (FRS) of rigid particle–flow interactions in complex flows. *Journal of Computational Physics*, 228(8):2712 – 2738, 2009.

[8] F. Auricchio, L. Beirão Da Veiga, T. J. R. Hughes, A. Reali, and G. Sangalli. Isogeometric collocation methods. *Mathematical Models and Methods in Applied Sciences*, 20, No. 11:2075–2107, 2010.

[9] G. Avalos, I. Lasiecka, and R. Triggiani. Higher regularity of a coupled parabolic-hyperbolic fluid-structure interactive system. *Georgian Mathematical Journal Volume*, 15:403–437, 01 2008.

[10] G. Avalos and R. Triggiani. *The coupled PDE system arising in fluid/structure interaction. I. Explicit semigroup generator and its spectral properties*, volume 440, pages 15–54. 01 2007.

[11] G. Avalos and R. Triggiani. Semigroup well-posedness in the energy space of a parabolic-hyperbolic coupled stokes–lamé pde system of fluid-structure interaction. *Discrete and Continuous Dynamical Systems - Series S*, 2:417–447, 09 2009.

[12] G. Avalos and R. Triggiani. Fluid-structure interaction with and without internal dissipation of the structure: A contrast study in stability. 2013.

[13] V. E. Badalassi, H. D. Ceniceros, and S. Banerjee. Computation of multiphase systems with phase field models. *Journal of Computational Physics*, 190(2):371 – 397, 2003.

[14] J. W. Banks, W. D. Henshaw, A.K. Kapila, and D. W. Schwendeman. An added-mass partition algorithm for fluid–structure interactions of compressible fluids and nonlinear solids. *Journal of Computational Physics*, 305:1037 – 1064, 2016.

[15] J. W. Banks, W. D. Henshaw, and D. W. Schwendeman. Deforming composite grids for solving fluid structure problems. *Journal of Computational Physics*, 231(9):3518 – 3547, 2012.

[16] Y. Bazilevs, L. Beirão Da Veiga, J. A. Cottrell, T. J. R. Hughes, and G. Sangalli. Isogeometric Analysis: Approximation, stability and error estimates for h-refined meshes. *Mathematical Models and Methods in Applied Sciences*, 16(7):1031–1090, 2006.

[17] Y. Bazilevs, V. M. Calo, T. J. R. Hughes, and Y. Zhang. Isogeometric fluid-structure interaction: Theory, algorithms, and computations. *Computational Mechanics*, 43(1):3–37, 2008.

[18] Y. Bazilevs, K. Takizawa, and T. E. Tezduyar. *Computational Fluid-Structure Interaction: Methods and Applications*. Wiley, 2013.

[19] D. Bhaga and M. E. Weber. Bubbles in viscous liquids: shapes, wakes and velocities. *Journal of Fluid Mechanics*, 105:61–85, 4 1981.

[20] O. Botella and R. Peyret. Benchmark spectral results on the lid-driven cavity flow. *Computers & Fluids*, 27(4):421–433, 1998.

[21] F. Boyer. A theoretical and numerical model for the study of incompressible mixture flows. *Computers and Fluids*, 31(1):41–68, 2002.

[22] D. Braess. *Finite Elements: Theory, Fast Solvers, and Applications in Solid Mechanics*. Cambridge University Press, 3rd edition, 2007.

[23] S. Brenner and L. R. Scott. *The Mathematical Theory of Finite Element Methods*. Texts in Applied Mathematics. Springer New York, 2002.

[24] M. Breuer, G. De Nayer, M. Münsch, T. Gallinger, and R. Wüchner. Fluid–structure interaction using a partitioned semi-implicit predictor–corrector coupling scheme for the application of large-eddy simulation. *Journal of Fluids and Structures*, 29:107 – 130, 2012.

[25] C.-H. Bruneau and M. Saad. The 2D lid-driven cavity problem revisited. *Computers & Fluids*, 35(3):326–348, 2006.

[26] J. Bueno, Y. Bazilevs, R. Juanes, and H. Gomez. Wettability control of droplet durotaxis. *Soft Matter*, 14:1417–1426, 2018.

[27] J. Bueno, C. Bona-Casas, Y. Bazilevs, and H. Gomez. Interaction of complex fluids and solids: theory, algorithms and application to phase-change-driven implosion. *Computational Mechanics*, 55(6):1105–1118, Jun 2015.

[28] J. Bueno, H. Casquero, Y. Bazilevs, and H. Gomez. Three-dimensional dynamic simulation of elastocapillarity. *Meccanica*, 53(6):1221–1237, 2018.

[29] A. Buffa, C. De Falco, and G. Sangalli. IsoGeometric Analysis: Stable elements for the 2D Stokes equation. *International Journal for Numerical Methods in Fluids*, 65(11-12):1407–1422, 2011.

[30] A. Buffa and G. Sangalli. *IsoGeometric Analysis: A New Paradigm in the Numerical Approximation of PDEs - Cetraro, Italy 2012*, volume 2161. Springer International Publishing, 1st edition, 2016.

[31] P. Causin, J. F. Gerbeau, and F. Nobile. Added-mass effect in the design of partitioned algorithms for fluid-structure problems. *Computer Methods in Applied Mechanics and Engineering*, 194(42-44):4506–4527, 2005.

[32] L. Chen, S. V. Garimella, J. A. Reizes, and E. Leonardi. The development of a bubble rising in a viscous liquid. *Journal of Fluid Mechanics*, 387:61–96, 1999.

[33] P. G. Ciarlet. *Mathematical Elasticity Volume I: Three-dimensional elasticity*, volume 20 of *Studies in Mathematics and its Applications*. Elsevier Science Pulishers B. V., 1988.

[34] R. Clift, J. R. Grace, and M. E. Weber. *Bubbles, Drops, and Particles*. Academic Press, 1978.

[35] M. Coquerelle and G.-H. Cottet. A vortex level set method for the two-way coupling of an incompressible fluid with colliding rigid bodies. *Journal of Computational Physics*, 227(21):9121 – 9137, 2008. Special Issue Celebrating Tony Leonard's 70th Birthday.

[36] G.-H. Cottet, E. Maitre, and T. Milcent. Eulerian formulation and level set models for incompressible fluid-structure interaction. *ESAIM: M2AN*, 42(3):471–492, 2008.

[37] J. A. Cottrell, T. J. R. Hughes, and Y. Bazilevs. *Isogeometric Analysis: Toward Integration of CAD and FEA*. Wiley Publishing, 1st edition, 2009.

[38] J. A. Cottrell, T. J. R. Hughes, and A. Reali. Studies of refinement and continuity in isogeometric structural analysis. *Computer Methods in Applied Mechanics and Engineering*, 196(41-44):4160–4183, 2007.

[39] D. Coutand and S. Shkoller. Motion of an Elastic Solid inside an Incompressible Viscous Fluid. *Archive for Rational Mechanics and Analysis*, 176(1):25–102, 2005.

[40] D. Coutand and S. Shkoller. The Interaction between Quasilinear Elastodynamics and the Navier-Stokes Equations. *Archive for Rational Mechanics and Analysis*, 179(3):303–352, 2006.

[41] P-.G. de Gennes. Wetting: statics and dynamics. *Rev. Mod. Phys.*, 57:827–863, Jul 1985.

[42] P.-G. de Gennes, F. Brochard-Wyart, and D. Quere. *Capillarity and Wetting Phenomena: Drops, Bubbles, Pearls, Waves*. Springer, 2010.

[43] A. Debussche and L. Dettori. On the cahn-hilliard equation with a logarithmic free energy. *Nonlinear Analysis*, 24(10):1491–1514, 1995.

[44] DFG benchmark 2D-1 (RE20, laminar). `http://www.featflow.de/en/benchmarks/cfdbenchmarking/flow/dfg_benchmark_re20.html` [Online; accessed 01-Oct-2014].

[45] DFG benchmark 2D-2 (RE100, periodic). `http://www.featflow.de/en/benchmarks/cfdbenchmarking/flow/dfg_benchmark2_re100.html` [Online; accessed 01-Oct-2014].

[46] H. Ding, P. D. M. Spelt, and C. Shu. Diffuse interface model for incompressible two-phase flows with large density ratios. *Journal of Computational Physics*, 226(2):2078 – 2095, 2007.

[47] J. Donea, A. Huerta, J.-Ph. Ponthot, and A. Rodríguez-Ferran. *Arbitrary Lagrangian–Eulerian Methods*, chapter 14. American Cancer Society, 2004.

[48] Q. Du, M. D. Gunzburger, L. S. Hou, and J. Lee. Analysis of a linear fluid-structure interaction problem. *Discrete and Continuous Dynamical Systems - DISCRETE CONTIN DYN SYST*, 9, 05 2003.

[49] Q. Du, M. D. Gunzburger, L. S. Hou, and J. Lee. Semidiscrete finite element approximations of a linear fluid-structure interaction problem. *Society for Industrial and Applied Mathematics*, 42:1–29, 01 2004.

[50] N. Dubash and I. Frigaard. Conditions for static bubbles in viscoplastic fluids. *Physics of Fluids*, 16(12):4319–4330, 2004.

[51] T. Dunne. An Eulerian approach to fluid–structure interaction and goal-oriented mesh adaptation. *International Journal for Numerical Methods in Fluids*, 51(9-10):1017–1039, 2006.

[52] T. Dunne. *Adaptive Finite Element Approximation of Fluid-Structure Interaction Based on Eulerian and Arbitrary Lagrangian-Eulerian Variational Formulations*. PhD thesis, University of Heidelberg, June 2007.

[53] L. F. R. Espath, A. F. Sarmiento, P. Vignal, B. O. N. Varga, A. M. A. Cortes, L. Dalcin, and V. M. Calo. Energy exchange analysis in droplet dynamics via the navier–stokes–cahn–hilliard model. *Journal of Fluid Mechanics*, 797:389–430, 6 2016.

[54] J. A. Evans and T. J. R. Hughes. Isogeometric Divergence-conforming B-splines for the Steady Navier-Stokes Equations. *Mathematical Models and Methods in Applied Sciences*, 23(8):1421–1478, 2013.

[55] H. Fang, Z. Wang, Z. Lin, and M. Liu. Lattice Boltzmann method for simulating the viscous flow in large distensible blood vessels. *Phys. Rev. E*, 65:051925, May 2002.

[56] Z.-G. Feng and E. E. Michaelides. The immersed boundary-lattice Boltzmann method for solving fluid–particles interaction problems. *Journal of Computational Physics*, 195(2):602 – 628, 2004.

[57] M. Á. Fernández and M. Moubachir. A newton method using exact jacobians for solving fluid–structure coupling. *Computers & Structures*, 83(2):127 – 142, 2005. Advances in Analysis of Fluid Structure Interaction.

[58] `http://www.featflow.de/en/benchmarks/cfdbenchmarking/fsi_benchmark.html` [Online; accessed 06-May-2019].

[59] `http://www.featflow.de/en/benchmarks/cfdbenchmarking/bubble.html` [Online; accessed 08-Feb-2016].

[60] J. E. Flaherty. Lecture Notes - CSCI-6860 / MATH-6860: Finite Element Analysis. Rensselaer Polytechnic Institute, `http://www.cs.rpi.edu/~flaherje`, 2000.

[61] S. Frei. *Eulerian finite element methods for interface problems and fluid-structure interactions*. PhD thesis, 2016.

[62] T. G. Gallinger. *Effiziente Algorithmen zur partitionierten Lösung stark gekoppelter Probleme der Fluid-Struktur-Wechselwirkung*. PhD thesis, Technical University of Munich, November 2010.

[63] S. Ganesan, G. Matthies, and L. Tobiska. On spurious velocities in incompressible flow problems with interfaces. *Computer Methods in Applied Mechanics and Engineering*, 196(7):1193–1202, 2007.

[64] F. Gazzola and M. Squassina. Global solutions and finite time blow up for damped semilinear wave equations. *Annales de l'Institut Henri Poincare (C) Non Linear Analysis*, 23(2):185 – 207, 2006.

[65] U. Ghia, K. N. Ghia, and C. T. Shin. High-Re Solutions for Incompressible Flow using the Navier-Stokes Equations and a Multigrid Method. *Journal of Computational Physics*, 48(3):387–411, 1982.

[66] F. Gibou and C. Min. Efficient symmetric positive definite second-order accurate monolithic solver for fluid/solid interactions. *Journal of Computational Physics*, 231(8):3246 – 3263, 2012.

[67] R. Glowinski, T.-W. Pan, T. I. Hesla, and D. D. Joseph. A distributed lagrange multiplier/fictitious domain method for particulate flows. *International Journal of Multiphase Flow*, 25(5):755 – 794, 1999.

[68] R. Glowinski, T.-W. Pan, and J. Periaux. A fictitious domain method for external incompressible viscous flow modeled by navier-stokes equations. *Computer Methods in Applied Mechanics and Engineering*, 112(1):133 – 148, 1994.

[69] C. Grandmont. Existence for a three-dimensional steady state fluid-structure interaction problem. *Journal of Mathematical Fluid Mechanics*, 4(1):76–94, Feb 2002.

[70] J.-L. Guermond and L. Quartapelle. A projection FEM for variable density incompressible flows. *Journal of Computational Physics*, 165(1):167 – 188, 2000.

[71] Z. Guo, P. Lin, and J. S. Lowengrub. A numerical method for the quasi-incompressible cahn–hilliard–navier–stokes equations for variable density flows with a discrete energy law. *Journal of Computational Physics*, 276:486 – 507, 2014.

[72] M. E. Gurtin. *An Introduction to Continuum Mechanics*, volume 158 of *Mathematics in Science and Engineering*. Academic Press, 1981.

[73] M. E. Gurtin. *Topics in Finite Elasticity*. Society for Industrial and Applied Mathematics, 1981.

[74] M. E. Gurtin, D. Polignone, and J. Vinals. Two-phase binary fluids and immiscible fluids described by an order parameter. *Mathematical Models and Methods in Applied Sciences*, 6(6):815–831, 1996.

[75] H. Gómez, V. M. Calo, Y. Bazilevs, and T. J. R. Hughes. Isogeometric Analysis of the Cahn-Hilliard phase-field model. *Computer Methods in Applied Mechanics and Engineering*, 197(49-50):4333–4352, 2008.

[76] H. Gómez, T. J. R. Hughes, X. Nogueira, and V. M. Calo. Isogeometric analysis of the isothermal Navier-Stokes-Korteweg equations. *Computer Methods in Applied Mechanics and Engineering*, 199(25-28):1828–1840, 2010.

[77] R. Haelterman, A. Bogaers, J. Degroote, and N. Boutet. Quasi-newton methods for the acceleration of multi-physics codes. *International journal of pure and applied mathematics*, 47:352–360, 2017.

[78] C. W. Hirt and B. D. Nichols. Volume of fluid (VOF) method for the dynamics of free boundaries. *Journal of Computational Physics*, 39(1):201 – 225, 1981.

[79] P. C. Hohenberg and B. I. Halperin. Theory of dynamic critical phenomena. *Reviews of Modern Physics*, 49:435–479, Jul 1977.

[80] B. S. Hosseini and M. Möller. Phase Field-Based Incompressible Two-Component Liquid Flow Simulation. In H. van Brummelen, A. Corsini, S. Perotto, and G. Rozza, editors, *Numerical Methods for Flows. Lecture Notes in Computational Science and Engineering*, volume 132, pages 165–176. Springer, Cham, 2020. doi:10.1007/978-3-030-30705-9_15.

[81] B. S. Hosseini, M. Möller, and S. Turek. Isogeometric Analysis of the Navier-Stokes equations with Taylor-Hood B-spline elements. *Applied Mathematics and Computation*, 267:264 – 281, 2015.

[82] B. S. Hosseini, S. Turek, M. Möller, and C. Palmes. Isogeometric Analysis of the Navier–Stokes–Cahn–Hilliard equations with application to incompressible two-phase flows. *Journal of Computational Physics*, 348:171–194, 2017.

[83] J. Hron and S. Turek. A MONOLITHIC FEM SOLVER FOR AN ALE FORMULATION OF FLUID-STRUCTURE INTERACTION WITH CONFIGURATION FOR NUMERICAL BENCHMARKING. 2006.

[84] J. Hron and S. Turek. A Monolithic FEM/Multigrid Solver for an ALE Formulation of Fluid–Structure Interaction with Applications in Biomechanics. In H.-J. Bungartz and M. Schäfer, editors, *Fluid–Structure Interaction: Modelling, Simulation, Optimisation* (*Lecture Notes in Computational Science and Engineering*), volume 53, pages 146–170. Springer, Berlin, Heidelberg, 2006.

[85] P. Hu, L. Xue, S. Mao, R. Kamakoti, H. Zhao, N. Dittakavi, K. Ni, Z. Wang, and Q. Li. Material Point Method Applied to Fluid-Structure Interaction (FSI)/Aeroelasticity Problems. In *48th AIAA Aerospace Sciences Meeting Including the New Horizons Forum and Aerospace Exposition*. American Institute of Aeronautics and Astronautics, 01 2010.

[86] J. Huang, M. Juszkiewicz, W. H. de Jeu, E. Cerda, T. Emrick, N. Menon, and T. P. Russell. Capillary wrinkling of floating thin polymer films. *Science*, 317(5838):650–653, August 2007.

[87] T. J. R. Hughes. *The Finite Element Method: Linear Static and Dynamic Finite Element Analysis*. Dover Civil and Mechanical Engineering. Dover Publications, 2012.

[88] S. Hysing, S. Turek, D. Kuzmin, N. Parolini, E. Burman, S. Ganesan, and L. Tobiska. Quantitative benchmark computations of two-dimensional bubble dynamics. *International Journal for Numerical Methods in Fluids*, 60(11):1259–1288, 2009.

[89] J. Giesselmann and T. Pryer. Energy consistent discontinuous galerkin methods for a quasi-incompressible diffuse two phase flow model. *ESAIM: Mathematical Modeling and Numerical Analysis*, 49(1):275–301, 2015.

[90] D. Jacqmin. Calculation of two-phase navier–stokes flows using phase-field modeling. *Journal of Computational Physics*, 155(1):96–127, 1999.

[91] D. Jacqmin. Contact-line dynamics of a diffuse fluid interface. *Journal of Fluid Mechanics*, 402:57–88, 2000.

[92] E. R. Jerison, Y. Xu, L. A. Wilen, and E. R. Dufresne. Deformation of an Elastic Substrate by a Three-Phase Contact Line. *Phys. Rev. Lett.*, 106:186103, May 2011.

[93] V. John. Higher order finite element methods and multigrid solvers in a benchmark problem for the 3D Navier–Stokes equations. *International Journal for Numerical Methods in Fluids*, 40(6):775–798, 2002.

[94] C. Josserand and S. T. Thoroddsen. Drop impact on a solid surface. *Annual Review of Fluid Mechanics*, 48(1):365–391, 2016.

[95] H. P. Kavehpour. Coalescence of drops. *Annual Review of Fluid Mechanics*, 47:245–268, 2015.

[96] K. Königsberger. *Analysis 2*. Number 2, erweiterte Auflage in Springer-Lehrbuch. Springer, 1997.

[97] M. Krafczyk, M. Cerrolaza, M. Schulz, and E. Rank. Analysis of 3d transient blood flow passing through an artificial aortic valve by lattice–boltzmann methods. *Journal of Biomechanics*, 31(5):453 – 462, 1998.

[98] W. M. Lai, D. Rubin, and E. Krempl. *Introduction to Continuum Mechanics (Fourth Edition)*. Butterworth-Heinemann, Boston, fourth edition edition, 2010.

[99] H. Lee, J. S. Lowengrub, and J. Goodman. Modeling pinchoff and reconnection in a hele-shaw cell. I. The models and their calibration. *Physics of Fluids*, 14(2):492–513, 2002.

[100] H. Lee, J. S. Lowengrub, and J. Goodman. Modeling pinchoff and reconnection in a hele-shaw cell. II. Analysis and simulation in the nonlinear regime. *Physics of Fluids*, 14(2):514–545, 2002.

[101] G. R. Lester. Contact angles of liquids at deformable solid surfaces. *Journal of Colloid Science*, 16(4):315 – 326, 1961.

[102] L. Li, W. D. Henshaw, J. W. Banks, D. W. Schwendeman, and A. Main. A stable partitioned FSI algorithm for incompressible flow and deforming beams. *Journal of Computational Physics*, 312:272 – 306, 2016.

[103] L. Limat. Straight contact lines on a soft, incompressible solid. *The European Physical Journal E*, 35(12):134, Dec 2012.

[104] J. Liu, L. Dedè, J. A. Evans, M. J. Borden, and T. J. R. Hughes. Isogeometric analysis of the advective cahn-hilliard equation: Spinodal decomposition under shear flow. *Journal of Computational Physics*, 242:321–350, 2013.

[105] J. Lowengrub and L. Truskinovsky. Quasi–incompressible cahn–hilliard fluids and topological transitions. *Proceedings of the Royal Society of London A: Mathematical, Physical and Engineering Sciences*, 454(1978):2617–2654, 1998.

[106] L. E. Malvern. *Introduction to the Mechanics of a Continuous Medium*. Prentice-Hall series in engineering of the physical sciences. Prentice-Hall, 1969.

[107] A. Marchand, S. Das, J. H. Snoeijer, and B. Andreotti. Contact angles on a soft solid: From young's law to neumann's law. *Phys. Rev. Lett.*, 109:236101, Dec 2012.

[108] J. E. Marsden and T. J. R. Hughes. *Mathematical Foundations of Elasticity*. Dover Civil and Mechanical Engineering Series. Dover, 1994.

[109] M. Mitrea and S. Monniaux. Maximal regularity for the Lamé system in certain classes of non-smooth domains. *Journal of Evolution Equations*, 10:811–833, 11 2010.

[110] M. Münsch and M. Breuer. Numerical simulation of fluid–structure interaction using eddy–resolving schemes. In H.-J. Bungartz, M. Mehl, and M. Schäfer, editors, *Fluid Structure Interaction II*, pages 221–253, Berlin, Heidelberg, 2010. Springer Berlin Heidelberg.

[111] G. Nabh. *On High Order Methods for the Stationary Incompressible Navier-Stokes Equations*. PhD thesis, University of Heidelberg, 1998.

[112] M. Nickaeen, A. Ouazzi, and S. Turek. Newton multigrid least-squares FEM for the V-V-P formulation of the Navier-Stokes equations. *Journal of Computational Physics*, 256:416–427, 2014.

[113] R. W. Ogden. *Non-Linear Elastic Deformations*. Dover Civil and Mechanical Engineering Series. Dover, 1997.

[114] C. Palmes, B. Funke, and B. S. Hosseini. Nonparametric low-frequency lévy copula estimation in a general framework. *Journal of Nonparametric Statistics*, 30(3):523–555, 2018.

[115] R. Pericet-Camara, G. K. Auernhammer, K. Koynov, S. Lorenzoni, R. Raiteri, and E. Bonaccurso. Solid-supported thin elastomer films deformed by microdrops. *Soft Matter*, 5:3611–3617, 2009.

[116] C. S. Peskin. Numerical analysis of blood flow in the heart. *Journal of Computational Physics*, 25(3):220 – 252, 1977.

[117] C. S. Peskin. The immersed boundary method. In Arieh Iserles, editor, *Acta Numerica 2002*, volume 11 of *Acta Numerica*, page 479–518. Cambridge University Press, 2002.

[118] C. S. Peskin and D. M. McQueen. A three-dimensional computational method for blood flow in the heart I. Immersed elastic fibers in a viscous incompressible fluid. *Journal of Computational Physics*, 81(2):372 – 405, 1989.

[119] L. A. Piegl and W. Tiller. *The NURBS book*. Monographs in visual communication. Springer, 1995.

[120] C. Pozrikidis. *Introduction to Theoretical and Computational Fluid Dynamics*. Oxford University Press, 2011.

[121] C. Py, P. Reverdy, L. Doppler, J. Bico, B. Roman, and C. N. Baroud. Capillary origami: Spontaneous wrapping of a droplet with an elastic sheet. *Phys. Rev. Lett.*, 98:156103, Apr 2007.

[122] T. Richter. Goal-oriented error estimation for fluid–structure interaction problems. *Computer Methods in Applied Mechanics and Engineering*, 223:28–42, 2012.

[123] T. Richter. *Fluid-structure Interactions: Models, Analysis and Finite Elements*. Lecture Notes in Computational Science and Engineering. Springer International Publishing, 2017.

[124] T. Richter and T. Wick. Finite elements for fluid–structure interaction in ALE and fully Eulerian coordinates. *Computer Methods in Applied Mechanics and Engineering*, 199(41):2633 – 2642, 2010.

[125] M. E. Rognes, R. C. Kirby, and A. Logg. Efficient Assembly of $H(\mathrm{div})$ and $H(\mathrm{curl})$ Conforming Finite Elements. *SIAM J. Sci. Comput.*, 31:4130–4151, 2009.

[126] B. Roman and J. Bico. Elasto-capillarity: Deforming an elastic structure with a liquid droplet. *Journal of Physics Condensed Matter*, 22(49), 2010.

[127] A. I. Rusanov. On the thermodynamics of deformable solid surfaces. *Journal of Colloid and Interface Science*, 63(2):330 – 345, 1978.

[128] R. Sandboge. Fluid-structure interaction with openfsitm and md nastrantm structural solver. Ann Arbor, 2010. 1001-48105.

[129] M. Schäfer, S. Turek, F. Durst, E. Krause, and R. Rannacher. Benchmark computations of laminar flow around a cylinder, January 1996.

[130] D. Schillinger, J. A. Evans, A. Reali, M. A. Scott, and T. J. R. Hughes. Isogeometric collocation: Cost comparison with galerkin methods and extension to adaptive hierarchical nurbs discretizations. *Computer Methods in Applied Mechanics and Engineering*, 267:170–232, 2013.

[131] L. Schumaker. *Spline Functions: Basic Theory*. Cambridge Mathematical Library. Cambridge University Press, 3rd edition, 2007.

[132] B. Schweizer. *Partielle Differentialgleichungen*. Springer Spektrum, 2013.

[133] G. Scovazzi and T. J. R. Hughes. Lecture Notes on Continuum Mechanics on Arbitrary Moving Domains. Technical Report 2007-6312P, Sandia National Laboratories, November 2007.

[134] P. Seppecher. Moving contact lines in the Cahn-Hilliard theory. *International Journal of Engineering Science*, 34(9):977 – 992, 1996.

[135] J. A. Sethian. *Level Set Methods and Fast Marching Methods: Evolving Interfaces in Computational Geometry, Fluid Mechanics, Computer Vision, and Materials Science*. Cambridge Monographs on Applied and Computational Mathematics. Cambridge University Press, 1999.

[136] J. Shen and X. Yang. A phase-field model and its numerical approximation for two-phase incompressible flows with different densities and viscosities. *SIAM Journal on Scientific Computing*, 32(3):1159–1179, 2010.

[137] E. Shirani, N. Ashgriz, and J. Mostaghimi. Interface pressure calculation based on conservation of momentum for front capturing methods. *Journal of Computational Physics*, 203(1):154–175, 2005.

[138] P. Ŝolín. *Partial Differential Equations and the Finite Element Method*. Pure and Applied Mathematics: A Wiley Series of Texts, Monographs and Tracts. Wiley, 2005.

[139] K. Stein, T. Tezduyar, and R. Benney. Mesh Moving Techniques for Fluid-Structure Interactions With Large Displacements. *Journal of Applied Mechanics*, 70:58, 2003.

[140] R. H. Stogner and G. F. Carey. C^1 macroelements in adaptive finite element methods. *International Journal for Numerical Methods in Engineering*, 70(9):1076–1095, 2007.

[141] R. W. Style, R. Boltyanskiy, Y. Che, J. S. Wettlaufer, L. A. Wilen, and E. R. Dufresne. Universal Deformation of Soft Substrates Near a Contact Line and the Direct Measurement of Solid Surface Stresses. *Physical Review Letters*, 110(6), 2013.

[142] Y. Sun and C. Beckermann. Sharp interface tracking using the phase-field equation. *Journal of Computational Physics*, 220(2):626–653, January 2007.

[143] A. Tagliabue. Isogeometric Analysis for Reduced Fluid-Structure Interaction Models in Haemodynamic Applications. 2012. Thesis developed at EPFL under an Erasmus Placement contract with University of Insubria, Como, Italy.

[144] A. Tagliabue, L. Dedè, and A. Quarteroni. Isogeometric Analysis and Error Estimates for High Order Partial Differential Equations in Fluid Dynamics. *Computers & Fluids*, 102:277–303, 2014.

[145] T. E. Tezduyar, M. Behr, S. Mittal, and A. A. Johnson. Computation of unsteady incompressible flows with the stabilized finite element methods: Space-time formulations, iterative strategies and massively parallel implementations. volume 246, pages 7–24, 1992.

[146] G. Tryggvason. Numerical simulations of the Rayleigh-Taylor instability. *Journal of Computational Physics*, 75(2):253–282, April 1988.

[147] S. Turek. *Efficient Solvers for Incompressible Flow Problems - An Algorithmic and Computational Approach*, volume 6 of *Lecture Notes in Computational Science and Engineering*. Springer, 1999.

[148] S. Turek and J. Hron. Proposal for Numerical Benchmarking of Fluid-Structure Interaction between an Elastic Object and Laminar Incompressible Flow. In H.-J. Bungartz and M. Schäfer, editors, *Fluid–Structure Interaction: Modelling, Simulation, Optimisation (Lecture Notes in Computational Science and Engineering)*, volume 53, pages 371–385. Springer, Berlin, Heidelberg, 2006.

[149] S. Turek, J. Hron, M. Razzaq, H. Wobker, and M. Schäfer. Numerical Benchmarking of Fluid-Structure Interaction: A comparison of different discretization and solution approaches. *Lecture Notes in Computational Science and Engineering*, 73 LNCSE:413–424, 2010.

[150] S. Turek, A. Ouazzi, and J. Hron. On pressure separation algorithms (PSepA) for improving the accuracy of incompressible flow simulations. *International Journal for Numerical Methods in Fluids*, 59(4):387–403, 2009.

[151] E. H. van Brummelen, M. Shokrpour Roudbari, G. Şimşek, and K. G. van der Zee. Binary-fluid–solid interaction based on the Navier–Stokes–Cahn–Hilliard Equations. In S. Frei, B. Holm, T. Richter, T. Wick, and H. Yang, editors, *Fluid-Structure Interaction*, Radon Series on Computational and Applied Mathematics, pages 283–323. Walter de Gruyter GmbH, Germany, 2017.

[152] E. H. van Brummelen, M. Shokrpour Roudbari, and G. J. van Zwieten. Elasto-capillarity Simulations based on the Navier–Stokes–Cahn–Hilliard Equations. In Y. Bazilevs and K. Takizawa, editors, *Advances in Computational Fluid-Structure Interaction and Flow Simulation: New Methods and Challenging Computations*, pages 451–462. Springer International Publishing, Cham, 2016.

[153] J. D. van der Waals. The thermodynamic theory of capillarity under the hypothesis of a continuous variation of density. *Journal of Statistical Physics*, 20(2):200–244, 1979.

[154] D. Vella, M. Adda-Bedia, and E. Cerda. Capillary wrinkling of elastic membranes. *Soft Matter*, 6:5778–5782, 2010.

[155] E. Walhorn, A. Kölke, B. Hübner, and D. Dinkler. Fluid–structure coupling within a monolithic model involving free surface flows. *Computers & Structures*, 83(25):2100 – 2111, 2005.

[156] W. A. Wall. *Fluid-Struktur-Interaktion mit stabilisierten Finiten Elementen*. PhD thesis, Inst. für Baustatik der Universität Stuttgart, 1999.

[157] W. A. Wall and E. Ramm. *Fluid Structure Interaction Based Upon a Stabilized (ALE) Finite Element Method*. Bericht. SFB 404, Geschäftsstelle, 1998.

[158] J. H. Weijs, B. Andreotti, and J. H. Snoeijer. Elasto-capillarity at the nanoscale: on the coupling between elasticity and surface energy in soft solids. *Soft Matter*, 9:8494–8503, 2013.

[159] J. H. Weijs, J. H. Snoeijer, and B. Andreotti. Capillarity of soft amorphous solids: A microscopic model for surface stress. *Phys. Rev. E*, 89:042408, Apr 2014.

[160] T. Wick. *Adaptive Finite Element Simulation of Fluid-Structure Interaction with Application to Heart-Valve Dynamics*. PhD thesis, University of Heidelberg, November 2011.

[161] T. Wick. Fluid-structure interactions using different mesh motion techniques. *Computers & Structures*, 89(13):1456 – 1467, 2011.

[162] T. Wick. Flapping and contact FSI computations with the fluid–solid interface-tracking/interface-capturing technique and mesh adaptivity. *Computational Mechanics*, 53(1):29–43, June 2013.

[163] J. Wloka. *Partial Differential Equations*. Cambridge University Press, Cambridge, 1987.

[164] P. Wriggers. *Nonlinear Finite Element Methods*. Springer, 2008.

[165] P. Yue and J. J. Feng. Wall energy relaxation in the Cahn–Hilliard model for moving contact lines. *Physics of Fluids*, 23(1):012106, 2011.

[166] P. Yue, C. Zhou, and J. J. Feng. Spontaneous shrinkage of drops and mass conservation in phase-field simulations. *Journal of Computational Physics*, 223(1):1 – 9, 2007.